The Formation and Late Quaternary Palaeoenvironmental History of Sediment Mounds in the Amundsen Sea, West Antarctica

JENNIFER ROSE HORROCKS

The Formation and Late Quaternary Palaeoenvironmental History of Sediment Mounds in the Amundsen Sea, West Antarctica

Jennifer Rose Horrocks

Department of Geography

Durham University

British Antarctic Survey

Thesis submitted for the degree of Doctor of Philosophy

September 2017

The Formation and Late Quaternary Palaeoenvironmental History of Sediment Mounds in the Amundsen Sea, West Antarctica

Jennifer Rose Horrocks

Abstract

This thesis presents the first high-resolution palaeoceanographic study of environmental changes in the Amundsen Sea sector of the West Antarctic continental margin during the Late Quaternary. This part of the West Antarctic Ice Sheet (WAIS) is currently experiencing rapid mass loss and longer-term records can provide important context for these changes.

Four piston cores, covering the last *c.* 375 kyrs, have been studied from two of the five large sediment mounds which stand on the continental rise of the eastern Amundsen Sea. Four of the mounds have been previously been identified in the literature as sediment drifts. The cores were analysed for sedimentology (grain size, physical properties, spectrophotometry), mineralogy (clay minerals, sand fraction composition) and geochemistry (XRF, biogenic silica content, TOC, $CaCO_3$). These data were used to infer the supply of terrigenous material from the West Antarctic Ice Sheet, the amount of biological productivity and the nature of the bottom current. Age constraints for the ≤375 kyr records are derived from relative palaeomagnetic intensity, diatom biostratigraphy, AMS ^{14}C dates, tephrochronology and lithostratigraphy.

Analysis of the sediments together with new geophysical and bathymetric data suggests the mounds are mixed contourite-turbidite drifts. Turbidity currents were initiated at the margins of, and between, the mouths of Pine Island Trough East and West and Abbot Trough. The turbidity currents eroded channels in the slope, some of which connect to the deeply incised, maximum 20 km wide and 400 km long channels separating the drifts. The fine-grained fraction of the turbidity currents was pirated and deposited on the drift crests by the weak, eastwards-flowing bottom current, which may be Antarctic Bottom Water or Lower Circumpolar Deep Water. The coarse-grained component of the turbidity currents was largely constrained to the channels, with occasional spill-over depositing sand and sandy muds on the drift flanks. The drifts are long (250-433 km), narrow (38-130 km), stand up to 900 m above the sea floor and are asymmetric, with a

gently-sloping western flank and steeper eastern flank resulting from sediment interaction with the bottom current.

The sediments exhibit strong cyclicity corresponding to glacial-interglacial cycles. During glacial periods, deposition was mostly of grey, terrigenous, typically laminated contourites with dispersed ice rafted debris and locally-sourced kaolinite and illite. Sedimentation rates ranging from 0.1 to 17.2 cm/kyr reflect WAIS advance and retreat across the shelf. Bottom currents captured the fine grained fraction of turbidity currents and deposited laminated sediments, similar to those reported in the drifts west of the Antarctic Peninsula, attributed to a steady bottom current and the absence of bioturbation under perennial sea-ice. Manganese contents suggest suboxic conditions during glacial periods. A laminated sand and sandy mud turbidite deposit is present in a drift flank core.

Olive-brown, bioturbated, diatom-bearing and often calcareous-foraminifera-bearing, mixed contourite and hemi-pelagic muds were deposited in interglacial periods. Sedimentation rates range from 0.2 to ≥3.7 cm/kyr reflecting changes in productivity that were mostly controlled by sea-ice coverage. The smectite content of surface samples from the drifts are larger than any other known sample from the Amundsen Sea shelf or rise and suggest that the bottom current also deposits far-travelled clay.

There are no major depositional anomalies or thick IRD layers in the drift cores that might indicate collapse of the WAIS. However, millennial-scale cyclical variations in the provenance of terrigenous material in PS58/255-2 during mid-late MIS 6 may reflect changes in ice dynamics.

Table of Contents

Chapter Three

Chapter Four

Chapter Five

Chapter Seven

List of Tables

Chapter Two

Chapter Three

Chapter Four

Chapter Five

Chapter Six

Chapter Seven

List of Figures

Chapter One

Chapter Two

Chapter Three

Chapter Four

Chapter Five

Chapter Six

Chapter Seven

List of Equations

Chapter Four

List of Abbreviations

AABW	Antarctic Bottom Water
ACC	Antarctic Circumpolar Current
ASE	Amundsen Sea Embayment
ASS	Amundsen Sea Sector
ASW	Antarctic Surface Water
AWI	Alfred Wegener Institute, Helmholtz Centre for Polar and Marine Research
ARM	Anhysteretic remanent magnetisation
BAS	British Antarctic Survey
BC (prefix)	Box core
CDW	Circumpolar Deep Water
cmbsf	Centimetres below sea floor
CTD	Conductivity-Temperature-Depth
DBD	Dry bulk density
EAS	Eastern Amundsen Sea
EAIS	East Antarctic Ice Sheet
EPICA	European Project for Ice Coring in Antarctica
HSSW	High Salinity Shelf Water
IBCSO	International Bathymetric Chart of the Southern Ocean
IRD	Iceberg-rafted debris
ka	Thousand years before present
kyr	Thousand years
LCDW	Lower Circumpolar Deep Water
LGM	Last Glacial Maximum
LSSW	Low Salinity Shelf Water
MAR	Mass accumulation rate

mbsf	Metres below sea floor
MIS	Marine Isotope Stage
MS	Magnetic susceptibility
MSCL	Multi-sensor core logger
NRM	Natural remanent magnetisation
PC (prefix)	Piston core
PPM	Parts per million
PS (prefix)	RV Polarstern
RPI	Relative Palaeomagnetic Intensity
RPM	Rotations per minute
RSBW	Ross Sea Bottom Water
sACC	Southern boundary of the ACC
sACCf	Southern ACC front
SST	Sea surface temperature
TC	Total Carbon
TIC	Total Inorganic Carbon
TOC	Total Organic Carbon
UCDW	Upper Circumpolar Deep Water
VADM	Virtual Axial Dipole Moment
VIS	Visible
WAIS	West Antarctic Ice Sheet
WBD	Wet bulk density
XRF	X-ray Fluorescence

Declaration

I confirm that no part of the material presented in this thesis has previously been submitted for a degree in this or any other university. In all cases the work of others, where relevant, has been fully acknowledged.

A summary of the contributions from collaborators in this research is as follows:

Claus-Dieter Hillenbrand provided multi-sensor core logger data (wet bulk density and magnetic susceptibility) for PC494 and PC496. Gerhard Kuhn provided multi-sensor core logger data (wet bulk density and magnetic susceptibility), F sensor, dry bulk density, porosity, VIS-reflectance, Total Organic Carbon and Total Inorganic Carbon data for PS58/253-1 and PS58/255-2. Core logs for PS58/253-1 and PS58/255-2 were provided by Claus-Dieter Hillenbrand.

Amanda Hayton conducted the organic elemental analysis on PC494 and PC496 which provided total carbon and total inorganic carbon data. Werner Ehrmann conducted clay mineralogical analysis on all samples from the four cores, and also provided unpublished data from surface samples used in the discussion in Chapter 7.3.1.

Oliver Esper (PS58/253-1 and PS58/255-2) and Claire Allen (PC496) identified diatom species used for biostratigraphic constraints (outlined in Chapter 6.2.1.2). Andreas Mackenson conducted oxygen isotopic analysis on PS58/253-1, although the results were not suitable for chronological purposes.

Chuang Xuan provided tuition in taking u-channels from PC494, operating a magnetometer and assessing the suitability of relative palaeomagnetic intensity proxies for developing a chronology.

3.5 kHz TOPAS sub-bottom profiler data presented here were collected during cruise JR179 of the RRS James Clark Ross in February-April 2008 and provided by Kelly Hogan. All multi-beam swath bathymetry data displayed in this thesis have been obtained from the International Bathymetric Chart of the Southern Ocean (IBSCO) in Arndt et al., 2013. Many comparisons have been drawn between the four cores presented here and the analysis of sediment core PS58/254-1 by Hillenbrand et al. (2009a).

Statement of Copyright

Signed:

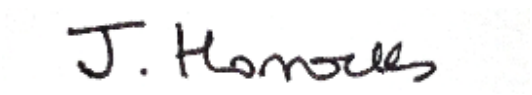

Jennifer Rose Horrocks

Durham University

September 2017

Acknowledgements

Firstly, my sincere, grateful thanks go to my supervisors, Colm Ó Cofaigh, Jerry Lloyd and Claus-Dieter Hillenbrand for their support, guidance, expert knowledge and patience during the last four years. A special thanks must go to Claus-Dieter for his technical expertise and for helping to establish partnerships with many of the collaborators whose data and guidance greatly enhanced this research.

This research was made possible through a Durham Doctoral Scholarship and my grateful thanks go to Durham University. A generous grant from the Trans-Antarctic Association allowed me to spend a month at the Alfred Wegener Institute, Helmholtz Centre for Polar and Marine Research, during which time I was able to sample and XRF scan PS58/253-1 and PS58/255-2 and to measure the biogenic silica content of the samples from all four cores. A place on the NERC-funded training course 'Advanced techniques in sediment core analysis and core data visualisation' included instruction in the operation of a multi-sensor core logger and XRF machine and the analysis and interpretation of the data, which enhanced my understanding of these techniques and the interpretations put forward in this thesis.

I am hugely grateful to the Collaborative Gearing Scheme and my supervisors for giving me the opportunity to work aboard the James Clark Ross in the Bellingshausen Sea and understand so much more about the process of collecting, processing and logging cores. I would also like to thank NERC and the British Antarctic Survey for my place on the 'Safe and effective fieldwork in the polar regions' Advanced Training Course, which gave me the rare opportunity to spend time in the Arctic and develop a greater appreciation for the many aspects of the polar environment which contribute to marine sedimentation.

I am grateful to the captain, scientists and crew of cruises JR179 and ANT-XVIII/5a for the collection of the marine sediment cores and sub-bottom profiler data (JR179) used in this research.

This research has benefitted greatly from discussions with, and data provided by, Rob Larter, James Smith, Claire Allen, Kelly Hogan (British Antarctic Survey), Oliver Esper, Gerhard Kuhn, Andreas Mackenson (Alfred Wegener Institute, Helmholtz Centre for Polar and Marine Research), Werner Ehrmann (University of Leipzig), Chuang Xuan (National Oceanography Centre and University of Southampton), Frank Nitsche

(Lamont-Doherty Earth Observatory) and Javier Hernandez-Molina (Royal Holloway, University of London). Particular thanks go to Gerhard Kuhn for providing access to PS58/253-1 and PS58/255-2 for sampling and XRF scanning, providing existing data from the two cores and their associated trigger cores and multi-cores, and for his hospitality and time during a four week visit to the Alfred Wegener Institute. Chuang Xuan has been very generous with his time and support, providing access to the palaeomagnetic laboratory at the National Oceanography Centre, training in the use of the magnetometer and assistance with analysing and interpreting the data.

The advice and assistance of laboratory and technical staff at many institutions has been instrumental in producing the data presented in this thesis. My grateful thanks go to Nick Farley (British Antarctic Survey), Susanne Weibe and Rita Froehlking (AWI), Alison George, Amanda Hayton, Katherine Melvin, Chris Longley, Jean Swales, Neil Tunstall and Frank Davies (Department of Geography, Durham University), Ian Tan (National Oceanography Centre), Suzie MacLachlan and Mike Edwards (British Ocean Sediment Core Research Facility).

I would like to thank all those in the Department of Geography at Durham University for being such a friendly, supportive community, particularly those in the Ice Sheets and Sea Level cluster. Thank you to my friends in the office and the GIS room for sharing the highs and the lows together, especially Rosie, Hannah, Jack, Jess, Bertie, Charlotte, Marisa, Richard, Sophie and Siobhan.

A primary school friend recalls me saying at 8 years old that one day I would work at the British Antarctic Survey; thank you to everyone there for making me feel so welcome during my busy visits, especially Tom, Kathy and Ashleigh.

I owe a huge debt of gratitude to my family, particularly my late Gran and Grandma, without whom “The Three Degrees” would not have been possible.

The support and guidance of my partner, Dave, has been incredible over the past four years. Your love, patience and encouragement have been unwavering.

This thesis is dedicated to my parents, Shirley and Steve, for their incredible sacrifices, hard work and commitment to giving me the best possible education.

Chapter 1: Introduction

1.1. Context and rationale

The past twenty years have seen a large increase in the scientific interest in the Amundsen Sea, West Antarctica, and the one-third of the West Antarctic Ice Sheet (WAIS) which drains into it, as an area apparently vulnerable to climatic change. During at least the last four decades, the largely marine-based glaciers draining into the Amundsen Sea (hereafter referred to as the Amundsen Sea Sector (ASS)) have undergone acceleration, rapid thinning and grounding line retreat at an ever increasing rate, particularly since the early 1990s (e.g. Rignot et al., 2002, 2008; Shepherd et al., 2002; Joughin et al., 2003, 2010; MacGregor et al., 2012; Sutterley et al., 2014). Annual mass loss of the glaciers draining into the Amundsen Sea increased by 77% in the period 1973 to 2013 (Mouginot et al., 2014). This has been linked to the upwelling of relatively warm Circumpolar Deep Water (CDW) onto the shelf, driven by westerly winds, which is able to reach the inner shelf and undersides of ice shelves via deep palaeo-ice stream troughs crossing the Amundsen Sea shelf (Thoma et al., 2008; Wåhlin et al., 2010; Steig et al., 2012). This has increased sub-ice shelf melt and reduced the buttressing effect of ice shelves on glacier flow (Rignot and Jacobs, 2002; Joughin et al., 2010).

It is likely that any large scale disintegration of the WAIS will be initiated in the ASS, as instability there is likely to shift ice divides and cause rapid mass loss elsewhere in the WAIS, with potential for ca. 3.3 m of sea level rise (Feldmann & Levermann, 2015). The rapid mass loss of Pine Island Glacier in particular has been a focus of attention for decades (e.g. Rignot et al., 2002; Smith et al., 2017). Indeed, unstoppable grounding line retreat of Thwaites Glacier, which together with Pine Island Glacier drains into Pine Island Bay in the easternmost Amundsen Sea, may have already begun (Joughin et al., 2014). In the light of the modern changes, the nickname “weak underbelly of the WAIS”, which was given to Pine Island Bay decades ago (Hughes, 1981), seems to be appropriate.

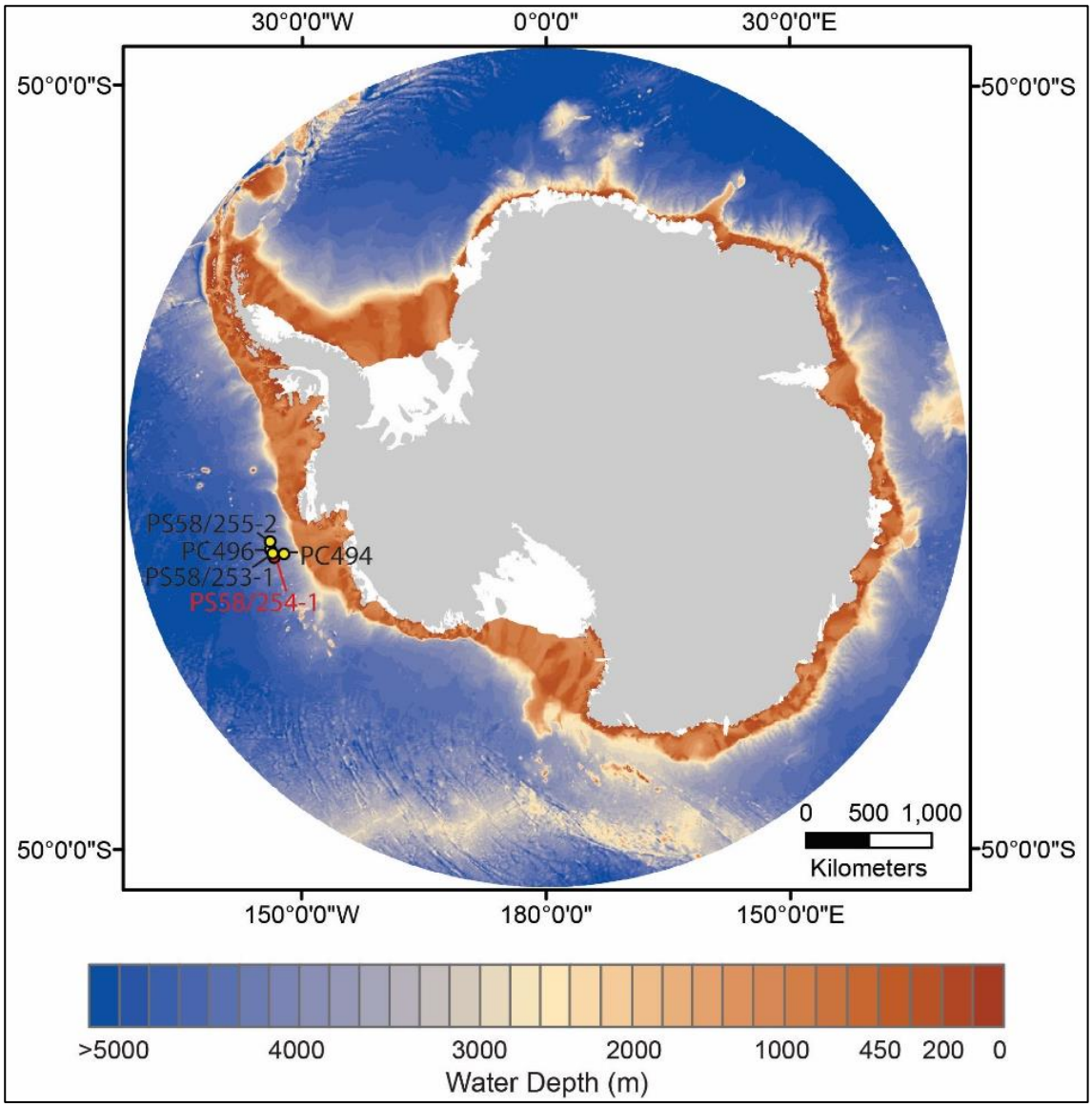

Figure 1.1: Map of Antarctica with core sites indicated (yellow circles indicate cores presented in this thesis, the red circle indicates site PS58/254-1 (Hillenbrand et al., 2009a)). Bathymetry taken from International Bathymetric Chart of the Southern Ocean (IBCSO) (Arndt et al., 2013). Grey areas mark the extent of grounded ice, white areas indicate ice shelves (according to BEDMAP2, Fretwell et al., 2013).

It is crucial to put the modern observations into a longer term context. Long-term reconstructions of environmental change in the region offer a new perspective on the modern-day changes, improve model inputs and allow for improved predictions of future change. However, there are currently very little data from either onshore or offshore areas of the ASS to reconstruct past environmental conditions prior to the Last

Glacial Maximum (LGM), 23-19 ka (Larter et al., 2014; Smith et al. 2014). Marine sediment cores taken from the continental rise offer the potential for high resolution, continuous or nearly continuous records of environmental change over multiple glacial-interglacial cycles, without erosion from glacial-overriding or highly variable sedimentation rates that are common at ice-proximal shelf sites. Marine sediment cores also offer the unique potential to reconstruct a wide range of environmental conditions. For example, there is the potential to make inferences about coincident changes in the behaviour of the ice sheet (e.g. by observing the amount and provenance of IRD), the nature of the bottom current (e.g. by using sortable silt as a proxy for bottom current speed) and the degree of marine productivity (e.g. by quantifying the biogenic silica content), which, in the eastern Amundsen Sea, is closely linked to sea ice coverage (Hillenbrand et al., 2009a).

In particular, the location of the eastern Amundsen Sea continental rise, offshore of an area of the WAIS currently deemed vulnerable, means that marine sediment cores taken from the area have a high potential of recording any past major disintegrations or collapses of the WAIS. Models suggest WAIS collapse would result in a large discharge of icebergs into the Southern Ocean (Bentley, 1998). The direction of surface currents means icebergs drifting over the core sites should capture any large influx of ice rafted debris from Marie Byrd Land. Possible evidence for a WAIS collapse in the past million years is widely debated (e.g. MacAyeal, 1992; Scherer et al., 1998). However, Hillenbrand et al. (2002) suggested appropriate criteria for the observation of WAIS disintegration in marine sediment cores in this region are the amount of lithogenic material and the gravel content (to identify changes in the input of glaciogenic material) and variations in the $CaCO_3$ content, reflecting productivity changes associated with a more stratified ocean.

Differentiation in key proxies from the typical glacial-interglacial characteristics can also be suggestive of ice sheet instabilities. Hillenbrand et al. (2009a) identified a depositional anomaly in PS58/254-1 during MIS 15-13 and suggested that the proxies for biological productivity and terrigenous sediment supply were characteristic of a prolonged interglacial period with no glacial signal. No direct evidence was found to suggest a collapse. However, based on the evidence put forward by other authors for a Late Quaternary WAIS collapse, Hillenbrand et al. (2009a) suggested this was the most

likely time frame, had a collapse occurred in the last 800 kyr. Therefore, although such cores cannot be used to definitively show or exclude a WAIS collapse, they can provide useful information to put other work into context and provide further information on palaeoenvironmental conditions.

Despite this, only one marine sediment core from the eastern Amundsen Sea continental rise, PS58/254-1, has been used for a comprehensive pre-LGM palaeoenvironmental reconstruction (Hillenbrand et al., 2009a; Konfirst et al., 2012).

Mechanisms of Mound Formation

Core PS58/254-1 was taken from the second westernmost of a series of large sediment mounds which sit at the base of the continental slope between 120°W and 100°W, aligned roughly perpendicular to the shelf break. The mounds have been interpreted, based on this core and a suite of geophysical data (multi-channel seismic, 3.5 kHz, single and multi-beam swath bathymetry), to be mixed sediment drifts deposited by eastward-flowing contour currents carrying pirated, fine-grained, terrigenous material from turbidity currents, and bounded by channels with coarse-grained beds (Nitsche et al., 2000; Hillenbrand et al., 2009a; Uenzelmann-Neben and Gohl, 2012, 2014).

Mixed contourite-turbidite drifts form when the fine grained component of turbidity currents becomes entrained in the nepheloid layer and is deposited by the action of bottom currents that flow parallel to bathymetric contours (Rebesco et al., 2008). Recent work has suggested drift formation in this area may have begun 43 Ma (Lindeque et al., 2016). However, small-scale depositional features, such as thin coarse-grained layers deposited from individual turbidity currents, cannot be resolved from seismic data (Shanmugam, 2002) and more sediment cores are needed to test whether the mounds are contourite drifts or could be other mounded deposits, such as large turbidite levee deposits which have been identified elsewhere in the eastern and central Amundsen Sea (Uenzelmann-Neben and Gohl, 2012).

Palaeo-environmental Reconstructions

The Amundsen Sea mounds resemble, at least superficially, twelve contourite drifts located on the continental rise west of the Antarctic Peninsula. These drifts have been the focus of seismic studies (e.g. Rebesco et al., 1996, 1997, 2002). Both conventional sediment cores (e.g. Pudsey & Camerlenghi, 1998; Pudsey, 2000; Ó Cofaigh et al., 2001; Lucchi et al., 2002; Hillenbrand et al., 2008a) and drill cores from the drifts have been used to reconstruct environmental changes since 9.4 Ma (e.g. Barker et al., 2002; Hillenbrand and Ehrmann, 2005). Core PS58/254-1 showed that records from the Amundsen Sea mounds can also provide valuable palaeo-environmental information about the WAIS and oceanographic conditions through multiple glacial-interglacial cycles (Hillenbrand et al., 2009a; Konfirst et al. 2012). The 1200 kyr record of PS58/254-1 showed a near-continuous record of predominantly fine-grained terrigenous detritus initially eroded and supplied by the WAIS and biogenic material (mainly diatoms), which were, for example, used to suggest a possible WAIS collapse during Marine Isotope Stage (MIS) 15-13 (621-478 ka) (Hillenbrand et al., 2009a). However, the low temporal resolution of this record, which was recovered from a drift flank, restricted its use as a recorder of environmental changes on timescales shorter than a glacial or interglacial period. Further records of higher temporal resolution would allow for the detailed long term palaeo-environmental reconstruction that is otherwise lacking in the Amundsen Sea and would provide a crucial long-term perspective on the modern changes.

Scope of Research

This thesis presents high temporal resolution records of palaeo-environmental changes in the Amundsen Sea since MIS 10 (374-337 ka), reflecting changes in the size of the WAIS, bottom current strength and marine productivity, each closely connected to climatic changes. This is achieved through analysing the sedimentology, geochemistry and mineralogy of four piston cores recovered from two of the four previously identified sediment mounds on the Amundsen Sea continental rise. The sediment core data will be used in conjunction with previously published bathymetric and seismic data and new acoustic sub-bottom profiler data to decipher the processes involved in mound formation.

1.2. Research aims and objectives

The two over-arching aims of this thesis are to reconstruct the Late Quaternary depositional environments recorded in the sediments from the Amundsen Sea continental rise and to draw conclusions about the mechanisms responsible for the formation of the sediment mounds. These aims will be achieved through addressing the following five objectives:

1. To date four piston cores recovered from the Amundsen Sea sediment mounds and analyse them by a multi-proxy approach, which includes sedimentological, geochemical, mineralogical and micro-palaeontological investigations.

2. To use the core data in conjunction with acoustic sub-bottom profiles and published multi-beam swath bathymetry and multi-channel seismic data to examine the sediment composition and structure of the Amundsen Sea mounds. This information will be used to interpret the sedimentological processes and mechanisms involved in the formation and development of these features.

3. To compare the sediment mounds in the Amundsen Sea to the comparatively well studied sediment mounds west of the Antarctic Peninsula, which have been interpreted as contourite drifts.

4. To assess the evidence in the cores for past changes of the West Antarctic Ice Sheet (such as advance, retreat and collapse).

5. To reconstruct the Late Quaternary palaeo-environmental history of the Amundsen Sea based on the sediment core data.

1.3. Thesis structure

Chapter Two outlines the contemporary characteristics of the study area and the environmental factors which may affect deposition at the core sites, particularly the behaviour of the WAIS in the ASS, the local bathymetry, the oceanographic regime in the Amundsen Sea and the nature of, and controls on, biological productivity.

Chapter Three describes the depositional processes and resulting sediments which are commonplace on the Antarctic continental margin. This includes outlining the previous work conducted on both the mounds in the Amundsen Sea and the well-studied contourite drifts west of the Antarctic Peninsula.

Chapter Four describes the multi-proxy analyses carried out on the sediment cores from the Amundsen Sea mounds and the methods applied to bathymetric data in order to address the research aims.

Chapter Five presents new sub-bottom profiler data from the Amundsen Sea continental rise (Chapter 5.1) and uses the data, in conjunction with previously published multi-beam swath bathymetry and multi-channel seismic data, to interpret how the Amundsen Sea mounds may have formed (Chapter 5.2).

The first section of **Chapter Six** presents the results of the sedimentological, mineralogical and geochemical analyses, conducted on the cores. The second section of Chapter Six presents the results of dating techniques and the core chronologies. The third section of Chapter Six is an interpretation of the depositional processes and the environmental conditions under which different sediment units were deposited.

Chapter Seven discusses the implications of the interpretations made in the context of mound formation and palaeo-environmental history. The first part discusses how the Amundsen Sea mounds formed, presents a depositional model and compares the mounds to similar features found around Antarctica, particularly the contourite drifts west of the Antarctic Peninsula. The second part of this chapter discusses the implications of the new findings for the dynamical history of the WAIS and provides a reconstruction of the palaeo-environmental history of the Amundsen Sea since MIS 10.

Chapter Eight concludes the thesis by summarising the main findings and implications and by making recommendations for future areas of research.

Chapter 2: The Study Area

2.1. Introduction

This chapter outlines the bathymetry, glaciology, geology, atmospheric circulation and dust deposition, oceanography and marine productivity of the study area. This is to establish the present day environmental conditions at the core sites to aid in reconstructing past environments. Further information regarding the nature and styles of deposition on the West Antarctic continental margin is provided in Chapter 3.

2.2. Setting

The West Antarctic Ice Sheet (WAIS) encompasses three main drainage sectors: The Weddell Sea Sector, which drains north-eastwards via the Ronne Ice Shelf into the Weddell Sea; the Amundsen-Bellingshausen Sea Sector, which drains northwards via small ice shelves into the Amundsen and Bellingshausen Seas; and the Ross Sea Sector, which drains largely westwards via the Ross Ice Shelf into the Ross Sea (Bindschadler, 2006) (Figure 2.1).

The Amundsen Sea is part of the Pacific sector of the Southern Ocean and is here taken as the ocean between 100° and 135°W, south of 60°S, where the continental shelf break is located at c.71°S (Nitsche et al., 2007). The Amundsen Sea Sector refers to the sector of the WAIS which drains into the Amundsen Sea, mostly through the glaciers which drain into the Amundsen Sea Embayment (ASE; Figure 2.2), defined as the continental shelf between 100° and 120°W.

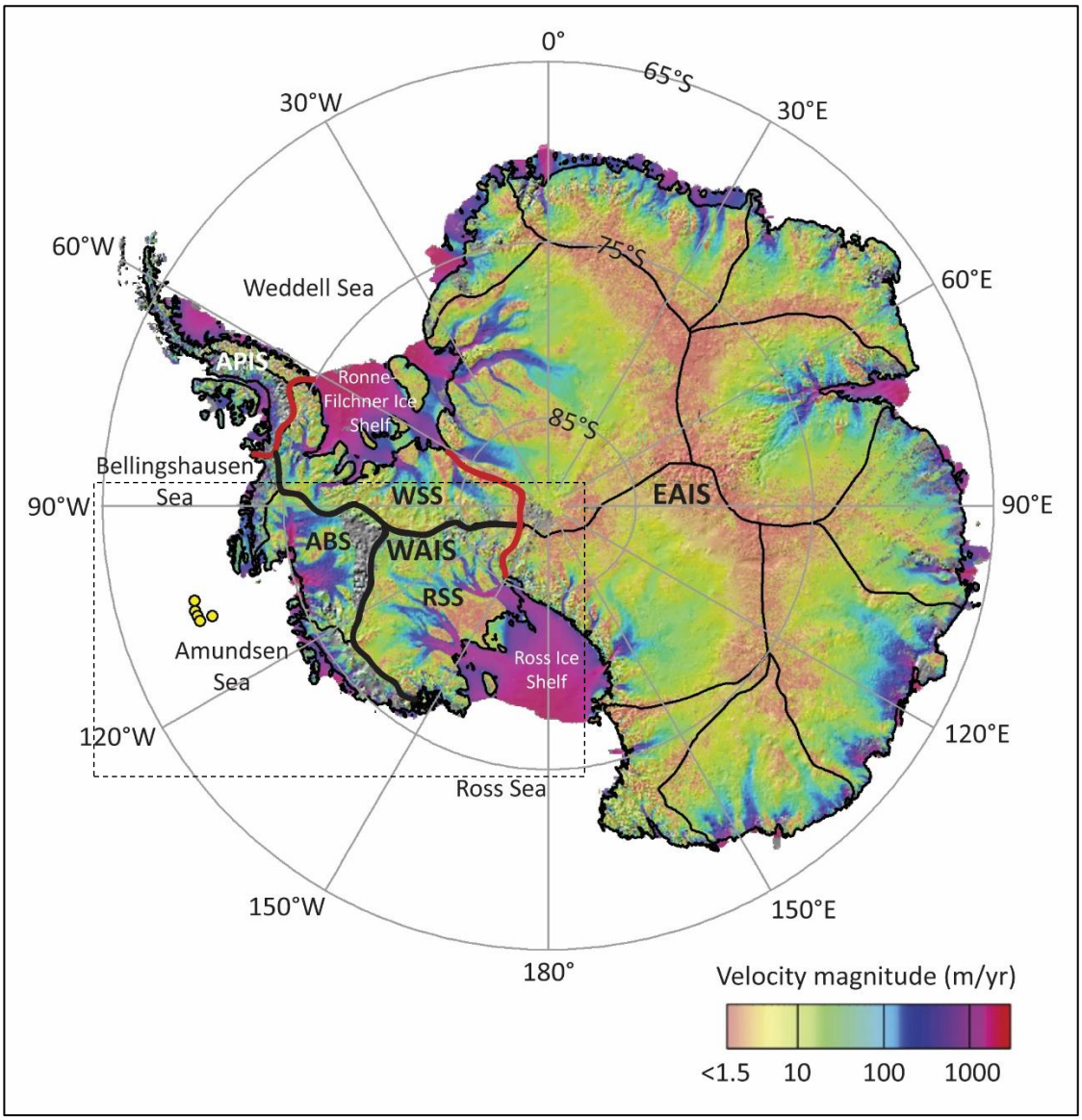

Figure 2.1: Ice flow velocity map of Antarctica (Rignot et al., 2011) with ice divides (Zwally et al., 2012) shown as black and red lines. Thick black lines also indicate the ice divides demarcating the boundaries of the Amundsen-Bellingshausen sector (ABS), Ross Sea sector (RSS) and Weddell Sea sector (WSS). Thick red lines indicate the ice divides demarcating the boundaries of the East Antarctic Ice Sheet (EAIS), West Antarctic Ice Sheet (WAIS) and Antarctic Peninsula Ice Sheet (APIS). Yellow circles indicate the positions of the four marine sediment cores investigated in this research, together with the location of core PS58/254-1 (Hillenbrand et al., 2009a). The position of Figure 2.2 is shown by the black dashed rectangle.

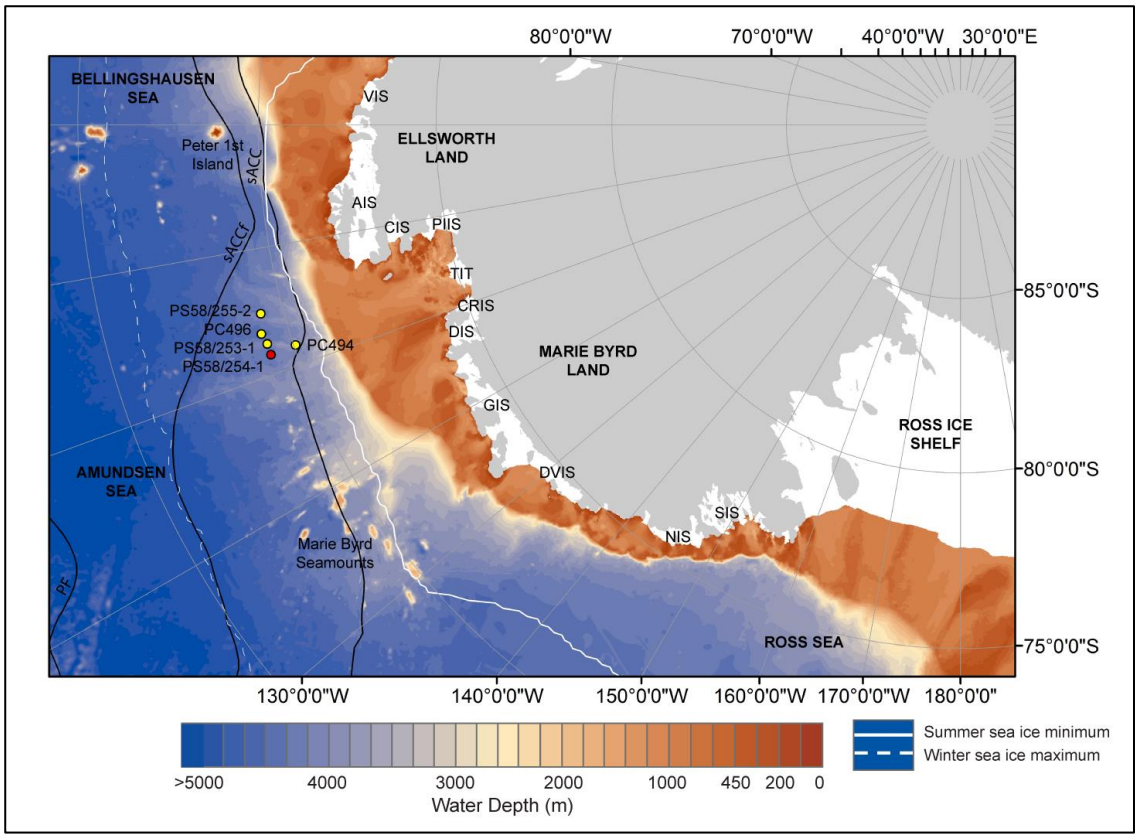

Figure 2.2: Bathymetric map of the western Bellingshausen, Amundsen and eastern Ross Seas. Major ice shelves are indicated and abbreviated as follows (from E to W): VIS Venable Ice Shelf, AIS Abbot Ice Shelf, CIS Cosgrove Ice Shelf, PIIS Pine Island Ice Shelf, TIT Thwaites Ice Tongue, CRIS Crosson Ice Shelf, DIS Dotson Ice Shelf, GIS Getz Ice Shelf, DVIS De Vicq Ice Shelf, NIS Nickerson Ice Shelf, SIS Sulzberger Ice Shelf. Yellow dots mark the positions of cores presented in this thesis. The red dot marks the position of core PS58/254-1. sACC, sACCf and PF mark the position of the Southern Boundary of the clockwise-flowing Antarctic Circumpolar Current (ACC), the Southern ACC Front and the Polar Front, respectively (Orsi et al., 1995). The grounded ice sheet is shown in grey and ice shelves in white. Bathymetric data from IBCSO (Arndt et al., 2013). Sea ice limits from NSIDC (2016).

2.3. Bathymetry

2.3.1. Bathymetry of the Amundsen Sea continental shelf

The continental shelf of the Amundsen Sea is up to 500 km wide (Noormets et al., 2009) and deepens landwards; repeated glacial erosion of the inner shelf has resulted in a shelf >1500 m deep in Pine Island Bay and in front of the Getz Ice Shelf and 400-500 m deep at the shelf break (Lowe and Anderson, 2002).

Large cross-shelf bathymetric troughs extend from the major glaciers and ice shelves (Figure 2.4). Streamlined subglacial bedforms, including mega-scale glacial lineations, observed along the floors of these troughs indicate they contained former ice streams (see Chapter 3.3.1.) (Nitsche et al., 2007). From East to West, the troughs in the ASE are:

- Abbot Trough, which was likely eroded by palaeo-ice streams emanating from the modern Cosgrove and Abbot ice shelves and which crosses the shelf break at 102-103°W at a water depth of 625 m (Hochmuth & Gohl, 2013; Klages et al., 2015).
- Pine Island Trough, which formed predominantly from ice flowing from Pine Island and Thwaites glaciers. This trough splits on the mid-shelf into Pine Island Trough East (PITE) which crosses the shelf break at 106°W in 550 m water depth and Pine Island Trough West (PITW) which crosses the shelf break at 114°W in 600 m water depth (Evans et al., 2006; Noormets et al., 2009; Graham et al., 2010).
- Dotson-Getz Trough comprises 3 separate troughs on the inner shelf, formed by palaeo-ice streams emanating from the modern Dotson Ice Shelf and the eastern parts of the Getz Ice Shelf (A and B). The three tributary troughs merge to form one larger trough on the mid and outer shelf. This trough crosses the shelf break at 118-119°W (Graham et al., 2009; Larter et al., 2009; Noormets et al., 2009).

2.3.2. Bathymetry of the Amundsen Sea continental slope

The continental slope of the Amundsen Sea in front of the palaeo-ice stream troughs typically contains slide scars, slumps, parallel ridges and mass flow deposits indicative of debris flows and mass wasting (Nitsche et al., 2000; Dowdeswell et al. 2006; Noormets et al., 2009; Gales et al. 2013). Mass wasting was apparently common during glacial periods, when glaciers at or close to the shelf break delivered large volumes of glacigenic sediment onto the upper slope and resulted in repeated progradation of sediment wedges, causing gravity-driven downslope sediment failure and turbidity currents (Nitsche et al., 2000; Noormets et al., 2009) (see Chapter 3.2.1.).

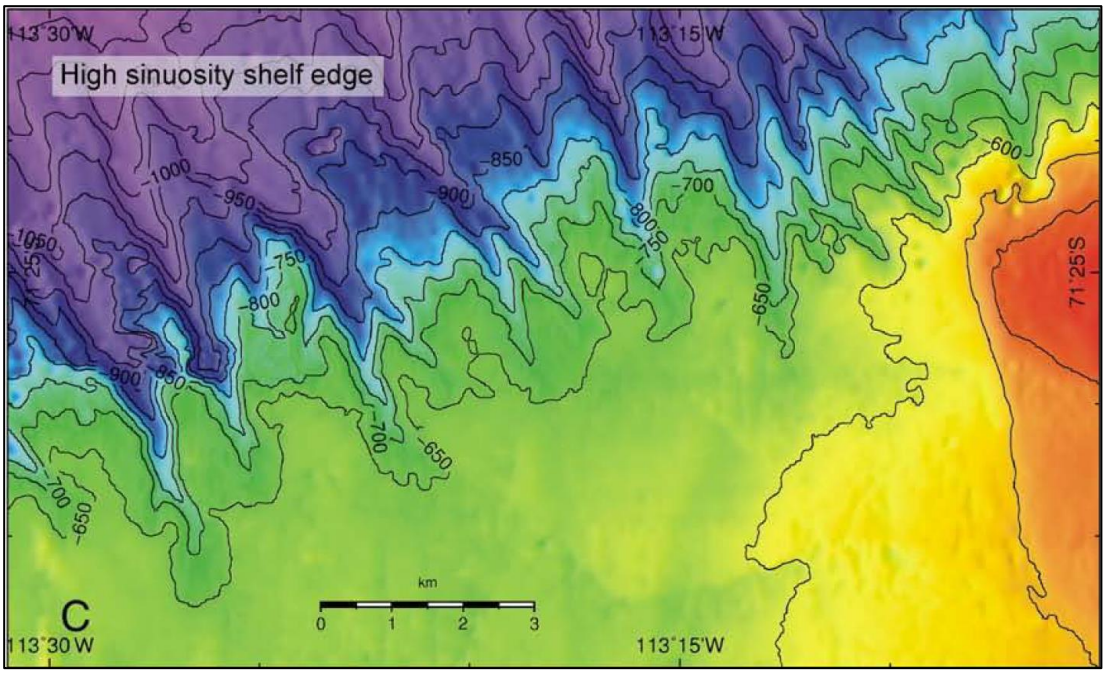

Figure 2.3: Bathymetric map of the shelf edge of PITW from Noormets et al. (2009), showing gullies cutting into the highly sinuous shelf edge (location shown in Figure 2.4).

The continental slope of the Amundsen Sea is steepest directly offshore of the shelf break and the upper slope is marked by a series of V-shaped, symmetrical gullies (Noormets et al., 2009; Figure 2.3.). The mean size of gullies in front of the PITW is 630 m wide, 50 m deep and 5-10 km long, with some gullies incising the shelf edge, creating a highly sinuous shelf edge, and some feeding into the larger channels seen on the mid and lower slope (Dowdeswell et al., 2006; Noormets et al., 2009). The gullies increase in both size and number towards the edge of the trough mouths, and, in the PITW, gullies are particularly large (but fewer in number) offshore from the eastern trough mouth

compared to further west (Noormets et al., 2009; Gales et al., 2013). The gullies are likely to have formed during initial deglaciation by meltwater-driven turbidity flows, but bottom waters produced from the melting of a glacier on the mid to inner shelf may also have contributed (Noormets et al., 2009; Gales et al., 2013).

2.3.3. Bathymetry of the Amundsen Sea Continental Rise

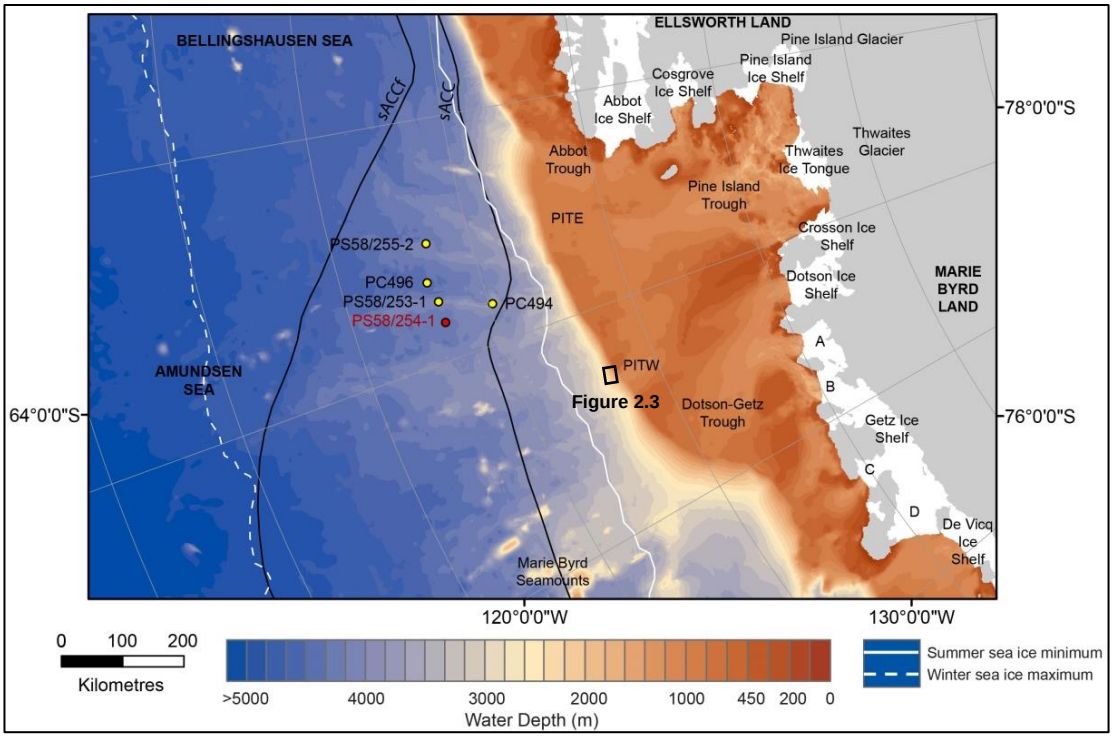

Figure 2.4: Bathymetric map of the central and eastern Amundsen Sea (for acronyms, symbols and references, see Fig. 2.2.). Major glaciers, ice shelves and bathymetric troughs are indicated. PITE indicates Pine Island Trough East, PITW indicates Pine Island Trough West. The location of Figure 2.3 is indicated by a black box.

Numerous sediment mounds have been identified on the continental rise of the Amundsen Sea using swath bathymetry and seismic profiles and identified as either contourite drifts or channel-levee/turbidite deposits (see Chapters 3.4.2 and 3.4.3) (Nitsche et al., 2000; Scheuer et al., 2006a; Uenzelmann-Neben and Gohl, 2012, 2014). Seismic profiles show some of the gullies and channels of the continental slope connect to channels on the continental rise, often merging to form larger channels and running alongside (predominantly the eastern side of) the four sediment mounds in the eastern

Amundsen Sea (Nitsche et al., 2000; Dowdeswell et al., 2006; Noormets et al., 2009). The central Amundsen Sea is also characterised by the Marie Byrd Seamounts (see Chapter 2.5).

2.4. Glaciology

2.4.1. Glaciology of the Amundsen Sea Sector

The sector of the WAIS which drains into the Amundsen and Bellingshausen Seas comprises a quarter of the WAIS by area (c.700,000 km²) but accounts for a third of its accumulation and discharge (Larter et al., 2014). Over 60% of this sector (by area) is drained by ice emanating from the Pine Island and Thwaites drainage basins (Larter et al., 2014), which contain 1.25 m sea level-equivalent of ice (Rignot et al., 2002).

20% of the WAIS by volume drains via the ASE, where 74% of the current mass loss of ice shelves occurs in response to their ocean-driven basal melting caused by the upwelling of relatively warm Circumpolar Deep Water (CDW) onto the shelf. In contrast, the ratio of ice-shelf loss by calving and basal melting, respectively, is roughly 50:50 for Antarctica as a whole (Depoorter et al., 2013; Rignot et al., 2013). The amount of ice-shelf mass loss through basal melting rather than through iceberg rafting may have important implications for sediment delivery to the continental rise. On average 1 m³ of Antarctic glacial ice contains 1 kg of sediment, 90% of which is generally deposited on the shelf in close vicinity to the source glacier (Raiswell et al., 2006), but this figure may be higher in the Amundsen Sea due to the high basal melt rates (e.g. Jacobs et al., 2011, 2013). Recent work found the present-day retreat of Pine Island Glacier began in the 1940s (Smith et al., 2017) and coincided with a strengthening in CDW upwelling (Hillenbrand et al., 2017), but that similar CDW incursions also occurred in the early Holocene for at least 2900 years, leading to enhanced melting of the glaciers in the eastern Amundsen Sea (Hillenbrand et al., 2017). The general lack of pre-LGM shelf records means it remains unknown whether similar CDW incursions have occurred prior to the Holocene, and therefore how the proportion of basal melt to ice rafting in the Amundsen Sea has changed during the Late Quaternary.

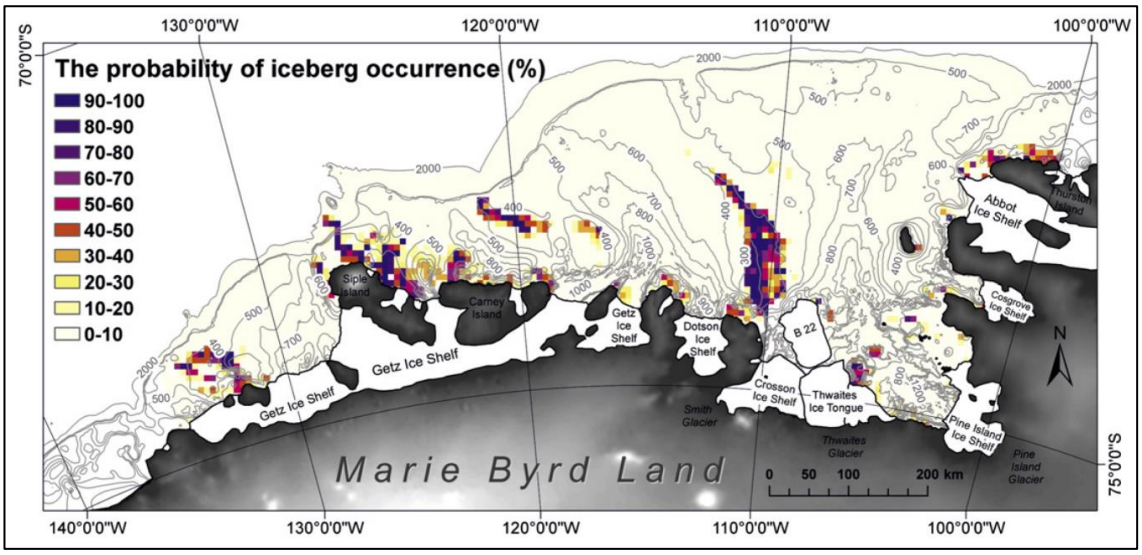

Figure 2.5: Probability of iceberg occurrence in the Amundsen Sea based on automatic iceberg detection from Advanced Synthetic Aperture Radar imagery (from Mazur et al., 2017).

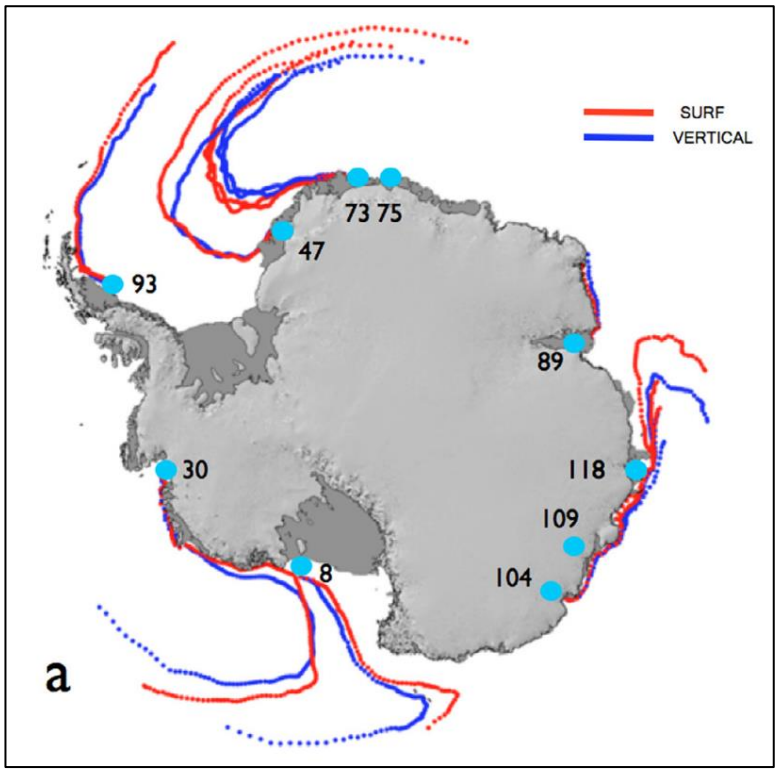

Figure 2.6: Modelled trajectories of medium-sized (73 m thick) icebergs from the source points indicated by blue circles. Red dotted trajectories are modelled based on drag at the ocean surface only. Blue dotted trajectories are modelled based on vertical integrated ocean drag. From Merino et al. (2016).

Icebergs calving from the small ice shelves in the ASE are today entrained within the westerly flowing, fast moving (40 cm/s^{-1} at 70 m water depth) Antarctic Coastal Current (Kim et al., 2016). Icebergs which drift north of the shelf break will then become entrained in the ACC, moving east towards the Bellingshausen Sea. Figure 2.5 highlights the westerly movement of icebergs but also shows icebergs calving off the Abbot Ice Shelf and the coast of western Ellsworth Land that may only be able to drift a short distance to the north-west before entering the ACC (see Figure 1 in Hillenbrand et al., 2003) and perhaps drifting over the sites of the cores investigated in this study. Figure 2.6 shows the modelled trajectories of medium-sized (73 m thick) icebergs, showing icebergs calving from Thwaites Glacier (74.76°S, 105.75°W) moving west, close to the continent, until becoming entrained in the ACC in the Ross Sea, before then moving north and then east-wards. As the sites of the studied cores sit within the ACC today, one would expect them to contain a reliable record of iceberg-rafted debris (IRD) sourced from ice to the south and east of the core sites (western Ellsworth Land and eastern Marie Byrd Land), as well as material sourced from further west (western Marie Byrd Land and the Ross Sea). However, the dominant source areas of the icebergs and their trajectories are expected to have varied, particularly between glacial and interglacial cycles, and must be considered when interpreting the palaeo record. The source of IRD deposited in the mounds will vary according to multiple factors, including for example, calving rates associated with ice dynamics, the proximity of grounding line positions to the mounds, the geographical and temporal extent of sea ice and the velocity or temperature of the surface currents.

2.4.2. Contemporary change

The present day highest rates of mass loss in Antarctica are concentrated in the glaciers of the ASE (King et al., 2012). The ice shelves of the ASE are relatively small but play a key role in buttressing the ice sheet, controlling rates of thinning and glacier flow speed upstream (Schoof, 2007). Upwelling of relatively warm CDW to the grounding line of numerous glaciers in the ASE is held responsible for ice shelf rifting, basal melt and collapse, leading to increases in the glacier thickness gradient, glacier velocity and glacier thinning (e.g. Rignot and Jacobs, 2002; Shepherd et al., 2002; MacGregor et al.,

2012; Pritchard et al., 2012). Thinning has been reported in all of the ASE ice shelves with the exception of the thinner Abbot Ice Shelf, which has a shallow draft above the water depth below that CDW is found (Pritchard et al., 2012; Cochran et al., 2014) (Figure 2.7).

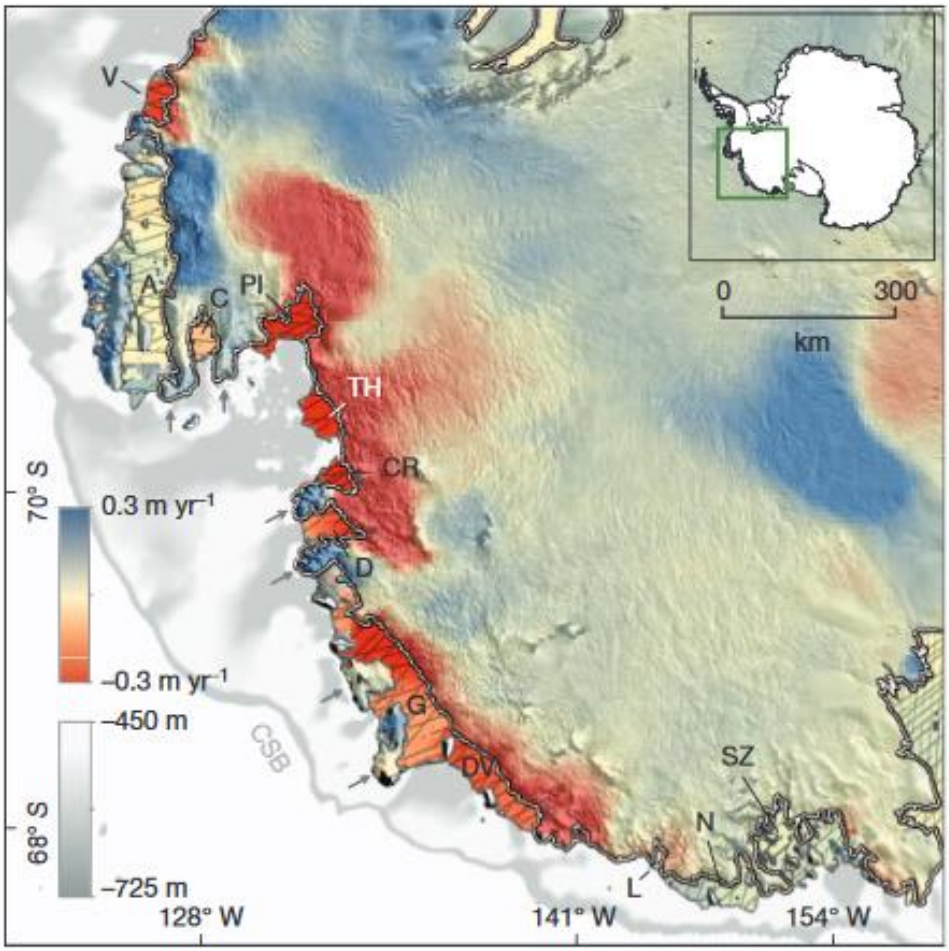

Figure 2.7: Changes in surface height of ice shelves and grounded ice in the ASE, 2003-2008. Arrows indicate grounded ice. The ice shelves have been labelled as follows: Venable (V), Abbott (A), Cosgrove (C), Pine Island (PI), Thwaites (TH), Crosson (CR), Dotson (D), Getz (G), De Vicq (DV), Land (L), Nickerson (N) and Sulzberger (SZ). CSB indicates the continental shelf boundary. From Pritchard et al. (2012).

Rignot and Jacobs (2002) recorded a strong correlation between ocean temperature and melt rates close to the grounding line of Antarctic outlet glaciers. A 1°C increase in ocean temperature at the grounding line could cause a 10 m/yr increase in basal melt just seaward of the grounding line, so the recent 0.2°C temperature increase may have

increased basal melt by 2 m/yr (Rignot and Jacobs, 2002). However, the dominant driver of this increased melt appears to be increased transport of the CDW onto the shelf, driven by stronger winds, rather than increases in the actual temperature of the CDW (Thoma et al., 2008; Pritchard et al., 2012), with the speed of CDW in Pine Island Bay increasing by 77% in the period 1994-2009 (Jacobs et al., 2011). The temperature, salinity and transport of CDW in the Amundsen Sea are also subject to interannual variability related to atmospheric forcing (Dutrieux et al., 2014; Turner et al., 2017).

This has resulted in Amundsen Sea ice shelves experiencing the highest rates of basal melt of any in Antarctica, with Pine Island Glacier experiencing 44 m/year basal melt of its ice shelf directly seaward of the grounding line, compared to an Antarctic average of 16.7 m/year (Rignot and Jacobs, 2002).

The increase in mass loss cannot be explained through atmospheric forcing as recent increases in accumulation have increased glacier flux within the ice sheets, meaning some of the ice shelves which are undergoing thinning are also advancing (Pritchard et al., 2012). The lower elevation of the WAIS compared to the EAIS means that high accumulation rates are not restricted to the coastal areas but can penetrate deep into the interior, resulting in accumulation rates typically >10 cm/yr (Bindschadler, 2006). Despite predicted further increases in accumulation, the rate of mass loss has accelerated over recent decades; models suggest a collapse of Thwaites Glacier, which has a grounding line 600 m below sea level, has already been initiated and a rapid disintegration could occur in 200 to 900 years (Joughin et al., 2014).

The impact of increased mass loss in the ASE is not restricted to the local region. The recent increase in basal melt (particularly beneath the Getz Ice Shelf) has been linked to freshening in the Ross Sea and changes in the properties of the Antarctic Bottom Water (AABW) produced there (Nakayama et al., 2014). There have also been suggestions that recent increases in freshwater input to the Ross Sea have aided the increased sea ice extent there by freshening surface layers, increasing stratification and reducing the flux of heat from intermediate waters to the surface (Zhang, 2007; Turner et al., 2009). Further mass loss may change ice divides and cause retreat in the Weddell and Ross Sea sectors (Feldmann & Levermann, 2015). Of the 4.3 m sea level equivalent stored in the WAIS, 3.4 m of it is grounded below present sea level (Fretwell et al., 2013), much of it

on a reverse-sloping bed (Joughin and Alley, 2011). This makes the WAIS potentially unstable under the marine ice sheet instability hypothesis, with the potential for further ice shelf loss and glacier thinning (Hughes, 1981; Schoof, 2007; Joughin and Alley, 2011).

2.4.3. Sea ice in the Amundsen Sea

All four cores presented in this thesis sit between the minimum (summer) and maximum (winter) sea ice limits in the Amundsen Sea. Sea ice at the site of PS58/253-1 was recorded at 81% in winter and 1% in summer (Schweitzer, 1995 *in* Esper et al., 2010).

Sea ice in the Amundsen Sea south of the sACC (approximately 71°S) drifts westwards due to wind stress; north of the sACC, locally-formed sea ice drifts eastwards with sea ice formed in the Ross Sea (Assman et al., 2005). The mean summer thickness of sea ice in the Amundsen Sea is approximately 100 cm, but can reach extremes of between 6 cm and 300 cm locally and is typically less than 100 cm thick north of 72°S (Assman et al., 2005; Xie et al., 2011).

Sea ice plays an important role in regulating ocean-atmosphere transfer of heat and gas, in controlling the earth's radiation budget through the albedo effect, and in modulating the availability of sunlight, oxygen and nutrients that may limit marine productivity (Parkinson and Cavalieri, 2012). Accumulation rates of the WAIS are highly sensitive to sea ice changes because the distance moisture-laden air masses need to travel to reach the WAIS interior depends on the sea-ice extent, with a 50 km increase in sea ice cover leading to a 10% decrease in mean annual precipitation over the WAIS (Zwally and Giovinetto, 1997). The extent of sea ice around Antarctica as a whole has increased since the late 1970s at a rate of 0.97% per decade, which models suggest may be due to natural variability (Turner et al., 2009). However, the Amundsen and Bellingshausen seas have seen the largest decline in sea ice extent, of -6.6% per decade (1978-2010), equivalent to -8200 ±1200 km^2/yr (Turner et al., 2009; Parkinson and Cavalieri, 2012). It is currently unclear whether this is also due to natural variability or linked to atmospheric conditions. It may be linked to increases in sea ice extent in the Ross Sea by stronger cyclonic atmospheric flow which carries warm air south over the Bellingshausen Sea and cold air from the ice sheet north over the Ross Sea (Turner et

al., 2009). This trend is expected to change as the stratospheric ozone hole recovers, following which, by 2081-2100, average model outputs suggest average annual sea ice extents around Antarctica will decline by 24% relative to the mean 1981-2000 extent due to the oceanographic and atmospheric impacts of increased greenhouse gas concentrations (Arzel et al., 2006).

2.5. Geology

West Antarctica is composed of four crustal blocks which were separated from the East Antarctic craton during the break-up of Gondwana and were then attenuated: Thurston Island, the Ellsworth-Whitmore Mountains, the Antarctic Peninsula and Marie Byrd Land (Dalziel and Lawver, 2001) (Figure 2.8). The placement and topography of these blocks strongly influences the placement of present-day ice divides (Bindschadler, 2006). Mafic material was then intruded into the area between the blocks and the East Antarctic craton (Dalziel and Lawver, 2001). Volcanic activity has occurred in Marie Byrd Land since at least 35 Ma, likely driven by a mantle plume under the "West Antarctic Rift" system which stretches from the Ross Embayment into Ellsworth Land (Dalziel and Lawver, 2001; Bingham et al., 2012). The extensive thinning and rifting across much of West Antarctica has led to a thin crust, just 15-24 km thick in the Ross Sea and 19-25 km thick in the ASE and its hinterland, compared to a global average of 35-40 km (Gohl et al., 2007; Diehl, 2008; Jordan et al., 2010), which has contributed to a large proportion of the WAIS being marine based.

Little is known about the rock types that encompass the Thurston Island and Marie Byrd Land crustal blocks of the ASE as there are few exposed outcrops. Eastern Marie Byrd Land is known to comprise many intrusive igneous rocks, particularly granite and granodiorite, likely dating from the Permian. Alkaline plutonic rocks dating from the Cretaceous are also found, mostly in western and central Marie Byrd Land (DiVenere et al., 1994; Pankhurst et al., 1998). Cenozoic volcanic activity has resulted in outcrops of basalts, andesites, rhyolites, ignimbrites and other volcanic rocks in Marie Byrd Land and westernmost Ellsworth Land (e.g. Le Masurier & Rex, 1991; DiVenere et al., 1994).

Between 114°-131°W and 68°-71°S are a series of volcanoes and smaller cones, the Marie Byrd Seamounts, which extend to ≤2800 m above the sea floor and formed since 65 Ma through rifting and volcanism (Kurentsova et al., 2008; Kipf et al., 2014).

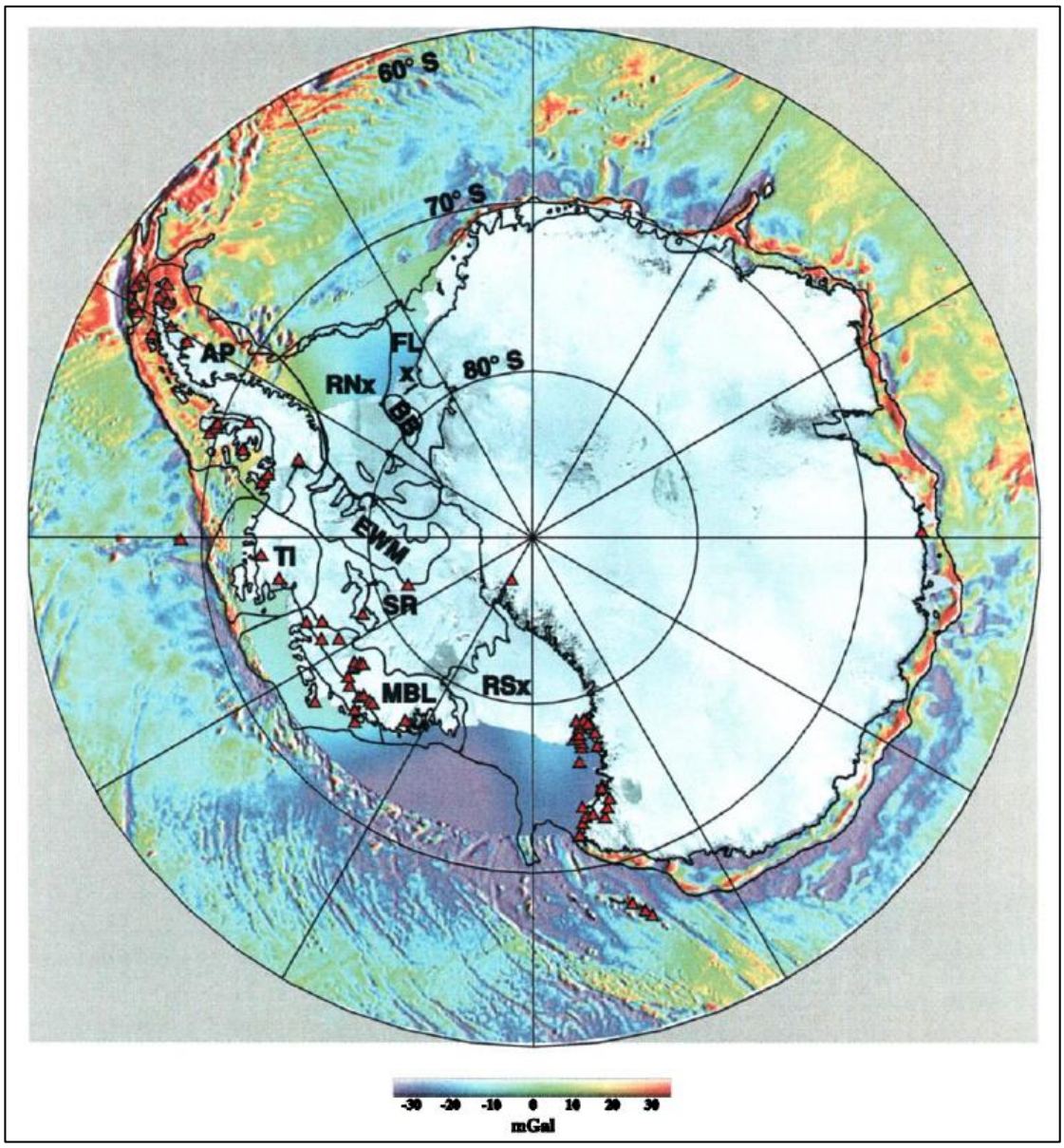

Figure 2.8: Combined Advanced Very High Resolution Radiometer and satellite gravity image of the present-day geological setting of Antarctica, showing the four crustal blocks making up West Antarctica, sub-ice lithospheric provinces and recently active volcanoes (red triangles) Abbreviations are as follows: FLx (Filchner extended lithosphere), RNx (Ronne extended lithosphere), AP (Antarctic Peninsula crustal block), TI (Thurston Island crustal block), EWM (Ellsworth-Whitmore Mountains crustal block), SR (Sinuous Ridge), MBL (Marie Byrd Land crustal block) and RSx (Ross Sea extended lithosphere). From Dalziel and Lawver (2001).

2.6. Atmospheric circulation

2.6.1. Amundsen Sea Low

The Amundsen Sea Low (ASL), also known as the Amundsen-Bellingshausen Seas Low, is a low pressure system centred over the Amundsen and Ross Seas to the north of the ASE (Turner et al., 2013; Turner et al., 2017). Climatic conditions throughout West Antarctica are affected by both the depth and position of the ASL, influencing winds which in turn affect accumulation rates, air temperatures and ablation rates, as well as sea ice extent and ocean upwelling (Turner et al., 2013). The ASL depth and position are affected in the short-term by climatic events including the Southern Annular Mode (SAM) and El Nino Southern Oscillation (ENSO), with the moisture-laden air masses oscillating between the Amundsen and Ross Seas (Kreutz et al., 2000; Bindschadler, 2006; Turner et al., 2013).

2.6.2. Dust

Models suggest only traces of dust reach the core sites today, mostly from Australia and New Zealand, driven by westerly winds and redistributed by ocean currents (Li et al., 2008). Dust deposition rates in the Pacific sector of the Southern Ocean were an estimated three times higher during glacial rather than interglacial periods during the Late Quaternary (Lamy et al., 2014).

2.7. Oceanography

2.7.1. Oceanic fronts and water masses in the Amundsen Sea

The core sites presented in this thesis sit between the present day Southern ACC Front (sACCf) and the southern boundary of the ACC (sACC), as identified by Orsi et al. (1995). This zone was referred to by Orsi et al. (1995) as the “Southern ACC Zone”. Compared to other zones of the ACC, the Southern ACC Zone exhibits relatively low temperatures at all water depths, high salinity in the upper 1000 m, moderate salinity at depth, low oxygen in the upper 300 m and high oxygen below 1000 m water depth (Orsi et al., 1995).

Fronts within the ACC are marked by increased transport and horizontal changes in density associated with changes in temperature, salinity and/or nutrients (Nowlin and Klinck, 1986). The position of the sACCf is influenced by topographic features, including the Antarctic-Pacific Ridge which extends to 145°W, and it has been suggested that anti-clockwise-moving eddies located at 135°W were generated by the sACCf (Orsi et al., 1995). Walker et al. (2013) suggested the sACCf is further south in the eastern Amundsen Sea than was suggested by Orsi et al. (1995). At 101°W, the westwards-flowing Antarctic Coastal Current is underlain by CDW which flows eastwards along the continental slope and penetrates onto the shelf via Abbot Trough (Walker et al., 2013). A weak flow then continues westwards before strengthening and again entering the shelf via the Abbot Trough at 103°W (Nakayama et al., 2013; Walker et al., 2013).

Orsi et al. (1995) defined the sACC as the southern-most extent of Upper Circumpolar Deep Water (UCDW) with no significant change in the density of surface waters. The sACC runs north of the ASE shelf and along the continental slope between 100°W and 55°W (Orsi et al., 1995).

South of the sACC, the Antarctic Coastal Current flows westwards towards the Ross Sea, driven by stress from easterly winds and by the density gradient created by meltwater inputs (Kim et al., 2016). The flow speed exhibits significant seasonal and spatial variation, with peak flow occurring in summer (October) (Kim et al., 2016). A weak south-westwards flow associated with the Antarctic Slope Front has also been identified by Jacobs et al. (2011) at 103°W and by Walker et al. (2013) at 113°-114°W.

The four water masses of the Amundsen Sea continental rise are described in Table 2.1. As the water masses exhibit variations in temperature and salinity, they are best identified by neutral density, as shown in Figure 2.9B. Figures 2.9.C and 2.9D display the seasonal differences in oceanographic conditions along 108.3°W, including the locations of PC494 and PS58/254-1 (National Oceanographic Data Centre, 2013). Temperature and salinity are relatively stable in the deep waters above the core sites year-round at 0 to 0.5°C and 34.70 to 34.71, respectively. Oxygen levels at depth are low and, to a small degree, seasonally dependent: Bottom waters at site PC494 (3450 m water depth) contain an average 4.8 ml/l oxygen in summer and 4.9 ml/l in winter, whilst at site PS58/254-1 (4014 m water depth), the opposite effect is noted (4.8-4.9 ml/l in summer

and 4.7-4.8 ml/l in winter). Below 4000 m water depth, oxygen levels during winter decrease significantly with depth when compared to summer conditions and higher oxygen levels in deep waters are constrained to a depth of approximately 2500-3500 m, close to the continental slope (Figure 2.9 D).

Water Mass	Abbreviation	Potential Temp. θ (°C)	Salinity	Neutral Density (kg m^{-3})	Reference
Antarctic Surface Water	ASW	<0.5°C	<34.40	<28.00	Orsi et al. (1995)
Upper Circumpolar Deep Water	UCDW	1.6 to 2.0°C	>34.60	28.00 to 28.18	Orsi et al. (1995)
Lower Circumpolar Deep Water	LCDW	>0	>34.70	28.18 to 28.27	Orsi and Wiederwohl (2009)
Antarctic Bottom Water	AABW	–0.2 to 0.2°C (Pacific sector)	34.70 to 34.72	>28.27	Orsi et al. (1999)

Table 2.1: Typical characteristics of water masses present within the ACC in the Pacific sector of the Southern Ocean.

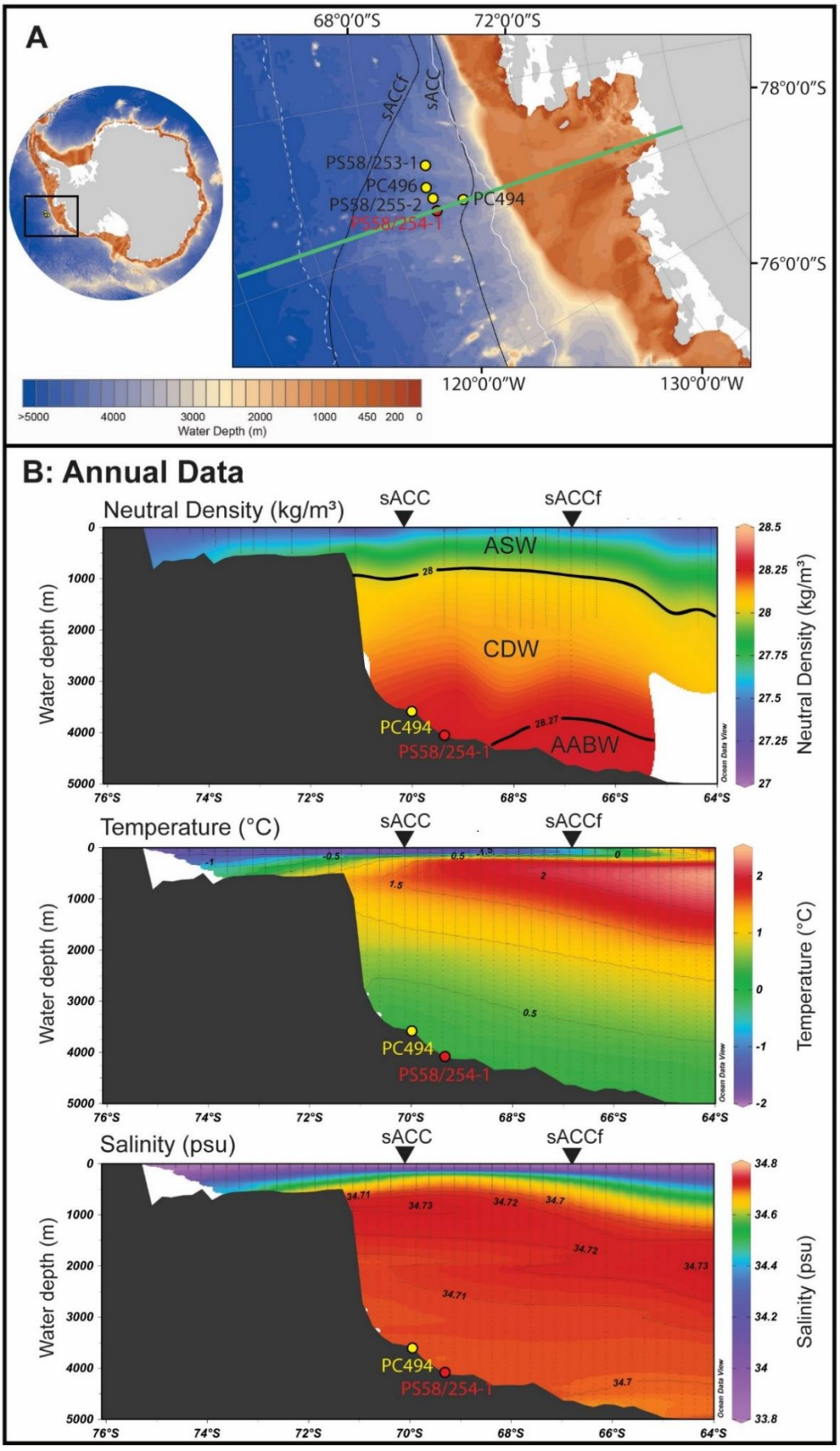
A
68°0′0″S
72°0′0″S
78°0′0″S
76°0′0″S
120°0′0″W
130°0′0″W
sACCf
sACC
PS58/253-1
PC496
PS58/255-2
PC494
PS58/254-1
>5000
4000
3000
2000
1000
450
200
0
Water Depth (m)
B: Annual Data
Neutral Density (kg/m³)
sACC
sACCf
ASW
CDW
AABW
28
28.27
PC494
PS58/254-1
Water depth (m)
Neutral Density (kg/m³)
Temperature (°C)
Salinity (psu)
Ocean Data View
76°S
74°S
72°S
70°S
68°S
66°S
64°S

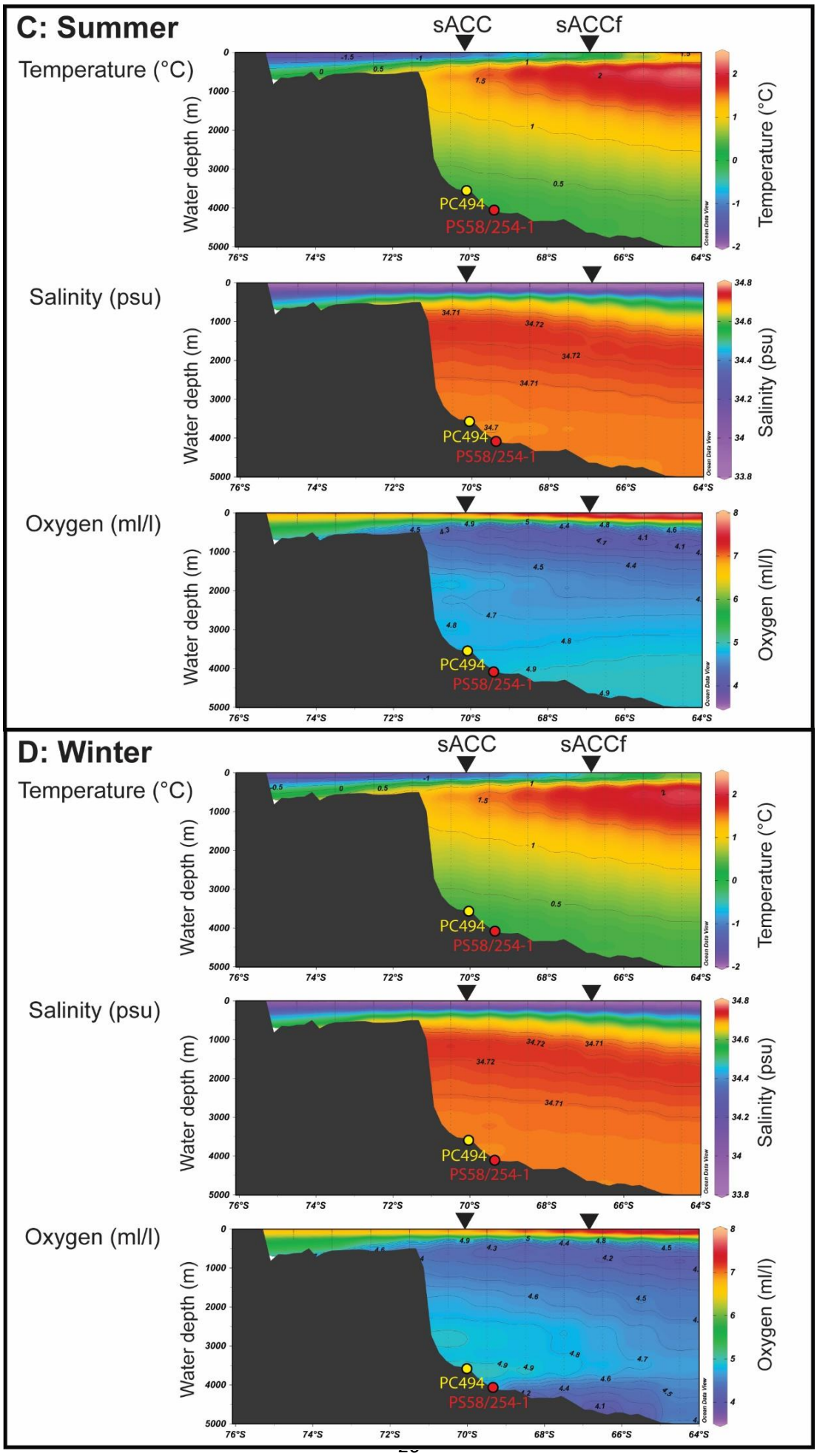
C: Summer
sACC
sACCf
Temperature (°C)
Water depth (m)
PC494
PS58/254-1
Temperature (°C)
Salinity (psu)
Salinity (psu)
Oxygen (ml/l)
Oxygen (ml/l)
D: Winter
sACC
sACCf
Temperature (°C)
Water depth (m)
PC494
PS58/254-1
Temperature (°C)
Salinity (psu)
Salinity (psu)
Oxygen (ml/l)
Oxygen (ml/l)

Figure 2.9. A-D (previous page): Interpolated profiles of temperature, salinity and oxygen in the eastern Amundsen Sea (along 108.3°W). Oceanographic data were obtained from the World Ocean Atlas 2013 (Boyer et al., 2013). All bathymetric data was obtained from IBCSO (Arndt et al., 2013). Plots were created in Ocean Data View (Schlitzer, 2017).

For all charts, temperature contours are shown in 0.5°C increments. Salinity contours are shown in 0.01 psu increments where salinity is >34.70. Oxygen contours are shown in 0.1 ml/l increments where oxygen is ≤5 ml/l. The position of cores PC494 and PS58/254-1 have been indicated as they lie on, or in close proximity to, the oceanographic transect. The position of the Southern Boundary of the Antarctic Circumpolar Current (sACC) and the Southern Antarctic Circumpolar Current Front (sACCf) are marked by black triangles. Dashed black lines indicate the boundaries of the interpolated grids.

(A) Bathymetric map of the eastern Amundsen Sea showing the location (green line) of the oceanographic profiles presented in parts B, C and D.

(B) Annual average neutral density, temperature and salinity. Neutral density was derived from the dataset, as outlined below. The 28.00 kg/m^3 and 28.27 kg/m^3 contours are shown in the neutral density plot and used to identify the water masses as Antarctic Surface Water (ASW), Circumpolar Deep Water (CDW) and Antarctic Bottom Water (AABW). Data have been interpolated with a weighted average gridded field over a 0.25° longitudinal and latitudinal area.

(C) Summer (January to March) water temperatures, salinity and oxygen contents. Data have been interpolated with a weighted average gridded field over a 1° longitudinal and latitudinal area.

(D) Winter (July to September) water temperatures, salinity and oxygen contents. Data have been interpolated with a weighted average gridded field over a 1° longitudinal and latitudinal area.

2.7.2. Surface and Intermediate Waters

During modern summer conditions, the uppermost water column of the Amundsen Sea contains Antarctic Surface Water (ASW): near-freezing (θ < 0.5°C), low salinity (S <34.40 psu) waters from melt of the nearby ice sheet (Orsi et al., 1995). Walker et al. (2013) found this surface layer to be similar across the shelf, slope and upper continental rise of the eastern Amundsen Sea, with θ < 0°C. Summer salinity and temperature measured at 10 m water depth above site PS58/253-2 were 33.43 psu and -0.62°C, respectively, with a mixed layer depth of just 4.42 m (values from the WOCE Global Hydrographic Climatology Atlas (Gouretski and Koltermann, 2004) and the LEVITUS 94 World Ocean Atlas (Monterey and Levitus, 1997) as quoted by Esper et al., 2010).

Below ASW, temperature and salinity both rise rapidly as this surface layer mixes with the underlying UCDW (Jacobs et al., 2011). UCDW is a warm (θ 1.6 – 2.0°C), saline (S >34.60 psu), low-oxygen and high-nutrient water mass (Orsi et al., 1995).

Beneath UCDW lies Lower Circumpolar Deep Water (LCDW), which is highly saline (S >34.70) and slightly cooler than UCDW (Orsi et al., 1995; Walker et al., 2013). Near the shelf break in the eastern Amundsen Sea, the core of LCDW lies at a water depth of ca. 700 m (Walker et al., 2013). In the eastern Amundsen Sea, the proximity of the sACC to the shelf break combined with the presence of ≤700 m deep palaeo-ice stream troughs on the shelf mean that while CDW is restricted to the continental rise in much of the Southern Ocean, in the ASE it is able to reach the grounding lines of glaciers (Orsi et al., 1995; Jacobs et al., 2011). Walker et al. (2013) reported CDW on the outer ASE shelf with a θ of 1.5-1.7 °C at ≥300 m water depth, with particularly large volumes of CDW flooding the centre of PITW. The CDW mixes with surface meltwater but still retains temperatures exceeding 1°C in the inner ASE (Wåhlin et al., 2010). This warm water is considered the main driver of the sub-ice shelf melting and associated grounding line retreat and ice-stream thinning in the ASE and its hinterland (Jacobs et al., 2011; Pritchard et al., 2012; Jenkins et al., 2016; Turner et al., 2017).

The water masses of the Amundsen Sea can be distinguished by their neutral densities: ASW has a neutral density of <28.00 kg/m^3, LCDW and UCDW have a neutral density of 28.00 - 28.27 kg/m^3 and Antarctic Bottom Water (AABW) has a neutral density of >28.27 kg/m^3 (Whitworth et al., 1998).

2.7.3. Bottom waters

There are three main potential sources of the bottom waters in the eastern Amundsen Sea: AABW derived from the Ross Sea to the west, modified Weddell Sea Deep Water (mWSDW) derived from the Weddell Sea far to the east or LCDW.

AABW is a relatively cold ($\theta \leq 0.2$°C) water body which, due to a range of potential temperatures and salinities derived from local mixing with other water masses, is best defined by the neutral density upper boundary of >28.27 kg m^{-3} (Orsi et al., 1999). In the Pacific sector of the ACC, AABW has a θ of –0.2 to 0.2°C and a salinity of 34.70 to 34.72 psu (Figs. 2.10, 2.11; Orsi et al., 1999). AABW feeds into all of the world's oceans and is a key driver of thermohaline circulation. AABW has four major source areas: the Ross Sea (170°E – 160°W), the western Weddell Sea (60 – 30°W), the Amery Basin (50 – 100°E) and the shelf offshore from Wilkes Land (120 – 160°E) (Orsi et al., 1999). Formation of AABW in the Pacific sector of West Antarctica (except the Ross Sea) is prohibited by the lack of dense pre-cursor water masses formed on the shelf as a result of the combination of small ice shelves and the presence of warm CDW on the shelf (Orsi et al., 1995, Jacobs et al., 2011).

There are two mechanisms of AABW pre-cursor water mass formation. The first, i.e. formation of High Salinity Shelf Water (HSSW), occurs during sea ice formation, when brine rejection into the underlying surface waters increases the density of this already cold water mass, causing it to sink. The second, forming Ice Shelf Water (ISW), occurs below ice shelves, as water moving under the ice shelf is forced to great depths by the thickness of the ice shelf. This water cools on contact with the ice, but the freezing point is reduced by the increased pressure, resulting in the 'super-cooling' of the water and formation of extremely cold water (θ >-2.3°C) (Orsi et al., 1999; Nicholls et al., 2009). The dense HSSW and ISW will mix with other water masses, typically CDW and its derivatives, to form AABW (Orsi et al., 1999).

Based on proximity and apparent flow directions, the most likely source for AABW in the Amundsen Sea is the Ross Sea. This water mass, also known as Ross Sea Bottom Water (RSBW), travels eastwards within the ACC and the Ross Sea Gyre. AABW in the northwest Ross Sea has the highest salinity and temperature of any of the AABW sources, with θ between -0.6°C and -0.3°C and S >34.72, due to the HSSW (S >34.8) from which it forms

(Orsi et al., 1999). In contrast, low-salinity AABW is formed in the eastern Ross Sea from Low-Salinity Shelf Water (LSSW) (S <34.70) (Orsi et al., 1999). AABW from the eastern Ross Sea can, together with LCDW, become entrained in the Ross Sea Gyre, a large cyclonic system south of the ACC which spans from 160°E (all water depths) to 140°W (upper and middle waters only) (Locarnini, 1991). Potential temperatures (θ <0.2°C) and dissolved silicate measurements suggest bottom waters within the gyre extend past 140°W, perhaps to between 90°W and 75°W where another cyclonic rotation has been observed (Locarnini, 1991).

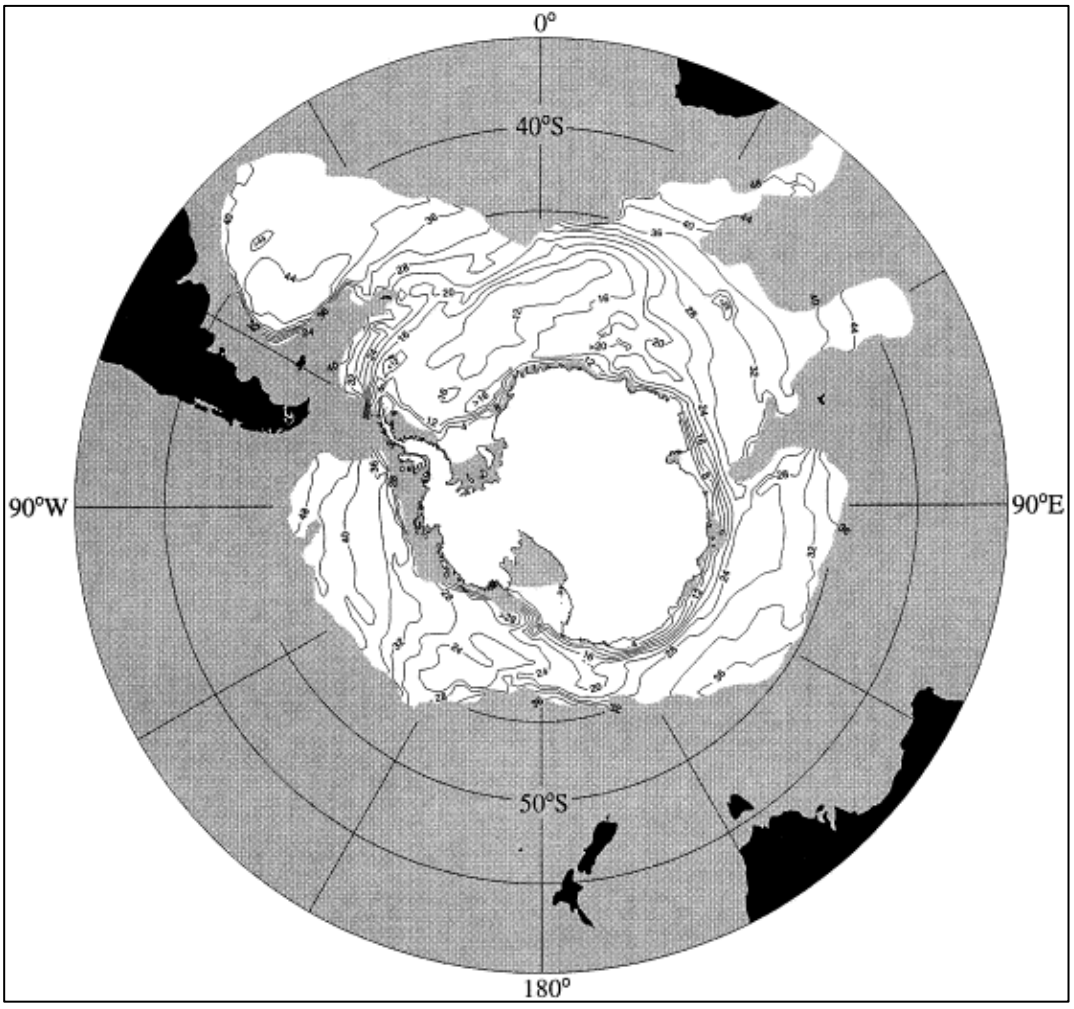

Figure 2.10: Extent (white areas) and depth of the top (contours in hundreds of metres) of Antarctic Bottom Water, based on the neutral density surface of 28.27 kg m^{-3}. From Orsi et al., 1999.

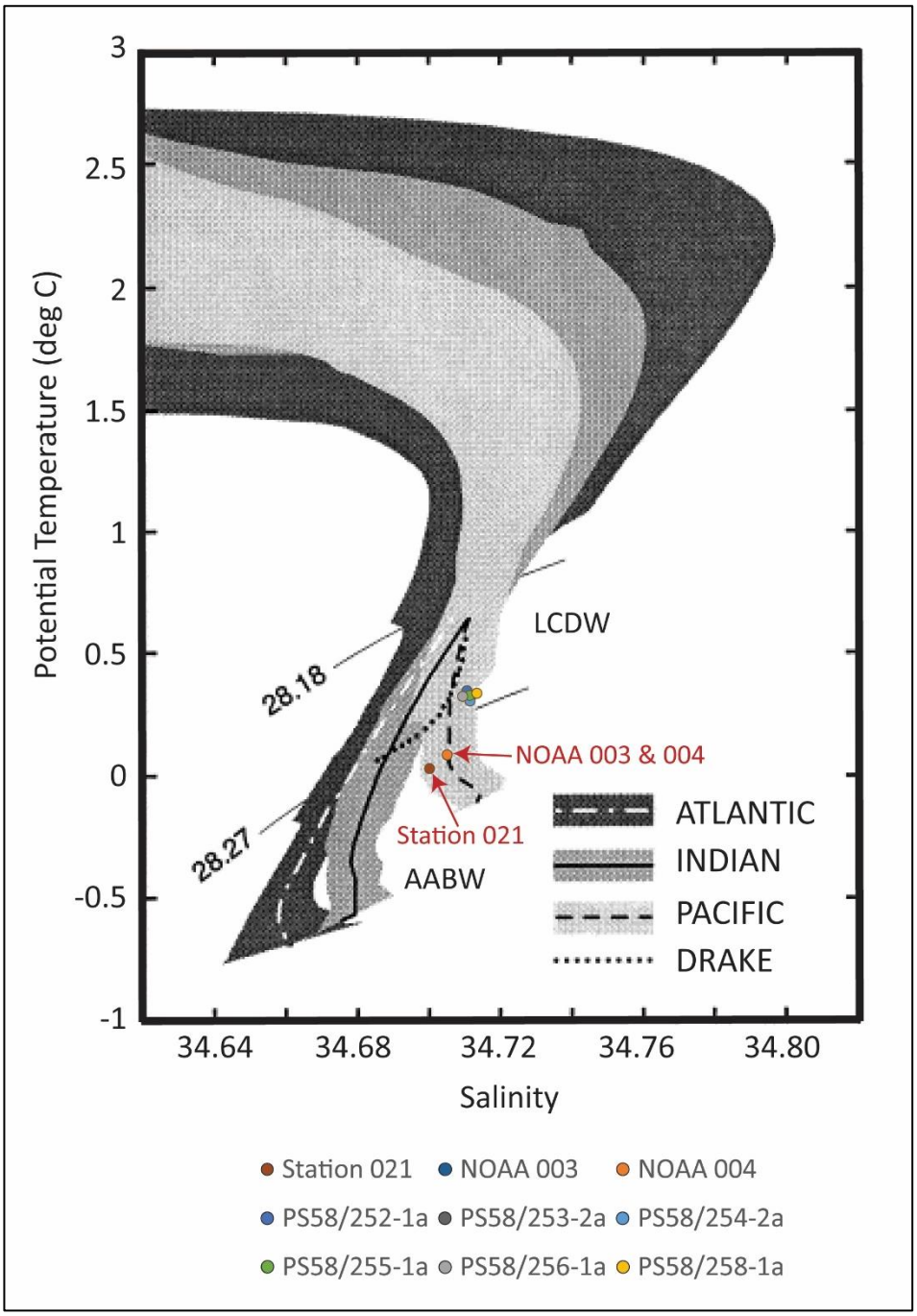

Figure 2.11: Potential temperature and salinity plot showing the average characteristics of deep water masses within the ACC, modified from Figure 5 of Orsi et al. (1999). LCDW and AABW are indicated, based on the neutral density surfaces of y^n=28.18 kg m^{-3} and y^n=28.27 kg m^{-3}. The potential temperature and salinity of bottom water at nine CTD stations from the eastern Amundsen Sea upper continental rise are plotted, and those with a neutral density indicating AABW (y^n>28.27 kg m^{-3}) have been labelled in red for clarity. The location of the CTDs is shown in Figure 2.12, and the references and further information are given in Table 2.2.

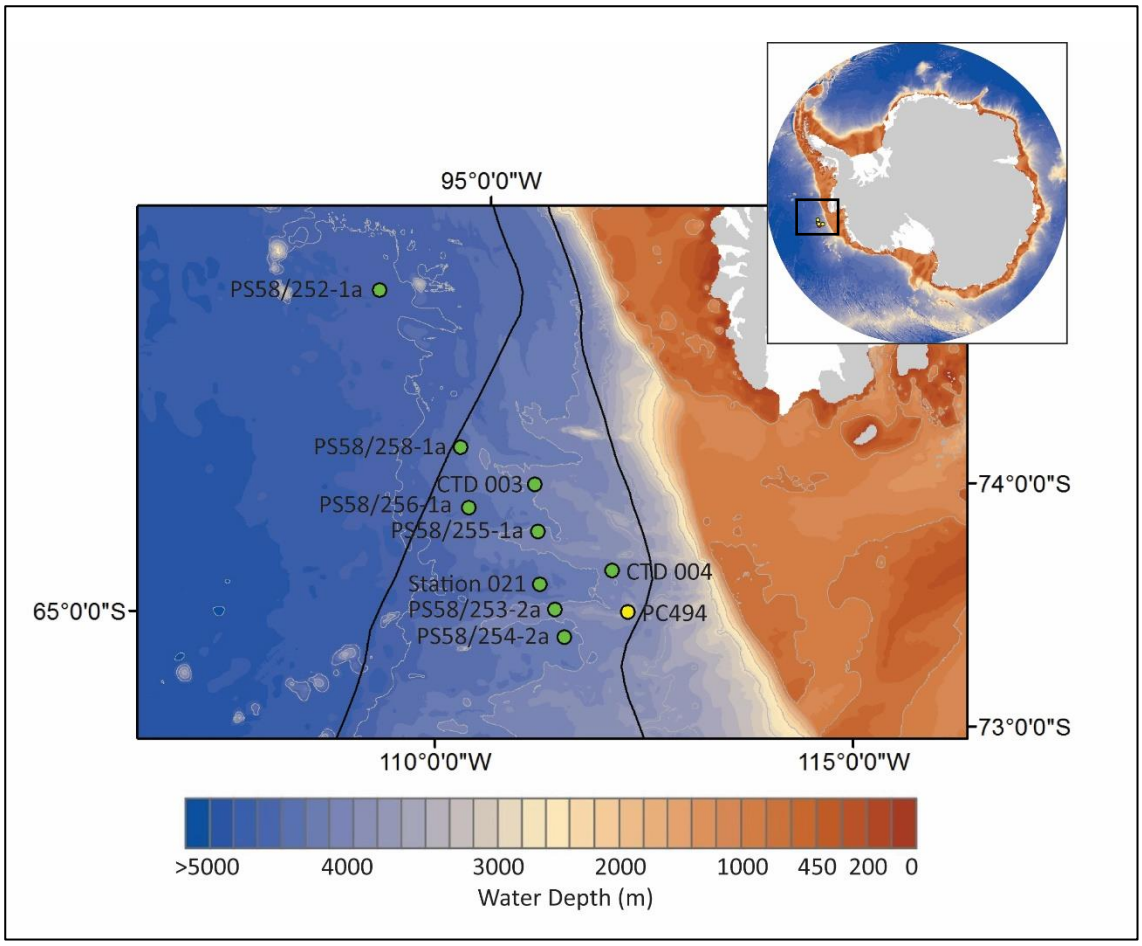

Figure 2.12: Bathymetric map indicating the location of the CTDs (green circles) referred to in Figure 2.11 and Table 2.2. The yellow circle indicates the position of core PC494; the locations of the other sediment cores are also sites of CTDs. The black rectangle on the inset map indicates the location of the main figure. Bathymetric data from IBCSO (Arndt et al., 2013).

CTD Name (Cruise)	Bottom depth (m)	Deepest CTD depth (m)	Potential temp. (°C) at bottom	Salinity at bottom	Water mass	Date of CTD	Data source
Station 021 (JR179)	4218	4208	0.03	34.70	AABW	March 2008	Carter et al. (2012)
CTD 003 (OSO1011)	3889	3849	0.09	34.71	AABW	Dec. 2010	NODC (2013)
CTD 004 (OSO1011)	3967	3951	0.09	34.71	AABW	Dec. 2010	NODC (2013b)
PS58/252-1a	4518	4468	0.35	34.71	LCDW	March 2001	Gersonde (2010)
PS58/253-2a	3722	3672	0.33	34.71	LCDW	March 2001	Gersonde (2010)
PS58/254-2a	4014	3972	0.31	34.71	LCDW	March 2001	Gersonde (2010)
PS58/255-1a	3795	3760	0.33	34.71	LCDW	March 2001	Gersonde (2010)
PS58/256-1a	4324	4217	0.33	34.71	LCDW	March 2001	Gersonde (2010)
PS58/258-1a	4255	3975	0.34	34.71	LCDW	March 2001	Gersonde (2010)

Table 2.2: Hydrographic data for the nine CTDs plotted in Figures 2.11 and 2.12. “NODC” is an abbreviated form of the National Oceanographic Data Centre.

Uenzelmann-Neben and Gohl (2012, 2014) suggested that a relatively weak form of AABW is present on the continental rise of the eastern Amundsen Sea. This is due to their interpretation of the sediment mounds (which are the focus of this research) as contourite drifts which began forming in the Eocene under an eastwards-flowing bottom current, prior to the existence of any evidence for CDW. They concluded that AABW, including its earliest ‘proto-AABW’ form, has been present and influenced sedimentation in the eastern Amundsen Sea since the Eocene. The AABW pathway, however, has changed as a result of glaciological, climatological and geological changes (Uenzelmann-Neben and Gohl, 2012). The lack of any bottom current influence on the uppermost seismic units of the channel-levee deposits of the central Amundsen Sea

implies the absence of AABW in this area since 4 Ma (Uenzelmann-Neben and Gohl, 2012).

The horizontal extent of AABW as defined by Orsi et al. (1999) lies close to the core sites in the eastern Amundsen Sea and is present below c.2800 m water depth (Figure 2.10). However, conductivity-temperature-depth (CTD) data from this area is sparse and the AABW suggested from the neutral density in Figure 2.9B is based only on three CTD profiles. Other CTDs taken in the vicinity of the mounds suggest both AABW and LCDW being present (Figure 2.11 and Table 2.2).

Uenzelmann-Neben and Gohl (2012) also suggest that the geometry of the southernmost section of the mounds/drifts of the eastern Amundsen Sea indicates they have been under the influence of a bottom current flowing towards the south-west since at least 21 Ma. Uenzelmann-Neben and Gohl (2012) suggested this was the result of eddies shed from the AABW, or that there may be a westwards extension of the mWSDW or modified LCDW which shaped the drifts west of the Antarctic Peninsula since at least 9.4 Ma (Hernandez-Molina et al., 2006; Hillenbrand et al., 2008). mWSDW has been observed as far west as 83°W and suggested to extend to 93°W, based on the geometry of contourite drifts and clay mineral distribution in seafloor surface sediments in the Bellingshausen Sea (Hillenbrand et al., 2003; Scheuer et al., 2006b), but there remains a need for more research in this area to further identify the extent of these water masses.

2.8. Marine productivity

Primary productivity in the Amundsen Sea is recorded in sediments as biogenic silica, $CaCO_3$ and organic carbon. An increase in the biogenic content of marine sediments may reflect a true increase in productivity, a reduction in grazing of microplankton by zooplankton, a reduction in dissolution or a reduction in dilution by terrigenous material (Vautravers et al., 2013). It is therefore crucial to examine the biogenic content in conjunction with a range of other palaeoenvironmental data.

2.8.1. Factors limiting biological productivity

The cores investigated in this thesis sit within the Antarctic Zone south of the Polar Front in nutrient-rich waters (Ehrmann et al., 2010). Measurements taken at 10 m water depth in summer at the site of PS58/253-1 recorded high nutrient contents, i.e. of phosphate (1.67 µmol L^{-1}), nitrate (25.53 µmol L^{-1}) and silica (43.36 µmol L^{-1}) (derived from the World Ocean Atlas 2005 (Garcia et al., 2006) by Esper et al., 2010). Therefore, the availability of nutrients is no limiting factor for phytoplankton production in the Amundsen Sea. Availability of dissolved iron is also less of a limiting factor than elsewhere in the Southern Ocean, here supplied predominantly via the near-surface presence of iron-rich UCDW at and south of the sACCf, and via the melting of glacial ice and sea ice (Hiscock et al., 2003; Gerringa et al., 2012).

The second significant control on primary productivity in the Southern Ocean is light availability (Gerringa et al., 2012). In the Amundsen Sea on a seasonal basis, light availability is controlled by the extent and duration of sea ice cover, which also influences nutrient supply (Lucchi and Rebesco, 2007). Light availability in the Amundsen Sea depends mainly on sea ice cover (Gerringa et al., 2012), although some diatom species are capable of surviving within the sea ice or within cavities (e.g. Esper et al., 2010). During the Last Glacial Maximum (LGM; ca. 19-23 cal. ka BP), it is believed that diatom production around the Antarctic continental margin was limited by perennial sea-ice cover, despite the high nutrient supply from increased CDW upwelling (Chase et al., 2003).

Primary productivity in the Southern ACC Zone of the Pacific sector of the Southern Ocean is greatest in late spring (December), when dissolved iron and silicic acid concentrations are high following increased upwelling of UCDW in winter, and when spring sea ice retreat increases the availability of light (Hiscock et al., 2003).

2.8.2. Biogenic Silica

Silicic acid in seawater is polymerised by diatoms, radiolaria, siliceous sponges and silicoflagellates into biogenic silica, which they use for building their hard parts (DeMaster, 1981). The production and burial of this biogenic silica is limited by the

availability of silicic acid (Anderson et al., 2009). The surface waters of the Antarctic Zone, south of the Antarctic Polar Front, have the highest concentration of dissolved silica in the Southern Ocean, favouring the production of biogenic silica (Pudsey, 2000; Esper et al., 2010). Nonetheless, due to the under-saturation of all ocean water with respect to silica, siliceous material must rapidly sink to the sea floor, typically by forming aggregates with other particles, in order to minimise dissolution and grazing (Esper et al., 2010). Grains smaller than 50 µm will take c.12 hours to sink 200 m through surface waters (Raiswell et al., 2006), making biogenic silica in the form of unicellular, silt-sized diatoms particularly vulnerable to dissolution in deep water given the long timescales involved. Further silica is then lost at the seafloor surface, when the siliceous microfossils are exposed to highly under-saturated bottom waters (through diffusion of silica into the overlying waters), and within the sediment along a concentration gradient, when under-saturated pore waters foster silica dissolution in the ca. uppermost 20 cm of the sediment column (DeMaster, 1981). The impact of any dilution with terrigenous material on preservation of biogenic microfossils is debated: rapid burial minimises exposure time and thus dissolution of the microfossils by corrosive bottom waters (e.g. DeMaster et al., 1996), but also causes silicic acid concentrations in the pore waters to decrease, which encourages dissolution of the biogenic silica (e.g. Esper et al., 2010). It has been estimated that only between 0.2 and 24% of the initially produced biosiliceous material will be preserved in deep-water sediments of the Southern Ocean, due to high rates of dissolution primarily in the upper water column and following deposition (Schlüter et al., 1998; DeMaster, 2002).

Diatoms comprise an average of 90% of the total phytoplankton biomass in the seasonally sea ice covered zone of the Amundsen Sea, and an average of 69.5% of the phytoplankton is grazed by microzooplankton each day in early summer (Yang et al., 2016). Diatoms bloom in stratified waters with high nutrient supply, so diatom production is relatively high in the vicinity of the core sites where melting sea ice and upwelling UCDW provide nutrients and the very shallow mixed layer creates a stable, upper water column (Fragoso and Smith, 2012).

Analysis of surface samples of diatom-bearing mud from site PS58/253 by Esper et al. (2010) found preservation was moderate to poor, indicating some dissolution, with a

biogenic silica content of 8.4 wt.% in the surface sediment. Esper et al. (2010) found a surface sample from PS58/254-2 (4016 m water depth) contained over three times the number of diatoms per weight of sediment than the sample from PS58/253-2 (3721 m water depth) (39.9 x 10^6 compared with 12.0 x 10^6 diatoms per g dry weight, respectively), and diatom preservation was also improved in PS58/254-2 (Esper et al., 2010). The sites feature near identical surface water chemistry and sea ice coverage, and the greater preservation is most likely related to differences in sediment condensation between the two sites. The surface samples were dominated by the common Southern Ocean open water species *Fragilariopsis kerguelensis* (>72% relative abundance) (Esper et al., 2010).

2.8.3. $CaCO_3$

Calcium carbonate is produced by organisms such as foraminifera, bryozoans, bivalves and brachiopods in the form of aragonite and calcite (Hauck et al., 2012). Most calcium carbonate on the West Antarctic continental margin is in the form of calcareous foraminifera, which grow either near the ocean surface (planktonic foraminifera) or ≤10 cm below the sediment-water interface (benthic foraminifera) (Jorissen, 1999). Benthic foraminifera can also be non-calcareous and have tests consisting of amalgamated biogenic and/or terrigenous grains (agglutinated foraminifera).

Carbonate is susceptible to dissolution by poorly ventilated water masses such as CDW as low-oxygen bottom waters enable high preservation of organic matter, which can later decompose and release organic acids (e.g. Diekmann et al., 2007; Majewski et al., 2016). Below the Carbonate Compensation Depth (CCD), sea water is permanently under-saturated in carbonate which leads to dissolution and a lack of carbonate preservation (Hauck et al., 2012). The depth of the CCD fluctuates according to climatic conditions and carbonate supply; during periods of high atmospheric CO_2, the additional CO_2 taken up by the ocean leads to ocean acidification, resulting in increased under-saturation and increased carbonate dissolution (Hauck et al., 2012). High melt rates increase stratification of the water column, which restricts mixing of the low-oxygen, high-nutrient bottom waters and can cause the CCD to rise (Lucchi and Rebesco, 2007).

Today, $CaCO_3$ concentrations in surface samples from the Amundsen Sea outer shelf (above the CCD) average 5.1 % and peak at c.15 % (Hauck et al., 2012), and most samples are dominated by the polar planktonic foraminifera species *Neogloboquadrina pachyderma* (sinistral) which can survive in sea ice (Dieckmann et al., 1991). Hillenbrand et al. (2003) estimated the water depth of the CCD in the Amundsen Sea at 4000 m, based on the distribution of $CaCO_3$-bearing sediments, and suggested the CCD rises between 120 and 70°W by at least 1200 m. Esper et al. (2010) identified a foraminifera and diatom bearing mud on the surface of PS58/254-2, though it is unclear whether the foraminifera were calcareous or agglutinated foraminifera. Hillenbrand et al. (2009a) found $CaCO_3$ in PS58/254-1 only in certain interglacials (MIS 19, 17 and 5), suggesting the CCD has been above 4014 m water depth for most of the Late Quaternary.

Chapter 3: Depositional Processes and Features of the Antarctic Continental Margin

3.1. Introduction

This chapter outlines the main depositional processes that occur on the continental margin of Antarctica and the nature of their deposits. The first part of the chapter outlines common depositional processes and describes their deposits. Particular emphasis is given to contourite deposits, as the mounds of the eastern Amundsen Sea have previously been interpreted as sediment drifts. Therefore, this part of the chapter also provides a review of the contourite drift deposits present on the Antarctic continental margin. The second part of the chapter describes the depositional processes and features of the Bellingshausen Sea continental margin to provide context for later work addressing the research aim of comparing the eastern Amundsen Sea mounds with the drifts located west of the Peninsula. The third part of the chapter describes the depositional processes and features of the Amundsen Sea, with particular emphasis on the eastern Amundsen Sea mounds.

3.2. Styles of deposition on the Antarctic continental margin

Three main modes of sedimentary deposition occur in the deep sea: down-slope density currents (forming turbidites), bottom currents (forming contourites) and pelagic settling (forming pelagites) (Rebesco et al., 2014). Turbidites and contourites are common features of the upper continental rise around Antarctica as a result of often significant down-slope deposition and the interaction of these deposits in some areas with bottom currents. Marine productivity and preservation of biogenic matter are often restricted on the continental rise by the presence of sea ice, limited nutrient supply and the dissolution of siliceous and calcareous material in deep water with often low terrigenous sedimentation rates.

3.2.1. Mass transport processes and deposits

Mechanisms for mass transport are common features of the continental slope around Antarctica, particularly where ice expanded to the outer continental shelf during glacial periods. High glacial sediment delivery to the outer shelf led to the accumulation of sediment near the shelf break, typically resulting in the development of prograding wedges over numerous glacial cycles (e.g. Nitsche et al., 2000; Noormets et al., 2009). These poorly compacted, poorly sorted sediments were then often subject to failure on the continental slope. Failures can be triggered by a wide range of factors (see Shanmugam and Wang, 2015) but rapid sediment accumulation, with the added impact of glacial loading and meltwater, was likely the most dominant cause of failure on the upper slope in the Amundsen Sea, where the slope failures largely pre-dated the formation of deep gullies and channels by meltwater following the LGM (Noormets et al., 2009). Slides, slumps and debris flows contain sediment concentrations of 25-100% by volume and lead to deposits (with increasing amounts of internal deformation) known as slides, slumps and debrites (Shanmugam and Wang, 2015). Debris flows also frequently initiate turbidity currents as shear on the upper surface of the debris flow encourages fine grains to become entrained in the seawater above (Parsons et al., 2007).

3.2.2. Turbidites

Turbidites are the deposits which result from turbidity currents; low-density (<25% sediment by volume and often <7%), gravity-driven, poorly sorted flows lasting minutes to days in which the sediment is held in suspension through turbulence and which are not classified as mass transport due to the low sediment concentration (Shanmugam, 2002; Parsons et al., 2007; Meiburg and Kneller, 2010). The flow is driven by the pressure gradient maintained by the density difference between the turbidity current and the surrounding seawater (Parsons et al., 2007).

Submarine turbidity currents are typically dominated by clay to medium sand sized grains and can carry grains no larger than coarse sand (Lowe, 1982; Parsons et al., 2007). Mud-rich sediments with a high water content can be subject to soft-sediment deformation (e.g. load and flame structures, sediment injections) as the turbidity current moves over the sea floor (Baas et al., 2014) and turbidity currents can both

entrain and deposit grains as they move (Meiburg and Kneller, 2010). Deposition occurs when bed shear falls as a result of decreasing sediment concentration (Parker et al., 1997) and occurs largely through suspension settling with larger grain sizes deposited first, resulting in normally graded depositional units (Lowe, 1982; Shanmugam, 2002). Single turbidity currents result in sediment units typically a few centimetres to tens of centimetres thick which cannot be resolved using multi-channel seismic profiles (Shanmugam, 2002).

Erosion resulting from turbidity currents is typically limited to the relatively narrow central portion of the flow, leading to channel formation (Parsons et al., 2007). In contrast, deposition typically occurs over a larger area, dependent on sediment concentration and shear velocity, and is particularly high at the edges of the channel, resulting in the deposition of levees which further constrain subsequent flows to the channel (Figure 3.1) (Parsons et al., 2007).

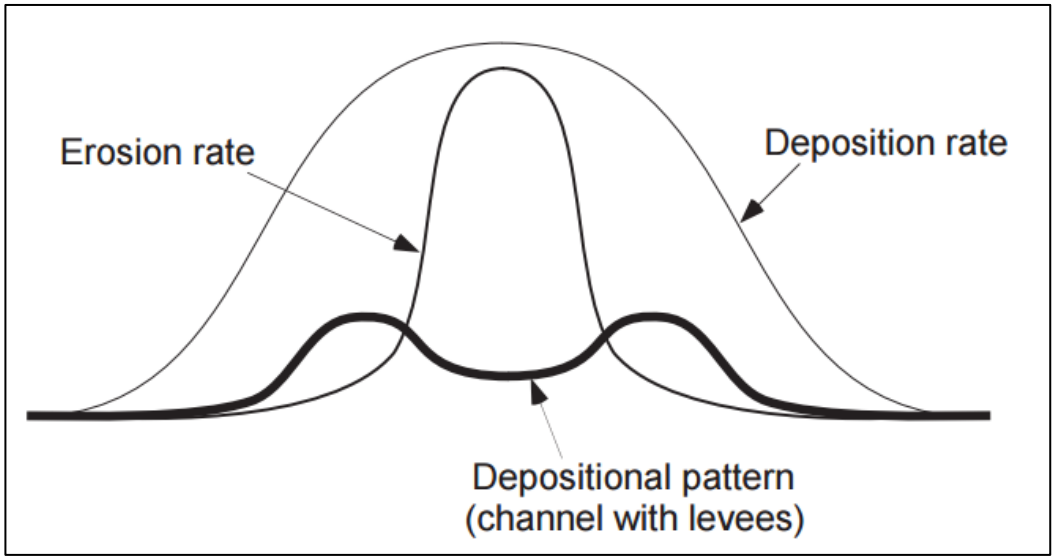

Figure 3.1: The distribution of erosion and deposition caused by a typical turbidity current. From Parsons et al. (2007).

Further down-slope, channels typically divide, meander and can be up to several thousand kilometres in length, and fan-shaped or sheet-like deposits can occur where some of the flow is unconfined (Parsons et al., 2007; Meiburg and Kneller, 2010). Over time, repeated erosion of the channel and deposition on the levees via overspill (where

the depth of the turbidity current flow exceeds the bank height of the channel) results in distinctive channel-levee deposits indicative of turbiditic action, which are generally more symmetrical than contourite drifts and do not rise as high above the sea floor (Scheuer et al., 2006b). Overspill generally accumulates slowly and can result in levees an order of magnitude wider than the channel (Parsons et al., 2007). In the southern hemisphere, the action of the Coriolis force means that the western levee will typically be larger than the eastern levee.

Bouma (1962) proposed an idealised vertical succession of deposits from turbidity currents, the Bouma Sequence. Intervals A-E represent differences in the grain size and structure of deposits resulting from the progressive stages of deposition from turbidity currents. Interval A reflects rapid sediment deposition with possible grading, no lamination and common water escape structures due to compaction and liquefaction. Interval B is parallel laminated and reflects bed transport of grains. Interval C is typically ripple cross-laminated and reflects suspension settling of grains whilst a current was active on the seabed. Intervals D and E reflect the settling of sand and silt grains from suspension, with some minimal grain sorting occurring in Interval D (Stow et al., 1996). However, this succession is only applicable to medium-grained turbidites and cannot be applied to fine-grained, silt-mud turbidites (Stow et al., 1996) which Stow (1977) divided into nine divisions termed T_0-T_8 reflecting the amount of traction and shear-sorting just prior to deposition. Some sequences may be missing or repeated (Stow et al., 1996).

Diagnostic criteria for the identification of turbidites include the following:

1. Overall architecture:
    - Many channel-levee deposits lie perpendicular to the margin, reflecting the down-slope movement of material.
    - Turbidites can be fan-shaped or sheet-like deposits up to a few hundred km² located either side of a channel. External levees are typically wedge-shaped (with the steep side facing the channel), <10 km wide and there is typically a negative correlation between grain size and the width of the levee (Hansen et al., 2015). Overspill deposits may be up to an order of magnitude wider than the channel (Parsons et al., 2007; Meiburg and

Kneller, 2010). Channel levees are typically of a similar size either side of a channel, but the western flank may be larger in the southern hemisphere due to the Coriolis effect (Maldonado et al., 2005).

- The inner, channel-facing walls of levees may be subject to mass wasting and collapse, resulting in the development of terraces, slide blocks and debrites (Hansen et al., 2015).
- Sediment waves are often present on the outer flank of the western levee (in the southern hemisphere), are typically 3-20 m high and tend to form at an angle oblique to the channel through overbank deposition (Migeon et al., 2001; Normark et al., 2002). Sediment waves may also be present where the turbidite has been deposited on irregular topography (Parsons et al., 2007).
- Channels are generally sinuous (Mayall et al., 2006) and exhibit systematic, morphological changes with distance from the margin (Nelson and Nilsen, 1984 *in* Maldonado et al., 2005).

2. Internal architecture and sedimentology:
    - Deep-water turbidites are rarely heavily bioturbated (the sudden nature of turbidite deposition may bury and kill benthic fauna, with bioturbation limited to the periods in between turbidite deposition) (Wetzel et al., 2008). Where there is bioturbation, this tends to decrease with distance from the channel (Hansen et al., 2015).
    - Thin-bedded (<10 cm thick beds) turbidites are commonly deposited on levees adjacent to deep-water turbidity current channels and often comprise inter-bedded sand, silt and mud (Garcia et al., 2015; Hansen et al., 2015). They typically form from the overspill of the upper, lower-density part of turbidity currents. Thicker beds, which may or may not be made of coarse grained sediment, are more typically confined to the channels (Hansen et al., 2015).
    - Proximal turbidites may be massive or contain only poorly developed lamination, if deposition occurred before grain movement by traction on the bed was sufficient to form laminae (Middleton, 1993).

- Distal turbidites may contain well-developed plane lamination or ripple cross-lamination (Middleton, 1993). Normal grading may be present on distal turbidites (as the low slope angle enables lateral grading to develop) (Walker, 1967). However, grading in fine-grained turbidites is often impossible to distinguish visually (Talling et al., 2012).
- A basic, idealised model for deposition of fine-grained turbidites suggests that where mud and silt laminae are present, they may be overlain by normally graded beds and then massive sediment, based on the behaviour of mud flocs (Stow and Bowen, 1978; Kranck, 1984).
- Laminated turbidite muds (T_{E-1} in Talling et al., 2012) are better developed in proximal sediments. They contain laminae typically 0.1 to <2 mm thick. Massive and graded muds (T_{E-2}) typically overlie the laminated muds. Massive ungraded muds (T_{E-3}) tend to be found in thicker intervals than T_{E-1} and T_{E-2} and are often deposited in ponds in topographic lows (Talling et al., 2012).
- Turbidite sediments recovered from close to the channel systems on the Antarctic Peninsula drifts contain frequently graded and/or laminated coarse-grained deposits with sandy intervals, silty layers up to 4 cm thick and erosive bases (Lucchi et al., 2002; Lucchi and Rebesco, 2007).
- Basal contacts can be sharp and/or erosional, whilst upper contacts can be gradational (Shanmugam, 2010).
- Material is often locally-derived and reflects local geologies.
- Shallow-water microfauna may be present (reworked from shelf sediments) (Howe, 2008).

3. Seismic attributes and facies:
    - Reflectors are approximately symmetrical either side of the channel, are continuous and thin towards the outer flanks of the levees, resulting in a so-called “gull-wing” geometry in some channel-levee systems (Nelson et al., 1993; Maldonado et al., 2005).

3.2.3. Trough Mouth Fans

Three large Trough Mouth Fans (TMFs) are present on the Antarctic upper continental rise; the 180 km wide Belgica TMF in the Bellingshausen Sea, the 100-150 km wide Crary TMF in the southern Weddell Sea and the 150 km wide Prydz Channel TMF off Prydz Bay (Ó Cofaigh et al., 2003; Dowdeswell et al., 2008). Smaller submarine fans are also present elsewhere around Antarctica (see Ó Cofaigh et al., 2003).

TMFs form when significant down-slope deposition (all three Antarctic TMFs lie offshore of ice streams) occurs on a continental slope of very low gradient (1-2°), leading to the accumulation of prograding, thick wedge-shaped deposits (Dowdeswell et al., 2008). The Belgica TMF is composed of diamictic sediment which was supplied, at least during the last glacial period, by an ice stream in the Belgica Trough which was probably grounded at the shelf edge and supplied sediment to the TMF via debris flows (Dowdeswell et al., 2008).

3.2.4. Contourites

Contourite deposits or drifts have been identified around Antarctica and attributed to both wind-driven currents (e.g. the ACC) and geostrophic, "contour currents" which flow along bathymetric contours (Rebesco et al., 2008). This thesis will use the definition of a contourite drift as proposed by Rebesco et al. (2008) of a sedimentary body affected and deposited by the action of any persistent current in contact with the sea floor, as opposed to purely contour currents, where the action of the current causes sediment re-suspension, entrainment, transport and/or deposition (Rebesco et al., 2008). At high latitudes, the sediment is commonly supplied by glacially-derived turbidity currents and debris flows, benthic storms (re-suspension of sediments from a short-term increase in current velocity), the vertical settling of biogenic, ice-rafted and volcanic material and the re-suspension of particles by benthic animals (He et al., 2008).

The particular type of drift deposited depends on a range of factors including the amount of sediment supply and load in the bottom current and nepheloid layer, the velocity of the bottom current and the basin physiography and tectonic structure (e.g. presence of steep slopes or ridges). There are numerous different types of contourite

drift, briefly summarised here but detailed further in Faugères and Stow (2008) and Stow et al. (2002).

Sheeted drifts can cover broad areas with uniform layers of sediment and form where basin physiography restricts current outflow and encourages the formation of a gyre (abyssal sheeted drifts), where currents up- or down-well and deposit sediments at the foot of a ridge or slope (slope sheeted drifts) or where unconfined currents run parallel to the foot of a ridge of slope (plastered drifts) (Faugères and Stow, 2008).

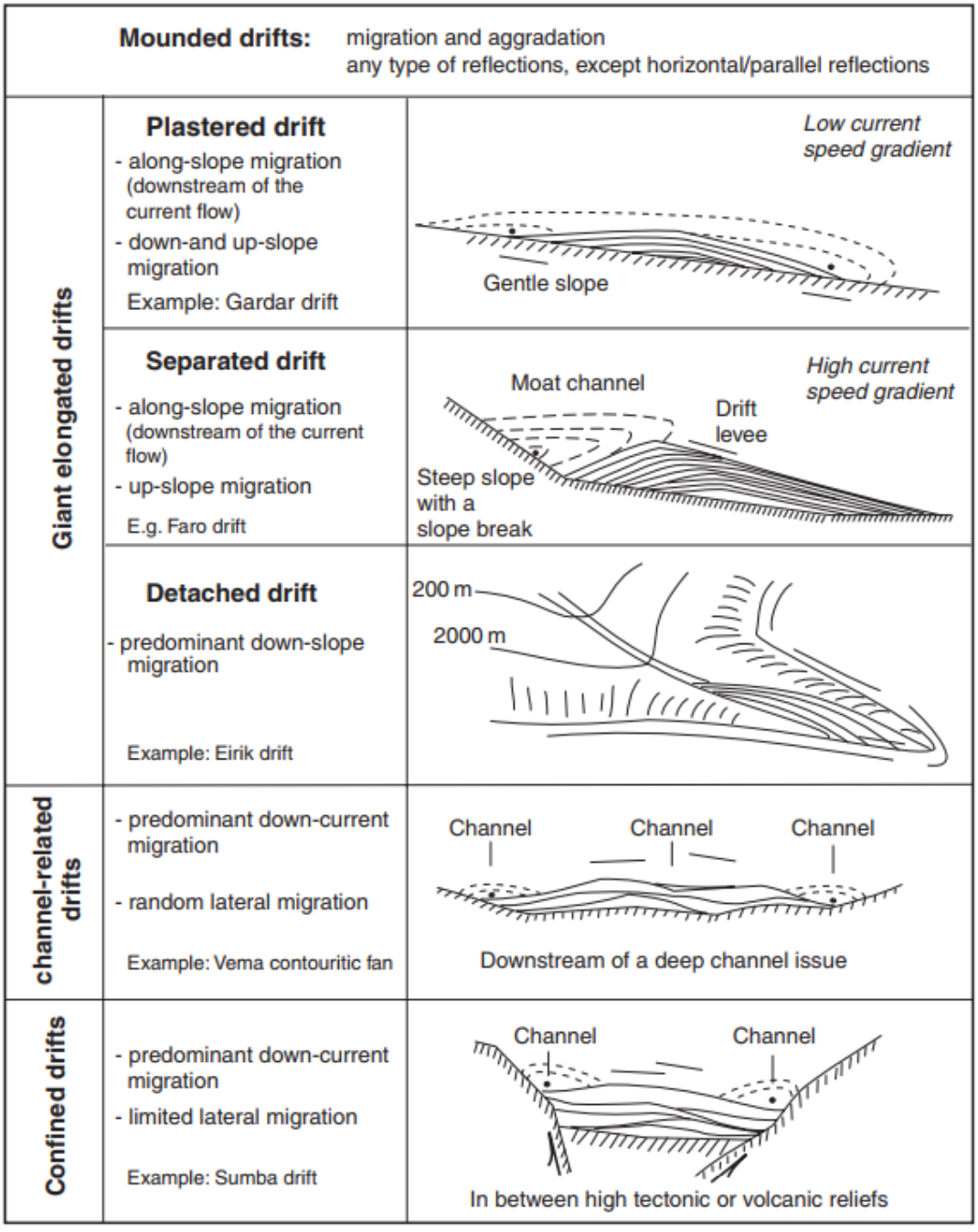

Figure 3.2: Types of mounded contourite drifts, from Faugères and Stow, 2008.

In contrast to sheeted drifts, mounded drifts are often elongate. Mounded drifts include plastered drifts, which are typically located on a low-gradient slope under a low-velocity bottom current (Figure 3.2). Separated drifts are found at the foot of often steep slopes and lie parallel to the margin, from which they are separated by a moat or channel. Detached drifts show progradation over time in response to margin changes or current interactions. Channel-related drifts are related to areas of constrained and higher velocity bottom current flow, whilst channel-patch drifts are small and restricted to the floor and walls of channels. Contourite fans are fan-shaped and deposited downstream of an area of constrained bottom current flow. Confined drifts form under low-velocity bottom currents in a confined areas such as a basin (Faugères and Stow, 2008).

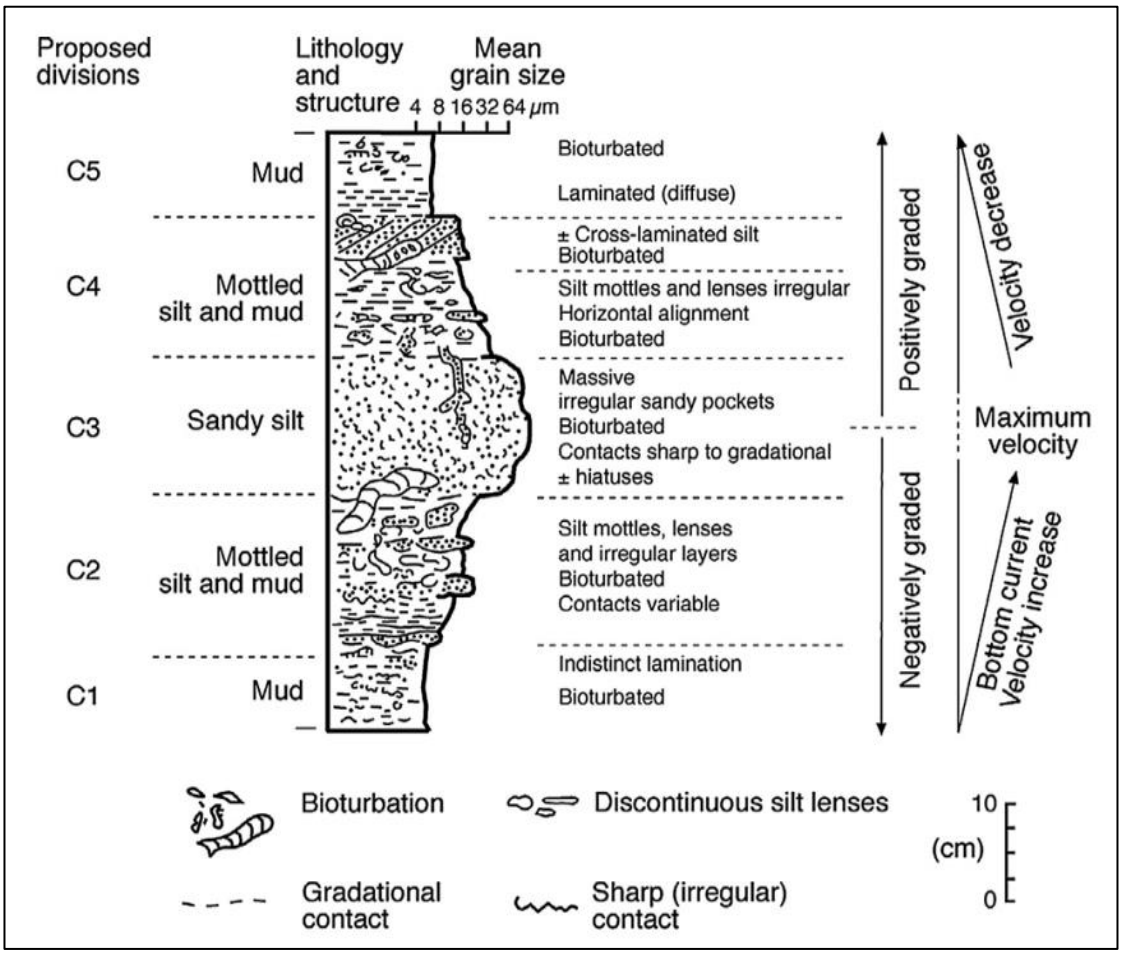

Figure 3.3: Contourite facies model from Stow and Faugères, 2008.

Criteria for identifying contourite deposits, particularly when distinguishing current-winnowed contourite sands from turbidite spill-over, are widely disputed (Rebesco et al., 2008, Nelson et al., 2003). A contourite facies model (Figure 3.3) suggests contourite deposits can show a five-stage vertical succession based on variability in bottom current velocity and/or sediment supply (Stow and Faugères, 2008). The five divisions of the sequence are described as follows (Stow et al., 2002; Stow and Faugères, 2008):

C5: Upper muddy contourite division

C4: Upper modelled silty contourite division

C3: Middle sandy contourite division

C2: Lower mottled silty contourite division

C1: Lower muddy contourite division

Partial sequences are at least as common as full sequences and are often the result of a period of erosion or non-deposition caused by an increase in bottom current velocity (Stow and Faugères, 2008).

Diagnostic criteria of mounded contourite drifts in particular can be considered under the following three headings (cf. Rebesco et al., 2008):

1. Overall architecture:
    - Contourites are typically orientated parallel to the continental margin due to the flow of bottom currents along bathymetric contours. However, they have also been identified lying oblique or perpendicular to the margin, particularly where down-slope deposition has been substantial such as the drifts located west of the Antarctic Peninsula (e.g. Rebesco et al., 1996) and in the Cosmonaut Sea (Kuvaas et al., 2005). This occurs as a result of the western levee being preferentially developed as a result of the Coriolis effect, leading to the channel and levees migrating east-wards, increasingly oblique to the margin (Faugères et al., 1999; Solli et al., 2007).

- Drifts often stand higher above the sea floor than channel-levee deposits (e.g. Scheuer et al., 2006b).
- Contourite drifts are typically asymmetric, with a gently-sloping flank facing into the flow and steeper flank facing away from the flow (e.g. Rebesco et al., 1997; Kuvaas et al., 2005).
- Furrows, moats and sediment waves are often present and aligned with the direction of flow (Wynn and Masson, 2008).

2. Internal architecture:
    - Frequently heavily bioturbated. The notion of bioturbation being a defining feature of contourites is disputed, with some authors arguing that bioturbation is also common in other marine deposits (e.g. Shanmugam, 2016). However, the consensus is that pervasive bioturbation is particularly common in contourite deposits due to slow, gradual deposition and the additional lateral supply of food (Stow and Faugères, 2008; Wetzel et al., 2008).
    - Lack of lamination. Widely disputed, with some laminated deposits interpreted as contourites due to depositional sorting (e.g. Shanmugam, 2008), but the consensus is that current speeds and sediment input are often too low to result in lamination through sorting, and any lamination that does occur is often masked through bioturbation (Rebesco et al., 2008).
    - Typically irregular grading (due to the persistent nature of a bottom current) (Howe, 2008). Muddy contourites are typically silty clay and poorly sorted (Stow and Faugères, 2008).
    - Far-travelled material present reflecting the source area and path of the bottom current.
    - Lack of shallow-water microfauna (Howe, 2008).

3. Seismic attributes and facies:
    - Reflectors are evenly spaced, lenticular, upwards-convex and asymmetric about the channel (Faugères et al., 1999; Kuvaas et al., 2005; Maldonado et al., 2005).
    - Reflectors diverge downstream and with distance from the main current path, where slower flow speeds allow for increased deposition (Maldonado et al., 2005; Kuvaas et al., 2005).

Contourites are common features of the Antarctic continental margin. Their presence usually coincides with areas of past or present significant down-slope transport as a result of sediment deposition on the outer shelf by repeated glacial advance, supplying bottom currents with large volumes of suspended sediment (e.g. the mixed contourite-turbidite drifts located west of the Antarctic Peninsula (Rebesco et al., 1996, 1997)). However, the development of contourites relates more to the effectiveness of the mode of down-slope transport than its specific nature (Michels et al., 2001).

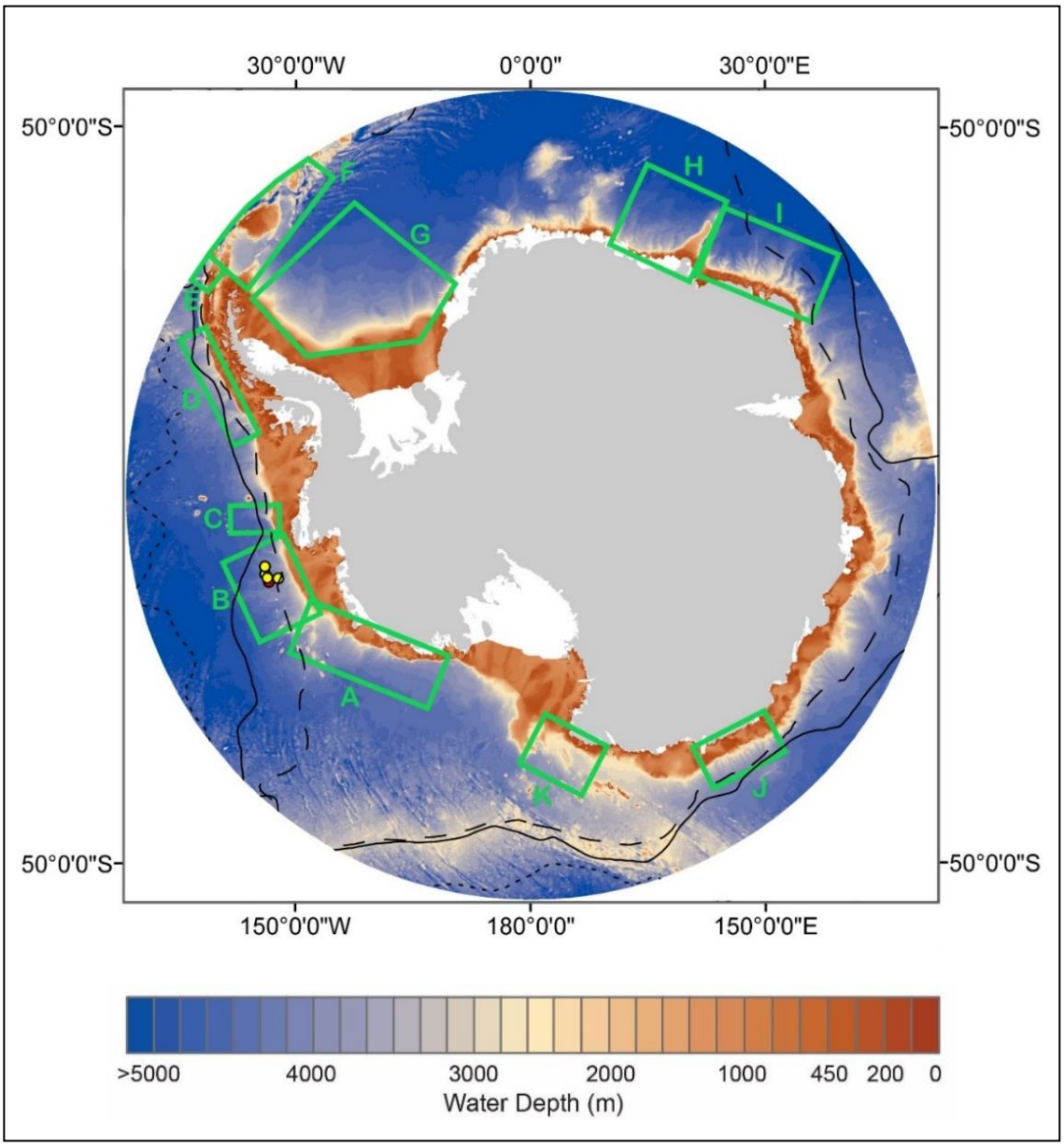

Figure 3.4: The location of contourites identified on the Antarctic continental margin. Green boxes indicate the locations of published work, with letters referred to in the main text below. The dashed black line indicates the sACC, the full black line indicates the sACCf and the dotted black line indicates the Polar Front. Grounded ice is shown in grey, ice shelves in white (BEDMAP 2, Fretwell et al., 2013). Bathymetric data from IBCSO (Arndt et al., 2013).

The following offers a brief description of contourites identified in the literature which are located south of 60°S and displayed in Figure 3.4:

A: Central and Western Amundsen Sea: In the central Amundsen Sea, topography has had a dominant control over the position of drifts, with elongate mounded and attached

drifts forming in the vicinity of the Marie Byrd Seamounts (Uenzelmann-Neben and Gohl, 2012, 2014) (see Chapter 3.4.2). In the western Amundsen Sea, stacked, mounded drifts dating to <68 Ma exhibit a geometry suggestive of an eastwards-flowing bottom current from the Ross Sea (Lindeque et al., 2016).

B: Eastern Amundsen Sea: The mounds featured in this research have been interpreted as "levee-drifts", having formed through a combination of turbiditic and contouritic processes, and have a geometry suggestive of being under the influence of an eastwards-flowing bottom current (Uenzelmann-Neben and Gohl 2012, 2014) (see Chapter 3.4.3).

C: Western Bellingshausen Sea: Three small sediment mounds and one large (130 km wide) elongate mounded drift, which is asymmetric, suggestive of a westwards-flowing bottom current flowing within 55 km of the continental slope. There is no channel separating the drift from the slope (Nitsche et al., 1997, 2000; Scheuer et al., 2006b, 2006c; Gohl et al., 2007) (see Chapter 3.3.1).

D: Bellingshausen Sea: 12 large elongate mounded drifts are present west of the Antarctic Peninsula, having formed through a combination of turbiditic and contouritic processes under the influence of the westwards-flowing Weddell Sea Deep Water (e.g. Rebesco et al., 1997) (see Chapter 3.3.2).

E: Southern Drake Passage: A range of buried and surface channels, sheeted drifts, plastered drifts and separated drifts and elongate-mounded drifts are present in an area of westward Weddell Sea Bottom Water (WSBW) flow and eastward LCDW flow within the ACC (Martos et al., 2013).

F: Northern Weddell Sea and Southern Scotia Sea: Seven different types of contourite drifts (giant elongated-mounded, elongated, plastered, basement/tectonic, levee, sheeted and transverse drifts) were identified by Maldonado et al. (2005) in the northern Weddell Sea. There is little down-slope deposition, so the type of drift is largely controlled by the speed of the WSBW bottom current (a function of the degree of confinement) and the basin physiography, particularly the position of large ridges. There are numerous giant elongated-mounded drifts located near the continental margin associated with the flow of bottom currents along the base of the slope in a moat. These stand up to 400 m higher than the surrounding seafloor, are 10-200 km long and 5-20

km wide and exhibit asymmetry, with a gently-sloping flank facing into a channel and the path of the WSBW. Sediment waves are also common and active in water depths of 2800-3100 m under AABW flow, with a typical amplitude of 20-50 m and wavelength of 2-4 km, which may have originally formed through turbidity current action but are now maintained by the action of AABW (Howe et al., 1998).

Two distinct areas of contourites were identified by Garcia et al. (2016) in the southern Scotia Sea. The Scan Basin contains a large (a few hundred kilometres wide) contourite fan related to the increased velocity of northwards-flowing WSDW as it flows through a constricted gateway, depositing the fan (also known as a channel-related drift) downstream. The area around Discovery Bank is under the influence of eastwards flow of both WSDW and dense CDW and contains sheeted drifts on flat areas, a plastered drift leading off from the continental slope and several small mounded drifts (<30 km long) fed by mass transport deposits and separated from the continental slope by a contourite moat.

G: Western Weddell Sea: Compared to the north-western Weddell Sea, higher sedimentation rates in the western Weddell Sea (due to increased proximity to glaciers leading to a higher sediment supply to the continental rise) combined with the less focused, lower velocity bottom current have resulted in the dominance of channel-levee deposits. Contourite drifts have developed in areas where multiple slide deposits have been identified on the slope. The drifts exhibit a similar 3-stage growth sequence as reported by Rebesco et al. (1997) in the drifts west of the Antarctic Peninsula (Michels et al., 2001).

H: Riiser-Larsen Sea: One large separated drift (300 km long, 120 km wide), one large plastered drift (150 km long, 50 km wide) and two small confined drifts (<70 km long) are present on the upper and mid continental rise in water depths of 3000 to 5000 m, fed by turbidity currents and the ACC. The turbidity currents, which previously delivered material to the lower continental rise and abyssal plain, were later restricted by the accumulated material, leading to turbidites being deposited progressively closer to the margin. Drift development occurred mostly in the mid to late Miocene after the intensification of the ACC, with the continued input from turbidity currents leading to larger western levees and eastwards migration of channels of the drifts on the upper continental rise (Solli et al., 2007).

I: Cosmonaut Sea: Elongate drifts are found on the lower continental rise, lying perpendicular to the continental margin, reflective of mixed turbidite and contourite deposition under the westward-flowing bottom current. The drifts lie in water depths of 3000-4500 m, are up to 100 km long and 70 km wide and, although lacking significant asymmetry, have seismic units which converge increasingly with distance from the channels which separate the drifts and some drifts feature sediment waves. On the upper continental rise, turbidity currents are the dominant control on deposition and mounded deposits, typically >100 km long, 10-100 km wide and 700-1200 m higher than the channels which separate them, with no consistent symmetry or asymmetry, have been interpreted as turbidites (Kuvaas et al., 2005). A buried plastered drift is also present on the upper continental rise running 1200 km along the margin, which may represent deposition by bottom currents before the initiation of large-scale glaciation on Enderby Land (Kuvaas et al., 2005).

J: Wilkes Land: Asymmetric sediment mounds, 25-50 km wide and 275-490 m high, reflective of mixed contourite and turbidite deposition are located on the upper continental rise in water depths of 2500 – 3000 m. The mounds have a gently-sloping flank facing east, with stratified and continuous reflectors on seismic profiles suggestive of deposition under the influence of the westward-flowing AABW. The steeper western flank frequently contains sediment waves and evidence of channel cutting. The mounds were largely constructed before c.2.5 Ma and deposition since then has been limited to low sedimentation rates (0.33-0.41 cm/kyr) and adding to, rather than changing, the mound geometry, similar to the “Drift Maintenance” stage of the Antarctic Peninsula drifts of Rebesco et al. (1997). Very large channel-levee deposits are also present (up to 900 m high above the surrounding seafloor) where turbidity currents have dominated the deposition (Escutia et al., 2002).

K: Pennell Coast and Adare Basin: The upper slope and shelf (water depths 200 to 1200 m) off the Pennell Coast have a surface layer of 10 to >100 cm thick sand interpreted as a contourite deposit under the influence of the ACC deposited since 9 ka. The interpretation was supported by the volcanic geology of the sand, suggesting westwards transport of 70 km, and an east to west decrease in grain size across the deposit (Rodriguez and Anderson, 2004). To the west, a series of turbidite deposits and contourite drifts have been identified in the Adare Basin, largely fed by turbidity currents

through the abundant channels cut into the steep continental slope and shaped by AABW in the Ross Sea Gyre. The AABW is channelled by the bathymetry of the trough which has resulted in greater sediment deposition in the west. Multi-channel seismic profiles were used to identify stages of drift development which match the drift growth and maintenance stages seen in the Bellingshausen and Weddell seas, suggesting that Antarctic-wide changes in the development of the ice sheet and ocean currents affected the deposition of contourites around the continental margin (Whittaker and Müller, 2006).

3.3. Depositional processes and features in the Bellingshausen Sea

3.3.1. Depositional features of the central and western Bellingshausen Sea

Sediment mounds and channel systems have been identified across much of the continental rise of the West Antarctic Pacific Margin. Off Ellsworth Land in the central and western Bellingshausen Sea, Nitsche et al. (1997, 2000), Dowdeswell et al. (2008), Gohl et al. (2007) and Scheuer et al. (2006b, 2006c) identified three minor sediment mounds and waves in the surrounding sea floor (Depocentre A), the Belgica Trough Mouth Fan (Depocentre B) and one very large (130 km wide and 700 m high) sediment mound, thought to be a contourite drift deposit, which suggests deposition under the influence of a westwards-flowing bottom current with a gently sloping eastern flank, containing sediment waves and two channels (one of which has migrated westwards), and a steep western flank (Depocentre C). It differs from the Antarctic Peninsula drifts in the absence of a channel separating the drift from the slope, perhaps related to the much lower slope gradient reducing the amount of energy contained in the gravity-driven debris flows, leading to sediment preservation rather than erosion (Nitsche et al., 2000). 55 km north of this drift lies a channel-levee structure which is narrower and exhibits the opposite asymmetry to the drift, with a gently sloping western flank and steep east flank facing the channel, suggesting bottom current intensity here decreases with distance from the margin, leading to the Coriolis effect being the dominant control over the mound asymmetry (Scheuer et al., 2006c).

3.3.2. Contourite drifts west of the Antarctic Peninsula

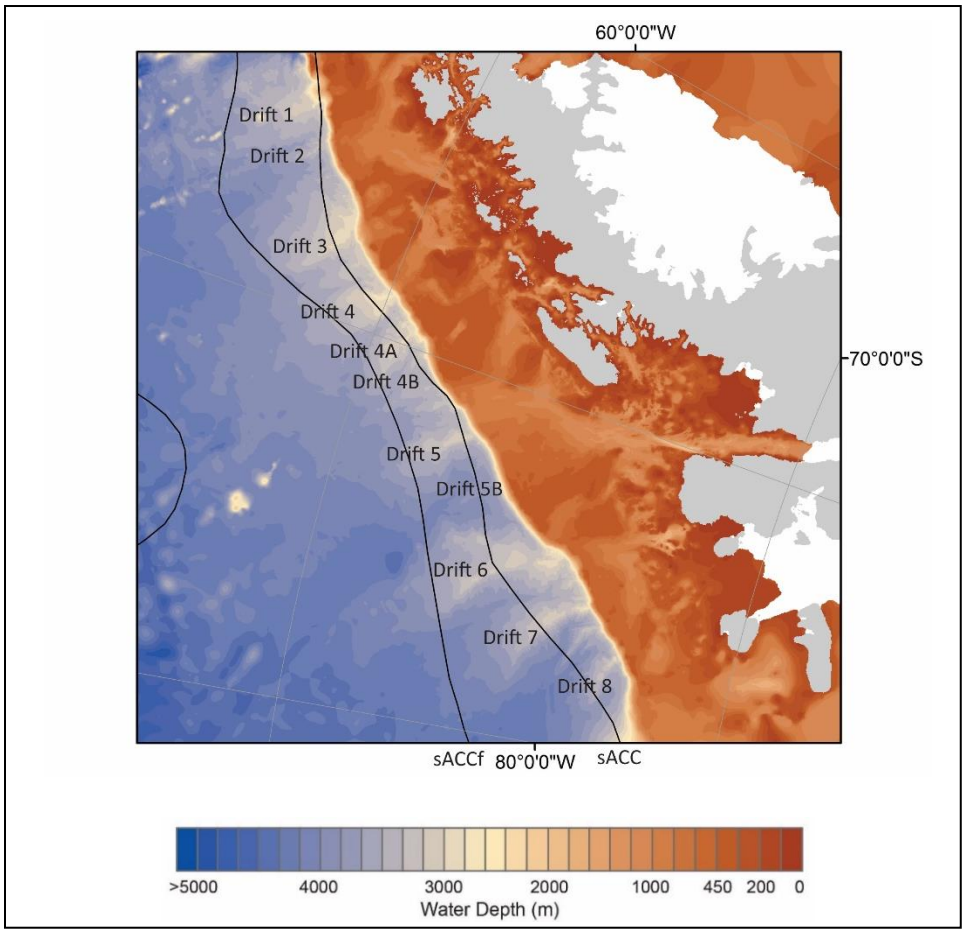

Figure 3.5: Bathymetric map of the contourite drifts located west of the Antarctic Peninsula in the Bellingshausen Sea. Bathymetry from IBCSO (Arndt et al., 2013). Position of the southern Antarctic Circumpolar Current front (sACCf) and the southern boundary of the Antarctic Circumpolar Current (sACC) from Orsi et al., 1995.

Twelve large mounds of hemipelagic sediment are located less than 200 km from the shelf break between 63° and 69°S on the continental rise of the Bellingshausen Sea, west of the Antarctic Peninsula (Rebesco et al., 1997; Hillenbrand et al., 2008a) (Figure 3.5). The mounds date to at least the mid-Miocene (Rebesco et al., 2002) and are widely accepted to be elongate, mounded contourite drifts (e.g. Lucchi et al., 2002; Hillenbrand et al., 2008a). Rebesco et al. (1996) first proposed this interpretation based on the mound asymmetry and geometry, the dendritic channel system, high sedimentation rates and the fine-grained nature of the mounds, which Stow et al. (2002) suggest developed according to their Modified Fan-Drift model. They are located in water depths between 2700 and 3700 m (Camerlenghi et al., 1997) under an ambient south-westwards flowing bottom current of modified Weddell Sea Deep Water (WSDW), a

form of AABW which has affected the drifts since at least 9.4 Ma (Rebesco et al., 1997; Hillenbrand et al., 2008a). Flow direction is generally in a south-west direction but there is some evidence to suggest the WSDW follows the bathymetric contours and flows in an anti-clockwise direction around at least one of the drifts (Camerlenghi et al., 1997).

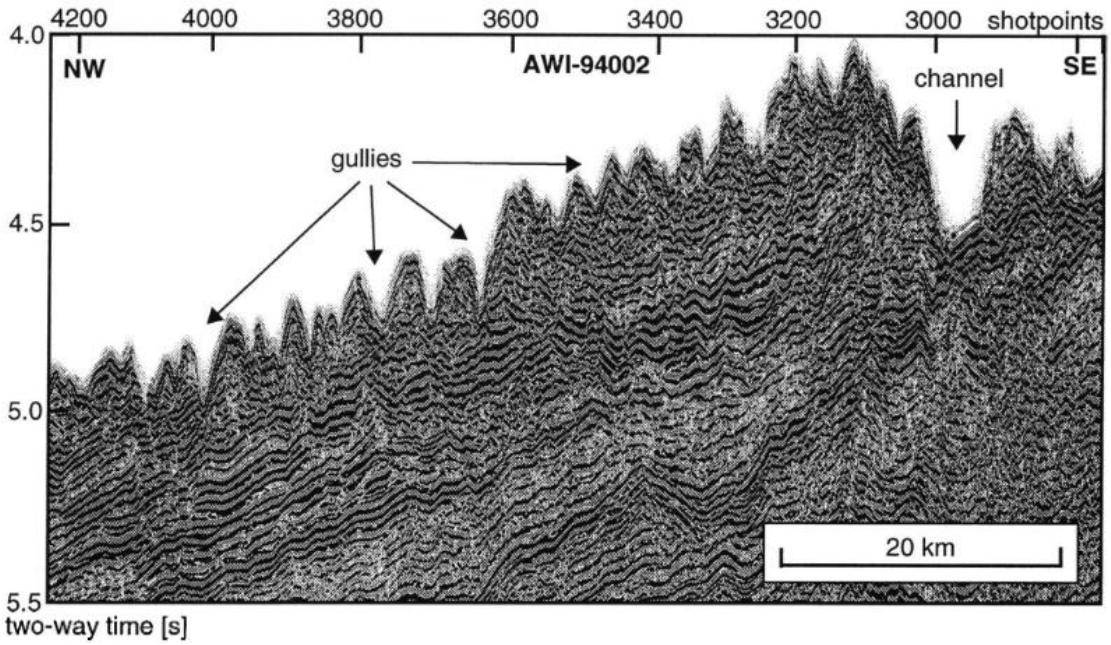

Figure 3.6: Multi-channel seismic profile of the south-western flank of Drift 8, located west of the Antarctic Peninsula, showing gullies on the gently-sloping, north-western flank and a channel at foot of the steeper, south-eastern flank (Figure 4 from Nitsche et al., 1997).

The long axes of the drifts lie perpendicular to the continental slope, aligned approximately north-west to south-east, and the largest drifts are up to 200 km long, 70 km wide and stand 1 km high above the sea floor (Rebesco et al., 2002). The continental slope is very steep (13-17° (Larter and Cunningham, 1993)) and the lower slope contains a series of channels which exhibit a dendritic pattern on the upper rise and run between the drifts (Rebesco et al., 1996; Rebesco et al., 2002). On each drift, the side facing the abyssal plain (generally facing the north-east) is gently-dipping (c.0.8°), with parallel reflectors suggesting laterally continuous sedimentation. The side facing the continental slope (generally facing the south-west), is steeper (c.2°), contains hiatuses, is unstable and subject to mass wasting, and contains small channels connected to the larger

channels which run between the drifts (Figure 3.6) (Rebesco et al., 1996, 1997, 2002; Camerlenghi et al., 1997).

Composition

Sediment cores have shown the drifts to be made of predominately fine-grained material, which is 70–90% terrigenous, even in interglacial periods (Camerlenghi et al., 1997). The uniform sedimentology of the terrigenous material suggests it was sourced from a local and limited region of the Peninsula, with little far-carried material (Pudsey, 2000). Sand-sized grains are primarily biogenic (Camerlenghi et al., 1997), with small amounts of mostly local IRD present in interglacial sediments amounting to 10-15% of the accumulation of terrigenous grains in the late Holocene (Hillenbrand et al., 2008).

Pudsey (2000) and Lucchi et al. (2002) carried out multi-proxy analysis of sediment cores taken primarily from Drift 7, and reported two main sedimentary types which suggest significant glacial-interglacial climatic control upon sedimentation.

1. Hemipelagic muds. Attributed to interglacial periods, these are brown, bioturbated muds with 5% sand and low sedimentation rates of 1.1 to 4.3 cm/kyr, and comprise mostly biogenic material from vertical settling and dispersed IRD. Diatoms and foraminifera are common, with ice-proximal cores containing up to 50% carbonate, although there are high modern rates of silica and carbonate dissolution by corrosive WSDW (Pudsey, 2000). These sediments typically contain high (≥25%) smectite (largely from the volcanic deposits of the South Shetland Islands) (Hillenbrand and Ehrmann, 2005) and up to 16% kaolinite (Lucchi et al., 2002), likely transported from the Amundsen Sea via iceberg rafting (Hillenbrand et al., 2008).
2. Terrigenous muds. Attributed to glacial periods, these are grey, laminated muds with <0.5% sand and >65% clay, with little biogenic content or IRD and sedimentation rates of 1.8 to 13.5 cm/kyr (Pudsey, 2000; Lucchi and Rebesco, 2007). The sediments are poorly sorted but sorting appears to increase and grain-size becomes finer with distance from the margin (Lucchi and Rebesco, 2007). Lucchi et al. (2002) proposed a variety of depositional processes to explain their origin, including turbidity currents, sediment plumes and reworking by

bottom currents. These units also contained laminated, silty layers or lenses, attributed by Lucchi et al. (2002) and Lucchi and Rebesco (2007) to the occasional spill-over of turbidity currents from the channels. IRD is limited to thin gravelly mud layers which contain <40% sand and gravel (Lucchi and Rebesco, 2007). Little carbonate or silica is preserved in these sediments, primarily indicating increased sea-ice cover during glacial periods, with diatom production largely restricted to polynyas (Pudsey, 2000). These sediments typically contain ≤20% smectite (likely due to increased dilution), relatively high (<42-60%) chlorite (due to increased terrigenous supply from the chlorite-rich Antarctic Peninsula during glacial periods) and no kaolinite (due to reduced ice-rafting from the Amundsen Sea) (Lucchi et al., 2002; Hillenbrand et al., 2008).

There are also clear transitional layers between glacial to interglacial periods and vice versa, when, in particular, colour and clay mineralogical characteristics are intermediate between the two main sedimentary types. This transition is marked by a gradual boundary in Late Quaternary sediments (Lucchi et al., 2002; Hepp et al., 2006). The sediments show the response of glaciers on the Antarctic Peninsula responded much faster to initial interglacial warmth than seen elsewhere on the continent, with increases in ice rafting occurring at the same time as increases in biogenic sedimentation (Pudsey, 2000). The transition from interglacial to glacial sediments is also commonly marked by gravel-rich mud layers, which have been attributed to IRD (Lucchi et al., 2002).

Formation

Rebesco et al. (1996, 1997) identified three key sections in the acoustic stratigraphy of the drifts which relate to drift development. Above the c.36 Ma basement:

1. The “Pre-Drift Stage”, >36 Ma to 15 Ma (Rebesco et al., 1997). Laterally continuous reflectors in the acoustic stratigraphy suggest only thin sediment drapes were deposited during the initial stages, suggesting sedimentation was mostly pelagic and the mounds were not yet being shaped (Rebesco et al., 1996). Later, filling then increased, probably as a result of increased terrigenous input (Rebesco et al., 1996). An erosional unconformity is then present, perhaps caused by a structural change

such as faulting, which led to the development of the mound crest (Rebesco et al., 1996). There is conflicting evidence for bottom current activity at this time, e.g. Rebesco et al. (1997) argue the laterally continuous, horizontal reflectors of internal stratigraphy suggest little to no bottom current activity, but Uenzelmann-Neben (2006) argued the drift geometry suggests a bottom current flowing towards the southwest was present on Drift 7 throughout this period, particularly strongly 25-15 Ma.

2. The "Drift Growth Stage", 15 Ma to 5 Ma (Rebesco et al., 1997). This stage saw high sedimentation rates and development of the mound shape, with the crests of the mounds migrating towards the north-east (Rebesco et al., 1997). The lack of erosional hiatuses suggests a persistent bottom current was present, which was both shaping the mounds and likely being diverted by the new topography (Camerlenghi et al., 1997). Glacial expansion onto the shelf is thought to have deposited the first prograding sequences at this time, supplying increased terrigenous material via turbidity currents (Rebesco et al., 1996; Rebesco et al., 1997).
3. The "Drift Maintenance Stage", 5 Ma to present (Rebesco et al., 1997). The present-day stage is characterised by parallel, gently dipping reflectors on the gently-sloping side of the drifts, suggesting deposition has continued, but without any significant changes to the drift shape or orientation (Rebesco et al., 1996).

The repeated presence of grounded ice near the shelf break has led to the deposition of sediment lobes and prograding wedges on the outer shelf (Lucchi et al., 2002). The failure of these lobes, and subsequent sediment slumps on the continental slope, led to small debris flows on the slope (Rebesco et al., 1997). Some of the debris flows evolved into turbidity currents, travelled in gullies on the slope and channels running between the drifts, and were particularly frequent during glacial periods due to the high sediment supply (Rebesco et al., 1997). The dominance of deposition on the north-east channel levee (the opposite of what would be expected due to the Coriolis effect), suggests the mounds are not overspill or levee deposits and are fed predominantly by along-slope, rather than down-slope processes (Rebesco et al., 1997). Rather, the fine grained components of the turbidity currents become entrained in the south-west flowing bottom current, which must have flown persistently since at least the Miocene as there

is no evidence to suggest a large hiatus or erosional episode (Rebesco et al., 1997). Some sediment also became entrained in the bottom current via meltwater plumes during peak glacial periods when the ice was close to the shelf break, particularly during MIS 6 (Pudsey, 2000). Deposition also occurs in the channels and on the steep, slope-facing side of the mounds, but this is largely removed by subsequent turbidity currents and slope instability, shown as small gullies cut into the steep side of the mounds (Rebesco et al., 1997).

The slow moving bottom current then allows the fine-grained terrigenous material from turbidity currents and meltwater plumes to be deposited, forming the mounds, together with current-transported material, biogenic matter, IRD and minor aeolian dust (from South America) which are deposited through vertical settling in the water column (Hillenbrand et al., 2008a). The bottom current also shapes the mounds, maintaining the elongate and asymmetric shape through deposition. WSDW flow was reduced during glacial periods (Rebesco et al., 1997), allowing for increased deposition of clay and poorly sorted sediments, but is still relatively weak today with mean current speeds 8 m above the bed either side of Drift 7 near-identical at c.6.2 cm s^{-1} and reaching a maximum velocity in a ten month period of 20 cm s^{-1} (Camerlenghi et al., 1997). These speeds are too low to erode sediments and are only capable of transporting clay and silt-sized grains, with flow speeds low enough (<5 cm s^{-1}) to enable clay deposition for only 30% of the ten-month period (Camerlenghi et al., 1997). Seismic stratigraphy of the mounds has allowed correlation of discrete layers between mounds 400 km apart, suggesting they have been subject to similar sedimentation rates and styles and synchronous changes in bottom current speeds (Rebesco et al., 1997).

3.4. Depositional processes and features in the Amundsen Sea

A series of sediment mounds have been identified on the upper continental rise of the Amundsen Sea using swath bathymetry and multi-channel seismic profiles (Yamaguchi et al., 1988; Gohl et al., 1997; Scheuer et al., 2006a, Uenzelmann-Neben and Gohl, 2012, 2014; Lindeque et al., 2016). Two sediment cores from the mounds have been studied to date and used to reconstruct WAIS behaviour and conditions in the Amundsen Sea

since 1.8 Ma (PS2547 in Hillenbrand et al., 2002; PS58/254-1 in Hillenbrand et al., 2009a and Konfirst et al., 2012).

Lindeque et al. (2016) mapped the seismic stratigraphy of the Amundsen Sea Basin. Table 3.1 shows how the four seismic units of the Amundsen Sea mounds, as outlined by Uenzelmann-Neben and Gohl (2012), correlate to other seismic units in the Amundsen Sea and Ross Sea and the estimated ages for each horizon.

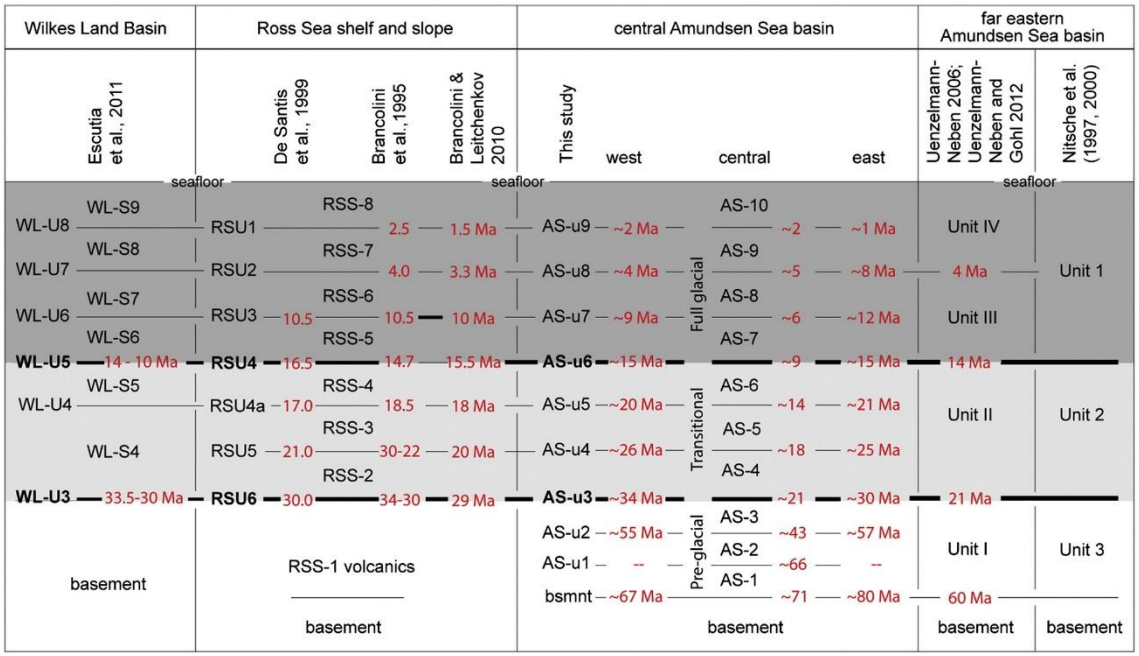

Table 3.1: Seismic stratigraphy correlation chart showing the seismic units and boundary horizons of the Ross Sea and Amundsen Sea, from Lindeque et al. (2016).

3.4.1. Sediment mounds in the western and central Amundsen Sea

Recent work has identified a series of sediment mounds throughout the western and central Amundsen Sea using seismic profiles (Lindeque et al., 2016). In the western Amundsen Sea, Lindeque et al. (2016) suggested the mounds are contourite drifts based on internal stratification and geometry. Drifts visible on the modern seafloor surface are generally stacked drifts, 50-100 km wide and 200-300 m high, with a gently sloping western flank and steeper eastern flank suggesting they are under the influence of an eastwards-flowing bottom current and have been since at least the mid-Miocene, 16 Ma (Lindeque et al., 2016).

In the central Amundsen Sea, the complex geological history means drift formation is largely controlled by the topography and faults, with inter-drift areas showing more variability in seismic structure than elsewhere in the Amundsen Sea (Gohl et al., 1997). Elongate drifts have formed in the vicinity of the Marie Byrd Seamounts and are fed largely by down-slope processes but are also affected by an eastwards flowing bottom current. This has resulted in a steep flank facing towards the seamounts, from which the drifts are separated by a channel, and a western levee which is generally larger than the eastern levee (Uenzelmann-Neben and Gohl, 2012).

Core P2547 was recovered from the distal crest of a sediment mound in the central Amundsen Sea, formed from the interaction of turbiditic and contouritic processes. IRD and foraminiferal tests comprise a greater amount of the sediment in PS2547 than cores taken from the surrounding continental rise, where the deeper sediments likely received less terrigenous input from ice rafting and foraminifera would be more prone to dissolution (Hillenbrand et al., 2002). The main glacial-interglacial variation in the mound sediments was in the carbonate content, with olive brown, bioturbated and IRD-rich mud deposited during both glacial and interglacial periods but $CaCO_3$ concentrations much higher during interglacials (e.g. 4 wt% in MIS 6 compared to 45 wt% in MIS 5). In contrast, sediments recovered from the surrounding continental rise showed grey, laminated, terrigenous mud deposited during glacial periods (Hillenbrand et al., 2002).

3.4.2. Sediment mounds in the eastern Amundsen Sea

Nitsche et al. (2000) identified four large sediment mounds in the eastern Amundsen Sea; the cores used in this study are taken from the central two mounds, and a fifth mound has also been identified by this study to the east (see Chapter 5). The mounds are elongate, lie approximately orthogonal to the continental slope and are asymmetric (Uenzelmann-Neben and Gohl, 2012). The mounds show the opposite asymmetry to those located west of the Antarctic Peninsula, with a gently sloping western flank (which, on at least one mound, contains sediment waves in the upper part) and steeper eastern flank, which dips towards a channel (Nitsche et al., 2000). The geometry of the mounds and their deposition to the west of the channels is consistent with both the

Coriolis effect and the action of a westward-flowing bottom current. However, Nitsche et al. (2000) suggested the mounds are too large for their geometry to be explained solely by the action of the Coriolis effect, but too little was known about the nature of the bottom currents in the Amundsen Sea or how they changed on glacial-interglacial timescales to draw further conclusions at the time.

Uenzelmann-Neben and Gohl (2012) used seismic profiles to suggest the mounds are levee-drifts formed through the interaction of turbidity currents in channels running between the mounds with the Coriolis force and a bottom current, forming a levee which is aligned to the direction of bottom water flow. Seismic profiles show channels coming off the slope, merging to form larger channels and running along (generally) the eastern side of the mounds (Nitsche et al., 2000). Compared to those found off the Antarctic Peninsula, these mounds are more distal to the continental slope and there are no channels parallel to the shelf break which separate the mounds from the slope (Nitsche et al., 2000). Sediment waves appear to be more common on the eastern Amundsen Sea mounds than those found west of the Antarctic Peninsula, which may be related to sedimentological differences, bottom current speed and stability, or perhaps that the Amundsen Sea mounds are much more distal (Nitsche et al., 2000).

Mound Formation

No cores dating to >1.3 Ma have yet been collected in the Amundsen Sea, but seismic profiles have allowed age attribution via tracing of sedimentary units to the ODP Leg 178 site 1095 core off the western Antarctic Peninsula and the IODP Leg 138 site U1356 off Wilkes Land (Lindeque et al., 2016). A core from DSDP Leg 35 Site 324 in the Bellingshausen Sea has not been used for age correlation due to poor recovery and sediments dating only to the Pleistocene and Pliocene (Uenzelmann-Neben and Gohl, 2012; Lindeque et al., 2016). Seismic profiles show the mounds have discontinuities at their base and in limited places within the mounds, which have been linked to major changes in bottom currents driven by plate tectonics and climate changes (Uenzelmann-Neben and Gohl, 2012) (Table 3.2).

Seismic unit	Proposed age (Ma)	Sedimentary features	Main area of occurrence	Oceanographic/ climatological interpretation
IV	**4-0**	Levee-drifts	Eastern Amundsen sea	Bottom water activity has shifted southwards, less intense
		Mass transport deposits	Near continental rise	Change in ice regime from wet to dry-based
III	**15-4**	Elongate drifts	Marie Byrd Seamounts	Intensified bottom water activity
		Levee drifts	Eastern Amundsen Sea	Cyclonic eddies shed from bottom water
		Mass transport deposits	Central/eastern Amundsen Sea	Advancing ice sheet
II	**21-15**	Elongate drifts	Marie Byrd Seamounts	Intensified bottom water activity
		Levee drifts	Eastern Amundsen Sea	Cyclonic eddies shed from bottom water?
I	**60-21**	Elongate sediment drifts	Marie Byrd Seamounts	Eastward flow of bottom water (proto-AABW?)

Table 3.2: The oceanographic and climatological model based on seismic horizons presented by Uenzelmann-Neben and Gohl (2012).

In contrast to the drifts west of the Antarctic Peninsula, where sediments overlying basement are from a “pre-drift stage” with no evidence of mound development (Rebesco et al., 1997), buried palaeo-drifts have been identified directly overlying basement in the western Amundsen Sea and in the vicinity of the Marie Byrd Seamounts (Uenzelmann-Neben and Gohl, 2012; Lindeque et al., 2016). The oldest assumed sediment mound identified in the Amundsen Sea is located in the western basin, which dates to >67 Ma and rests directly on the basement (Lindeque et al., 2016). The palaeo-current direction could not be inferred from the mound geometry, but the surrounding

bathymetry suggests flow was eastwards, perhaps as part of a proto-Ross Sea gyre (Lindeque et al., 2016). By the Eocene (57-40 Ma), numerous small mounds (possibly drifts) had begun to form, as well as a 3 km long and 400 m high levee-drift with a westwards-facing gently sloping flank also indicative of an eastwards flowing bottom current (Lindeque et al., 2016). Between 60 and 21 Ma, elongate drifts began to form close to the Marie Byrd Seamounts in the central Amundsen Sea under an eastwards flowing bottom current which may have been a proto-AABW from the Ross Sea, deflected and slowed by the presence of the newly-raised seamounts, leading to deposition of transported material around the seamounts but not on the upper continental rise (Uenzelmann-Neben and Gohl, 2012, 2014). This suggests an eastwards-flowing bottom current, likely sourced from the Ross Sea, was present on the lower continental rise of both the central and western Amundsen Sea during the Eocene and before the development of a significant ice sheet in West Antarctica. The current must have had a lower density than present AABW, given the drifts near the MBS rested on elevated bedrock at c.2000 m water depth (Uenzelmann-Neben and Gohl, 2014). Deposition in the eastern Amundsen Sea before 21 Ma was largely via a palaeo-delta near 106°W which crossed the outer shelf at the present site of PITE (Uenzelmann-Neben and Gohl, 2014).

The development of the ACC in the Oligocene aided the establishment of a continent-wide ice sheet and at least alpine glaciation in the Amundsen Sea hinterland in the early Miocene (Uenzelmann-Neben and Gohl, 2014; Lindeque et al., 2016). As sediment delivery to the continental rise increased, levee-drifts in the eastern Amundsen Sea began to develop between 21 and 14 Ma, with a geometry indicative of development under a south-west flowing bottom current, which may have been WSDW, LCDW or the result of cyclonic eddies coming off an eastwards-flowing proto-AABW (Uenzelmann-Neben and Gohl, 2012, 2014). The position of mass transport deposits and the drifts during this time suggests the main sediment sources were via glaciers occupying the Abbot Trough and the central and western Getz Troughs (Uenzelmann-Neben and Gohl, 2012).

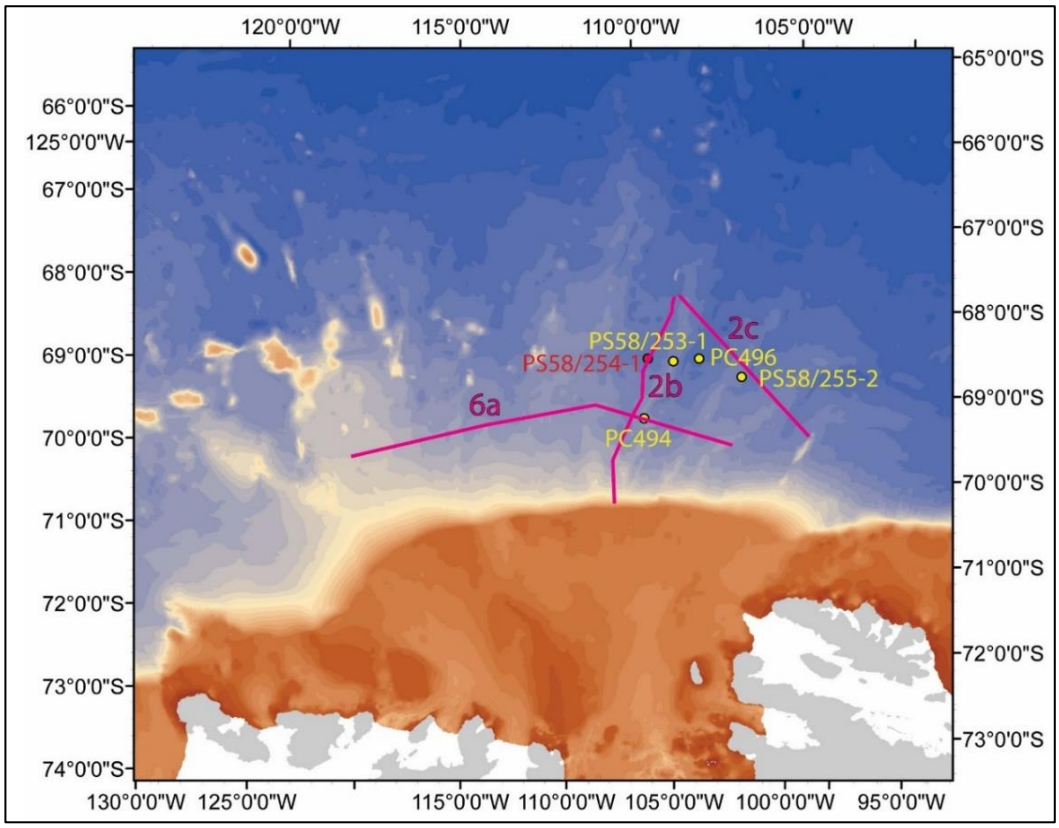

Figure 3.7: Bathymetric map of the Amundsen Sea (bathymetric data from IBCSO, Arndt et al., 2013) showing the location of the seismic lines presented in Uenzelmann-Neben and Gohl (2014): 6a (Figure 3.8), 2c (Figure 3.9) and 2b (Figure 3.10), and the location of sediment core sites analysed in this thesis (yellow) and by Hillenbrand et al. (2009a) (red, PS58/254-1).

After 15.5 Ma, the geometry of drifts throughout the Amundsen Sea suggests they were under the influence of an eastward flowing bottom current (Uenzelmann-Neben and Gohl, 2012; Lindeque et al., 2016). New attached drifts formed near the Marie Byrd Seamounts which had gently-sloping flanks facing south, suggesting the bottom current shifted to flow southwards (Uenzelmann-Neben and Gohl, 2012). Both ACC and AABW flow continued to strengthen and major glaciation began in West Antarctica c.14.1 Ma (Uenzelmann-Neben and Gohl, 2012). In the eastern Amundsen Sea, sedimentation rates increased between 14 and 4 Ma as modern depo-centres developed in the ASE, resulting in increased numbers of levee-drifts, with increased mass transport deposits in the central and eastern Amundsen Sea sourced particularly from glaciers in the Abbot Trough, PITE and PITW (Uenzelmann-Neben and Gohl, 2012, 2014; Lindeque et al., 2016). The crest of mounds 1 and 3 shifted temporarily westwards between 14.1 and 4 Ma (Figure 3.8). Buried and stacked drifts and channels are present in the central and

western Amundsen Sea, 50-100 km wide and 200-300 m high, with gently-sloping sides facing the west (Lindeque et al., 2016). The buried features suggest sedimentation rates and styles have been high but variable from the late Miocene to the present day (Lindeque et al., 2016).

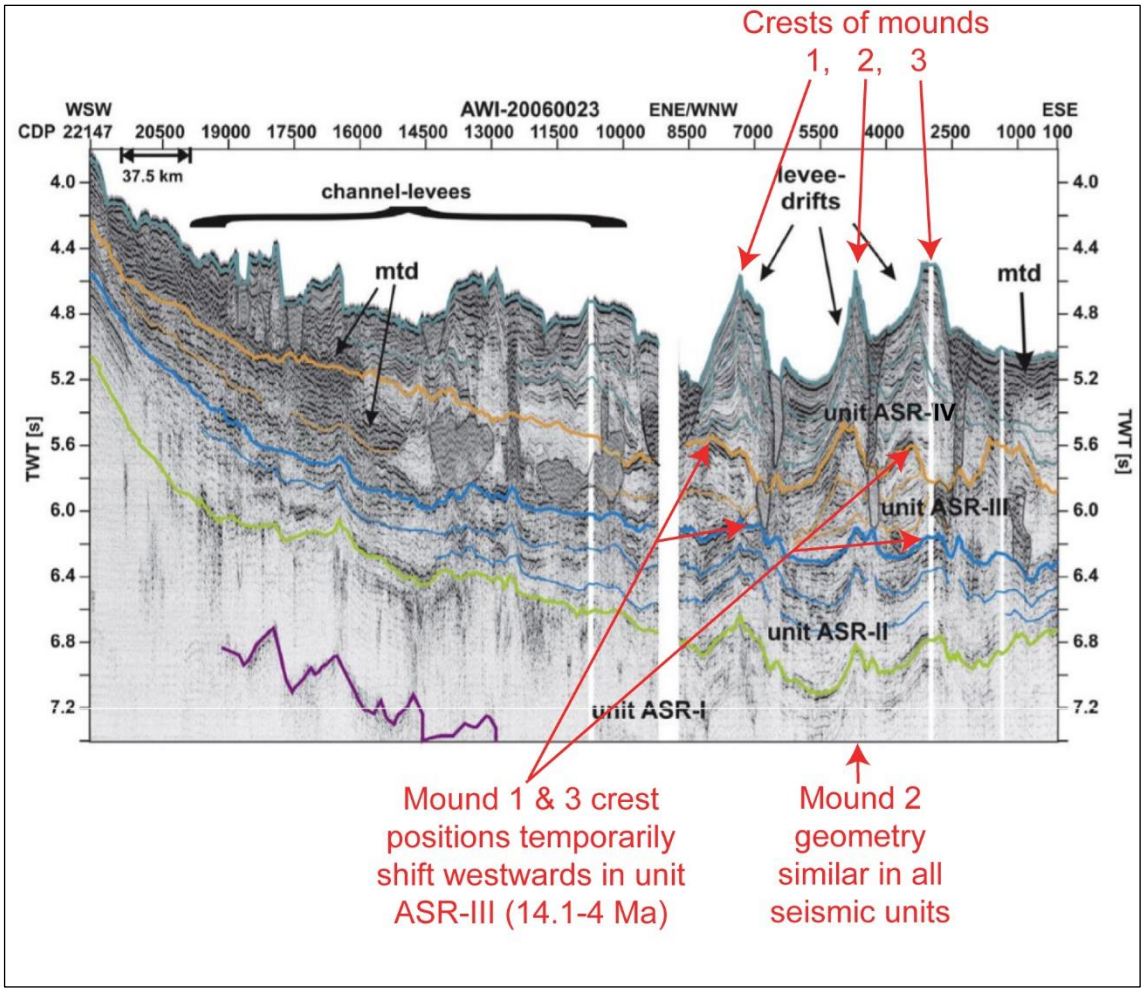

Figure 3.8: Multi-channel seismic profile AWI-20060023 (modified from Figure 6a in Uenzelmann-Neben and Gohl, 2014), shown as line 6a on Figure 3.7. Modifications are shown in red. Mounds have been labelled according to their nomenclature in this thesis. "mtd" indicates a mass transport deposit. Black lines indicate small-scale faults. Unit ages are as shown in Figure 3.9: unit ASR-I >21 Ma, unit ASR-II 21-14.1 Ma, unit ASR-III 14.1-4 Ma, unit ASR-VI 4 Ma-present.

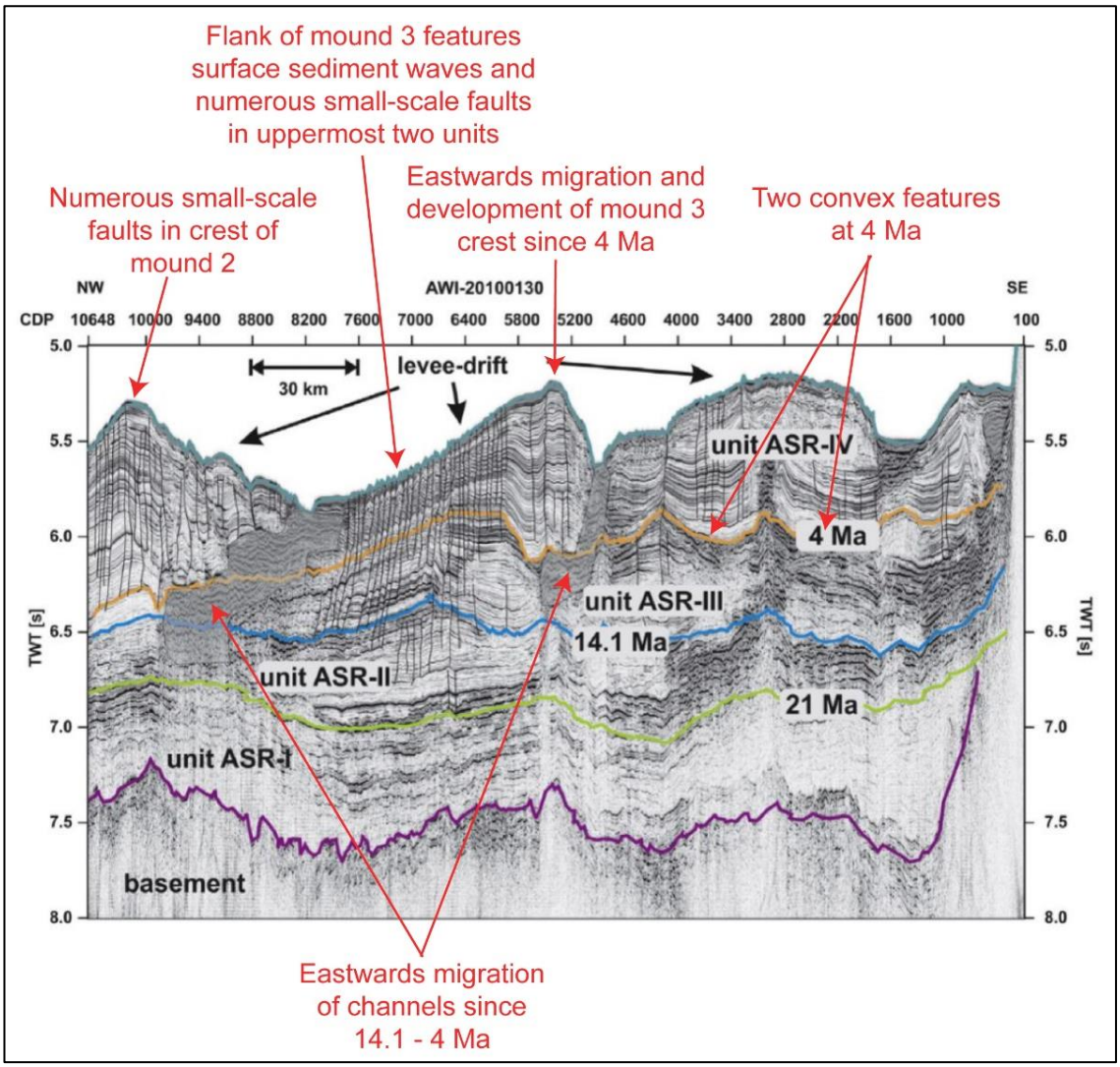

Figure 3.9: Multi-channel seismic profile AWI-20100132 (modified from Figure 2c in Uenzelmann-Neben and Gohl, 2014), shown as line 2c on Figure 3.7. Modifications are shown in red. Mounds have been labelled according to their nomenclature in this thesis. "mtd" is a mass transport deposit. Black lines indicate small-scale faults.

Fewer sediment drifts have formed in the Amundsen Sea since 4 Ma, suggesting decreased sedimentary input and a weaker bottom current; however, more channel-levee systems have developed in the central and eastern Amundsen Sea which is likely linked to the switch from wet to dry based ice, delivering more material to the continental rise (Uenzelmann-Neben and Gohl, 2012). Along-slope processes continue to play a major role in deposition in the eastern Amundsen Sea, and may offer an explanation for the eastwards migration of the channels to the west of mounds 3 and 4 since prior to 4 Ma and eastwards migration of the crest of mound 3 since 4 Ma (Figure

3.9) (Uenzelmann-Neben and Gohl, 2012). Turbidity currents sourced from the slope in front of PITW are a particularly dominant source of material to the channel-levees in the central Amundsen Sea, whilst Abbot Trough and PITE are thought to be the dominant source of material to the eastern Amundsen Sea drifts (Uenzelmann-Neben and Gohl, 2012, 2014). A mass transport deposit is visible on the lower continental slope on the seismic profile through mound 2, located between PITE and PITW, shown in Figure 3.10.

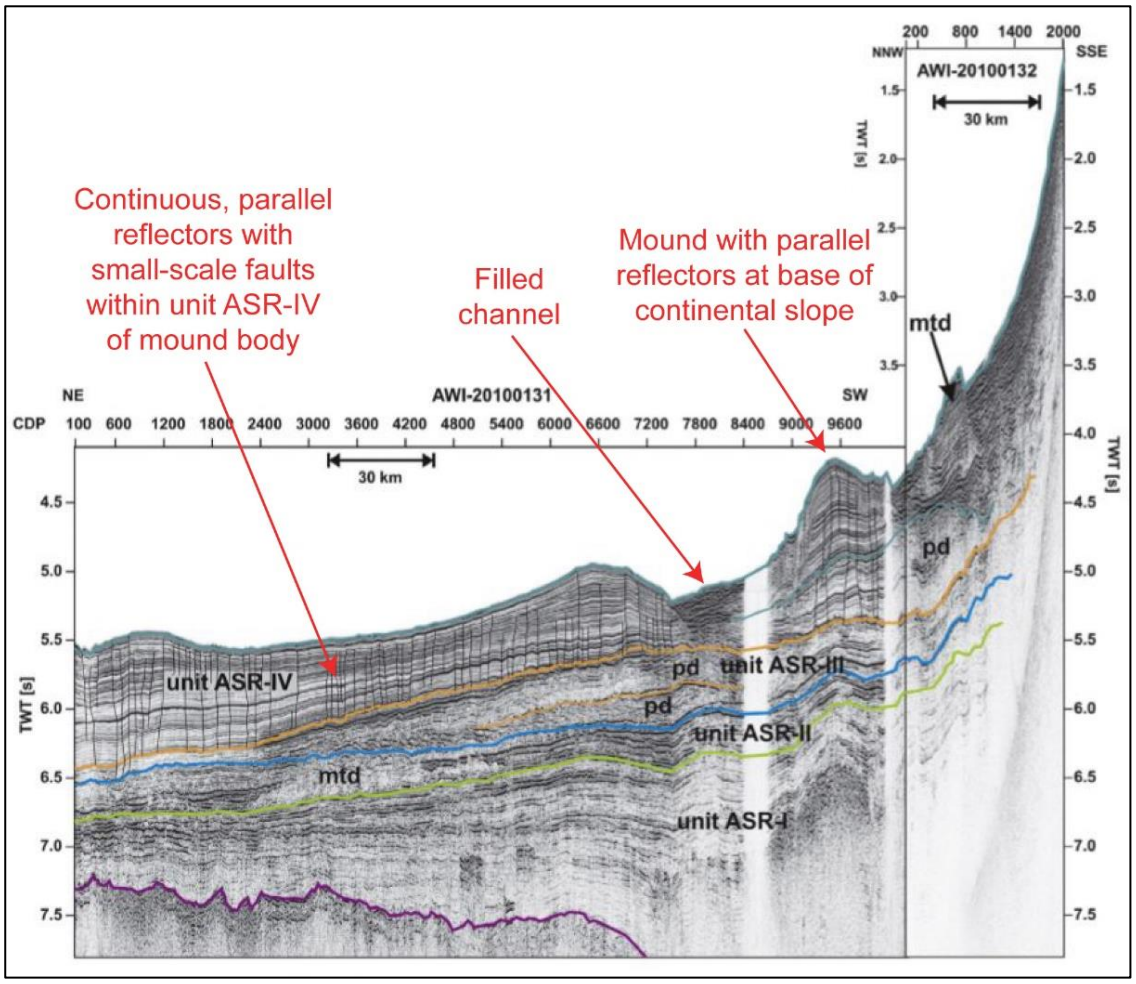

Figure 3.10: Multi-channel seismic profile AWI-20100131/20100132 (modified from Figure 2b in Uenzelmann-Neben and Gohl, 2014), shown as line 2b on Figure 3.7. Mounds have been labelled according to their nomenclature in this thesis. “mtd” is a mass transport deposit. “pd” indicates a patched drift. Black lines indicate small-scale faults.

Composition

Only one core has yet been analysed from the mounds of the eastern Amundsen Sea: PS58/254-1 (Hillenbrand et al., 2009a; Konfirst et al., 2012). The core, taken from an ice-distal area on the gently sloping, western flank in 4014 m water depth, was collected from the same mound as PC494 (ice-proximal, mound crest) and PS58/253-1 (ice-distal, mound crest). Interglacial sediments are characterised by diatom-bearing muds featuring high Ba/Al ratios of 4-8, high biogenic opal contents of typically 20-30 wt.% and low wet (1.25-1.4 g/cm^3) and dry (0.3-0.45 g/cm^3) bulk densities. Carbonate is rare. Glacial sediments are characterised by lithogenic muds with low Ba/Al ratios of <1.5, low biogenic opal contents of <7 wt.%, and high wet (1.4-1.6 g/cm^3) and dry (0.55-0.9 g/cm^3) bulk densities (Hillenbrand et al., 2009a). Clay mineralogy is dominated by illite (30-50 %), but kaolinite and smectite exhibit significant glacial-interglacial variability, with kaolinite percentages increasing from <10 % in interglacials to 10-28 % in glacials as a result of increased locally-derived sediment supply from a kaolinite source area in the ASE (Hillenbrand et al., 2009a). Smectite exhibits the opposite effect, decreasing from c.30-50 % in interglacials to 12-25 % in glacials (Hillenbrand et al., 2009a).

There is no consistent pattern in sedimentation rates, with both glacial and interglacial sedimentation rates varying between 0.7 and 4.4 cm/kyr in the late Quaternary, but not exceeding 2.7 cm/kyr since the start of MIS 15, 620 ka (Hillenbrand et al., 2009a). Similarly, gravel mass accumulation rates are variable (0.05-0.7 grains/10cm^2/kyr) and are often, though not always, higher in glacials rather than interglacials (Hillenbrand et al., 2009a).

3.4.3. Late Quaternary depositional processes in the Amundsen Sea

Little is known about the pre-LGM depositional environments of the Amundsen Sea. Progradation of the outer shelf is present throughout the Amundsen Sea, suggesting ice has reached the outer shelf on numerous occasions (Nitsche et al., 1997). Nitsche et al. (1997, 2000) identified prograded foresets on the outer shelf near 105°W and a series of debris flow deposits on the upper slope indicative of mass wasting. Channels were also identified in the slope to the east of Mound 4.

Analysis of core PS58/254-1 from the eastern Amundsen Sea revealed major glacial-interglacial changes in lithogenic and biogenic content occurred throughout the Late Quaternary and varied in accordance with the oxygen isotope record (Hillenbrand et al., 2009a). During interglacial periods, PS58/254-1 records biogenic opal contents of up to 32 wt.%, suggesting limited to no sea ice cover. During glacial periods, low biogenic opal contents (typically < 5 wt.%) suggest perennial sea ice cover restricted productivity, whilst the high terrigenous content suggests sediment delivery to the continental rise greatly increased. The exception to this is MIS 14, which lacks a typical glacial-period signal of decreases in productivity and increases in lithogenic material, and it has been suggested MIS 15-13 may therefore represent a single interglacial period, possibly indicative of WAIS collapse (Hillenbrand et al., 2009a). Records from the central Amundsen Sea (PS2547) reflect similar glacial-interglacial changes in terrigenous and biogenic content over the 1.8 million years of the Pleistocene but with no evidence of a WAIS collapse (Hillenbrand et al., 2002).

During the Last Glacial Maximum (LGM) (23-19 ka), ice advanced up to 500 km across the shelf to, or close to, the shelf break of the Amundsen Sea (Figure 3.7) (Larter et al., 2014). Evidence for this includes AMS ^{14}C dates from well-preserved, streamlined bedforms and the thin sediments that overlie them (Larter et al., 2014 and references therein). However, recent geophysical and sediment core data suggest ice in Abbot Trough did not advance to the shelf break and reached a maximum LGM extent 100 km from the shelf break (Klages et al., 2017).

LGM ice flow and sediment delivery to the outer shelf were greatest in the ice streams that sat in the cross-shelf troughs Pine Island Trough East (PITE) and Pine Island Trough West (PITW), which meet the shelf break at 106°W and 114°W, respectively. Graham et al. (2010) suggested PITE was the more dominant outlet for ice from the Pine Island-Thwaites system at the LGM, with the majority of flow likely switching from PITW to PITE in MIS 2 prior to the LGM. Ice was at least 715 m thick on the outer shelf of PITE and sat within 68 km of the shelf break (Graham et al., 2010). Large volumes of sediment-laden meltwater carved channels along the upper continental slope and most connect to channels further down-slope, particularly those located in front of the cross-shelf troughs (Dowdeswell et al., 2006) suggesting delivery of material to the upper continental rise may have been greatest directly in front of the ice streams.

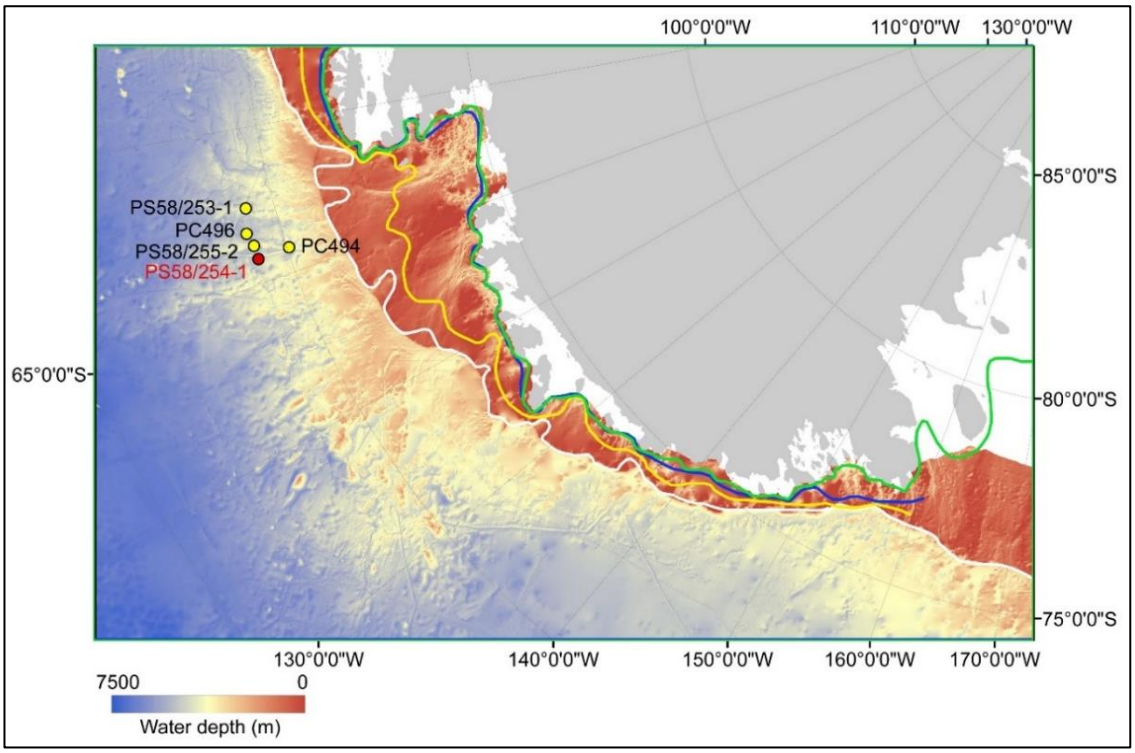

Figure 3.11: Reconstruction of post-LGM retreat of ice in the Amundsen Sea from the compilation of Larter et al., 2014. Line colours refer to years as follows: white, 20 ka; yellow, 15 ka; blue, 10 ka; green, 5 ka. Bathymetric data from IBCSO (Arndt et al., 2013). The present-day location of grounded ice is shown in grey and ice shelves shown in white (data from BEDMAP2, Fretwell et al., 2013). The location of cores presented in this thesis are shown as yellow circles and the location of PS58/254-1 as a red circle.

Retreat following the LGM was rapid, particularly on the over-deepened basins of the inner shelf, and the ice had reached close to its present position by 10 ka (Figure 3.11) (Larter et al., 2014). The presence of two grounding zone wedges in PITE and three in the central PIT suggest the retreat of the ice streams was episodic, likely as a result of geological variations and bathymetry constraining the flow (Graham et al., 2010; Jakobsson et al., 2012).

Chapter 4: Material and Methods

4.1. Introduction

This chapter describes the collection and analysis of the geophysical and sediment core data presented in this thesis. The chapter begins with an overview of the geophysical data. The second part of the chapter describes the collection, processing and analysis of the sediment cores, focusing first on the collection of continuous data and then discrete data from sediment samples. Finally, a description is given of the methods used to constrain chronology of the sediment cores and to develop age models.

4.2. Geophysical data

4.2.1. TOPAS sub-bottom profiles

A Kongsberg Simrad TOPAS PS018 sub-bottom profiler was run almost continuously during British Antarctic Survey (BAS) cruise JR179 aboard RRS James Clark Ross (JCR) between February and April 2008. The TOPAS system was typically run on a fixed ping cycle in deep water to avoid interference with other systems on board and in 'chirp' transmission mode to suppress 100 Hz noise (Shipboard Party JR179, 2008). The data are used in this research to examine the internal structure of the sediment mounds from which the cores were taken. TOPAS profiles presented in this thesis were displayed using Kongsberg TOPAS Mark II software.

4.2.2. Swath bathymetry

Bathymetric data presented in this thesis have been obtained from the International Bathymetric Chart of the Southern Ocean (IBCSO) (Arndt et al., 2013). The IBCSO bathymetric model has a 500 m x 500 m resolution and is based on a compilation of single and multi beam data with predicted bathymetry where no data exist. Data have been displayed using ArcMap and ArcScene software on a polar stereographic projection with true scale at 65°S.

4.3. Sediment cores

4.3.1. Core Collection

Piston cores (PC) PC494 and PC496 and box core (BC) BC495 were taken during cruise JR179 between February and April 2008 (see Table 4.1). Piston cores PS58/253-1 and PS58/255-2 were collected during cruise ANT-XVIII/5a of the RV Polarstern between February and April 2001 by the Alfred Wegener Institute, Helmholtz Centre for Polar and Marine Research (AWI). Over-penetration was noted in PS58/253-1, indicating loss of surface sediment. All cores were stored in the scientific cool room on board the respective ship at 4°C.

Core ID	**PC494**	**BC495**	**PC496**	**BC497**	**PS58/ 253-1**	**PS58/ 255-2**	***PS58/ 254-1***
Cruise	JR179	JR179	JR179	JR179	ANT-XVIII/5a	ANT-XVIII/5a	*ANT-XVIII/5a*
Device	Piston	Box	Piston	Box	Piston	Piston	*Piston*
Location on drift	Drift crest	Drift crest	Drift flank	Drift flank	Drift crest	Drift crest	*Drift flank*
Latitude	-70.04960	-70.04879	-69.23008	-69.23008	-69.3080	-69.3700	*-69.3130*
Longitude	-108.33701	-108.34936	-106.68016	-106.68016	-107.5580	-105.1180	*-108.4530*
Water depth (m)	3450	3468	4230	4230	3720	3795	*4014*
Core length (cm)	1041	52	937	17	1452	1253	*1831*

Table 4.1: Location and key details of all cores used in this study, including PS58/254-1 (italics) (Hillenbrand et al., 2009a).

Comparisons will also be made with the only other published core collected from the mounds of the eastern Amundsen Sea, PS58/254-1 (Hillenbrand et al., 2009a), the details of which are listed in Table 4.1.

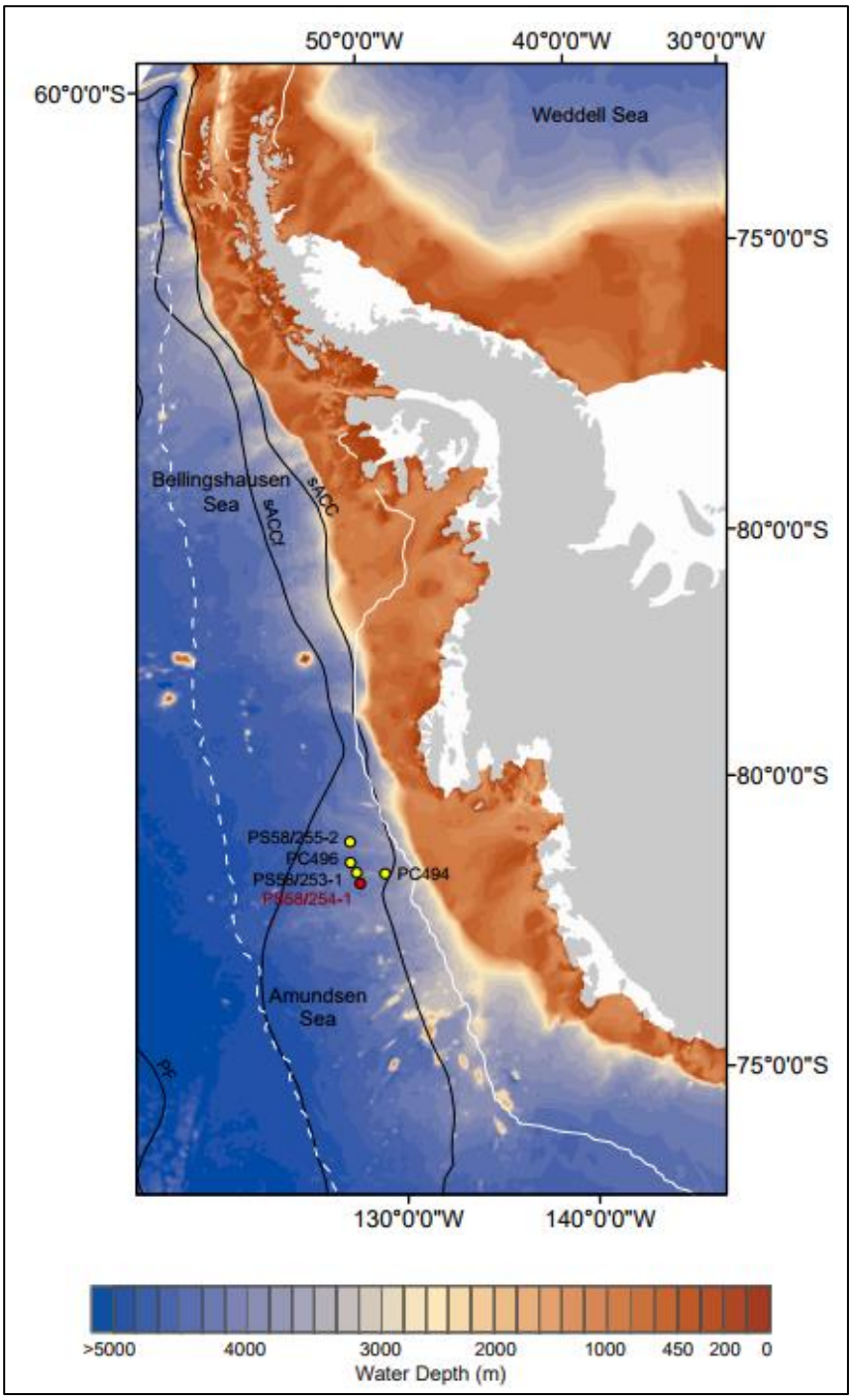

Figure 4.1: Bathymetric map of the western margin of Antarctica showing the location of the four cores used in this thesis and PS58/254-1 (Hillenbrand et al., 2009a). Bathymetry data are taken from IBCSO (Arndt et al., 2013). sACC marks the southern boundary of the ACC, sACCf marks the southern boundary of the ACC Front, PF marks the Polar Front. The white dashed and full lines indicate the winter and summer sea ice extents, respectively. Sea ice data are from the National Snow and Ice Data Centre (2016). Grey areas mark the extent of grounded ice, white areas indicate ice shelves (according to BEDMAP2, Fretwell et al., 2013).

4.3.2. Core splitting, logging and sampling

PC494, BC495 and PC496 were split at BAS in October 2013. PS58/253-1 and PS58/255-2 were split aboard RV Polarstern in February-April 2001. Photographs of the cores were taken immediately after splitting and line-scan images were also later taken of PS58/253-1 and PS58/255-2. X-radiographs were taken of the archive halves of cores PC494 and PC496 and of a 1 cm thick, 10 cm wide sediment slice taken from the split cores of PS58/253-1 and PS58/255-2.

A core description was conducted on the archive halves of each split core immediately following photography. PC494, BC495 and PC496 were logged at BAS by Jennifer Horrocks. PS58/253-1 and PS58/255-2 were logged during ANT-XVIII/5a by Dr. Claus-Dieter Hillenbrand. Features described included: lithological units, their thickness, nature of contacts between units, sediment colour (hue, value and chroma according to a Munsell Soil Colour Chart), lithology and grain size, sedimentary structures (such as laminations, stratifications, grading or mottling), occurrence of microfossils and large clasts, coring disturbance and any other notable features. Smear slides were also taken from each major unit and used to estimate diatom and foraminifera content. X-radiographs were also used at a later date to add further information on sub-surface features and sedimentary structure.

Discrete, 1 cm-thick samples were then taken from the working halves of each core for various measurements. All cores were sampled at ≤30 cm resolution, with higher resolution chosen for surface sediments, thin units, sections of low WBD and sections which included interesting features or potentially dateable material (e.g. microfossils or tephra) (Table 4.2).

4.3.3. Core processing and analysis of continuous data

The four sediment cores have undergone a range of analyses both as whole cores, producing continuous data, and as discrete samples. Figure 4.2 outlines the processes of analyses applied to the cores.

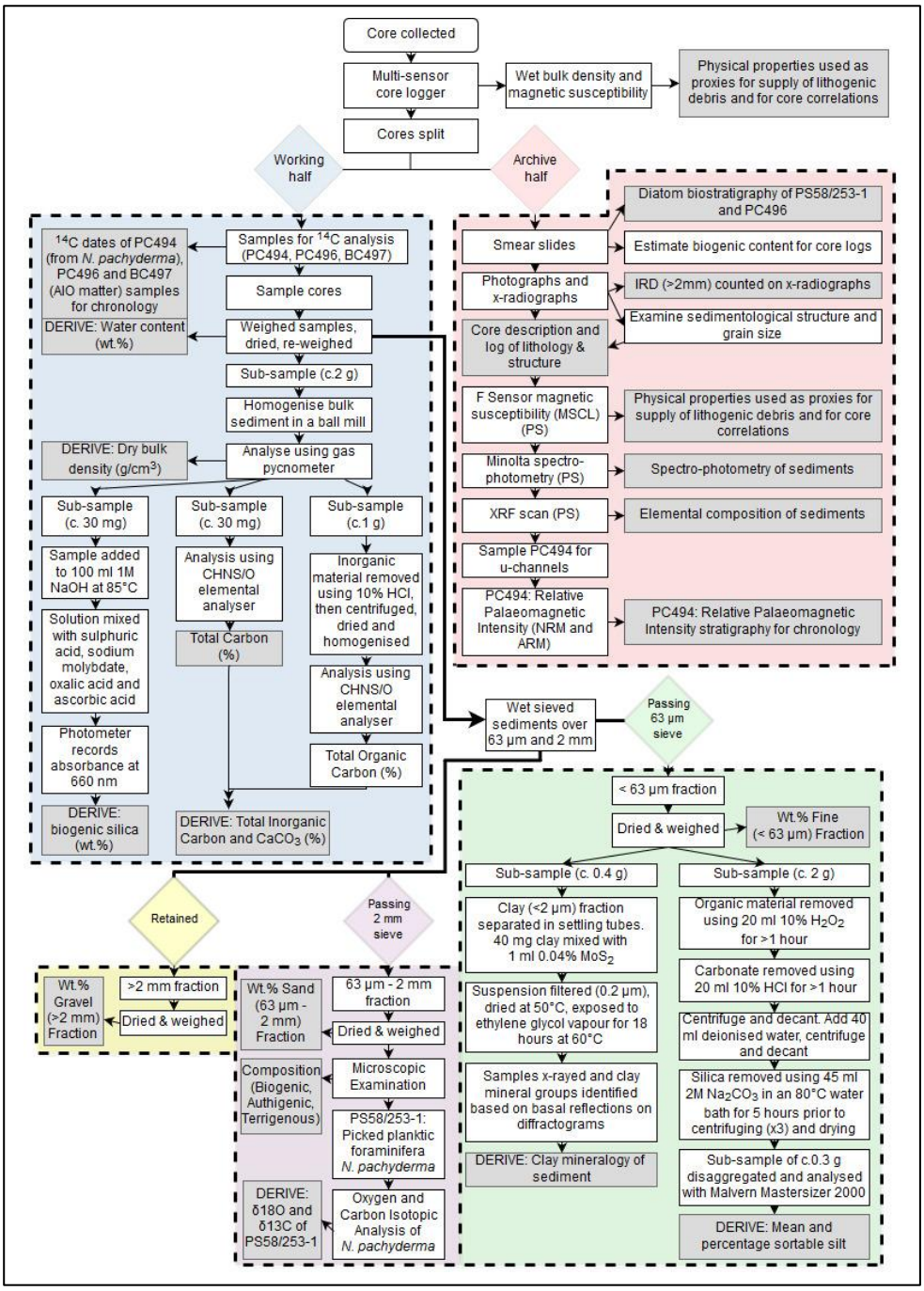

Figure 4.2: Flowchart to show the processes of analyses used in this research. The red box indicates analyses applied to the archive half of the cores. The blue box indicates analyses applied to the working half of the cores and the bulk sediment samples. The green, purple and yellow boxes indicate analyses applied to the <63 µm, 63 µm-2 mm and >2 mm fractions, following wet-sieving. Grey boxes indicate end data produced. (PS) indicates analyses applied only to PS58/253-1 and PS58/255-2. Abbreviations are as follows: ARM: Anhysteretic Remanent Magnetisation, IRD: Iceberg-rafted debris, MSCL: Multi-sensor core logger, NRM: Natural Remanent Magnetisation. Methods and references are outlined in the chapter text.

Analysis/Core	PC494	PC496	PS58/253-1	PS58/255-2
Wet bulk density (WBD)	1 cm	1 cm	1 cm*	1 cm*
Magnetic Susceptibility (MSCL)	1cm	1 cm	1 cm*	1 cm*
Magnetic Susceptibility (F sensor)			1 cm*	1 cm*
Visible reflectance spectrophotometry			1 cm*	1 cm*
Ice Rafted Debris (counts on X-radiographs)	1 cm	1 cm	1 cm	1 cm
X-ray fluorescence (XRF)			2 mm (10 and 30 kv), 10 mm (10, 30 and 50 kv)	2 mm (10 and 30 kv), 10 mm (10, 30 and 50 kv)
Grain size (sieving and Coulter Counter)	3 – 20 cm	5 – 20 cm	6 – 30 cm	3 – 30 cm
Water content and dry bulk density (DBD)	3 – 20 cm	5 – 20 cm	6 – 30 cm	3 – 30 cm
$CaCO_3$/TC/TOC/TN	3 – 20 cm	5 – 20 cm	5 – 15 cm*	5 – 30 cm*
Biogenic silica	3 – 20 cm	5 – 20 cm	4 – 16 cm	5 – 30 cm
Clay mineralogy	3 – 20 cm**	5 – 20 cm**	6 – 30 cm**	3 – 30 cm**
Sand fraction composition	3 – 20 cm	5 – 300 cm	6 – 30 cm	5 – 210 cm

Table 4.2.: The resolution of analyses carried out on the cores. TC: Total Carbon. TOC: Total Organic Carbon. TN: Total Nitrogen.

* Data provided by Dr. Gerhard Kuhn (AWI).

** Data provided by Dr. Werner Ehrmann (University of Leipzig).

4.3.3.1. Multi sensor core logging

Wet Bulk Density (WBD) and Magnetic Susceptibility (MS) were determined non-destructively on whole sediment cores using a GEOTEK multi-sensor-core logger (MSCL) at 1 cm resolution (Table 4.2). Measurements were conducted at the British Ocean Sediment Core Research Facility on PC494 and PC496 and at AWI on PS58/253-1 and PS58/255-2. The data from PS58/253-1 and PS58/255-2 were provided by Dr. Gerhard Kuhn.

Physical properties of marine sediment cores closely reflect variations in sediment composition, particularly the amount of terrigenous and biogenic material and the grain-size of sediments (Weber et al., 1997). WBD can be used as an estimation of biogenic silica content as the two are typically found to be negatively correlated (e.g. Hillenbrand et al., 2009a; Sprenk et al., 2013). WBD was measured via the degree of attenuation of gamma rays through the core (Weber et al., 1997).

High magnetic susceptibility values are indicative of abundant magnetic grains and low values are indicative of biogenic material, quartz and feldspar (Rothwell and Rack, 2006). Magnetic susceptibility was measured with a loop sensor which creates a slightly smoothed signal by measuring magnetic susceptibility of sediments ≤10 cm either side of the sensor (Weber et al., 1997). However, the loop sensor has a high signal to noise ratio making it suitable for sediments of a low magnetic susceptibility (Rothwell and Rack, 2006). Once split, the cores were also analysed at 1 cm resolution using an F sensor which provides greater spatial resolution than a loop sensor (Rothwell and Rack, 2006).

4.3.3.2. Visible reflectance

Visible (VIS) reflectance data for PS58/253-1 and PS58/255-2 were supplied by Dr. Gerhard Kuhn. The archive halves of the cores were covered with transparent film and scanned on cruise ANT-XVIII/5a for VIS-reflectance at 1 cm resolution (Table 4.2) using a Minolta CM-2002 Spectrophotometer (lens diameter 8 mm, field of view 0.8 cm) connected to a desktop PC. Data measured were: L* colour space (sediment lightness from 0% (black) to 100% (white)); a* colour space (green-red components, from -4 (green) to 16 (red)); b* colour space (blue-yellow component, from 0 (blue) to 40

(yellow)) (Sprenk et al., 2014); red, green and blue values; colour reflectance (percentage) in 10 nm steps from 400 to 700 nm; chroma, hue and value according to the Munsell Soil Colours. The spectrophotometer was calibrated at the beginning and end of each core section to account for potential drift.

4.3.3.3. Ice rafted debris counts on X-radiographs

Ice rafted debris (IRD) may contain grains of all sizes. However, the mud fraction cannot be distinguished from mud with the same provenance which may be deposited by bottom currents or turbidity currents. As weak bottom currents and turbidity currents cannot transport grains larger than medium sand, it is assumed that any grains >2 mm in the mounds must have been transported by ice rafting and therefore are a proxy for IRD. A major benefit of this technique is that the presence of particularly large grains does not over-represent the IRD content of a sample as it would when using the weight percentage of IRD in the bulk sediment (Grobe, 1987).

All grains with a middle axis larger than 2 mm were counted on the X-radiographs per 1 cm core depth (equivalent to 19.24 cm^3 in PC494, PC496 and BC495 and 10 cm^3 in PS58/253-1 and PS58/255-2), according to the method presented in Grobe (1987). Grain counts were then converted to number of grains per 10 cm^3 to normalise counts between cores. Following the development of the age models, the mass accumulation rate of gravel based on this data (MAR_{gravel}) was calculated by multiplying the number of grains per 1 cm^3 by the linear sedimentation rate (Hillenbrand et al., 2002).

4.3.3.4. X-ray fluorescence

The archive halves of PS58/253-1 and PS58/255-2 and associated trigger cores were scanned using an Avaatech X-ray fluorescence (XRF) core scanner at AWI. XRF scanning is a rapid and non-destructive method of analysing the elemental composition of marine sediments at high resolution (Hennekam and de Lange, 2012, and references therein). The sediment cores are subjected to X-ray radiation, which causes the inner shell of an atom to lose an electron. In its place, an electron from the outer shell moves to the inner shell. The difference in energy between the two shells is emitted and each element emits

a unique wavelength of electromagnetic radiation. The peak amplitude of the emitted radiation corresponds to the concentration of each particular element at that sample depth (Richter et al., 2006).

The cores were covered with a 4 µm–thick polypropylene film during the analysis to prevent contamination of the scanner. XRF scanning provided the Area, DArea and Chi Squared data for the elements Al, Si, P, S, Cl, K, Ca, Ti, Cr, Mn, Fe, Rh (10 kV at 2 mm and 10 mm resolution), Cu, Zn, Ga, Br, Rb, Sr, Y, Zr, Nb, Mo, Pb, Bi (30 kV at 2 mm and 10 mm resolution), Ag, Cd, Sn, Te and Ba (50 kV at 10 mm resolution only).

At least 2 cm of data were deleted from each section end where errors are likely to occur. Some elements are known to be significantly influenced by pore water contents in accordance with Moseley's Law, particularly lighter elements such as Si (Tjallingii et al., 2007). These elements will therefore not be used for environmental analysis as it is impossible to quantify the extent to which they are reflecting the water content. However, division of elemental counts by these lighter elements can account for the variation in water content down-core and the corresponding impact on the amplitude of emitted radiation. Elements are therefore typically presented in the thesis as ratios to Ti.

4.3.4. Analysis of discrete samples

4.3.4.1. Water content and dry bulk density

Samples from PC494, PC496 and BC495 were weighed immediately after they had been taken, then oven dried at 40°C and re-weighed after drying. Samples from PS58/253-1 and PS58/255-2 were put into pre-weighed bags, which were then sealed and kept refrigerated at 4°C aboard RV Polarstern; the samples were then weighed at AWI, freeze dried and re-weighed. Assuming a mass ratio of salt to water of 0.0363 at 3.5% salinity (Kuhn et al., 2017), salt-corrected (sc) water content (w) was calculated from:

$$\mathrm{wsc}\ (\%) = \frac{\mathrm{wet\ weight} - \mathrm{dry\ weight}}{\mathrm{wet\ weight}} * 100 * 1.0363$$

Equation 4.1: Salt-corrected water content (Kuhn et al., 2017).

A 2 g sub-sample from each sample was homogenised in a ball mill to be suitable for analysis in a gas pycnometer, and later for TC, TIC and biogenic silica analysis. Each sample was then weighed and analysed with a gas pycnometer.

Porosity (φ) and dry bulk density (DBD) were measured using water content (w), the pycnometer reading (ρ), the assumed density of the pore water (1.024 g/cm^3 (Weber et al., 1997)) and the equation after Weber et al. 1997 and Niessen et al. 2013:

$$\varphi\ (\%) = \ 100 * \frac{\frac{\mathrm{w} * 100}{96.5 * 1.024}}{\frac{100 - \mathrm{w}}{\rho} - \mathrm{w} * \frac{3.5}{96.5 * 2.1} + \mathrm{w} * \frac{100}{96.5 * 1.024}}$$

Equation 4.2: Porosity (φ) (%) (Weber et al., 1997).

$$\mathrm{DBD} = \mathrm{WBD} - 1.024 * \frac{\varphi}{100}$$

Equation 4.3: Dry bulk density (DBD) (Weber et al., 1997).

4.3.4.2. Grain size

Each dried bulk sample was weighed before 20 ml distilled water and 2 ml of 6% sodium hexametaphosphate solution were added to disaggregate the sample. Samples were shaken on an orbital shaker for 8 hours. Samples remained in the solution for at least two days prior to wet-sieving. Samples were then wet-sieved over a 63 µm and 2 mm sieve in order to separate the mud (combined clay (0 – 2 µm) and silt (2 – 63 µm)) fraction from sand (63 µm – 2 mm) and gravel (> 2 mm). The first 250 ml of the <63 µm fraction was captured in a beaker and the rest discarded. This fraction was left to settle for at least one day, decanted to c.100 ml and left to dry at 40°C in an oven. The 63 µm – 2 mm fraction was washed into a 50 ml beaker using distilled water and placed in an oven for drying at 40°C. The >2 mm fraction was left to air dry at room temperature. The mud and sand fractions were then weighed and calculated as weight percentages of the bulk sediment.

A Coulter Counter was used to determine the particle size distribution in the <63 µm fraction to allow calculation of sortable silt to reconstruct changes in bottom current vigour and identify possible episodes of winnowing. Sortable silt is a proxy for near-bottom current speed based on the principle that terrigenous silt grains <10 µm behave like clay (<2 µm) and are cohesive, whilst grains 10-63 µm are increasingly non-cohesive and undergo increased amounts of size sorting the faster the current flows (McCave et al., 1995). The size of grains in the 10-63 µm "sortable silt" fraction is dependent on selective deposition at flow speeds below 10-15 cm^{-1} and both selective deposition and winnowing above these speeds (McCave and Hall, 2006). The sortable silt proxies are used to infer relative changes in bottom current speeds. Recent work has attempted to calibrate the sortable silt proxy to bottom current speeds but has identified large regional differences in the calibration, reflecting differences in the grain size of material supplied to the bottom current (McCave et al., 2017).

There are two sortable silt proxies: Mean sortable silt is the mean size of grains in the 10 - 63 µm fraction, and percentage sortable silt is the percentage of the 10 - 63 µm fraction within the 0 - 63 µm grain-size fraction (McCave et al., 1995). Concerns raised by McCave and Hall (2006) regarding the use of a Coulter Counter to derive the percentage sortable silt proxy due to the failure to detect particles <2 µm are not relevant here, due to a minimum particle detection size of 0.04 µm and only rare particles present <0.20 µm.

It was important to first remove carbonate, organic material and biogenic silica which often have grain sizes concentrated in certain modes, particularly related to species size, as they can confuse the sortable silt signal (McCave and Hall, 2006). The following method for the removal of organic matter was taken from McCave et al. (1995). Approximately 2 g of dry <63 µm sediment was weighed into a plastic 50 ml centrifuge tube. To remove organic material, 20 ml 10% hydrogen peroxide (H_2O_2) was added to each sample. Tubes were vigorously shaken and then regularly stirred with glass rods for at least one hour until any reaction had stopped.

To remove carbonate (following the method in Wilson, 2013 which includes the use of a centrifuge, adapted from McCave et al., 1995), 20 ml of 10% hydrochloric acid (HCl) was then added to each sample, and again regularly stirred until any reaction had

stopped, before being centrifuged at 400 rotations per minute (rpm) for 20 minutes and decanted. 40 ml deionised water was added to each sample before being centrifuged again. Samples were decanted and left to dry in an oven at 40°C overnight, taking care not to fully dry out the samples as their high clay content meant keeping the samples in solution was important to avoid aggregation.

The following day, 45 ml of 2 Molar sodium carbonate (Na_2CO_3) were added to each sample to remove biogenic silica using the method in Morlock and Froelich (1989). Samples were vigorously shaken, then placed in a water bath at 80°C for five hours. Samples were stirred every 30 minutes with a glass rod and vigorously shaken after two and a half hours. Samples were then removed from the water bath and immediately centrifuged at 400 rpm for 20 minutes. A higher speed could not be used as the centrifugal force warped the hot centrifuge tubes. Samples were decanted, washed with 40 ml deionised water, centrifuged at 3750 rpm for five minutes, and repeated again. Samples were then left to dry out at 40°C in an oven.

c.0.3 g of the treated, dried sediment were then placed in a 50 ml plastic centrifuge tube, mixed with 2 ml sodium hexametaphosphate and 20 ml deionised water and put on an orbital shaker for several hours. Samples were regularly shaken vigorously and left overnight to disaggregate. Smear slides were taken from sample depths previously identified as containing diatoms to confirm that the treated samples were barren of diatoms.

Particle size measurements were carried out using a Beckman Coulter Counter at Durham University. The machine underwent rinsing after each sample and a longer rinse every hour, after which the obscuration and Polarization Intensity Differential Scattering values were recorded to ensure they fell within the expected operational range. This showed the Coulter Counter was clean and not retaining sediment from previous sample runs. If not, the machine was rinsed again until levels were acceptable. Samples were washed into the machine using deionised water. Each sample ran for 90 seconds on each run. Each sample was run at least twice and the results averaged. If any large differences were noted between the two runs, the sample runs were repeated until they sufficiently overlapped. A small number of samples were run a maximum of ten times (in which case, the last four runs showed sufficient overlap). The reason for the initial

discrepancies in runs is here attributed to the clay-rich nature of the sediments meaning the samples were prone to coagulation and clumping, which was overcome through the action of the Coulter Counter during repeat runs and through use of the ultrasonic feature to disaggregate flocs. Results were exported into a Microsoft Excel spreadsheet.

Mean sortable silt was calculated as the mean size of grains in the 10 - 63 µm fraction. Percentage sortable silt was calculated as the volume percentage of the 10 - 63 µm fraction within the 0 - 63 µm grain-size fraction (McCave et al., 1995).

Analysis of the Coulter Counter output to quantify sorting and skewness was carried out using the GRADISTAT software (version 8) (Blott and Pye, 2001) using the methods in Folk and Ward (1957).

4.3.4.3. Total Organic Carbon, $CaCO_3$ and biogenic silica

Total carbon (TC) and total organic carbon (TOC) were quantified using a Flash 2000 CHNS/O Organic Elemental Analyser. Analysis of PC494 and PC496 was carried out at Durham University Department of Geography. Analysis of PS58/253-1 and PS58/255-2 was done at AWI and data supplied by Dr. Gerhard Kuhn.

To analyse TC, approximately 30 mg of homogenised, dried bulk sediment was weighed into a small tin capsule and compressed tightly. The machine was calibrated before each batch of 21 samples using a blank tin capsule, followed by 0.5 mg, 1 mg, 1.5 mg, 2 mg and 2.5 mg standards of aspartic acid, $C_4H_7NO_4$. Carbon and nitrogen values were checked to ensure they were within 5 % of the certificated values for the aspartic acid standards (36.14 % w/w carbon, 10.47 % w/w nitrogen).

At the end of each batch, a further quality control check was performed with aspartic acid to check for drift. A sample of a Certified Reference Material soil was also run to ensure the machine was properly calibrated for analysing samples with a complex matrix, rather than a pure chemical, to better match the marine sediment samples. Analysed values needed to be within 7.5 % of the certificated CRM values (2.29 % w/w carbon, 0.21 % w/w nitrogen).

To remove the inorganic carbon and allow analysis of TOC, 40 ml of 10% hydrochloric acid (HCl) were then added to c.0.5 g of the remaining homogenised, dried bulk sediment in 50 ml plastic centrifuge tubes. Samples were stirred with glass rods and left for several hours until any reaction had stopped. The samples were then centrifuged at 3750 rpm for five minutes, decanted, washed with deionised water and repeated, then left to dry at 40°C in an oven. Once fully dried, samples were re-homogenised in a pestle and mortar before being immediately placed into sample bags and into a desiccator. 30 mg of each sample were then weighed into small tin capsules and compressed, and the method repeated as for the TC analysis.

The following equations were applied in order to calculate TC (%), TOC (%), TIC (%) and $CaCO_3$ (%) (Bernard et al., 1995):

$$\text{TC (\%)} = \frac{\text{Carbon (g)}}{\text{Dry sample weight (g)}}$$

Equation 4.4: Total carbon (%) (Bernard et al., 1995).

$$\text{TOC (\%)} = \frac{\text{Organic Carbon (g)}}{\text{Dry sample weight (g)}}$$

Equation 4.5: Total organic carbon (%) (Bernard et al., 1995).

$$\text{TIC (\%)} = TC - TOC$$

Equation 4.6: Total inorganic carbon (%) (Bernard et al., 1995).

$$\text{CaCO}_3\ \text{(\%)} = (TC - TOC)\ x\ 8.33$$

Equation 4.7: $CaCO_3$ (%) (Bernard et al., 1995).

Biogenic silica was analysed at AWI using the automated wet-leaching method described by Müller and Schneider (1993). A known weight of c.30 mg of dried, homogenised, bulk sediment were weighed into tin capsules, then decanted into a stainless steel cylinder containing 100 ml 1M sodium hydroxide, NaOH. The cylinder sat in a water bath held at 85°C. A stainless steel lid was added, to minimise evaporation, with a stirring rod

attached to a drill to maintain constant agitation at a set speed (80 rpm). Two capillary tubes carried the leaching solution to the auto-analyser, via a paper filter to exclude particles >2 µm. The solution was mixed with 0.088 M sulphuric acid, sodium molybdate, oxalic acid and finally, ascorbic acid, each pumped through 1.2 mm tubes at a rate of 0.6 ml per minute. The solution was then run through a photometer, which measures absorbance at 660 nm, and prints results on a strip-chart recorder. Samples were left to run until the gradient of the line produced by the photometer had stabilised (Figure 4.3); typically 45 minutes. Between each sample, the paper filter was changed, capillary tubes were cleaned, the stainless steel cylinder was washed with deionised water and NaOH, and the photometer returned to the background reading.

The machine was calibrated at the start and end of each day using solutions with standard silica concentrations, typically 10 and 20 mg/L silica, but adjusted depending on the range of concentrations analysed in the batch. Biogenic silica was calculated according to equation 4.8 (Müller and Schneider, 1993), then corrected for the average 10 % water content of silica and for salt-content:

$$SiO_2\ (\text{wt.}\%) = \frac{ABR_{spl}\ x\ Si_{std}\ x\ 21.39\ x\ mV_{spl}}{ABS_{std}\ x\ Wt\ x\ mV_{std}}$$

Equation 4.8: Biogenic silica (Müller and Schneider, 1993).

Where: ABS_{spl} is the absorbance value for the sample, read by extrapolating the gradient of the photometer reading. ABS_{std} is the absorbance value for the standard silicon solution. Si_{std} is the concentration of the standard silicon solution (mg). Wt is the weight of the sample (mg). mV_{spl} and mV_{std} are the (usually identical) gain settings used for the sample and solution, respectively (Müller and Schneider, 1993).

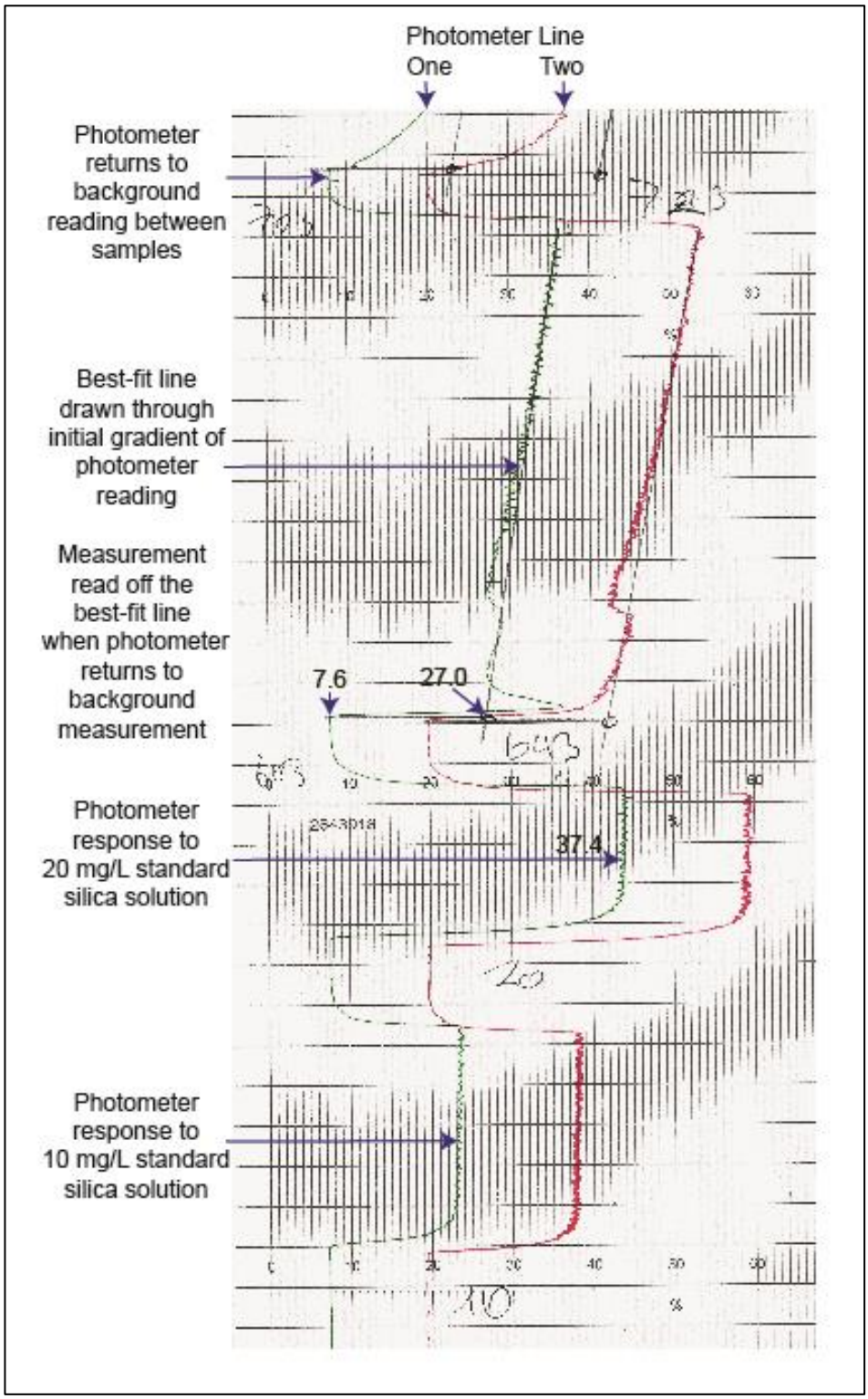

Figure 4.3: Annotated photometer output from the automated wet-leaching method of analysing biogenic silica content. The green and red lines (photometer lines one and two) reflect the absorbance measurement of the sample and standard silica solutions. By extrapolating a line of best fit through the readings, the absorbance values for the sample can be read and inputted into the equation as ABS_{spl} (the absorbance value of the sample) and ABS_{std} (the absorbance value of the standard).

4.3.4.4. Composition of the coarse fraction

The 63 µm to 2 mm fraction of each sample was, where sample quantities allowed, sampled using a sample splitter to avoid bias towards larger grains. The grains were arranged on a black gridded tray and categorised and counted using a microscope at up to 60x magnification. A minimum of 300 grains were identified and counted according to the categories given in the following (representative photographs of each category are shown in Figures 4.4 and 4.5):

- Terrigenous particles: Rock fragments, quartz & feldspar, mica, mafic minerals, volcanic glass, other minerals.
- Authigenic particles: Micro-manganese nodules.
- Biogenic components: Planktonic foraminifera, benthic calcareous and agglutinated foraminifera, calcareous foraminiferal fragments, radiolaria, sponge spicules and biogenic unspecified.

Counts were then converted into percentages of the bulk sediment.

Figure 4.4 (overleaf): Photographs of typical terrigenous and authigenic components of the 63 µm-2 mm fractions.

Terrigenous components:

A: Rock fragments from PC496 3.5 cmbsf.

B: Mafic minerals from PC496 3.5 cmbsf.

C: Mica from PC496 3.5 cmbsf.

D: Volcanic glass from PS58/255-2 133 cmbsf.

Authigenic components:

E: Micro-manganese nodules from PS58/253-1 476 cmbsf.

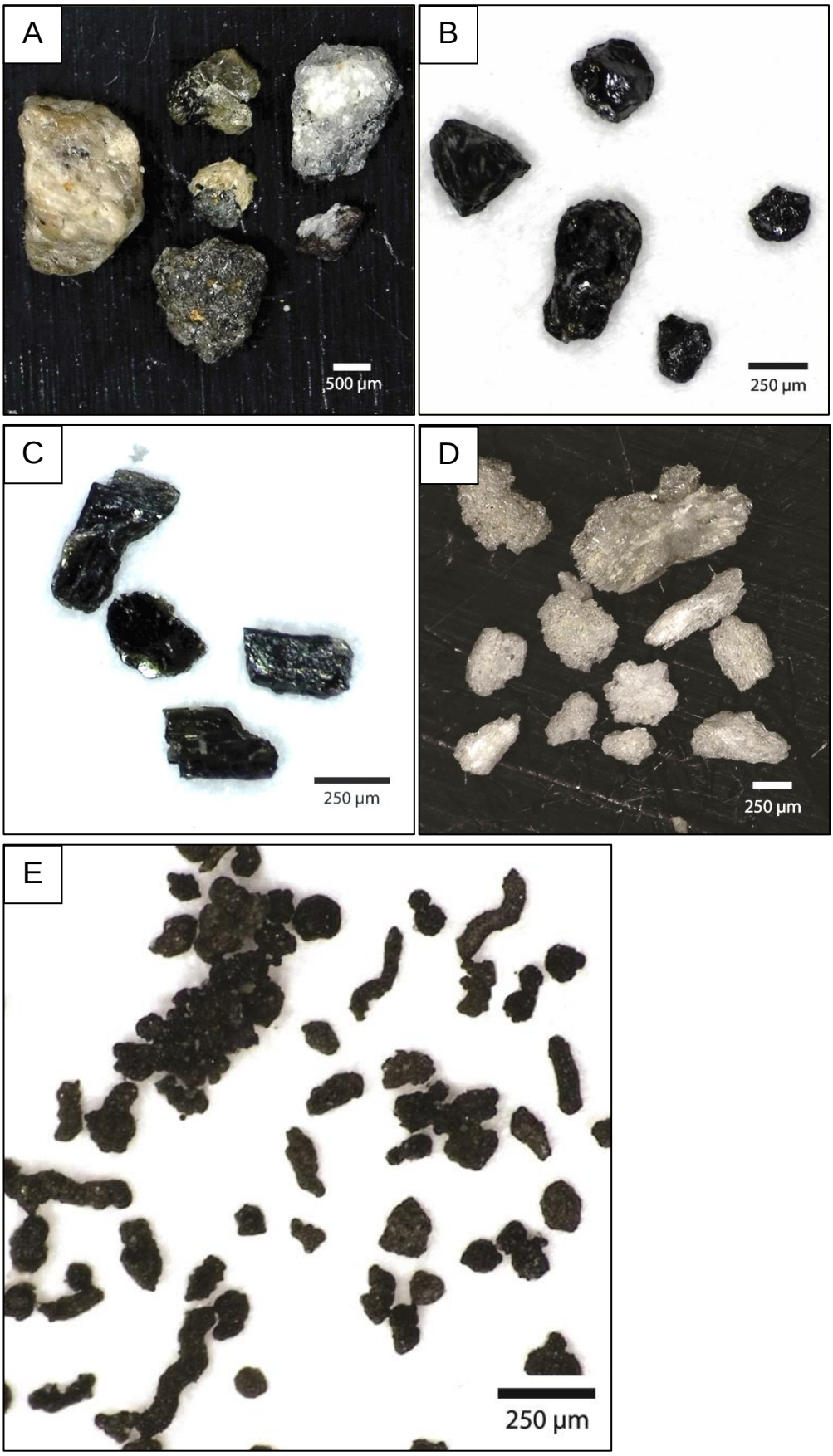
A
500 µm
B
250 µm
C
250 µm
D
250 µm
E
250 µm

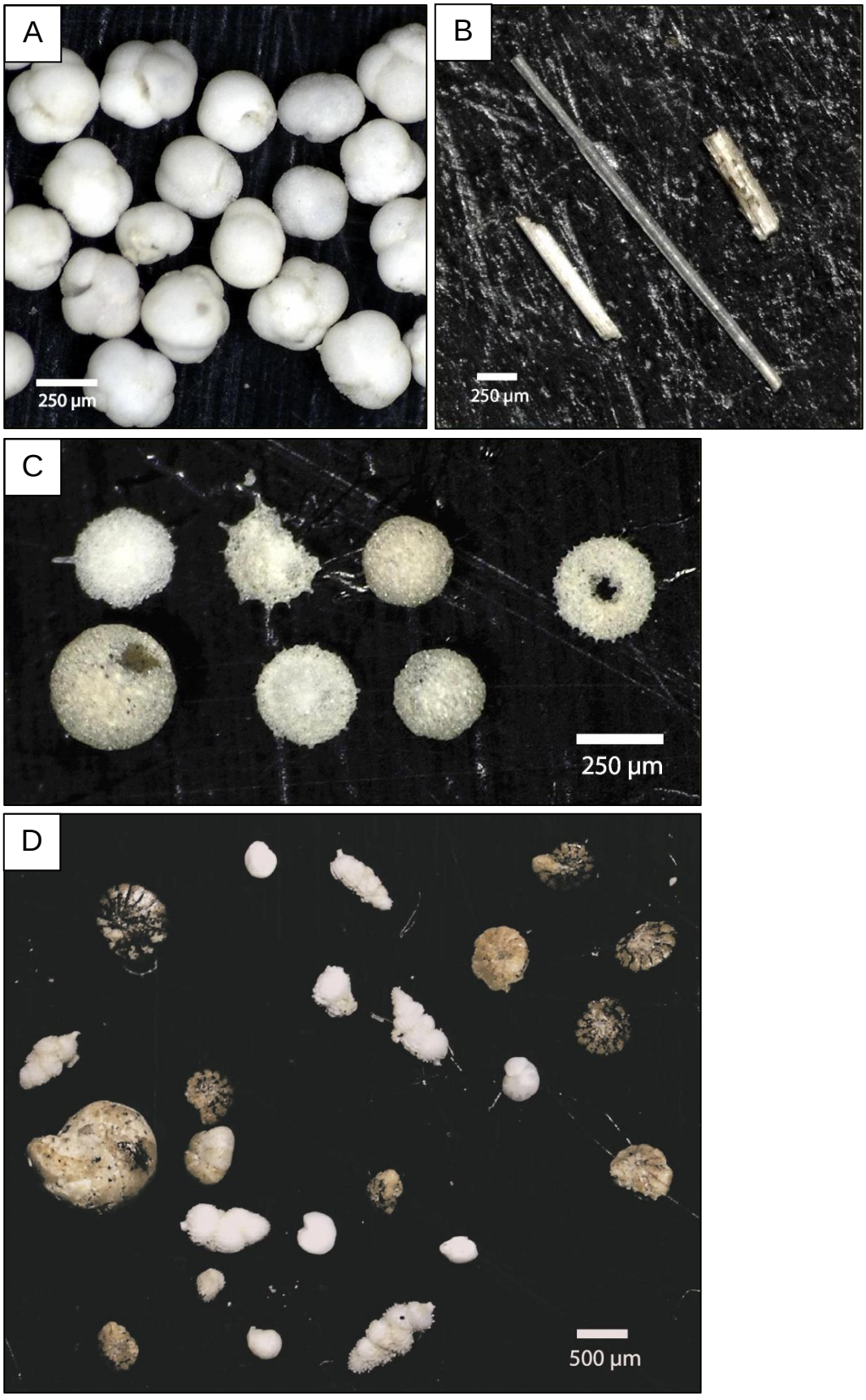
A
250 µm
B
250 µm
C
250 µm
D
500 µm

Figure 4.5 (previous page): Typical biogenic components of the 63 µm-2 mm fractions. A: Planktonic foraminifera from PS58/253-1 365 cmbsf.

B: Sponge spicules from BC495 2 cmbsf.

C: Radiolaria from PC496 3.5 cmbsf.

D: Benthic foraminifera from BC495 2 cmbsf.

4.3.4.5. Clay mineralogy

XRD clay mineral analysis was carried out at the University of Leipzig by Prof. Werner Ehrmann. The method is described in Petschick et al. (1996) and Ehrmann et al. (2011). The clay (<2 µm) fraction was placed in suspension with a standard, filtered through a 0.2 µm filter and the filter paper was dried and exposed to ethylene glycol vapour. The samples were X-rayed on a Rigaku New Miniflex with CoKα radiation (30 kV, 15 mA). Smectite, illite, chlorite and kaolinite were identified based on their basal reflections on the diffractograms. Duplicate analyses were carried out if samples recorded a clay mineralogical change unaccompanied by lithological change, or if diffractograms were unclear (e.g., because of preparation issues or high opal contents) to aid in evaluation.

4.3.5. Chronological methods

Age models for the cores have been developed from chronological constraints in the form of ^{14}C dates, diatom biostratigraphy, tephrochronology and Relative Palaeomagnetic Intensity, together with variability in physical properties, sedimentology and geochemistry of the sediment cores (Figure 4.6). Age constraints are restricted to glacial-interglacial boundaries with the exception of core PC494, for which the correlation of the relative palaeomagnetic intensity record with a global stack has allowed for the attribution of ages within individual marine isotope stages.

The dates of each marine isotope stage (MIS) referred to in this thesis are as in Lisiecki and Raymo (2005), as follows:

MIS boundary	Age (ka)
1/2	14
2/3	29
3/4	57
4/5	71
5a (peak)	82
5b (peak)	87
5c (peak)	96
5d (peak)	109
5e (peak)	123
5/6	130
6/7	191
7/8	243
8/9	300
9/10	337
10/11	374

Table 4.3: Marine Isotope Stage ages, from Lisiecki and Raymo (2005).

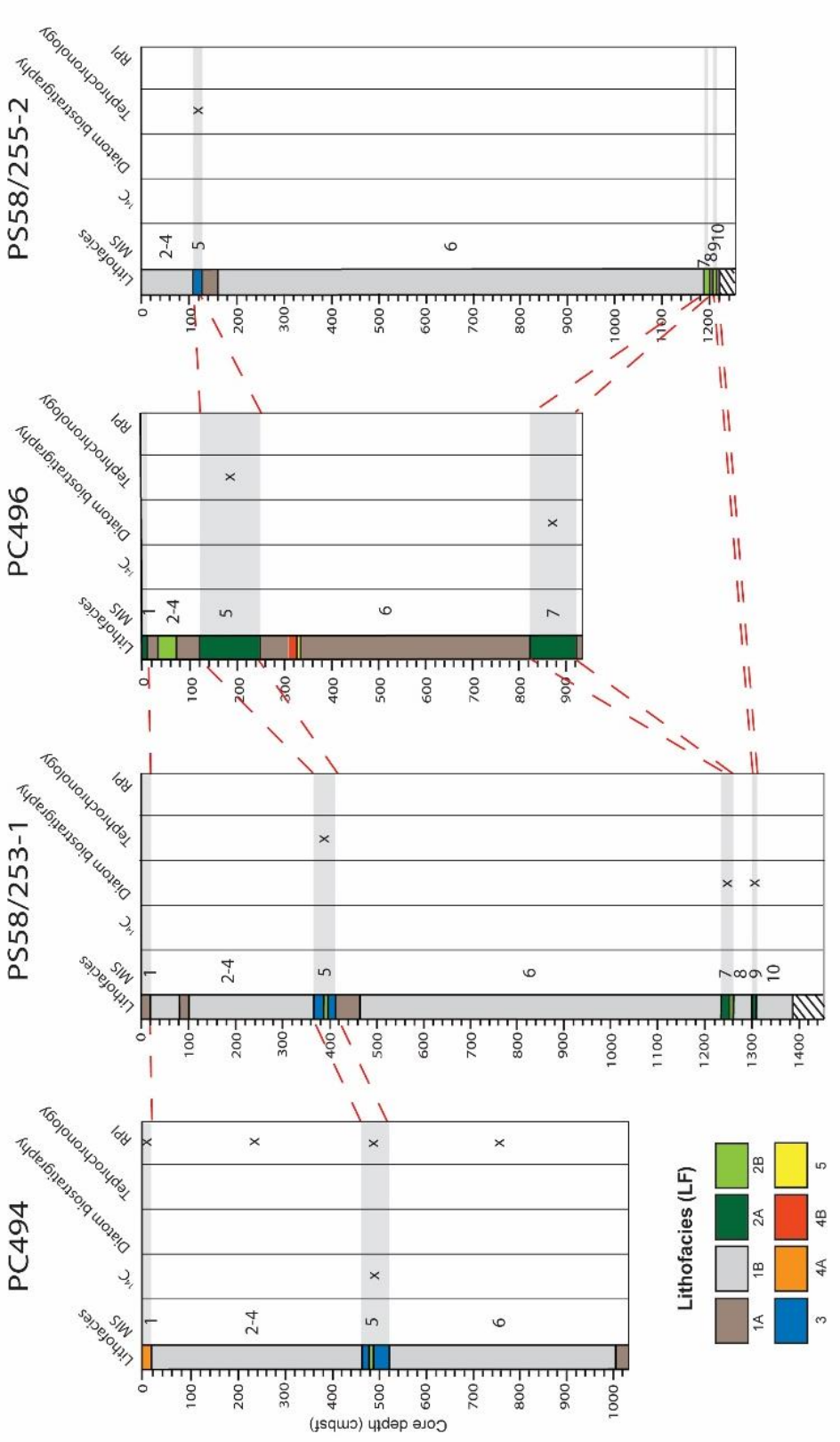

Figure 4.6: Summary of the chronological methods that were used in conjunction with variability in physical properties, sedimentology and geochemistry of the sediment cores to identify glacial-interglacial cycles and correlate between cores. Further information is provided in Chapter 6.2.

4.3.5.1. Radiocarbon Dating

Accelerator Mass Spectrometer (AMS) ^{14}C dating was carried out at BETA Analytic Inc. (Miami, Florida, U.S.A.). One sample of planktonic foraminifera of the species *Neogloboquadrina pachyderma* sinistral was dated from core PC494 (474 cmbsf). Two samples of bulk sediment were taken from PC496 (190 and 873 cmbsf) and one from BC497, taken from the same location as PC496 (surface sample), due to the lack of carbonate material in these cores, and AMS ^{14}C dating was carried out on the acid-insoluble organic matter. Conventional ages were calibrated using the Marine13 calibration curve of Reimer et al. (2013) and the Calib Rev 7.0.4 software (Stuiver et al., 2017). The results of the AMS ^{14}C dating are presented in Chapter 6.2.1.1.

4.3.5.2. Stable oxygen and carbon isotope analysis

$\delta^{18}O$ and $\delta^{13}C$ analyses were carried out on planktonic foraminifera of the species *Neogloboquadrina pachyderma* sinistral picked from PS58/253-1. However, this method did not produce viable results for developing a chronology, probably because many of the picked tests showed signs of dissolution and/or reworking, and because of analytical issues (i.e. samples were not weighed before analysis, resulting in unreliable data). Therefore, the results are not shown.

4.3.5.3. Diatom biostratigraphy

Diatom biostratigraphy was carried out by Dr. Oliver Esper at AWI on five samples from PS58/253-1 and by Dr. Claire Allen at BAS on two samples from PC496. Key indicator species were identified regarding both environmental conditions (e.g. the presence of *Fragilariopsis kerguelensis* suggesting pelagic, open-ocean conditions (Crosta et al., 2005)) and chronological constraints (e.g. the presence of *Hemidiscus karstenii*, which has a first abundant occurrence datum of 420 ka and last occurrence datum of 180 ka) (Zielinski et al., 2002; Zielinski and Gersonde, 2002).

4.3.5.4. Tephrochronology

Distinct, disseminated layers of volcanic glass had been noted in MIS 5 and late MIS 6 marine sediments in the Amundsen and Bellingshausen seas. Hillenbrand et al. (2008b) reported occurrence of up to three tephra layers in 28 marine sediment cores and ice cores, referred to as tephra layers A, B and C. The chemical composition of the volcanic glass indicated Marie Byrd Land as the volcanic source. There, Wilch et al. (1999) and Dunbar et al. (2008) had investigated tephra layers at Mt. Moulton, which had been deposited during Plinian eruptions of the nearby Mt. Berlin volcano.

Litho-, bio-, magneto- and chemostratigraphy were used to derive approximate ages for the tephra layers detected in the marine sediment cores, whilst correlation to tephra layers in EPICA Dome C and Vostok ice cores suggested the following ages: tephra layer A, late MIS 5 (c. 92 ka); tephra layer B, MIS 5.5 (c. 136 ka); and tephra layer C, the end of MIS 6 (c. 142 ka) (Hillenbrand et al. 2008b). These ages correspond to $^{40}Ar/^{39}Ar$ dates of discrete tephra layers at Mt. Moulton (Wilch et al. 1999, Dunbar et al. 2008). Core PS2551 (69.815°S, 117.025°W) was the only core in the Amundsen Sea, in which Hillenbrand et al. (2008b) found a single tephra layer that they identified as layer B. It is thought that tephra layer A may have not been sampled in the core due to the typically disseminated nature of this layer, and that tephra layer C was likely prohibited from reaching the sea floor by sea ice at this southerly location, which may have retained perennial sea ice further into the MIS 6-5 transition than the more northerly cores included in the study (Hillenbrand et al., 2008b). Major and trace metal analysis of the three tephra layers showed chemical signatures indistinguishable from each other. Nevertheless, any elevated concentrations of volcanic glass found in the sand fraction of cores investigated in this study potentially offer “loose” chronostratigraphic constraints, identifying sediments deposited during late MIS 6 or MIS 5.

4.3.5.5. Relative Palaeomagnetic Intensity

U-channels were taken from the archive half of PC494 at the British Ocean Sediment Core Research Facility (BOSCORF) in Southampton. The 2 x 2 cm diameter u-channels were cut exactly to length and pushed into the sediment, ensuring no air was trapped.

Gravel grains were removed where this would not disturb the surrounding sediment. Any remaining gravel grains, voids, sediment disturbance or other notable features were recorded. The u-channels were removed with the aid of nylon line and capped with a lid and the ends were sealed with non-magnetic tape.

Firstly, magnetic susceptibility of the u-channel sediments was measured using a Bartington MS3 meter and a Bartington MS2C loop sensor of 40 mm diameter. Each u-channel was analysed twice in 1 cm increments for consistency and checked to ensure it correlated with the magnetic susceptibility data previously obtained for the whole core using a MSCL.

Relative Palaeomagnetic Intensity (RPI) analysis was carried out on the u-channels of core PC494 at the National Oceanography Centre, Southampton, in collaboration with Dr. Chuang Xuan.

Natural Remanent Magnetisation (NRM) is a record of both the primary magnetisation of a sample when it was deposited, plus any magnetisation acquired after deposition, and reflects both the strength of the earth's magnetic field and the amount of magnetic material in the sample. Anhysteretic Remanent Magnetisation (ARM) is a measure of the magnetic content of the sample and can therefore be used to remove the concentration effect from NRM (Bleil and von Dobeneck, 1999).

NRM and ARM measurements were carried out on a 2G Enterprises Superconducting Rock Magnetometer of 42 mm internal diameter, kept in a steel-lined room. Technical details of the magnetometer are described in Roberts (2006). The u-channels entered the magnetometer automatically on a plastic tray which was cleaned physically with methanol after every sample and cleaned magnetically using 100 mT degauss at the start of each day. NRM and ARM were measured in 1 cm steps down-core.

Each u-channel was run first for NRM analysis at 10, 20, 30, 40, 50, 65, 80 and 100 mT on the XYZ axes. ARM demagnetisation was then carried out, which applied 100 mT and a 0.5 Gauss Direct Current field to the sample to suppress the magnetism of almost all minerals. An ARM acquisition signal was then obtained by applying the same mT steps as for NRM, at 0.5 Gauss Alternating Field on the Z axis. Declination and inclination were also recorded, showing the dipping angle of the magnetic vector, varying between 0°

(horizontal) and 90° (vertical); the latter would be expected at this site due to the high latitude location.

Two estimations of RPI were created: the slope of the best fit line between NRM/ARM demagnetisation and NRM/ARM acquisition, where the ARM values are the mean values measured at 20-50 mT. The UPmag software for MATLAB was used to display and analyse the data and to produce the two RPI proxies (Xuan and Channell, 2009). Each RPI estimation is accompanied by a correlation coefficient value (R) of the best-fit which provides an indication of the quality of the data and suitability for correlation to other records. The ratio of NRM to the respective normaliser was also calculated, which can be used as an RPI estimate, but the accompanying standard deviation data suggested the data were more uncertain than the slope angles of the best fit lines.

The RPI records were then compared to similar records obtained in the South Pacific and with global stacks, e.g. SINT-800 (Guyodo and Valet, 1999) and PISO1500 (Channel et al., 2009). The SINT-800 record was found to have the greatest similarity with PC494 RPI and was used to identify tie points and develop an age model. Inclination was analysed to identify the 41 ka Laschamp magnetic reversal event, though the 110-120 ka Blake event was not identified (Langereis et al., 1997; Singer et al., 2009).

The magnetic grain size proxy ARM demagnetisation at 0 mT/magnetic susceptibility was also calculated in order to examine changes in grain size.

Chapter 5: Results and Interpretation of the Bathymetric Analysis of the Amundsen Sea Mounds

5.1. Introduction

This chapter presents the analysis of existing multi-beam swath bathymetry data (IBCSO, Arndt et al., 2013) and new sub-bottom profiler data. The available data for each mound are presented together with a brief description. Section 5.3 draws on these data to make interpretations as to how the mounds formed. The evidence for influence of turbidity currents and bottom currents on mound formation are considered separately. This includes the interpretation of how slope-parallel channels and sediment waves may have formed.

5.2. Results of the bathymetric analysis of the Amundsen Sea mounds

5.2.1. Overview of mound morphology

The sediment mounds of the eastern Amundsen Sea will be referred to here as mounds One to Five (M1 to M5) (west to east) (Figure 5.1). The existence of four asymmetric sediment mounds in the eastern Amundsen Sea has long been established in the literature (e.g. Yamaguchi et al., 1988; Nitsche et al., 2000), corresponding to the mounds labelled Am1-4 by Scheuer et al. (2006a), but here we also identify a fifth mound located to the east of those previously identified (at approximately 70°S, 103°W). Single and multi-beam swath bathymetry data from the IBCSO compilation suggest M5 exhibits a similar size and morphology to M3 and M4.

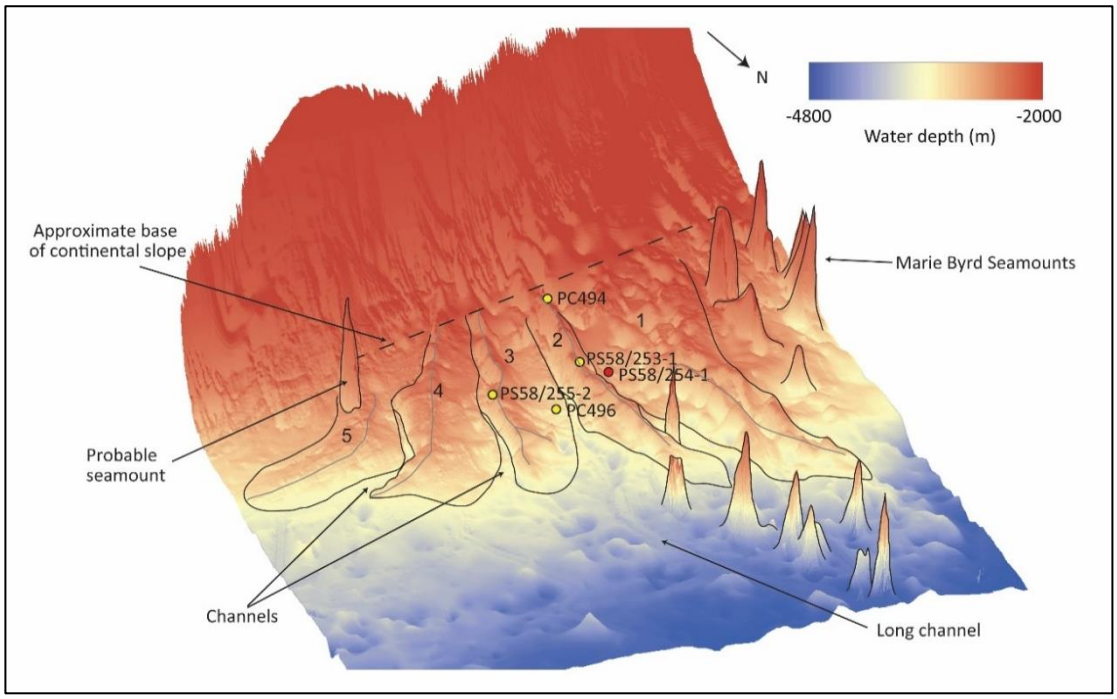

Figure 5.1. 3D bathymetric image of the lower continental slope and upper continental rise of the eastern Amundsen Sea (location shown in Figure 5.2). The sediment mounds (labelled 1-5) and prominent seamounts have been outlined and notable features labelled. Blue circles indicate the position of the sediment cores analysed in this research and the pink circle indicates the position of core PS58/254-1. Bathymetric data are from IBCSO (Arndt et al., 2013). Bathymetry shown with 150x vertical exaggeration.

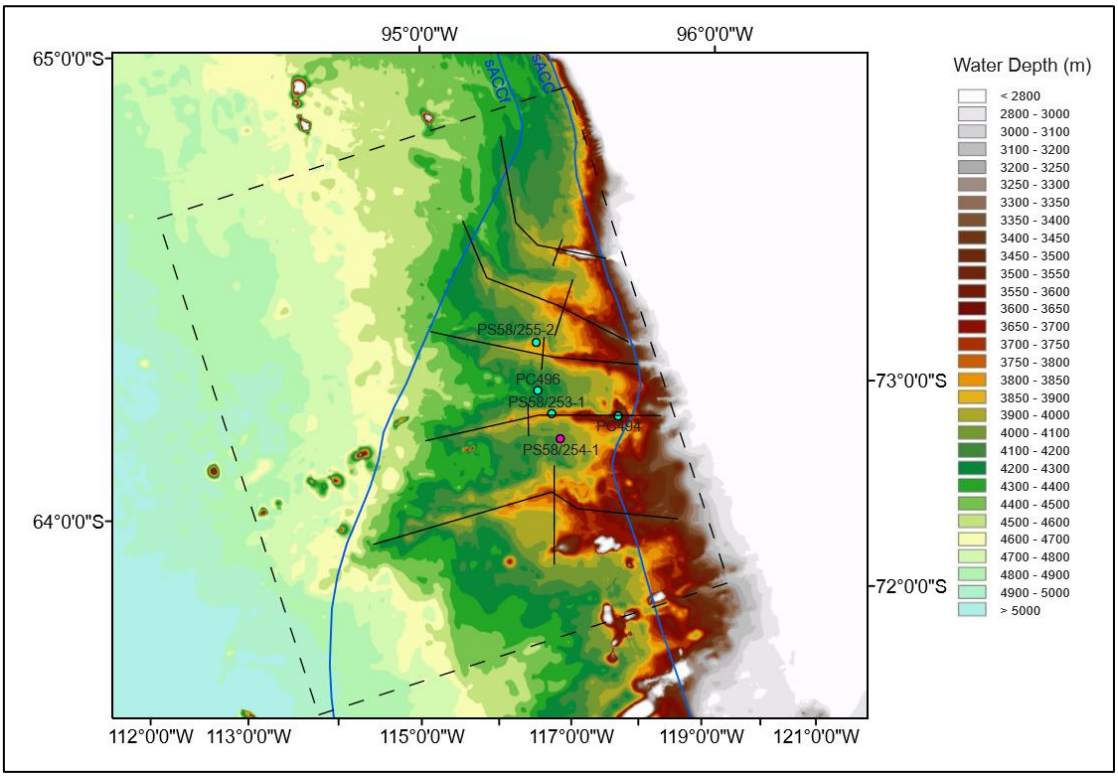

Figure 5.2: Bathymetric map of the upper continental rise of the eastern Amundsen Sea. Black lines mark the approximate position of the mound crest and maximum width used to measure the dimensions, as given in Table 5.1. The black dashed box indicates the location of Figure 5.1. Position of the sACC and sACCf taken from Orsi et al., 1995. Bathymetric data from IBCSO (Arndt et al., 2013).

Mound number	Length (km)	Maximum width (km)	Shallowest water depth of crest (m)	Maximum height above sea floor (m)
M1	433	130	3400	900
M2	315	45	3500	800
M3	280	42	3500	800
M4	290	78	3650	650
M5	250	36	3800*	500

Table 5.1: Dimensions of the five mounds. Figure 5.2 shows the locations of the profiles along which the mound length and width were measured. Maximum height above sea floor has been calculated based on a 4300 m water depth sea floor to the east of the mounds. Mound 5 * indicates the measurements do not include the height of the seamount.

Mound length (Table 5.1) was measured approximately along the main axis of the mounds from 3400m water depth at the base of the continental slope to 4400m water depth on the continental rise. The mounds vary from 250 to 433 km in length and, typically, the mounds become progressively smaller in length and height above the seafloor in an eastward direction. The maximum width of the mounds varies from 36 to 130 km. The mounds are partially joined and so the areas between mounds have water depths of approximately 3850-4000 m close to the continental slope and 4300-4400 m at about 250 km from the base of the slope.

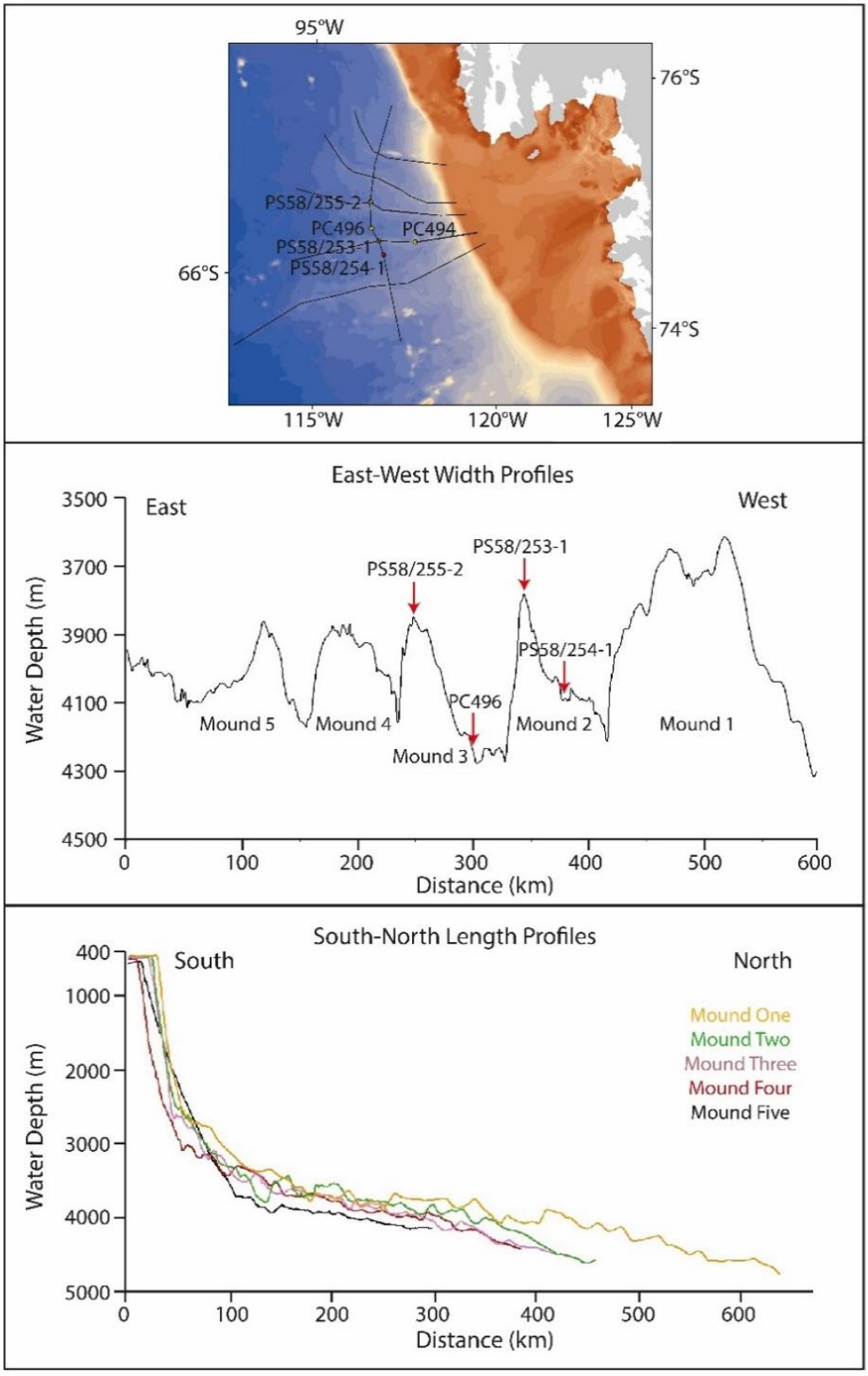

Figure 5.3: Strike and dip topographic profiles of the mounds in the eastern Amundsen Sea.

5.2.2. Mound One

M1 is the widest, longest and tallest of the five mounds, standing up to 900 m above the surrounding sea floor in 3600-4300 m water depth. M1 corresponds to mound Am4 of Scheuer et al. (2006a). The mound is attached to the base of the continental slope with no evidence of a channel in between. The most proximal third of M1 is roughly symmetrical (cross profiles 5 and 6 on Figure 5.5). The mound here is over 150 km wide but its eastern flank, which lies at the base of a particularly low-angle section of the continental slope, is dissected by a deep depression and therefore its easternmost part appears partially detached from the main body of the mound. This easternmost section is shown in the TOPAS image of Figure 5.6, and its crest is labelled as “secondary mound crest”.

Approximately 100 km from the base of the continental slope at c.70°S, the wide mound crest narrows and turns eastwards, so that the central third of the length of M1 is asymmetrical (cross profile 4 on Figure 5.5), with a gently sloping flank to the west and a steep flank facing east, bordered by a channel. Here, the mound crest has two branches. The western branch contains sediments that have accumulated around seamounts and extends no further north than 69°S, whilst the eastern branch continues much further north. Figure 5.6 shows that the sediments on the eastern part of the mound are acoustically stratified, with the exception of sections of the undulating surface and the 2° sides of the channels separating the three mound sections. The channels have steeper western flanks and large western levees when compared to the east.

The most distal third of M1 has a particularly complex and undulating topography. The crest of the eastern branch exhibits several changes in orientation and changes in height of up to 300 m. Its crest splits into two branches, as shown in cross profile 3 of Figure 5.5, probably due to the development by a new channel. A pronounced depression, approximately 200-250 m deep (with a base at 4100 m water depth) and 50 km wide, is present in the western branch, marked by the red arrow in strike profile B in Figure 5.4, approximately 300 km from the base of the continental slope. The northern terminus of this mound branch is particularly undulating and relatively steep, with its water depth increasing by 400 m over a distance of 30 km.

The channel to the east separates M1 from M2, is 6 km wide and has a steep western flank (Figure 5.6). This channel is visible on cross profiles 3 to 6 (Figure 5.5), implying that it extends for at least 200 km, and it turns westwards further north, thereby approaching the eastern edge of M1.

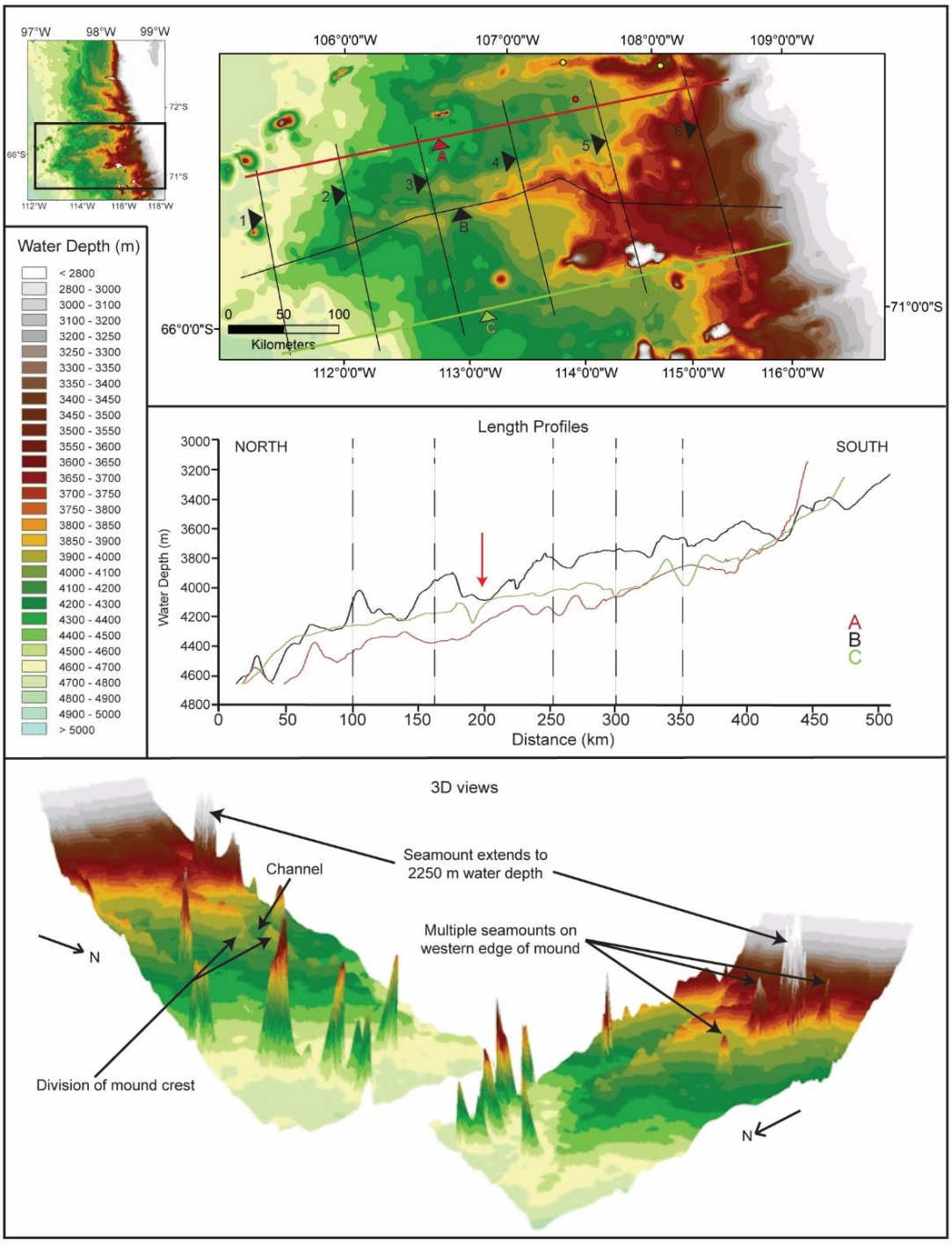

Figure 5.4: 2D, strike profiles and 3D views of M1. The position of the red (A), black (B) and green (C) lines on the 2D map show the location of the profiles along the long axis of M1. Dashed lines indicate changes in direction along the profile; the colour of the dashed line indicates to which profile the change corresponds. The red arrow on the profile marks the position of a prominent depression. The position of the black lines labelled 1-6 on the 2D map mark the location of the profiles across M1 in Figure 5.5. All 3D views are shown at 100x vertical exaggeration. Bathymetric data are from IBCSO (Arndt et al., 2013).

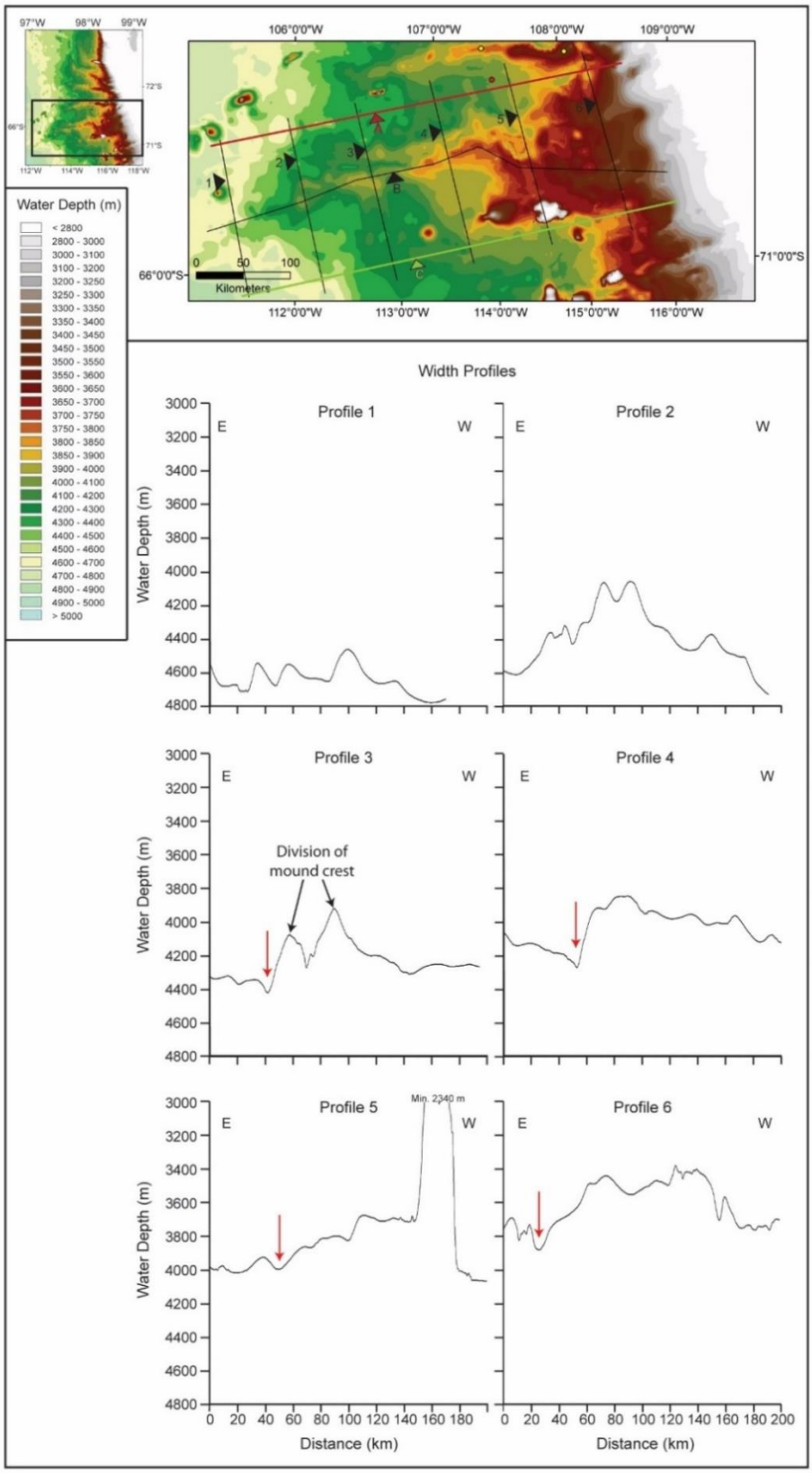

Figure 5.5: Profiles across M1, taken approximately perpendicular to the mound crest. The positions of the black lines labelled 1-6 on the 2D map mark the locations of the profiles. Red arrows on the profiles mark the position of the flanking channel to the East of M1.

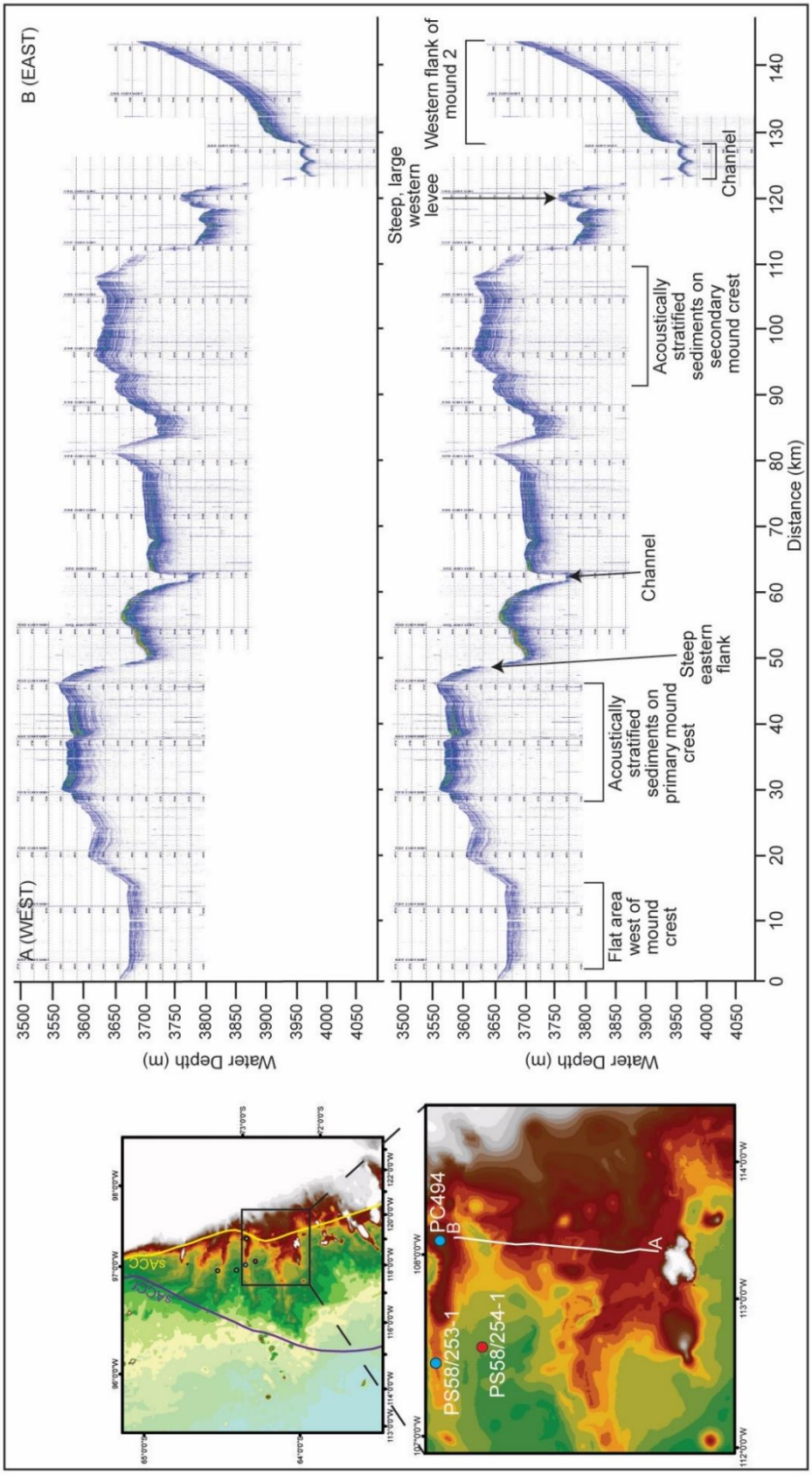

Figure 5.6: TOPAS sub-bottom profile extending from M1 to M2 across the channel separating the two mounds.

To the west of M1, between the mound and the large bathymetric high west of approximately 118°W (Figure 5.2), the lower continental slope and rise are characterised by a complex and rough seafloor topography. The continental slope here is at a particularly low slope angle of c.2° and its base is sinuous. However, there is also a feature with a geometry and acoustic profile somewhat similar to the five mounds identified in this research (Figure 5.7). This dome-like feature rises up to 400 m above the surrounding sea floor, is c.70 km wide (parallel to the shelf break) and c.50 km long; although connected to the continental slope, which would make the mound c.150 km long, channels appear to partially separate it from the slope, making this mound a more distinct feature.

Figure 5.7, particularly the line between point A and point B, shows a channel with an acoustically hard bed lying to the west of a mounded structure. The mound features a gently sloping western flank with acoustically stratified sediments, a relatively flat and broad mound crest (c.10 km wide) and a steeper eastern flank, which culminates in a steep-sided channel. The seafloor to the east of the channel, in the vicinity of a seamount, is characterised by gullies or sediment waves of varying wavelengths that are a few metres to 30 m deep. East of the seamount, sediment waves are seen to be developed in the acoustically stratified sediments.

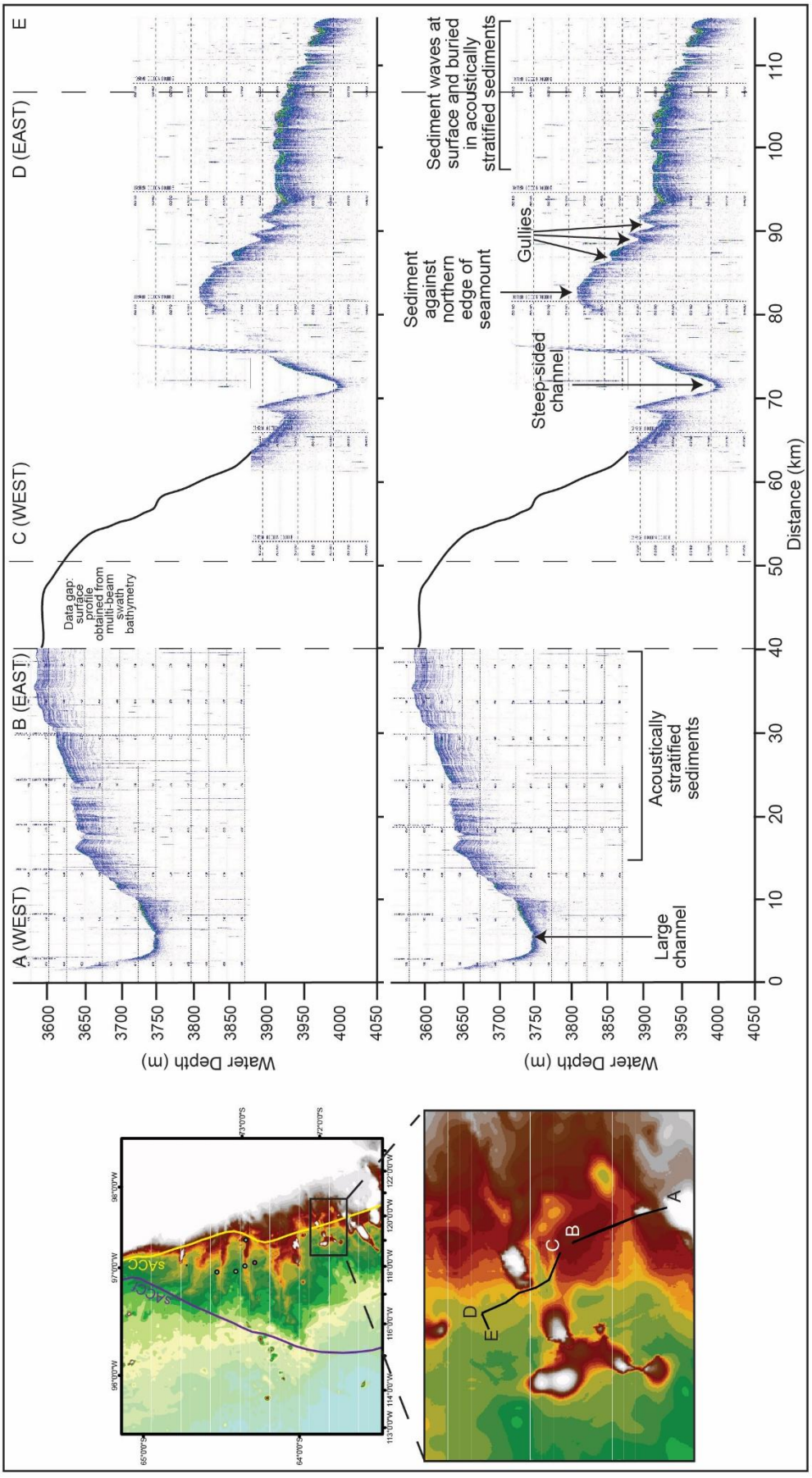

Figure 5.7: TOPAS sub-bottom profile of the area west of M1.

5.2.3. Mound Two

M2 is a particularly long but narrow and steep-sided mound (Figures 5.8 and 5.9) which extends north almost perpendicular to the continental shelf along its length, thereby only slightly turning to the west. M2 corresponds to mound Am3 of Scheuer et al. (2006a). The surface topography of M2 is moderately undulating, with the mound crest exhibiting height differences of up to 200 m over a distance of 10-20 km. With a gradient of 0.46°, the northern terminus of the mound is the steepest section, with the water depth of the mound crest increasing by 400 m over 50 km.

A 26 km wide, 460 m deep, shelf-parallel, asymmetrical channel separates the mound from the base of the slope, with a gently sloping (1-2.3°) southern side but a steeper (3.8°) northern flank, rising by 400 m northwards over 5 km (profile B in Figure 5.8). The northern bank of this channel is located 10 km south of site PC494.

M2 is separated from M1 to the west by a deep 6 km wide channel. Its eastern levee forms the base of the western flank of M2, which is acoustically stratified and smooth, while its higher but narrow western bank forms the base of the steep eastern flank of M1 (Figure 5.10). Two small steps are present in the western flank of M2 (Figure 5.10). The western flank rises eastwards to a very flat and acoustically stratified mound crest, from where core PC494 and, at a more distal location, core PS58/253-1 were collected (Figures 5.11, 5.12).

Up to a distance of at least 150 km from the base of the continental slope, profiles taken perpendicular to the shelf edge suggest the sides of M2 are particularly steep and symmetrical (profiles 4 and 5 on Figure 5.9). However, the orientation of the mound crest is highly variable and the multi-beam swath bathymetry data and profile 3 (Figure 5.9) show profiles taken perpendicular to the mound crest suggest the mound is asymmetric, with a gently sloping western flank and steeper eastern flank.

The channel separating M2 from M3 to the east was profiled at different locations with TOPAS (Figures 5.11, 5.12). Its floor is acoustically hard and approximately 5 km wide closer to the base of the continental slope (Figure 5.11).

Further north its bed is up to 10 km wide, sloping away from M2. This channel also appears to deflect eastwards further north, increasing the distance from the crest of M2,

and can be traced to at least the position of profile 3 (Figure 5.10) and possibly even of profile 1, some 400 km from the continental slope. This channel was noted in the cruise report of JR179 as having an asymmetrical floor and geometry typical of a channel eroded by turbidity currents (Shipboard Party JR179, 2008).

The eastern flank of M2 (Figures 5.11 and 5.12) is highly irregular and cut by numerous small gullies, typically <20 m deep (maximum 50 m deep) at water depths of c.4100m in moderately acoustically stratified sediments. The gullies are particularly extensive on the north-eastern flank (Figure 5.12). The seabed between M2 and M3, including the location of core PC496 on the distal flank of M2, slopes gently northwards and is acoustically stratified (Figures 5.11, 5.12).

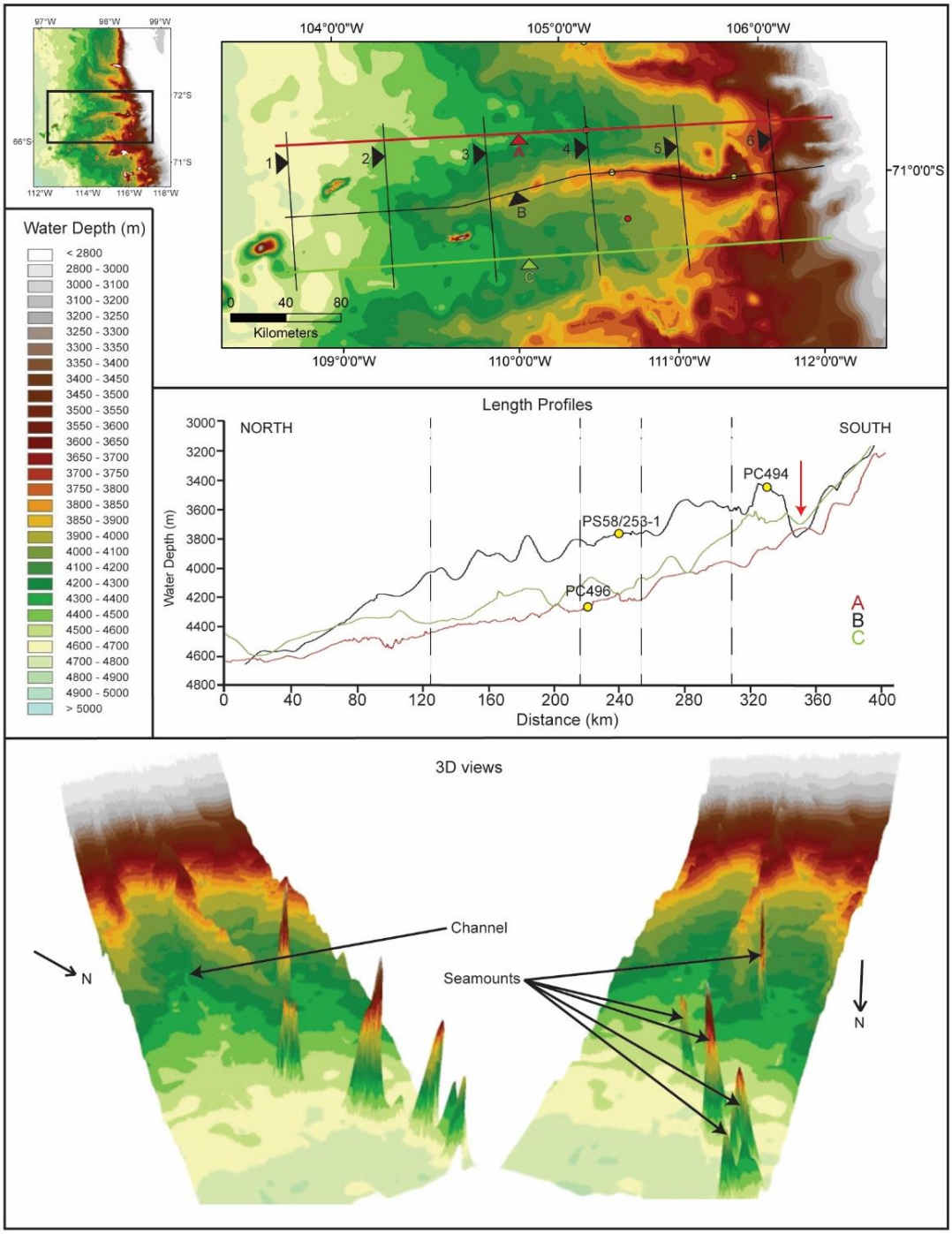

Figure 5.8: 2D, strike profiles and 3D views of M2. The positions of the red (A), black (B) and green (C) lines on the 2D map show the locations of the profiles along the long-axis of M2. Dashed lines indicate changes in direction along the profile; the colour of the dashed line indicates to which profile the change corresponds. The red arrow on the profile marks the position of the channel separating M2 from the continental slope. The position of the black lines labelled 1-6 on the 2D map mark the location of the profiles across M2 in Figure 5.9. All 3D views are shown at 100x vertical exaggeration. Bathymetric data are from IBCSO (Arndt et al., 2013).

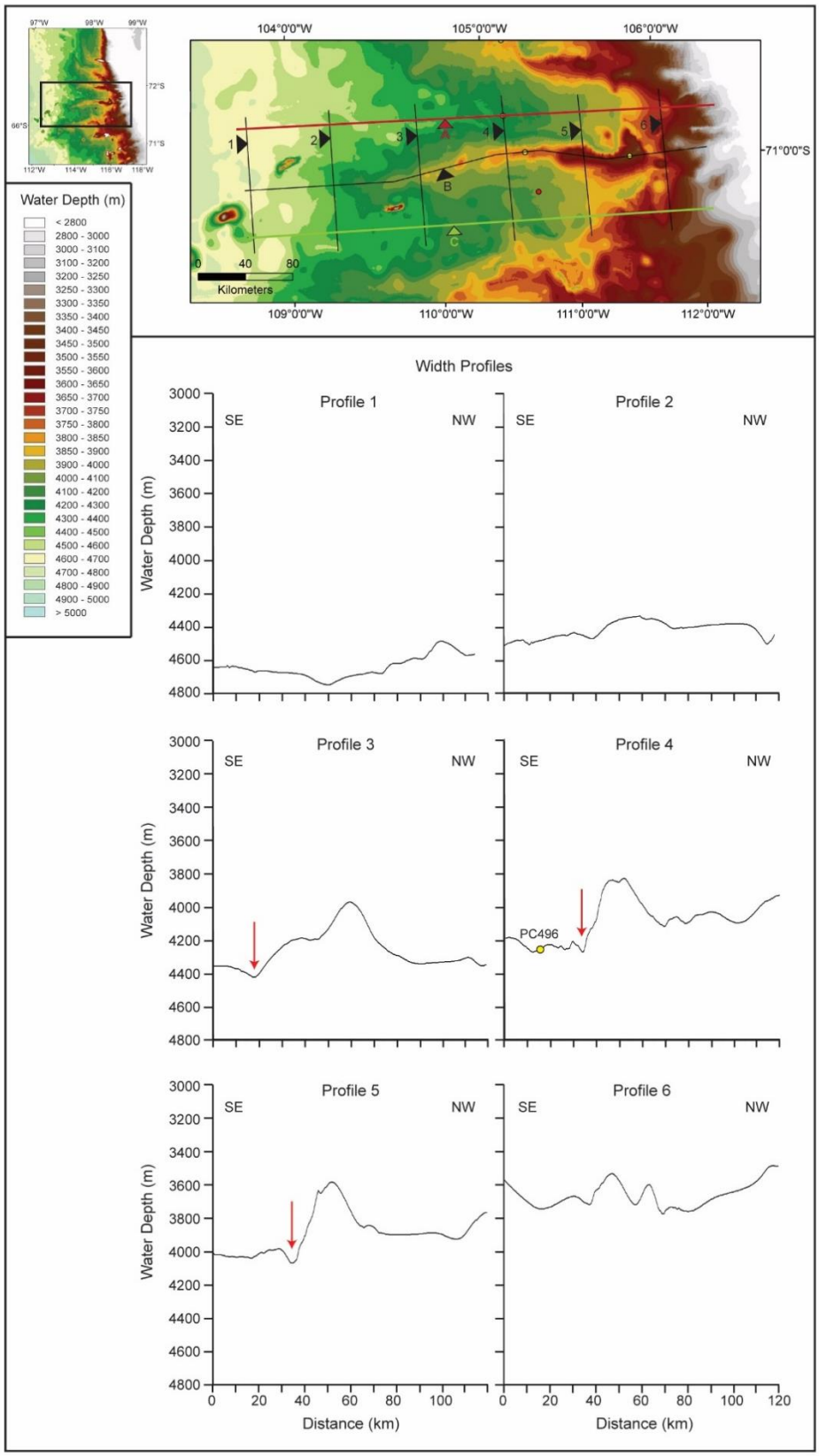

Figure 5.9: Profiles across M2, taken approximately perpendicular to the mound crest. The positions of the black lines labelled 1-6 on the 2D map mark the locations of the cross profiles. Red arrows on the profiles mark the position of the channel system separating M2 from M3 to the east.

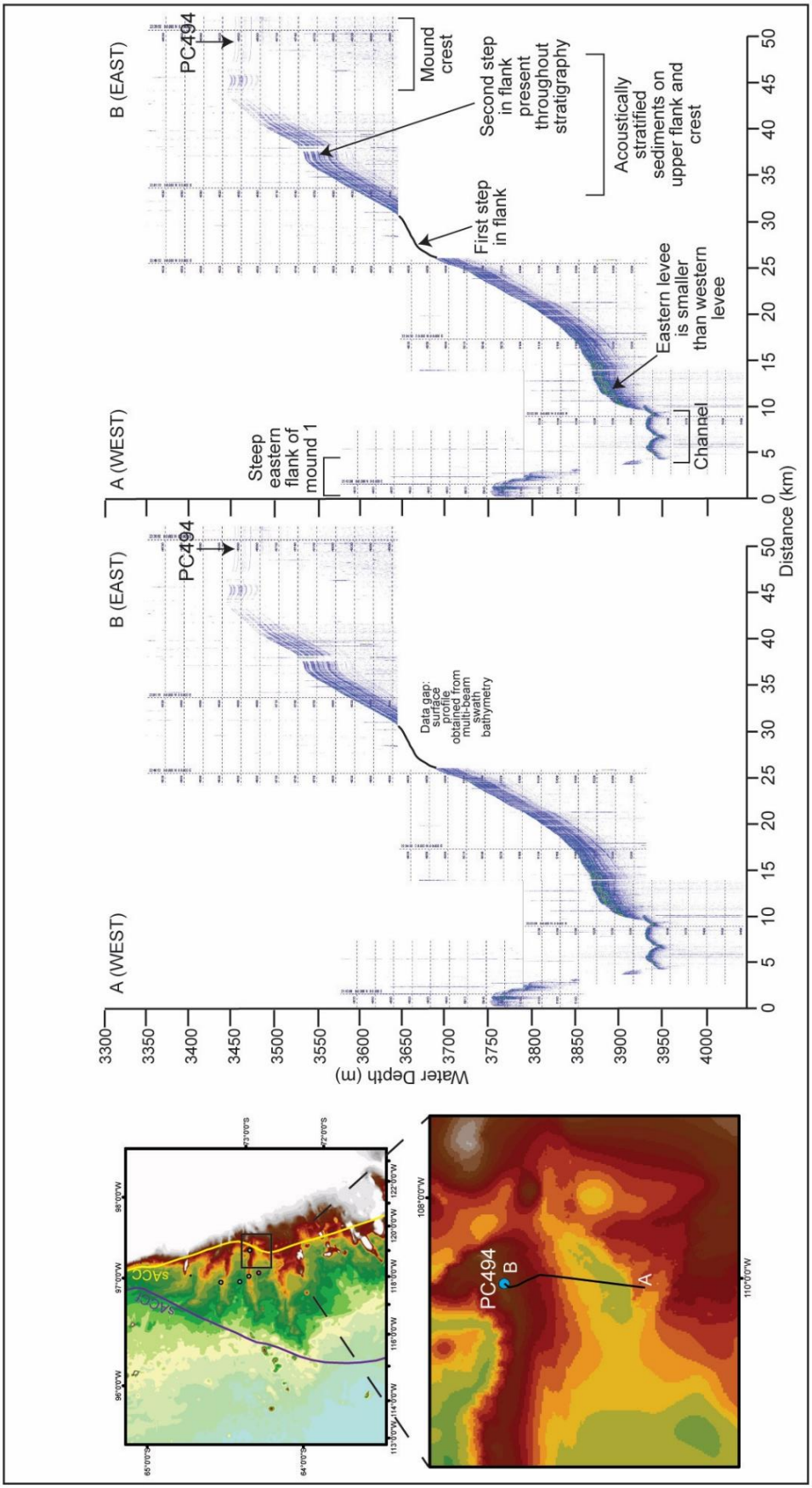

Figure 5.10: TOPAS sub-bottom profile extending from the eastern flank of M1 to the crest of M2.

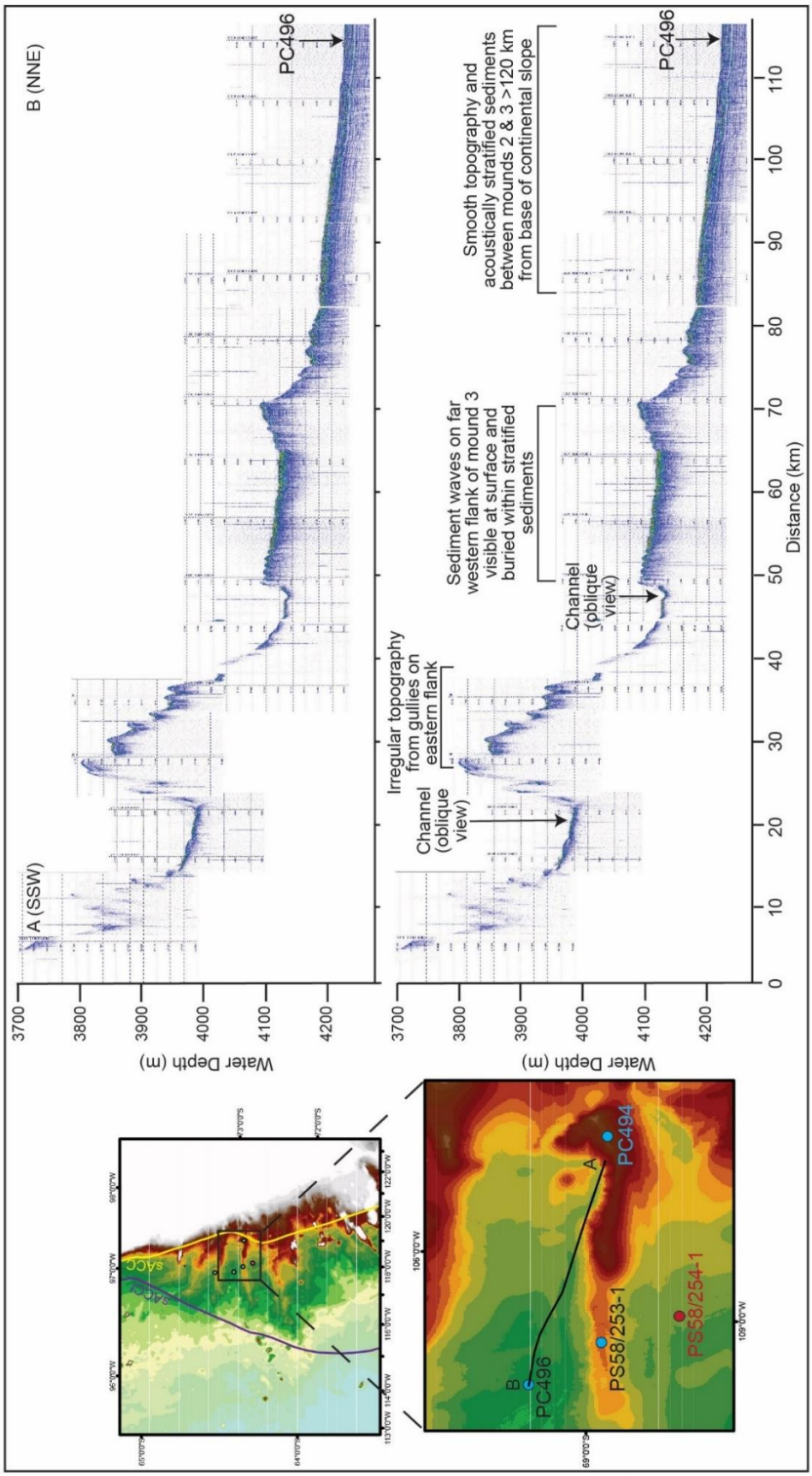

Figure 5.11: TOPAS sub-bottom profile extending from the proximal to the distal part of M2 along its eastern flank and across the channel separating M2 from M3.

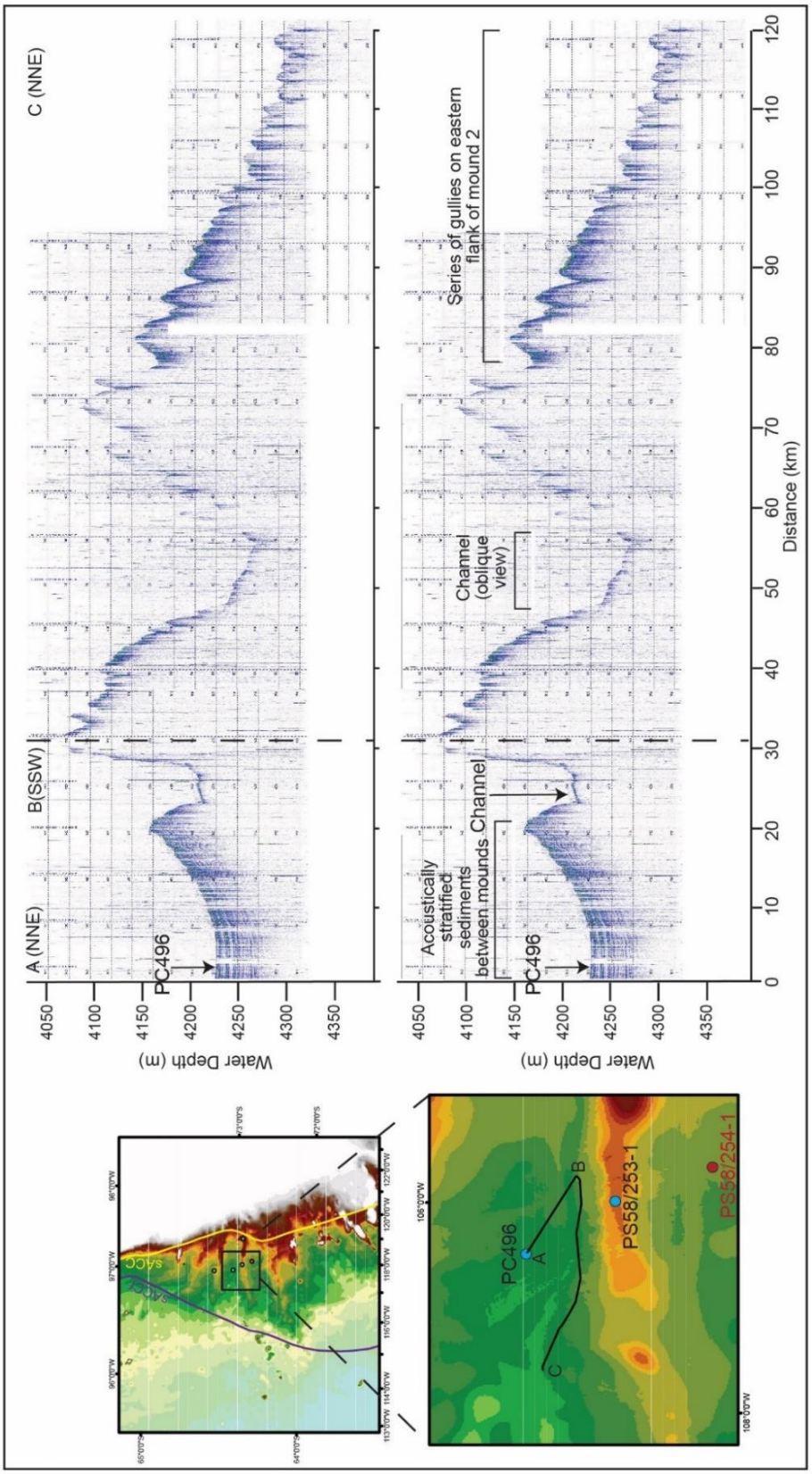

Figure 5.12: TOPAS sub-bottom profile on the distal eastern flank of M2 and across the channel separating M2 from M3.

5.2.4. Mound Three

M3 is relatively long and narrow and strikes NNE, i.e. its long axis is orientated approximately 30° to the shelf break. M3 corresponds to mound Am2 of Scheuer et al. (2006a). The mound crest 'kinks' towards the east at approximately 69.5°S, retaining its proximal orientation for a further 30 km north. The mound has a smooth and gently seaward sloping profile along its length (Figure 5.13).

A 26 km wide, 160 m deep, shelf-break parallel depression, which is possibly a channel, partially separates the mound from the base of the continental slope (indicated on Figure 5.13). The depression has a symmetrical, smooth bed and gentle flanks (≤1.6°).

The proximal-half of M3 shows a moderate degree of asymmetry with a gently-sloping NW flank and a steeper SE flank, which is bordered by a channel (see cross profiles 4 and 5 in Figure 5.14). This channel, which originates between profiles 6 and 5 (40 to 80 km from the base of the continental slope), continues to the position of profile 2 (270 km from the slope) and possibly profile 1 (320 km from the slope) in a more westerly position (Figs. 5.13, 5.14).

The asymmetry is not observed north of the 'kink' in the crest orientation. M3 has a more symmetrical geometry and a more undulating surface topography at a distance more than c.200 km away from the base of the slope. The complex topography includes a 200 m deep, 30 km wide depression in the mound crest at c. 280 km distance from the base of the continental slope, which may be due to mass wasting (indicated on Figure 5.13).

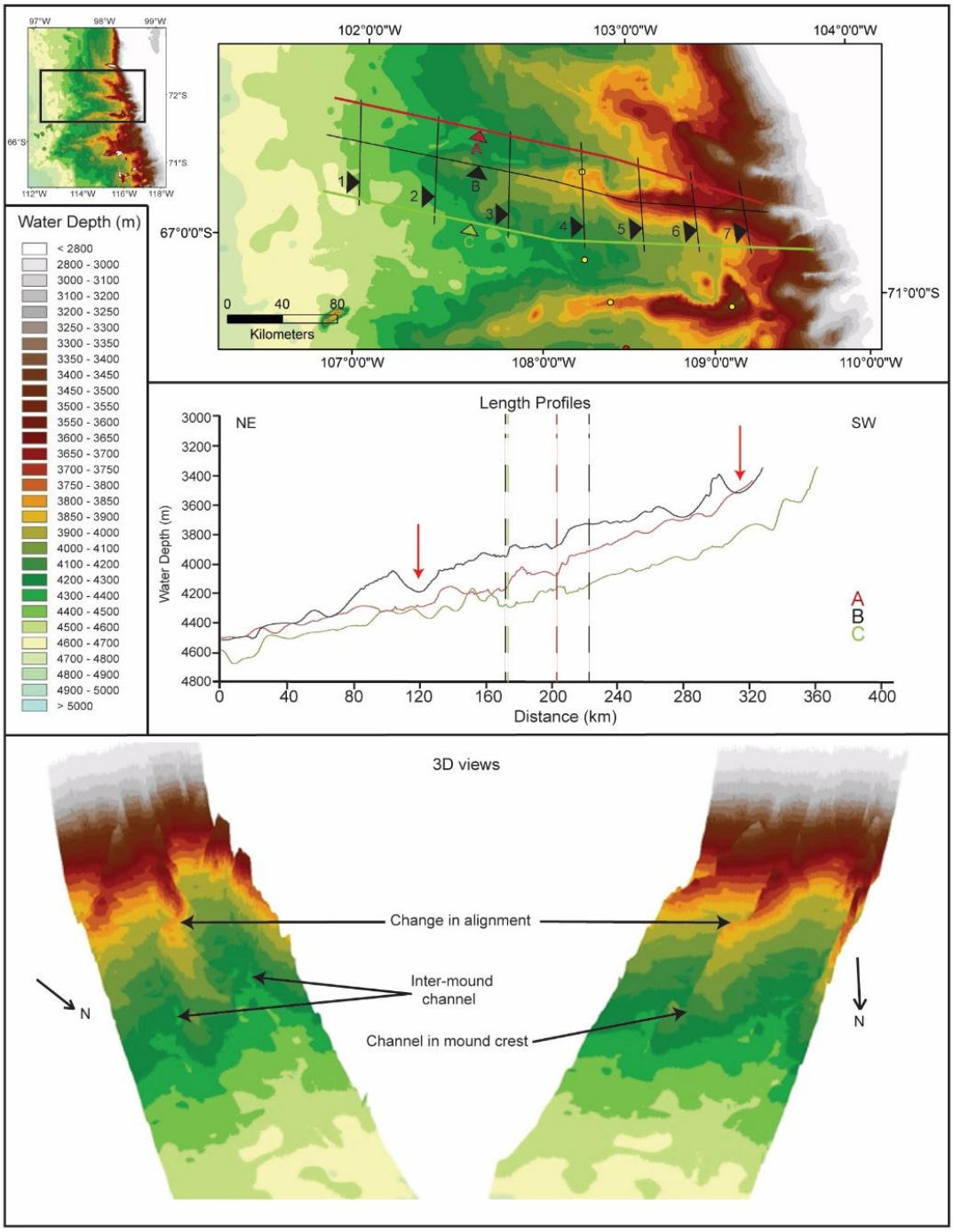

Figure 5.13: 2D, strike profiles and 3D views of M3. The position of the red (A), black (B) and green (C) lines on the 2D map show the locations of the profiles along the long axis of Mound Three. Dashed lines indicate changes in direction along the profile; the colour of the dashed line indicates to which profile the change corresponds. Red arrows on the profiles mark the position of prominent depressions. The position of the black lines labelled 1-6 on the 2D map mark the location of the cross profiles in Figure 5.14. All 3D views are shown at 100x vertical exaggeration. Bathymetric data are from IBCSO (Arndt et al., 2013).

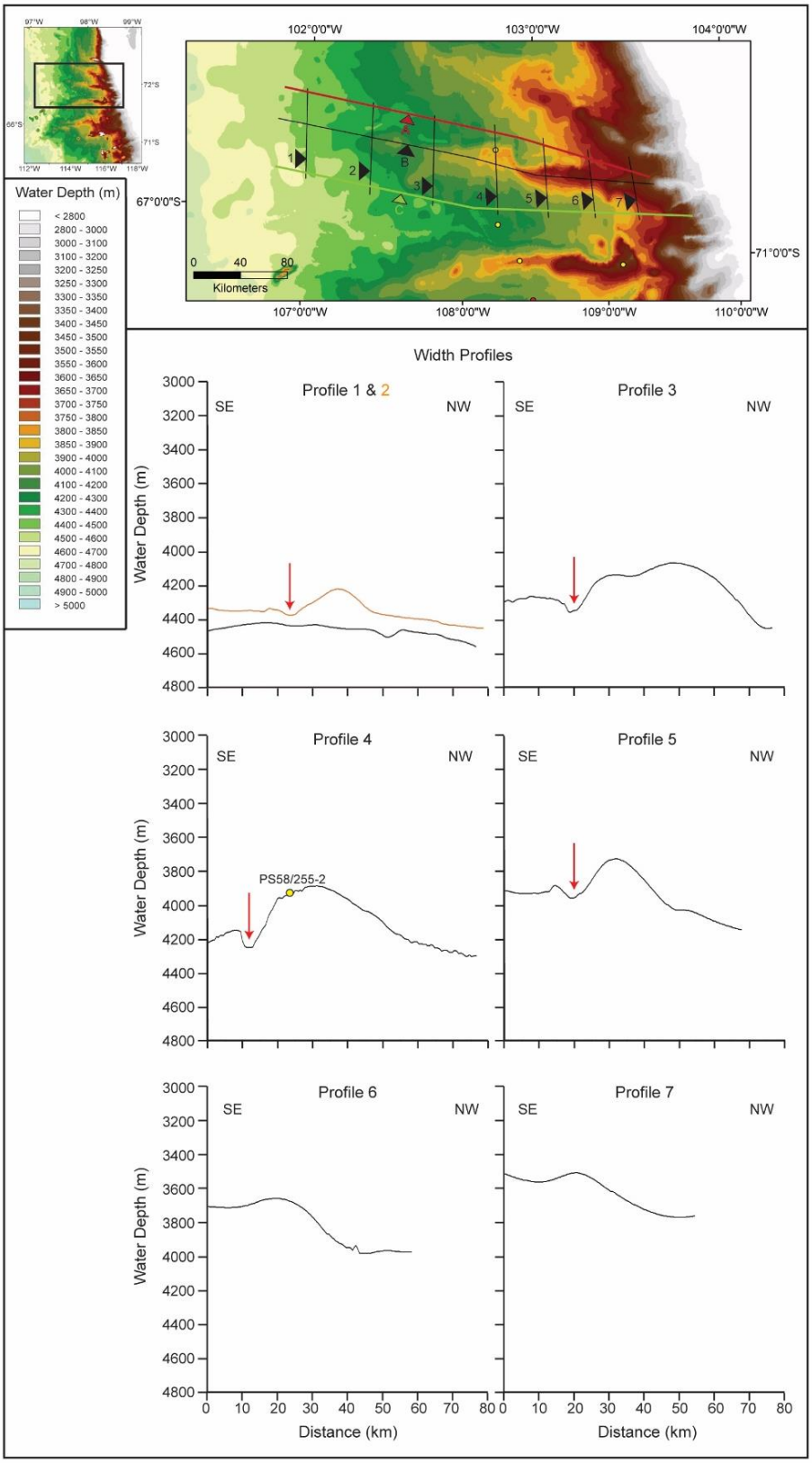

Figure 5.14: Profiles across M3, taken approximately perpendicular to the mound crest. The position of the black lines labelled 1-7 on the 2D map mark the locations of the profiles. Red arrows on the profiles mark the positions of the channel separating M3 from M4 to the East.

5.2.5. Mound Four

At the base of the continental slope, the southernmost part of M4 is indistinguishable from, and amalgamated with, M3. M4 corresponds to mound Am1 of Scheuer et al. (2006a). A 130 m deep, 22 km wide, symmetrical depression incises M4 and is present at the foot of the continental slope and runs parallel to the shelf break (Figure 5.15).

In the most proximal part of the mound, its crest has a NE-SW orientation, i.e. at an angle of approximately 45° to the continental shelf break. This orientation extends to 69°S, 200 km from the base of the continental slope, where the mound crest becomes further orientated towards the east, i.e. to an angle of approximately 10° to the shelf break. The height of the mound crest also increases by 100 m in the area of this change in orientation.

The symmetry of M4 is complicated by the change in orientation of its long axis. Close to the continental slope, the mound has a gently sloping western flank and steeper eastern flank (profile 8 on Figure 5.16). Further north, but south of the eastward change in orientation, M4 shows near symmetry (profiles 5 to 7 in Figure 5.16). Northwards of the point of the change in orientation, the multi-beam data and profiles 1-3 (Figure 5.16), although taken oblique to the mound crest, suggest the mound asymmetry is the same as in the proximal part. Profiles 4, 5 and 6 (Figure 5.16) show the channel separating M4 from M5 to the East. This channel is 5 km wide and steep-sided with an acoustically hard floor (see later Figure 5.20).

A TOPAS profile on the western flank of M4 shows sediment waves formed at water depths of 3750-3850 m in acoustically stratified sediments (Figure 5.17). The sediment waves have wavelengths of c. 600 m and are <10 m high.

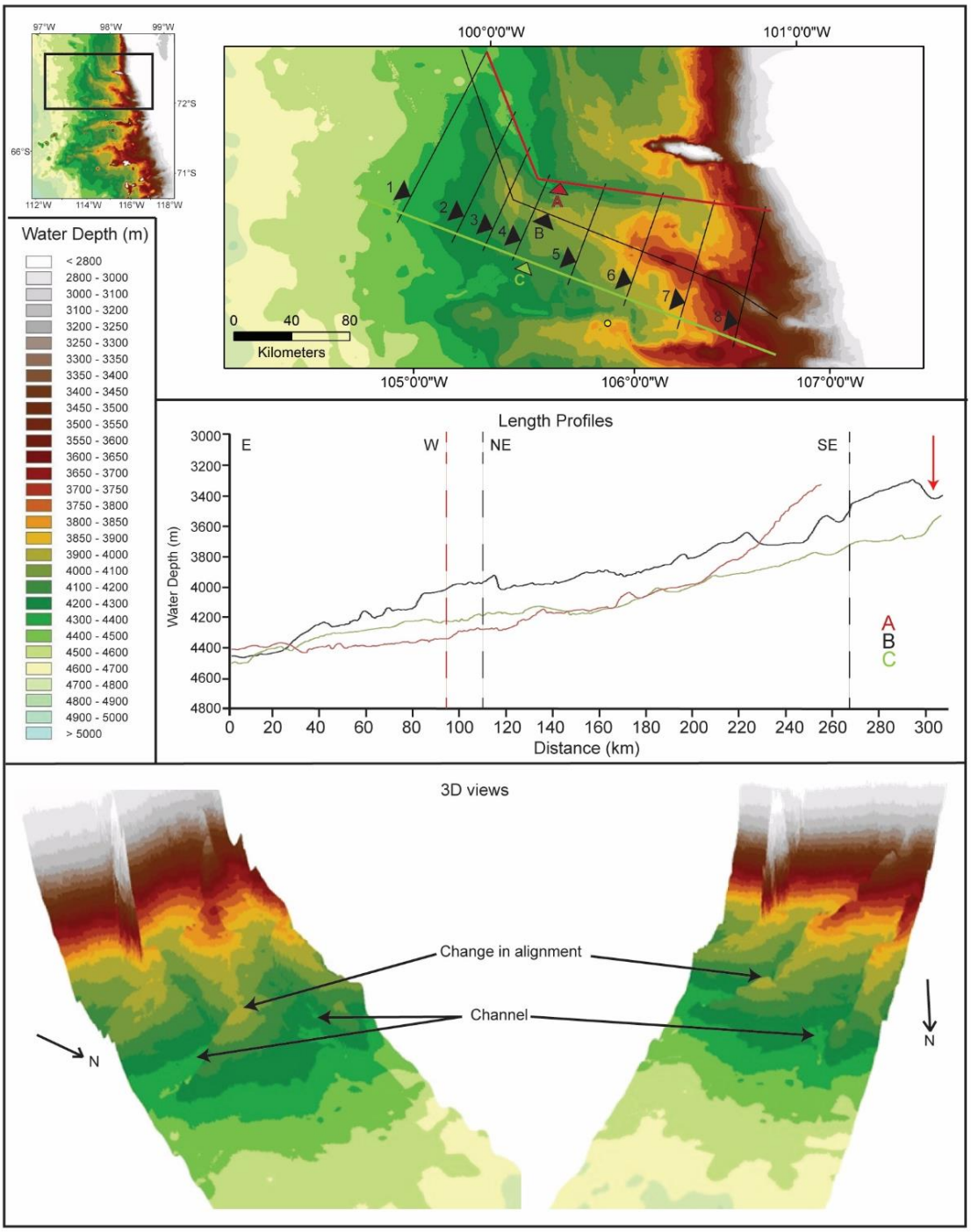

Figure 5.15: 2D, strike profiles and 3D views of M4. The positions of the red (A), black (B) and green (C) lines on the 2D map show the location of the profiles along the long axis of M4. Dashed lines indicate changes in direction along the profile; the colour of the dashed line indicates to which profile the change corresponds. The red arrow on profile B marks the position of a possible channel. The positions of the black lines labelled 1-6 on the 2D map mark the locations of the cross profiles in Figure 5.16. All 3D views are shown at 100x vertical exaggeration. Bathymetric data are from IBCSO (Arndt et al., 2013).

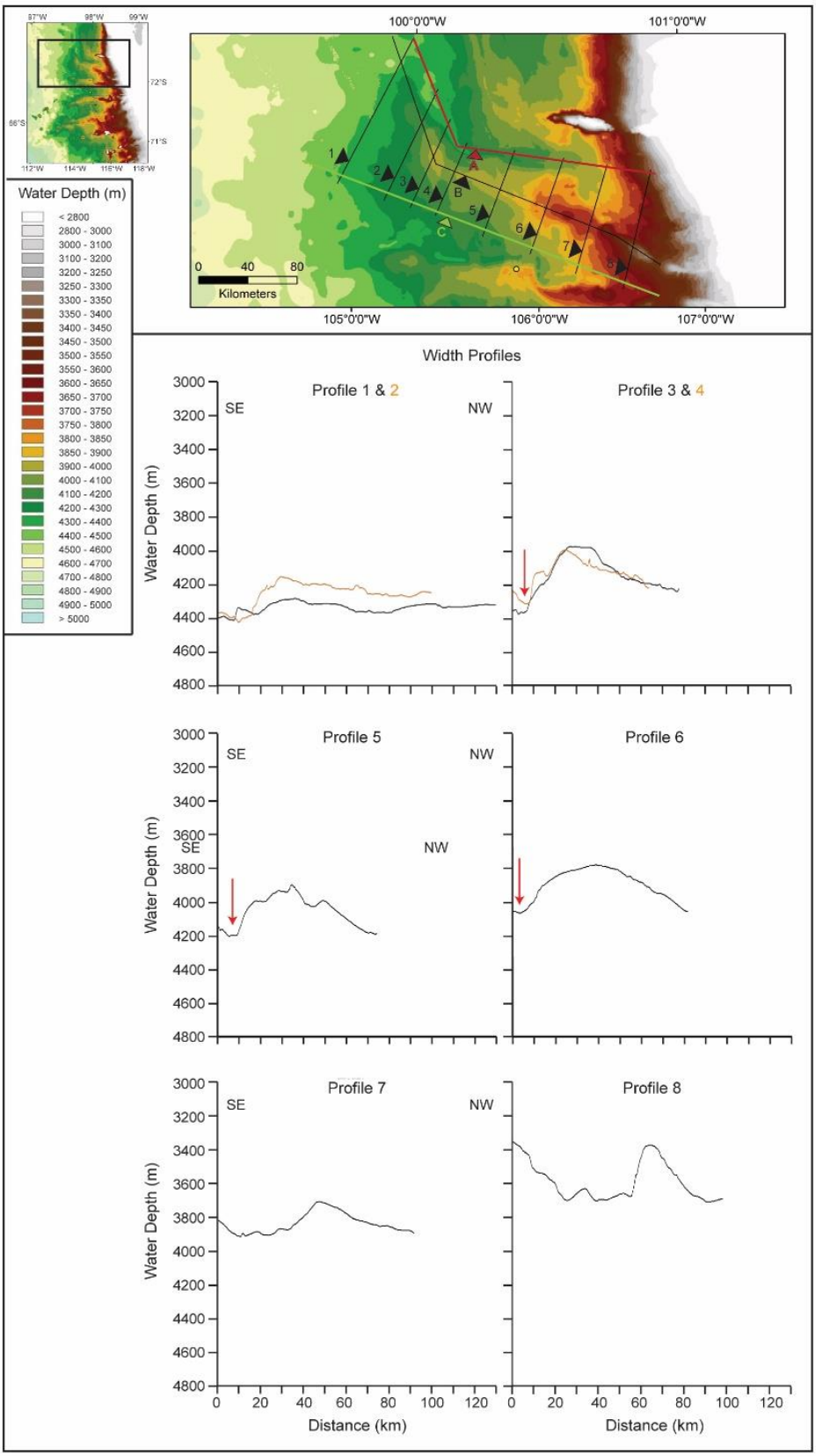

Figure 5.16: Profiles across M4, approximately perpendicular to the long axis of M4. The positions of the black lines labelled 1-8 on the 2D map mark the locations of the profiles. Red arrows on the profiles mark the positions of channel separating M4 from M5 to the East.

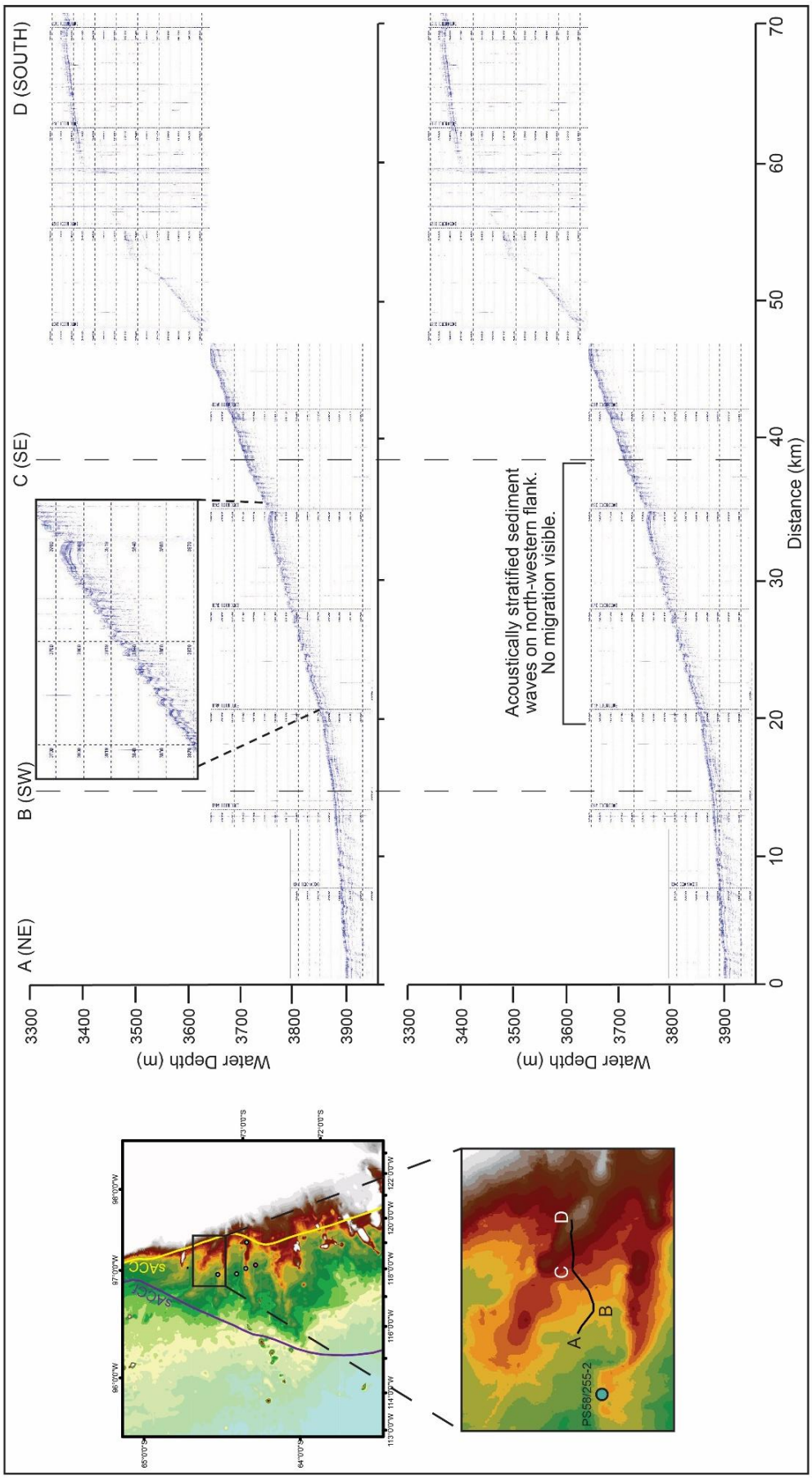

Figure 5.17: TOPAS sub-bottom profile on the western flank of M4.

5.2.6. Mound Five

M5 is the smallest mound in the eastern Amundsen Sea in both height and length (Table 5.1). It formed around a prominent bathymetric high which is probably a seamount (F. Nitsche, *pers comms*). M5 has not been previously identified as a mound in the literature. Only up to a distance of 80 km away from the continental slope and in the vicinity of the seamount the surface of M5 is above 3900 m water depth (Figure 5.18), with the remaining c.170 km long offshore section of the mound exhibiting a smooth topographical profile with a low and consistent slope angle.

M5 is particularly prominent for the distinct and significant eastward turn in orientation at approximately 69.5°S to an angle almost parallel to the shelf break.

M5 does not show any significant asymmetry. However, it is noteworthy that the flanks of M5 are of a lower angle (≥0.11°) than those of the other mounds and that its main body does not stand as high above the surrounding sea floor. Profiles 3 and 4 (Figure 5.19) show the gently-sloping western flank. The eastern flank is particularly wide at depths below 4200 m water depth, extending over 100 km from the mound crest to the continental slope.

Whilst profile 4 (Figure 5.19) shows the channel separating M4 and M5, there is no evidence for any major channel located to the east of M5 in the multi-beam or TOPAS data. The TOPAS data (Figure 5.20) instead show acoustically stratified sediments with a relatively smooth surface below 4100 m to the east of the mound and acoustically hard sediments on the mound crest and its flanks.

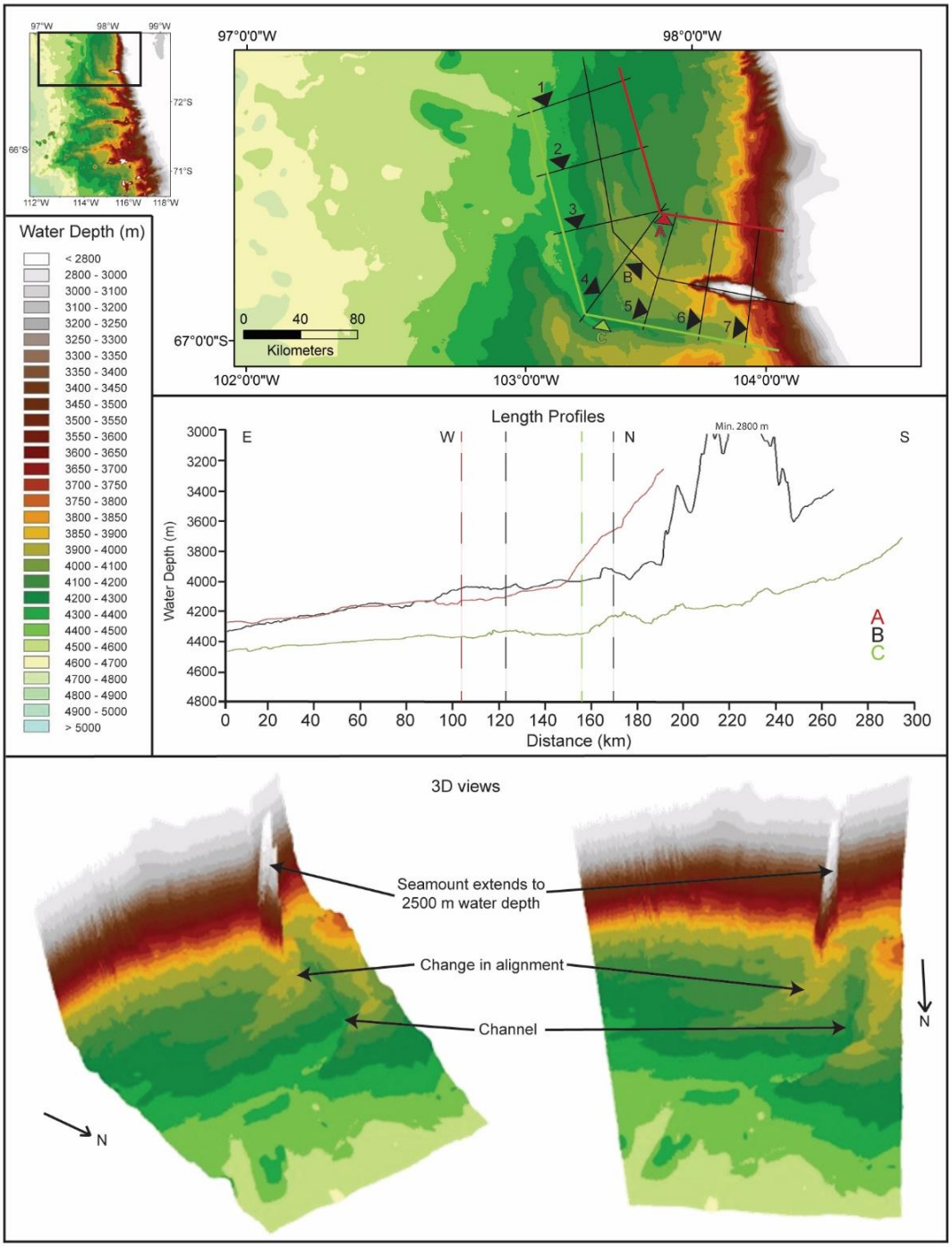

Figure 5.18: 2D, strike profiles and 3D views of M5. The positions of the red (A), black (B) and green (C) lines on the 2D map show the locations of the profiles along the long axis of M5. Dashed lines indicate changes in direction along the profile; the colour of the dashed line indicates to which profile the change corresponds. The positions of the black lines labelled 1-6 on the 2D map mark the locations of the cross profiles in Figure 5.19. All 3D views are shown at 100x vertical exaggeration. Bathymetric data are from IBCSO (Arndt et al., 2013).

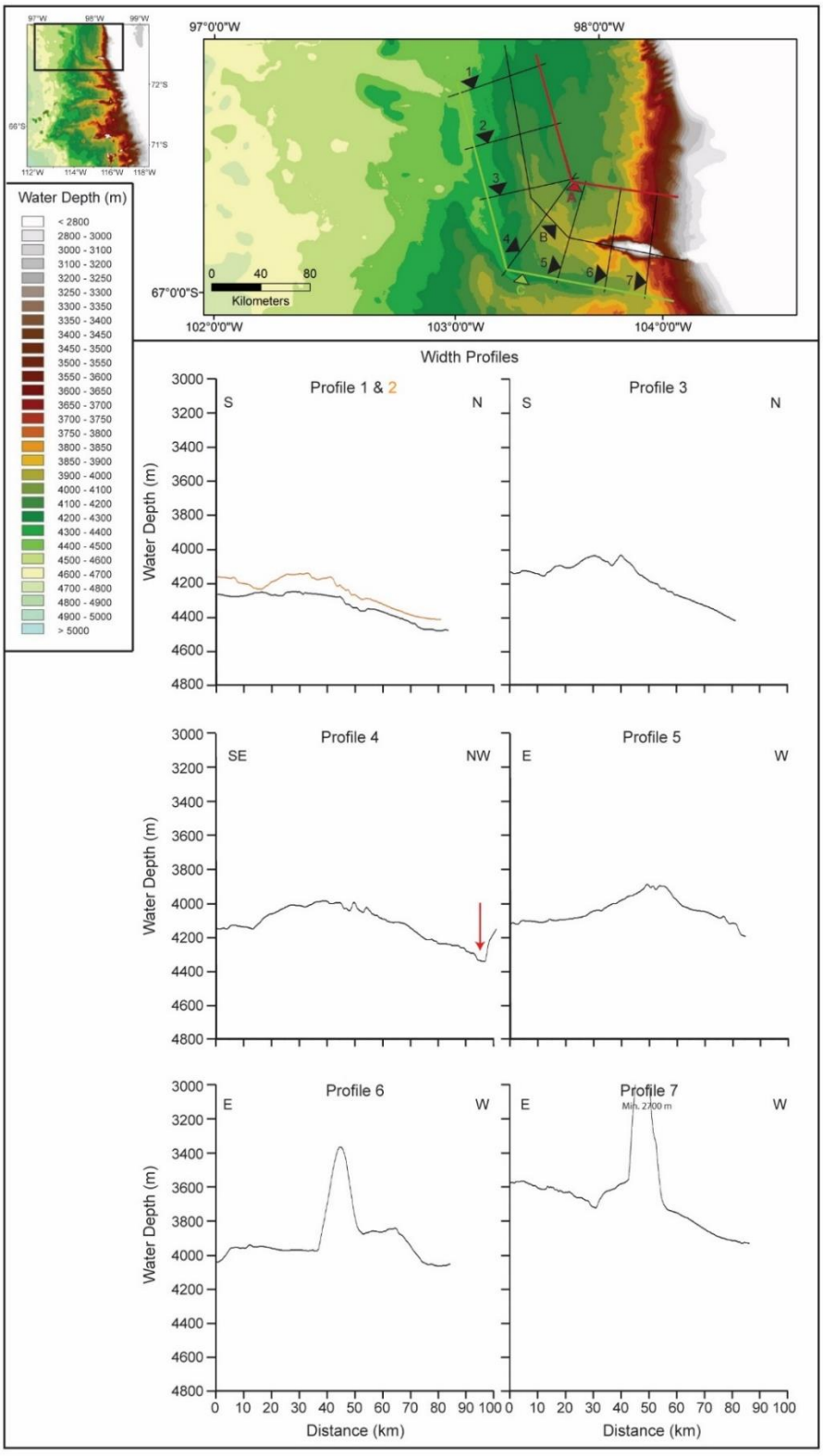

Figure 5.19: Profiles across M5, approximately perpendicular to the mound crest. Profiles 6 and 7 include a seamount which extends to 2500 m water depth (2700 m water depth in Profile 7). The positions of the black lines labelled 1-7 on the 2D map mark the locations of the profiles. The red arrow in profile 4 marks the position of the channel separating M5 from M4.

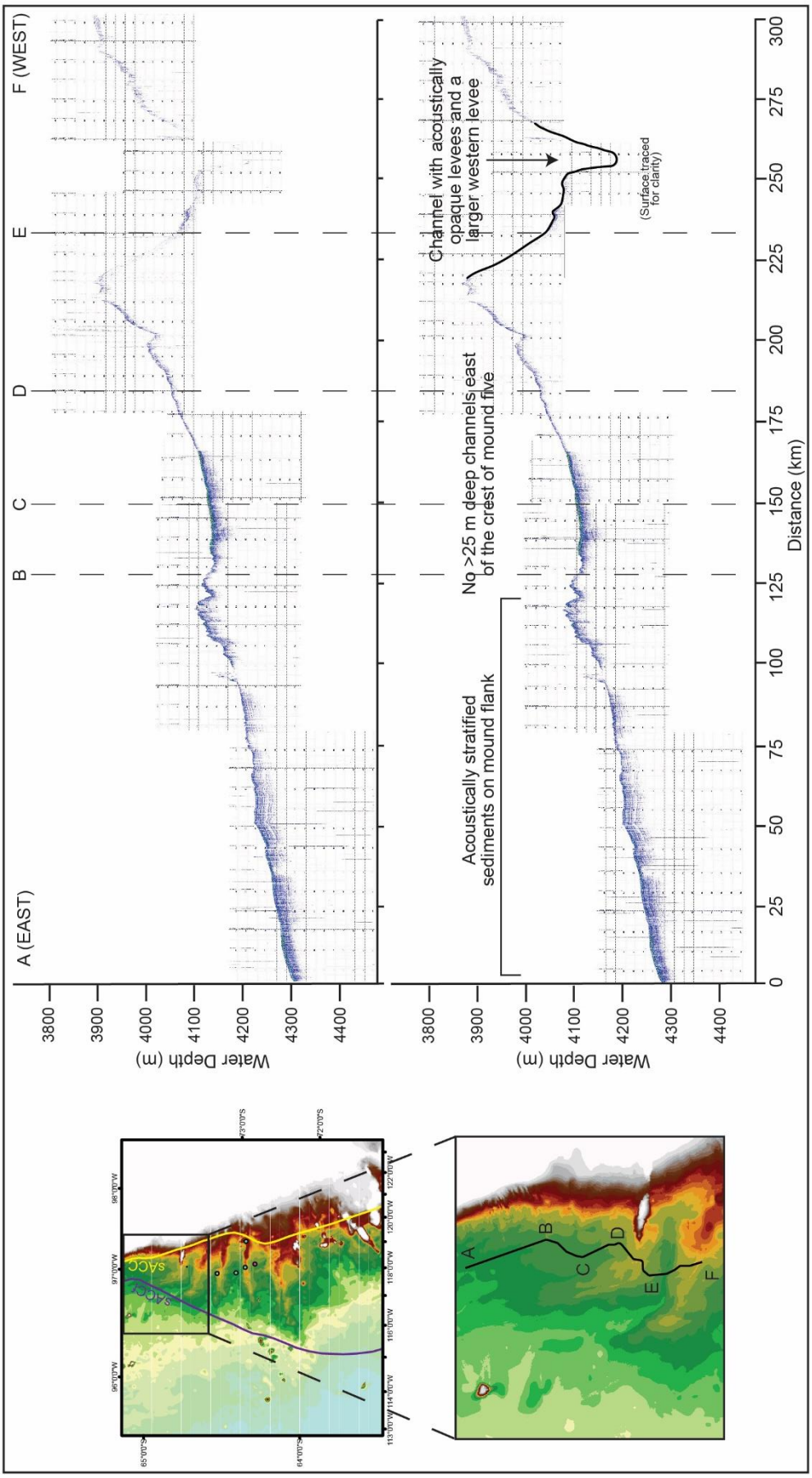

Figure 5.20: TOPAS sub-bottom profile of M4 and M5.

Mound	One (West)	Two	Three	Four	Five (East)
Size (LxWxH) (km)	433 x 130 x 0.9	315 x 45 x 0.8	280 x 42 x 0.8	290 x 78 x 0.65	250 x 36 x 0.5
Orientation	Perpendicular to shelf	Perpendicular to shelf, kinks eastwards at 70°S	Aligned slightly eastwards, 70° to the slope	Aligned eastwards, 30° to the slope, slope-parallel north of 69.5°S	Aligned eastwards, 45° to slope, parallel to slope north of 69.5°S
Asymmetry	Typically a gently sloping western flank and steeper eastern flank.	Slight; the eastern flank is slightly steeper than the western flank.	Only in the proximal half, with a gently sloping western flank and steeper eastern flank.	Generally a gently sloping western flank and steeper eastern flank.	No significant asymmetry.
Structure	3 distinct sections of mound crest. Crest is acoustically stratified. Undulating mound crest cut by a depression 300 km from the slope.	Lots of gullies present on the eastern flank. Western flank is acoustically stratified and smooth with the exception of two steps.	Gullies on the eastern flank. Far western flank contains sediment waves. Undulating mound crest cut by a depression 200 km from slope.	Western flank contains sediment waves. The mound crest increases in height by 100 m at the point of the change in orientation.	The eastern flank is particularly extensive with smooth, acoustically stratified sediments extending over 100 km east.
Shelf-parallel channel at base of slope?	No	Yes: 26 km wide, 460 m deep, asymmetrical channel.	Yes: 26 km wide, 160 m deep, symmetrical channel	Yes: 17 km wide, 130 m deep, symmetrical channel.	No
Channel alongside mound	Up to 200 m deep. Extends for over 200 km along the eastern edge of the mound, 5 km wide, migrating westwards offshore. Western levee is >2x the height of the eastern levee.	70-150 m deep. Runs alongside eastern mound edge, 5-10 km wide, migrates eastwards offshore. Acoustically hard bed slopes away from mound. Western levee is 5x the height of the eastern levee.	c.100 m dee, 5-10 km wide channel runs along the eastern edge of the mound. The western levee is c.4x the height of the eastern levee (= western flank of M4).	Up to 100 m deep, 5 km wide channel runs along the eastern edge of the mound. The western levee is c.4x the height of the eastern levee (= western flank of M5).	No channel to the east; only the channel to the west as described under M4.

Table 5.2: Summary of key characteristics of the mounds of the eastern Amundsen Sea.

5.3. Interpretation of the bathymetric data from the Amundsen Sea mounds

5.3.1. Role of turbidity currents in mound formation

Based on the bathymetry data presented and summarised in Table 5.2, there are numerous features of the eastern Amundsen Sea mounds which are consistent with formation through the action of turbidity currents travelling down the continental slope and depositing material on the upper continental rise under the influence of the Coriolis effect. The most striking feature for a turbiditic origin is the association of the mounds with the channels in the intra-mound areas. Some of these channels can be seen on the lower slope. Various authors have previously identified gullies incised into the upper continental slope and noted that some gullies extend from the shelf break down the slope and have been used to document the major role of gravitational down-slope processes in shaping the Amundsen Sea continental margin (e.g. Nitsche et al., 2000; Dowdeswell et al., 2006; Noormets et al., 2009; Gales et al., 2013). A direct link between the gullies of the upper slope and the intra-mound channels of the lower slope and upper rise has not been observed. However, the resolution of the bathymetric data for the mid slope region is poor and the presence of a link cannot be excluded. Chapter 3.1.2 outlines the identifying criteria for turbidites upon which the following points are based.

Mound Position and Orientation

1. The mounds are positioned at the base of the continental slope and, with the exception of the most distal parts of M4 and M5, the mounds extend offshore approximately perpendicular to the shelf break with length:width ratios of up to 7:1, consistent with a substantial down-slope supply of material.
2. Mounds 3, 4 and 5 each feature a change in mound orientation towards the east, with the mound crests following a change in orientation of the associated turbidite channels running between the mounds. The orientation of deep-sea sediment mounds is a function of the direction of the dominant flow (here, either down-slope turbidity currents or along-slope bottom currents), the interaction of the dominant flow with (other) currents, changes in morphology (e.g. slope steepness, interaction with seamounts) and the impact of the Coriolis effect

(Faugères et al., 1999). No major changes in morphology or tectonic features are present in the seismic data (Uenzelmann-Neben and Gohl, 2012, 2014), with the exception of the seamount at the foot of the slope in M5, which cannot explain the change in orientation in M5, given the lack of any moat around the seamount excludes any major change in the bottom current velocity. Elsewhere, the inter-drift channels are sinuous and meander but the degree and similarity of change in the channels between these mounds is much greater than seen in the other channels. A possible explanation is the preferential deposition of sediment from turbidity currents on the western levee of the channels under the Coriolis effect led to the eastwards migration of the channels. Alternatively, bottom currents may have influenced the geometry (see Chapter 5.2.2).

Mound Structure

3. Acoustic sub-bottom profiles show the mound sediments are typically acoustically stratified with strong internal reflectors, a common feature of turbidites, whereas contourites typically show low reflectivity and no internal layers (Stow and Lovell, 1979).
4. The mounds thin offshore, suggesting the dominant source of sediment was down-slope transport. In contrast, the sub-bottom profiles show similar thicknesses of stratified sediments across much of the mound crests, with thinning only on the steeper slopes near the channels to the East, implying along-slope deposition was probably less important (Pudsey, 2000).
5. The crest of M1 is divided into three crests separated by channels aligned approximately perpendicular to the shelf break, suggesting the channels were a route for supply of material to the mound crests and explaining why the mound is more symmetric than the other mounds. An alternative explanation is that the large depocentre was subject to mass wasting and turbidity currents may have been generated on the mound crests, eroding channels separating the mound into smaller sections.
6. Sediment waves are present on the western flanks of M3 (Figure 10a in Nitsche et al., 2000) and M4 (Fig. 5.17), which can occur in both turbidite and contourite sediments (Keevil et al., 2008; Wynn and Stow, 2002). It is unclear from the

TOPAS data whether migration of the sediment waves has occurred, but the seismic data presented by Nitsche et al. (2000) show sediment waves on the distal part of M3 displaying some eastwards migration (Figure 10a in Nitsche et al., 2000).

Channel Systems

7. Channels run along the eastern flanks of M1-M4, are orientated roughly perpendicular to the slope, and can be traced from >20 km from the base of the continental slope for up to 300 km seawards (Figure 5.21). The channels are at least as long as the neighbouring mounds, suggesting they are a conduits for supplying sediment some distance from the continental slope via turbidity currents. The distance between the channels may explain why the mounds are particularly long and narrow if the channels prohibit one mound merging into another by consistently eroding the area between the mounds.
8. Channels running between the mounds have acoustically hard bases suggesting repeated erosion of fine-grained material and deposition of coarse grained sediment. The channel between M1 and M2 is deeply incised, indicative of repeated, highly-erosive flows, such as turbidity currents. Erosion of the channels by bottom currents would require flow velocities in excess of any known from the region or suggested by the mound sedimentology.

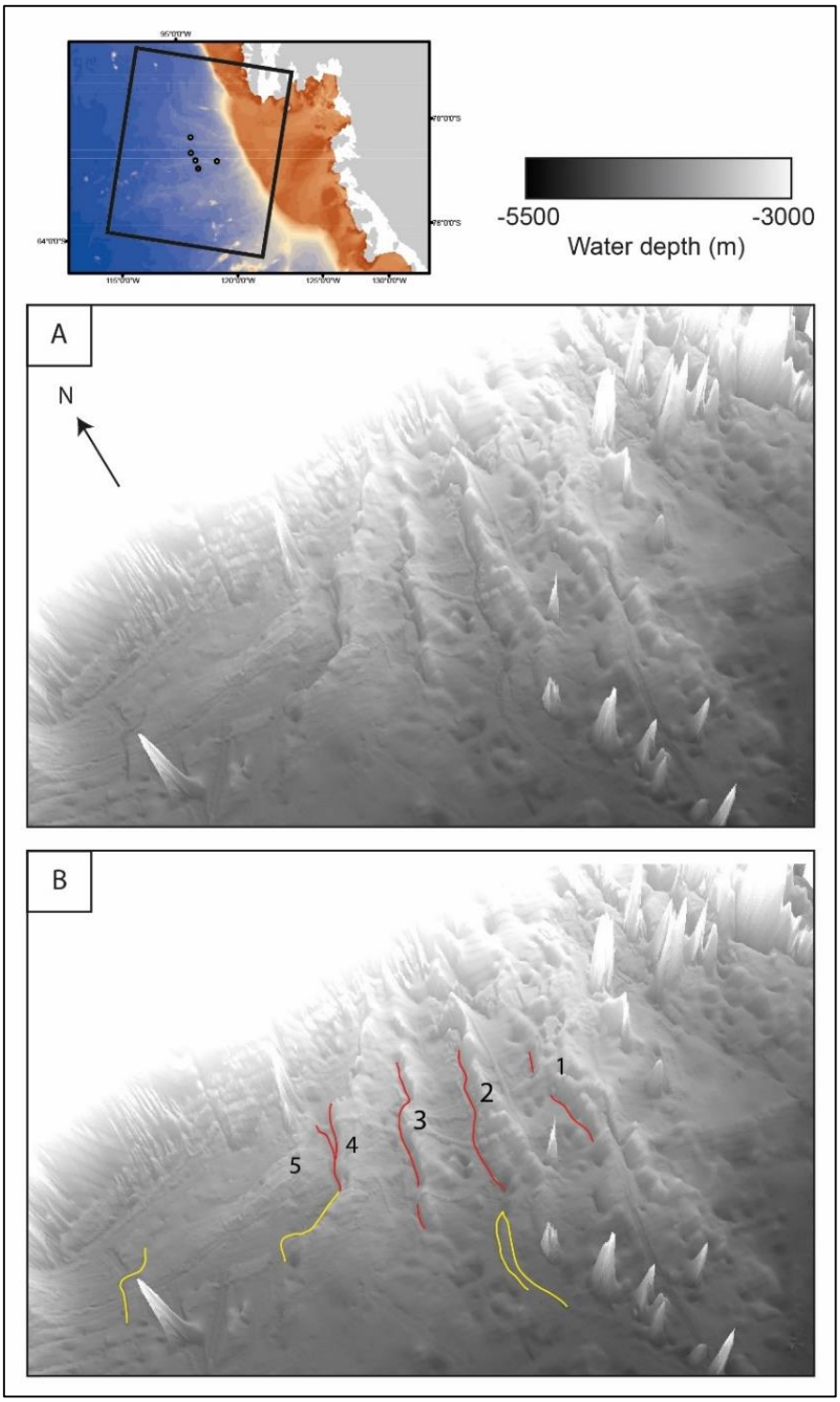

Figure 5.21: Inter-mound channels on the upper continental rise. 3D image from IBSCO (Ardnt et al., 2013) with the five mounds numberered. Red lines indicate locations of channels identified based on sub-bottom profiler and seismic data (Uenzelmann-Neben and Gohl, 2012, 2014). Yellow lines indicate areas inferred to be channels based on the multi-beam swath bathymetry only.

9. The 36-130 km wide mounds are up to an order of magnitude wider than the

channels, which are typically 5-10 km wide. This width is within the expected size of turbidity current overspill deposits (Parsons et al., 2007; Meiburg and Kneller, 2010).

10. The channels are sinuous and have typically smaller levees with distance from the continental slope, suggesting the material is being supplied from the slope (and ultimately the shelf).
11. The western levee of each of the major channels is larger than the eastern levee in all of the presented TOPAS and swath bathymetry profiles. This is consistent with an interaction of settling material with the Coriolis effect, which acts to the left in the southern hemisphere (Maldonado et al., 2005).
12. There is no channel to the west of M1, only one to the east, which runs alongside this particularly large mound for over 200 km. This suggests deposition of sediment supplied by turbidity currents and deposited under the influence of the Coriolis effect is a likely mechanism for formation, as the predominantly eastwards-flowing currents in this region would require a channel lying to the west of the mound to supply material.

5.3.2. Role of bottom currents in mound formation

Based on the bathymetry data presented, there are also numerous features of the eastern Amundsen Sea mounds which suggest deposition has primarily occurred via, or under the influence of, an eastward-flowing bottom current. Chapter 3.1.4.1 outlines the identifying criteria for contourites upon which the following points are based.

Mound Position and Orientation

1. The large size of the mounds, standing up to 900 m above the surrounding sea floor, is more characteristic of deposition by bottom currents than turbidity currents (Rebesco et al., 1996).
2. The eastwards turn seen in the distal ends of M3, M4 and M5 could also be explained by along-slope processes. Contourites are typically aligned and elongated with the direction of flow (Rebesco et al., 2013), here parallel to the continental slope. The

sACCf (as defined by Orsi et al., 1995) is at a more southerly location over the offshore ends of M3, M4 and M5 than over M1 and M2. The increase in bottom current speeds associated with the front may therefore have resulted in an increased amount of along-slope transport at the ends of these three mounds, compared to M1 and M2, leading to along-slope elongation. The exact mechanism of this is unclear and further seismic data from the region would help to establish whether the mounds and channels have exhibited this alignment since mound development began, suggestive of a tectonic control, or whether the alignment has developed progressively, suggestive of a bottom current control.

Mound Structure

3. The mounds do not show the typical 'gull-wing' geometry of turbidites (Maldonado et al., 2005) and instead are predominantly asymmetric with a gently sloping western flank and a steeper eastern flank. This is consistent with deposition under an eastwards-flowing bottom current.
4. Sub-bottom profiles show the mounds have largely continuous, parallel reflectors, showing deposition is extensive over the mounds. Sedimentation rates appear highest on the mound crests, not on channel levees, suggesting sediment is redistributed from where a turbidity current would deposit most material.
5. The sediment waves on the western flanks of mounds 3 and 4 could also suggest a bottom current influence. The sediment waves show parallel, wavy reflectors, and no significant downstream changes in wavelength or amplitude which are typically seen in sediment waves formed by turbidity currents (Faugères et al., 1999; Wynn and Stow, 2002). The wavelength, amplitude and extent are similar in both turbidite waves and contourite waves so cannot be used here to distinguish a depositional environment (Faugères et al., 1999).
6. Mounds One and Three are cut by depressions in their distal sections, i.e. approximately 300 and 200 km, respectively, from the base of the continental slope (Figures 5.4 and 5.13). These depressions are aligned parallel to the shelf break and have a relatively smooth, symmetrical profile, which may suggest erosion by an east or westwards flowing bottom current. Alternatively, the depression may have been caused by mass wasting of the mound crest.

Channel Systems

7. The lack of a channel to the east of M5 suggests the sediment of this mound was delivered via the western channel, in which case the Coriolis effect deflecting a turbidity current would have led to the build-up of the western levee (M4), with relatively minor deposition on the eastern levee (M5). Redistribution of sediment by an eastwards-flowing bottom current is needed to explain the development of M5 and particularly its extensive eastern flank.

5.3.3. Slope-parallel channels

M2, M3 and M4 have a slope-parallel channel separating the base of the slope from these mounds. The channels, which may also have been eroded by turbidity currents, are of a similar width (17-26 km) and their upper banks are located in water depths of 3300 – 3400 m. M2 features the channel eroded deepest into the surrounding seafloor (460 m); the northern edge of this channel is located 10 km south of site PC494. The channels in M3 and M4 have a similar geometry with a smooth, symmetrical floor and a maximum floor depth of 160 m (M3) and 130 m (M4) below the surrounding seafloor (Figure 5.22).

Coverage of the channels by sub-bottom profiler and seismic data is unfortunately sparse. Uenzelmann-Neben and Gohl (Figure 2b, 2014) displayed a seismic profile (see Figure 3.9 on p. 67) from just west of the channel south of M2, which has a partial data gap in the channel but shows a partially infilled, slightly V-shaped channel, present in the uppermost seismic unit (dating to 4 Ma to present) and possibly present in the underlying seismic unit (14.1 – 4 Ma), suggesting the channel has not been recently eroded. The sediments show distinct, tightly packed reflectors suggesting the deposition of coarse grained sediments.

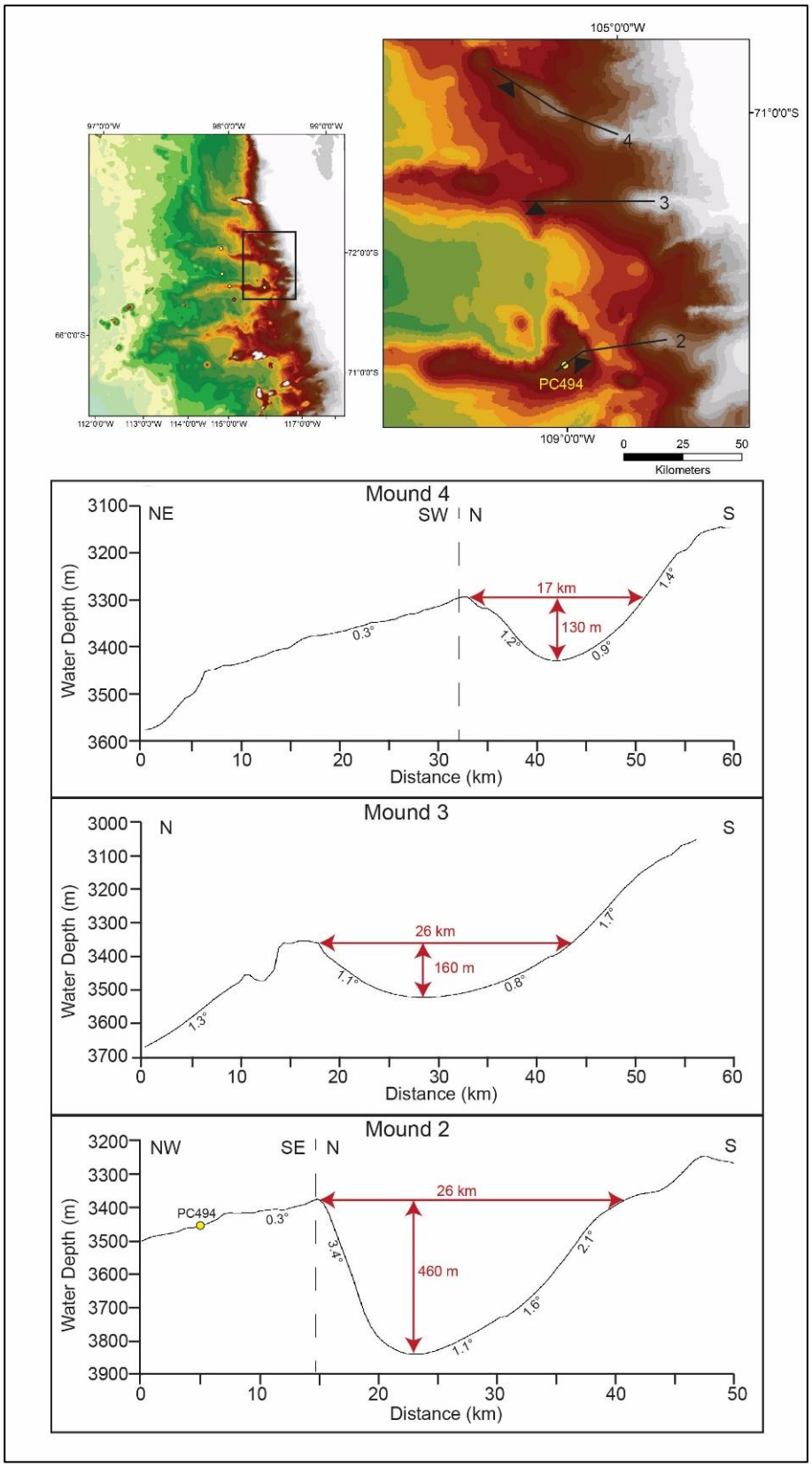

Figure 5.22: Profiles across the areas between M2, M3 and M4 and the adjacent continental slope. The locations of profiles are highlighted as black lines on the map. The maximum depth and width (based on the height of the northern bank) are shown in red.

Channels separating the slope from sediment mounds are also a common feature of contourite systems, where a focused bottom current hugs the base of the slope and erodes a contourite channel or moat (Rebesco et al., 2014) (Figure 5.23). Bottom current velocities exceeding 20 cm/second are needed to erode moat channels (Mulder et al., 2008), a speed which is seen only rarely in the generally weak WSDW-derived, westward-flowing bottom current off the western Antarctic Peninsula margin (Camerlenghi et al., 1997) and is probably similarly rare in the eastern Amundsen Sea, given the high clay content of the sediments. The absence of a slope-parallel channel in M1 or M5 also suggests the channel is unlikely to have been eroded by bottom currents.

An alternative hypothesis for the formation of the slope-parallel channels is that the channels are the product of turbidity currents running parallel to the shelf before turning and running between the mounds. None of the turbidite channels or gullies on the slope are seen to connect directly to any slope-parallel channel; however, this does not exclude the possibility, given many channels will be too small to be resolved in the multi-beam data. Rebesco et al. (1997) suggested this mechanism was the reason for <50 km wide channels separating the drifts on the continental rise west of the Antarctic Peninsula from the base of the slope. The channel was absent from a section of one drift and attributed to reduced down-slope mass wasting during recent times, with fewer slumps and debris flows and more fine-grained turbidity currents resulting in less erosion at the slope base (Rebesco et al., 1997). A similar mechanism may help explain the lack of a slope-parallel channels in M5, as few gullies or channels are evident on the continental slope and M5 is the smallest of the Amundsen Sea mounds, implying sediment delivery to this mound may have been less than to the other mounds.

The notion of the channels being turbidity current related is also supported by the low angle of the continental slope in the eastern Amundsen Sea. Pratson et al. (2000) found that turbidity currents on slopes ≤1.5° cannot gain enough momentum to erode sediments sufficiently to counteract the dilution of the flow, resulting in minimal sedimentation which is deposited only on the slope (Figure 5.23). A slope angle of 2.25° provides the ideal angle for turbidity currents to erode sediments and sustain the flow, eroding the slope and upper continental rise within 2 km from the base of the slope, and depositing sediments over a further 20 km in model experiments. Slope angles >2.25° result in a progressive decrease in the ability of flows to erode sediment, leading to less

erosion on the slope and at the foot of the slope, and a decrease in the thickness of deposits and their distance from the slope. The slope angle of 2-4° in the eastern Amundsen Sea therefore provides the ideal angle for the generation of turbidity currents which heavily erode the slope, can account for the erosion of a channel-shaped feature at the base of the slope, and explain the large height and length of the mounds (when compared to the Antarctic Peninsula drifts where slope angles are up to 16°).

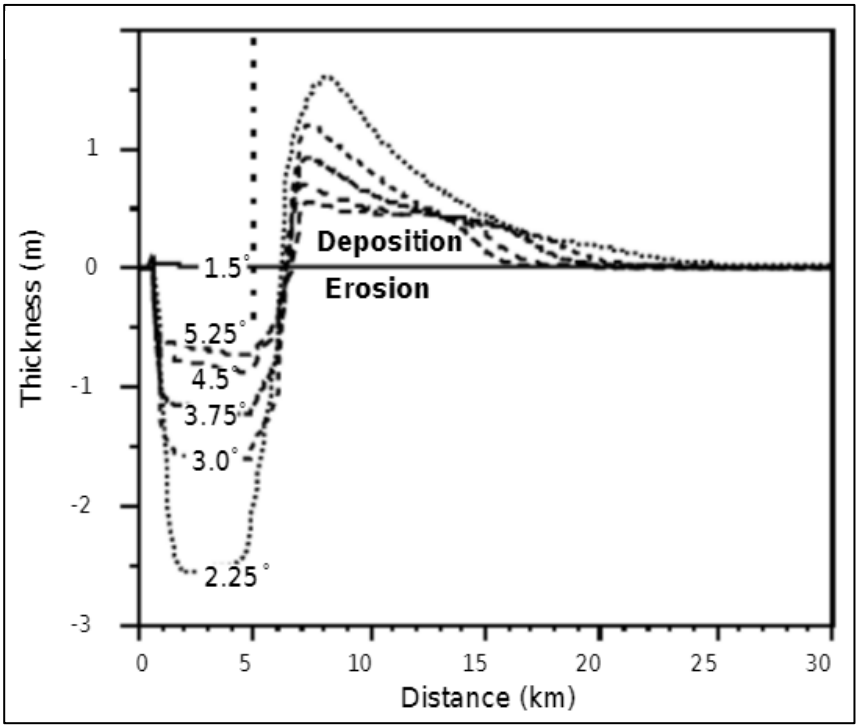

Figure 5.23: Turbidity current deposition and erosion based on a varying slope angle. The dashed line indicates the base of the continental slope. Figure 9B modified from Pratson et al. (2000).

5.3.4. Sediment waves

On the western flank of both drift 3 and drift 4 are sediment waves with a wavelength of around 600 m and crest height of <10 m (Figures 5.11 and 5.17). Sub-bottom profiler data show that there are areas with no sediment waves separating both wave fields from the nearest channels. It is unclear from the geophysical data what the spatial extent or orientation of the sediment waves are, and high resolution multi-beam swath bathymetry in combination with multi-channel seismic data would be needed to make a more confident assumption of how the waves formed.

The waves are present on low-angle (around 0.37° on both M3 and M4) drift flanks which are plausible sites for wave creation by the low velocity bottom currents, unconfined turbidity currents or via sediment deformation (Wynn and Stow, 2002). The sediments appear acoustically transparent on sub-bottom profiler data, suggesting they are fine grained and within the size constraints of waves formed by all three processes. However, no sediment cores have been taken from the waves so grain size cannot be confidently assumed.

Sediment waves formed by contour currents and by turbidity currents are often similar in dimensions and morphology (Faugères and Stow, 1993). The dimensions of the waves are small compared to what is typical of both contourite mud waves (mainly 1 to 2.5 km wavelength and up to 150 m high) and turbidite waves (mainly 0.75 to 2.5 km wavelength and up to 80 m high) (McCave, 2017). It is noted that the wave height in particular is unusually low for large-scale, fine-grained sediment waves (Symons et al., 2016). However, Migeon et al., 2001 and Normark et al., 2002 reported that a height of 3-20 m may be more typical of waves on turbidity current levees. Due to the Coriolis effect, in the southern hemisphere, waves formed by turbidity current action most commonly develop on the left-hand levee (when looking down-channel), here the western levee (Wynn and Stow, 2002). As deposition on the crests of the other drifts studied was found to be dominantly contouritic with no direct turbiditic deposition, this suggests little sediment from turbidity currents was directly deposited over the crests or western flanks of the drifts. This suggests that if the waves did form through turbidity current action, they may spilled over from the channels lying to the left or west of the

wave field, meaning the waves developed on the right-hand levee, the opposite to what is expected.

Fine-grained sediment waves formed by bottom currents typically become smaller and less symmetrical towards the edge of the wave field (Wynn and Stow, 2002). The waves typically migraine upslope and up-current. Fine-grained sediment waves formed from turbidity currents typically have dimensions which progressively decrease downslope, and the waves typically become more symmetrical with distance downslope (Wynn and Stow, 2002). However, given the direction of flow over the Amundsen Sea drift, waves formed by either turbidity or bottom current action will both typically migrate upslope. The seismic data presented by Nitsche et al. (2000) show sediment waves on the distal part of M3 displaying a small degree of up-slope migration (Figure 10a in Nitsche et al., 2000). Sparse data coverage means it is not possible to observe changes across the whole wave field. However, the sub-bottom profiler data show that the sediment in the waves is stratified, can be traced across the drift and there is no notable decrease in the distance between the stratifications down-slope, which is commonly observed in turbidity current deposits as sediments thin with distance from the channel (Wynn and Stow, 2002).

Similar wave-shaped features can also arise through soft sediment deformation, particularly on slopes with a high gradient and high sedimentation rates (Symons et al., 2016). Creep folds are most common on slopes >2°, have broad, flat crests and narrow troughs, and do not laterally migrate (Wynn and Stow, 2002). Compaction in thick, fine-grained sediments can lead to de-watering and faulting (Wynn and Stow, 2002). Syn-sedimentary faulting has been described in the Humboldt Slide off the California coast by Gardner et al. (1999) (though later questioned by Lee et al., 2002). According to Gardner et al. (1999), compression of the main body of the Humboldt Slide has led to the development of folds, with the sediments deformed through translation and shallow rotation, and the stresses led to compressional folding on the lower body of the slide.

Based on these criteria, the up-slope migrating, rounded-topped waves on slopes c.0.37° are unlikely to be creep folds and no displacement along fault planes is visible on sub-bottom profiler data. Similarly, the stratification on the geophysical data can be traced between waves and is not disrupted by faulting. The seismic data presented by Nitsche

et al. (2000) also show the sediments do not have any significant faulting, do migrate up-slope, and that parallel stratifications are present throughout the sediment with no evidence of deformation. Obtaining higher resolution multi-beam swath bathymetry data from this area may help to rule out this hypothesis, as waves formed through this process often appear polygonal in plan view (Wynn and Stow, 2002).

Similar sediment waves are common on other Antarctic contourite and mixed contourite-turbidite drifts (e.g. Howe et al., 1998 (Northern Weddell Sea), Nitsche et al., 2000 (Bellingshausen Sea), Michels et al., 2001 (Western Weddell Sea), Escutia et al., 2002 (Wilkes Land) and Kuvaas et al., 2005 (Cosmonaut Sea)). As a result of the evidence for up-slope migration, the morphology of the waves, the presence of the waves in relation to channels and the common presence of current-related sediment waves on similar contourites and mixed drifts around Antarctica, the waves are tentatively deemed more likely to have been formed by the action of a bottom current than a turbidity current and are deemed unlikely to be the result of sediment deformation.

5.3.5. Bathymetry Interpretation

Based purely on the bathymetry presented here, there is evidence to suggest both turbidity currents and bottom currents have influenced deposition of the mounds and that, as a whole, the position, structure and channel systems associated with the mounds cannot be explained by one depositional process alone. Evidence for a turbidity current influence on deposition includes the location, size and down-slope elongation and thinning of the mounds, the nature of the well-developed channel systems and the larger size of the western levees compared to the eastern levees (Figure 5.24). Evidence for a bottom current control on deposition includes the size and asymmetry of the mounds, lack of a ‘gull-wing’ geometry and seaward changes in the long-axis orientation of the mounds. Chapter 7 will discuss this evidence in more detail in conjunction with the sedimentological results and previously published work.

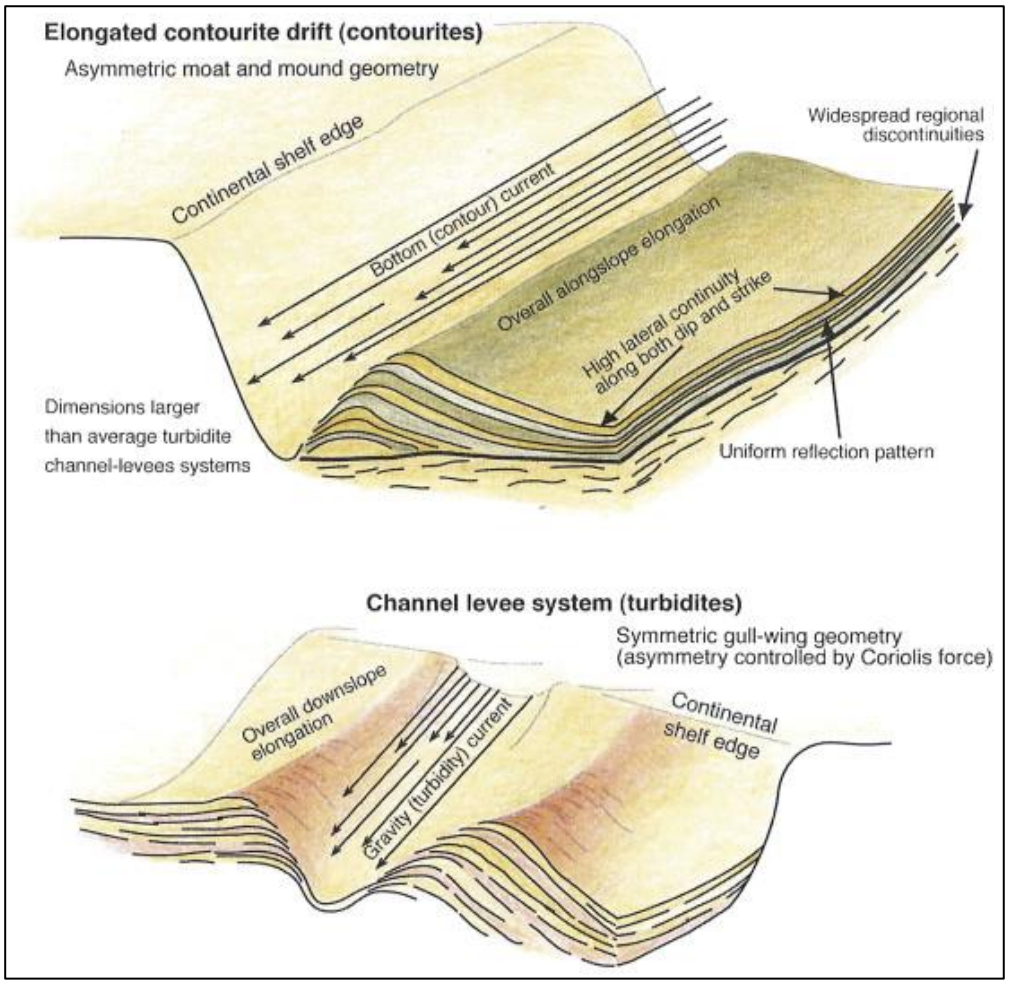

Figure 5.24: "Schematic model showing ideal, large-scale differences between contourite drifts and channel-levee systems" (from Rebesco et al., 2014).

Chapter 6: Results and Interpretation of the Analysis of Sediment Cores from the Amundsen Sea Mounds

6.1. Introduction

The results of the analysis of the four sediment cores are presented in this chapter. For each core, the sediments are first described by unit in terms of the key sedimentological, geochemical and mineralogical data. The sediments are then correlated to lithofacies which have been identified across the four cores based on key criteria.

The results of the methods used to obtain chronological constraints are then presented and used in conjunction with cross-core correlations to develop a chronology for the cores. The characteristics of each lithofacies is then used in conjunction with the core chronologies to interpret the depositional environment in which each lithofacies may have formed.

6.2. Results of the analysis of sediment cores from the Amundsen Sea mounds

6.2.1. Development of lithofacies

In the following sections, the sediments of each core are first described and then correlated to lithofacies which have been identified across the four cores based on key criteria. The criteria (grain size, structure, biogenic content, physical properties and clay mineralogy) were selected as they show significant down-core variability and primarily reflect changes in sediment supply, sediment provenance and productivity that are needed to address the research aims. The criteria used to define each lithofacies are summarised in Table 6.1. Additional data demonstrating the typical grain size distribution of each lithofacies are given in Table 6.2.

Lithofacies 1a is homogenous to slightly mottled mud of relatively high wet bulk density (1.5-1.9 g/cm^3) and low water content (40-55%). It comprises the majority of the glacial sediments in PC496 on the mound flank but is only found in discrete units less than 27 cm thick on the mound crests. It is composed of typically >95% mud, but contains IRD both dispersed and in thin, rare laminae of up to 30 wt.% sand and gravel. The mud

fraction is poorly sorted and has a mean grain size of very fine silt, which is slightly coarser at the more distal core site of PS58/253-1 (3.9 μm) where the mud fraction is 33% clay (by volume) than at the proximal site of PC494 (2.7 μm) where the mud fraction is 40% clay. The clay mineralogy contains relatively high kaolinite (12-30%) and low smectite (10-27%). $CaCO_3$ content is low (<2%). Biogenic silica content varies depending on whether the core is from the deeper water, mound flank site (PC496, <15 wt.% biogenic silica) or in shallower water on the mound crests (3-10 wt.%).

Lithofacies 1b is laminated to stratified mud of relatively high wet bulk density (1.5-1.9 g/cm^3) and low water content (40-55%). It is found at each of the three mound crest sites but not at the mound flank site. The laminae are slightly bioturbated in limited sections of PC494 but are not bioturbated in other cores. It is composed of typically >95% mud, but contains thin, rare laminae of up to 70 wt.% sand and gravel. The mud fraction is poorly sorted, approximately a third clay (by volume) and has a mean grain size of very fine silt, which is similar (3.4-3.5 μm) at both the proximal and distal core sites. The clay mineralogy contains relatively high kaolinite (12-30%) and low smectite (10-27%). $CaCO_3$ content is low (<2%). Biogenic silica content varies depending on whether the core is from the more proximal site in shallower water depth (PC494, <15 wt.% biogenic silica) or at a more distal site in deeper waters (<7 wt.%). IRD is dispersed throughout the lithofacies.

Lithofacies 2a is a diatom-bearing, slightly to heavily bioturbated mud containing 15-40 wt.% biogenic silica. It has a relatively low wet bulk density (<1.5 g/cm^3) and high water content (55-75%). It is found in the three distal cores (i.e. not PC494) and particularly characterises interglacial sediments at PC496, the mound flank site. The mud fraction is poorly sorted, c.20% clay (by volume) and has a mean grain size of fine silt. It is predominantly mud, but <10 wt.% sand and <10 wt.% gravel are dispersed throughout the lithofacies. The clay mineralogy contains relatively low to moderate kaolinite (5-24%) and high smectite (24-38%). $CaCO_3$ content is moderate (<10%).

Lithofacies 2b is a slightly to heavily bioturbated mud with diatoms, containing 8-15 wt.% biogenic silica. It has a relatively low wet bulk density (<1.5 g/cm^3) and high water content (55-75%). It is found on mound crests in maximum 11 cm thick units, and at the mound flank site in a 42 cm thick unit attributed to MIS 2-4. It is predominantly mud,

but <10 wt.% sand and <10 wt.% gravel are dispersed throughout the lithofacies. The mud fraction is poorly sorted and has a mean grain size of fine silt, which is slightly coarser at the more distal core site of PS58/253-1 (6.2 μm) than at the more proximal core site of PC494 (4.4 μm). The clay mineralogy contains relatively little kaolinite (5-17%) and high smectite (24-33%) in all cores except PC496 (minimum 16% smectite). $CaCO_3$ content is moderate (<10%).

Lithofacies 3 is a slightly to heavily bioturbated, calcareous foraminifera-bearing mud. It is found only in MIS 5 sediments on the mound crests. In PC494 and PS58/253-1, it is present in two distinct units separated by lithofacies 2b. The foraminifera are predominantly planktonic foraminifera of the species N. Pachyderma (sinistral), with <0.1% benthic foraminifera present in PC494 and PS58/253-1. It has a relatively low wet bulk density (<1.4 g/cm^3) and moderate water content (50-60%). Lithofacies 3 contains <30 wt.% sand which is almost entirely biogenic (mostly N. Pachyderma) and is reflected in the high $CaCO_3$ of 10-40%. Gravel contents are low at <1 wt.% and IRD is dispersed throughout the sediment. The mud fraction is poorly sorted and has a mean grain size of fine silt, which is slightly coarser at the more distal core site of PS58/253-1 (6.9 μm) than at the proximal site of PC494 (5.6 μm). The clay mineralogy contains relatively little kaolinite (5-15%) and high smectite (24-33%).

Lithofacies 4a is a slightly to heavily bioturbated sandy mud, containing 25 wt.% sand and gravel, of which 56% of the sand is biogenic. It is present only in the upper 21 cm of PC494, the proximal mound crest site. It has a relatively low wet bulk density (1.4-1.5 g/cm^3) and moderate water content (53%). The mud fraction is poorly sorted and has a mean grain size of fine silt. The clay mineralogy contains relatively low to moderate amounts of both kaolinite (16%) and smectite (22%). $CaCO_3$ content is moderate at 6.5%. IRD contents are large, mostly as sand, and dispersed throughout.

Lithofacies 4b is a moderately bioturbated sandy mud, containing 7.6 wt.% quartz and feldspar sand and no gravel. It is found only in late MIS 6 sediments in the mound flank site, PC496, overlying lithofacies 5. It has a relatively moderate to very high bulk density (1.4-2.0 g/cm^3) and very low water content (23%). The clay mineralogy contains relatively moderate amounts of both kaolinite (19%) and smectite (22%). The lithofacies contains only 0.2% $CaCO_3$, 2.3 wt.% biogenic silica, 0.1% TOC and no gravel.

Lithofacies 5 is a horizontally laminated, very fine to fine sand lithofacies. It is found only in late MIS 6 sediments in the mound flank site, PC496, underlying lithofacies 4b. 85% wt.% of the sediment is sand and 15 wt.% is mud. It has a very high bulk density (2.0 g/cm^3) and very low water content (20%). The clay mineralogy contains relatively moderate amounts of both kaolinite (22%) and smectite (20%). The lithofacies contains 0.1% $CaCO_3$, 3.4 wt.% biogenic silica, 0.1% TOC and no gravel.

Each core section includes graphs highlighting the key sedimentological, mineralogical and geochemical data per core. On each graph, interglacial periods are highlighted as grey bars and lithofacies, structure and lithology of the sediments are indicated as in Figure 6.1. A stratigraphic log indicating where chronological constraints have been developed can be found at Figure 6.21 on p.199.

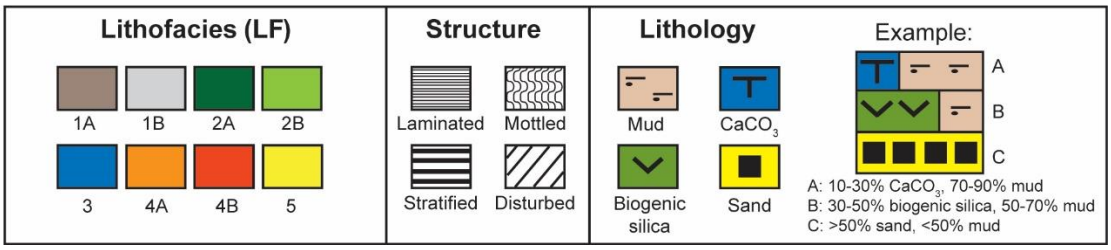

Figure 6.1. Key to the lithofacies, structure and lithology of the sediment cores used in Figures 6.2-6.10.

Lithofacies	Description	Grain size	Structure	Water content (%)	Wet bulk density (g/cm³)	Kaolinite %	Smectite %	Biogenic silica (wt. %)	$CaCO_3$ (%)
1a	Homogenous terrigenous mud	Mud with typically <5 wt.% sand & gravel, with thin, rare layers	Typically homogenous to slightly mottled	40 – 55	1.5 – 1.9	12 – 30	10 – 27	< 15	< 2
1b	Laminated to stratified terrigenous	Mud with typically <5 wt.% sand & gravel, with thin, rare layers	Typically laminated or stratified	40 – 55	1.5 – 1.9	12 – 30	10 – 27	< 15	< 2
2a	Diatom-bearing mud	Mud with <10 wt.% sand & <10 wt.% gravel	Slightly to heavily mottled	55 – 75	< 1.5	5 – 24	24 – 38	15 – 40	< 10
2b	Mud with diatoms	Mud with <10 wt.% sand & <10 wt.% gravel	Slightly to heavily mottled	55 – 75	< 1.5	5 – 17	24 – 33 (min. 16 in PC496)	8 – 15	< 10
3	Calcareous foraminifera-bearing mud	Mud with <30 wt.% sand & <1 wt.% gravel	Slightly to heavily mottled	50 – 60	< 1.4	5 – 15	24 – 33	< 10	10 - 40
4a	Sandy mud	Mud with 25 wt.% sand and gravel. Sand is 56% biogenic	Slightly to heavily mottled	53	1.4 – 1.5	16	22	7.1	6.5
4b	Sandy mud	Mud with 7.6 wt.% quartz & feldspar sand and no gravel	Moderately mottled	23	1.4 – 2.0	19	22	2.3	0.2
5	Very fine to fine sand	Very fine to fine sand (85% sand, 15% mud)	Horizontally laminated	20	2	22	20	< 5	< 1

Table 6.1: Description of the sedimentological, geochemical and mineralogical criteria used to define the seven lithofacies in PC494, PC496, PS58/253-1 and PS58/255-2.

	PC494 (mound crest, proximal)				PS58/253-1 (mound crest, distal)			
LFA	Mean grain size (µm)	Clay (% <2µm of the 0-63µm fraction)	Skewness (Sk_G)	Sorting (σ_G)	Mean grain size (µm)	Clay (% <2µm of the 0-63µm fraction)	Skewness (Sk_G)	Sorting (σ_G)
1a	2.65 *Very fine silt*	40.2%	-0.016 *Symmetrical*	3.03 *Poorly sorted*	3.92 *Very fine silt*	32.6%	-0.003 *Symmetrical*	3.47 *Poorly sorted*
1b	3.49 *Very fine silt*	34.1%	-0.041 *Symmetrical*	3.36 *Poorly sorted*	3.67 *Very fine silt*	32.7%	-0.050 *Symmetrical*	3.48 *Poorly sorted*
2a	-	-	-	-	6.60 *Fine silt*	20.0%	-0.042 *Symmetrical*	3.91 *Poorly sorted*
2b	4.36 *Fine silt*	23.3%	-0.091 *Symmetrical*	3.14 *Poorly sorted*	6.22 *Fine silt*	19.4%	-0.061 *Symmetrical*	3.54 *Poorly sorted*
3	5.61 *Fine silt*	20.9%	-0.087 *Symmetrical*	3.48 *Poorly sorted*	6.93 *Fine silt*	16.8%	-0.098 *Symmetrical*	3.61 *Poorly sorted*
4a	4.69 *Fine silt*	21.9%	-0.076 *Symmetrical*	3.14 *Poorly sorted*	-	-	-	-

Table 6.2: Comparison of the mean grain size, modal grain size and degree of sorting, averaged for all samples taken from the respective core and lithofacies, in PC494 and PS58/253-1 according to the Folk and Ward method and geometric graphical measures (Folk and Ward, 1957) (calculated using GRADISTAT v8, Blott and Pye, 2001).

6.2.2. Results of analysis of PC494

1031 - 1004 cmbsf

Olive brown mud containing rare foraminifera 1029-1024 cmbsf and which is slightly mottled 1007-1003 cmbsf. WBD and MS values both increase rapidly from the core base to reach relatively large values (e.g. at 1018 cmbsf, WBD of 1.68 g/cm^3 and MS of 31.6 10^{-5} SI). Typically trace amounts of IRD are present, reflected in the grain size at 1024 cmbsf which contained no gravel and only 0.14 wt.% sand. Both mean and percentage sortable silt are close to core-average values, at 16.18 µm and 11.93%, respectively. At 1024 cmbsf, biogenic silica contents are moderately low at 7.7 wt. % whilst TOC is relatively high at 0.95% and there is zero $CaCO_3$. Clay mineralogy is dominated by illite and kaolinite (at 1024 cmbsf, 13.1 % smectite, 44.4% illite, 13.6% chlorite, 29.0% kaolinite).

1004 - 956 cmbsf

Foraminifera-bearing, olive brown mud. 1003-970 cmbsf is laminated, 995-990 cmbsf is slightly mottled, and layers of coarser grains are present at 1020-1017, 995 and 988 cmbsf. Physical properties are both relatively high, with average unit values of WBD of 1.70 g/cm^3 and MS of 28.5 10^{-5} SI). IRD is present in low amounts throughout the unit, and no gravel was found in any of the discrete samples which were >98.5 wt.% mud. The clay mineralogy is similar to the underlying unit, but smectite concentration increases towards the top of the unit from c.12.7% (at 984 cmbsf) to 17.3% (at 957 cmbsf), with a corresponding decline in kaolinite from 29.0% to 24.9%. Mean and percentage sortable silt are of moderate values, e.g. at 984 cmbsf, 16.01 µm and 16.49%. TOC exhibits core-average values of 0.63-0.71%, but biogenic silica concentrations are low, at 4.6-5.9 wt.% and relatively low contents of $CaCO_3$ are also present (≤0.13%).

956 – 524 cmbsf

Olive brown to greyish brown mud, with a coarse grained layer of mostly fine sand 934.5-936 cmbsf. The majority of the unit is laminated, with slight to moderate mottling

at 902-894, 807-772, 755-587 and 554-550 cmbsf, and heavy mottling at 549-537 and 530-524 cmbsf.

WBD and MS values are both relatively large and MS exhibits particularly high variability, with values for WBD of 1.51-1.85 g/cm^3 and MS of 19.0-32.6 10^{-5} SI. Low IRD contents are present throughout the unit, but are found in particularly high concentrations of ≤15 grains/10 cm^3 at 942-921, 882-879, 669-645 and 549-524 cmbsf. However, mud still constitutes ≥96.2 wt.% of all discrete samples in this unit, with the exception of a sample from the coarse-grained layer at 935.5 cmbsf, which contained 10.8 wt.% gravel, 31.2 wt.% sand and only 57.9 wt.% mud. Clay mineralogy is relatively consistent throughout the unit, dominated by illite (c. 41%) and kaolinite (c. 28%), with the exception of 604 and 584 cmbsf, when smectite concentration temporarily increases from 15.8% at 624 cmbsf, to 19.4% at 604 cmbsf and 22.3% at 584 cmbsf, with kaolinite seeing the largest concurrent decrease. Mean sortable silt exhibits little variation, with a range of 15.9-19.2 µm, but percentage sortable silt is more variable throughout the unit, ranging from 11.7-26.3%. Biogenic silica contents are close to average core-values at 5.0-10.0 wt.%, whilst the TOC content varies between 0.36-1.21%.

522 - 465 cmbsf

Foraminifera-bearing, olive brown mud (522-482 cmbsf) to mud with foraminifera (482-465 cmbsf) with dispersed clasts throughout. Slightly mottled 520-512 and 497-490 cmbsf, moderately mottled 482-473 cmbsf and heavily mottled 490-482 cmbsf.

WBD and MS both exhibit low values for the entirety of this unit, with mean values of WBD 1.40 g/cm^3 and MS 15.1 10^{-5} SI. MS exhibits a double minima (495 and 475 cmbsf). IRD is present throughout the unit and in relatively high concentrations, with a mean concentration of 4.0 grains/10 cm^3 and a maximum of 12 grains/10 cm^3. This is reflected in the discrete grain size data, which contain 1.2-15.2 wt.% gravel, 5.8-18.4 wt.% sand and 72.0-88.4 wt.% mud.

Mean and percentage sortable silt values are both slightly above core-average and peak at 474 cmbsf at 25.04 µm and 41.76%, respectively. Kaolinite concentrations are low,

with chlorite increasing the most from the underlying unit as kaolinite decreases, reaching a low at 484 cmbsf (25.3% smectite, 41.2% illite, 25.2% chlorite, 8.3% kaolinite).

$CaCO_3$ contents are the highest of the core and exhibit a double peak of 16.1% at 494 cmbsf and 14.9% 474 cmbsf separated by 6.9% at 484 cmbsf. Biogenic silica contents are relatively low (5.9-10.2 wt.%), and TOC contents are slightly below average for the core (c. 0.5%).

465 – 21 cmbsf

Light olive brown mud with alternating layers of olive grey mud 178-102 cmbsf, and particularly thin units of each 178-151 cmbsf. The unit is mostly laminated from 449-187, 150-121 and 102-31 cmbsf, with mottling in thin sections throughout but particularly concentrated 212-199 and 121-111, 58-51 cmbsf (heavily mottled), 195-187, 178-151, 102-70, 43-21 cmbsf (slightly to moderately mottled). MS and WBD both exhibit moderately high values for the entirety of this unit, with mean values of WBD 1.54 g/cm^3 and MS 23.2 10^{-5} SI, but with significant variability, reaching particular minima at 173 and 112 cmbsf. IRD is present mostly in discrete bands 462-439, 410-412, 404-387, 229-225, 178-168, 144-141, 117-101 and 41-21 cmbsf, with a maximum of 16 grains/10 cm^3.

Sortable silt data are generally moderately high and show little variation, with the significant exception of discrete samples at 124 and 95 cmbsf which record very high values. At 124, 102 and 95 cmbsf, mean sortable silt is 21.8, 17.2 and 33.6 µm, whilst percentage sortable silt is 33.0%, 7.2% and 58.2%, respectively.

Clay mineralogy is dominated by illite (c. 44%) and kaolinite (c. 27%), and is relatively consistent with the exception of 102 cmbsf, which sees a temporary near doubling of chlorite and halving of kaolinite concentrations. For example, at 124 cmbsf, 13.4% smectite, 46.5% illite, 13.9% chlorite, 26.2% kaolinite, whereas at 102 cmbsf, 18.3% smectite, 42.1% illite, 26.1% chlorite and 13.5% kaolinite.

Biogenic silica contents are low (5.4-11.4 wt.%) whilst TOC contents very between 0.39-0.78%. There is no $CaCO_3$ in this unit.

21 - 0 cmbsf

Olive grey (21 – 3 cmbsf) to light olive brown (3 – 0 cmbsf) sand-bearing and slightly mottled mud. WBD and MS are of relatively moderate values, lower than the underlying unit, with mean values of WBD 1.40 g/cm^3 and MS 17.6 10^{-5} SI. The unit contains large amounts of IRD, from 1-17 grains/10 cm^3, giving an average of 9.5 grains/10 cm^3. Only one discrete sample was taken from this unit, from 3 cmbsf, which comprised 8.5 wt.% gravel, 16.6 wt.% sand and 75.0 wt.% mud. Sortable silt data are slightly higher than in the underlying unit, with a mean sortable silt of 19.2 µm and a percentage sortable silt of 25.4%. Clay mineralogy shows a small increase in smectite and decrease in kaolinite from the underlying unit (at 3 cmbsf, 22.0% smectite, 42.5% illite, 19.8% chlorite, 15.7% kaolinite). $CaCO_3$ is present in this unit at a relatively high content of 6.25%. TOC content increases slightly towards the core-top to 0.62%, but biogenic silica contents are relatively low at 6.8 wt.%.

Lithofacies attribution

Base (cmbsf)	Top (cmbsf)	Lithofacies Description	Lithofacies Number
21	0	Sandy mud	4a
465	21	Laminated to stratified terrigenous mud	1b
479	465	Calcareous foraminifera-bearing mud	3
489	479	Mud with diatoms	2b
522	489	Calcareous foraminifera-bearing mud	3
1004	522	Laminated to stratified terrigenous mud	1b
1031	1004	Homogenous terrigenous mud	1a

Table 6.3: Depths and descriptions of lithofacies in core PC494.

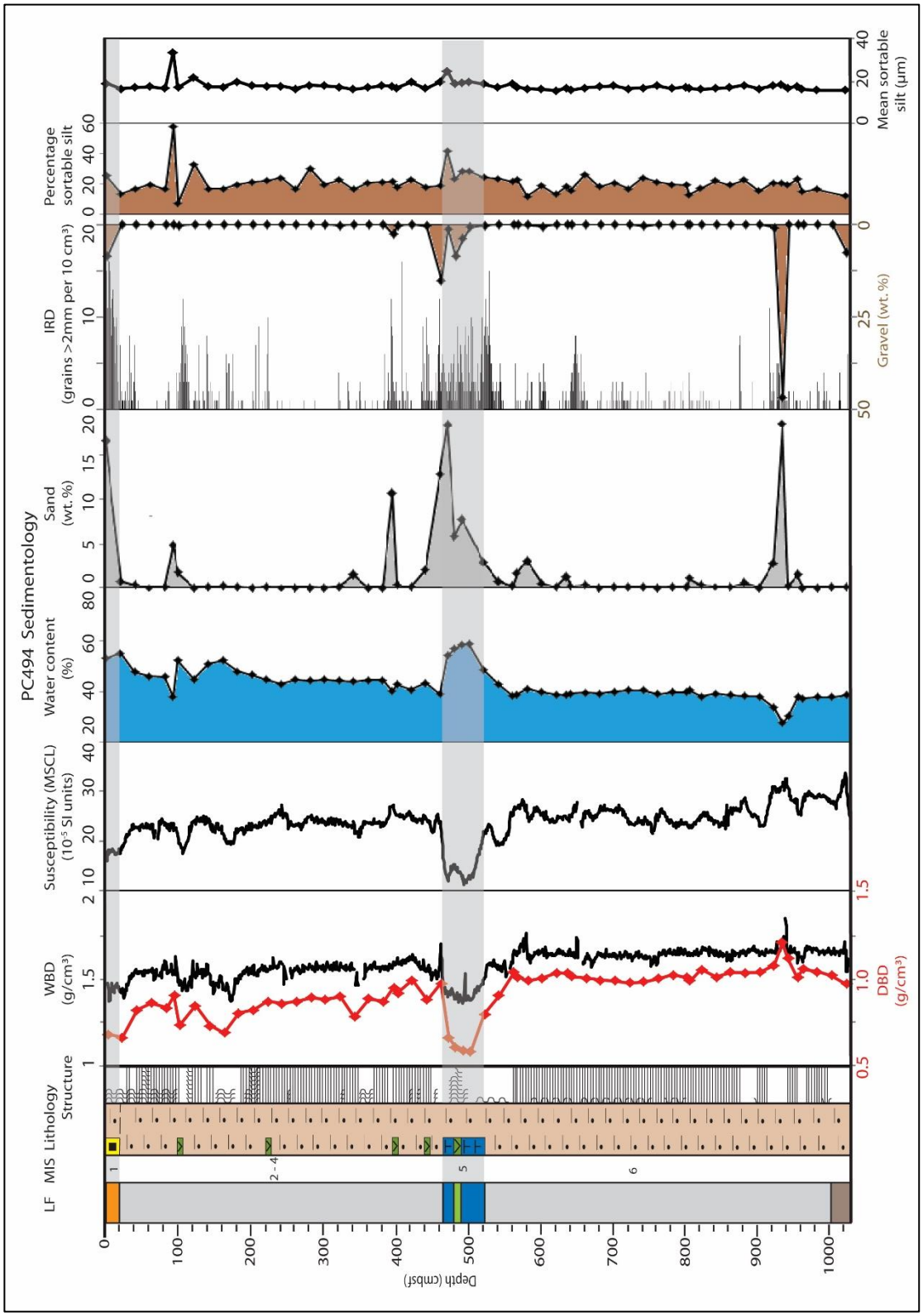

Figure 6.2: Lithology and structures, physical properties and grain size distribution in core PC494.

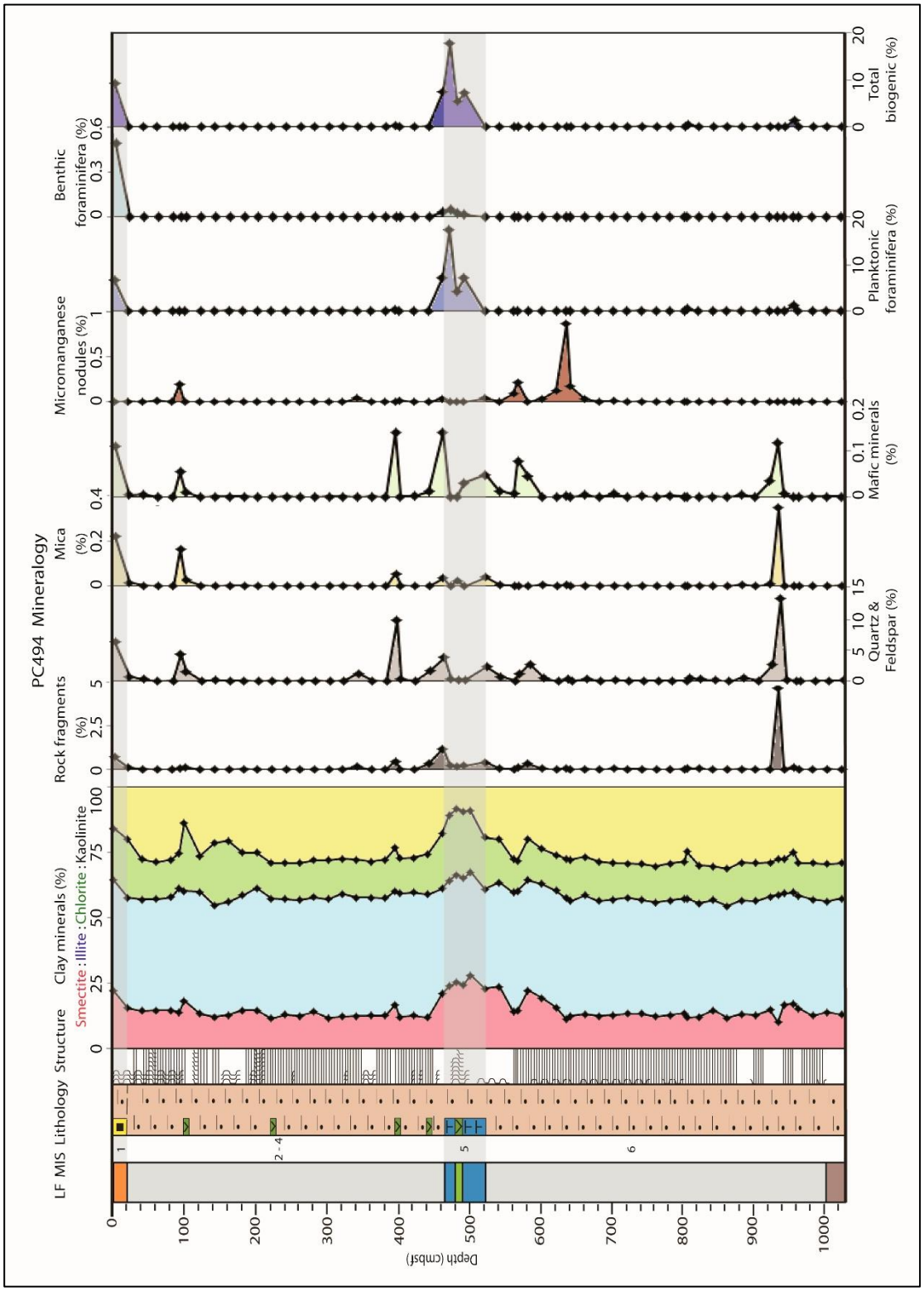

Figure 6.3: Clay mineralogy and composition of the sand fraction in core PC494.

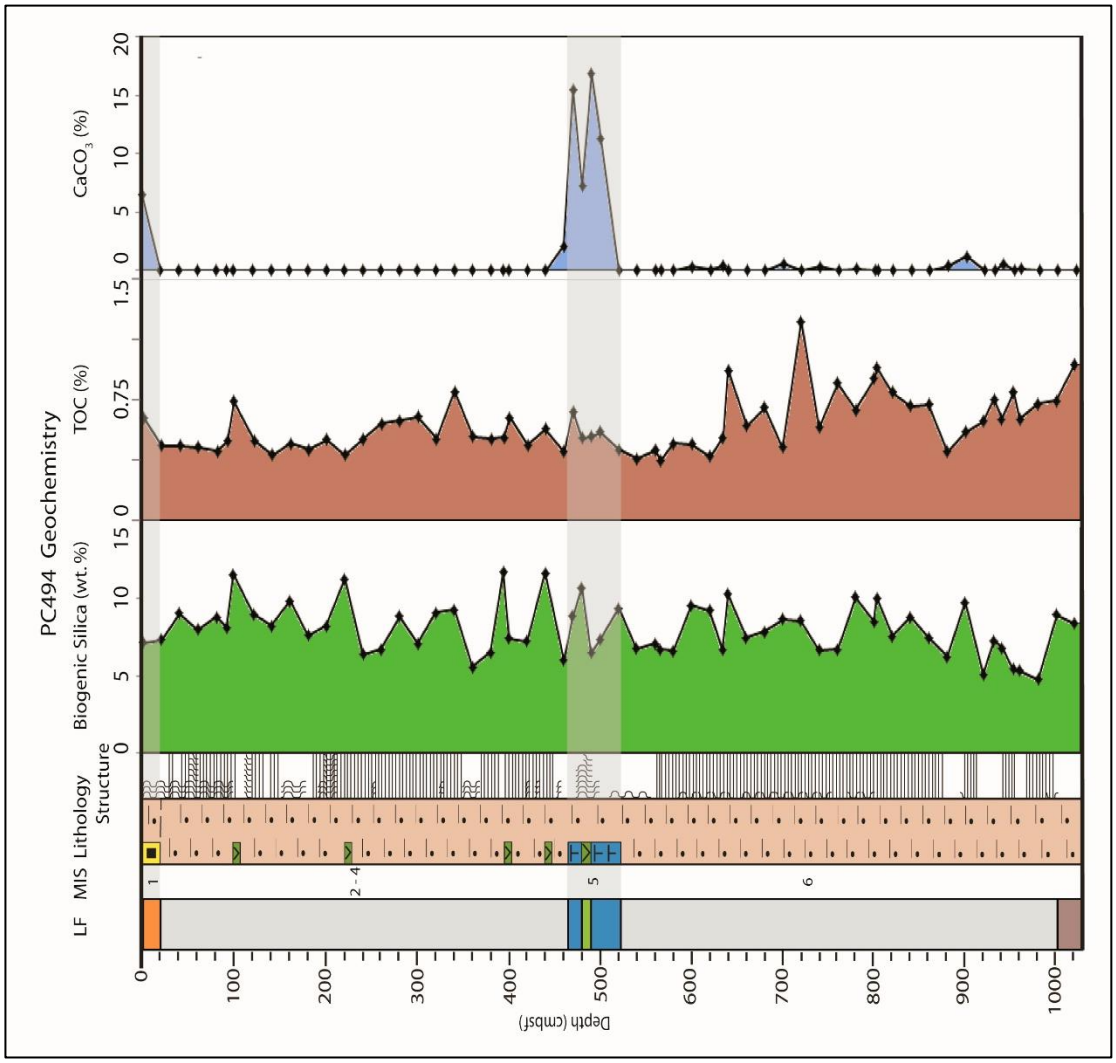

Figure 6.4: Biogenic silica, TOC and $CaCO_3$ contents of core PC494.

6.2.3. Results of analysis of PC496

Sediment description

936 - 931 cmbsf

Moderately mottled, light brownish-grey mud. Physical property values are low at the core base but increase towards the overlying unit (e.g. at 933 cmbsf, WBD of 1.42 g/cm^3 and MS of 16.91 10^{-5} SI). No discrete samples were taken from this unit.

931 - 922 cmbsf

Light olive brown mud, which is moderately (934-924 cmbsf) to slightly (924-922 cmbsf) mottled. Physical property values are relatively large, e.g. at 926 cmbsf, WBD of 1.54 g/cm^3 and MS of 16.83 10^{-5} SI The one discrete sample analysed from this unit (923 cmbsf) contains no $CaCO_3$ but a relatively large TOC content of 1.10% and a core-average biogenic silica content of 14.5 wt.%. Only trace amounts of IRD and sand are present, with 99.15 wt.% <63 µm. Mean and percentage sortable silt are both of roughly average values for the core, at 15.5 µm and 21.5%, respectively. Clay mineralogy is dominated by illite with approximately equal contents of smectite and kaolinite (18.6% smectite, 47.6% illite, 12.9% chlorite, 21.0% kaolinite).

922 - 824 cmbsf

Olive brown to brownish grey mud (922-896.5 and 825-824 cmbsf) and diatomaceous ooze (896.5-825 cmbsf). Slightly mottled throughout. Physical property values decrease in the lowermost 4 cm of the unit and remain low, with mean values of WBD 1.34 g/cm^3 and MS of 12.62 10^{-5} SI. Small amounts of IRD are consistently found throughout the unit, but the <63 µm fraction is never less than 98 wt.% of the discrete samples. Mean and percentage sortable silt exhibit slight increases compared to the underlying unit, with respective maximum values of 20.6 µm and 37.4%. Clay mineralogy is dominated by smectite and illite, with very low relative contents of kaolinite (e.g. at 863 cmbsf, 36.7 % smectite, 38.0% illite, 20.7% chlorite, 4.6% kaolinite). This unit contains no $CaCO_3$ and TOC decreases up-unit from 0.98% at 903 cmbsf to 0.64% at 843 cmbsf. However,

biogenic silica contents are high, always >20 wt.% and peaking at 32.1 wt.% at 883 cmbsf.

824 – 583 cmbsf

Dark greyish-brown mud which is slightly mottled 824-817, 645-640 and 615-611 cmbsf, moderately mottled 743-740 cmbsf, and laminated 769-671 and 655-594 cmbsf. 3 mm thick coarser grained layers are present at 718, 699 and 672 cmbsf.

The physical property values exhibit moderately high values for the entirety of this unit, with mean values of WBD 1.58 g/cm^3 (and a gradual decrease up-core) and MS 21.10 10^{-5} SI. IRD is present throughout in small quantities and discrete bands (1-10 grains per 10 cm^3). 11 of the 13 discrete samples have mud contents greater than 99.4 wt.%.

Sortable silt values are generally low, but percentage sortable silt in particular exhibits large variations, with ranges of mean sortable silt of 11.4-16.4 μm and percentage sortable silt of 6.2-33.6%.

Clay mineralogy is relatively consistent throughout, with significant changes only occurring close to the boundary with the overlying unit. Illite and kaolinite dominate, with low concentrations of smectite and chlorite. For example, at 683 cmbsf, 10.3% smectite, 44.5% illite, 15.7% chlorite, 29.5% kaolinite.

Biogenic silica contents are relatively low to moderate throughout the unit at 6.5-10.2 wt.%. TOC is also relatively high at 0.50-0.79%. This unit contains no $CaCO_3$.

583 - 264 cmbsf

Alternating layers of brown, grey and light olive brown mud, with particularly thin alternating layers 484-454 cmbsf. A layer of laminated fine to medium sand is present 329/335-324 cmbsf, and overlain by sandy mud 324-309 cmbsf. Slight to moderate mottling is present 568-540, 508-486, 472-453, 378-329, 319-314, heavy mottling is present 516-506, 484-480, 474-472, 420-385, 314-309, and laminated sections are 542-

529, 514-512, 449-396, 331-324 cmbsf. Sand lenses are present at 578, 555 and 546 cmbsf and 2 mm layers of fine sand are found at 301 and 299 cmbsf.

The physical property values are moderately high throughout the unit, with mean values of WBD 1.55 g/cm^3 and MS 24.51 10^{-5} SI. Both MS and WBD exhibit three distinct peaks at 328, 302 and c.271 cmbsf, correlating to sand layers. IRD is highly concentrated in select bands, which contain between 1 and 26 grains per 10 cm^3, at 583-578, 566-563, 543 -538, 470-458, 437-432, 396-380 and 352-330 cmbsf. The discrete samples have largely missed these IRD-rich layers, with the exception of the 463 cmbsf sample which contains 25.6 wt.% gravel.

Sortable silt values are generally low, with the significant exception of discrete samples between 328 and 303 cmbsf (in the sandy mud layer) which record very high values, with mean sortable silt peaking at 44.2 µm and percentage sortable silt peaking at 88.4%.

Clay mineralogy is dominated by illite but there is a large amount of variation, particularly in smectite and kaolinite concentrations. For example, at 523 cmbsf, 12.4 % smectite, 45.8% illite, 16.1% chlorite, 25.7% kaolinite, whereas at 503 cmbsf, 19.5% smectite, 42.3% illite, 25.5% chlorite and 12.7% kaolinite.

Biogenic silica contents are relatively low to moderate at 2.3-14.5 wt.%., whilst TOC exhibits an initial increase, peaking at 423 cmbsf at 0.74%, before decreasing to just 0.11% at 328 cmbsf and increasing again in the overlying unit. Traces of $CaCO_3$ (≤0.25%) are present from 343 cmbsf up to the overlying unit.

<u>264 - 112 cmbsf</u>

Olive brown diatomaceous mud with some sand (264-257 and 142-116 cmbsf), diatom-bearing mud with rare sand (116-112 cmbsf), diatomaceous mud (257-210 and 164-142 cmbsf), and diatomaceous ooze (210-164 cmbsf).

Physical property values are low, with mean values of WBD 1.27 g/cm^3 and MS 9.87 10^{-5} SI. Small amounts of IRD are present throughout the unit (typically 1-3 grains cm^3/10, max. 9 grains/10 cm^3. Grain size analysis showed the samples were 89.6-98.2 wt.% mud,

with the remainder mostly sand, with gravel only present in 2 of the 9 discrete samples from this unit. Sortable silt values are moderately large and variable, with a range of mean sortable silt of 14.4-21.6 μm and range of percentage sortable silt of 15.9-36.6%. Clay mineralogy is dominated by illite with particularly low contents of kaolinite (e.g. at 163 cmbsf, 30.6% smectite, 40.7% illite, 24.6% chlorite, 4.1% kaolinite). TOC and biogenic silica contents are relatively small at the start and end of the unit, but both exhibit higher values towards the centre of the unit, with TOC peaking at 0.75% at 163 cmbsf, and biogenic silica peaking at 34.0 wt.% at 183 cmbsf. The sample at 183 cmbsf also contains just 0.25% $CaCO_3$, 163 cmbsf contains zero $CaCO_3$, but it reappears in the overlying samples 143-113 cmbsf at the highest values for the core, peaking at 123 cmbsf at 5.2%.

112 - 63 cmbsf

Homogenous (112-98 cmbsf) to slightly mottled (98-63 cmbsf) light olive brown mud. Physical property values fluctuate but with little overall change (WBD 1.33-1.44 g/cm^3, MS 15.9-19.3 10^{-5} SI).

IRD occurs in three distinct bands from 111-99 cmbsf (which contains up to 25 grains per 10 g/cm^3), 87-80 cmbsf and 69-64 cmbsf. This is reflected in the grain size data, with up to 0.42 wt.% >2mm and 2.44 wt.% sand (at 103 cmbsf). Mean and percentage sortable silt are close to average values and fluctuate little, with mean values of 13.99 μm and 17.12%, respectively. Clay mineralogy is dominated by illite, with near-equal concentrations of smectite and kaolinite (e.g. at 83 cmbsf, 20.1% smectite, 43.6% illite, 15.6% chlorite, 20.7% kaolinite). The unit contains no $CaCO_3$ and moderate concentrations of TOC (0.44-0.53%) and biogenic silica (10.4-13.2 wt.%).

63 - 35 cmbsf

Slightly to moderately mottled, greyish brown to olive grey mud. Coarser grains are dispersed in the mud at 40-38 cmbsf. MS decreases towards the core top throughout the unit, but WBD experiences a clear minimum at 53 cmbsf of 1.28 g/cm^3, with values at either end of the unit of c.1.37 g/cm^3. Only traces amounts of IRD are present with

the exception of 38 and 39 cmbsf, when 20 and 11 grains are present (per 10 cm^3). The discrete sample at 43 cmbsf reveals a content of 98.6% mud, with mean and percentage sortable silt values of 22.9 µm and 12.5%, respectively. Clay mineralogy is dominated by chlorite and illite, with relatively little kaolinite (18.7% smectite, 39.7% illite, 33.2% chlorite, 8.5% kaolinite). TOC concentrations are moderately high (0.60%) and biogenic silica values are close to average values for the core (15.0 wt.%).

35 - 9 cmbsf

Greyish brown mud (35-18/15 cmbsf) to olive brown, sand-bearing mud (18/15-9 cmbsf). Slightly to moderately mottled 35-18/15 cmbsf, strongly mottled 14-10 cmbsf. Physical property values are relatively large and consistent throughout the unit, with a mean WBD of 1.42 g/cm^3 and mean MS of 15.23 10^{-5} SI. Only one discrete sample has been analysed from this unit, at 23.5 cmbsf. The sample was 97.8% mud with no gravel, which concurs with the generally small amounts of IRD found in the unit. Mean and percentage sortable silt values are low, at 13.6 µm and 13.5%, respectively. Clay mineralogy is dominated by illite, with relatively high amounts of kaolinite (22.7% smectite, 39.9% illite, 19.2% chlorite, 18.2% kaolinite). The samples contain relatively low amounts of biogenic material, with 11.5 wt.% biogenic silica, 0.62% TOC and zero $CaCO_3$.

9 - 0 cmbsf

Olive brown, homogenous, sand-bearing mud. Physical properties decline 9-6 cmbsf and then stabilise at relatively low amounts (e.g. at 3 cmbsf, WBD of 1.29 g/cm^3 and MS of 10.07 10^{-5} SI), with a corresponding high water content of 63.2%. IRD is present throughout and increases towards the core top, where it is present in relatively high amounts, e.g. at 1 cmbsf, 15 grains per 10 cm^3. Only one discrete sample was taken from this unit, at 3.5 cmbsf, which contained 9.73 wt.% sand and 1.07 wt.% gravel. Mean and percentage sortable silt were relatively high, at 19.0 µm and 28.3 %, respectively. Clay mineralogy exhibited almost a halving of percentage kaolinite compared to the underlying unit, with a simultaneous increase in smectite (29.6% smectite, 40.8% illite,

19.9% chlorite, 9.7% kaolinite). Biogenic silica content was an approximately core-average value of 17.5 wt.% and TOC was 0.92%.

Lithofacies attribution

Base (cmbsf)	Top (cmbsf)	Lithofacies Description	Lithofacies Number
9	0	Diatom-bearing mud	2a
34	9	Homogenous terrigenous mud	1a
76	34	Mud with diatoms	2b
120	76	Homogenous terrigenous mud	1a
251	120	Diatom-bearing mud	2a
309	251	Homogenous terrigenous mud	1a
324	309	Sandy mud	4b
335	324	Very fine to fine sand	5
824	335	Homogenous terrigenous mud	1a
922	824	Diatom-bearing mud	2a
936	922	Homogenous terrigenous mud	1a

Table 6.4: Depths and descriptions of lithofacies in core PC496.

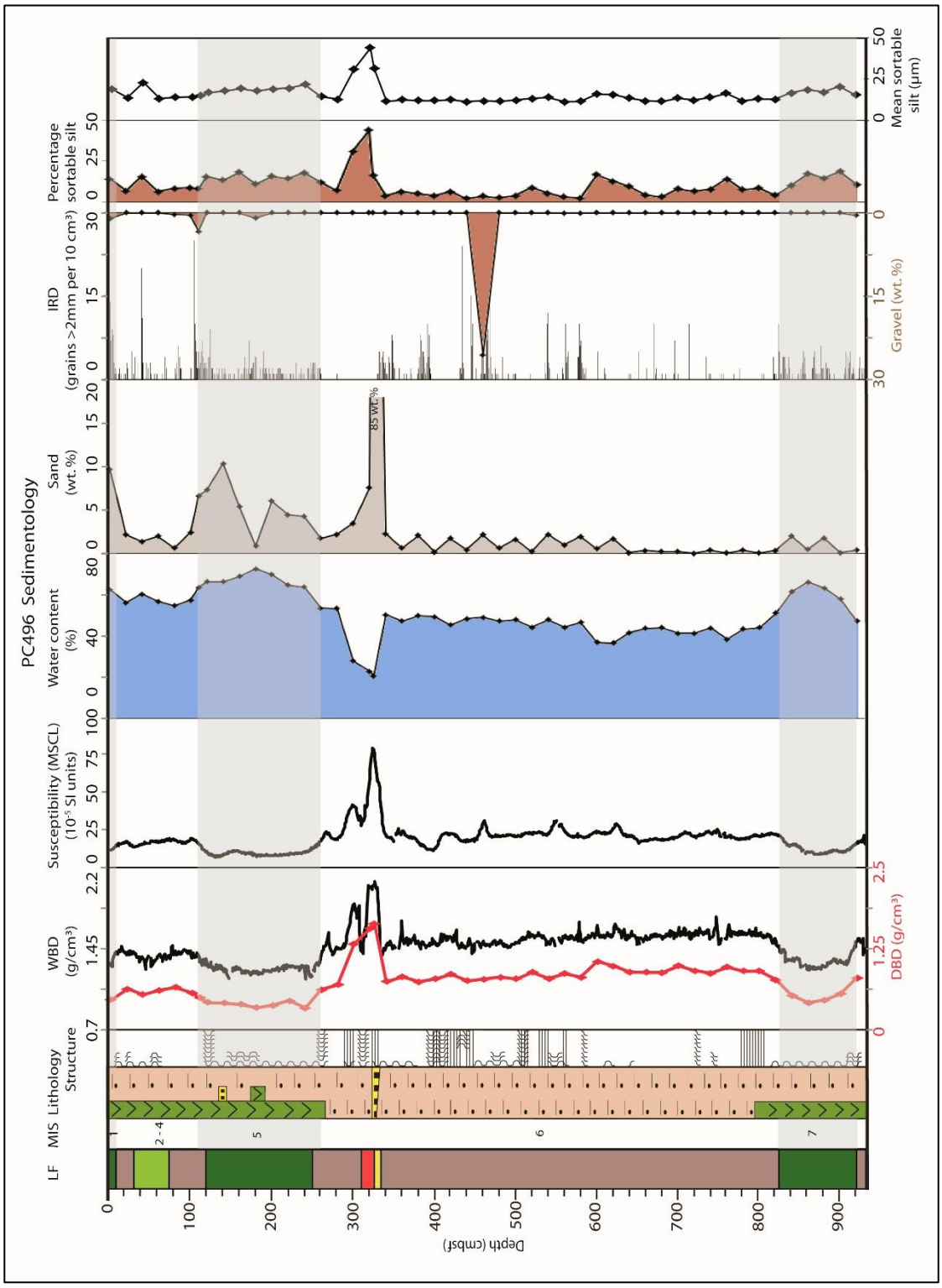

Figure 6.5: Lithology and structures, physical properties and grain size distribution in core PC496.

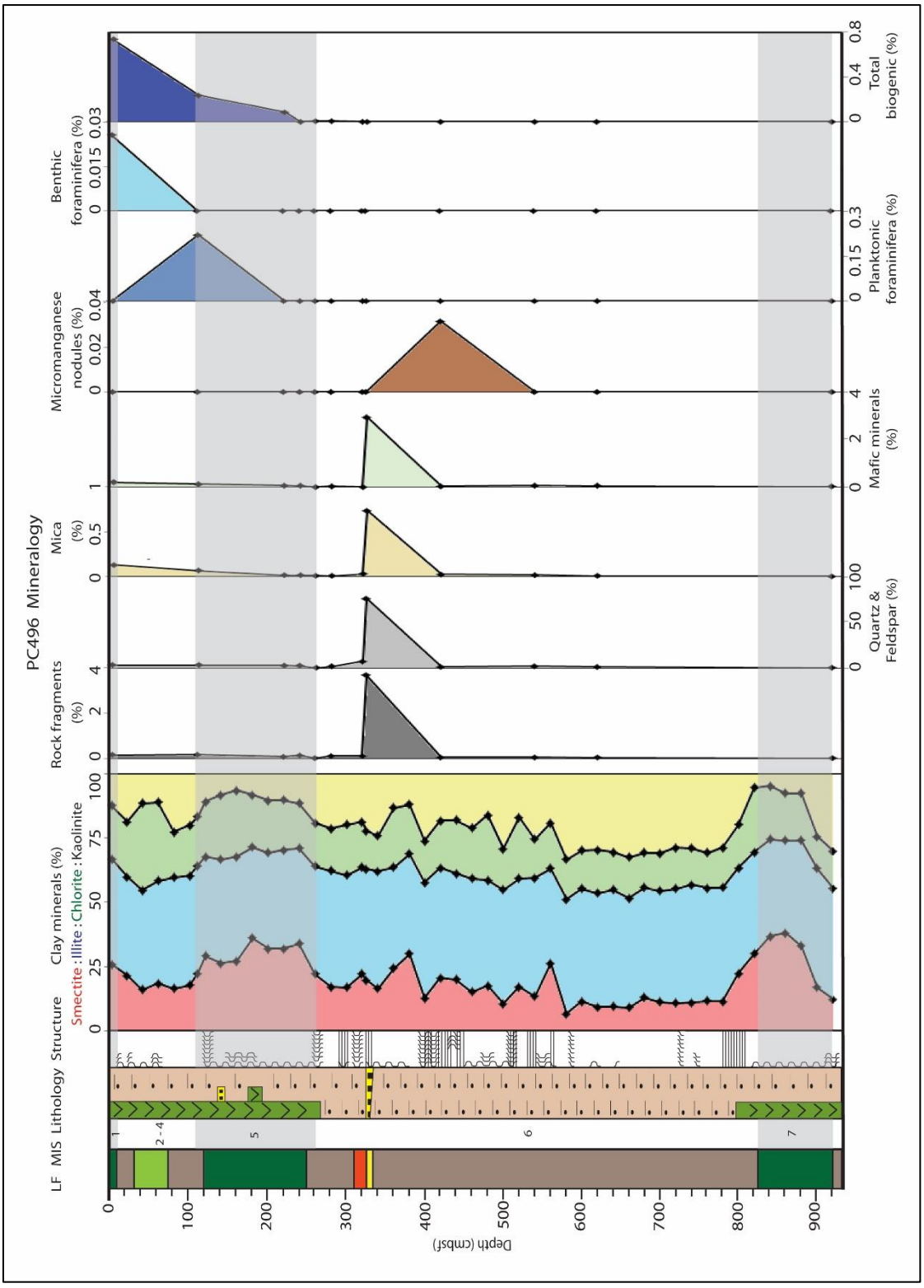

Figure 6.6: Clay mineralogy and composition of the sand fraction in core PC496.

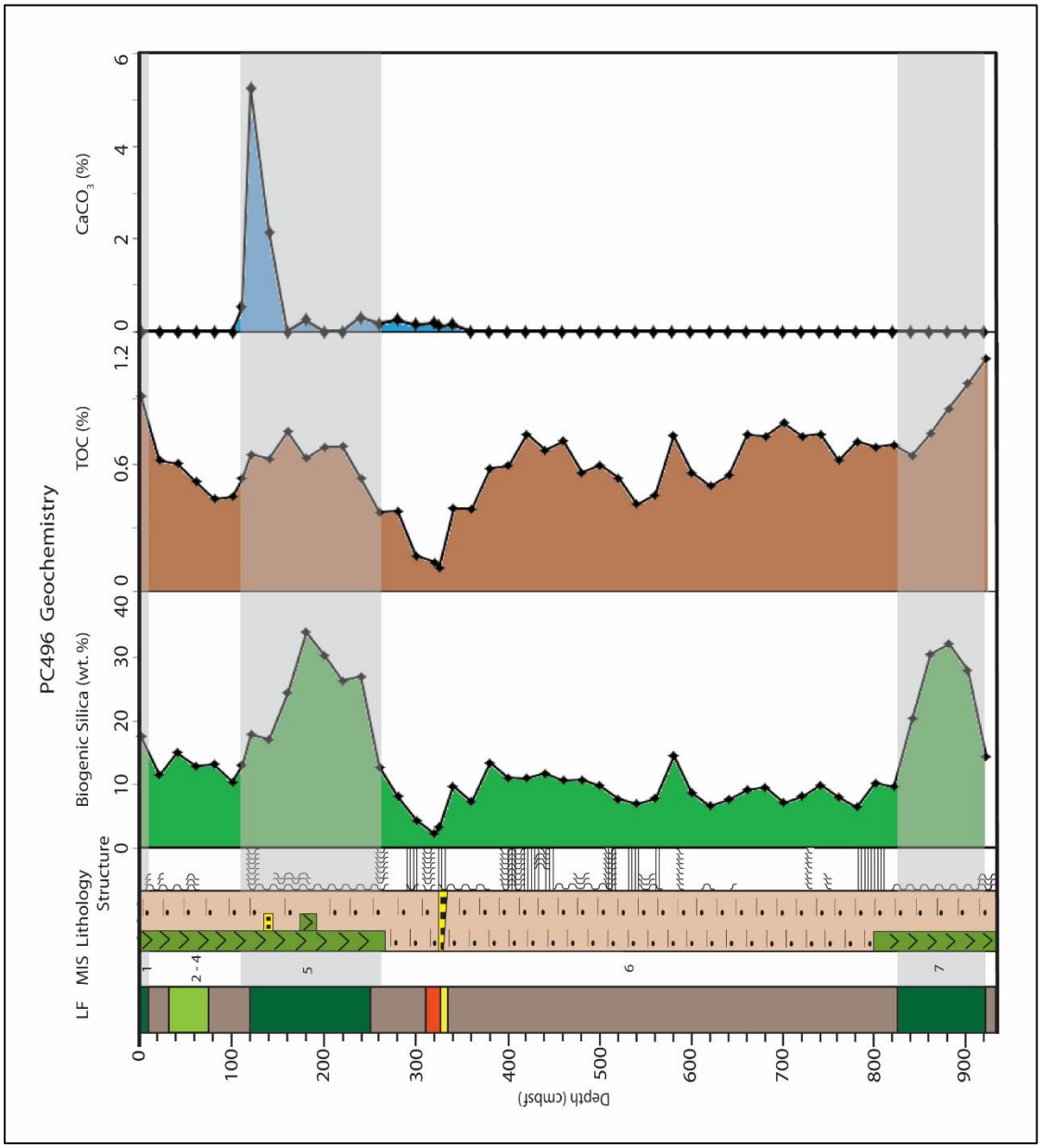

Figure 6.7: Biogenic silica, TOC and $CaCO_3$ contents of core PC496.

6.2.4. Results of analysis of PS58/253-1

1452 – 1315 cmbsf

Olive brown, strongly laminated mud, which is disturbed due to infill from 1452-1386 cmbsf. The unit contains rare dispersed gravel. MS and WBD are relatively large and show little variation throughout the unit, with a mean WBD of 1.78 g/cm^3 and MS of 84.0 10^{-5} SI. Mean and percentage sortable silt are between 17.6-21.6 µm and 22-38%, respectively. Clay mineralogy is dominated by chlorite and kaolinite throughout (e.g. at 1366 cmbsf, 15.3% smectite, 45.9% illite, 13.4% chlorite and 25.4% kaolinite). Sand makes up less than 0.6 wt.% of the bulk sediment in the unit and sand mineralogy is dominated throughout by quartz and feldspar, although micro-manganese nodules are present throughout (peaking at 0.11 wt.% of the bulk sediment at 1331 cmbsf) and trace planktonic foraminifera are present at 1351 cmbsf. $CaCO_3$ values reflect this, with a peak of 0.7% at 1355 cmbsf, compared to values of 0.2% at both 1365 and 1350 cmbsf. Biogenic silica content remains consistently low throughout the unit (2.3-4.4 wt.%). Ba/Ti data are missing for all but the uppermost 34 cm, which has low values of 0.09-0.14.

1315 – 1299 cmbsf

Green-brown, highly mottled diatomaceous ooze (mud with >50% diatoms) with dispersed gravel. Significant changes are present in all physical properties with respect to the underlying and overlying units; a WBD minima of 1.41 g/cm^3 and MS minima of 43.2 10^{-5} SI occur at 1307 cmbsf. Mean and percentage sortable silt both peak at 1306 cmbsf at 23.1 µm and 35.5%, respectively. This unit shows a large increase in biogenic silica from 4.4% (1315 cmbsf) to 16.3% (1305 cmbsf), and an increase in Ba/Ti from 0.16 (1315 cmbsf) 0.37 (1310 cmbsf). This is also accompanied by a small peak in Fe/Ti, minor increases in TOC (max. 0.12%) and traces of $CaCO_3$ (max. 0.5%). There is only one clay mineralogy sample from this unit at 1306 cmbsf, which reveals an almost doubling of chlorite and decrease in kaolinite compared to the underlying unit (26.9% smectite, 45.1% illite, 22.1% chlorite and 5.8% kaolinite). Micro-manganese nodules constitute

0.10 wt.% of the bulk sediment, with the remainder quartz and feldspar and traces of volcanic glass, planktonic foraminifera, mafic minerals and rock fragments.

1299 – 1265 cmbsf

Olive brown, moderately stratified mud with some dispersed gravel. MS and WBD are generally high with little variation (average WBD of 1.74 g/cm^3 and MS of 69.7 10^{-5} SI). Towards the top c.12 cm of the unit, there is an increase in IRD and sand content. This coincides with a biogenic silica minima of 2.3 wt.% at 1275 cmbsf, and a slight increase in smectite. No micro-manganese nodules were found in the discrete samples, but the Mn/Ti ratio (max. 0.43) suggests dispersed manganese is present throughout the unit. Sortable silt values are moderate and show little fluctuation (mean sortable silt 17.6-19.6%).

1265 – 1235 cmbsf

Green-brown (becoming green-grey from c. 1250 cmbsf) highly mottled diatomaceous ooze with dispersed gravel and abundant foraminifera. MS and WBD values are relatively low and MS reaches a minima of 31.5 10^{-5} SI at 1251 cmbsf (WBD data is missing for 1257-1247 cmbsf). Water content is high, peaking at 62.9% at 1250 cmbsf. Small amounts of IRD and sand are present throughout the unit (max. 3.9 wt.% sand). Mean and percentage sortable silt both increase significantly to peak at 1246 cmbsf before rapidly decreasing. This peak is most notable in the percentage sortable silt, which decreases from 42.6% at 1246 cmbsf to 13.8% at 1236 cmbsf. This unit sees the highest concentrations of biogenic silica in the whole core, peaking at 21.4 wt.% at 1250 cmbsf, also reflected in the high Ba/Ti ratio which peaks at 0.48 at 1254 cmbsf (1253-1249 cmbsf values missing). $CaCO_3$ is present, typically 6.2-8.2%, but exhibits a short-lived minima at 1250 cmbsf which is also reflected in minima in the the Fe/Ti and Ca/Ti ratios. TOC is low (0.08-0.17%) but increases up the unit. The sand fraction was composed mainly quartz, feldspar and benthic foraminifera. The clay mineralogy is relatively smectite-rich and kaolinite-poor compared to the underlying unit (at 1246 cmbsf, 30.8% smectite, 39.5% illite, 22.2% chlorite and 7.5% kaolinite).

1235 – 463 cmbsf

Olive brown mud, strongly laminated with the exception of three homogenous sections, each less than 5 cm thick. IRD is present throughout the section, both dispersed and in thin layers, and thin silt layers are present between 1228 and 974 cmbsf. Otherwise, only traces of >63 μm material are present. MS and WBD values exhibit few fluctuations and are generally high (mean WBD 1.74 g/cm^3, mean MS 74.3 10^{-5} SI). Sortable silt fluctuates but is generally low below c.650 cmbsf (mean sortable silt 14.9-21.7 μm, percentage sortable silt 12.2-31.8%). Upwards of c.640 cmbsf, both sortable silt measurements exhibit large fluctuations, with percentage sortable silt decreasing from 32.3% at 632 cmbsf to 16.4% at 572 cmbsf. Clay mineralogy is highly consistent throughout the unit with the exception of 572 cmbsf, when smectite concentrations increase from 13.9% (602 cmbsf) to 26.4%, recuing the illite and kaolinite concentrations. Micro-manganese nodules, present in trace amounts until 572 cmbsf, constitutes a maximum of 0.11 wt.% of the bulk sediment at 476 cmbsf. This is also reflected in the Mn/Ti ratio, with manganese consistently present in the sediment from 575 to 460 cmbsf and peak values found at 575 and 483 cmbsf. TOC is highly variable throughout, with contents from 0.06 to 0.37, particularly low from 571 cmbsf which continue into the overlying unit. Biogenic silica contents (0.7-10.7 wt.%, average 3.0 wt.%) and Ba/Ti (0.09-0.12) are relatively low throughout this unit.

463– 414 cmbsf

Slightly (463-442 cmbsf) to strongly (442-414 cmbsf) mottled green-brown mud with dispersed gravel. WBD (1.62-1.44 g/cm^3) and DBD decline (0.85-0.56 g/cm^3) gradually up the unit, with a concurrent rise in water content (44.9-59.0%). MS exhibits an initial decline, then increases to 56.2 10^{-5} SI at 442 cmbsf, before declining again. The sand:mud ratio is low but increases up the unit to 0.03 by 415 cmbsf, accompanied by the consistent presence of low amounts of IRD. The two sortable silt measurements are low but begin to rise rapidly at the top of the unit, particularly percentage sortable silt which increases from 11.7% at 436 cmbsf to 39.5% at 415 cmbsf. Similarly, biogenic silica contents and Ba/Ti begin to increase from 456 cmbsf. Smectite levels are high (24.8-

27.9%), with low chlorite values in the base of the unit increasing above 426 cmbsf, with a simultaneous decrease in kaolinite content to 11.8%.

414 – 366 cmbsf

Olive brown (414-c.385 cmbsf) to green-brown (c.385-366 cmbsf), foraminifera-bearing (15-30% foraminifera), diatomaceous (30-50% diatoms) mud. The sediment is highly mottled with dispersed gravel. Physical properties, declining gradually in the underlying unit, are low (WBD 1.35-1.46 g/cm^3, MS 25.0-35.6 10^{-5} SI) until they begin to increase from 368 cmbsf. IRD is present throughout, though never more than 4 grains per 10 cm^3. The sand:mud ratio is the highest of the core, peaking at 0.35 at 375 cmbsf. The sand consists mostly planktonic foraminifera (25.2 wt.% of the bulk sediment at 375 cmbsf) with traces of benthic foraminifera and radiolaria. Mean and percentage sortable silt values are highest towards the base of the unit (28.7 µm and 43.5%, respectively at 395 cmbsf) and decline (20.7 µm and 23.0 %, respectively) before peaking again. This double peak is also seen in Fe/Ti, Ca/Ti, $CaCO_3$ and Ba/Ti, though not in the biogenic silica, which peaks at 11.3 wt.% at 389 cmbsf. TOC content is low (0.09 at 414 cmbsf) but gradually increases throughout the unit (0.20 at 369 cmbsf). Illite, smectite and chlorite contents are high with low kaolinite (at 375 cmbsf, 25.9% smectite, 42.4% illite, 22.9% chlorite and 8.8% kaolinite).

366 – 102 cmbsf

Strongly laminated, green-brown mud. MS and WBD values are relatively high and consistent (average WBD 1.64 g/cm^3, average MS 65.1 10^{-5} SI) with the exception of a short-lived DBD and water content fluctuation at 266 cmbsf and a gradual decrease in density towards the core top. Small amounts of IRD are present in discrete bands, with only traces of sand which comprises mostly micro-manganese nodules (max. 0.03 wt.% of bulk sediment). Biogenic silica (1.0-5.8 wt.%) and Ba/Ti (0.09-0.16) vary little. TOC content varies between 0.10% and 0.33%. Only trace amounts of $CaCO_3$ are present (≤1.0 %). Clay mineralogy is relatively kaolinite-rich and shows little variation throughout (e.g. at 247 cmbsf, 16.7% smectite, 44.6% illite, 14.1% chlorite and 24.6% kaolinite).

102 – 82 cmbsf

Homogenous (102-96 cmbsf) to moderately mottled (96-82 cmbsf) diatom-bearing (15-30% diatoms) mud. Gravel is dispersed between 96-82 cmbsf. Foraminifera were noted during core logging at the top of the unit but this has not been sampled in the discrete samples, with a $CaCO_3$ high of just 2.3%. Biogenic silica peaks at 8.3 wt.% at 98 cmbsf. This double peak is also seen in Fe/Ti. Clay mineralogy is relatively kaolinite-rich and similar to that of the unit below (e.g. at 91 cmbsf, 14.3% smectite, 43.4% illite, 18.1% chlorite and 24.2% kaolinite).

82 – 19 cmbsf

Strongly laminated, olive brown mud. WBD and MS values are both high at the base and top of the unit (c. 1.57 g/cm^3 and 58 10^{-5} SI), but experience a minima at 59 cmbsf. This short-lived sedimentological change is also indicated by increases in kaolinite and reduction in chlorite (from 17.0 % kaolinite and 22.9% chlorite at 62 cmbsf to 21.4% kaolinite and 15.9% chlorite at 56 cmbsf) and an almost doubling of TOC (0.14% at 70 cmbsf to 0.26% at 55 cmbsf). Both sortable silt measurements decrease from the high values of the underlying unit, reaching a minima of 16.9 µm (mean sortable silt) and 19.5% (percentage sortable silt) at 56 cmbsf. Sand is present in only trace amounts and comprises mostly quartz, feldspar, mica and rock fragments. Mn/Ti values indicate manganese is consistently present from 43 cmbsf, and micro-manganese nodules comprise 0.11 wt.% of the bulk sediment at 44 cmbsf.

19 – 0 cmbsf

Moderately mottled, olive brown mud, with dispersed gravel. Physical properties decrease throughout the unit (WBD from 1.55 (19 cmbsf) to 1.45 (7 cmbsf); MS from 57.4 (19 cmbsf) to 46.5 (1 cmbsf)). Small quantities of IRD and sand (4 wt.% at 4 cmbsf) are present. Mean and percentage sortable silt are close to average values for the core at 18.7 µm and 16.6%, respectively. The sand fraction of 4 cmbsf contained mostly

quartz, feldspar and rock fragments, but also had small quantities (0.05% bulk sediment each) of planktonic and benthic foraminifera and radiolaria, reflected in a slight core-top increase in $CaCO_3$ from 0.3% at 13 cmbsf to 1.5% at 3 cmbsf. Ba/Ti and Fe/Ti are not available for the uppermost 13 cm, but biogenic silica contents are higher than in the underlying unit, peaking at 6.9 wt.% (13 cmbsf).

Lithofacies attribution

Base (cmbsf)	Top (cmbsf)	Lithofacies Description	Lithofacies Number
19	0	Homogenous terrigenous mud	1a
82	19	Laminated or stratified terrigenous mud	1b
102	82	Homogenous terrigenous mud	1a
366	102	Laminated or stratified terrigenous mud	1b
385	366	Calcareous foraminifera-bearing bearing mud	3
395	385	Mud with diatoms	2b
414	395	Calcareous foraminifera-bearing bearing mud	3
463	414	Homogenous terrigenous mud	1a
1237	463	Laminated or stratified terrigenous mud	1b
1253	1237	Diatom-bearing mud	2a
1262	1253	Mud with diatoms	2b
1302	1262	Laminated or stratified terrigenous mud	1b
1310	1302	Diatom-bearing mud	2a
1386	1310	Laminated or stratified terrigenous mud	1b
1452	1386	Disturbed	-

Table 6.5: Depths and descriptions of lithofacies in core PS58/253-1.

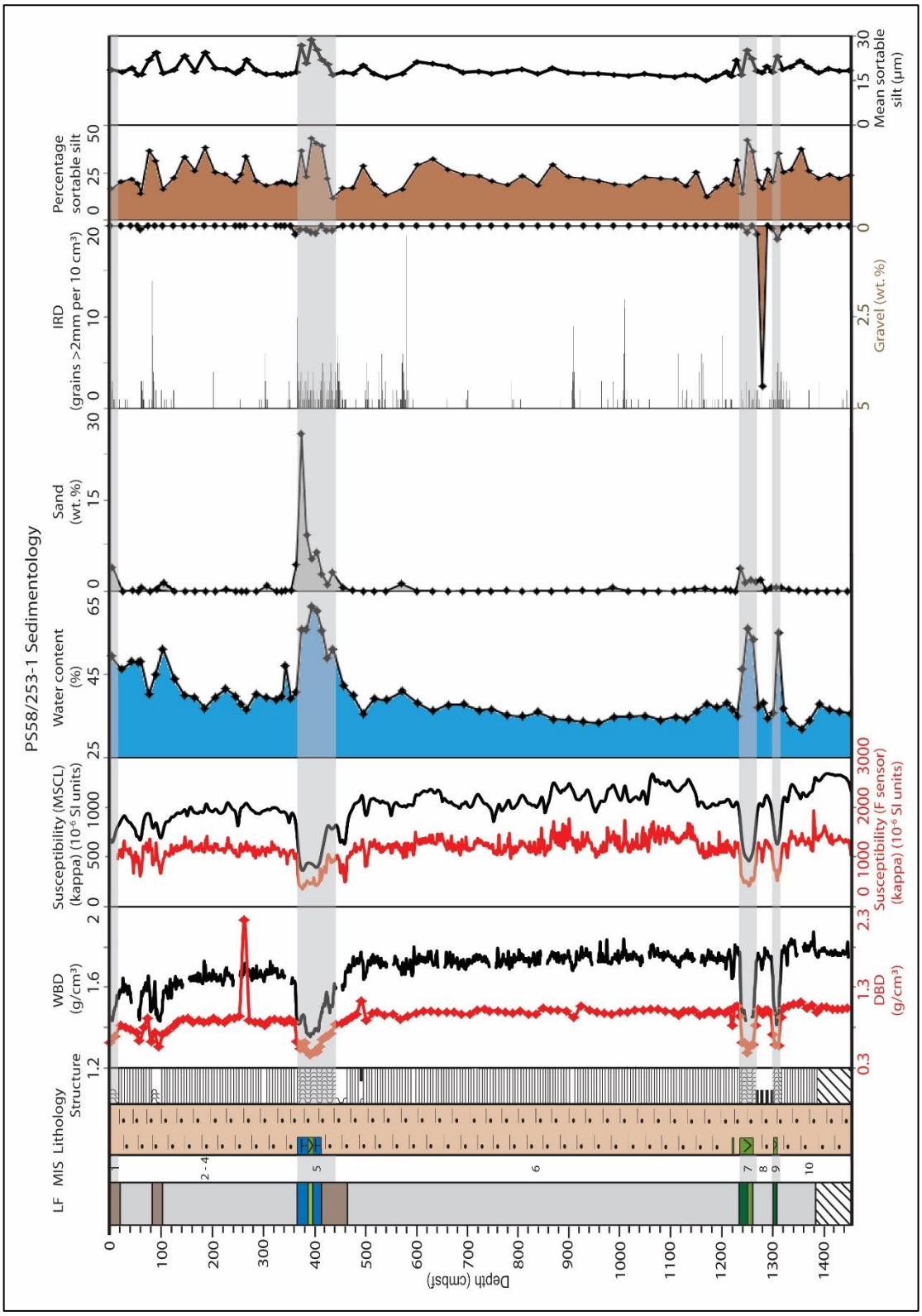

Figure 6.8: Lithology and structures, physical properties and grain size distribution in core PS58/253-1.

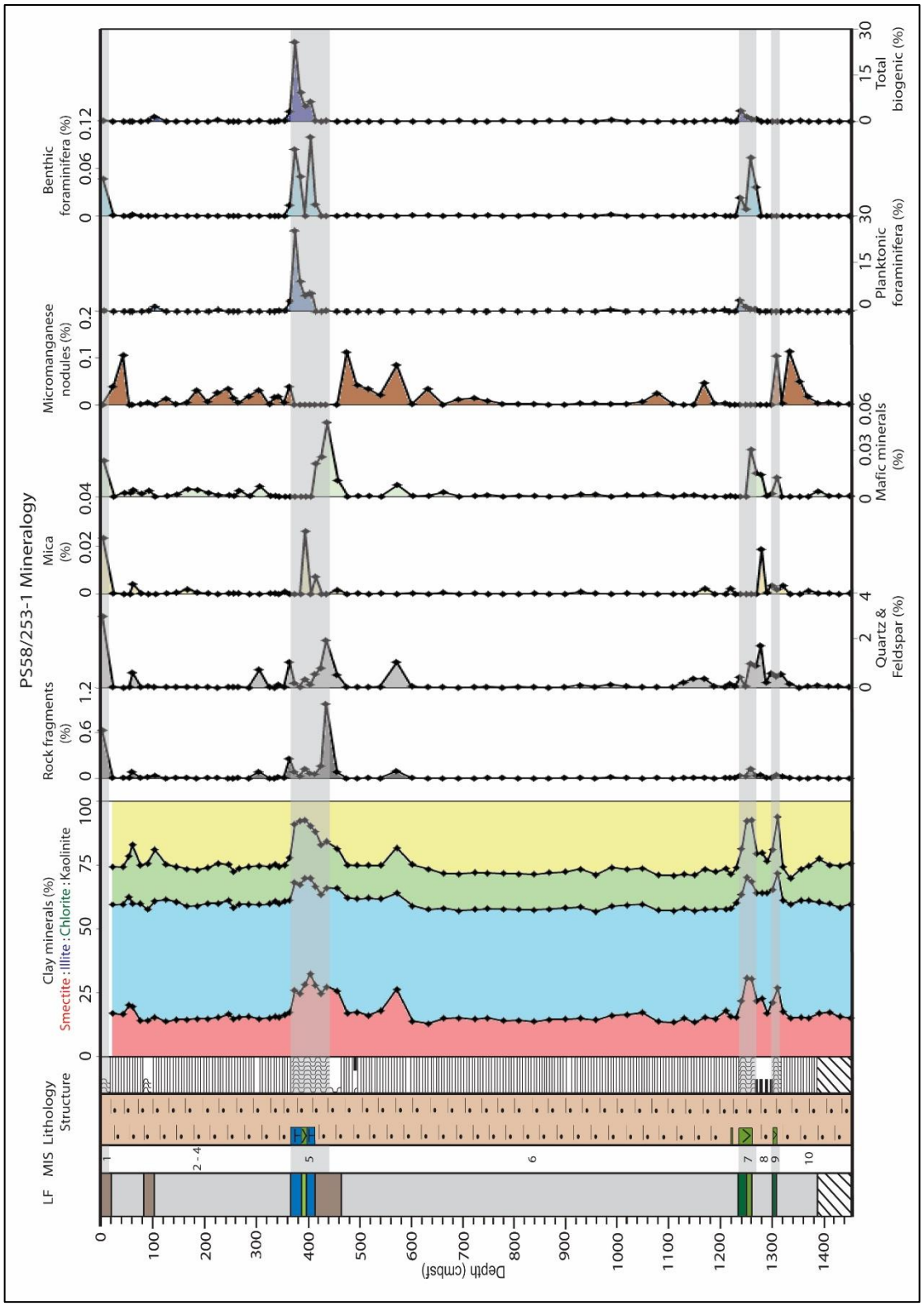

Figure 6.9: Clay mineralogy and composition of the sand fraction in core PS58/253-1.

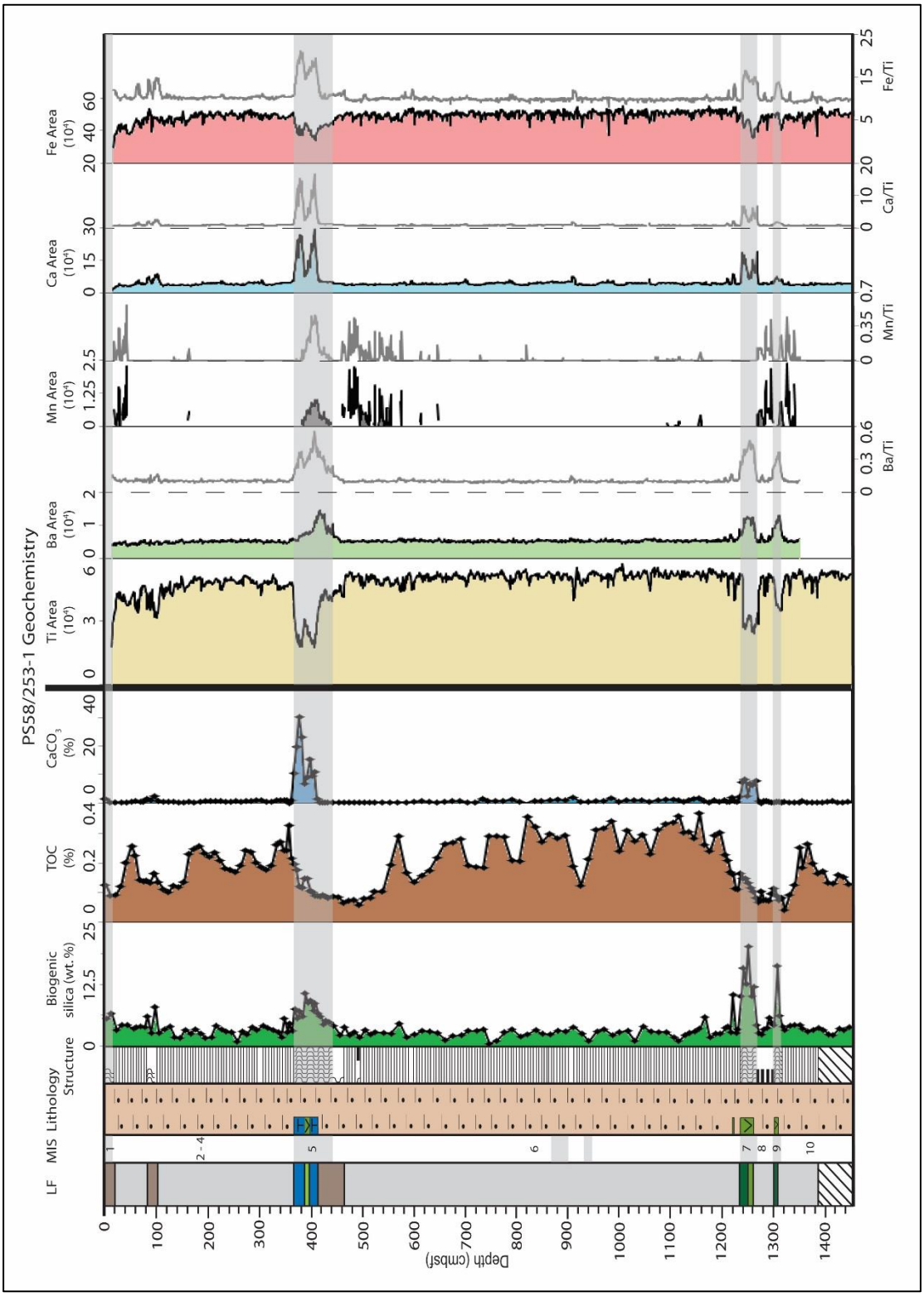

Figure 6.10: Biogenic silica, TOC and $CaCO_3$ contents and XRF elemental composition of core PS58/253-1.

6.2.5. Results of analysis of PS58/255-2

Sediment description

1253 - 1219 cmbsf

Disturbed (due to inflow), olive brown mud. WBD and MS values are high (average WBD 1.86 g/cm^3) and MS decreases gradually up-unit, from 104.1 10^{-5} SI at 1244 cmbsf to 79.4 10^{-5} SI at 1220 cmbsf. Only traces of IRD are present, reflected in the ≥97.9 wt.% mud, 0.89-1.78 wt.% sand and ≤0.36 wt.% gravel in the four discrete grain size measurements. Mean and percentage sortable silt exhibit moderate values with a peak at 1241 cmbsf of 20.5 µm and 35.2%. Clay mineralogy shows a relatively high kaolinite concentration (e.g. at 1241 cmbsf, 17.2% smectite, 43.2% illite, 11.1% chlorite, 28.5% kaolinite). $CaCO_3$ is present at low concentrations (≤0.3%), as are TOC (≤0.05 %) and biogenic silica (<3.7 wt.%). Ba/Ti (0.11-0.17) and Fe/Ti (8.9-9.9) values are low. Mn/Ti is present and relatively high throughout the unit, peaking at 0.45 at 1224 cmbsf.

1219 - 1211 cmbsf

Highly mottled, dark greyish olive diatomaceous ooze, with dispersed IRD. MS and WBD are low and reach a minima at 1215-1214 cmbsf, with a WBD of 1.52 g/cm^3 and MS of 61.9 10^{-5} SI. IRD is consistently present 1216-1211 cmbsf with up to 6 grains/10 cm^3. Only one discrete grain size sample was taken from this unit, at the boundary with the overlying unit of 1211 cmbsf. It contained 96.9 wt.% mud, 2.8 wt.% sand and 0.3 wt.% gravel. Mean and percentage sortable silt are both relatively low, with values at 1211 cmbsf of 14.0 µm and 14.4%. Clay mineralogy showed relatively very high smectite and chlorite concentrations, with moderate illite and low kaolinite (at 1211 cmbsf, 25.9% smectite, 40.5% illite, 24.8% chlorite, 8.7% kaolinite). At 1215 cmbsf, $CaCO_3$ (0.3%) and TOC (0.08%) contents remain low, but the biogenic silica content is moderately high at 8.02 wt.%. There is a distinct maximum in Ba/Ti (0.33) and Fe/Ti (12.8) at 1218-1213 cmbsf.

1211 - 1205 cmbsf

Slightly stratified, light olive brown mud with dispersed IRD. Physical property values are relatively high, particularly WBD, and reach a maximum of WBD 1.81 g/cm^3 (1210 cmbsf) and MS 68.8 10^{-5} SI (1208 cmbsf). Traces of IRD are present at the unit base, but grain size measurements are lacking from this unit (see 1219 – 1211 cmbsf description for results of sample at 1211 cmbsf). Geochemical data from 1210 cmbsf reveal low levels of $CaCO_3$ (0.3%), TOC (0.08%) and biogenic silica (2.96 wt.%). There are also moderately low levels of Ba/Ti (0.11 – 0.23) and Fe/Ti (10.1 – 11.2).

1205 - 1194 cmbsf

Highly mottled, dark greyish olive diatomaceous ooze. Physical property values are low and reach a minima at 1201 cmbsf, with a WBD of 1.47 g/cm^3 and MS of 55.7 10^{-5} SI. VIS-reflectance data show a minima of a* and b* at 1197 cmbsf, but high L*. IRD is dispersed throughout the unit, particularly 1204-1196 cmbsf which contains up to 5 grains/10 cm^3 which are unsorted and ≤7 mm diameter. This is reflected in the relatively high sand concentration of a sample from 1201 cmbsf, which contained 96.8 wt.% mud, 2.8 wt.% sand and 0.4 wt.% gravel. Mean and percentage sortable silt values are relatively high, with values at 1201 cmbsf of 21.9 μm and 40.8%. Clay mineralogy showed very high smectite and chlorite concentrations, with low kaolinite (at 1201 cmbsf, 28.3% smectite, 39.5% illite, 23.0% chlorite, 9.1% kaolinite). At 1200 cmbsf, biogenic silica is at the core-high value of at 10.0 wt.%, whilst $CaCO_3$ is slightly higher than underlying units (4.0%) and TOC is very low (0.1%). There are distinct maxima in Ba/Ti (0.34 at 1201 cmbsf), Fe/Ti (16.1 at 1200 cmbsf) and Ca/Ti (5.64 at 1200 cmbsf).

1194 - 700 cmbsf

Laminated, dark greyish brown mud. Physical property values are high with moderate levels of fluctuation, with average values of WBD 1.82 g/cm^3 and MS 100.3 10^{-5} SI, and a range of WBD 1.70 - 2.04 g/cm^3 and MS (80.7 – 123.3 10^{-5} SI). Small amounts of IRD are present in thin layers throughout the unit and grain size of 18 discrete samples revealed the samples are ≥98.9 wt.% mud and only one sample contained any gravel

(0.12 wt.% at 1181 cmbsf). Mean and percentage sortable silt are of moderately high values and peak at 1191 cmbsf (24.1 µm, 57.2%), 901 cmbsf (26.4 µm, 60.4%) and 841 cmbsf (22.4 µm, 54.0%). Clay mineralogy is dominated by illite and kaolinite, with values of 11.2 – 16.3% smectite, 40.2 – 45.8% illite, 13.7 – 17.7% chlorite and 24.4 – 29.5% kaolinite. This unit contains relatively moderate amounts of TOC (≤ 0.41%), low contents of biogenic silica (1.0 – 3.6 wt.%) and moderate amounts of $CaCO_3$ (≤ 1.9%). Ba/Ti and Fe/Ti are relatively low, with little variability and average values (respectively) of 0.11 and 9.75. Mn/Ti values are low for this unit, but peak at 0.18 at 1069 cmbsf.

700 - 138 cmbsf

Dark greyish brown mud (700-317 cmbsf), olive brown mud (317-270 cmbsf), olive grey mud (270-40 cmbsf) and light olive brown mud (240-138 cmbsf). Laminated 655-572, 567-564, 556-469, 446-440, 437-254 and 250-187 cmbsf. Slightly to moderately mottled 572-568, 187-159 (also moderately stratified). Heavily mottled 146-138 cmbsf.

WBD and MS values are moderately high, though lower than the underlying unit, and do vary. The average value of WBD is 1.73 g/cm^3 and MS 78.5 10^{-5} SI, with a range of WBD 1.55-2.26 g/cm^3 and MS (30.4-111.5 10^{-5} SI). Notable minima in both WBD and MS occur at c. 706, 660, 600, 561, 467, 360 and 263 cmbsf. The order of magnitude of each of these fluctuations is of WBD c. 0.10-0.20 g/cm^3 and MS c. 13-30 10^{-5} SI. VIS-reflectance data show minima in a* and b*, and concurrent maxima in L*, at 660, 560, 463, 360, 335 and 269-258 cmbsf. Ba/Ti, Fe/Ti and Ca/Ti also show change at these depths, e.g. at 462 cmbsf, Ba/Ti is 0.14, Fe/Ti is 13.62 and Ca/Ti is 2.10. This compares to values at 470 cmbsf of 0.11 (Ba/Ti), 10.76 (Fe/Ti) and 1.09 (Ca/Ti), Mn/Ti values are not available for much of the unit below 275 cmbsf (and only traces are present, where it is available) but consistent measurements from 233 cmbsf shows a Mn/Ti peak of 0.58 at 160 cmbsf.

IRD is located in discrete, thin layers throughout, particularly in the intervals of 622-617 (sand-rich), 658-655, 564-556, 440-437 (sand-rich), 428-408, 253-250, 221-201 and 155-138 cmbsf. The only gravel present in the discrete samples is at 211 cmbsf (1.02 wt.%), otherwise the samples are ≥97.6 wt.% mud with an average sand content of 0.52 wt.%.

Both sortable silt values are highly variable, with ranges of mean sortable silt from 11.7-25.3 µm, and percentage sortable silt from 8.3-57.2%. Peak values occur at 616 (25.3 µm, 57.2 %), 541 (22.3 µm, 45.3%) and 451 (22.6 µm, 34.6%) cmbsf.

Clay mineralogy exhibits a relatively high degree of variability, particularly in smectite and kaolinite contents. Particularly notable increases in smectite and decreases in kaolinite occur at 661, 556, 421, 361, 271, 241 cmbsf. The largest change in smectite occurs between 301 cmbsf (14.5% smectite, 44.4% illite, 14.6% chlorite, 26.5% kaolinite) and 271 cmbsf (46.1% smectite, 27.9% illite, 16.4% chlorite, 9.6% kaolinite). Similar to the underlying unit, this unit contains moderately high amounts of TOC (≤ 0.32%), low to moderate contents of biogenic silica (1.4-4.5 wt.%) and moderate amounts of $CaCO_3$ (≤ 1.9%).

138 - 108 cmbsf

Light olive brown mud (138-130 cmbsf), olive brown diatomaceous mud (130-120 cmbsf) and diatom- and foraminifera-bearing mud (120-108 cmbsf), all strongly mottled. Physical property values are low, reaching a minima of WBD 1.39 g/cm^3 (at 124 cmbsf) and MS 27.8 10^{-5} SI (at 115 cmbsf). The very top of the unit (c.117 - 109 cmbsf) is marked by a minima of a* and b* in VIS-reflectance, and concurrent maximum in L*. IRD is present in moderate concentrations throughout the unit (≤5 grains/10 cm^3, particularly concentrated 122-111 cmbsf. This unit contains the highest sand contents of the core in each of the discrete samples, particularly 118, 111 and 108 cmbsf which contain a maximum of 19.58 wt.% sand and 6.65 wt.% gravel. Sortable silt values are high throughout the unit (mean sortable silt ranges from 18.6-25.4 µm), particularly percentage sortable silt which always exceeds 31.1% and reaches a maximum of 51.2% at 133 cmbsf.

Clay mineralogy is notable for the lowest kaolinite concentrations of the whole core, with concurrent increases largely in smectite, e.g. at 123 cmbsf, 28.7% smectite, 40.0% illite, 24.2% chlorite, 7.1% kaolinite.

Biogenic silica contents are relatively high and consistent, measuring 5.4-5.9 wt.% in the four discrete samples. $CaCO_3$ is exceptionally high for the core, increasing up the unit and peaking at 24.1% at 112 cmbsf. TOC remains low (≤0.15 %).

XRF scanning shows the principal element ratios are all relatively high: Ba/Ti (max. 0.35 at 125 cmbsf), Fe/Ti (max. 20.26 at 114 cmbsf), Ca/Ti (max. 13.21 at 114 cmbsf), Mn/Ti (max. 0.23 at 123 cmbsf (no data for 119-108 cmbsf)).

108 - 0 cmbsf

Olive brown, laminated (106-103 and 100-12 cmbsf) mud. The upper 12 cm has been disturbed by inflow. Thin coarse grained (mostly fine sand) layers are present at 103-100, 91, 75, 40, 37 and 30 cmbsf.

The physical property values are moderately high and consistent, with average values of WBD 1.64 g/cm^3 and MS 66.1 10^{-5} SI. IRD is present in small amounts (typically 1-3 grains/10 cm^3) in discrete layers, particularly at 108-107, 100-97, 40-37 and 30-27 cmbsf. No gravel is present in the discrete samples and only traces of sand (≤0.65 wt.%). Mean and percentage sortable silt are variable, with high values low in the unit (e.g. at 93 cmbsf, 23.4 µm, 36.2%), a minima at 53 cmbsf (13.7 µm, 19.0%), and peaking again at 13 cmbsf (22.6 µm, 49.7%).

Clay mineralogy is dominated by illite and kaolinite, with approximately equal proportions of smectite and chlorite (e.g. at 53 cmbsf, 14.6% smectite, 44.8% illite, 14.0% chlorite, 26.6% kaolinite).

Biogenic silica contents are relatively low to moderate, peaking at 4.05 wt.% at 12 cmbsf but otherwise ranging from 1.2-3.5 wt.%. $CaCO_3$ contents are low following the 6.5% recorded at 107 cmbsf, with an average value of 0.6%, and TOC values do not exceed 0.21%. Ba/Ti (0.10-0.16), Fe/Ti (9.35-13.05) and Ca/Ti (0.70-2.22) are all relatively low. Mn/Ti data are only available for 44 – 35 cmbsf, which were of low values (0.01-0.03).

Lithofacies attribution

Base (cmbsf)	Top (cmbsf)	Lithofacies Description	Lithofacies Number
108	0	Laminated or stratified terrigenous mud	1b
126	108	Calcareous foraminifera-bearing mud	3
159	126	Homogenous terrigenous mud	1a
1194	159	Laminated or stratified terrigenous mud	1b
1205	1194	Mud with diatoms	2b
1211	1205	Laminated or stratified terrigenous mud	1b
1219	1211	Mud with diatoms	2b
1220	1219	Homogenous terrigenous mud	1a
1253	1220	Disturbed	-

Table 6.6: Depths and descriptions of lithofacies in core PS58/255-2.

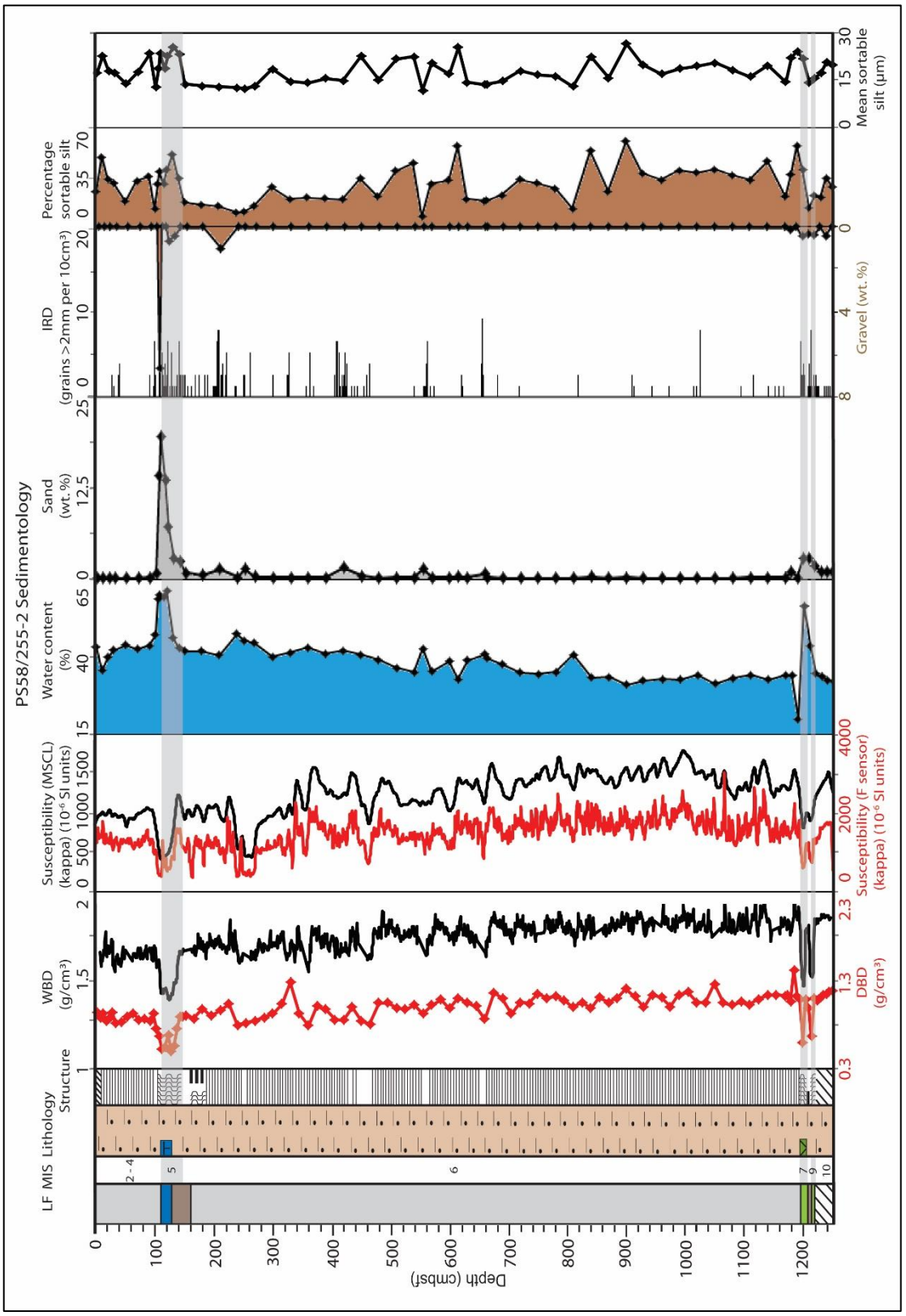

Figure 6.11: Lithology and structures, physical properties and grain size distribution in core PS58/255-2.

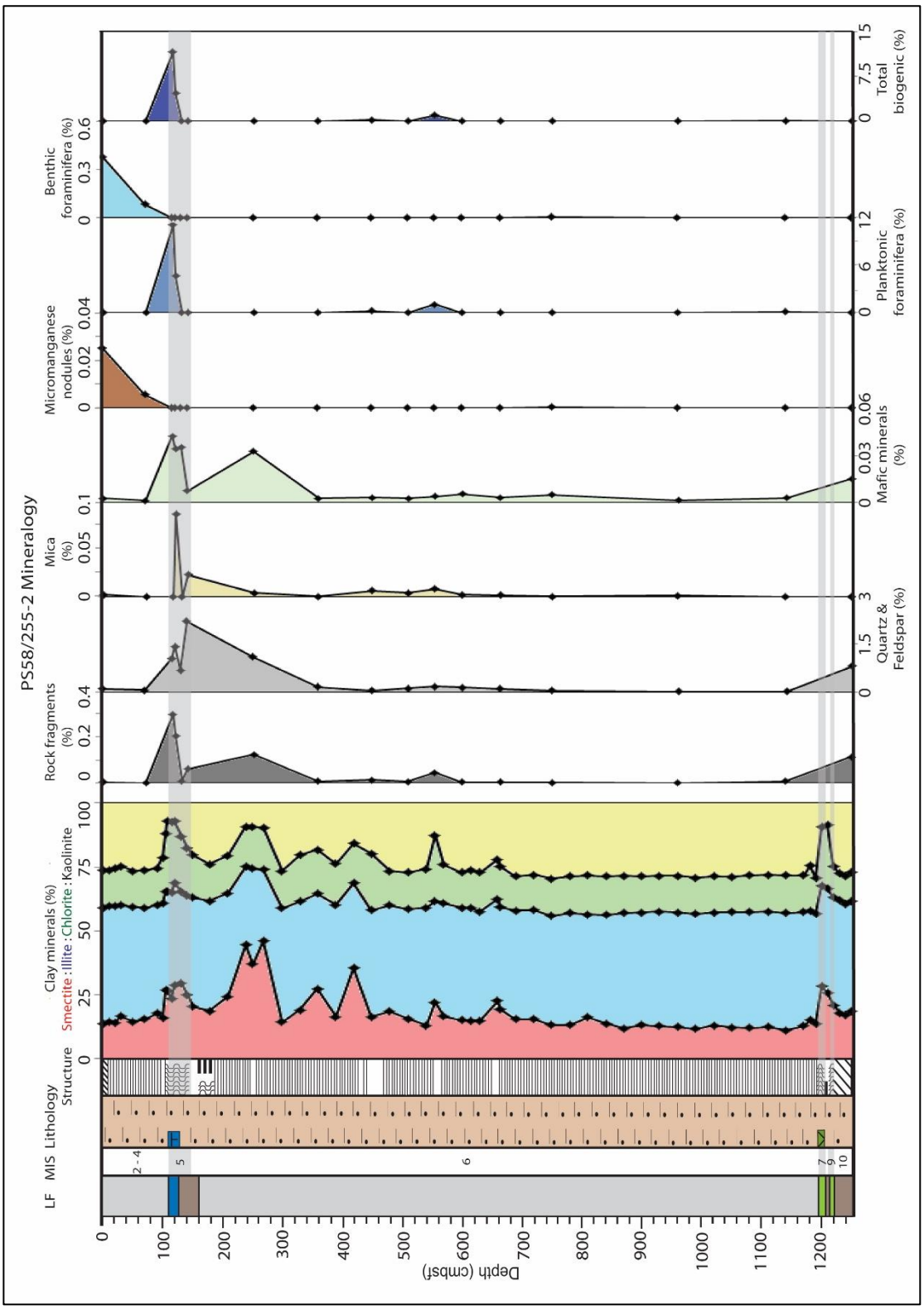

Figure 6.12: Clay mineralogy and composition of the sand fraction in core PS58/255-2.

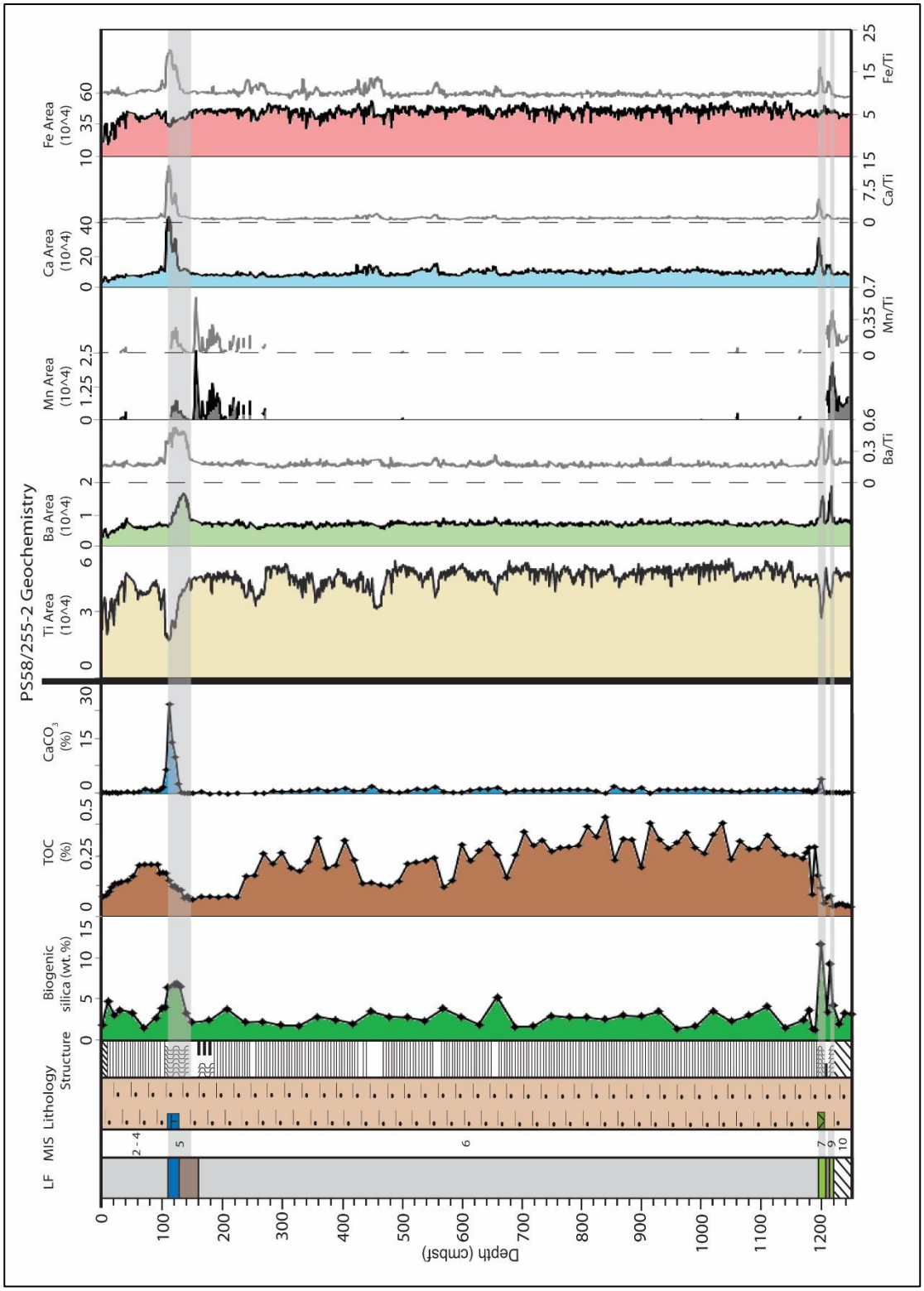

Figure 6.13: Biogenic silica, TOC and $CaCO_3$ contents and XRF elemental composition of core PS58/255-2.

6.3. Chronology of the sediment cores

6.3.1. Direct age constraints

6.3.1.1. AMS ^{14}C Radiocarbon dates

A ^{14}C date was obtained from planktonic foraminifera of the species *Neogloboquadrina pachyderma* sinistral of PC494 474 cmbsf. The sample contained no residual ^{14}C, indicating it dates to >40 ka.

A ^{14}C date obtained from the acid-insoluble organic matter of a bulk sediment sample from the surface of BC497 suggested the surface sediments contain significant amounts of reworked fossil organic carbon, resulting in an age of 6105-5626 BP, much older than the marine reservoir effect for the Southern Ocean of 1300±100 years (Berkman and Forman, 1996). In addition, bioturbation could have contributed to the old age of the surface sediment sample.

The two AIO ^{14}C dates from lithofacies 2A sediments in PC496 record Holocene ages and an age reversal. Age reversals of AIO dates are common features of Southern Ocean sediments, frequently caused by the varying contamination of young organic matter with reworked fossil organic carbon (e.g. Pugh et al., 2009). The recording of a younger age at 873 cmbsf compared to 190 cmbsf, separated by partly-laminated lithofacies 1A, 4 and 5 sediments indicates that coring disturbance or sediment reworking by a slump, slide or debris flow can be ruled out as cause of the reversal. Regardless of the age reversal, the MIS 2 AIO ages are not consistent with other chronological constraints for this core and are therefore discarded.

Core	Depth (cmbsf)	Lab ID	Sample type	Modern Carbon (%)	Conventional Age (years BP)	ΔR	ΔR uncertainty	Two sigma calibration from Marine13 (cal. years BP)
BC497	0.5	373595	AIO	45.5 ± 0.2	6330 ± 40	900	100	6105-5626
PC496	190	370535	AIO	9.5 ± 0.1	18870 ± 90	900	100	21696-20885
PC496	873	373596	AIO	15.6 ± 0.1	14950 ± 60	900	100	16929-16172
PC494	474	382342	*N. pachyderma*	<0.4	>43500	-	-	-

Table 6.7: ^{14}C ages obtained from acid insoluble organic matter from PC496 and BC497 and from the calcareous foraminifera *N. pachyderma* in PC494. Conventional ages have been calibrated using CALIB 7.1 (Stuiver et al., 2017) using the Marine13 calibration curve (Reimer et al., 2013). Delta R has been calculated by subtracting the radiocarbon reservoir correction for the Southern Ocean of 1300 ± 100 years (Berkman and Forman, 1996) from the already-incorporated global reservoir correction of 400 years.

6.3.1.2. Diatom Biostratigraphy

PS58/253-1

Diatoms indicative of particular time periods were identified in five samples from PS58/253-1 (data supplied by Dr. Oliver Esper) (biostratigraphic information as given in Zielinski and Gersonde, 2002 and Zielinski et al., 2002).

371 and 392 cmbsf: Abundant (30-60% of assemblage) *Fragilariopsis kerguelensis* and *Thalassiosira lentiginosa*, less abundant (15-30%) *Thalassiothrix antarctica* and few (3-15%) *Fragilariopsis separanda* and *Chaetoceros* resting spores. This diatom assemblage is typical of the Late Quaternary (e.g. Zielinski and Gersonde, 2002; Konfirst et al, 2012).

1248 and 1252 cmbsf: Assemblage as found in 371 and 392 cmbsf, with traces (0.5%) of *Hemidiscus karstenii* (first abundant occurrence datum (FAOD) 420 ka, MIS 11, last occurrence datum (LOD) 180 ka, MIS 6).

1306 cmbsf: Assemblage as found in 371 and 392 cmbsf, with the addition of traces of *Rouxia constricta* (first occurrence datum (FOD) 1.6 Ma, LOD 280 ka, MIS 8) and traces of *Actinocyclus ingens* (FOD 2.3 Ma, LOD 380 ka, MIS 11).

The presence of traces of *H. karstenii* at 1248 and 1252 cmbsf suggests these sediments pre-date the start of MIS 6 and may be attributed to MIS 7. It is possible that these diatoms were reworked, however, this is deemed unlikely due to the presence of traces in two distinct samples and also in a similar stratigraphic position in neighbouring core PC496. Traces of *R. constricta* at 1306 cmbsf suggest these sediments pre-date the start of MIS 8 and may be attributed to MIS 9. The traces of *A. ingens*, which would imply these sediments date to MIS 11 or earlier, have not been used as a chronological constraint as there is no indication from the sediment core analyses of an interglacial-style signal (e.g. low WBD, high Ba/Ti, high biogenic silica) between 1298 and 1268 cmbsf, which would have suggested the sediments attributed to MIS 8 actually represent MIS 8, 9 and 10. The 2 mm to 10 mm resolution of the XRF data suggests significant changes in composition are unlikely to have been missed by the sampling resolution. However, one cannot rule out the possibility of MIS 9 sediments being absent due to a hiatus, or that sediments deposited during MIS 9 show characteristics which are here deemed more typical of sediments deposited during glacial periods.

PC496

Diatom assemblages of two samples from PC496, 4.5 cmbsf and 882 cmbsf, were also analysed. Both samples are dominated by the pelagic, open-ocean species *Fragilariopsis kerguelensis* (Crosta et al., 2005), which comprise 65% of the surface sample and 71% of a sample from 882 cmbsf (when counted with *Fragilariopsis* colonies in girdle view, deemed likely to be *Fragilariopsis kerguelensis*). The sample from 4.5 cmbsf contains abundant *Thalassiosira* group, which are also typical of an open ocean (Crosta et al., 2005).

Diatoms in both samples were well preserved, with relatively high percentages of girdle bands suggesting both higher productivity and/or better preservation of diatoms at 882 cmbsf compared to surface sediments. Warnock et al. (2015) noted silica preservation

in PS58/254-1 was higher during interglacial periods when compared to glacials. This supports the notion that sediments of 882 cmbsf were deposited in an interglacial period with open ocean conditions, productivity at least as high as the present day and/or more preferable conditions for silica preservation. This is further supported by the abundance of diatoms in each sample, with the 882 cmbsf sample containing 65 mature valves per gram compared to 27 mature valves per gram at 4.5 cmbsf.

The presence of 3 well-preserved frustules of *H. karstenii* among 320 diatom frustules counted at 882 cmbsf does, as in PS58/253-1, suggest these sediments pre-date the start of MIS 6.

6.3.1.3. Tephrochronology

Maxima in volcanic glass content were detected in the sand fraction samples of three of the four studied cores (PC496: 223 cmbsf: (0.1% of the bulk sediment, 3.1% of the sand fraction) and 243 cmbsf (1.4% of the bulk sediment, 31.6% of the sand fraction); PS58/253-1: 415 cmbsf (2.2% of the bulk sediment, 75.6% of the sand fraction); PS58/255-2: 118 cmbsf (0.6% of the bulk sediment; 4.1% of the sand fraction), 123 cmbsf (0.6% of the bulk sediment, 8.5% of the sand fraction) and 133 cmbsf (2.0% of the bulk sediment and 72.0% of the sand fraction). In each core, volcanic glass was present in amounts greater than 0.06% of the bulk sediment only in a particular stratigraphic position, i.e. at the base of a diatom or calcareous foraminifera-rich unit with low WBD (lithofacies 1A, 2A and 3). Cross-core correlations suggest this low represents MIS 5, identified using the >40 ka ^{14}C date from PC494 474 cmbsf and Relative Palaeomagnetic Intensity analysis of PC494. This supports the notion that the layer of volcanic glass likely represents the eruptions at the time of the MIS 5/6 boundary identified by Hillenbrand et al. (2008b).

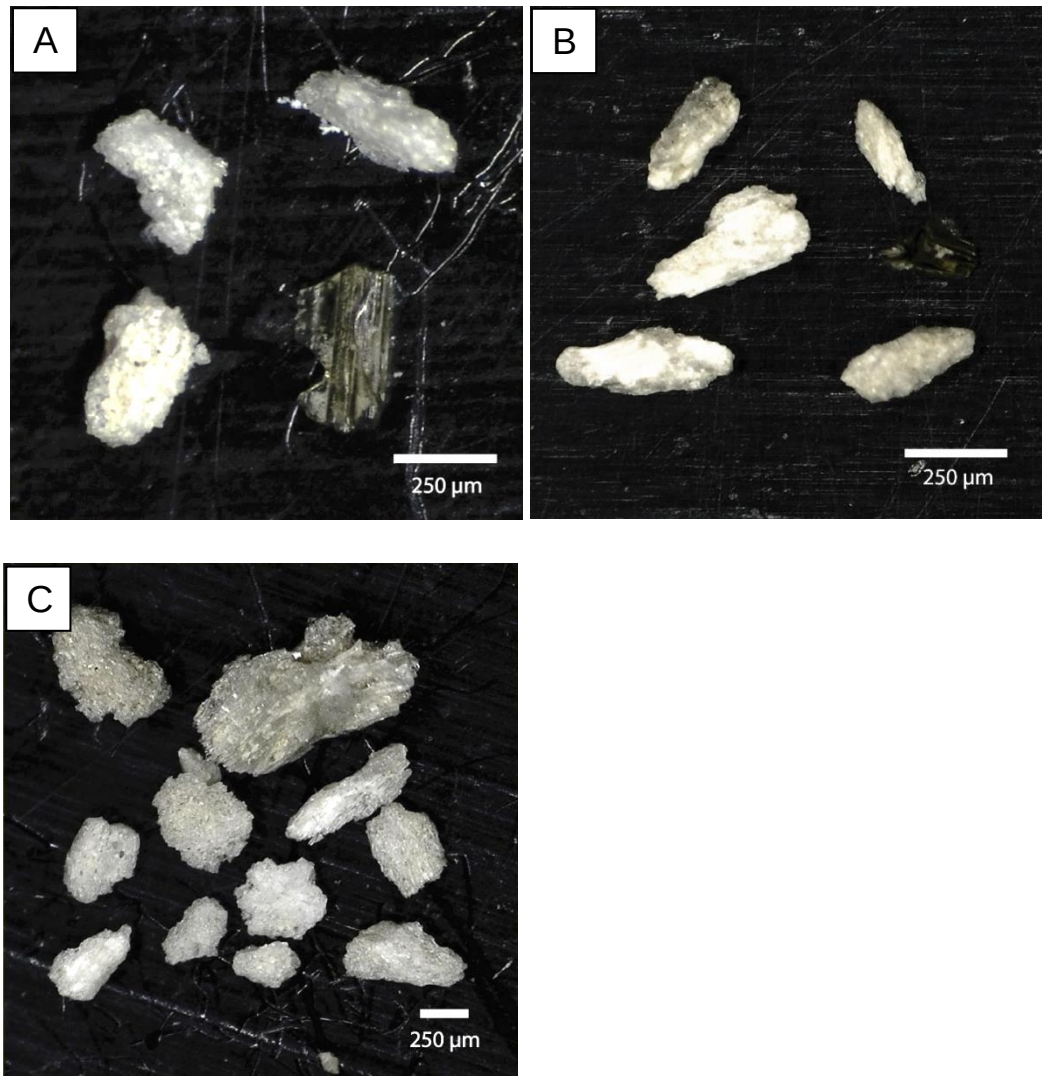

Figure 6.14: Examples of volcanic glass found in the sand fraction of (A) PC496 243 cmbsf, (B) PS58/253-1 415 cmbsf, (C) PS58/255-2 133 cmbsf.

The volcanic glass shards are alike in their whitish colour, typical size of 250-500 µm and glassy, jagged appearance. Only one shard was found which was atypical from this description (the lower right hand shard shown in Figure 6.14A from PC496, 243 cmbsf), which was pale green and sheet-like but of a similar size to the other shards. The absence of other shards matching these characteristics suggests the source volcano may be distant or may have had only a small eruption compared to that which produced the more numerous shards.

The white glass shards, based on their stratigraphic position, lack of glass elsewhere in the cores, similarity in appearance under a microscope (Figure 6.14) and the very similar amount of glass (c.2 % of the bulk sediment) in each core suggest they likely came from the same eruption or series of eruptions, perhaps that at 136 ka, corresponding to

tephra layer B identified previously in core PS2551 from the Amundsen Sea by Hillenbrand et al. (2008b).

The absence of volcanic glass in the sand fraction samples of PC494 is probably a function of the 20 cm sample spacing and the relatively high sedimentation rate (6.8 cm/kyr) at the end of MIS 6 causing high rates of dilution and burial by terrigenous material. Sea-ice coverage at this more southerly site may also have been present for more months of the year, or persisted for longer during the glacial-interglacial transition, than the more northerly sites, which may have prevented or delayed deposition of the glass at PC494. There is no evidence from the RPI analysis of PC494 of a significant hiatus.

6.3.1.4. Relative Palaeomagnetic Intensity (RPI)

NRM, ARM acquisition and ARM demagnetisation intensities were measured under alternating magnetic field strengths of 10, 20, 30, 40, 50, 65, 80 and 100 mT (Figure 6.15). Two RPI proxies were calculated and analysed in order to establish a chronology: the angle of the best-fit lines between NRM and ARM acquisition, and between NRM and ARM demagnetisation, where both ARM values are taken as the mean values measured at 20-50 mT (Figure 6.16). R values >0.98 indicate that the NRM and ARM are strongly correlated and that both RPI proxies are of good quality and suitable for comparison to other records.

The dating constraints listed previously were used in conjunction with cross-core correlations to establish tie points, and RPI used to establish a high resolution chronology between the tie points (Table 6.8). The RPI proxies were compared to the global records of SINT-800 (Guyodo and Valet, 1999) and PISO-1500 (Channel et al., 2009) (Figure 6.17) and to the 75 ka Antarctic Peninsula drift record (Vautravers et al., 2013).

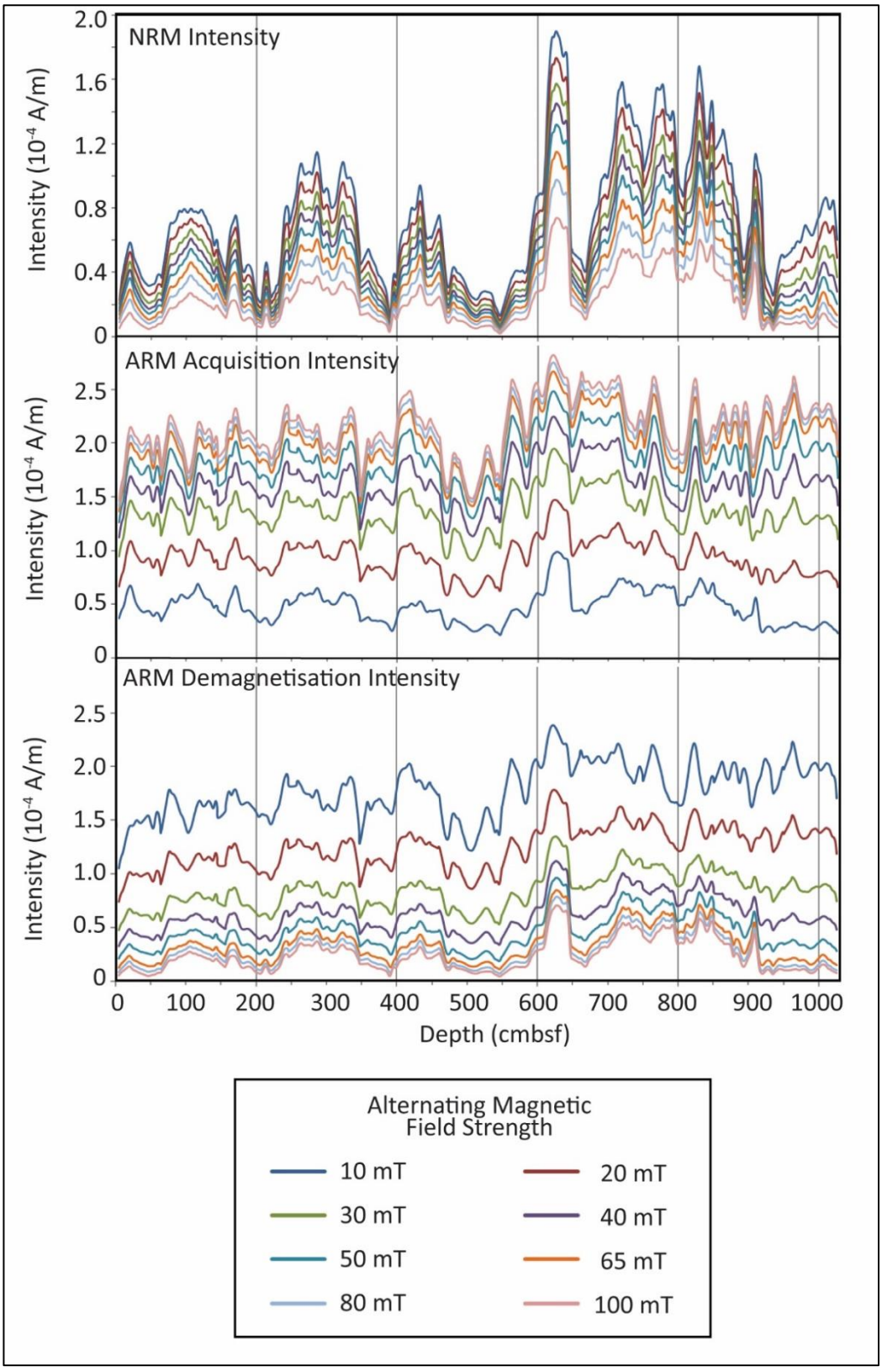

Figure 6.15: NRM, ARM acquisition and ARM demagnetisation intensity at each of the eight alternating magnetic field strengths applied (10-100 mT).

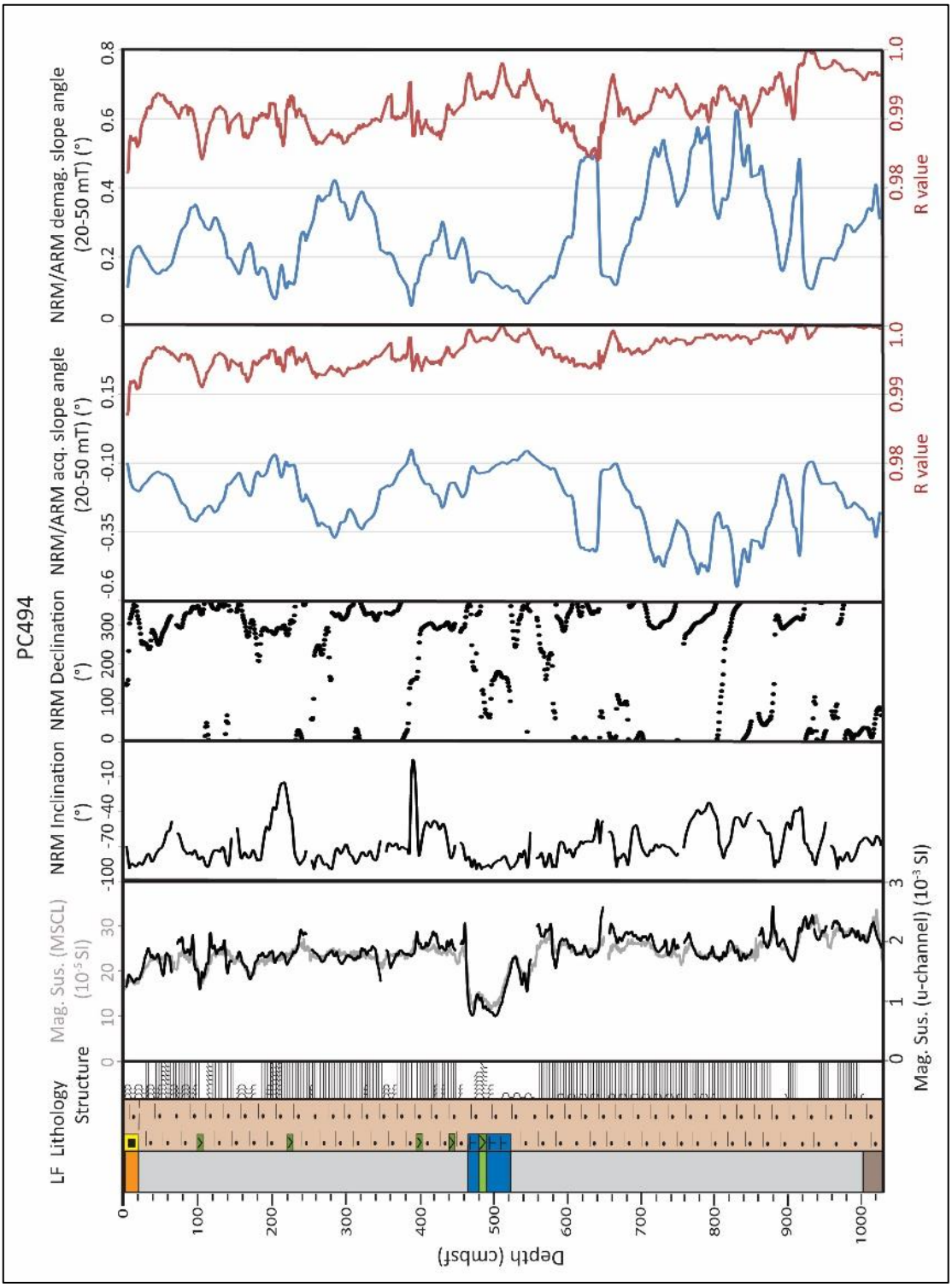

Figure 6.16: Palaeomagnetic data obtained from a u-channel of sediment core PC494.

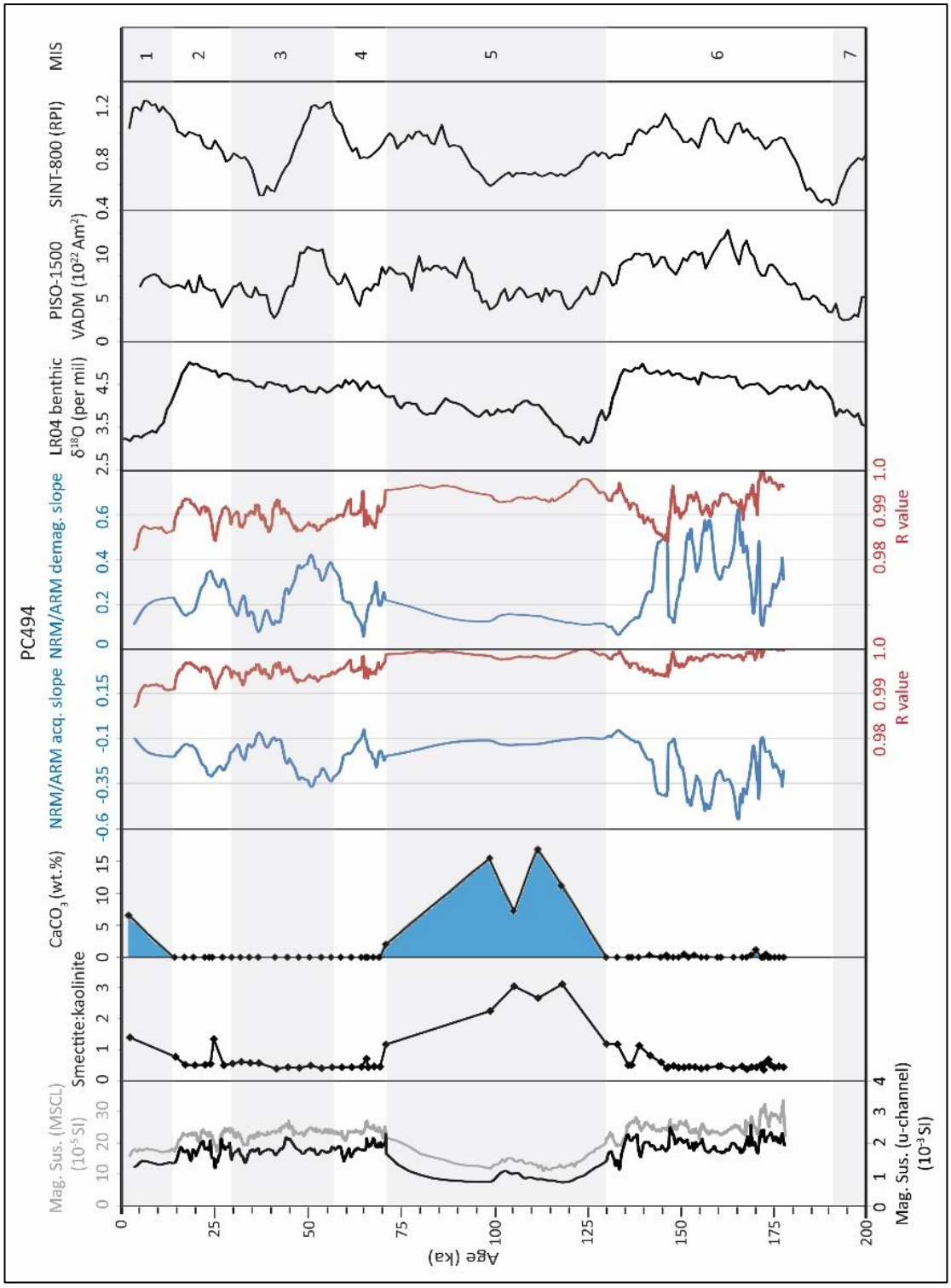

Figure 6.17: Comparison of PC494 RPI with PISO-1500 (Channel et al., 2009) and SINT-800 (Guyodo and Valet, 1990), the LR04 δ^{18}O benthic stack (Lisiecki and Raymo, 2005) and indicators of sediment composition and provenance. All data are plotted against the age model derived from correlation of PC494 RPI with SINT-800.

Both of the RPI proxies showed particularly good correlation to the independently dated SINT-800 RPI reference record (Guyodo and Valet, 1999), which was then used to identify tie points between the two records within individual glacial and interglacial periods (Figure 6.18, Table 6.8). A peak in inclination dated to 40.1 ka (following a tie-point between PC494 and SINT-800 at 41 ka) may represent the Laschamp event, a geomagnetic excursion (Singer et al., 2009).

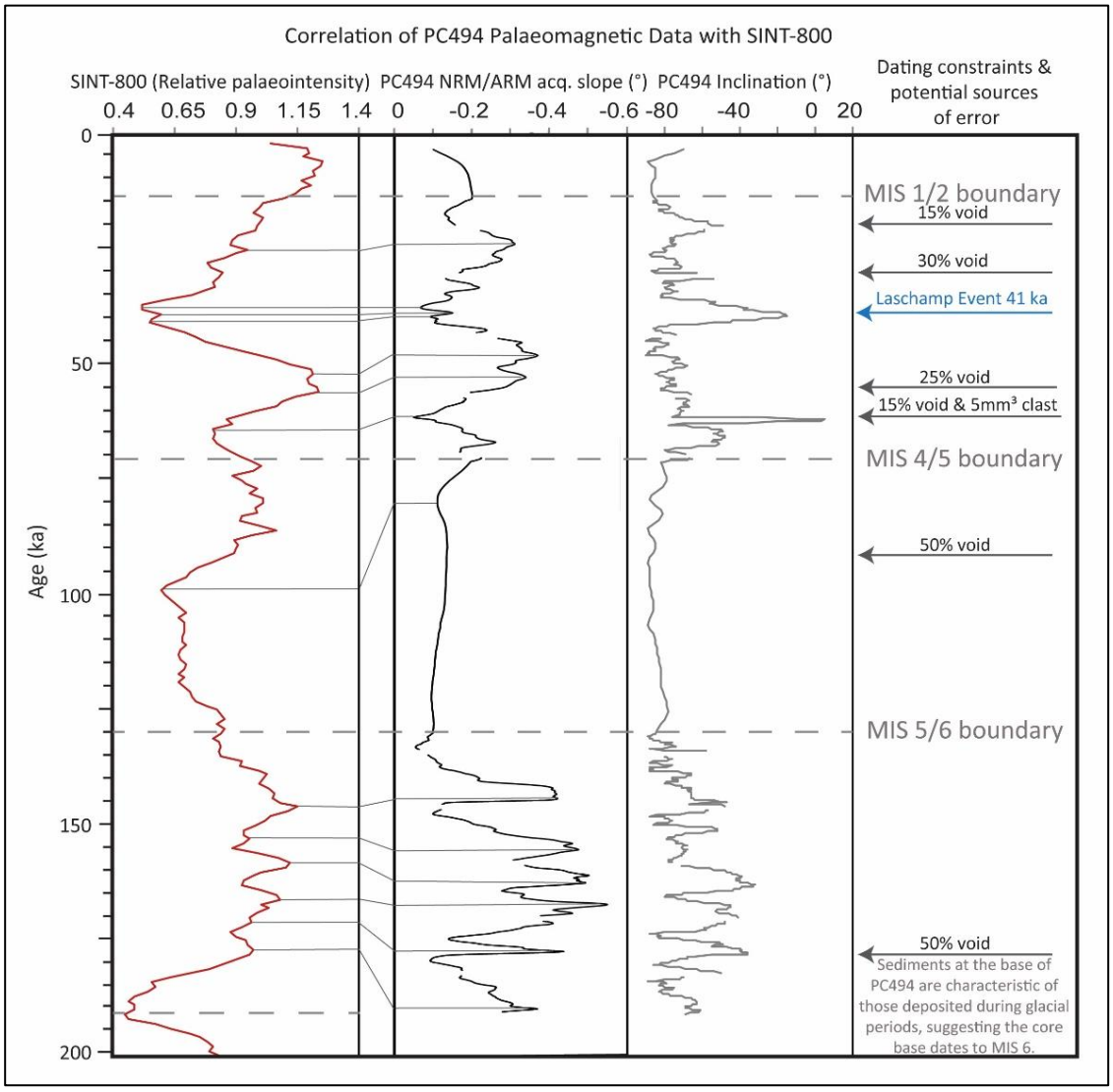

Figure 6.18: Correlation of the PC494 RPI data with the SINT-800 record of Guyodo and Valet (1999), the inclination record, dating constraints and identification of potential sources of error. Dashed grey lines indicate the MIS boundaries which were determined through lithostratigraphy and correlation to other cores. Whole grey lines indicate tie points between SINT-800 and the PC494 RPI record. The inclination record is presented and Laschamp Event indicated. Large voids and clasts in the u-channel are noted as potential sources of error in the RPI data.

PC494 Depth (cmbsf)	Age (from correlation of RPI proxy to SINT-800 RPI) (ka)	Age (from core correlations and lithostratigraphy) (ka)	Sedimentation rate (cm/kyr)
0		0	1.50
21		14	7.64
105	25		8.42
206	37		4.00
214	39		3.50
221	41		6.50
286	51		7.00
321	56		7.56
389	65		12.67
465		71	0.32
474	99		1.55
522		130	6.81
631	146		14.14
730	153		12.40
792	158		5.00
832	166		15.40
909	171		1.50
1008	177		>1.64
1031		<191	-

Table 6.8: Tie-points used to develop the age model of PC494 from relative palaeomagnetic intensity and changes in sedimentology, geochemistry and mineralogy suggestive of glacial-interglacial cycles correlated with PC496, PS58/253-1 and PS58/255-2. Tie points are based on: 1. Correlating the PC494 RPI proxy of NRM/ARM acquisition slope angle (20-50 mT) to the SINT-800 RPI record. 2. Cross-core correlations and sedimentological, geochemical and mineralogical evidence for glacial-interglacial transitions, particularly through increases in $CaCO_3$ and an increase in the smectite-kaolinite ratio suggestive of changes in the provenance of terrigenous material.

One particular aim of the RPI analysis was to determine whether "interglacial sediments" represented all of the material deposited during an interglacial, or only that deposited during the peak interglacial. This was particularly the case for demarcating MIS 5 (which lasted 59 kyr) rather than MIS 5e (which lasted c.10 kyr). However, the low sedimentation rates during MIS 5 prevented development of a high-resolution chronology during this period, with only one tie point identified between PC494 RPI and SINT-800.

The RPI correlation revealed highly variable sedimentation rates within MIS 6, with a linear sedimentation rate of 1.5 cm/kyr from 177-171 ka followed by 15.4 cm/kyr from 171-166 ka (Table 6.8, Figure 6.19).

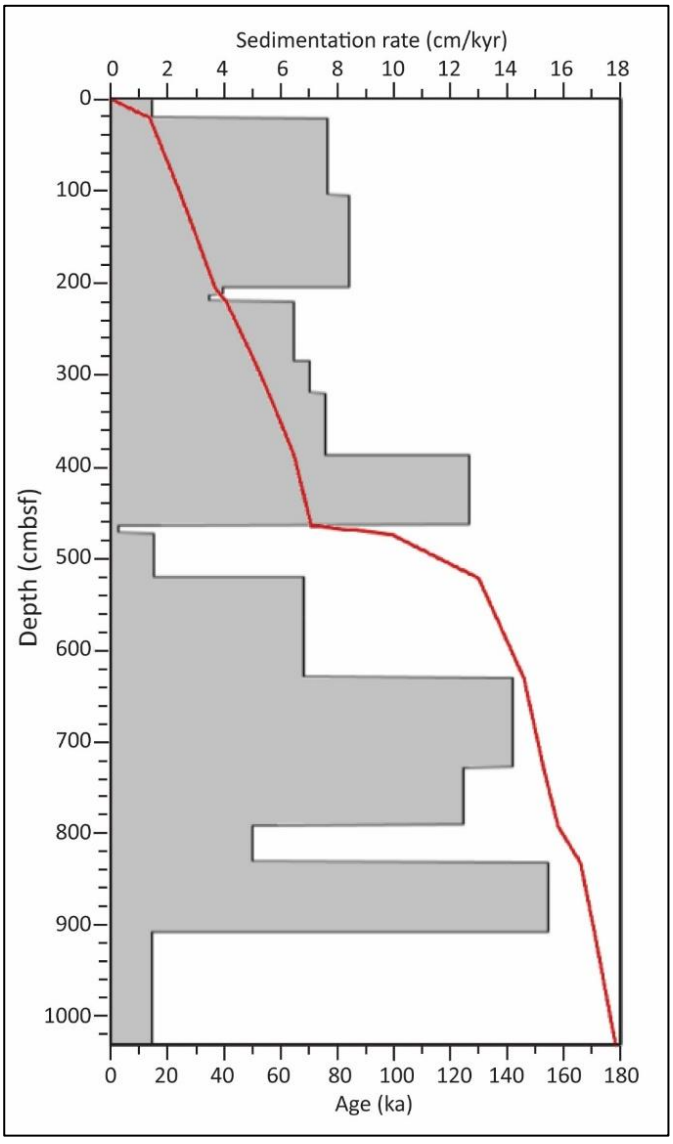

Figure 6.19: Age vs depth plot (red line) and sedimentation rates (grey boxes) for PC494 following development of an age model using RPI.

The surface sediments of PC494 were difficult to correlate with any other RPI record and no tie points could be identified from the RPI correlation for sediments dating to <25 ka. Similar discrepancies are present between the RPI record from Peninsula Drift 4 (Vautravers et al., 2013) and PISO-1500 and SINT-800 (Figure 6.21), with Vautravers et al. (2013) able to correlate minima at 25, 40 and 64 ka but unable to identify stratigraphic tie points from the RPI for sediments <25 ka.

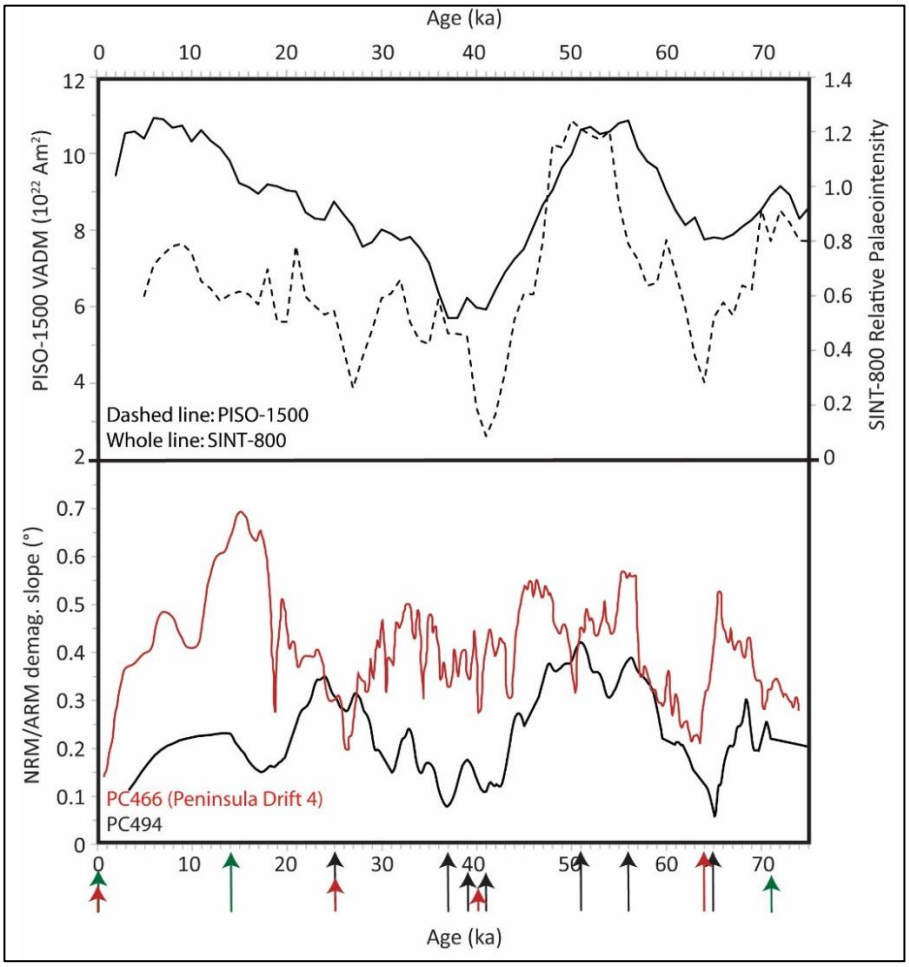

Figure 6.20: PC494 RPI (NRM/ARM demagnetisation slope angle) (black line, lower plot) compared to the Peninsula Drift 4 RPI record (NRM/ARM demagnetisation slope angle) (Vautravers et al., 2013) (red line, lower plot), PISO-1500 (Channel et al., 2009) (black dashed line, top plot) and SINT-800 (Guyodo and Valet, 1999) (black whole line, top plot). Black arrows indicate tie points between the RPI of PC494 and the SINT-800 record. Green arrows indicate tie points of glacial-interglacial boundaries identified from the sediment analyses of PC494 and cross-core correlations. Red arrows indicate tie points between the Peninsula Drift 4 RPI record and the PISO-1500 record (from Vautravers et al., 2013).

6.3.2. Lithostratigraphy and attribution of MIS

Lithological successions have been routinely used in sediment cores from the Peninsula drifts to suggest whether sediments were deposited under glacial or interglacial conditions and to develop and support age models (e.g. Pudsey 2000; Lucchi et al., 2002; Vautravers et al., 2013). In the Amundsen Sea, biogenic silica content in core PS58/254-1 is positively correlated with Ba/Al, suggesting biogenic silica is a suitable proxy for productivity which is known to vary in this area depending on climatic state (Hillenbrand et al., 2009a). Biogenic silica content was found to fluctuate with, and was then correlated to, the global $\delta^{18}O$ stack (Lisiecki and Raymo, 2005), following development of an age model based on palaeomagnetism and lithostratigraphy (Hillenbrand et al., 2009a). Biogenic silica was also positively correlated with the sediment water content and negatively correlated with magnetic susceptibility, WBD and DBD (Hillenbrand et al., 2009a). Correlation of the $CaCO_3$ record is not possible due to PS58/254-1 lying below the CCD for much of the Late Quaternary (Hillenbrand et al., 2009a). Interglacial periods were also characterised by increased smectite contents and decreased kaolinite contents (Hillenbrand et al., 2009a).

Following the model of cores from the Peninsula drifts and core PS58/254-1, glacial-interglacial periods in the cores were demarcated based on significant changes in physical properties (particularly WBD), clay mineralogy and particularly biogenic content (biogenic silica, Ba/Ti and $CaCO_3$). Cross-core correlations allowed for dating constraints to be extrapolated and applied to the other cores (Figure 6.22). Cores were correlated primarily based on the dating constraints in conjunction with lithofacies and the WBD record, which was available for every centimetre of core and found to fluctuate closely in sync with water content and biogenic silica. IRD and XRF data were also particularly helpful for core correlations due to their 10 mm and 2-10 mm resolution, respectively.

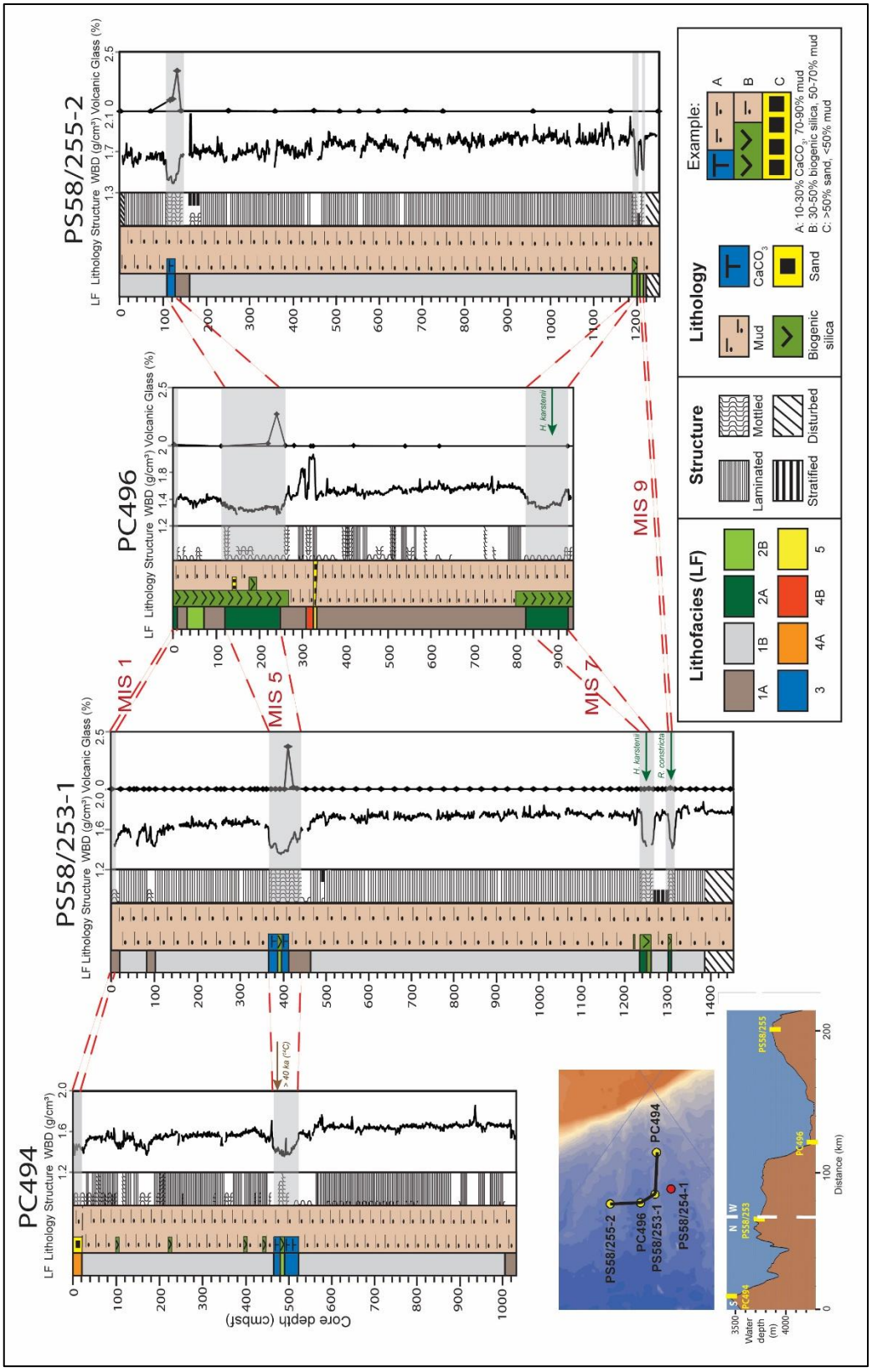

Figure 6.21: Lithofacies, lithology, structure, WBD and volcanic glass (% of the bulk sediment) with cross-core correlations. Volcanic glass is not shown for PC494 as none was identified in the sand fraction. Interglacial periods are highlighted as grey bars.

With the exception of the RPI-based chronology of PC494, MIS 3 has not been separated from MIS 2-4 due to the difficulties of accurately identifying the sediments deposited during this short lived (28 kyr) interglacial with relatively low amplitude changes in temperature compared to MIS 2 and 4. The following paragraphs focus on possibly contentious issues faced when assigning MIS to the cores, particularly with regard to surface sediments.

PC494

The core top of PC494 appears relatively intact. There is an increase in $CaCO_3$ content at the surface from 0 % at 23 cmbsf to 6.3 % at 3 cmbsf, due mostly to the presence of planktonic foraminifera (6.9 % of the bulk sediment) but also the appearance of benthic foraminifera (0.5 % of the bulk sediment). Unlike in PS58/254-1, which saw a 14 wt.% increase in biogenic silica content from late MIS 2-4 to the core top, there is no increase in biogenic silica at the core top. However, biogenic silica contents are of relatively moderate values (4.7-11.7 wt.%) throughout the core and show none of the glacial-interglacial variability seen in the other cores. PC494, the most ice-proximal core site, featured the highest MIS 2-4 sedimentation rate of the four cores and a MIS 6 sedimentation rate of >8.3 cm/kyr. The high flux of terrigenous material to the core site would bury diatoms, minimising dissolution and therefore potentially preserve more biogenic silica in the sediments of PC494 than the other core sites (Warnock et al., 2015). This shows the need to consider various aspects of the sediment properties when developing a lithostratigraphy. Other indicators of interglacial conditions from core PS58/254-1 are present, such as an increased concentration of IRD, decreases in physical properties from 21 cmbsf to the core top and an increase in the smectite:kaolinite content.

PC496

PC496 was difficult to correlate with the other cores as the physical properties did not exhibit the same degree of glacial-interglacial variation as in PC494, PS58/253-1 and PS58/255-2. This was further complicated by the presence of a sand and sandy mud

layer and an age reversal in the ^{14}C dating. The identification of MIS relied more heavily on the biogenic silica content and clay mineral assemblage than in the other cores. An increase in biogenic silica and an increased smectite:kaolinite ratio, together with a decrease in WBD, suggest the core top and modern-day sedimentation may be preserved.

MIS 3 has not been separated from MIS 2-4, but a low in physical properties (WBD < 1.40 g/cm^3), low kaolinite (11%), high chlorite (31-34%) and relatively high biogenic silica (13-15 wt.%) suggest the sediments between 77 and 34 cmbsf may have been deposited during MIS 3. If this is the case, it would mean sedimentation rates in MIS 2 of 1.7 cm/kyr, MIS 3 of 1.5 cm/kyr, and MIS 4 of 2.5 cm/kyr, compared to a MIS 2-4 average of 2.0 cm/kyr.

A 14 cm layer of sediment at the base of PC496 has been attributed to MIS 8. This is based on WBD and magnetic susceptibility being high (WBD > 1.45 g/cm^3) and increasing down-core to the core base (although it is noted an edge effect may be influencing the lowermost core sediments) and the analysis of a sample at 923 cmbsf which recorded relatively low biogenic silica (14.5 wt.%) and low smectite:kaolinite ratio (0.71), found to be more typical of a glacial period in PS58/254-1 (Hillenbrand et al., 2009a).

PS58/253-1

Modern-day sediments appear to be missing from the core top of PS58/253-1, as there is no significant increase in biogenic material or IRD at the core top. This is probably related to disturbance and/or over-penetration during coring. However, the MIS 1/2 contact has been identified based on reductions in WBD and magnetic susceptibility and a small increase in biogenic silica.

PS58/255-2

Sediments dating to the Holocene appear to be absent from PS58/255-2. Lithofacies 1B is present from the beginning of MIS 2-4 sediments to the core top. Physical properties, biogenic content and clay mineralogy all exhibit values typical of sediments deposited

during glacial periods, with none of the changes seen in the other cores and in PS58/254-1 at the core top which differentiate the Holocene from MIS 2-4 sediments. The Holocene sediments are likely to have been lost through coring disturbance; the uppermost 12 cm of the core was described as disturbed on the core log.

Table 6.9 shows the depths in each core of the MIS, and Table 6.10 shows the associated sedimentation rate per MIS. An age-depth plot is given in Chapter 7.1.2 (Figure 7.4).

MIS boundary	Age (ka)	PC494 (depth, cmbsf)	PC496 (depth, cmbsf)	PS58/253-1 (depth, cmbsf)	PS58/255-2 (depth, cmbsf)
Modern	0	0	0	0	
1 / 2-4	14	21	9	14	0
2-4 / 5	71	465	112	366	108
5 / 6	130	522	262	442	147
6 / 7	191		824	1235	1194
7 / 8	243		922	1268	1205
8 / 9	300			1298	1211
9 / 10	337			1317	1219
10 / 11	374				
Core base		1031	936	1452	1253

Table 6.9: Depths in each core (cmbsf) which correspond to the boundaries of Marine Isotope Stages (MIS) (ages as defined by Lisiecki and Raymo, 2005).

MIS	PC494	PC496	PS58/253-1	PS58/255-2
1	≥ 1.50	≥ 0.64	≥ 1.00	
2 – 4	7.79	1.81	6.18	1.89
5	0.97	2.54	1.29	0.66
6	> 8.34	9.21	13.00	17.16
7		1.88	0.63	0.21
8		> 0.25	0.53	0.11
9			0.51	0.22
10			> 3.65	> 0.92

Table 6.10: Sedimentation rates (cm/kyr) for each MIS. Sediments at the core top and core base are given as minimum sedimentation rates due to the lack of evidence for MIS boundaries.

6.4. Interpretation of the analysis of sediment cores from the Amundsen Sea mounds

Lithofacies 1a (LF 1a)

The homogenous, terrigenous, mud-rich sediment of Lithofacies 1a (LF 1a) is interpreted as a contourite deposit consisting primarily of locally sourced, fine-grained sediment that was originally supplied to the nepheloid layer by turbidity currents. Dating constraints and lithostratigraphy (described in Chapter 6.2.2) suggest LF 1a was deposited mainly during glacial periods on the mound flanks (PC496) and at glacial-interglacial and interglacial-glacial transitions on the mound crests.

The relatively high kaolinite contents typically seen in this lithofacies suggest the ASE, and perhaps the Thwaites Glacier system (Ehrmann et al., 2011), is the dominant source of the detritus. The sediment was predominantly supplied during glacial periods when ice advanced to, or close to, the shelf break, delivering large amounts of kaolinite-rich sediment onto the continental slope (cf. Hillenbrand et al., 2002, 2009a). The relatively uniform clay mineral, grain size and sand fraction compositions of this lithofacies suggest the source area did not vary greatly throughout the period of deposition. Most of the lithofacies is homogenous, with only minor bioturbation, high clay content, low mean and percentage sortable silt and low biogenic content, suggesting primary structure is unlikely to have been overprinted post-depositionally by benthic organisms or bottom currents. The low $CaCO_3$ and biogenic silica contents, together with only minor bioturbation, reflect reduced levels of primary productivity from perennial sea ice coverage during glacial periods (cf. LGM and glacial reconstructions of Hillenbrand et al., 2002, 2009a and Benz et al., 2016).

The presence of up to 30 wt.% terrigenous sand and gravel in discrete, poorly sorted layers is indicative of periodic input of ice rafted debris (IRD). The low contents of IRD between these layers suggests either relatively high sedimentation rates, consistent with regular and/or large amounts of sediment supply from turbidity currents, or rare passage of melting icebergs across the mounds. The absence of bioturbation is consistent with high sedimentation rates (Mulder et al., 2008). The lack of bioturbation could also result from low plankton production in response to perennial sea-ice cover.

As this lithofacies occurs primarily close to a channel and is only present on mound crests during periods of climatic transition, this suggests it is linked to the supply of down-slope material. It is thought that both the frequency of turbidity currents and the volume of sediments within them will vary according to factors including meltwater production and sediment loading and so it is feasible that the climatic transitions resulted in variations in the numbers or volumes of turbidity currents.

Turbidites are typically associated with moderate to good sorting and silts are often positively skewed, as opposed to poor to moderate sorting and low positive or negative skew in contourites (Stow and Faugères, 2008). However, the absence of coarse layers and any obvious grading is not uncommon for fine grained turbidites (Stow and Bowen, 1978; Stow et al., 1996). Poorly sorted turbidites lacking laminae have been identified elsewhere in Td sediments of the Bouma Sequence and linked to the cohesion of clay particles within a turbidity current, leading to rapid deposition and the 'trapping' of silt-sized grains (Piper, 1973; Alonso et al., 2016). Alternatively, the lack of sorting and laminae may be due to low sediment concentrations in the nepheloid layer preventing the depositional sorting that can result in laminae in fine-grained turbidites, or may be due to a very low turbidity current velocity (Stow and Faugères, 2008).

The poor sorting and absence of primary structure can also be explained by a bottom current influence on sedimentation. Lithofacies 1a occurs in thick, featureless units, typical of the muddy contourites described by Stow and Faugères (2008). The absence of bioturbation may be linked to perennial sea ice cover during glacial periods with a corresponding low nutrient supply to the sea bed, as proposed for a similar (though laminated) facies deposited during glacial periods off the Antarctic Peninsula by Lucchi and Rebesco, 2007 which is further described for lithofacies 1b. At a distal core site (PS58/253-1), clay content is lower and mean grain size in the mud fraction is larger (32.6% and 3.92 μm) than at a more proximal core site on the same mound (PC494) (40.2% and 2.65 μm). This concurs with the increase in mound asymmetry with distance from the margin suggestive of a larger bottom current influence. Sedimentation rates of this lithofacies are similar on both the mound flank and crest, rather than thinning away from a channel as seen in typical channel-levee structures.

Cores taken from the flanks of the Antarctic Peninsula drifts and interpreted as turbidite facies have contained graded silt to fine sand layers up to 60 mm thick (Pudsey, 2000, Unit D) and silty laminae and lenses, interbedded with laminated mud and containing no IRD (Lucchi et al., 2002; Lucchi and Rebesco, 2007). The thickness and frequency of these layers and laminae decrease with distance from the channel (Lucchi et al., 2002). Such features are not present in LF 1a.

The homogeneity of the sediments, both in terms of the lack of structure and in terms of their consistency in properties within and between cores suggests bottom currents have influenced their deposition. The favoured hypothesis is therefore that this lithofacies is a contourite deposit but that the bulk of its sediment was supplied to the nepheloid layer by turbidity currents.

Lithofacies 1b (LF 1b)

The laminated to stratified, terrigenous, mud-rich sediment of Lithofacies 1b (LF 1b) is interpreted as a contourite deposit, largely composed of material supplied to the nepheloid layer by turbidity currents. This lithofacies has the same characteristics as LF 1a, but also has extensive, horizontal, parallel laminae. It is unclear (due to the thin laminae and amount of sample needed for grain-size analysis) whether the laminae are purely colour banded or represent grain size changes; bulk grain-size analysis shows the sediments are poorly sorted silts and clays.

Laminated, rarely bioturbated, fine grained sediments with occasional IRD layers are common in contourites around the Antarctic margin and have been interpreted as contourites deposited during glacial periods (e.g. Gilbert et al., 1988 in the Weddell Sea, Lucchi and Rebesco, 2007 in the Bellingshausen Sea). West of the Antarctic Peninsula, the attribution of this facies to contourite rather than turbidite processes was based on the presence of IRD, both in layers and sparsely distributed throughout the sediments, suggestive of a slow sedimentation rate, together with low TOC contents (usually <0.2%) and poor sorting (Lucchi et al., 2002; Lucchi and Rebesco, 2007). Similar characteristics are present in LF 1b, with IRD both dispersed throughout the sediments and present in layers, and sediments being poorly sorted. However, the Peninsula drift sediments are

negatively skewed, unlike the symmetrical skewness in LF 1b, whilst the TOC contents are more variable and may reflect different sea ice and palaeoceanographic conditions, typically <0.4% in PS58/253-1 and PS58/255-2 and 0.4-0.8% at PC494. A contourite influence on sedimentation would also help to explain why LF 1b is only found on the crests of the Amundsen Sea mounds and not in the core from the mound flank, with bottom currents having a more dominant influence on sedimentation than turbidity currents on the crests of the mounds ≤800 m above the sea floor channels.

However, in the Antarctic Peninsula drifts, turbidity currents were postulated to provide the bulk of the sediment to the bottom current via the nepheloid layer, explaining the high sedimentation rates in this facies as opposed to the interglacial sediments (Lucchi et al., 2002). The IRD layers can be attributed to periods between turbidity currents when sedimentation rates may have been low. The laminae may be attributed to fluctuations in the supply of mud from turbidity currents (Rebesco et al., 2002) or, less likely, given the uniform grain size and sorting in this lithofacies, to fluctuations in the velocity of the bottom current (Stow and Bowen, 1978). Sediment from turbid plumes is also thought to have contributed due to turbidity currents undergoing a hydraulic jump at the base of the 16° slope off the Peninsula (Lucchi et al., 2002). This is unlikely to be a major influence on sedimentation in the eastern Amundsen Sea where the slope is 2-4°.

The near-absence of bioturbation in the contourite facies has been attributed to oxygen-reduced deep waters and to the low primary productivity (due to persistent sea-ice cover) resulting in low nutrient supply to bottom waters (Lucchi and Rebesco, 2007). Similarly laminated, clay-rich, glacial facies have been identified in other places around the Antarctic margin but are absent where there is evidence for polynyas, supporting this hypothesis and suggesting such sediments were common where sea-ice expansion combined with an oxygen-reduced circumpolar current (Lucchi and Rebesco, 2007). A similar environment may have existed in the Amundsen Sea, evidenced by the low biogenic opal, TOC and $CaCO_3$ contents in this facies and the presence of micro-manganese nodules towards the top of these units suggestive of redox conditions.

The well-defined, continuous nature of the laminations suggests the bottom current was persistent, as fluctuations in flow velocity have been linked to irregular and wispy laminations (Lucchi et al., 2002).

Lithofacies 2a (LF 2a)

The bioturbated, diatom-bearing sediment of Lithofacies 2a (LF 2a) is interpreted as a mixed contourite-hemipelagite, with its fine-grained terrigenous components mainly deposited by bottom currents and its IRD and biogenic components mainly deposited by vertical settling of diatoms in a (seasonally) open ocean setting during interglacial periods. The continuous and intensive bioturbation, rare laminae, poor sorting and high clay content are characteristic of the 'muddy contourite' and contourite facies C1, as defined by Stow and Faugères (2008). However, the large biogenic component (≤40%) also suggests a large pelagic contribution above the ≤20-30% typically expected in a muddy contourite (Stow and Faugères, 2008).

Large smectite (higher than any smectite content known from the ASE shelf, e.g. Ehrmann et al., 2011 (see Chapter 7.2.1)) and low kaolinite contents suggest the dominant source of the terrigenous material in LF 2a was not local and that far-travelled clay was deposited on the mounds by bottom currents. LF 2a and 2b contain more coarse grains than LF 1a and 1b, which is likely due to the low sedimentation rate resulting in less dilution of IRD than during glacial periods. An increase in bottom current strength, resulting in winnowing and the creation of IRD lag layers, is supported by increases in percentage and mean sortable silt in PS58/253-1 from LF 1b to LF 2a and 2b. However, no significant change has been noted in the other cores, suggesting this effect may be more localised and not a major influence on lithofacies development.

The relatively large biogenic content (15-40 wt.% biogenic silica) suggests a large component of hemi-pelagic settling, probably under at least a seasonally open ocean as biogenic contents are similar to those of surface samples. This is supported by PC494 containing only LF 2b, with a lower biogenic silica content than LA 2a, which may be linked to increased sea ice coverage at this more southerly core site. Pervasive bioturbation suggests the sediments were deposited in a low-energy environment with

a low sedimentation rate and good supply of nutrients to the seabed (Pudsey, 2000). Moderate amounts of $CaCO_3$ are also present, suggesting the CCD was below 4230 m water depth (PC496).

A similar greyish brown, bioturbated mud facies containing typically 5-30 wt.% biogenic silica with low magnetic susceptibility was deposited during interglacial periods in the drifts west of the Antarctic Peninsula and also attributed to mixed contourite and hemipelagic deposition (units A, C and E in Pudsey, 2000).

Lithofacies 2b (LF 2b)

Lithofacies 2b consists of bioturbated mud with 8-15 wt.% biogenic silica and is interpreted as a contourite with a minor hemi-pelagic contribution. LF 2b was deposited in a similar environment as LF 2a, but with a lower biogenic silica content. This is deemed more likely to be the result of variations in the amount of dissolution rather than changes in sea ice coverage, given the deepest core site at PC496 does not contain LF 2b but the other cores, on a similar or more southerly latitude do contain LF 2b.

Lithofacies 3 (LF 3)

Lithofacies 3 consists of $CaCO_3$-bearing mud and is interpreted as a mixed contourite-hemi-pelagite, deposited in a seasonally open ocean with relatively high primary productivity, evidenced by high Ba/Ti of 0.3-0.6. The CCD was situated below 3795 m water depth (PS58/255-2). However, the moderate to low contents of biogenic silica suggest diatom production was reduced compared to LF 2a and 2b, that some dissolution of silica may have occurred and/or that $CaCO_3$ contents diluted the biogenic silica. High smectite and low kaolinite contents suggest that the source of terrigenous mud was distal and fine-grained terrigenous detritus was deposited by bottom currents, as for LF 2a and 2b. Pervasive bioturbation in LF 3 is consistent with high productivity, low sedimentation rates and contourite deposition. Low gravel contents suggest IRD deposition was minimal and/or that dilution by finer grained material was high.

Lithofacies 4a (LF 4a)

Lithofacies 4a consists of terrigenous sandy mud, found only in the upper 21 cm of PC494, and is interpreted as a contourite deposit with a minor hemi-pelagic component of biogenic material and IRD. The relatively high smectite and low kaolinite contents are consistent with deposition of far-travelled clay particles by bottom currents (Ehrmann et al., 2011) rather than locally-sourced deposition by turbidity currents. The presence of bioturbation and benthic foraminifera are more consistent with a contouritic than a turbiditic origin of LF 4a, given the low sedimentation rates required (Wetzel et al., 2008).

The moderate values of biogenic silica content (7.1 wt.% biogenic silica) and relatively high contents of planktonic and benthic foraminifera and radiolaria (6.5% $CaCO_3$) suggest biological productivity occurred under (at least seasonally) open-marine conditions, with siliceous and carbonate organisms being deposited via pelagic settling.

85.7% of the mud in LF 4a is terrigenous and approximately half of the sand grains are terrigenous, dominated by quartz and feldspar. Relatively large gravel contents (8.5 wt.%) suggest much of the terrigenous sediment was supplied as IRD and that deposition was gradual, rather than the rapid deposition expected of a turbidite deposit. The other half of the sand content is biogenic and reflects the high biogenic sand content commonly found in contourites (Stow and Lovell, 1979; Stow et al., 2002). The mean (19.2 μm) and percentage (25.4%) sortable silt values do not indicate any significant winnowing.

Lithofacies 4b (LF 4b)

Lithofacies 4b consists of terrigenous, bioturbated sandy mud and is interpreted as a turbidite deposit, found only at site PC496 on the distal flank of Mound Two in sediments suggested to date from late MIS 6 (Figure 6.22).

Interpretation of this lithofacies is limited by the loss of the sediment from the archive half of the core during splitting and disturbance of the remaining sediments in the working half, meaning structure may have been lost. The presence of LF 4b only on a mound flank site, in close proximity to a turbidity current channel, suggests the

sediments represent spill-over from numerous turbidity currents. LF 4b overlies LF 5, a well sorted, laminated, medium sand deposit which has also been interpreted (below) as a turbidite deposit. Walker (1967) noted one characteristic of proximal turbidites is the presence of laminated or rippled sand with a sharp base and a top which grades into finer sediment. It is unclear whether laminae or grading may have been present in LF 4b prior to bioturbation or disturbance during core splitting. Based on context, with the lithofacies overlying a Tb division sediment, and the presence of bioturbation and burrows, this sediment may tentatively be classified as a Tc division sediment (Bouma, 1962) with ripples perhaps visible on a larger scale than seen in a narrow piston core, but no definitive classification can be given.

The relatively high kaolinite and low smectite contents of this lithofacies concur with a dominant local source for the terrigenous fine-grained material (Chapter 7.2.1; Ehrmann et al., 2011). Low contents of $CaCO_3$ and biogenic silica in LF 4b indicate its deposition during a glacial period under perennial sea ice cover, consistent with the age assignment to MIS 6. However, despite the probable low nutrient supply to the seafloor, the lithofacies is slightly bioturbated, suggesting sedimentation rates may have been relatively low.

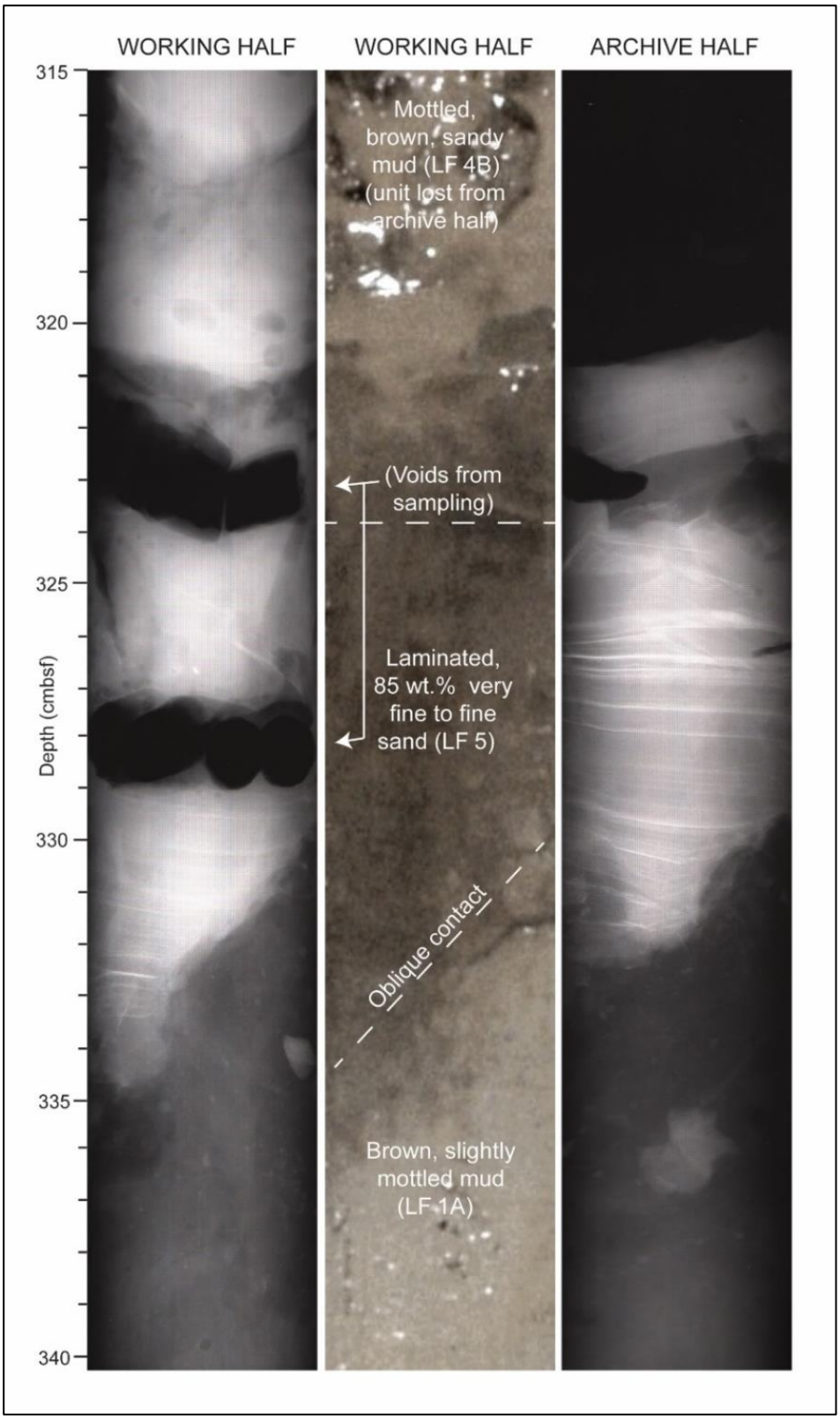

Figure 6.22: X-radiograph of the working half (left) and archive half (right) of the section from 315-340 cmbsf of core PC496, with the core photograph displayed in the centre. Notable sedimentological features and lithofacies are indicated in the photo. Note that the uppermost 5 cm of this section was lost from the archive half during core splitting.

Lithofacies 5 (LF 5)

Lithofacies 5 consists of horizontally-laminated, well sorted, very fine to fine terrigenous sand with an erosional base, and is present only at site PC496 on the flank of Mound Two in late MIS 6 sediments (Figure 6.22). LF 5 is interpreted as a turbidite spill-over deposit originating from a turbidity current traveling through the nearby channel.

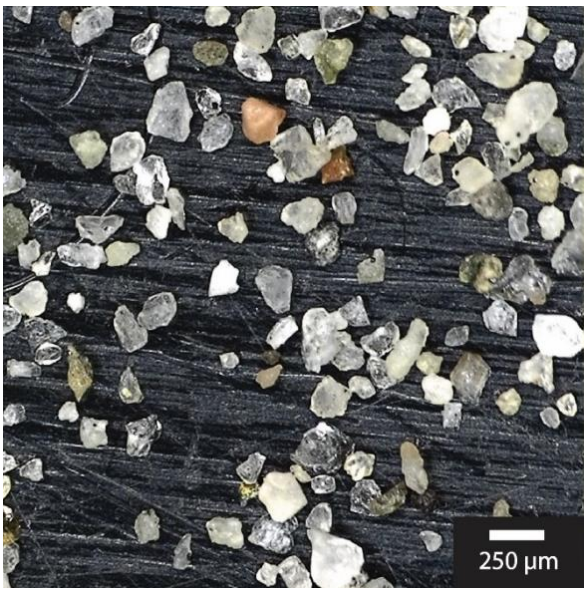

Figure 6.23: Microscope image of the 63 µm - 2 mm fraction of the sample taken from 328 cmbsf in core PC496; the sample is dominated by quartz and feldspar grains <250 µm in diameter (very fine to fine sand).

A sample taken from LF 5 revealed that the sand was almost entirely terrigenous (bulk sediment: 3.5% combined biogenic silica, $CaCO_3$ and TOC) and dominated by very fine to fine sand-sized quartz and feldspar grains (77% of the bulk sediment) (Figure 6.23). If LF 5 had been deposited by a bottom current, as opposed to a turbidity current, one would expect other grains coarser than fine sand to be present, reflecting pelagic settling of unsorted IRD and possibly planktonic foraminifera and/or radiolarians. The singular geology of the sand grains is supportive of a turbidity current influence, carrying sediment eroded from a particular source area, rather than the more mixed geologies and biogenic components typical of the rest of the core and therefore expected if it was a lag layer caused by bottom current winnowing (Rebesco et al., 2014). Bottom current deposits are also typically poorly sorted, bioturbated and contain sand concentrated in thin layers, in contrast to this well sorted, laminated, 11 cm thick sand unit (Stow and Lovell, 1979; Rebesco et al., 2014).

The lithofacies has an erosive and oblique contact with the underlying mud, suggestive of either a turbidity current or a bottom current of higher velocity than has been suggested by clay content and sortable silt data. Parallel laminated very fine to medium sand units require current speeds on the order of 40-200 cm/s (Rebesco et al., 2014), which are hard to reconcile with the evidence for sluggish bottom currents in this area and the lack of any similar lithofacies in the other four cores. LF 5 also does not exhibit the typical coarsening-upwards or any traction structures other than horizontal lamination which would be expected in a bottom-current reworked sand (Rebesco et al., 2014).

Based on its well-sorted and fine sand grain size, the dominance of quartz, the high kaolinite and low smectite contents of the clay fraction, the rare biogenic material, absence of coarse IRD and bioturbation, and the location of core PC496 on the mound flank near a turbidite channel, LF 5 is interpreted to be the lateral spill-over of turbidity currents from the channel. Parallel laminae in deep-water sands are characteristic of division Tb of the Bouma sequence (Bouma, 1962). Talling et al. (2012) further subdivided this category and attributed finely planar laminated sand ($T\text{-}_{B2}$) to the lateral shearing of sediments, produced predominately by high-density turbidity currents. The oblique contact with the underlying LF 1a documents erosion by the turbidity current of the pre-existing sediments (Figure 6.22). Individual laminae may represent deposition from individual turbidity currents.

A similar lithofacies was recovered from the north-east flank of Antarctic Peninsula Drift 7 close to the Alexander Channel system in sediments deposited during MIS 2. In the upper reaches of the channel (core SED-11), laminated, very-fine sand topped other sandy and silty layers which Lucchi and Rebesco (2007) suggested represented scattering of the turbidity current flow. Core SED-18 from the lower reaches of the channel contained a 19 cm thick turbidite deposit comprised of four separate intervals of graded and laminated fine to medium sand, each capped by a mud layer (Lucchi et al., 2002). Therefore, this lithofacies is similar to those found in a comparable position relative to turbidity current channels on the mixed contourite-turbidite drifts west of the Peninsula, where they form part of a thicker turbidite deposit.

Chapter 7: Discussion

7.1. Introduction

This chapter will discuss the data obtained from the sediment cores and the geophysical data and their implications for mound formation and palaeoenvironmental history, addressing the two primary research aims.

The first part of this chapter will focus on the mechanisms involved in mound formation. The sub-chapters will discuss the characteristics of the mounds (Chapter 7.2), the characteristics of the bottom current (Chapter 7.3), mechanisms of mound formation and a depositional model (Chapter 7.4), and make a comparison of the mounds with other Antarctic sediment drifts (Chapter 7.5).

The second part of this chapter discusses the palaeoenvironmental data obtained from the sediment cores and their implications for ice sheet and oceanographic history. The first part of the section focuses on WAIS history and evidence for local and regional changes in the ice sheet preserved in the sedimentology and mineralogy of the sediment cores (Chapter 7.6). The second part of the section focuses on the palaeoenvironmental history of the eastern Amundsen Sea, particularly changes in productivity and the nature of the bottom current (Chapter 7.7). The final section summarises the key implications of the observations made regarding the nature of the WAIS and Amundsen Sea for MIS 1 – MIS 10 (Chapter 7.8).

7.2. Characteristics and formation of sediment mounds in the eastern Amundsen Sea

7.2.1. Bathymetry

The bathymetry of the five mounds in the eastern Amundsen Sea suggests that both down-slope and along-slope processes have been key factors in their development. Bottom currents have prevented the development of the “gull-wing” geometry that is typical of some channel-levee systems and results from interaction of sediment with the Coriolis effect. By pirating suspended sediment from turbidity currents and redistributing it eastwards, depositing clays and silts on the mound flanks and

particularly the crests, bottom currents have resulted in a reduction in the size of the eastern levee and increase in the size of the western levee, relative to what would be expected for a 'pure' turbidite levee. This has created asymmetrical mounds with gently-sloping western flanks and a steeper eastern flanks (Figure 7.1).

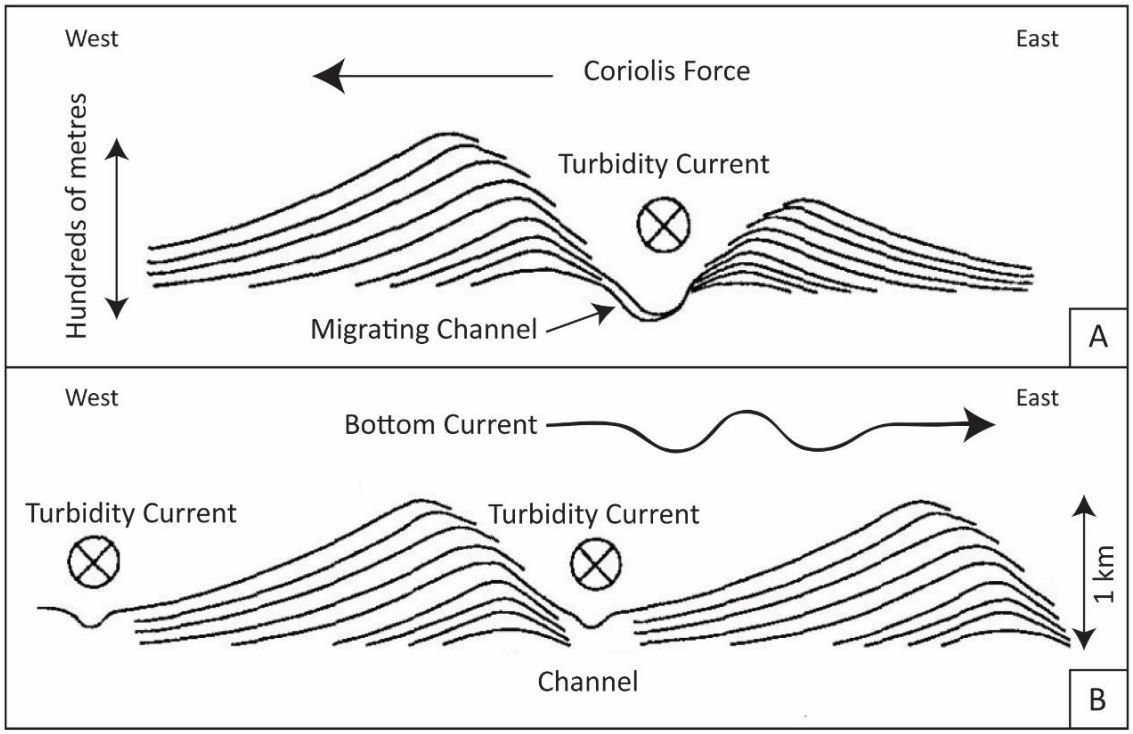

Figure 7.1: Idealised model of deposition of the fine-grained component of turbidity currents under A) The Coriolis effect, and B) Interaction with an eastwards-flowing bottom current. Modified from Figure 6 in Rebesco et al. (1996).

TOPAS sub-bottom profiles show laterally extensive, thick sediment packages on the mound crests, reflecting the relatively large amounts of turbiditic deposition on the western levee (under the Coriolis effect), together with the persistent eastward transport and deposition of fine grained sediment by bottom currents. The long axes of M3, and particularly M4 and M5, show a change in alignment towards the east which is associated with a change in orientation of the turbidity current channels lying between the mounds and may also reflect eastward along-slope transport by bottom currents. However, for the most part, the mounds are generally aligned perpendicular to the slope, suggesting the dominant sediment supply is down-slope via turbidity currents.

Turbidity current channels running between the mounds are incised and have acoustically hard beds, suggesting repeated, high-energy flows and coarse-grained beds.

Channel systems linking the continental slope to the rise and running between the mounds were identified previously (e.g. Nitsche et al., 2000; Uenzelmann-Neben and Gohl, 2012, 2014). Some channels on the lower slope appear to connect to channels on the mid slope; it is assumed that some of these are the channels which were found to connect to gullies on the uppermost slope by Dowdeswell et al. (2006) and Noormets et al. (2009). Eastward channel migration and some infilling are evident on the seismic profiles presented by Uenzelmann-Neben and Gohl (2012, 2014), typical features of turbidity current channels where deposition rate has exceeded erosion rate or mass wasting has occurred on the steep levees (Faugères et al, 1999). Erosion by turbidity currents can cause failure on their levees by 'under-cutting', leading to channel infill, if not subsequently eroded (Stow and Mayall, 2000). However, no infilling of the channels is visible on the sub-bottom profiler data, suggesting the turbidity currents may have been active in the recent past. Common acoustic stratification on the mounds may reflect long-term grain size variations in turbidity currents or variability in winnowing related to changes in bottom current strength, potentially related to wider climatic changes.

The finding of mixed contourite-turbidite deposition is consistent with the observations and interpretations of multi-channel seismic data by Uenzelmann-Neben and Gohl (2012, 2014), who identified sub-parallel internal reflectors within lenticular, upwards-convex seismic units, key characteristics of contourite drifts (Faugères et al., 1999). Laterally extensive internal discontinuities were attributed to major changes in deposition linked to ice sheet development and bottom current changes (Uenzelmann-Neben & Gohl, 2012), another feature of contourite drifts not typically seen in turbidite systems (Faugères et al., 1999). Multi-channel seismic data show eastwards migration of some of the channels and mound crests by up to 30 km since 4 Ma (Uenzelmann-Neben and Gohl, 2012, 2014), which could indicate along-slope transport under an eastwards-flowing bottom current. Otherwise, the orientation and positions of the mounds and channels changed little, implying the source area and the importance of down-slope deposition have been consistent since at least 14 Ma when mass transport deposits on the continental rise became more common (Uenzelmann-Neben and Gohl, 2014). This concurs with the work of Gohl et al. (2013), who interpreted seismic data to suggest the position of PITE and PITW, and therefore the flow paths of the major palaeo-

ice stream in the eastern ASE retained the same position on the mid and outer shelf since the earliest glacial advances in the Miocene. This consistency in drainage pattern offers an explanation for the large size of the mounds, similar to those located west of the Antarctic Peninsula (Amblas et al., 2006).

Although Uenzelmann-Neben and Gohl (2012, 2014) attributed the gently sloping western flank and steeper eastern flank of the mounds to an eastwards-flowing bottom current, they also concluded from the geometry of the mounds the influence of a south-westward bottom current at the base of the slope. This interpretation is here questioned, with no evidence in the multi-beam swath bathymetry or sub-bottom profiler data of a gently sloping eastern flank and steeper western flank that would be expected under a westwards-flowing bottom current. Rather, the geometry is interpreted as the product of an eastwards-flowing bottom current in combination with preferential deposition of turbidity currents on the western channel levees caused by the Coriolis effect.

However, although dominantly asymmetric with a gently-sloping eastern flank and a steeper western flank, the mounds are approximately symmetric in many places indicating spatial differences in mound development. The more symmetric mound sections are typically located close to the continental slope and therefore probably reflect the relatively large amount of down-slope deposition in this area, exerting more control over the morphology than the weak bottom current. Sediments in PC494 are typically more clay-rich than the more distal sediments in PS58/253-1, which may reflect downslope trends in grain size associated with turbidity currents. Alternatively, this, together with the spatial differences in asymmetry, could be the result of the bottom current being of a higher velocity >100 km from the margin, leading to a greater degree of selective deposition.

7.2.2. Sedimentology

The data from the four cores presented in this research, plus from core PS58/254-1 (Hillenbrand et al,. 2009a), reveal the mounds of the eastern Amundsen Sea are composed of mixed contourites and turbidites, with fluctuations between the two end members related to glacial-interglacial cycles and spatial variations between the mound flank and crest. Sedimentation rates during glacial periods are up to seventeen times greater than during interglacial periods and likely reflect increased input of material to the nepheloid layer via turbidity currents in response to an expanded ice sheet. Sediments deposited during glacial periods on mound crests are primarily contourites comprised of locally sourced, fine-grained (>95 wt.% clay and silt), laminated sediment largely supplied by turbidity currents and which are similar to glacial contourite facies found elsewhere on the Antarctic margin. Sediments taken from the mound flank close to a channel also contain turbidite spill-over in the form of an 11 cm thick layer of very fine to fine sand present in PC496 (335/329 - 324 cmbsf) (Lithofacies 5) overlain by sandy mud (Lithofacies 4b). Sediments deposited during interglacial periods are also contourites (C1 and C5) (Stow and Faugères, 2008) or mixed contourites and hemi-pelagites predominantly composed of far-travelled clays and biogenic material.

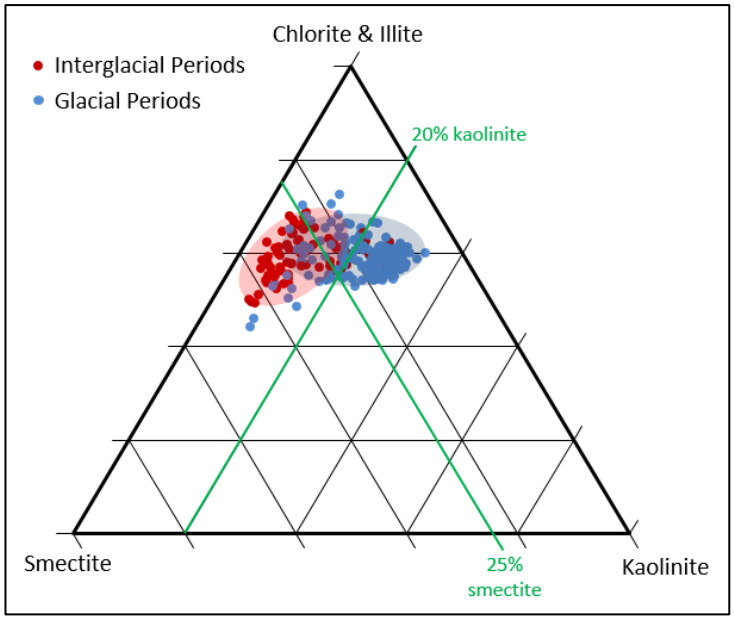

Figure 7.2: Ternary plot of glacial-interglacial changes in clay mineral composition in the sediments from the eastern Amundsen Sea mounds. Data from PC494, PC496, PS58/253-1, PS58/255-2 with post-MIS 11 data from PS58/254-1 obtained from Hillenbrand et al. (2009a).

The variability in the amount of down-slope and along-slope sourced sediment is reflected in the clay mineral composition of the sediments (Figure 7.2). Core-top smectite contents from the mounds exceed the smectite contents of shelf samples known from anywhere in the Amundsen Sea (see Chapter 7.3.1). This suggests clay is transported (most likely eastwards from the sub-Antarctic South Pacific and the central and western Amundsen Seas (see Chapter 7.3.1) and that Holocene deposition is largely controlled by along-slope bottom currents. This may also be the case for chlorite, though to a lesser degree than smectite, with the mounds recording slightly higher chlorite than seen on the outer shelf. Low core-top contents of kaolinite and illite, lower than many shelf samples from the ASE, suggest dilution by far-travelled clay occurs on the continental rise. In contrast, mound sediments deposited during glacial periods contain relatively high amounts of kaolinite and low smectite, suggesting down-slope sediment delivery was dominant over along-slope transport, with clay sourced from the ASE and particularly Thwaites Glacier (Ehrmann et al., 2011). Kaolinite and smectite contents in the five cores are negatively correlated (R^2=0.79) (Figure 7.3).

In the drifts west of the Antarctic Peninsula, it is under debate whether the clay mineral changes between glacials and interglacials are related entirely to the changes in amount of down-slope sediment delivery and the associated sediment dilution, or whether bottom currents also varied the amount of sediment deposited (Hillenbrand and Ehrmann, 2001; Lucchi et al., 2002). Sortable silt data from the Amundsen Sea drifts suggest bottom current speeds were faster in interglacial than glacial periods in PS58/253-1, but there was no consistent glacial-interglacial variability in the other cores, suggesting clay mineralogical changes are controlled by sediment dilution. Spatial differences in clay mineral contents across the mounds suggest more turbiditic material is deposited in inter-mound sites and on mound crests: PC496, taken from the mound flank and the deepest water depth of the five cores, and PC494, the most proximal and shallowest site, contain more kaolinite and less smectite than the other cores studied. This likely reflects an increased amount of down-slope transport to the proximal areas of the mound and to the inter-mound channel areas by turbidity currents.

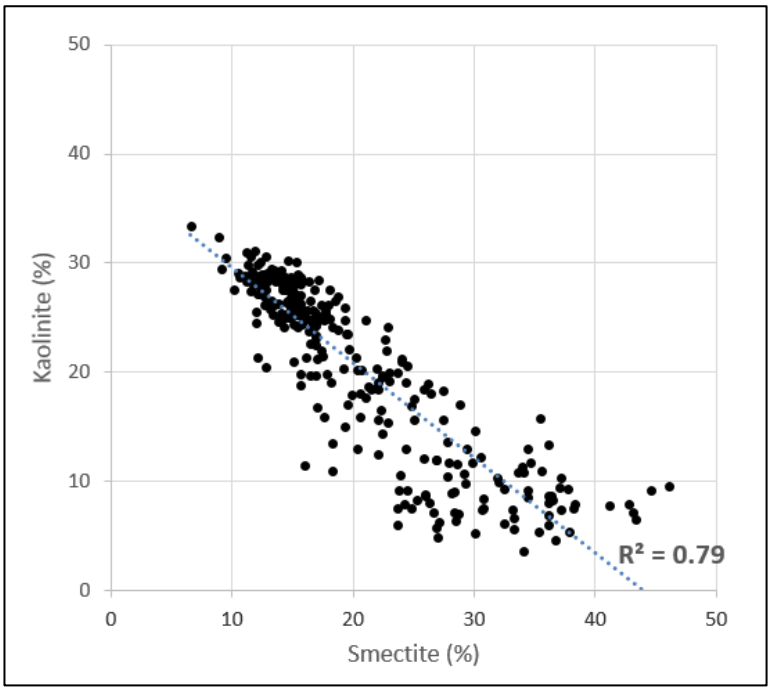

Figure 7.3: Percentage smectite and kaolinite contents of all samples from the five cores with a linear trend line and R^2 value. PS58/254-1 data taken from Hillenbrand et al. (2009c).

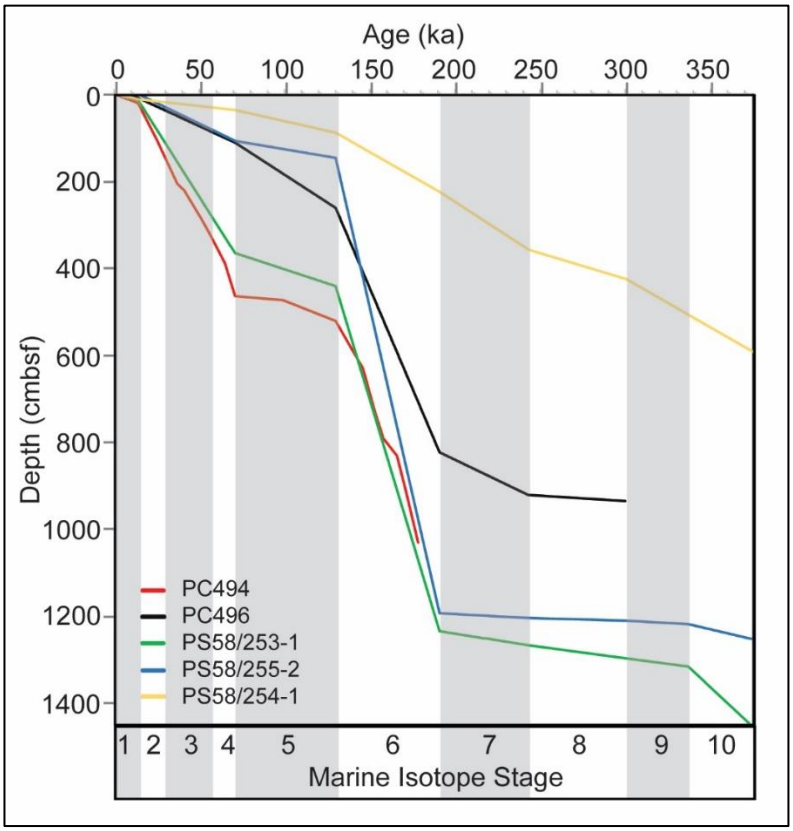

Figure 7.4: Age-depth profile for all cores. Grey bars indicate interglacial periods. Age model from PS58/254-1 taken from Hillenbrand et al. (2009c).

Sedimentation rates are typically higher in glacials than in interglacial periods but vary greatly from 0.1 to 17.2 cm/kyr (Figure 7.4). Glacial sedimentation rates are generally highest on mound crests (PC494, PS58/253-1 and PS58/255-2) than the flanks (PC496, PS58/254-1), probably as a result of the accumulation of fine-grained sediment on mound crests by the bottom current. The large variation in sedimentation rates between individual glacial periods may reflect how far the ice advanced across the shelf and the position of the ice margin relative to the gullies and channels that acted as a 'feeder system' for the mounds. The episodic, spatially variable nature of sediment supply to the nepheloid layer by turbidity currents may be reflected in the different sedimentation rates during MIS 6 in mound crest cores PS58/253-1 (13.0 cm/kyr) and PS58/255-2 (17.2 cm/kyr), with different mounds experiencing different sedimentation rates due to the spatially variable supply of material from the shelf break. Of the five cores, PC494 is the most proximal and had the highest sedimentation rate in the last glacial period, MIS 2-4, eight times higher than during MIS 5. In conjunction with the clay mineralogy, this high sedimentation rate may reflect the high volume of sediment supplied to the nepheloid layer by turbidity currents close to the margin rather than further offshore. The large variation in sedimentation rate within a single glacial period inferred from the relative palaeomagnetic intensity analysis of core PC494 (5 to 16.5 cm/kyr within MIS 6) highlights the episodic nature of turbidity currents supplying sediment to the nepheloid layer.

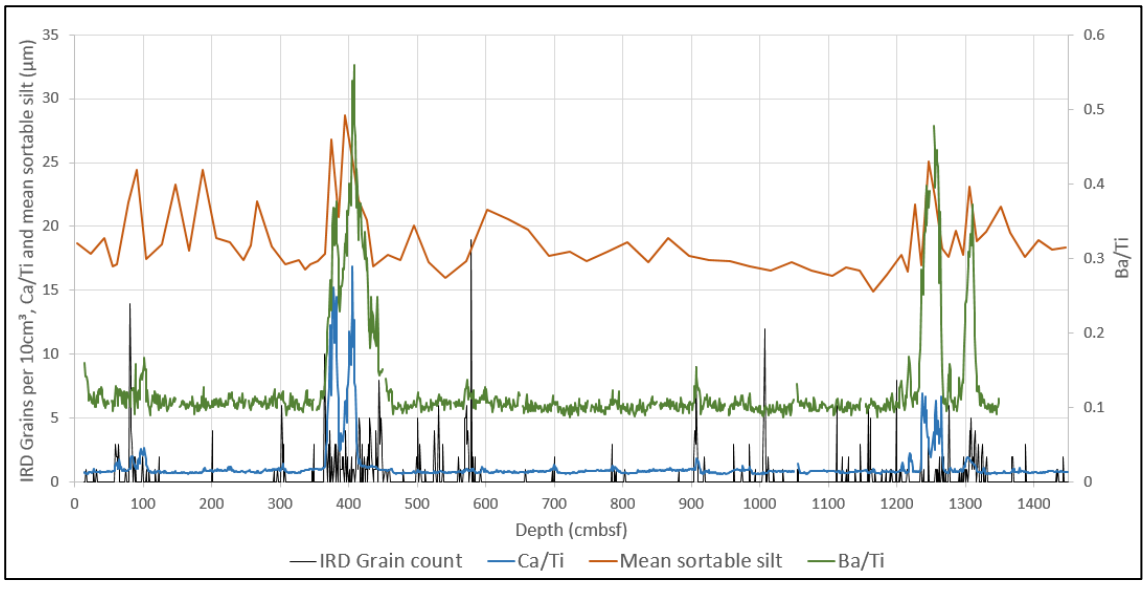

Figure 7.5: PS58/253-1 IRD grain counts (grains per 10 cm³, counted on x-radiographs), Ba/Ti, Ca/Ti and mean sortable silt (µm).

Sediments deposited during interglacial periods show a significant bottom current influence with an equal or minor pelagic component. Interglacial sedimentation rates are low (0.2-2.2 cm/kyr) and the highest sedimentation rate of 2.2 cm/kyr was found for MIS 5 in the mound flank core PC496. Sedimentation rates between the flanks and crests are similar during interglacial periods due to a greater proportion of the sediment comprising biogenic material largely supplied via vertical settling, with little to no input from turbidity currents after deglaciation of the adjacent shelf. There is no evidence for significant winnowing. Stow and Lovell (1979) suggested that bottom current winnowing might lead to lag deposits of biogenic material, but there are few correlations between Ba/Ti, Ca/Ti, mean sortable silt and the IRD grain counts outside of the general glacial-interglacial variations (Figure 7.5). There are no indications for hiatuses in the core data or age models. This suggests the bottom current bathing the mounds was too weak during the Late Quaternary to actively winnow and erode sediments, and its role was probably restricted to transport and selective deposition of clays and silts.

7.2.3. Evidence for a bottom current influence on mound formation

A large body of evidence has been presented in Chapters 5 and 6 that suggest down-slope deposition by turbidity currents has been a major influence on the presence and structure of the mounds. This includes the location of the mounds (lying largely perpendicular to a prograded margin where ice streams are known to have reached the shelf edge), their relationship to channel systems, previous authors' identification of gullies and mass transport deposits on the continental slope, the presence of a laminated sand layer in PC496 close to a channel, the kaolinite content of sediments suggesting an ASE source area and the large difference in the sedimentation rate of terrigenous material in glacial periods compared to interglacial periods.

No single piece of evidence suggested below is solely diagnostic of a contour current influence and there are limitations to the points raised below. It is recognised that, where flows of two different speeds interact, the sediments will be dominated by the record of the most energetic flow (Mulder et al., 2008). Criteria for identifying contour current and turbidity current interaction at the facies level are debated and it is generally accepted that mixed drifts are best identified through the study of multi-channel seismic

data (Mulder et al., 2008; Rebesco et al., 2014). In particular, the high clay content of the drifts suggests the bottom current has been persistently low velocity, with no evidence for ripples, hiatuses, winnowed coarse-grained lag layers or other features commonly associated with faster velocity currents. However, taken as a whole, the new facies-level and bathymetry data do concur with the suggestion that the mounds are mixed contourite-turbidite drifts put forward by Uenzelmann-Neben and Gohl (2012, 2014) using multi-channel seismic data.

Facies-level evidence that is suggestive of the mounds having had a bottom current influence on sedimentation is outlined in Chapter 6.4 as part of the lithofacies interpretation. Key points are summarised as follows:

Sediment grain size

- With the exception of the sand-rich lithofacies 4b and 5, all of the terrigenous material in the cores is clay and silt-rich and poorly sorted. Although some mud-rich turbidites can be poorly sorted (Piper, 1973), poor sorting is particularly common in contourites (Rebesco et al., 2008).
- There are no sandy layers or lenses in the cores from the drift crest, suggesting deposition of at least the coarse-grained fraction of the turbidity currents is restricted to the channel (Rebesco et al., 2002).
- IRD is typically dispersed throughout the sediments with concentrated IRD layers only occurring in lithofacies which also contain dispersed IRD. This is indicative of slow accumulation and does not concur with deposition purely from periodic turbidity currents.
- PC496, taken from the drift flank close to a channel, contains the smallest core-averaged percentage sortable silt value of all four cores (18.6%), followed by PC494 (20.8%), compared to values of 24.0% in PS58/253-1 and 30.6% in PS58/255-2. This along-slope grain size trend may represent selective deposition by bottom currents.
- Similarly, PC494 contained a higher percentage of clay and a finer mean grain size in all lithofacies than PS58/253-1, located on a more distal part of the same drift crest. This may represent changes in down-slope deposition with distance from the margin. However, it could also be the result of selective deposition by

a bottom current may be occurring at the more distal sites and is either weaker or has less of an influence on sedimentation on the more proximal parts of the drift. This concurs with the finding that the drifts are roughly symmetric close to the margin and asymmetric >100 km from the margin, reflecting the increased influence of a bottom current with distance from the margin.

- Sortable silt does not show any consistent variation between glacial and interglacial periods in three of the four cores. This is suggestive of a steady influence on grain size deposition common to both climatic states.
- Mean and percentage sortable silt are strongly correlated, with R^2 values of 0.78 in PC494, 0.82 in PC496, 0.80 in PS58/253-1 and 0.85 in PS58/255-2. Mean and percentage sortable silt are expected to show little correlation in a sediment which has not been current-sorted, such as a turbidite, and a strong correlation in current-sorted sediments.
- There is no correlation between sediments containing relatively large amounts of IRD and the mean sortable silt value, suggesting the mean sortable silt value is reflecting current-sorting rather than variations in the amount or size of IRD input (Roberts, 2017) (Figures 7.6 and 7.7).

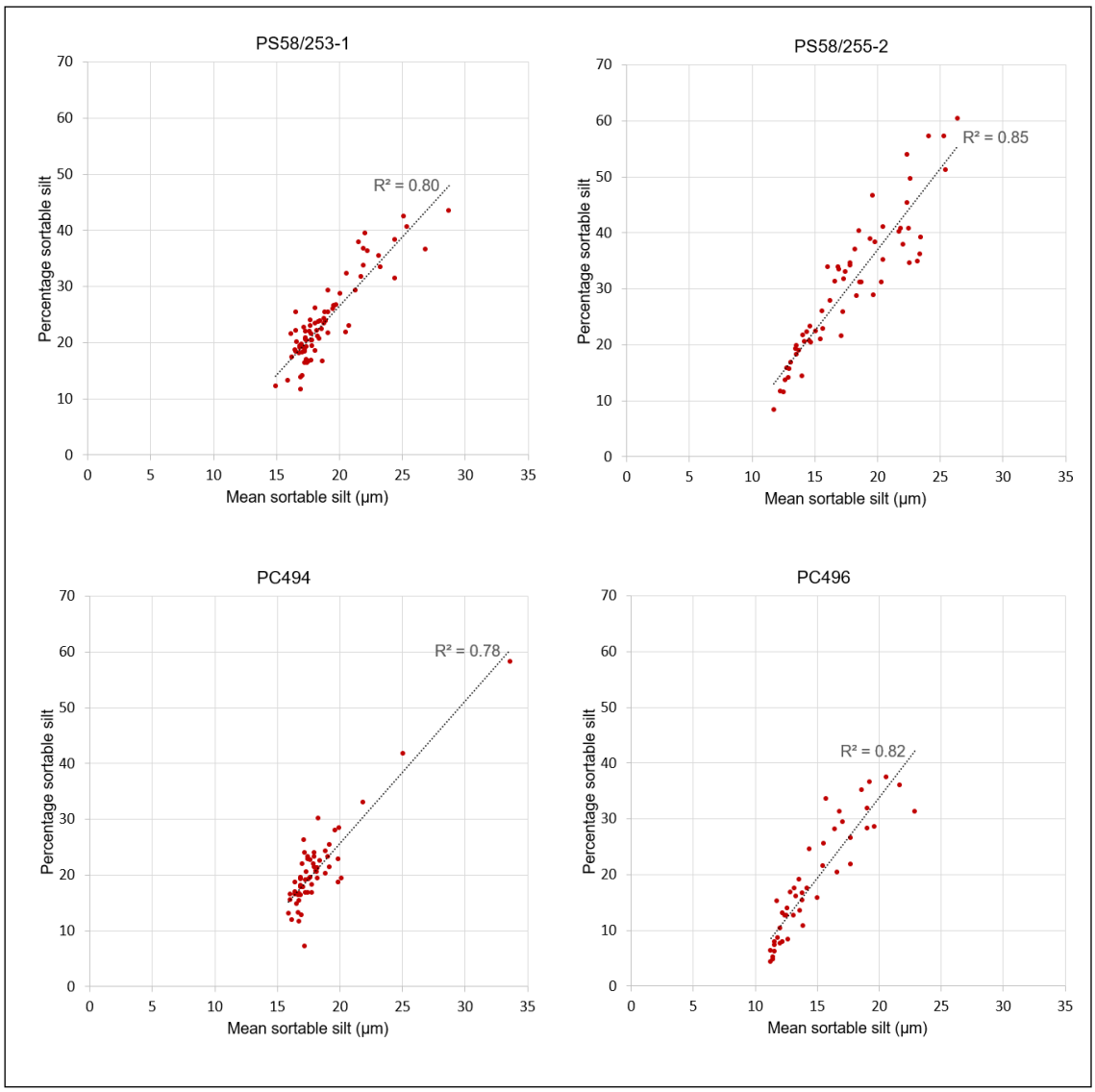

Figure 7.6: Mean sortable silt versus percentage sortable silt for the four cores.

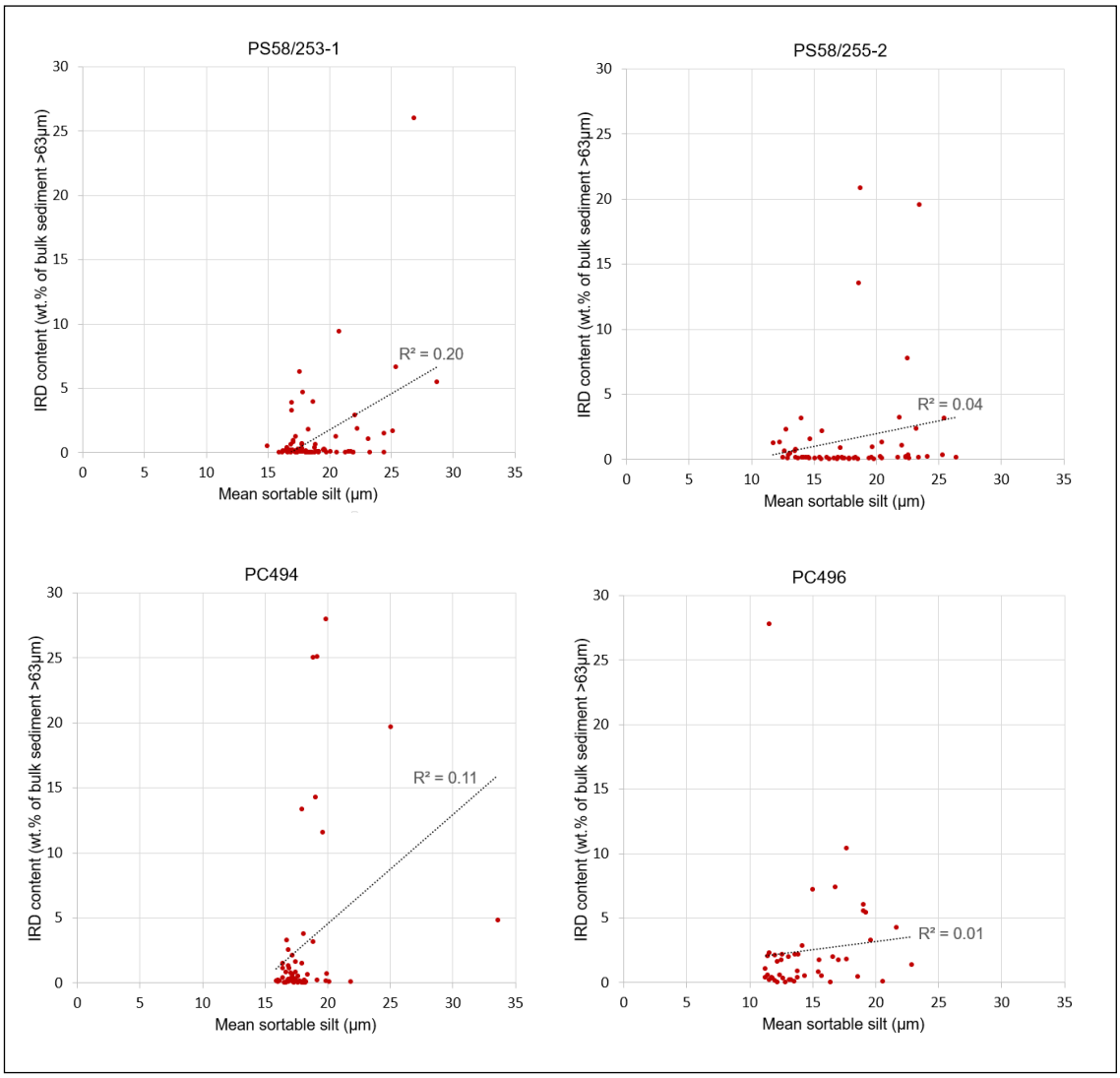

Figure 7.7: Mean sortable silt versus IRD content (wt.% of the bulk sediment >63 µm) for the four cores. Analyses from samples taken from the sand layer in PC496 (lithofacies 5) have been excluded given their likely turbidite source.

Sediment mineralogy and geochemistry

- The smectite content of surface samples from all four cores is greater than any known sample from the Amundsen Sea shelf or rise. This suggests the dominant source of the smectite is not in the Amundsen Sea Embayment and that the smectite has been transported and deposited by bottom currents (Chapter 7.3.1).

- Within each lithofacies and generally within each glacial and interglacial period, sediment composition is uniform and consistent. XRF and VIS-reflectance data showed sediments within each lithofacies were consistent in their geochemistry and spectral response, with no evidence of alternating or interbedded sediments. Similarly, biogenic silica and $CaCO_3$ contents, analysed at 1-10 cm resolution, showed little variation within each lithofacies. This suggests the sediments are unlikely to be turbidites with interbedded contourites or hemi-pelagites, and that the sediments likely reflect a consistent depositional environment and mix of sediment sources within each lithofacies (Stow and Lovell, 1979; Stow, 1985).
- Micro-manganese nodules present in the sediments, typically deposited towards the end of glacial periods, require low sedimentation rates in order to form and are therefore more suggestive of slow deposition under a bottom current than rapid, periodic deposition under a turbidity current.

Sediment structure and deposition

- Sedimentation rates, though highly variable between glacial and interglacial periods, are low to moderate in all cores. The high resolution chronology developed for PC494 using relative palaeomagnetic intensity showed sedimentation rates were moderately uniform within each lithofacies. Sedimentation rates for each individual lithofacies found in several locations on the drifts are within an order of magnitude of each other and there is no evidence for the highly spatially and temporal sedimentation rates expected of turbidite deposits. This is more in keeping with rates expected from typical contourites than from direct deposition from turbidity currents (Stow and Faugères, 2008).
- Laminated, rarely bioturbated sediments containing IRD, similar to those in LF 1b, are also common on the crests of the drifts located west of the Antarctic Peninsula and have been interpreted as contourites deposited during glacial periods (Lucchi and Rebesco, 2007). This interpretation was based on the presence of IRD, both in layers and sparsely distributed throughout the

sediments, low TOC contents and poor sorting, which are also characteristic of LF 1b. (Lucchi et al., 2002; Lucchi and Rebesco, 2007) (Chapter 6.4).

- Bioturbation and laminae occur together in Lithofacies 1b sediments of PC494 dating to MIS 2-4, which indicates low sedimentation rates and therefore concurs with the laminae being the product of bottom currents.
- Bioturbation in lithofacies 2a and 2b is pervasive and occurs throughout the units, typical of contourites, rather than being episodic and concentrated near the tops of beds as is more typical of turbidites (Stow and Faugères, 2008).
- No grading was identified in the core sediments. Normal grading and graded laminated units are common features of turbidites and may have been lost by the action of a bottom current (Stow and Bowen, 1980; Rebesco et al., 2002; Stow and Faugères, 2008).
- Sedimentation rates during glacial periods are similar at the drift flank site to the drift crest site. This is in contrast to turbidite sediments identified on Drift 7 west of the Antarctic Peninsula by Lucchi et al. (2002), who reported sedimentation rates decreasing with distance from the drift flank up the drift crest.
- Lithofacies 1a occurs in thick, featureless units, more typical of the muddy contourites described by Stow and Faugères (2008) than of turbidite deposits.
- Lithofacies 2a and 2b were commonly deposited during interglacial periods. Their bioturbated, grey-brown, mud-rich sediments of low magnetic susceptibility are similar to interglacial sediments from the Antarctic Peninsula drifts interpreted as mixed contourite-hemi-pelagites by Pudsey (2000). The high smectite content also suggests deposition of far-travelled clay by a bottom current.

The new bathymetry data are also suggestive of an along-slope influence on mound development. For example:

- Rebesco et al. (2002) used the large dimension of the Peninsula drifts to aid in their interpretation as mixed drifts, stating that the drifts are generally wider than 40 km and the crests stand over 400 m above the channel thalweg. The

Amundsen Sea drifts are of similar dimensions and stand up to 900 m above the channel.

- The drifts typically have continuous, parallel reflectors on their gently-sloping side and chaotic, truncated reflectors on their steeper side. These criteria were also used to support the interpretation of the Antarctic Peninsula drifts as mixed drifts by Rebesco et al. (2002).
- The asymmetry of the mounds is suggestive of sediment deposition under an eastwards-flowing bottom current. In turbidite levee deposits, the sediments generally thin way from the channels but this is only true for the right-hand levee in the Amundsen Sea, with the left-hand levee thickening with distance from the channel towards a crest. A similar geometry was used to support the notion of contourite sedimentation in the Scotia Sea by Escutia et al. (2002).
- The asymmetry is only evident over 100 km from the base of the continental slope, suggesting this is the point where the bottom currents and turbidity currents had similar energy and the bottom current influence was large enough to affect deposition and mound morphology.
- The easternmost two mounds have a distinct change in orientation eastwards, which may be due to the redistribution of sediment by an eastwards flowing bottom current leading to downstream extension and elongation of the mound.

7.2.4. Mixed Contourite-Turbidite Drifts

The bathymetry data from the five mounds, in conjunction with sedimentological, mineralogical and geochemical core data from M2 and M3, suggest the five mounds of the eastern Amundsen Sea formed by the interaction of down-slope (turbiditic) and along-slope (contouritic) processes. Biogenic and ice-rafted components constitute only minor amounts of the sediment. This continuum between deposition from turbidity currents, bottom currents and vertical settling has been identified as a common problem when differentiating depositional settings (Stow and Lovell, 1979; Shanmugam, 2016). This interaction, combined with their relatively large size and drift-like morphology and architecture, means the Amundsen Sea mounds can be classified as mixed turbidite-

contourite, elongate, mounded, levee-drift deposits. The five mounds will therefore be referred to as drifts 1-5 in the following chapters.

This concurs with the larger-scale conclusions drawn by other authors from analysis of bathymetric and multi-channel seismic data. Nitsche et al. (1997) and Uenzelmann-Neben and Gohl (2012, 2014) identified the mounds as mixed contourite-turbidite drifts. Lindeque et al. (2016) provided the context for their development in the Amundsen Sea basin. Uenzelmann-Neben and Gohl, 2014 interpreted the seismic data as showing evidence of interaction of the drifts with an eastwards-flowing bottom current since perhaps 60 Ma.

7.3. Nature of the Bottom Currents

7.3.1. Path of the Bottom Currents

The clay mineral composition of the sediments can be used as a geological tracer to identify potential source areas of the material deposited on the drifts (e.g. Hillenbrand and Ehrmann, 2001; Hillenbrand et al., 2003). As described in Chapter 7.1.2, the smectite content of the surface sediments of the eastern Amundsen Sea drifts (PC494: 22%, BC495: 22%, PC496: 26%, PS58/253-2: 36%, PS58/254-2: 38%, PS58/255-1: 38% (latter 3 results sourced from Ehrmann et al., 2011) is greater than on the adjacent shelf (typically <25%) (references given in Figure 7.8), where smectite is predominantly sourced from Ellsworth Land and western Marie Byrd Land (Ehrmann et al., 2011). This suggests that smectite-enriched clays from an unknown source are transported to the drifts by bottom currents.

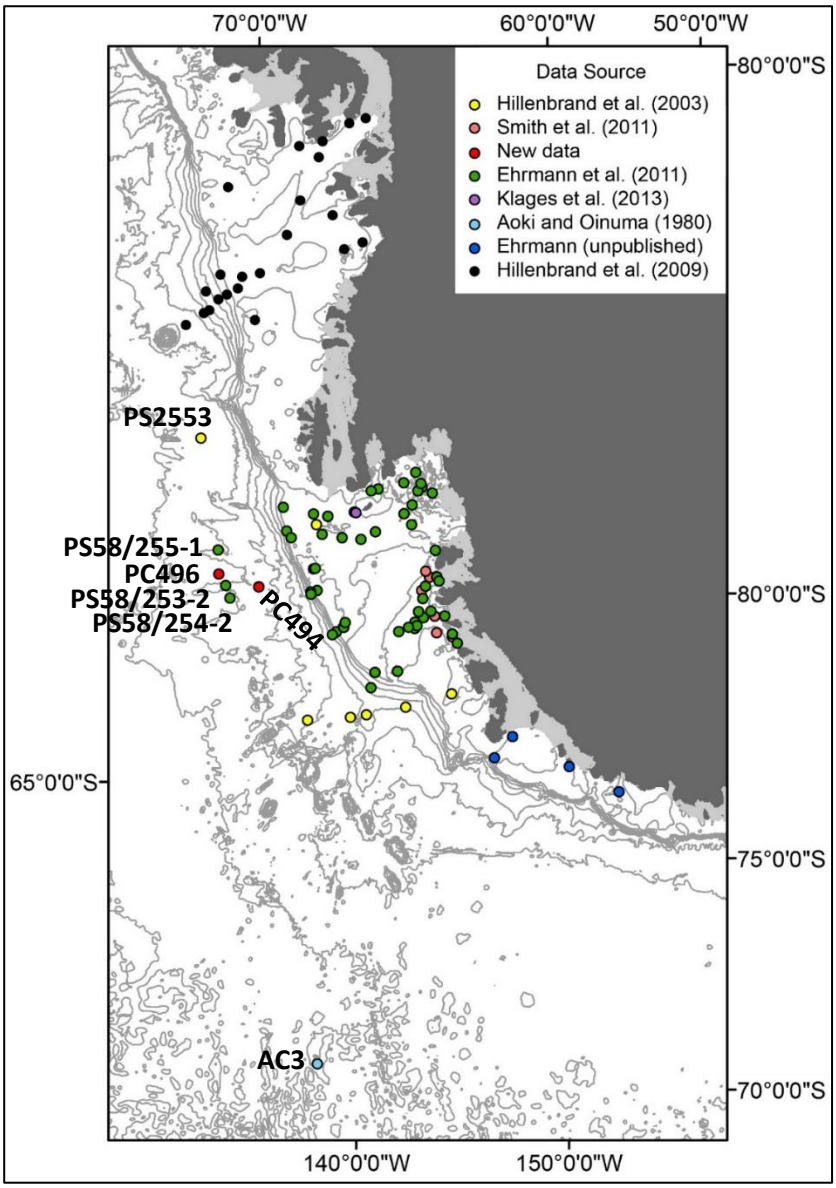

Figure 7.8: Locations of surface sediment samples providing the clay mineral reference data used in Figure 7.9. 500 m bathymetric contours are shown. Grounded ice is shown in dark grey, ice shelves are shown in light grey. Bathymetry (with 500 m contours) sourced from the IBCSO of Arndt et al. (2013).

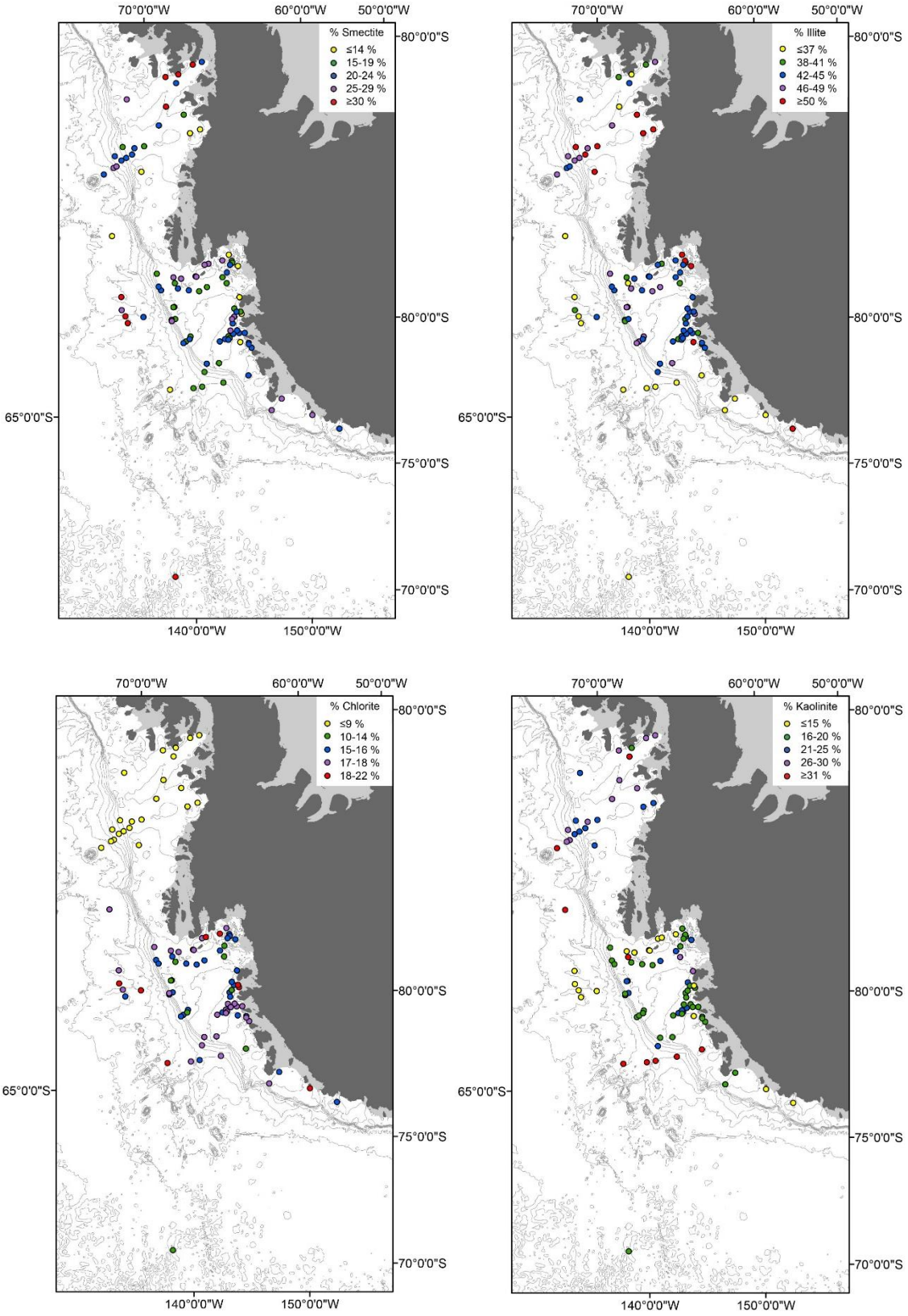

Figure 7.9: Smectite, illite, chlorite and kaolinite contents in core-top samples from the West Antarctic margin (for data sources, see Figure 7.6). Grounded ice is shown in dark grey, ice shelves are shown in light grey. Bathymetry (with 500 m contours) from IBCSO (Arndt et al., 2013).

The following scenarios are considered as explanations for the high smectite delivery to the eastern Amundsen Sea:

1. Westwards extension of modified WSDW

Uenzelmann-Neben and Gohl (2012) inferred from seismic profiles the influence of a south-west flowing bottom current on the drifts in the eastern Amundsen Sea since 21 Ma, albeit weakly since 4 Ma. The authors related this current to modified WSDW or LCDW flow from the Bellingshausen Sea or eddies shed from AABW. The surface drift geometry does not support this hypothesis, but a weak westward flow constrained to the base of the slope cannot be ruled out.

The high chlorite content (sourced from the Antarctic Peninsula) of a drift in the western Bellingshausen Sea (PS2556 from the Depocentre C of Scheuer et al., 2006b) suggests the westward flow of modified WSDW extends to at least 94°W (Hillenbrand et al., 2003). The dilution of chlorite by smectite and kaolinite at 97°W (PS2553) suggests this flow may not extend beyond c.94°W (Hillenbrand et al., 2003). Alternatively, the flow may continue weakly, as the high 37% smectite content of PS2553 suggest clay transport from the smectite-rich volcanic rocks of Peter 1st Island by a westward-flowing bottom current to at least 97°W (Hillenbrand et al., 2003).

The drift at 94°W shows the decreasing influence of a bottom current with distance from the margin: At a distance >55 km from the margin its geometry can be entirely explained by the influence of the Coriolis effect on deposition (Scheuer et al., 2006b). This suggests the westwards flow is weak and confined to the base of the continental slope. In contrast, the bottom current affecting the eastern Amundsen Sea drifts appears to be active along the whole length of the drifts, up to 400 km from the margin, making it unlikely that modified WSDW is the dominant water mass affecting the drifts, but that a narrow, slope-hugging, weak current could be present.

2. Southward-flowing current from the South Pacific

Ehrmann et al. (2011) suggested that the smectite may be being carried in an unknown southward-flowing bottom current from smectite-rich sediments in the sub-Antarctic

South Pacific, which were reported by Nayudu (1971). However, there are currently no clay mineral records from between the two regions to expand on this hypothesis.

3. Eastward-flowing current from the Ross Sea

Ehrmann et al. (2011) suggested smectite could be transported to the drifts from a source in the Ross Sea or western Amundsen Sea by an eastwards-flowing bottom current. Clay mineral data were only published for one core within the ACC to the west of the drifts (core AC3, see Figure 7.8), which is located in a similar position relative to the sACCf as the Amundsen Sea drifts. With 42% smectite (Aoki and Oinuma, 1980), this core recorded the highest smectite content on the West Antarctic continental rise. The eastward-flowing ACC, flowing within the Ross Sea Gyre, may erode sediments in the vicinity of AC3 and deposit them further east on the drifts. The low smectite content in the vicinity of the Marie Byrd Seamounts does not invalidate this hypothesis as each of the five surface samples in this area lie south of the sACC (Hillenbrand et al., 2003; Figure 7.8).

The smectite is unlikely to be sourced from the Ross Sea continental shelf because surface sediments in the western Ross Sea (and within the Ross Sea Gyre) contain only 20% smectite (Quaia et al., 1996 *in* Marinoni et al., 2000). The source of this smectite is possibly McMurdo volcanic rocks cropping out on the inner shelf, which are glacially eroded and the detritus is then carried north by bottom currents. Smectite content increased during glacial periods after MIS 9, peaking during late glacial periods at ≤36% (Quaia et al., 1996 *in* Marinoni et al., 2000), but even this is not high enough to explain the high smectite contents of the eastern Amundsen Sea.

4. Unidentified smectite source in the eastern Amundsen Sea

A further possibility is that there is a smectite-rich source in the vicinity of the drifts which has not been identified. A potential source may be the seamounts which lie within the drifts, particularly Drift One. As Peter 1st Island is a known smectite-rich province, these seamounts, which are also of volcanic origin, may be enriching bottom currents with smectite which has remained unidentified due to sparse sampling in the area.

Although poorly evidenced due to sparse spatial coverage, the clay mineral data suggest an eastwards flowing bottom current influencing the eastern Amundsen Sea drifts, in agreement with the interpretations of the bathymetry and sedimentological data (Chapter 7.1). The most likely source of the smectite are sediments in the South-East Pacific Basin, which were eroded and transported by the ACC and Ross Sea Gyre. Therefore, it is assumed the water mass influencing the drifts must be either LCDW or AABW sourced from the Ross Sea.

7.3.2. Bottom Current Strength

The typically fine grain size of the sediments indicates a low bottom current velocity which was too weak to winnow sediments, transport coarse grains or cause sediment resuspension (cf. Camerlenghi et al., 1997). WSDW bottom current speeds around Antarctic Peninsula Drift 7, which consists of sediments of a similar grain size (e.g. Lucchi et al., 2002), were typically between 4 and 6.2 cm/second (Camerlenghi et al., 1997). Stow et al. (2009) argued bottom current speeds in excess of 10 cm/second are required for sediment transport needed for drift development, suggesting the current may have had a faster velocity upon entering the eastern Amundsen Sea in order to transport the far-travelled sediments. The presence of mud waves suggests a steady and persistent flow velocity of <20 cm/second (Rebesco et al., 2014). The division C1 and C5 contourites are typically deposited under low velocity bottom currents (Shanmugam, 2016), and evidence for erosion or non-deposition by higher velocity flows is lacking in the contourite lithofacies of the Amundsen Sea cores. The lack of grading in the contourite units suggests the bottom current was consistently weak (cf. Shanmugam, 2016).

Micro-manganese nodules are present in discrete layers in the turbidite lithofacies of the drifts (reaching a maximum of 1% of the bulk sediment in LF 5 in core PC494). Small nodules have been associated with slower bottom currents, typically unconstrained by topography, than areas with larger manganese nodules and pavements (Faugères and Stow, 1993).

The presence of the drifts themselves may cause the ACC to slow south of the sACCf. Johnson and Hill (1975, *in* Nowlin and Klinck, 1986) suggest that topographical features

with a relief of 20% of the total water depth (i.e. a drift of 800 m height with a surrounding sea floor of 4000 m depth) may result in ACC transport decreasing by 85%, relative to a smooth, flat topography. However, more typically bottom waters are seen to speed up around obstacles due to the change in slope of the sea bed and the water mass being restricted vertically by density (e.g. Hernandez-Molina et al., 2006). Alternatively, other possible oceanographic reasons for current slow-down include:

1. The bottom current may be AABW, a density-driven current, the speed of which (in topographically unconstrained areas) depends on the slope of the bed and the density difference between the AABW and the overlying water (Rebesco et al., 2014). As the density difference between AABW and LCDW is large, AABW may have been at a relatively high velocity upon entering the eastern Amundsen Sea. However, Orsi et al. (1999) notes that AABW flowing within the ACC will constantly mix with the overlying CDW and, once heat gain passes a critical point, becomes entrained within the CDW. This mixing may have reduced the density difference, causing the AABW to progressively slow, given the long transport distance from the site of AABW production in the Ross Sea and lack of any bottom water production in the Amundsen Sea to replenish the dense water mass.

2. The bottom current may be LCDW and slowing due to the presence of the weak, westward-flow of modified WSDW detected near the continental slope at ca. 94°W and possibly extending further west (Hillenbrand et al., 2003). Ridges of sediment form along the margins of areas where a slow-moving current comes into contact with a faster, sediment-carrying current flowing in the opposite direction (Stow and Lovell, 1979). The seawards ends of the drifts are positioned under, or just south of, the sACCf, which reaches to within 100 km of the base of the continental slope at 95°W (Figure 7.10). Further to the east, from at least 80°W to 63°W, the ACC rises above the dense modified WSDW and only affects the upper c.1000 m of the water column above the Antarctic Peninsula drifts (Hillenbrand et al., 2008a). The confluence of these two water masses may cause the ACC to slow and deposit sediment. A similar process has been proposed for Prydz Bay, where the eastward-flowing ACC meets the westwards-flowing Antarctic Coastal Current, leading to the slow down and possibly diversion of bottom currents,

and resulting deposition of sediment in mixed turbidite-contourite drifts and ridges (Kuvaas and Leitchenkov, 1992).

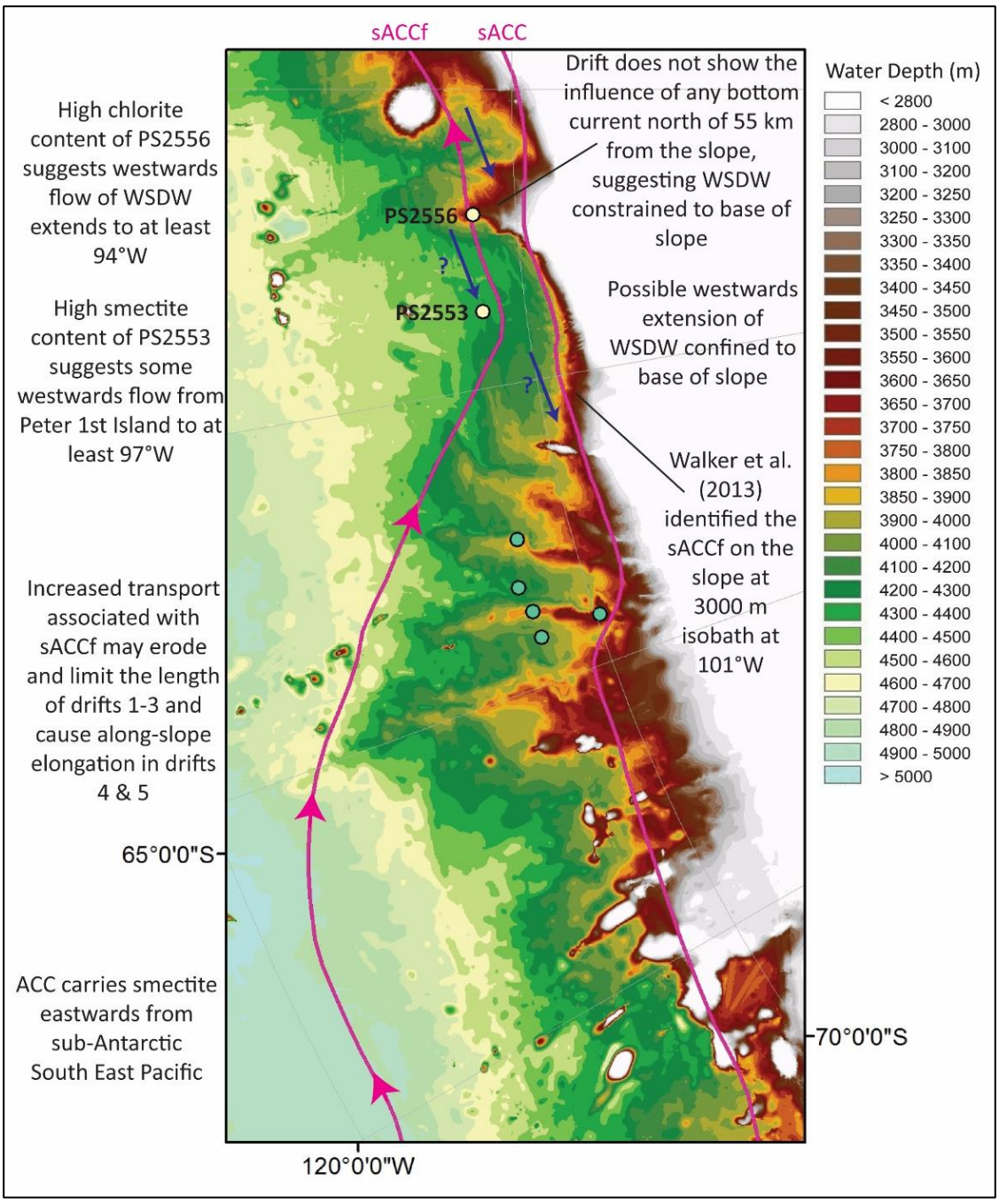

Figure 7.10: Illustration of the main oceanographic features of the eastern Amundsen Sea and western Bellingshausen Sea. Pink arrows illustrate flow within the ACC, blue arrows indicate flow of WSDW. Bathymetry from IBCSO (Arndt et al., 2013). Suggestions for bottom current flow around sites PS2553 and PS2556 are from Hillenbrand et al. (2003).

7.3.3. Potential Water Masses

There are two known possible water masses which flow eastwards through the Amundsen Sea within the ACC and could have influenced the drifts: LCDW and AABW.

Uenzelmann-Neben and Gohl (2012, 2014) suggested that AABW sourced from the Ross Sea was the water mass responsible for drift development. However, CTD data (Chapter 2.6.1) are ambiguous in that respect, with ODV profiles showing that LCDW directly overlies the core sites today with AABW present only over the northern tip of the mounds (north of 68.5°S along 108.3°W), but a CTD at site PC496 suggesting AABW presence there. The consistent asymmetry of the drifts along most of their lengths suggests the bottom current is active up to 400 km from the base of the slope. The $CaCO_3$ content of the cores, though generally zero in glacial periods, is typically >20% in interglacial periods, suggesting the bottom current is less corrosive to carbonate than the modified WSDW which bathes the Antarctic Peninsula drifts. The well-ventilated AABW is typically considered highly corrosive to carbonate, although the AABW in the Amundsen Sea may have been modified and become less corrosive than the modified WSDW due to mixing with overlying LCDW. No further inferences regarding the bottom water mass can be made from the sedimentology or bathymetry, and it remains unclear which water mass is ultimately responsible for the drift development and maintenance.

7.3.4. Influence of the ACC on Drift Morphology

Whether the main water mass influencing the drifts is LCDW or AABW, they are both transported within the ACC. The ACC is wind-driven and speeds propagate to the sea floor (Howe et al., 1997), so the increase in transport and flow velocity associated with fronts (Nowlin and Klinck, 1986) such as the sACCf will have an influence on bottom current speeds. The proximity of the ACC to Antarctic Peninsula Drift 1 has been suggested as a cause of its undulating topography and the fact that it has the lowest height of the 12 Antarctic Peninsula drifts (Pudsey, 2000).

Uenzelmann-Neben and Gohl (2012) found no evidence from multi-channel seismic data for any influence of a bottom current on channel-levee deposits in the central Amundsen Sea since 4 Ma. In contrast, the drifts of the eastern Amundsen Sea do show

the influence of a bottom current during this time. This could be attributed to the sACCf lying much further offshore in the central Amundsen Sea, with the front extending further south in the east and being in much closer proximity to the upper continental rise.

In the eastern Amundsen Sea, drifts 4 and 5 have the lowest heights of the five drifts and the point of change in orientation in each drift, north of which the elongation is more along-slope than down-slope, lies approximately 100 km south of the present day position of the sACCf according to Orsi et al. (1995). However, Walker et al. (2013) suggested the position of the sACCf is temporally highly variable, and identified the sACCf lying closer to the continental shelf in this area than defined by Orsi et al. (1995), with the sACCf located at the 3000 m water depth isobath on the continental slope at 101°W, just south of Drift Five. This implies the sACCf could (at least sometimes) lie directly over the position of the change in orientation of the drifts, leading to their along-slope elongation parallel to the axis of the front. The erosion or non-deposition of material by the sACCf could also explain why drift length generally decreases towards the east, following the southward movement of the sACCf, with increased current velocities at the front preventing deposition north of the sACCf. This hypothesis is based only on the present-day oceanography of the area. It is unclear how the sACCf may have migrated over the period of drift development.

7.4. Formation of the drifts

It is important to note that the following observations and interpretations are limited by the spatial coverage and sampling resolution of the sediment core analyses, and particularly the spatial coverage and resolution of geophysical data. It is acknowledged that the identification of certain features, such as channels and gullies, may be biased towards areas of better coverage, and that the presence of such features on areas of the margin with poorer coverage of geophysical data cannot be excluded.

7.4.1. Mechanisms of down-slope sediment delivery

The formation of bedforms on the upper continental rise depends on the morphology of the continental slope (gradient, sinuosity, presence/absence of channels) together with the composition, and rate of delivery and transfer of detritus to the continental rise (O'Grady and Syvitski, 2002). The continental slope on glaciated margins, where ice streams delivered large amounts of clay-rich detritus to the outer shelf are considered an "inherently unstable system" (pp. 76, Elverhøi et al., 2002), where mass wasting and redeposition of the poorly consolidated, rapidly deposited till material with high pore pressures may occur without an external trigger. Sediment failure on the continental slope occurs largely through a reduction in sediment shear strength, which in this setting is likely related to sediment loading on the outer shelf, high sediment flux to the upper slope and changes in hydrostatic and pore-water pressures due to meltwater production and glacial loading on the outer shelf (Noormets et al., 2009; Shanmugam, 2013).

The longest drifts (drifts 1, 2 and 3) in the eastern Amundsen Sea lie offset from the mouths of the cross-shelf troughs (PITE and PITW) (Figure 7.11). Reconstructions of the Last Glacial Maximum (LGM) show ice reached the shelf edge outside the troughs (Larter et al., 2014), however, the slower-moving ice would have resulted in lower sediment flux to the slope, usually too low to result in development of a trough mouth fan (Dowdeswell and Ó Cofaigh, 2002).

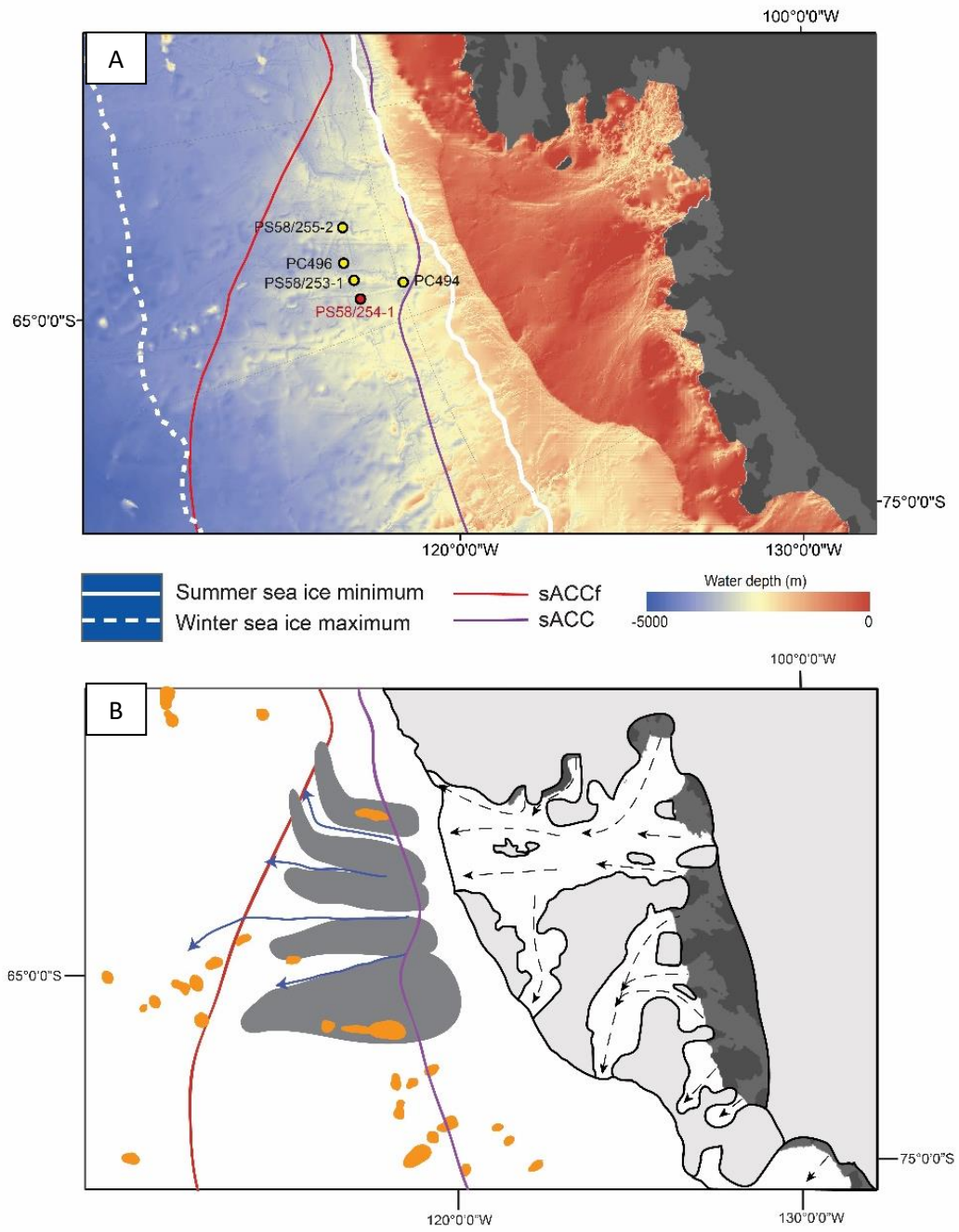

Figure 7.11: A) Bathymetric map of the eastern Amundsen Sea. Dark grey areas represent grounded ice and medium grey areas represent ice shelves. Bathymetry from IBCSO (Arndt et al., 2013). The position of the sACCf and sACC are from Orsi et al. (1995). Sea ice maxima are from NSIDC (2015).

B) Illustration of the approximate paths of ice stream flow at the LGM (dotted black arrows) and the location of turbidity current channels (blue arrows) in the eastern Amundsen Sea. The sediment drifts are shown in dark grey. Light grey indicates parts of the continental shelf shallower than 500 m water depth. Orange areas indicate seamounts. The red line indicates the sACCf, the purple line indicates the sACC.

The shelf edge in this area is highly sinuous due to gullies incising back into the shelf, particularly to the east of mouth of PITW (Noormets et al., 2009). The gullies are V-shaped, an average of 50 m deep and were interpreted to have been eroded by sediment-carrying meltwater flows, likely debris flows during glacial maxima and turbidity currents as the ice retreated (Noormets et al., 2009). Some of these gullies connect to channels on the mid-slope (Dowdeswell et al., 2006; Evans et al., 2006). Noormets et al. (2009) found that gullies on the upper slope below the PITW mouth flanks are more abundant than below the trough centre, which is probably linked to the subglacial production of more meltwater by the slower moving ice on the shallow banks outside of PITW.

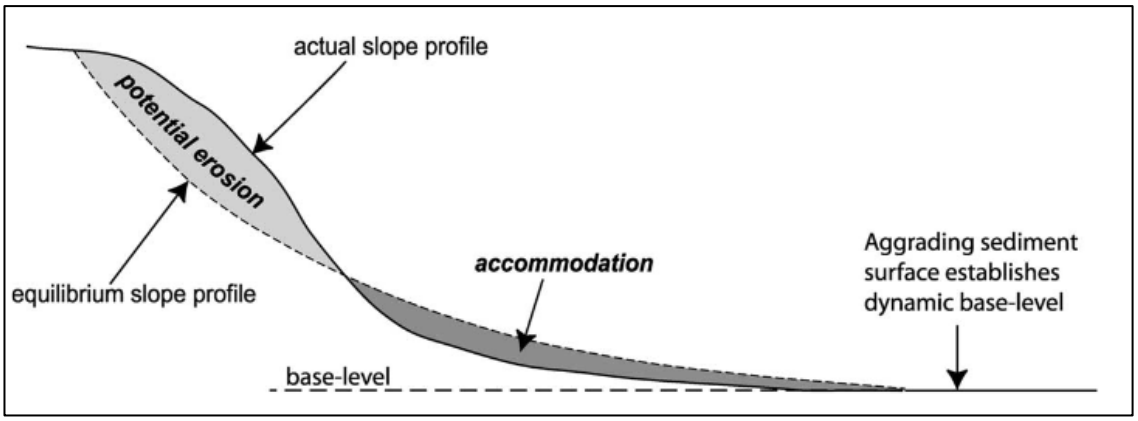

Figure 7.12: Illustration of an equilibrium slope profile, actual slope profile and intervening zones of potential erosion and accommodation. Figure from Kneller (2003).

Slope angle appears to have influenced gully incision, with incision increasing with increasing slope angle (Noormets et al., 2009). Similar observations were made elsewhere in Antarctica, e.g. Ó Cofaigh et al. (2003) and Dowdeswell et al. (2004) noted gully development in front of Marguerite Trough was more common on steeper slopes at the trough mouth edges than on the gentler slope in front of the trough centre. This is a common feature of turbidity current channels, as slope gradient is proportional to the force of the flow, which is loosely equated (depending on grain size) to the amount of erosion caused by the flow (McHargue et al., 2011). This may be related to steeper slopes having a greater distance between what would be an equilibrium slope profile and what the slope surface actually is, giving a larger zone of potential erosion for turbidity currents (Kneller, 2003) (Figure 7.12). The gullies may also have been pathways

for turbidity currents that developed at the shelf break, rather than transforming from other gravitational down-slope processes (e.g. debris flows), if subglacial meltwater production was high enough (Noormets et al., 2009). As the slope below the eastern PITW flank has more channels and apparently more meltwater was released there than in the central trough, enabling the development of turbidity currents at the shelf break, the eastern edge of the trough probably played a more dominant role in sediment delivery to the drifts than the central trough.

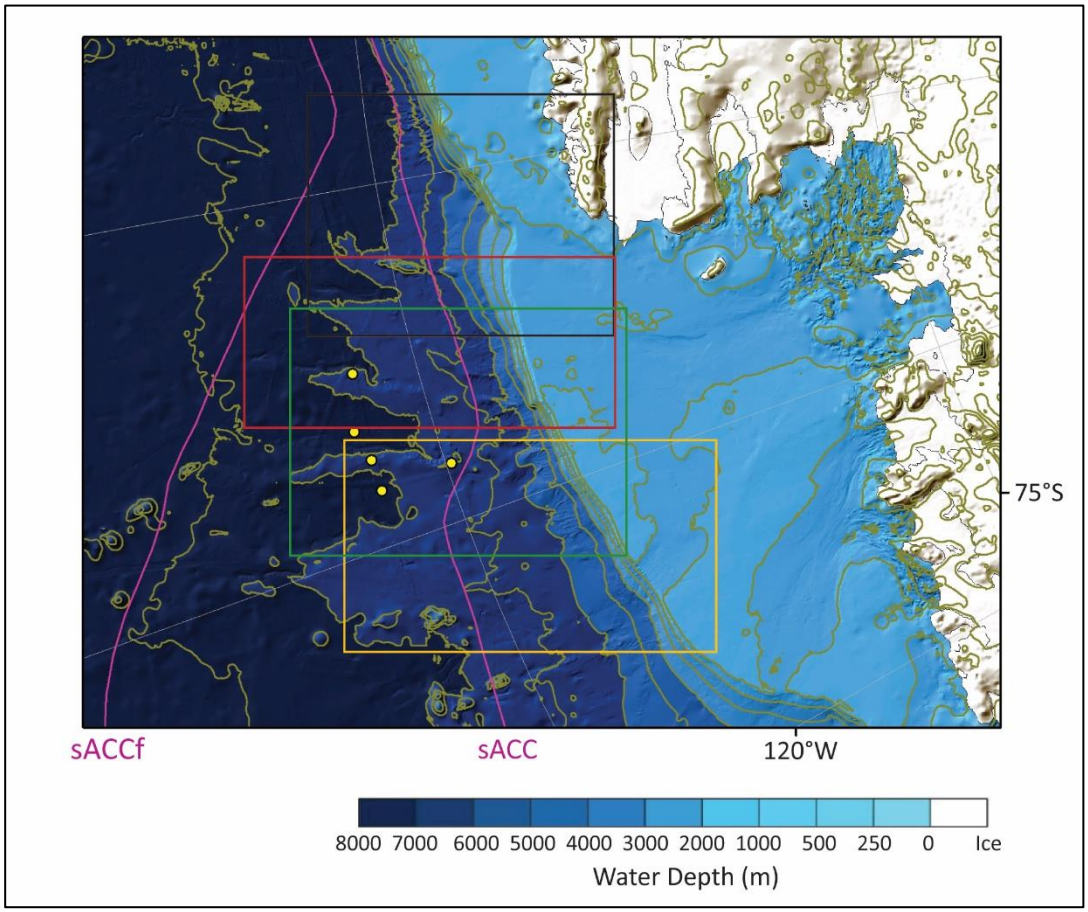

Figure 7.13: Bathymetric map of the eastern Amundsen Sea showing the location of Figures 7.14 (yellow), 7.15 (green), 7.17 (red) and 7.18 (black). Bathymetry data (with 500 m contours) from IBCSO (Arndt et al., 2013). ACC positions from Orsi et al. (1995).

7.4.1.1. Drift One

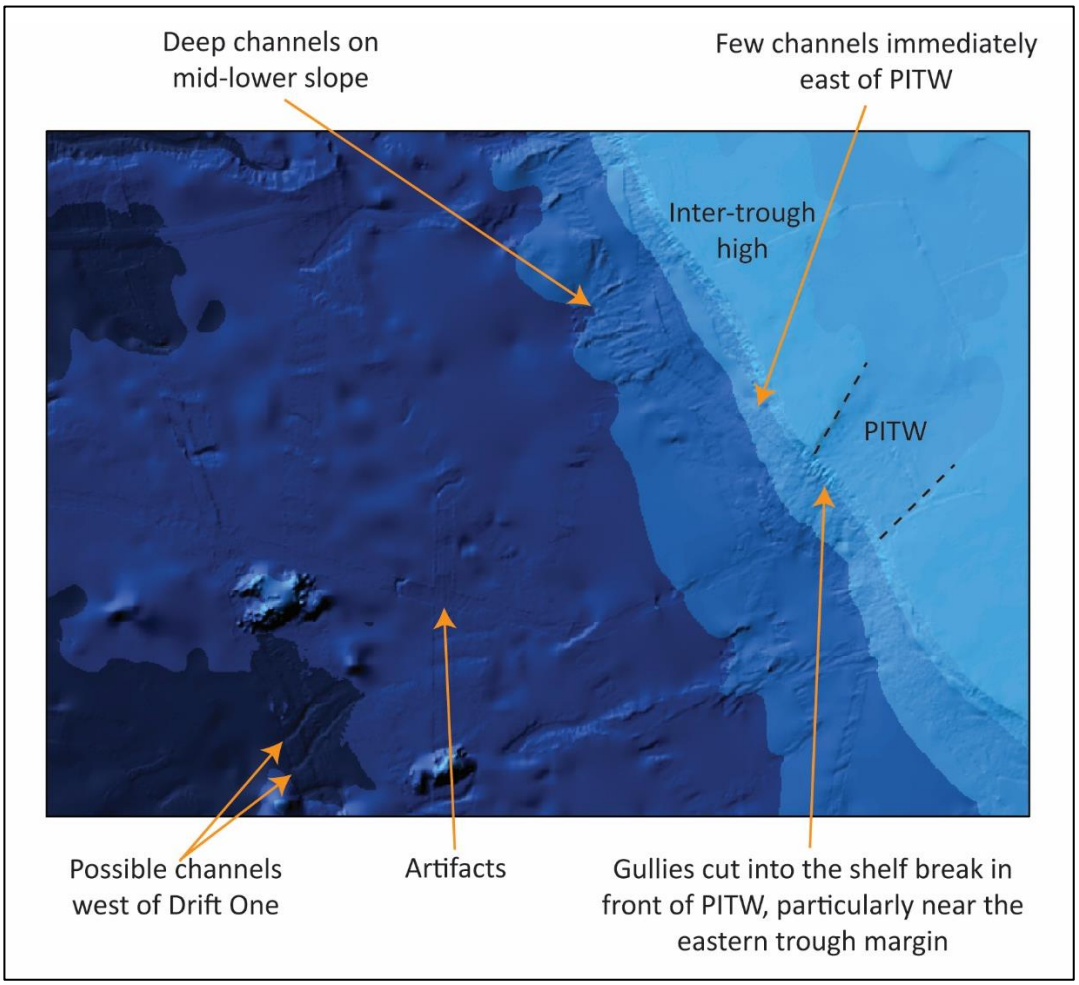

Figure 7.14: Bathymetry of the outer shelf, continental slope and upper continental rise at the southern end of Drift One. Bathymetry data from IBCSO (Arndt et al., 2013).

Few gullies or channels are visible on the slope in front of the central section of Drift One, according to IBCSO data (Figure 7.14). Areas without large numbers of gullies contain slide scars and are interpreted as areas that received weak subglacial meltwater flow (Noormets et al., 2009), meaning the glacial meltwater dynamics on the outer shelf had a significant impact on transport of material down-slope and the formation of gully and channel systems. Similar areas bordering Marguerite Trough contain few gullies and were interpreted by Dowdeswell et al. (2004) as the result of only small amounts of meltwater and sediment. This helps to explain the geometry of Drift One; the large sediment supply from the gullies below the eastern edge of PITW to the western part of Drift One through channels on the drift surface and possible minor channels to the west of the drift (Figure 7.14). The lack of a large channel to the west of the drift may be

related to the low number of gullies on the slope, which may reflect debris flows and sediment slumps and slides, rather than turbidity currents, given the relatively low meltwater and sediment fluxes compared to the trough margins. The eastern part of the drift is fed by the deep and long channel systems present in front of the inter-trough shelf bank, implying the occurrence of regular turbidity currents. These turbidity currents were constrained to the deep, incised channel separating Drift One from Drift Two, with the Coriolis effect responsible for the build-up of the western levee, i.e. the eastern part of Drift One.

Between these two areas, slumps, slides and debris flows may have blocked channels and led to the amalgamation of the two drifts into one. As Drift One has three distinct sections of drift crest and few channels are visible on the bathymetry data connecting Drift One to the continental slope, this drift is interpreted as the amalgamation of (at least) two smaller drifts. Variations in the angle of the slope off the Greenland margin were linked to development of secondary mound crests in the Eirik Drift (Hernández-Molina et al., 2008). Drift One may also have undergone large-scale mass wasting due to the large size of the drift, creating slide scars. However, the amalgamation of drifts is the preferred interpretation here due to the large-scale plateau shape of the drift and the distinct difference in length between the longer eastern section of the drift and the shorter western section. The high sediment flux to this drift from multiple sources and amalgamation of two drifts accounts for this being the longest, widest and tallest of the eastern Amundsen Sea drifts and lacking the asymmetry seen in the other drifts. Amalgamation of drifts has been identified elsewhere, such as Drift 6 off the western Antarctic Peninsula (Rebesco et al., 1998) where, like here, the drift shows symmetry and a plateau geometry. These features suggest turbidity currents had a more dominant role in shaping the geometry and structure of Drift One than of the other drifts, which is likely to be related to greater sediment delivery and the placement of channels on the drift surface. The presence of these shallow surface channels implies the structure of this drift may still be evolving.

The spatially dispersed seamounts around and within the drifts likely interacted with the bottom current and led to short-term increases in flow velocity, particularly on the southern edge of the seamounts, assuming an eastwards-flowing bottom current (cf. Hernandez-Molina et al., 2006). This may explain why the westernmost section of Drift

One ends c.10 km south of a seamount, around which flow speeds likely increase, possibly enough to cause down-stream erosion. Turbidity currents have also been known to be deflected by seamounts and to separate into smaller flows (Faugères et al., 1999; Stow and Mayall, 2000). Uenzelmann-Neben and Gohl (2012) identified moats in the sediment either side of a seamount at the seaward end of Drift One.

Similarly, the main area of the Marie Byrd Seamounts lies 500 km west of Drift One so any increase of flow velocity there should not impact on flow velocity above the mounds. Although there is no significant channel located to the immediate west of Drift One, a further sediment mound was identified further west, bounded by channels and separated from Drift One by a series of seamounts but lying directly under the sACC (see Chapter 5.1.2). One hypothesis is that these seamounts led to diversion and increased velocity of the bottom current, causing erosion of any depositional features on the upper continental rise and helping to explain the lack of mounds due north of PITW, leading to the deposition of Drift One once flow velocity dropped.

7.4.1.2. Drifts Two and Three

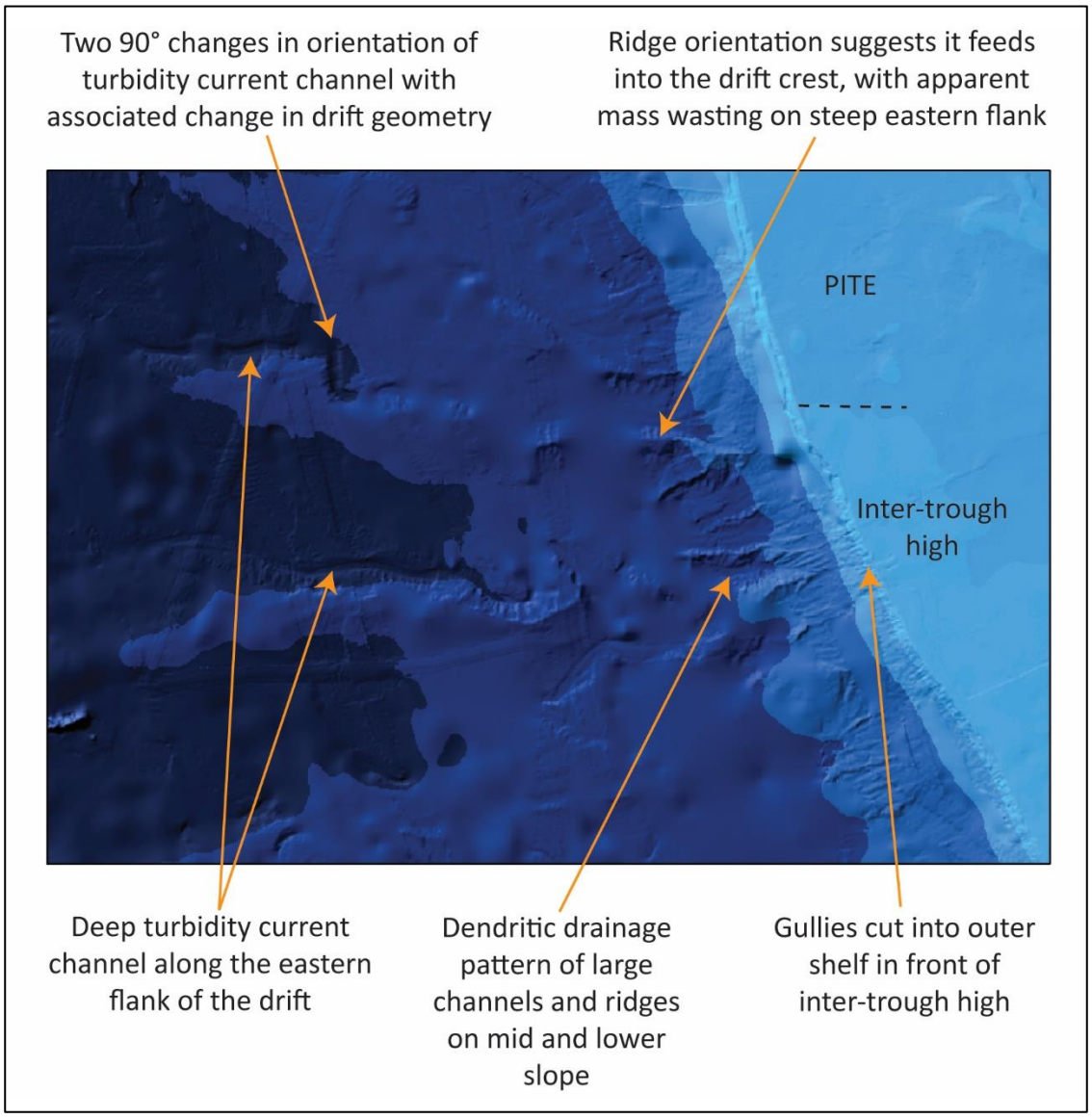

Figure 7.15: Bathymetry of the outer shelf, continental slope and upper continental rise at the southern end of Drifts Two and Three. Bathymetry data from IBCSO (Arndt et al., 2013).

Further east, the shelf break and upper slope in front of the inter-trough area separating PITE from PITW contains many gullies and channels, some of which are seen to connect via a dendritic drainage pattern to channels on the mid and lower slope (Figure 7.15). Channels are particularly large and numerous on the eastern edge of the inter-trough area. Multi-beam swath bathymetry data show that the lower slope, particularly at the southern end of Drifts Two and Three, contains many ridge-like deposits and channels. The ridge-like deposits are assumed to connect to the drift crests as they share the same

orientation and have a similar height above the surrounding seafloor. In particular, the orientation of the ridge feeding into the crest of Drift Three has the same angle to the shelf break as the rest of the drift, suggesting the orientation of this drift is controlled by down-slope deposition rather than along-slope modification. The 50 m-deep incision of the channel separating Drift One from Drift Two suggests repeated erosion by turbidity currents sourced from the slope. Similarly, the channel separating Drift Two from Drift Three is particularly long, extending past the northern ends of the drifts up to 400 km from the base of the slope, and suggests the turbidity currents eroded substantial amounts of sediment in the channels along their flow, in order to counteract the dilution of the flow and sustain the turbulence.

It is therefore inferred that the meltwater produced by the slow-moving ice sitting on the shelf bank between PITE and PITW led to the development, possibly at the shelf break, of turbidity currents. Erosional gullies in front of the inter-trough area have previously been identified by Dowdeswell et al. (2006) (Figure 7.16). The slope in this area is the steepest of the eastern Amundsen Sea, probably resulting in greater erosion of the slope by turbidity currents to the equilibrium slope profile and producing deep gullies (Kneller, 2003). The gullies and channels directed subsequent flows, channelling the sediment towards and onto the drifts.

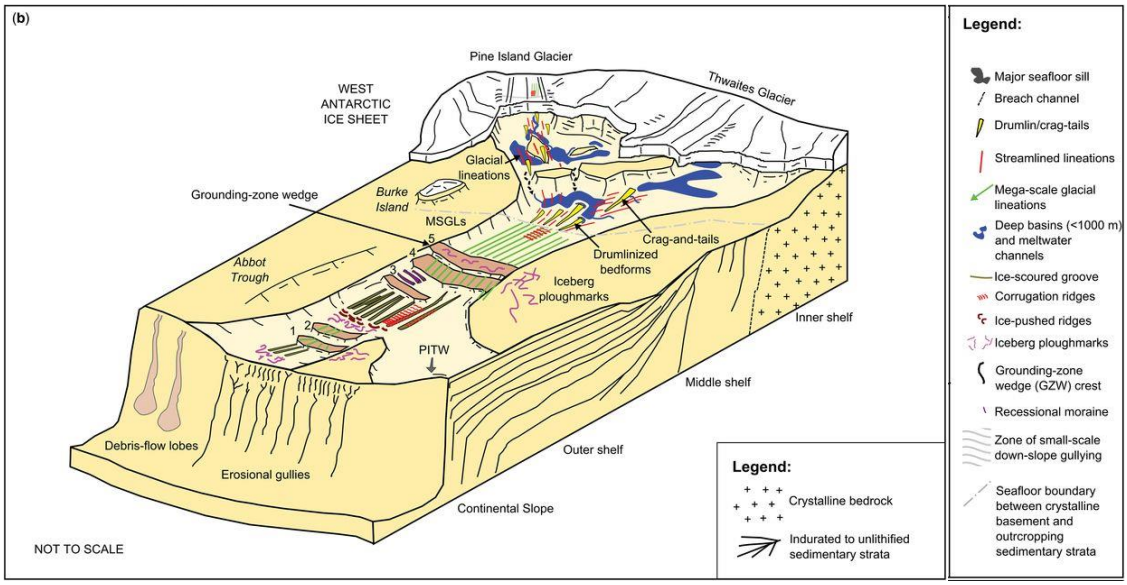

Figure 7.16: Illustration from Graham et al. (2016) highlighting the sub-glacial landforms in Pine Island Trough and bedforms on the adjacent slope.

Graham et al. (2010) discussed the possibility of ice stream flow in this area being divergent and occurring in PITW, the inter-trough area and PITE at the same time in a sheet-like fashion, but concluded that this was unlikely given the lack of modern analogues. At the last deglaciation, ice is assumed to have retreated from the outer shelf in PITW by c.25 ka and PITE by c.20 ka, but remained at the shelf break in the inter-trough area until >16.4 ka (Graham et al., 2010; Kirshner et al., 2012; Larter et al., 2014; Smith et al., 2014). The presence of such slow-moving ice, grounded at the shelf break and producing large amounts of meltwater helps to explain the production of turbidity currents, eroding the gullies and delivering sediment to the upper continental rise via channels. The extensive nature of the channel and gully system implies similar processes occurred in previous glaciations.

7.4.1.3. Drift Four

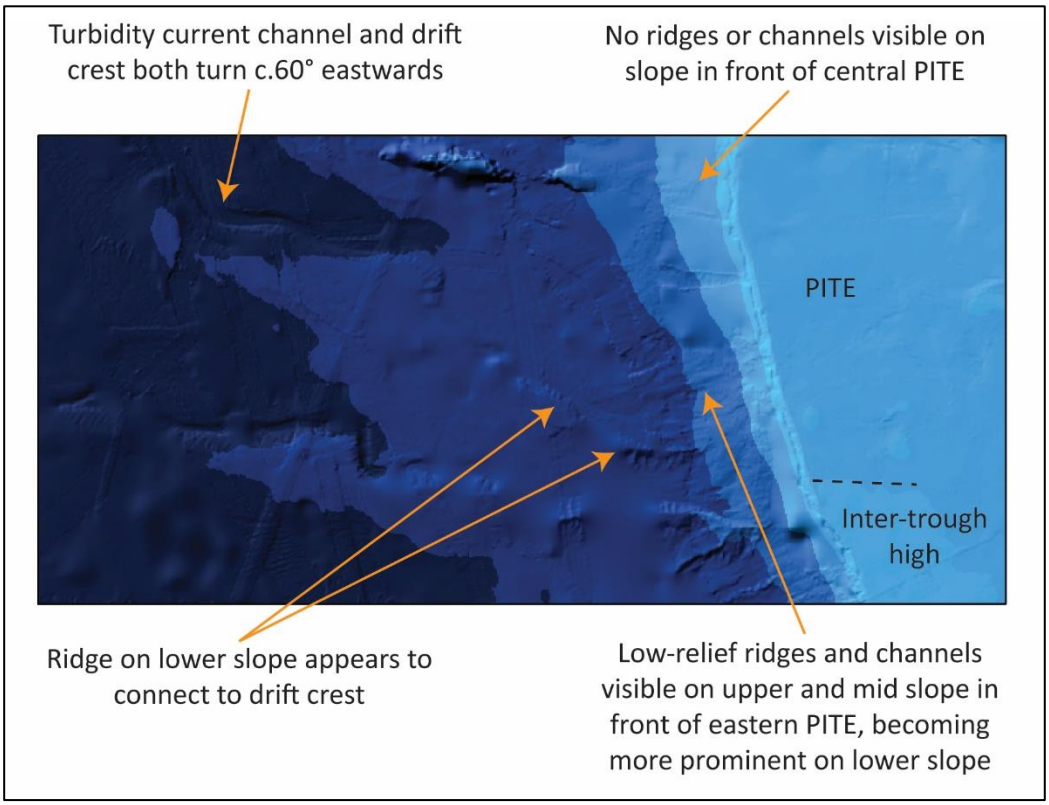

Figure 7.17: Bathymetry of the outer shelf, continental slope and upper continental rise at the southern end of Drift Four. Bathymetry data from IBCSO (Arndt et al., 2013).

Drift Four lies directly north of the mouth of PITE, which was the site of a high amount of sediment flux to the outer shelf during at least the LGM (e.g. Larter et al., 2014). The drift crest emanates from a ridge on the lower slope, around which a series of channels connected to channels further up on the slope is observed (Figure 7.17). The position of the western channel separating Drift Three from Drift Four suggests the far western edge of PITE was the source for most, if not all of the down-slope supply of sediment to the eastern part of Drift Three and most of Drift Four. As in Drift Three, the long axis of Drift Four is orientated at an angle to the shelf break and the main body of the drift follows this orientation. A key exception is the seaward end of the drift, which turns eastward. The turbidite channel to the east of the drift also turns eastwards, but with no obvious tectonic or topographical features to explain the change. The change in orientation is therefore suggested to be the result of sediment transport and deposition by the eastwards-flowing ACC, given the proximity of this end of the drift to the sACCf, with the turbidite channel being forced to mimic the change in orientation as the position of the drift blocked northward erosion by turbidity currents. The large angle of the channel bend may cause some sediment to spill over directly onto the eastern flank of Drift Four, which may explain the undulating height of the end of this drift (Wynn and Stow, 2002).

7.4.1.4. Drift Five

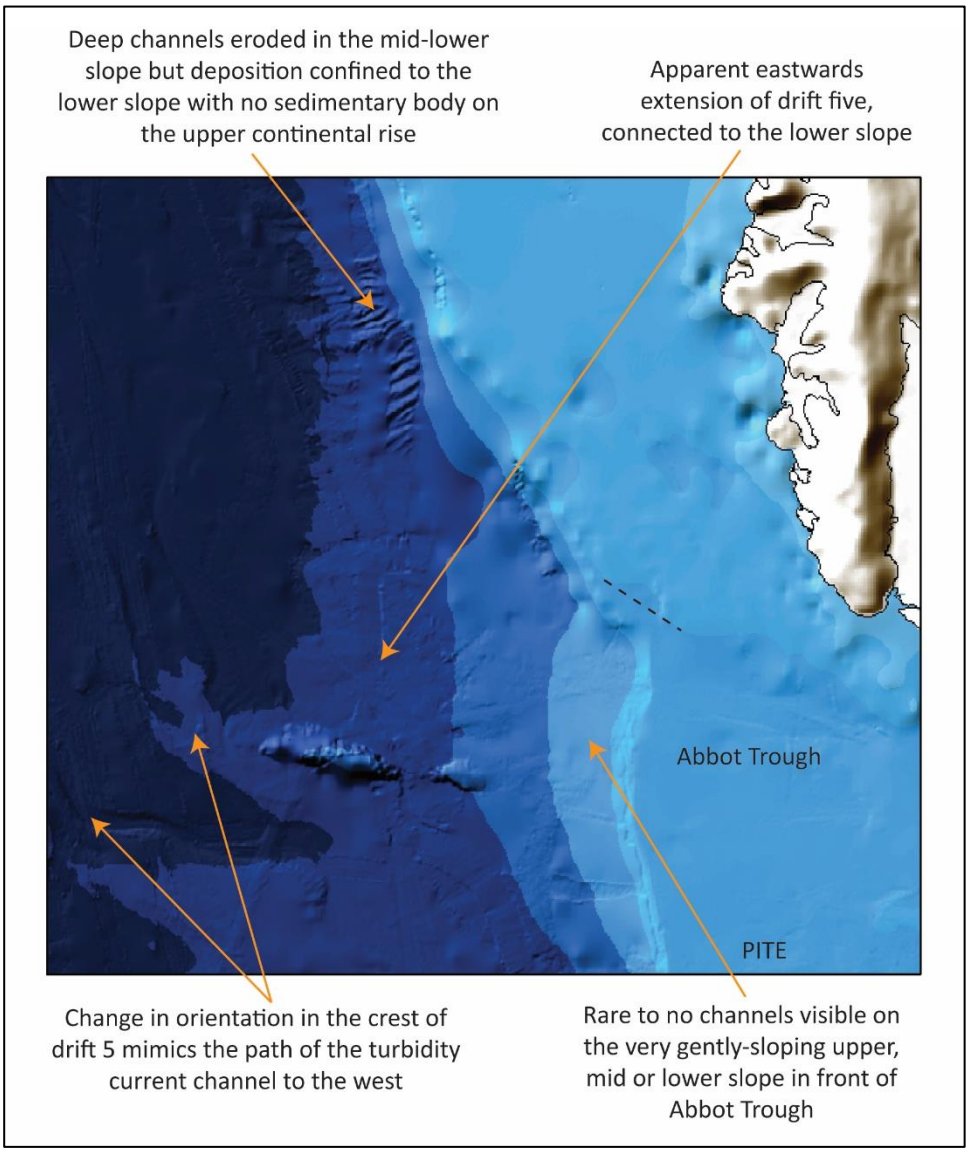

Figure 7.18: Bathymetry of the outer shelf, continental slope and upper continental rise at the southern end of Drift Five. Bathymetry data from IBCSO (Arndt et al., 2013).

Drift Five lies directly north of the Abbot Trough. With a turbidite channel to the west of the drift and none to the east, the bulk of the drift is fed by turbidity currents from sediments supplied from the ice once grounded on the outer shelf between PITE and Abbot Trough (Figure 7.18). The absence of any ridge-like system leading from the lower slope to the drift crest supports the hypothesis that the eastward turn of the seaward-end of the drift crest is related to along-slope transport of sediment by the ACC. The ACC may directly cause along-slope orientation of the end of this drift, or the turn may result from the change in orientation in Drift Four, which caused the turbidity current

separating the two drifts to turn eastwards and therefore Drift Five to mimic the orientation of the channel. However, it is unclear whether the sediment accumulated south of the drift crest, following the change in orientation, is a product of down-slope transport of sediment from Abbot Trough and/or further along-slope deposition of sediment.

If the sediment was primarily supplied by down-slope transport, the absence of significant turbidite channels, at least those visible in the 500 m resolution data, suggests the sediment may have been delivered primarily via slides, slumps and/or debris flows. Debris flow deposits are present on the slope in front of Abbot Trough (Graham et al., 2016) (Figure 7.16). The sediments in this eastern section of Drift Five appear to be banked against the slope and their northernmost extent corresponds to the position of the drift crest following the eastwards turn, rather than gradual offshore thinning. This suggests the debris flows may have been restricted from being transported further onto the continental rise by the existing drift. Submarine debris flows on low-angle slopes (<2°) can have particularly long run-out distances onto the continental rise due to hydroplaning (Elverhøi et al., 2002). The more dilute a debris flow is, the further it will travel (Shanmugam, 2013), but the apparent absence of large channels in the area based on the available data suggests few debris flows were diluted enough to become turbidity currents and sediment volumes were high, with sediment being deposited close to the base of the slope.

The apparent absence of a large channel to the east of the drift may explain the different orientation of this drift, as the presence of turbidity currents in channels separating the other drifts would have eroded any sediments deposited in the channels, preventing along-slope progradation. Sub-bottom profiler data show the drift sediments are acoustically stratified and the stratification can be traced for at least 100 km on a line running parallel to the shelf break (Figure 5.20), suggesting the sediments were deposited by a laterally extensive bottom current, rather than sporadically deposited by gravitational processes. The interpretation of the sediments being delivered by along-slope transport is therefore preferred, with sediments sourced from the PITE/Abbot Trough boundary becoming entrained in turbidity currents, running in channels down the slope between drifts Four and Five, and the fine fraction being transported eastward

by a bottom current before being deposited. Debris flow deposits may also contribute to the sediments closer to the slope.

Near the base of the continental slope, Drift Five contains a basement feature assumed to be a seamount, which is approximately 60 km long (north to south), 15 km wide (east to west) and extends to 2500 m water depth. Turbidity currents can be deflected or separated by topography (Stow and Mayall, 2000), but geophysical data coverage here is too poor to analyse whether this has occurred.

7.4.2. Comparison to previous research

Scheuer et al. (2006a) suggested the large height of Drift One (Am4) and Drift Two (Am3) may be related to high accumulation of sediments in this area sourced from PITW. Here, Drift One is interpreted as the amalgamation of at least two smaller drifts, with surface turbidity channels supplying down-slope material from PITW and from the inter-trough area between PITE and PITW. The down-slope component of Drift Two is sourced entirely from this inter-trough area.

Uenzelmann-Neben and Gohl (2014) suggested Abbot Trough, PITE and the inter-trough area between PITE and PITW were the sources of glaciogenic sediment in the eastern Amundsen Sea since 4 Ma. The position of turbidite channels concurs with this hypothesis, with the exception of Drift One, which has the additional input of glaciogenic sediment supplied from PITW. Interestingly, the seismic data suggest sedimentation rates for Drift One are higher in the uppermost seismic unit (4 Ma to present) than the previous unit dated 14.1-4 Ma, despite PITW being the dominant source of sediment in the eastern Amundsen Sea during that time (Uenzelmann-Neben and Gohl, 2012, 2014). This suggests the source of glaciogenic material to at least Drift One was temporally variable, particularly over millions of years.

7.4.3. Depositional Model

Sedimentation in the drifts during the Late Quaternary occurred mostly during **glacial periods**, when down-slope sediment supply by turbidity currents and the subsequent pirating of the fine-grained material by bottom currents led to the deposition of thick terrigenous mud units (Figure 7.19a). Ice expansion across the ASE shelf led to large fluxes of sediment being delivered to the outer shelf and upper slope, marked by the slope progradation (e.g. Nitsche et al., 2000). Some of this sediment was then subject to mass wasting on the continental slope due to the impact of sediment loading and high pore-water pressure on sediment shear strength. In areas of high meltwater production relative to sediment load, particularly at the eastern edge of PITW and the inter-trough area separating PITW from PITE, turbidity currents were initiated at the shelf break and repeated flows eroded deep gullies into the outer shelf and upper slope. Some gullies connect to smaller channels on the mid and lower slope, where some connect dendritically to form large channels running between the drifts and onto the surface of Drift One. The action of turbidity currents on the 2-4° slope provided near-optimum conditions for erosion at the base of the slope, resulting in a channel partially separating drifts Two, Three and Four from the slope.

The sediment cores suggest the dense base of the turbidity currents largely followed the bathymetry and remained in the channels, with coarse material deposited along channel floors. Occasionally, the coarse grained fraction could spill over the channel banks, resulting in the laminated, terrigenous sand layer observed in core PC496. Some sediment may have been deposited as channel levees, particularly on the western levee, due to deflection by the Coriolis effect. However, drift geometry suggests much of the fine grained material was captured by the bottom current, transported eastwards and deposited on the drift crests. The steep, western flanks of the drifts facing the channels were probably maintained through a combination of mass wasting and bottom current action, as in the drifts west of the Antarctic Peninsula (Camerlenghi et al., 1997; Pudsey, 2000).

Fine grained material from a turbidity current can remain in suspension for more than a month in the absence of a bottom current (e.g. Stow and Bowen, 1978) and become entrained in the nepheloid layer. A bottom current with a velocity of 5 cm/second could,

theoretically, move clay grains c.130 km in a month, the same distance as the width of Drift One. As the other drifts are much narrower, and given the high clay content of the drift sediments, it is inferred that repeated erosion by turbidity currents in the intra-drift channels prevented the drifts from merging with each other and becoming elongated along-slope (with the exception of the offshore ends of Drifts Four and Five).

During glacial periods terrigenous detritus in the nepheloid layer was largely dominated by the locally-derived, fine-grained component of turbidity currents (cf. Camerlenghi et al., 1997). Minor components were also supplied via the erosive action of bottom currents on seafloor sediments (sortable silt data suggest bottom currents were too weak to erode sediments in the Amundsen Sea, but clay mineral data suggest clays were transported from further afield, perhaps from the sub-Antarctic South East Pacific), by vertical settling of biogenic material and volcanic glass, IRD deposition and re-suspension of sediments via the action of burrowing organisms (Faugères and Stow, 1993). The nepheloid layer during glacials was largely barren of biogenic material, due to both the northwards expansion of the sea ice limit (e.g. Benz et al., 2016) and possibly increases in carbonate and biogenic silica dissolution.

Interaction of this sediment in the nepheloid layer with an eastwards-flowing, weak bottom current led to the mixing of the locally sourced, kaolinite-rich sediment with far-travelled, smectite-rich clay being supplied by the bottom current. There is little evidence for erosion, with no obvious hiatuses or lag deposits, and the impact of the bottom current is mostly from selective deposition. A reduction in the velocity of the bottom current then led to clay deposition. The high clay content of the majority of the drift sediments suggests the bottom current was very weak but fast enough to transport clay and silt grains for typically <50 km from channel levees to drift flanks and crests. Sediments deposited during glacial periods are therefore a combination of fine grained material initially supplied by turbidity currents and transported and deposited by bottom currents, grains (clay to fine sand) deposited as rare overspill deposits by turbidity currents, a minor component of far-travelled clay deposited by the bottom current, IRD and rare biogenic material deposited by vertical settling.

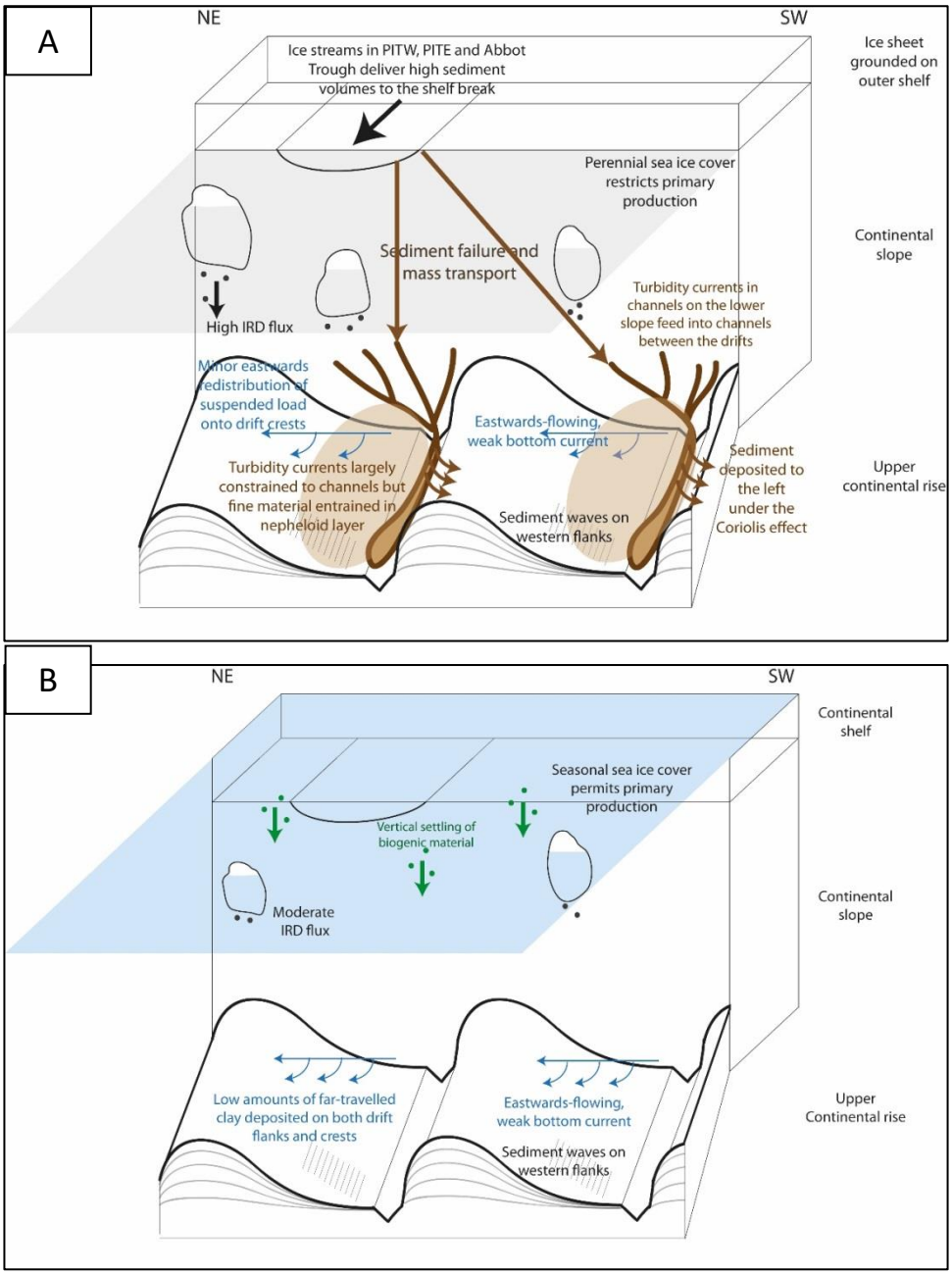

Figure 7.19: Schematic (not to scale) showing idealised processes of drift maintenance in the eastern Amundsen Sea during Late Quaternary A) Glacial periods and B) Interglacial periods. Inferences regarding primary production and sea ice coverage have been made using biogenic silica and Ba/Ti data. IRD flux has been inferred using gravel counts on X-radiographs and the sand and gravel content of sediment samples: MAR_{IRD} was higher during glacial than interglacial periods.

Although it is clear that bottom currents were persistent and affected sedimentation in the drifts throughout both glacial and interglacial periods in the late Quaternary, the

sortable silt data show consistent glacial-interglacial variability only in core PS58/253-1, which was suggestive of a faster bottom current speed during interglacials. Any enhancement in smectite deposition during glacial periods was likely diluted by the local inputs of relatively kaolinite-rich clay. The position of the ACC fronts may have shifted northwards due to the extensive, perennial sea ice cover and so it remains unclear how the drifts were affected (Rebesco et al., 1997; Brackenridge et al., 2011).

Deposition during **interglacial periods** was dominated by along-slope smectite-rich bottom currents, but low sedimentation rates allowed for pervasive bioturbation (Figure 7.19b). Bottom currents were weak, resulting in clay-rich sediments, but may have been faster than during glacial periods, based on the sortable silt data of PS58/253-1. Down-slope transport during peak interglacial periods was minimal to non-existent, as sediment delivery to the slope was reduced and sediment shear stress stabilised. The reduced extent of sea ice compared to glacial periods led to increased biogenic activity, leading in turn to increased carbonate and biogenic silica deposition via pelagic settling, possibly reduced dissolution and increased preservation of biogenic material.

The morphology of the drifts has therefore arisen primarily through deposition, with the sediment core chronologies and particularly the seismic data (Uenzelmann-Neben and Gohl, 2012, 2014) indicating long-term accumulation of sediments and changes in morphology of the drift-channel systems related to major palaeoenvironmental changes. Erosion by turbidity currents has led to the development of gullies on the slope and a channel system running between the drifts. Mass wasting is probably responsible for maintaining the steep, channel-facing side of the drift crests and for the undulating surface of Drift One.

7.4.4. Present Day Deposition

The presence of surface sediment waves, possibly active turbidity current channels (with no infill) and contourite-hemipelagite surface sediments dating to c.5.6-6.1 ka (^{14}C date of BC497 surface sample) suggest both contourite and turbidite processes may have been active on the drifts in the recent geological past. However, the sediments visible in the sub-bottom profiler data show the structure of the drifts did not change in the recent

geological past, with well-established channels and most drift crests showing laterally extensive acoustic stratification and continuous, parallel reflectors.

The typically low sedimentation rates at the core sites compare with an estimated sedimentation rate of 16 cm/kyr by Scheuer et al. (2006a) for Drift Two (Am3) since 5.3 Ma. The sedimentation rate was 17 cm/kyr in MIS 6 at site PS58/255-2, but this was atypical for the average sedimentation rate across the drifts, suggesting sedimentation today is lower than it was in the Pliocene and/or early Pleistocene. Similarly, Uenzelmann-Neben & Gohl (2014) calculated a sedimentation rate of 14.5 cm/kyr for the uppermost seismic unit (ASR-IV) of the drifts, which began to form at 4 Ma. However, this was the highest sedimentation rate of the four seismic units in the drifts, with sedimentation rates of 5.9 cm/kyr for unit ASR-III (14.1-4 Ma), 8.7 cm/kyr for unit ASR-II (21-14.1 Ma) and 4.5 cm/kyr for ASR-I (c.60-21 Ma) (Uenzelmann-Neben and Gohl, 2014), suggesting drift growth is continuing. This is at odds with the reduced number of mass transport deposits visible in ASR-IV and interpreted by Uenzelmann-Neben & Gohl (2012) as indicative of less sediment delivery to the slope and upper continental rise following the switch from a warm to a cold based ice sheet. Gohl et al. (2013) noted the positions of both PITE and PITW have not changed since the first glacial advances at 19.2-16 Ma, which suggests they possibly acted as conduits for sediment to the drifts since their formation began 60-21 Ma ago (Uenzelmann-Neben and Gohl, 2012).

If the calculated sedimentation rates of Uenzelmann-Neben and Gohl (2014) are not taken into account, the presence of a very weak bottom current and the low sedimentation rates suggest that the drifts grow slowly now and their shape is enhanced rather than changed, with spatial differences in sedimentation being too low to cause a significant change in their shape or structure. The drifts are therefore in a stage comparable to the “drift maintenance stage” identified by Rebesco et al. (1996) for the drifts west of the Antarctic Peninsula, with the depositional environment allowing for slow growth and enhancement of the drifts but no change in structure. However, if the calculated sedimentation rates for the seismic units by Uenzelmann-Neben and Gohl (2014) are correct, classification as the “drift growth stage” may be more appropriate. The apparent amalgamation of two or three smaller drifts to Drift One suggest it may be in a drift growth stage. The drilling of IODP site 379 in early 2019 may help to address this question by providing further constraints on the age of the seismic units.

7.4.5. Style of deposition

Other areas of the Antarctic continental slope with a similar low gradient (<3°) to that of the eastern Amundsen Sea typically feature a trough mouth fan (Dowdeswell et al., 2004, 2008). Investigation of seismic data by Nitsche et al. (2000) and Uenzelmann-Neben and Gohl (2012, 2014) does not suggest any link between the morphology of the underlying basement and the drift formation and geometry, as has been suggested for a drift in the western Bellingshausen Sea (Nitsche et al., 2000).

Trough mouth fans (TMFs) typically form where high sediment flux to the shelf break by ice streams coincides with a slope of <1° (Ó Cofaigh et al., 2003). The eastern Amundsen Sea features a wide continental shelf and several large palaeo-ice streams advanced across the shelf during past glacials (Nitsche et al., 2000; Lowe and Anderson, 2002; Evans et al., 2006; Graham et al., 2009; Larter et al., 2009, 2014; Jakobsson et al., 2012; Gohl et al., 2013; Hochmuth and Gohl, 2013). Sediment supply is unlikely to be a factor in restricting TMF formation, given the shelf is up to 500 km wide and both the mid and outer shelf have a sedimentary substrate ≤7 km thick (Lowe and Anderson, 2002; Gohl et al., 2013). Instead, the mode of sediment delivery, related to slope angle, is probably the critical factor. The gradient of the continental slope, typically 2-4°, is too high for ideal TMF development as slope angles greater than 1° encourage turbidity currents to form, eroding gullies and leading to sediment bypass of the upper slope, rather than forming the debris flows needed for TMF formation (Ó Cofaigh et al., 2003). For comparison, the Belgica TMF is on average 3 km thick with a maximum thickness of 4 km (Nitsche et al., 2000; Dowdeswell et al., 2008), whereas the maximum height of the Amundsen Sea drifts is only 900 m. This is a significant difference, even taking into account the redistribution of sediment in the drifts by a bottom current.

7.5. Comparison to other Antarctic mixed drifts

Regarding all contourite drifts from around Antarctica, the drifts of the eastern Amundsen Sea (henceforth referred to as the EAS drifts) are most similar to those found west of the Antarctic Peninsula (AP drifts), where mixed drift development is associated with turbidity current channels. With particular emphasis on comparisons with the AP

drifts, the following observations are made, with key similarities between the two sets of drifts summarised in Table 7.1 and key differences in Table 7.2.

Similarities	Amundsen Sea drifts	Antarctic Peninsula drifts
Dimensions	38-130 km wide, ≤400 km long, standing 500-900 m above the sea floor	Dimensions: 50-100 km wide, ≤200 km long, standing ≤1000 m above the sea floor (Rebesco et al., 2002)
Orientation	Lie predominantly perpendicular to the slope	
Amalgamation	Drift One may be two amalgamated drifts	AP drifts 6 and possibly 4 are amalgamated (Rebesco et al., 2002)
Grain size	Spatial variability in grain size is restricted to drift crests vs drift flanks, with significant no down-slope changes	
Channels	Channels running between the drifts are typically 5-10 km wide and 70-200 m deep	Channels running between the drifts are typically <10 km wide and ≤150 m deep (Pudsey, 2000)
Sediment composition	Sediments in both sets of drifts are poorly sorted and typically brown, bioturbated and IRD-rich in interglacial periods and grey, laminated and fine grained in glacial periods (Pudsey, 2000).	
Grain size	0.2-2.2 cm/kyr (interglacial) and 0.1-17.2 cm/kyr (glacial)	1.1-4.3 cm/kyr (interglacial) and 1.8 to 13.5 cm/kyr (glacial) (Pudsey, 2000)
Drift formation	Similar mechanism proposed for both; in glacial periods, turbidity currents supply nepheloid layer with fine-grained material, which is pirated and deposited down-stream by the bottom current. Interglacial sediments are mixed contourites-hemipelagites. Drifts now in 'drift maintenance' stage.	

Table 7.1: Key similarities between the Eastern Amundsen Sea drifts and the Antarctic Peninsula drifts.

Table 7.2 (overleaf): Key differences between the Eastern Amundsen Sea drifts and the Antarctic Peninsula drifts.

Differences	Amundsen Sea drifts	Antarctic Peninsula drifts	Possible reasons for difference
Geometry	Elongate and narrow	Oval shaped	May be related to continental slope angle and length, affecting how far turbidity currents travel
Asymmetry	Gently sloping western flank, steeper eastern flank	Gently sloping eastern flank, steeper western flank	Reflects the influence of different bottom currents flowing in opposite directions
Orientation	Three drifts are aligned oblique to the margin, to varying degrees	Drifts are mostly perpendicular to the margin	May be related to along-slope elongation by bottom current or in response to turbidity current channel migration
Sediment waves	Sediment waves more common on the EAS drifts than on the AP drifts		May be related to bottom current speed and directional stability
Relation to palaeo-ice stream troughs	The channels mostly originate in front of the inter-trough area	The channels mostly originate in front of palaeo-ice stream troughs	May be related to slope angle impacting on gully formation, or to differences in meltwater production/sediment flux
Slope gullies	Deep gullies incise the shelf edge, suggesting turbidity currents were initiated at the shelf break	The upper slope is dominated by debris flows; turbidity currents maybe initiated on the lower slope or upper rise (Rebesco et al., 1997)	May be related to slope angle. Unknown potential differences in glacial and/or meltwater dynamics
Connection to slope	All drifts are connected to the slope but 3 drifts have an erosional depression at the foot of the slope	Mostly detached drifts with channels separating drifts from slope	Possibly due to steeper slope off the AP
Clay mineralogy	Kaolinite is abundant, particularly during glacial periods.	No kaolinite in glacial sediments, ≤16% during interglacial periods in Drift 7 (Lucchi et al., 2002).	Reflects icebergs from kaolinite source area in ASE reaching AP drifts only in interglacials.
CCD depth	$CaCO_3$ present (planktonic foraminifera) at core top, 3450 m water depth	$CaCO_3$ absent from surface sediments in water depths of 2729-3662 m (Pudsey, 2000)	Modern CCD shallower above AP drifts than EAS drifts, possibly linked to corrosivity of bottom current
Biogenic silica content	5-20 wt.% biogenic silica (mostly diatoms) during glacial periods	<5 wt.% biogenic silica during glacial periods	Unclear; possibly fewer polynyas off AP or more corrosive bottom current

Morphology

The EAS drifts are large but of a comparable size in terms of width (38-78 and 130 km) and height (500-900 m above the sea floor) to other Antarctic mixed drifts where sediments have been largely supplied via ice streams to the shelf edge: drifts in the Cosmonaut Sea are 10-100 km wide and 700-1200 m tall (Kuvaas et al., 2005), drifts off Wilkes Land are 25-50 km wide and 275-490 m high (Escutia et al., 2002) and the AP drifts are 50-100 km wide and ≤1000 m tall (Pudsey, 2000; Rebesco et al., 2002).

Both the AP and EAS drifts are bounded by turbidity current channels which appear to limit the width of the drifts. The turbidite channels around the AP drifts have resulted in the drifts being oval shaped, with a wide centre and narrowing at their proximal and distal ends, with their long axes orientated perpendicular to the slope (Rebesco et al., 2002) (Figure 7.20 and 7.). In contrast, the EAS drifts are elongate and narrow, with the exception of Drift One, which may be the result of the amalgamation of two elongate drifts. This difference is probably related to the large differences in continental slope gradient between the two areas, which has an impact on the mode of sediment delivery (e.g. how far the turbidity currents will extend onto the continental rise) and the geometry of the resultant deposits.

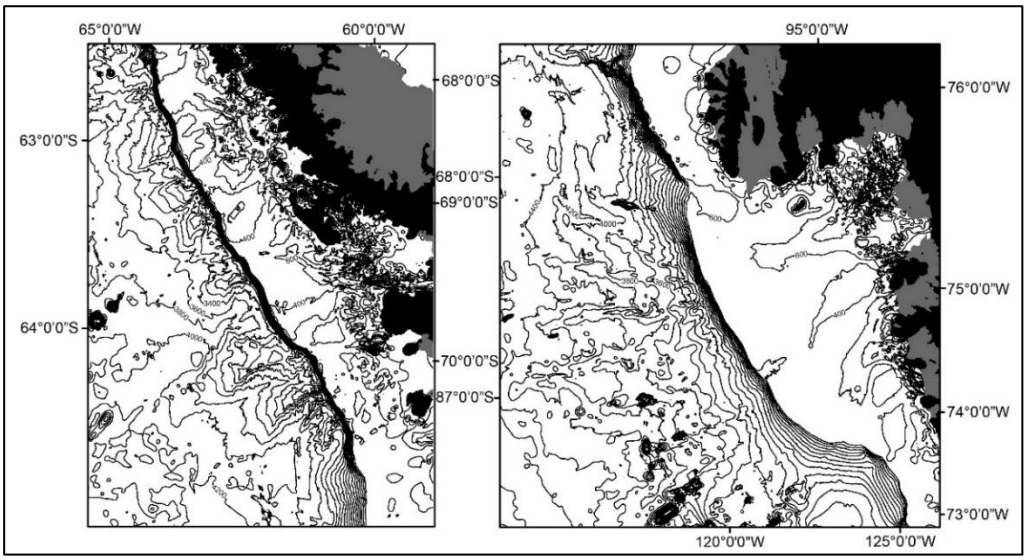

Figure 7.20: Bathymetric maps of the Antarctic Peninsula drifts (left) and the Amundsen Sea drifts (right) on the same spatial scale with 200 m contours. Dark grey areas of the continent indicate ice shelves; black areas indicate grounded ice. Bathymetry from IBCSO (Arndt et al., 2013).

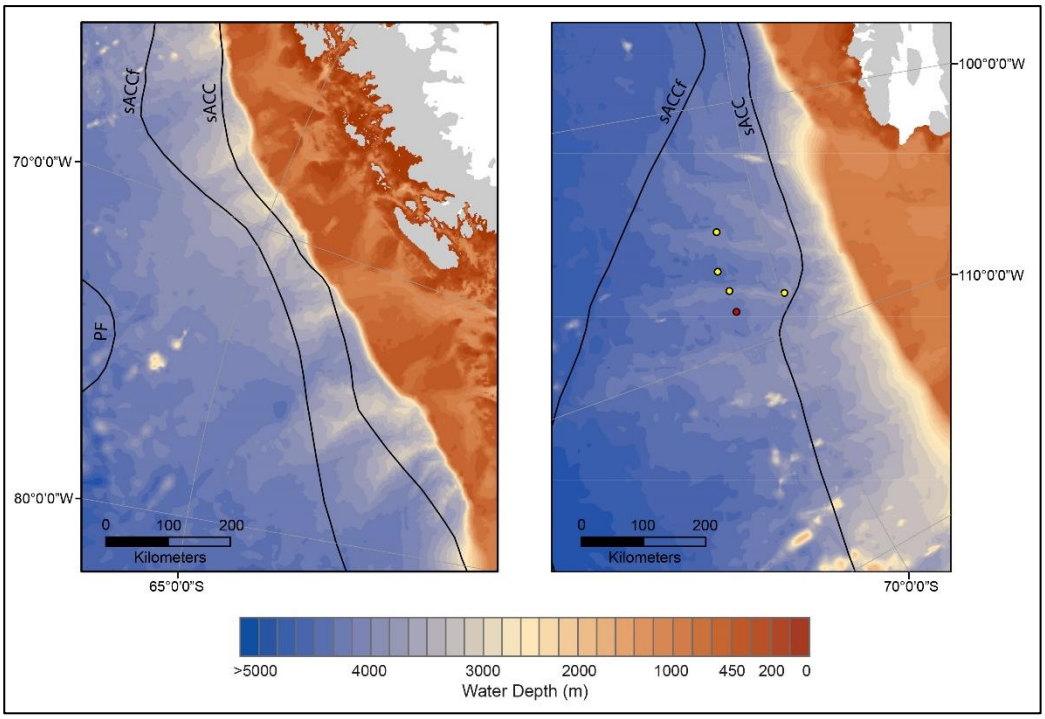

Figure 7.21: Bathymetric maps showing the Antarctic Peninsula drifts (left) and Amundsen Sea drifts (right) on the same spatial (with identical colour coding for water depth). White areas of the continent indicate ice shelves; Grey indicates grounded ice. ACC fronts according to Orsi (1995) are also shown. Bathymetry from IBCSO (Arndt et al., 2013).

At 250-433 km in length the EAS drifts are relatively long when compared to other Antarctic drifts (e.g. <200 km in the northern Weddell Sea (Maldonado et al., 2005), mostly >100 km in the Cosmonaut Sea (Kuvaas et al., 2005) and 100-300 km for the AP drifts (Pudsey, 2000)). However, they are not uniquely long, as turbidity currents have been identified at 400 km from the slope in the Cosmonaut Sea and >500 km from the slope in the Weddell Sea in large channel systems feeding from cross-shelf trough, where they have formed channel-levee deposits (Michels et al. 2002; Kuvaas et al., 2005). The Cosmonaut Sea levees and EAS drifts both have relatively low angle continental slopes of 4-6° (in the eastern sector of the Cosmonaut Sea, where the long turbidity current channel is located) and 2-4°, respectively. Pratson et al. (2000) suggested the length of the continental slope is a factor for the travel distance of turbidity currents (Figure 7.22).

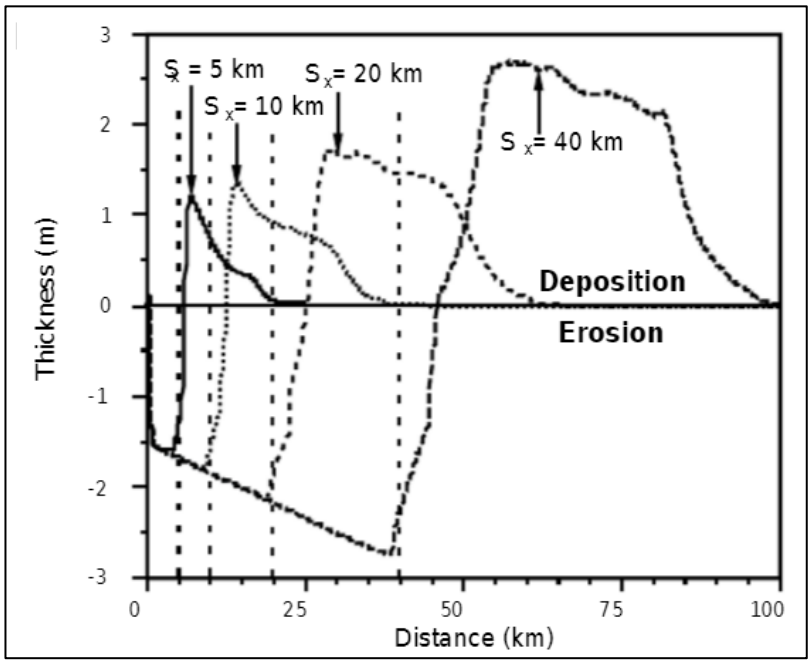

Figure 7.22: Variation in the thickness of turbidite beds and length of turbidity currents with increasing slope length (S_x). The dashed line indicates the base of the continental slope. From Pratson et al. (2000).

Based on a slope angle of 3° and a slope height of 3000 m (500 m water depth at the shelf break and 3500 m water depth on the upper continental rise), the slope in the EAS is 57 km long. In comparison, based on a slope angle of 16° and a slope height of 2100 m (500 m water depth at the shelf break and 2600 m water depth on the upper continental rise), the slope west of the AP is 7.6 km long. Individual turbidity currents in

the EAS are therefore expected to travel more than three times further. This highly simplified mechanism could offer at least a partial explanation as to why the drifts in the two areas have similar heights but the EAS drifts are typically much longer.

Most mixed contourite-turbidite drifts lie perpendicular to the slope, and the degree of change in orientation in the sea-ward ends of EAS drifts 4 and 5 is rare amongst the other Antarctic drifts studied to date. Some drifts in the Cosmonaut Sea feature a change in orientation to a lesser degree, or are aligned at an angle of <90° to the slope (in their entirety) (Kuvaas et al., 2005). In both the Cosmonaut Sea and the EAS, the drift crest runs parallel to the turbidity current channel, from which the drifts are supplied with sediment. The change in direction of the channels is assumed to be related to along-slope elongation by the sACCf in the EAS and to topographical deflection in the Cosmonaut Sea.

The asymmetry of the AP drifts, with a steep south-western flank containing hiatuses and gullies, and gently-sloping, laterally continuous north-eastern flank, corresponds to the action of the westward-flowing modified WSDW (Camerlenghi et al., 1997), and the reverse asymmetry is seen in the EAS drifts, characteristic of an eastwards-flowing bottom current. Both sets of drifts show parallel, laterally continuous reflectors and acoustic stratification on the gently-sloping flanks (Rebesco et al., 1996). The similarities in asymmetry and the high clay content of the drift sediments suggest the bottom currents affecting the two sets of drifts are similarly weak. However, in the Cosmonaut Sea, Kuvaas et al. (2005) noted drifts which were asymmetric in both directions, with the drift geometry linked to the distribution of turbidity current channels and therefore the supply of down-slope sediment. This suggests bottom current flow has a greater impact on drift geometry, relative to turbidity currents, in the EAS and offshore from the western AP than it does in the Cosmonaut Sea. This may be a function of the down-slope sediment flux (i.e. the frequency of turbidity currents and the amount of sediment transported to the drifts), or to the strength or persistence of the bottom current.

EAS Drift One is likely composed of two amalgamated drifts, resulting in a plateaued profile. AP Drift 6 and possibly also Drift 4, as well as the levees in the Cosmonaut Sea, have similar geometries and are also interpreted as amalgamated drifts (Kuvaas et al.,

2005; Rebesco et al., 2002).

Many areas of the Antarctic continental rise are characterised by mixed drifts in close proximity to, or even adjoined to, channel-levee deposits, where turbiditic deposition dominated over an unfocused and/or low velocity bottom current (e.g. western Weddell Sea (Michels et al., 2001), western Bellingshausen Sea (Scheuer et al., 2006b, 2006c). The bottom current in the EAS must therefore be faster (which is unlikely, given the high clay content of the sediments and evidence for a weak bottom current) or more laterally extensive than the bottom currents elsewhere as the asymmetry of the EAS drifts extends along their whole length.

As in the case of the AP drifts (Rebesco et al., 2002), there are no spatial patterns identified in grain size composition of the sediments from the EAS drift crests, with spatial variability restricted to drift crests vs drift flanks. This concurs with the finding that turbidity currents are restricted to the inter-drift channels, with no channels on the drift crest (with the exception of EAS Drift One, which has a complex system of channels on the drift surface attributed to a possible amalgamation of two drifts), and suggests the bottom current is of a similar strength along the length of each drift.

Nitsche et al. (2000) noted that sediment waves were more common on the EAS drifts than the AP drifts and related this to sedimentological differences, bottom current speed and directional stability of flow, or perhaps that the EAS drifts are more distal. No cores have been collected from the sediment wave areas of the EAS drifts, but cores from elsewhere on the drifts suggest the drift sediments are similar to the AP drifts. Sediment waves were identified on the western flanks of EAS drifts 3 and 4 c.100 km from the base of the continental slope, thus proximity to the slope does not appear to be a factor, given the AP drifts are longer than 100 km. The prevalence of sediment waves on the EAS drifts compared to the AP drifts is therefore most likely related to differences in bottom current speeds and/or directional stability or to increased amounts of turbidity current overspill from the channels.

Turbidity Current Channels

The EAS drifts are fed by channels mostly sourced from the inter-trough area on the outer shelf between PITE and PITW, with EAS Drift One receiving some sediment via PITW and Drift Five receiving the bulk of its sediments via the Abbot Trough. In contrast, the placement of the channels feeding the AP drifts is controlled by the location of palaeo-ice stream troughs on the outer shelf, with drift crests aligned approximately with the inter-trough areas (Amblas et al., 2006), although channel heads are also found offshore from the inter-trough areas (Pudsey, 2000; Dowdeswell et al., 2004). This difference may be linked to differences in the meltwater production or sediment flux in the inter-trough area of the ASE compared to similar areas on the AP shelf, resulting in the generation of more turbidity currents (usually slopes off inter-trough areas are characterised by slumps and slides), or to differences in the slope angle impacting on the degree of erosion by gullies, with a steeper slope angle leading to deeper gully erosion and more constraint over the steering of flows. The implications of this difference on sediment supply are unclear.

Deep gullies traced down-slope from the upper slope suggest turbidity currents were initiated at the shelf break in the EAS whereas debris flow deposits on the lower slope off the AP suggest turbidity currents there were initiated on the lower slope or upper rise (Rebesco et al., 1997), with the gullies observed on the upper slope (Dowdeswell et al., 2004) mainly eroded by subglacial meltwater (Gales et al., 2013).

Channels running between the EAS and AP drifts are of a comparable width and depth, typically <10 km wide and ≤150 m deep (Pudsey, 2000). Turbidity current channels are present between other mixed drifts (e.g. eastern Riiser-Larsen Sea (Solli et al., 2007)), suggesting highly erosive turbidity current flows are a common feature on the Antarctic continental margin.

The EAS drifts are connected to the slope, although a channel, thought to be turbidity current related, partially separates drifts Two, Three and Four from the slope. The AP drifts are mostly detached drifts with a steeply-dipping south-eastern flank facing the

slope. The drifts are partially separated from the continental slope by 10-20 km wide turbidity current channels which run parallel to the shelf break before turning and running oblique to the margin between the drifts (Rebesco et al., 1997, 1998, 2002).

Composition of Drift Sediments

Both the EAS and AP drifts are composed predominately of fine-grained, terrigenous sediments, which show cyclical sedimentological changes related to climatic variations. The sediments are typically brown, bioturbated and IRD-rich in interglacial periods and grey, laminated and fine grained in glacial periods (Pudsey & Camerlenghi, 1998; Pudsey, 2000; Lucchi et al., 2002). The poor sorting and fine grain size of sediments in both sets of drifts suggest bottom currents of a similarly low velocity (Camerlenghi et al., 1997). Sedimentation rates are also comparable: 1.1-4.3 cm/kyr (interglacial) and 1.8 to 13.5 cm/kyr (glacial) on the AP drifts (Pudsey, 2000) and 0.2-2.2 cm/kyr (interglacial) and 0.1-17.2 cm/kyr (glacial) on the EAS drifts. Sedimentation rates are typically higher in glacial periods, reflecting increased sediment flux in response to grounded ice sheet advance across the continental shelf in both areas. Whilst sedimentation rates in the AP drifts are typically highest in MIS 2-4, sedimentation rates in the EAS drifts are greatest during MIS 6, reflecting glaciological differences in the source area and possibly variations in the mode of sediment delivery, with Pudsey (2000) suggesting meltwater plumes were more dominant than turbidity currents in delivering sediment to the AP drifts during MIS 2-4.

The AP drifts show a decrease in sedimentation rate during glacial periods with increasing distance from the margin, but no such offshore decrease in interglacials (Pudsey, 2000). The EAS drifts similarly show a decrease in MIS 2-4 sedimentation rate between site PC494 and the more distal site PS58/253-1, with similar interglacial sedimentation rates along the drift crests. This reflects the dominant down-slope supply of sediment during glacial periods depositing progressively less material with distance offshore, compared to the largely pelagic settling and deposition from bottom currents during interglacial periods resulting in a more even lateral distribution of sediments.

The clay mineral assemblages of the EAS and AP drifts highlight the different geologies of their sediment source areas. Kaolinite is abundant in the EAS drifts, particularly during glacial periods, but is absent from the glacial sediments of AP Drift 7 and present in only small quantities (≤12 %) during interglacial periods (Lucchi et al., 2002). This may reflect the relatively large amount of kaolinite supplied to the EAS drifts by ice sheet expansion and erosion of the kaolinite source rocks and sediments in the ASE hinterland and on the ASE shelf during glacial periods, compared to the AP drifts, with no kaolinite source known from the AP hinterland (Hillenbrand and Ehrmann, 2001). During interglacial periods, the clay mineral assemblage of the EAS drifts reflects a decrease in kaolinite supply and increased dilution by smectite deposited by bottom currents and probably sourced from the sub-Antarctic South Pacific. Smectite contents also increase in the AP drifts during interglacial periods, transported by bottom currents from the South Shetland Islands (Hillenbrand et al., 2003). Kaolinite contents in the AP drifts reflect deposition by icebergs sourced from the Amundsen Sea during interglacial periods (Lucchi et al., 2002), which rarely reach the AP during glacial periods due to perennial sea ice cover (Hillenbrand et al., 2003; Ehrmann et al., 2011).

The AP drifts, like the EAS drifts, lie mostly between the present winter and summer sea ice limits, and are ice-free for between 3 and 9 months a year (Pudsey, 2000). Pudsey (2000) found no calcareous organisms in the surface sediments from the AP drifts. However, foraminifera are also absent from Holocene sediments in the Amundsen Sea at all sites except PC494 which, at 3450 m water depth, is the shallowest core studied (at 3.5 cmbsf, approximately 6.8 % of the bulk sediment is planktonic foraminifera and 0.4 % is calcareous benthic foraminifera, total 6.5 % $CaCO_3$). The cores studied by Pudsey (2000) were in water depths of 2729-3662 m. This suggests the modern CCD is shallower off the western Antarctic Peninsula than in the Amundsen Sea as previously concluded by Hillenbrand et al. (2003). This suggests the bottom current in the EAS is less corrosive to carbonate than the corrosive WSDW which led to poor carbonate preservation in the AP drifts (Pudsey, 2000), or that the primary productivity in the EAS during an interglacial peak is lower than offshore from the western AP (Hillenbrand et al., 2003).

Biogenic silica contents during glacial periods are generally low in the AP drifts (<5 wt.%)

(Pudsey, 2000; Hillenbrand and Fütterer, 2001). Smear slide analysis indicated dissolution of diatoms in glacial sediments in the Amundsen Sea but biogenic silica contents are typically 5-20 wt.%. As sedimentation rates are similar between the two areas, this suggests that during glacial periods WSDW was more corrosive to siliceous microfossils than the bottom water in the EAS, or that sea ice, nutrients and/or oxygen conditions are more conducive to diatom production in the EAS than offshore from the AP. Sea ice cover on the Amundsen Sea margin during glacial maxima was probably less severe than on the western AP margin because of polynyas (Thatje et al., 2008; Lu et al., 2016). Interglacial biogenic silica contents between sediments of the two drift sets are similar (10-35 wt.%), while TOC contents are low (<0.5 %) and show no spatial or temporal trends (see Chapter 6.1.2-6.1.5; Pudsey, 2000).

Drift Formation

The EAS and AP drifts formed via similar processes, with sediment largely supplied via turbidity currents in erosional channels, the fine-grained components entering the nepheloid layer and being transported by a bottom current too weak to retain the sediment in suspension, leading to deposition on a drift down-stream. Both the EAS and AP drifts suggest turbidity currents were the dominant mechanism of sediment delivery during glacial periods and deposition of far-travelled material from bottom currents, in combination with vertical settling of biogenic material and IRD, were dominant during interglacial periods (Rebesco et al., 2002, 2007). Pudsey (2000) also suggested that meltwater plumes supplied fine-grained sediment to the AP drifts, particularly during MIS 2-4, but spatial coverage of cores in the EAS drifts is not sufficient to note whether the thickness of the sediments deposited during MIS 2-4 is consistent with deposition from meltwater plumes along the upper slope, with the shelf break acting as a line source (Pudsey, 2000). It is plausible to consider that meltwater plumes contributed to drift development, given the present day upwelling of warm CDW onto the Amundsen Sea shelf. However, the sedimentation rates at proximal site PC494 are similar to those at distal site PS58/253-1, and the long length of the EAS drifts, with only minor thinning offshore, suggest that turbidity currents were the dominant mode of terrigenous sediment delivery to the drifts.

Various types of contourite drifts are commonly found in close proximity, such as in the northern Weddell Sea (Maldonado et al., 2005) and the Riiser-Larsen Sea (Solli et al., 2007). The absence of other drift types in the EAS is indicative of the point-source nature of the sediment delivery, with the drift development heavily reliant on, and orientated around, the position of turbidity current channels.

The turbidity current channels remain active with no evidence in sub-bottom profiles of recent infilling, in contrast to the former turbidity current channels in the western Weddell Sea which, following a reduction in turbidity current activity, are now largely infilled or maintained by contour currents (Michels et al., 2001).

According to Uenzelmann-Neben & Gohl (2012, 2014), drift growth in the eastern Amundsen Sea began 60-21 Ma. Uenzelmann-Neben and Gohl (2014) suggest this was initiated by sediment supply from a delta off PITE, meaning a pre-existing channel system and down-slope sediment supply were active before drift growth. In contrast, drifts in the western Weddell Sea developed from sediment slumps on the upper continental rise as contourites, with no evidence of turbidite channels during the initial phases of drift growth (Michels et al., 2001).

Seismic profiles and age models suggest the EAS drifts experienced progressive accumulation of detritus along their full lengths, with laterally extensive deposition within each drift (Uenzelmann-Neben and Gohl, 2012, 2014). This is also shown by the Late Quaternary sediments studied here (Chapter 7.1). This style of deposition contrasts with the drifts of the eastern Riiser-Larsen Sea, where initial drift deposition on the lower continental rise was followed by deposition progressively closer to the slope, with sediment build-up preventing deposition further seawards (Solli et al., 2007).

7.6. The Record of Late Quaternary West Antarctic Ice Sheet History

7.6.1. Is there an 'ice sheet signal' preserved in the drifts?

The Late Quaternary terrigenous sediments of the eastern Amundsen Sea contourite drifts are composed mostly of locally sourced, kaolinite-rich sediments deposited during glacial periods when sedimentation rates were relatively high (≤17.2 cm/kyr). Cyclical variations in clay mineralogy reflect changes in the proportion of locally derived sediments as opposed to far-travelled sediments, reflecting glacial-interglacial fluctuations in the extent of the WAIS in the ASE. Delivery of terrigenous sediment to the drifts has primarily occurred via turbidity currents, ice rafting and the transport of sediment within ocean currents on the continental rise and, to a lesser degree, flowing off the ASE shelf (Walker et al., 2013). Dust flux to the Pacific sector of the Southern Ocean was three times greater during glacial periods than during interglacial periods, but was still present in only trace amounts (Lamy et al., 2014).

During glacial periods, high rates of delivery of locally-sourced sediment mean a localised ice sheet signal is preserved. During interglacial periods, IRD contents increase but MAR_{IRD} decreases, reflecting decreased deposition from icebergs over the core sites but possibly a more regional signal due to reduced sea ice coverage (cf. Pudsey, 2000). Typically low sedimentation rates and an increase in the smectite:kaolinite ratio during interglacial periods reflect a large decrease in the local ice sheet signal and may reflect a much more regional signal, with terrigenous material transported to the drifts by bottom currents and iceberg rafting. The eastwards-flowing, circumpolar nature of the ACC, with AABW sourced from the Ross Sea, suggests terrigenous material deposited by the bottom current in the eastern Amundsen Sea will be largely sourced from the Amundsen and Ross Seas and areas of the sub-Antarctic South East Pacific within the Ross Sea Gyre (Chapter 7.2.1).

It is therefore inferred that the ice sheet signal preserved in terrigenous sediments deposited during interglacial periods reflects inputs from a large, regional source area with (at least) a large proportion of sediments supplied by the sectors of the WAIS that

drain into the Amundsen and Ross Seas. In contrast, the ice sheet signal preserved in terrigenous sediments deposited during glacial periods is much more localised to the WAIS in the ASE.

7.6.2. Glacial-interglacial variability in glacigenic sediment delivery

The supply of glacigenic sediment (the "ice sheet signal") is particularly large in the drift sediments deposited during glacial periods. The mean MAR_{terr} (mass accumulation rate of terrigenous sediments) of sediments deposited during glacial periods (8.5 g/cm²/ka) is seventeen times the MAR_{terr} of sediments deposited during interglacial periods (0.5 g/cm²/ka) in PS58/253-1 (Figure 7.23). Clay mineralogy has been used to show the terrigenous sediments in the drifts are primarily sourced from the ASE (Chapter 7.2.2). The relatively kaolinite-rich clay mineralogy is consistent with the supply of terrigenous sediment from the Pine Island and Thwaites glaciers (Ehrmann et al., 2011), which expanded into PITE and PITW during at least the LGM (Larter et al., 2014). High sedimentation rates are indicative of large volumes of sediment being supplied to the drifts primarily via turbidity currents, with glacigenic sediment supplied by ice in PITE, PITW and the area separating the two troughs (Chapter 7.3.3). The offshore thinning of the drifts and the decrease in MIS 2-4 sedimentation rate from the proximal PC494 (7.8 cm/kyr) to the distal PS58/253-1 (6.2 cm/kyr) reflect the down-slope supply of terrigenous, locally sourced sediment. The high sedimentation rates suggest the grounding line of the ice sheet was on the outer shelf and at, or close to, the shelf break for much of MIS 2. This is consistent with shelf-based inferences of the LGM ice sheet extent in the eastern Amundsen Sea (Larter et al., 2014) (Figure 7.24).

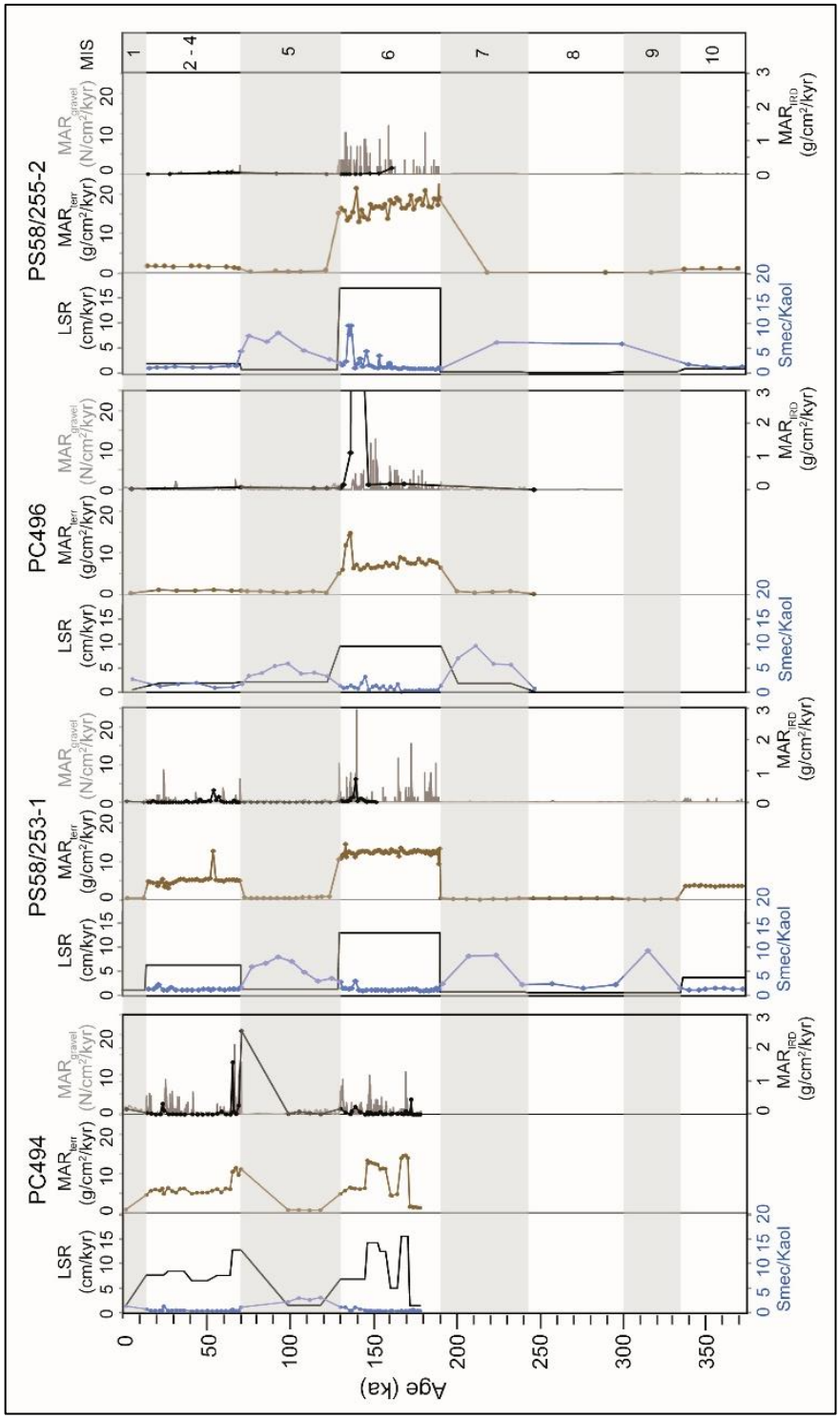

Figure 7.23: Sedimentological and mineralogical indicators of glacigenic sediment delivery vs. age in the four sediment cores. LSR: Linear sedimentation rate (based on RPI in PC494, averaged based on glacial/interglacial boundaries in the other cores). Smec/Kaol: Smectite/kaolinite ratio. MAR_{terr}: Mass accumulation rate (MAR) of terrigenous material in the bulk sediment. MAR_{gravel}: MAR of grains >2 mm counted on x-radiographs. MAR_{IRD}: MAR of terrigenous grains >63 µm. Grey shaded bars indicate interglacial periods, and non-shaded bars indicate glacial periods.

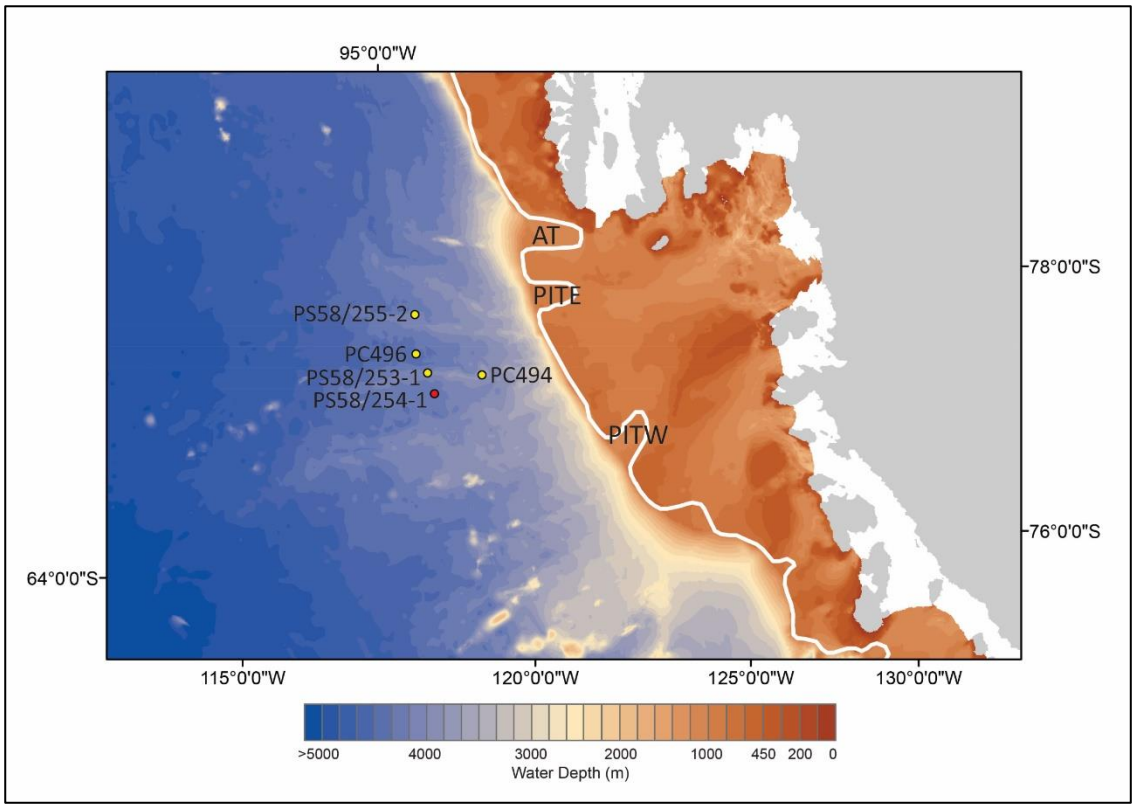

Figure 7.24: Reconstruction of the 20 ka grounding line of ice in the eastern Amundsen Sea (white line) (Larter et al., 2014). AT: Abbot Trough. PITE: Pine Island Trough East. PITW: Pine Island Trough West. Bathymetry from IBCSO (Arndt et al., 2013). Grey areas indicate the contemporary grounded ice sheet, white areas indicate contemporary ice shelves (Fretwell et al., 2013). The position of the sediment cores investigated in this research are indicated, along with the position of sediment core PS58/254-1 (Hillenbrand et al., 2009a).

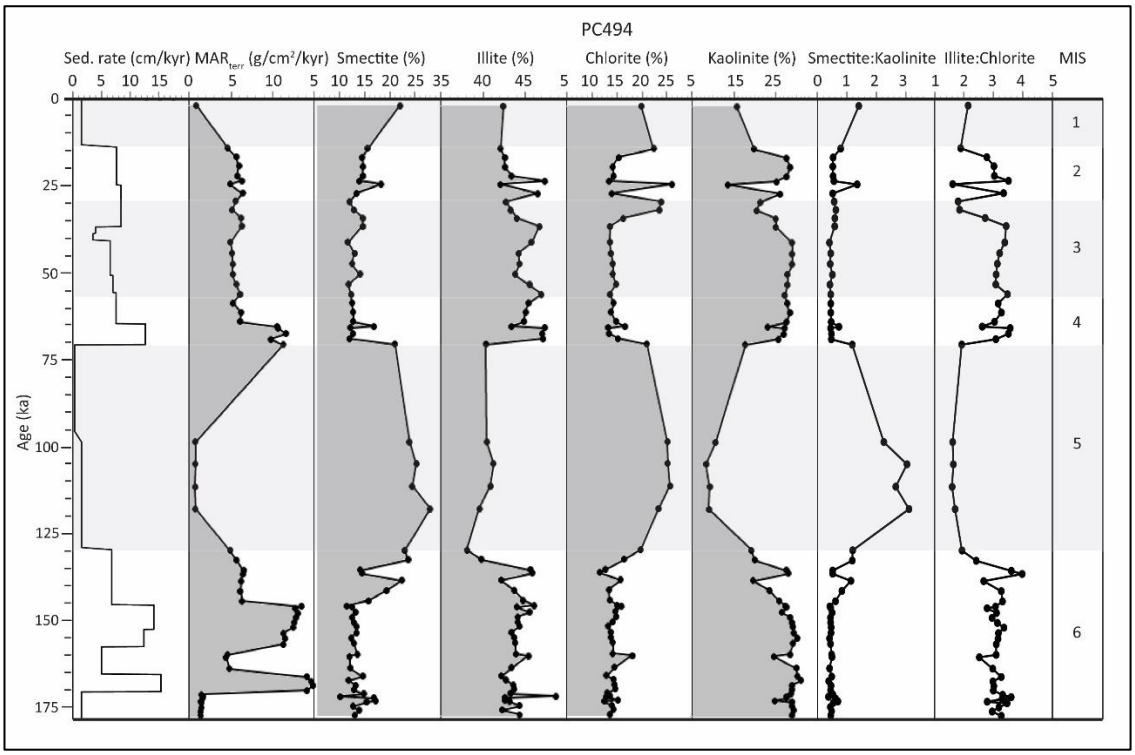

Figure 7.25: Clay mineralogy, sedimentation rate and MAR_{terr} vs. age of sediment core PC494.

The provenance of the terrigenous material deposited during interglacial periods reflects deposition primarily from the bottom current(s), providing a mix of far-travelled, relatively smectite-rich and chlorite-rich sediments (Figure 7.25). Sparse sampling of the Pacific sector of the Southern Ocean means it is unclear from which area the smectite has been sourced, however, it may have been entrained in the sub-Antarctic South East Pacific by the ACC (see Chapter 7.2.1). This would imply an offshore smectite source, meaning the ice sheet signal would be diluted and indistinguishable from terrigenous sediments sourced from elsewhere. In the central and western Amundsen Sea, the sACC lies hundreds of kilometres offshore and is unlikely to entrain much of the sediment supplied down-slope by mass wasting and turbidity currents. Terrigenous sediments deposited during interglacial periods therefore reflect a much more regional signal of both glacially-sourced and non-glacially-sourced material, with the glacially-sourced material most likely to have been sourced from the Ross Sea area, perhaps as far west as the westernmost limb of the Ross Sea Gyre at 160°E (Locarnini, 1994).

The input of large amounts of locally sourced, kaolinite-rich clay during glacial periods

means it is unclear to what extent (if any) the provenance of sediment carried and deposited by the bottom current may vary during glacial periods, although the sortable silt record suggests bottom current speed was similar in glacial and interglacial periods in three of the four cores. Any clay mineralogical signal from the ice sheets draining into the central and western Amundsen Sea is likely to be heavily diluted during transport and particularly during deposition on the drifts by the large amount of local input. Therefore, the regional ice sheet signal is best seen in the ice rafted debris record, with clay mineralogy most representative of local ice sheet variability.

7.6.3. Ice Rafted Debris

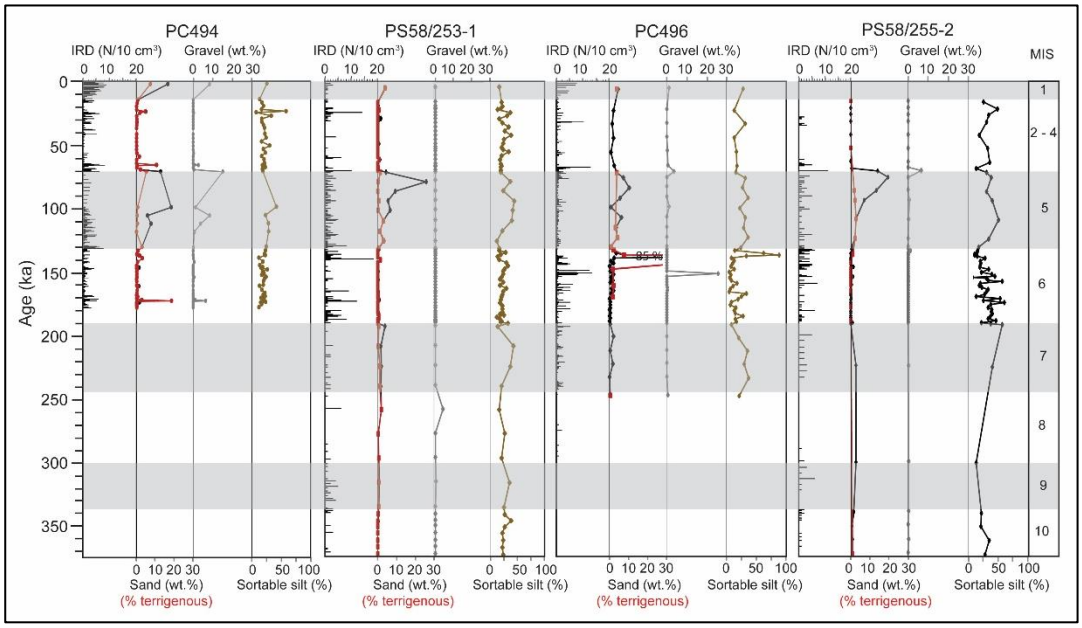

Figure 7.26: Ice rafted debris indicators and percentage sortable silt in cores PC494, PS58/253-1, PC496 and PS58/255-2. For each core, the IRD is shown as number of gravel grains per 10 cm^3, sand and terrigenous sand contents and gravel content.

The amount of IRD in the cores is comparable with the IRD contents of PS58/254-1 (Hillenbrand et al., 2009a), with a maximum of 19 grains per 10 cm^3 in the ≤375 kyr record but typical contents of 0-7 grains per 10 cm^3 (Figure 7.26). Both IRD counts and MAR_{IRD} are generally greater during glacial periods when the presence of IRD is also more continuous, as opposed to the more dispersed IRD that characterises interglacial

periods. This suggests icebergs were melting over the core sites near-continuously during glacial periods and more periodically during interglacial periods. It further suggests that IRD deposition during glacial periods was high enough that it was not diluted by fine-grained sediment input primarily from turbidity currents and bottom currents. This is in contrast to the Peninsula drifts, where lower IRD contents in glacial than interglacial periods have been linked to small amounts of ice rafting (a function of a thin ice sheet and small drainage basins) and IRD being subject to increased dilution during glacial periods by fine-grained sediments (Pudsey, 2000). The high IRD production during glacial periods in the eastern Amundsen Sea probably therefore reflects deposition from a large drainage area, which, given the movement of icebergs within the westwards-flowing Antarctic Coastal Current and entrainment within the eastwards-flowing ACC, likely includes all of the Amundsen Sea Sector and possibly the eastern Ross Sea (Chapter 2.3.1).

Minor increases in the IRD content towards the end of MIS 6 in PC496, PS58/253-1, PS58/255-2 and PS58/254-1 (Hillenbrand et al., 2009a) indicate a small increase in the amount of iceberg calving and/or the amount of icebergs melting over the core sites. This may reflect the start of deglaciation approximately 10-20 ka prior to the glacial-interglacial boundary. However, the IRD contents are likely too low to represent major ice sheet break-up, and the increase in IRD content may also reflect changes in surface water temperature or sea ice extent in the central and western Amundsen Sea (Hillenbrand et al., 2009a).

A small increase in IRD content is present at the MIS 5/4 transition in all cores (Figures 8.4 and 8.5), shown most clearly in Figure 7.27 as two separate peaks in MAR_{gravel} of PC494 at c.71-69 ka and 67-65 ka. The increase is also present in PS58/254-1 (Hillenbrand et al., 2009a). Explanations for this maxima include instability in the growing ice sheet or a rapid expansion of ice to the shelf break. A similar peak is seen in the IRD content of sediment core PC466 from Drift 4 off the Antarctic Peninsula, dating to c.71 ka (Vautravers et al., 2013), suggesting the IRD records may reflect regional increases in iceberg calving.

IRD contents during MIS 2 are lower and more dispersed than during MIS 6, which may suggest the ice sheet was more stable or less proximal to the core sites during MIS 2 or

that sea ice coverage was more of a restricting factor on iceberg drift in MIS 2 than MIS 6. There is no significant increase in IRD content at the MIS 2/1 boundary, i.e. the last deglaciation, in contrast to Peninsula Drift 4 (Vautravers et al., 2013). However, in keeping with the IRD record of Peninsula Drift 4 (Vautravers et al., 2013), the sediment cores feature an increase in IRD in the uppermost few centimetres. MAR_{gravel} and MAR_{IRD} in Holocene sediments are still relatively low compared to the rest of the cores. The sortable silt proxies also increase in the uppermost sample of PC494 and PC496 (Figure 7.24), suggesting increased amounts of selective deposition may have occurred due to a faster velocity bottom current.

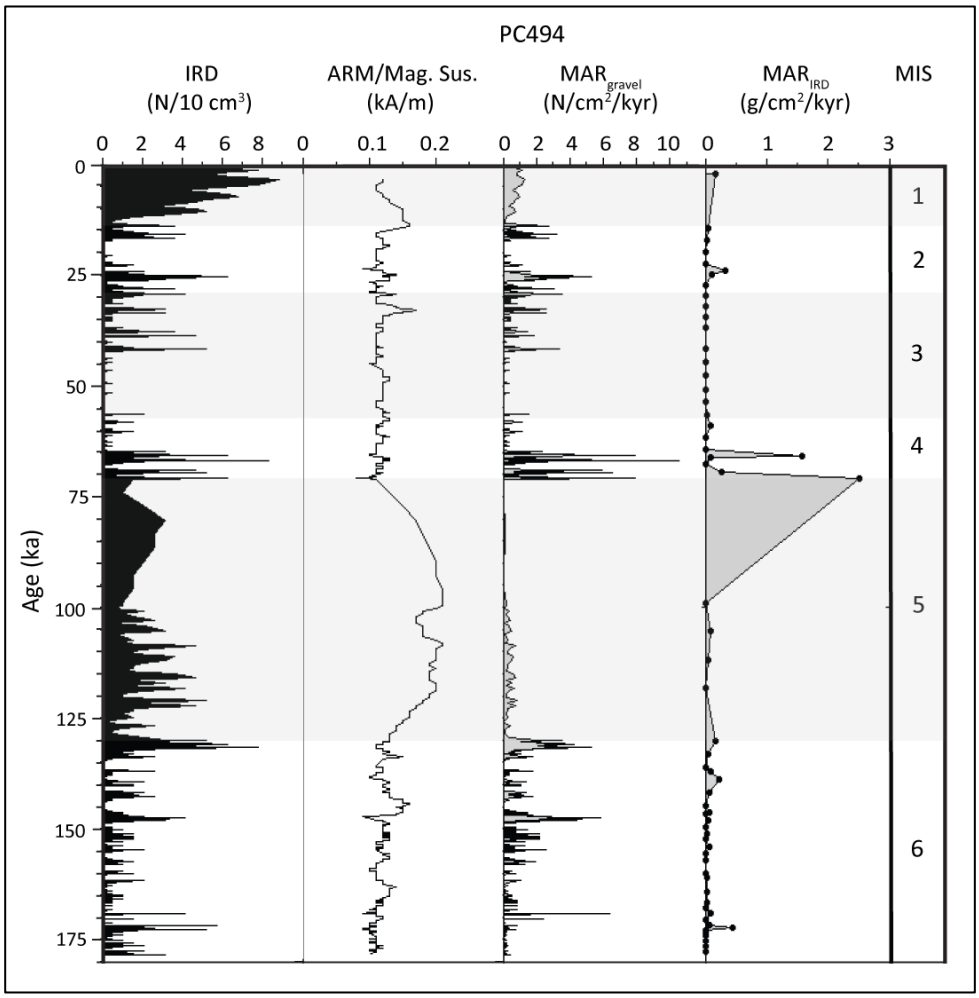

Figure 7.27: Ice rafted debris contents, mass accumulation rates and a magnetic grain size proxy in sediment core PC494. Anhysteretic remanent magnetisation (ARM) was acquired in an alternating magnetic field of 100 mT. Magnetic susceptibility (mag. sus) was measured on the same u-channel. MAR_{gravel} ($N/cm^2/kyr$) was calculated using counts of grains >2mm on x-radiographs. MAR_{IRD} ($g/cm^2/kyr$) was calculated from the percentage of terrigenous sand and gravel grains in each discrete sample.

Analysis of the sand fraction revealed quartz and feldspar dominated all samples, with minor components of mafic minerals, mica and assorted rock fragments. ARM/magnetic susceptibility ratios in PC494 and PS58/254-1 (Hillenbrand et al., 2009a) are relatively low during glacial periods (Figure 7.27), suggestive of a coarser magnetic grain size when compared to interglacial periods. The relatively small and dispersed terrigenous sand and gravel content and the poor correlation between the numbers of gravel grains (MAR_{gravel}) and the weight of sand and gravel (MAR_{IRD}) in PC494 (Figure 7.27) is conducive with the material being supplied by ice rafting rather than input of layers of coarse grained sediment by turbidity currents.

This is in contrast to the gneiss, mica schist and green schist IRD in the glacial-interglacial transition sequences dating to <75 ka in Peninsula Drift 4 (Vautravers et al., 2013), and suggests the IRD has not been deposited by icebergs drifting westwards from the Bellingshausen Sea. Instead, the source area during interglacial periods is likely to be the glaciers calving into the Amundsen Sea and possibly the Ross Sea, with icebergs drifting westwards within the Antarctic Coastal Current before becoming entrained in the eastwards-flowing ACC. During glacial periods, the advance of the ice sheet to the shelf break in many areas likely led to high calving rates and may have disrupted the westward movement of icebergs within the Antarctic Coastal Current, leading to the progression of increased numbers of icebergs northwards and eastwards over the core sites.

The increased IRD contents during glacial periods compared to interglacial periods may reflect increased proximity of the grounding line to the core sites. Alternatively, the lower temperature of the surface waters may have delayed melting and allowed far-travelled icebergs to travel further eastwards within the ACC than occurs in warmer, interglacial waters, particularly if the ice sheet was more proximal to the core sites. Summer sea surface temperatures over the core sites were 1-2°C cooler at the LGM than they are today (Benz et al., 2016). Similarly, the northwards expansion of the winter sea ice limit during the LGM meant that the core sites had perennial sea ice cover, which may have restricted iceberg drift compared to the seasonal sea ice cover of the present day (Benz et al., 2016). If similarly cold sea surface temperatures and perennial sea ice coverage were present in previous glacial periods, this may have slowed the drift of both locally-calved icebergs being produced by the more proximal grounding line, and far-travelled icebergs that may or may not have increased in number, resulting in greater

IRD deposition at the core sites. As many of the icebergs being transported by the ACC will be sourced from the glaciers of the Amundsen Sea, the similar lithology of samples deposited during both glacial and interglacial periods does not help in distinguishing the source of the IRD deposited on the drifts without further mineralogical analysis.

7.6.4. Indicators of ice sheet collapse

The sediment cores analysed in this study span the last 375 kyr but do not show any evidence for an episode(s) of major ice sheet disintegration. This is consistent with analysis of PS58/254-1 by Hillenbrand et al. (2009a).

The generally low mass accumulation rate of IRD in the cores suggests ice rafting to the drifts has been relatively low during the past 375 kyr. The clay mineralogy is highly correlated with glacial-interglacial periods and there is little change within any of these periods that might suggest collapse of part of the ice sheet. However, changes in sedimentation rate in PC494 and in colour, WBD and clay mineralogy in PS58/255-2 can be seen in the mid-late MIS 6 sediments in both cores and could represent variations in ice sheet dynamics at this time.

A major ice sheet collapse would likely lead to increased ocean stratification with large amounts of freshwater at the ocean surface reducing the production of sea ice and raising the CCD (Lucchi and Rebesco, 2007). Sea ice coverage is the dominant control restricting diatom growth in the eastern Amundsen Sea, but the sediment core records do not show any significant increases in biogenic silica or Ba/Ti or corresponding loss of $CaCO_3$ outside of the typical glacial-interglacial variability.

7.7. Late Quaternary palaeoenvironmental history of the Amundsen Sea

7.7.1. Productivity

Productivity proxies in the sediment cores suggest palaeoproductivity and/or dissolution were largely influenced by the climatic conditions with pronounced glacial-interglacial cyclicity in biogenic silica and $CaCO_3$ contents (Figure 7.28) related to both production and preservation.

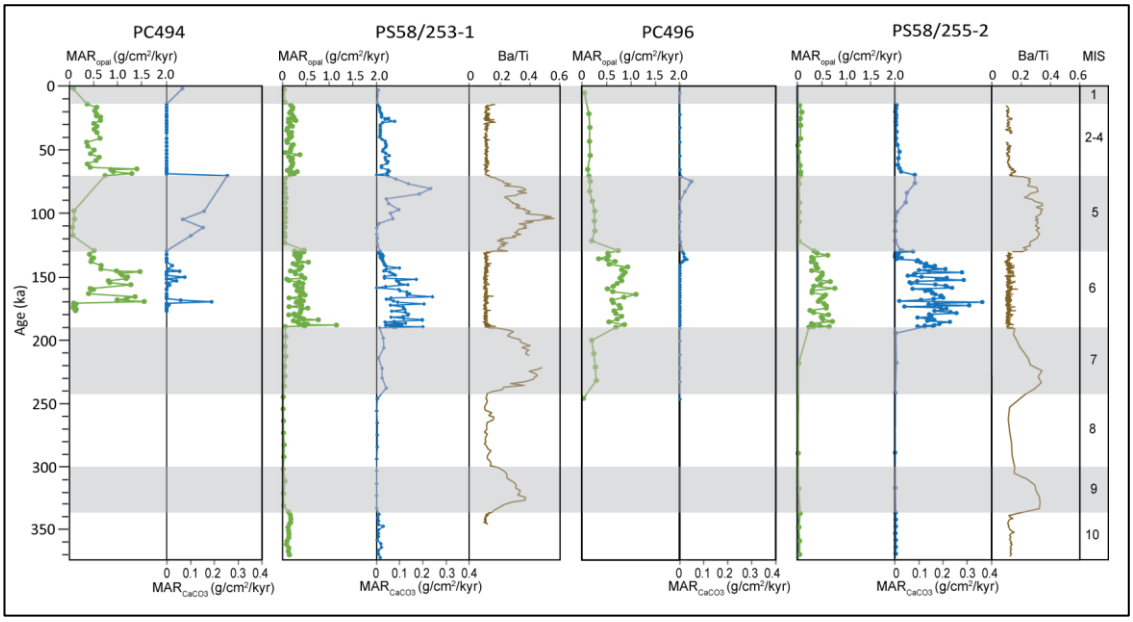

Figure 7.28: Productivity proxies in sediment cores PC494, PS58/253-1, PC496 and PS58/255-2. MAR_{opal}: Mass accumulation rate of biogenic silica. MAR_{CaCO3}: Mass accumulation rate of $CaCO_3$.

7.7.1.1. Biogenic silica

The biogenic silica content of the sediment cores is typically greater during interglacial than glacial periods. For example, the mean biogenic silica content of sediments deposited during interglacial periods in PS58/253-1 is 8.8 wt.% and peak biogenic silica content is 21.4 wt.%, compared to 3.2 wt.% and 10.7 wt.%, respectively, during glacial periods. Large differences in glacial-interglacial sedimentation rate are reflected in the MAR_{opal}, with mean MAR_{opal} in PS58/253-1 during interglacial periods of 0.05 g/cm²/kyr and during glacial periods of 0.26 g/cm²/kyr. The relatively high biogenic silica contents but low MAR_{opal} during interglacial periods are suggestive of reduced sea ice coverage

allowing for greater productivity, but greater dissolution compared to glacial periods when high inputs of terrigenous material would have buried the silica and minimised post-depositional dissolution.

Biogenic silica content is relatively high in PC494, particularly during MIS 2-4 with a mean content of 8.4 wt.% compared with mean contents of 3.5 wt.% in PS58/253-1 and 3.1 wt.% in PS58/255-2. This can be attributed to PC494 having a high linear sedimentation rate during MIS 2-4 of 7.8 cm/kyr (compared to 6.2 cm/kyr in PS58/253-1 and ≥1.9 cm/kyr in PS58/255-2), which led to more rapid burial of silica than at the other core sites and therefore minimised post-depositional dissolution (Warnock et al., 2015). However, biogenic silica content in MIS 2-4 is highest at the deepest water site, PC496, with a mean content of 12.6 wt.%. The enhanced preservation cannot be attributed to the linear sedimentation rate of just 1.8 cm/kyr, which has resulted in a low mean PC496 MIS 2-4 MAR_{opal} of 0.15 g/cm²/kyr compared to a mean PC494 MIS 2-4 MAR_{opal} of 0.62 g/cm²/kyr. A possible explanation is the nature of the deposition at site PC496 during glacial periods, with periodic deposition of spill-over from turbidity currents in the nearby channel leading to rapid burial of biogenic silica, minimising post-depositional dissolution, on a regular basis. Alternatively, PC496 may have been bathed by a different water mass, less corrosive to silica, than that affecting the cores at shallower water depths.

The glacial-interglacial cyclicity is also seen in the Ba/Ti ratio, which is positively correlated with biogenic silica and negatively correlated with wet bulk density, as in PS58/254-1 (Hillenbrand et al., 2009a).

Smear slides revealed diatoms comprised the overwhelming majority of the biogenic silica content of the sediment cores. Diatom production in the eastern Amundsen Sea is controlled mostly by sea ice coverage (Esper et al., 2010), and the glacial-interglacial cyclicity in biogenic silica content and Ba/Ti are therefore suggestive of perennial sea ice cover over the core sites during glacial periods and either seasonal coverage or an open ocean during interglacial periods. This concurs with the reconstruction of LGM sea ice extent of Benz et al. (2016) (Figure 7.29).

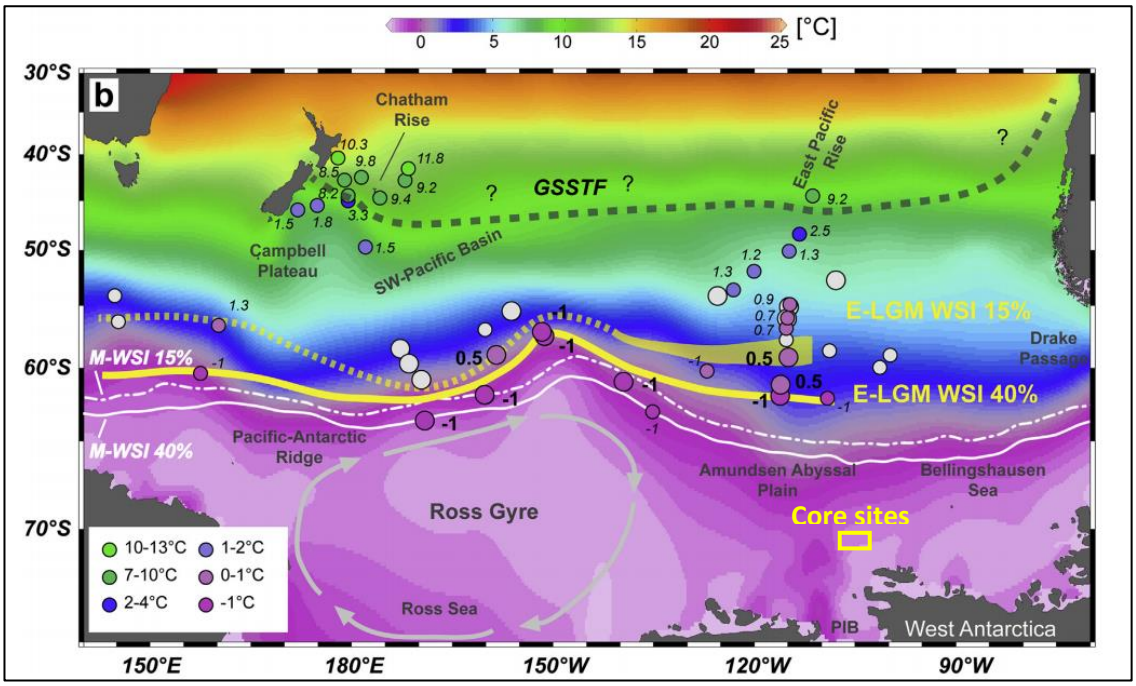

Figure 7.29: Estimated winter sea surface temperatures during the LGM (Benz et al., 2016). The approximate position of the sediment core sites presented in this thesis is indicated by the yellow box. GSSTF: Glacial Southern Subtropical Front. E-LGM WSI: Estimated LGM winter sea ice extent. E-LGM WSI 15% indicates the maximum winter sea ice extent (>15% September sea ice concentration). E-LGM WSI 40% indicates the extent of the average (40%) sea ice concentration. M-WSI 15% and 40% mark the corresponding modern sea ice extents.

7.7.1.2. $CaCO_3$

The $CaCO_3$ content of all samples is strongly controlled by the abundance of calcareous foraminifera in the sand fraction (Figure 7.28), which is almost entirely composed of *Neogloboquadrina pachyderma* sinistral. This species continues to dominate surface samples in the Amundsen Sea today and indicates polar conditions with seasonal seaice coverage persisted throughout the Late Quaternary (Chapter 2.7.3, Hauck et al., 2012). Calcareous and agglutinated benthic foraminifera are also present in trace amounts in sediments dating to MIS 7 (PS58/253-1), mid-late MIS 5 (PS58/253-1 and PC494) and the Holocene (all cores), suggesting the bottom water mass was oxygenated and the CCD below the core depths during these interglacial periods.

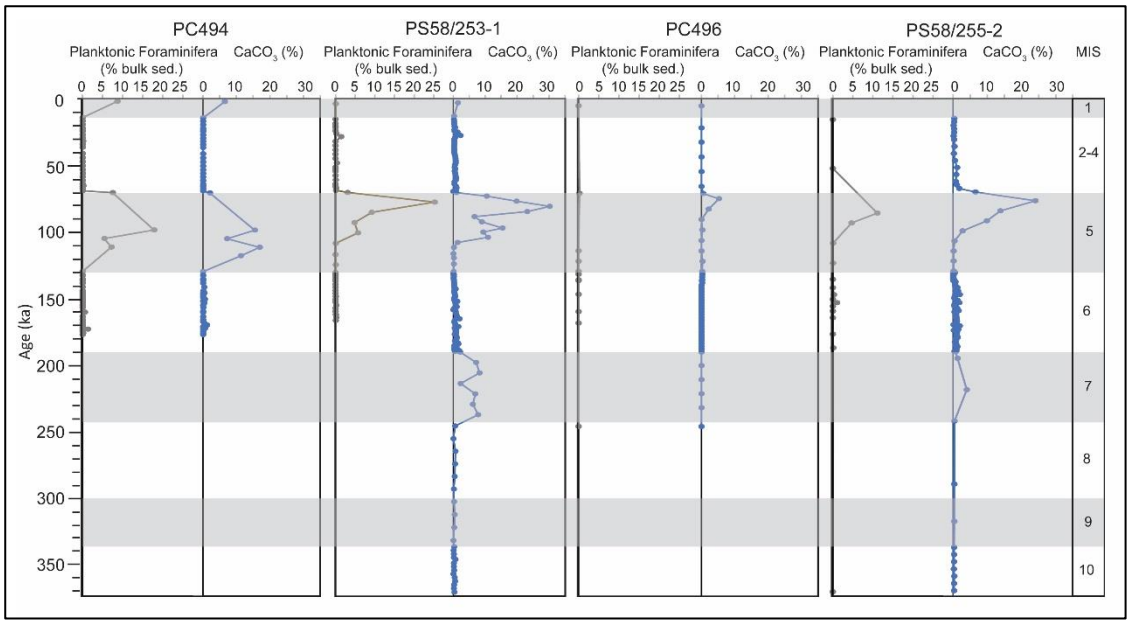

Figure 7.30: Calcareous planktonic foraminifera and $CaCO_3$ content of the four sediment cores.

$CaCO_3$ content is typically greatest during interglacial periods, whilst MAR_{CaCO3} is typically greatest during glacial periods and late interglacial periods, peaking at 0.4 g/cm^2/kyr in MIS 6 sediments in PS58/255-2. The low $CaCO_3$ contents but high MAR during glacial periods suggest productivity was restricted, probably by perennial sea ice cover, but the CCD remained below the core sites (except PC496) allowing the $CaCO_3$ to be preserved through rapid burial by the high terrigenous accumulation rates. The high $CaCO_3$ contents during interglacial periods suggest productivity increased, likely as a result of a reduction in the period of sea ice coverage over the core sites. Low MAR_{CaCO3} early in MIS 5 and the Holocene is probably a reflection of high rates of dissolution due to low sedimentation rates and a shallow CCD. This may be due to the low concentration of carbonate ions in seawater and large amounts of meltwater following deglaciation causing increased stratification and poor ventilation (Chapter 2.7.3). As productivity and therefore the concentration of carbonate ions in seawater increased during MIS 5 and the Holocene and ocean ventilation increased, the CCD was lowered, allowing for more $CaCO_3$ to be preserved.

$CaCO_3$ is present in only trace amounts prior to the MIS 7/6 transition, which suggests the CCD became shallower in the eastern Amundsen Sea c.191 ka. This concurs with the $CaCO_3$ record of PS58/254-1, which contains only traces of $CaCO_3$ from early MIS 17 (710 ka) to mid-MIS 5 (Hillenbrand et al., 2009a), suggesting the CCD lay below 4014 m water

depth during that period. With the exception of two samples from sediments dating to late MIS 5, which contain <6% $CaCO_3$, only traces of $CaCO_3$ are present in the deepest core, PC496, at 4230 m water depth. This suggests dissolution has been a major control on the $CaCO_3$ content of the sediments and that the CCD lay below 4230 m water depth during MIS 6 and fluctuated between 4014 m and 4230 m water depth post-MIS 6.

7.7.2. Nature of the Bottom Current

7.7.2.1. Flow speeds

The sortable silt data suggest the bottom current influencing the drifts has been weak for much of the last c.374 kyr, with an average percentage sortable silt value across all samples of 24.3% and mean sortable silt size of 17.9 μm. Based on correlation with current meters and sediment samples from the Weddell and Scotia Seas, this equates to a mean scalar flow speed of approximately 9.6 cm/sec^{-1} (McCave et al., 2017). However, based on a much wider, global database of samples, the sortable silt data suggest a mean scalar flow speed of approximately 3.0 cm/ sec^{-1} (McCave et al., 2017). Flow speeds less than 10-15 cm/sec^{-1} are too low to winnow sediments but would influence grain size via selective deposition (McCave and Hall, 2006). Most samples are clay-rich, with the average clay content (0.04-3.9 μm) of the <63 μm fraction of all samples 49.5% (by volume).

Both percentage and mean sortable silt values, particularly in PS58/253-1, are slightly higher during interglacial periods than glacial periods (Figure 7.31), suggestive of a faster bottom current speed. The particle size distribution of a typical interglacial sediment is skewed towards coarser grain sizes, with particularly less clay and more medium and coarse silt (Figure 7.32). In sediment core PS58/253-1 (the longest temporal record and most frequently sampled core), sediments deposited during interglacial periods had an average mean sortable silt value of 21.7 μm and average percentage sortable silt value of 29.3%, which decreased to 18.3 μm and 22.7%, respectively, during glacial periods. McCave et al. (2017) suggests these sortable silt values correspond to mean scalar flow speeds of 7.7 cm/sec^{-1} (based on global data) or 16.1 cm/ sec^{-1} (based on Weddell and Scotia Sea data) during interglacial periods, and 3.5 cm/ sec^{-1} or 10.3 cm/ sec^{-1},

respectively, during glacial periods. The large discrepancy between datasets has been attributed to the grain size of sediments supplied to the site of deposition (McCave et al., 2017). The scalar flow speeds based on global data are preferred here over the speeds inferred from Weddell and Scotia Sea data as the dataset is slightly larger and there is no evidence that the drift sediments have been extensively winnowed (e.g. periods of non-deposition in the high-resolution age model of PC494 or lag layers of high sand and gravel content), implying current speeds rarely, if ever, exceeded 10-15 cm/ sec^{-1} (McCave et al., 2017). The sortable silt proxy therefore suggests mean bottom current speeds in interglacial periods were approximately double that of glacial periods.

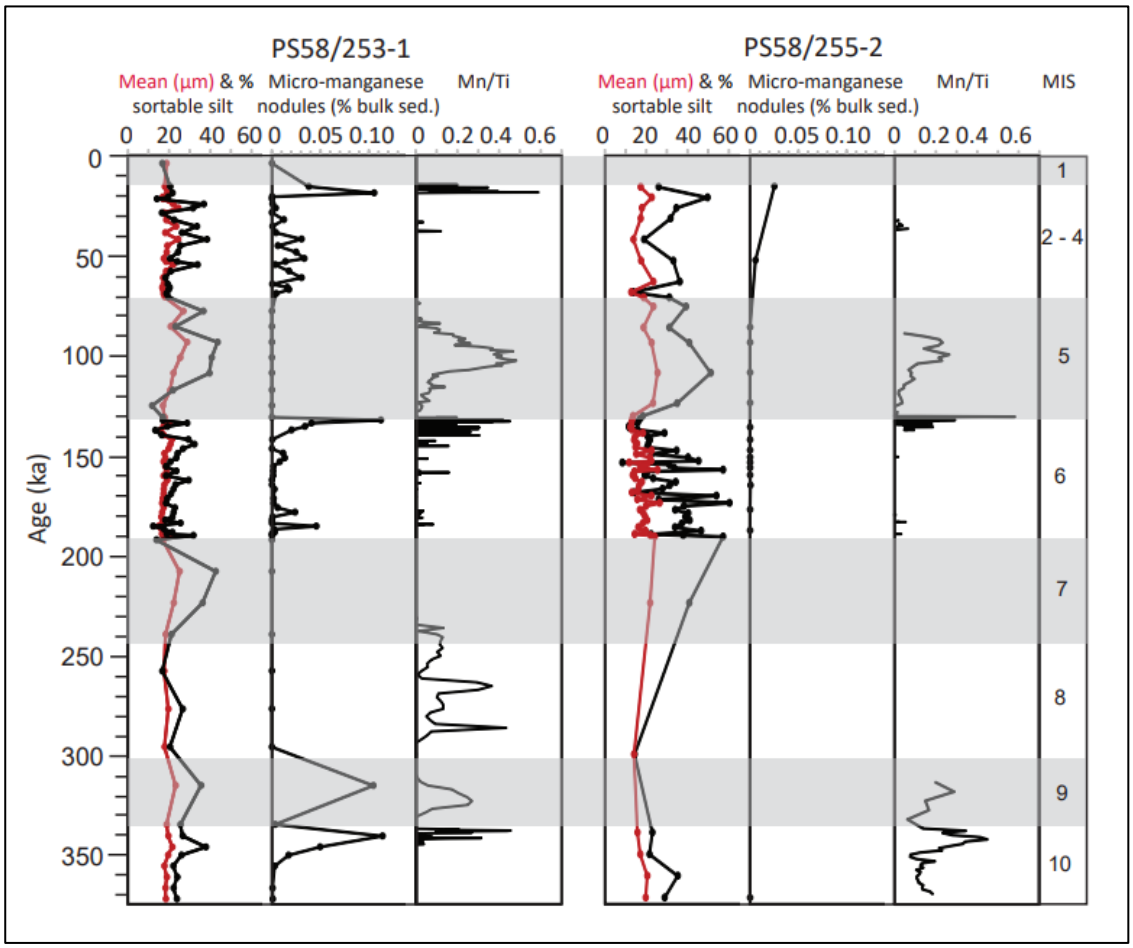

Figure 7.31: Sortable silt, micro-manganese contents and Mn/Ti of PS58/253-1 and PS58/255-2.

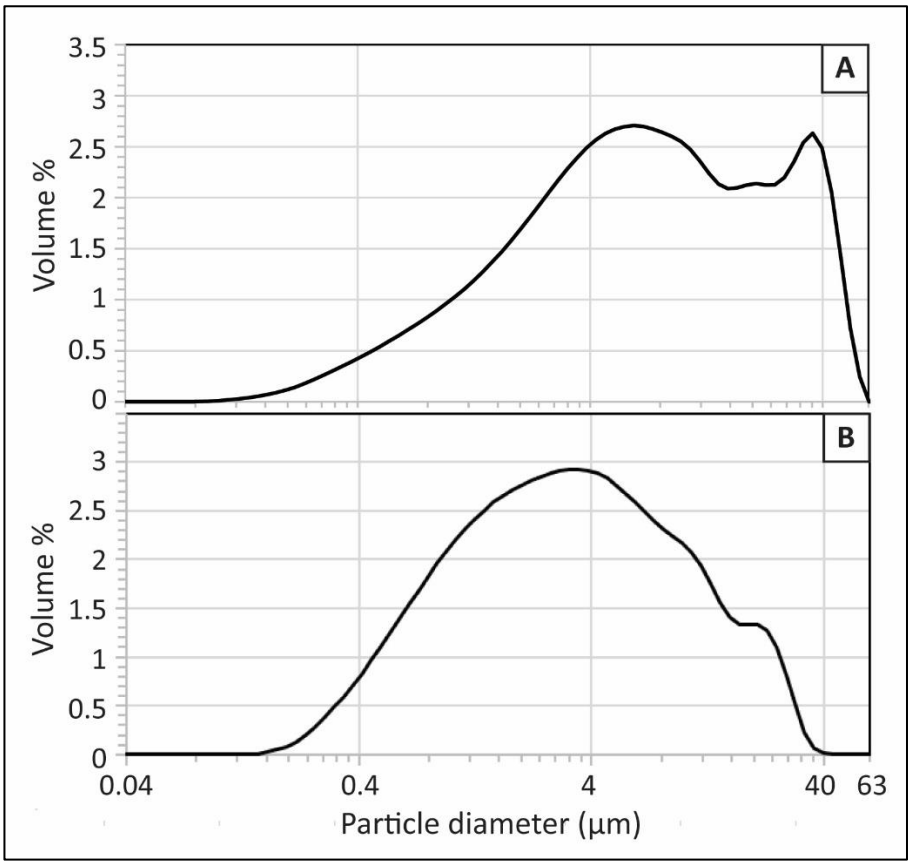

Figure 7.32: Example particle size distributions for representative interglacial (A) and glacial (B) sediments from PS58/253-1. Particle size is shown as a volume percentage of the 0-63 µm fraction. A: Sample from 405 cmbsf, the approximate mid-depth of MIS 5 sediments. B: Sample from 837 cmbsf, the approximate mid-depth of MIS 6 sediments.

It is unclear whether the bottom water mass in the eastern Amundsen Sea at the present day is LCDW or AABW (Chapter 7.2.1). However, AABW production was greater at the LGM than the present day, aided by brine rejection from the extended sea ice coverage, although models disagree on the extent of the production (Otto-Bliesner et al., 2007; Ferrari et al., 2014). AABW transport to the Amundsen Sea should therefore have been higher compared to the present day, and greater sortable silt values would be expected in MIS 2 than MIS 1 sediments. The opposite is true in the drift sediments, with the sortable silt data suggesting bottom current speeds are faster at present (and in previous interglacial periods) than they were in MIS 2 (and other glacial periods). One possible explanation for this is that, similar to the present day, LCDW is the dominant water mass over the drifts during interglacial periods and AABW during glacial periods, that the LCDW is of a higher velocity than the AABW and therefore that any glacial-interglacial change in AABW speed is not recorded in the sediments. A second possible explanation

is that the position of the sACCf fluctuates according to glacial-interglacial cycles and that the front lay closer to the drifts during interglacial periods than during glacial periods, with faster current speeds associated with the front leading to increased amounts of selective deposition. However, there is no correlation between sortable silt and smectite content within interglacial periods. A correlation between these values may have suggested increases in bottom current velocity were related to changes in the pathway of the current (such as movement of the sACCf away from the hypothesised source of smectite in the sub-Antarctic south Pacific) with a corresponding change in sediment provenance.

7.7.2.2. Ventilation

The presence of carbonate in post-MIS 7 sediments is suggestive of a well ventilated bottom water mass, which may have been less well ventilated prior to MIS 7, given the near absence of carbonate in PS58/254-1 between MIS 17 and MIS 5 (Hillenbrand et al., 2009a). Possible explanations include reductions in the sea ice coverage or stratification of the water column allowing for more ventilation, or a change in the water mass affecting the drifts. AABW is a more well ventilated water mass than CDW at the present day (Chapter 2.7.3, Majewski et al., 2016) and contrasts with the WSDW bathing the Peninsula drifts which is highly corrosive to carbonate (Pudsey, 2000).

Micro-manganese nodules are concretions of iron and manganese oxides <1 mm in diameter which form under redox conditions and low sedimentation rates and so can be used to comment upon bottom water ventilation (Mangini et al., 1990). Unlike larger manganese nodules, micro-nodules can form without a nuclei (such as a calcareous microfossil or siliceous test) (Chester and Jickells, 2012). Increases in the manganese content of late glacial and interglacial sediments have been identified in widely distributed marine sediment cores including in the Arctic Ocean (e.g. Jakobsson et al., 2000), North Atlantic Ocean (e.g. Mangini et al., 2001) and the Weddell Sea (Mangini et al., 1990).

Micro-manganese nodules are present in the sand fraction of PC494, PC496 and PS58/253-1 in sediments dating to late MIS 6. The sediments have been interpreted as contourites, largely composed of sediment supplied to the bottom current by turbidity currents. This suggests that, even if the nodules did not develop in-situ and were

perhaps transported to the drifts by turbidity currents, inferences about bottom current ventilation are still valid as the nodules were transported by bottom currents and were deposited without being dissolved. High Mn/Ti values also show increases in the manganese content of the sediments of both PS58/253-1 and PS58/255-2 in late MIS 6, with high Mn/Ti values initially present only intermittently, becoming more continuous in late MIS 6. High Mn/Ti values are also present in sediments dating to late MIS 10 (PS58/253-1 and PS58/255-2), MIS 9 (PS58/255-2) and MIS 8 (PS58/253-1 and PS58/255-2). Mn/Ti ratios in MIS 5 sediments are lower than in MIS 6 sediments and peak approximately half way through the interglacial sediments, but no micro-manganese nodules are found in any of the sediment samples. Mn/Ti ratios are low in early MIS 2-4 and increase towards the end of this period, when micro-manganese nodules are found in the three shallower cores. As manganese nodules are present in sediments dating to both glacial and interglacial periods and in lithofacies interpreted as contourites,

The increased Mn/Ti ratio and maxima in micro-manganese nodules at the end of glacial periods, particularly late in MIS 6, suggests a reduction in sedimentation rate and/or changes in the chemical characteristics of the bottom current may have occurred. Micro-manganese nodules require low sedimentation rates to avoid burial as they grow slowly, mainly at the sediment-water interface (Hesse and Schacht, 2011). However, the chronology developed for PC494, including the use of relative palaeomagnetic intensity analysis, suggests sedimentation rates in late MIS 6 were high at 14.1 cm/kyr (153-146 ka) and 6.8 cm/kyr (146-130 ka) and of a similar rate to sediments deposited during other periods which are barren of micro-manganese nodules. Bioturbation is believed to contribute to micro-manganese nodule development by keeping nodules at the sediment-water interface where most growth occurs (Hesse and Schacht, 2011). The presence of micro-manganese nodules and, in particular, the maxima in Mn/Ti do largely coincide with increases in bioturbation. However, the late MIS 6 increase in Mn/Ti begins in a laminated unit c.50 cm below bioturbated sediments, and there are also bioturbated units with no micro-manganese nodules. On the contourite drifts, the transport and possible winnowing of sediment by the bottom current may also have maintained the presence of nodules at the sediment-water interface. However, the sortable silt proxies are of low-moderate values in the sediments containing micro-manganese nodules and high Mn/Ti ratios and there is no evidence that the core

sediments have been winnowed.

The absence of micro-manganese nodules in Holocene sediments is attributed to the bottom waters being well oxygenated, leading to oxidation of almost all organic matter (Mangini et al., 1990). The precipitation of manganese from seawater requires reducing conditions in order for manganese to be mobilised in seawater in the reduced (or acidic) and soluble form Mn(II), then oxidising (or alkaline) conditions are required to oxidise the manganese to Mn(IV), which is insoluble, leading to precipitation (Mangini et al., 2001; Chester and Jickells, 2012). The presence of micro-manganese nodules could therefore indicate changes in the oxygen content of bottom waters, with suboxic conditions followed by oxic conditions occurring towards the end of the glacial periods. This is in keeping with increased manganese precipitation seen in late glacial sediments elsewhere (Mangini et al., 1990). Reducing conditions can occur if the oxygen content of a water mass is too low to oxidise organic matter (Mangini et al., 1990). This could occur if the water mass has a velocity of < 2 cm/s and/or if the ventilation of the water mass is reduced (Mangini et al., 1990). TOC contents, although generally low, do decrease at the end of glacial periods in the sediment cores which correspond to increases in Mn/Ti and micro-manganese counts, concurring with the hypothesis of anoxic or suboxic followed by oxic conditions. Similarly, sediments are typically laminated during the glacial periods but PC494, PS58/253-1 and PS58/255-2 are slightly bioturbated in the late glacial periods which continue into the interglacial periods, suggesting oxic conditions at the sea bed. Jakobsson et al. (2000) suggested a reduction in sea ice coverage at the onset of interglacial conditions increased ventilation and oxygen content at depth, leading to manganese precipitation in the Arctic Ocean.

The near-absence of micro-manganese nodules in the two cores from the deeper water depths, PC496 (4230 m water depth) and PS58/255-2 (3795 m water depth) suggests the deposition and/or preservation of micro-manganese nodules may be related to water depth, with these sites staying below the redoxcline. The position of PC496 on the drift flank close to a turbidite channel may also have been a factor, with possible episodic deposition of large volumes of sediment (via bottom current pirating of the nepheloid layer) preventing micro-manganese nodule growth, compared to the more gradual accumulation of sediment on the drift crests.

The increased manganese contents of the sediment cores during late glacial and interglacial periods is therefore interpreted as the result of a switch from suboxic conditions during glacial periods to oxic conditions in interglacial periods, leading to precipitation of manganese nodules. This concurs with the reduction in total organic content at the end of the glacial periods, for which one explanation is an increase in oxygen content. The occurrence of the nodules in the late glacial periods suggests the cause of the increase in oxygen content may be particularly sensitive to climatic changes, occurring several to tens of thousands of years prior to changes in clay mineralogy indicative of an ice sheet response. AABW is known to have been more poorly ventilated at the LGM compared to the present day, which has been attributed to increased sea ice cover (Ferrari et al., 2014). Sea ice coverage in the Ross Sea is therefore likely to have been the dominant control over ventilation, as the AABW is created there and then sinks below CDW. This suggests the sea ice in the Ross Sea was particularly sensitive to warming air temperatures, warming ocean temperatures or salinity changes associated with increased meltwater and stratification of the water column.

7.8. Observations by Marine Isotope Stage

Holocene/MIS 1

Moderate to high diatom and calcareous planktonic foraminifera contents are in keeping with the present day productivity under seasonal sea ice at the core sites but productivity is lower than the maxima reached in MIS 5. The near-absence of $CaCO_3$ in the core top of PC496 suggests the CCD is located between 3720 (PS58/253-1) and 4230 (PC496) m water depth. Bioturbated sediments and the presence of benthic calcareous foraminifera in the sand fraction suggest the bottom current is oxic and that sediments have accumulated slowly, which agrees with the low sedimentation rates suggested by the age models of ≥0.6 to ≥1.5 cm/kyr. Sortable silt proxies suggest the bottom current is weak and of a similar speed to that during MIS 2-4, probably causing a small amount of selective deposition. The smectite content of the surface samples is relatively high and typical of other interglacial periods, suggesting most deposition during the Holocene has been of far-travelled sediments. However, kaolinite contents are of intermediate glacial-interglacial values (e.g. 20% at 3.5 cmbsf in PC494), suggesting that small

amounts of sediment failure continue to occur on the slope and are deposited on the drifts via turbidity currents.

The deglaciation signal at the MIS 2/1 boundary is small, suggesting few icebergs melted over the drifts, possibly due to large volumes of meltwater reducing surface water temperatures and encouraging sea ice formation through increased stratification. However, an increase in the ARM/Magnetic susceptibility ratio at the MIS 2/1 boundary is indicative of an increase in magnetic grain size which continues into the early Holocene. Low but increasing IRD content towards the core tops suggests ice rafting has increased through the Holocene.

Low sedimentation rates and the inability to date the uppermost sediments of PC494 through relative palaeomagnetic intensity limit the observations that can be made regarding the timing of IRD peaks in the Holocene. However, based on a linear sedimentation rate between the MIS 2/1 boundary at 14 ka and the modern surface, IRD is not present in PC494 Holocene sediments until c.10 ka. There is no evidence for a response to Meltwater Pulse 1a or any of the episodes of iceberg rafting seen in the Scotia Sea which were interpreted as responses to global climatic events by Weber et al. (2014).

MIS 2-4

IRD content for much of the period is low but punctuated by episodes of moderate-high IRD content, particularly at the start and end of the period and at the MIS 3/2 boundary. This suggests the ice sheet was relatively stable with periodic large calving events. High kaolinite contents persisted throughout MIS 2-4 until the transition with MIS 1, suggesting large volumes of sediment continued to be supplied to the drifts after the ice had retreated from the outer shelf. A large increase in chlorite content of PC496 sediments (from 17.6% at 83 cmbsf to 30.5% at 63 cmbsf) and decrease in kaolinite content (from 22.6% at 83 cmbsf to 11.0% at 63 cmbsf) with little change in the proportion of smectite or illite probably reflects a change in source area of the terrigenous material supplied onto the slope. This may suggest variations in either the dominant ice stream supplying sediment to the core site, or to changes in the ice

dynamics and the rock types being eroded. The presence of micro-manganese nodules, which in PS58/253-1 are punctuated by samples containing no micro-manganese nodules, suggests the bottom current was oxic and sedimentation rates were often very low.

The lack of bioturbation, absence of calcareous foraminifera in the sand fraction, and low Ba/Ti, biogenic silica, Ca/Ti and $CaCO_3$ suggest productivity was low, probably due to perennial sea ice coverage, and/or that dissolution was common. Biogenic silica contents in the ice proximal site of PC494 are 6-12 wt.%, similar to that during MIS 5, suggesting the high sedimentation rate at this site may have led to faster silica burial and minimised post-depositional dissolution. This contrasts with the <5 wt.% biogenic silica content of PS58/255-2, which had a low sedimentation rate (≥1.9 cm/kyr) during MIS 2-4 and therefore less rapid burial of silica and carbonate.

MIS 5

The low but continuous presence of IRD in MIS 5 sediments suggests iceberg flux was the result of continual calving from the ice sheet with no major episodes of disintegration. The associated lithofacies are heavily bioturbated, with moderate-high biogenic silica contents (mostly diatoms) and high $CaCO_3$ contents (mostly planktonic foraminifera of the species *N. pachyderma* sinistral) reflecting high productivity. Biogenic silica and $CaCO_3$ contents are typically greater than they are in the Holocene sediments, which suggests sea ice coverage was less than at present, perhaps a perennially open ocean, or that the Amundsen Sea was less corrosive to silica and carbonate in MIS 5 than it is today. $CaCO_3$ contents in MIS 5 are slow to increase at the onset of the interglacial and are low during the peak MIS 5e period which suggests the CCD was slow to rise and most $CaCO_3$ was subject to dissolution at that time.

Sortable silt proxies in PS58/253-1 are greater in MIS 5 compared to MIS 6 and MIS 2-4, particularly percentage sortable silt. Sortable silt is slow to increase at the onset of the interglacial but peaks approximately mid-way through MIS 5, suggesting bottom current speeds increased and caused increased amounts of selective deposition. The distribution of high Mn/Ti values shows a similar distribution, peaking mid-way through

the MIS 5 sediments, suggesting bottom current changes were not limited to speed and may also have had an increase in oxygen content following the existence of reducing conditions early in MIS 5. The absence of micro-manganese nodules suggests the growth of nodules was restricted, possibly by sedimentation rates being too high and causing burial, restricting the size of the nodules to <63 µm.

MIS 6

Sedimentation rates in all four cores were highest in MIS 6 due to very high MAR_{terr} and high input of IRD, particularly in the latter half of the period. Very low smectite:kaolinite ratios reflect the large inputs of terrigenous material from the WAIS in the ASE which heavily diluted any far-travelled material deposited by the bottom current. The MAR_{terr} exceeds the values seen in MIS 2-4 in all four cores, suggesting ice was sitting at or near the shelf break and probably for a longer period of time than occurred at the LGM. There is no large increase in IRD associated with a deglaciation signal at the MIS 6/5 boundary.

Productivity is very low based on Ba/Ti and biogenic silica and $CaCO_3$ contents, but relatively high MAR_{opal} in all cores and MAR_{CaCO3} in all but the deepest core (PC496) suggest the high terrigenous sedimentation rates led to rapid burial, minimising dissolution of the biogenic silica and $CaCO_3$ that was being produced. The near-absence of $CaCO_3$ in MIS 6 sediments in PC496 suggests the CCD lay between 3795 (PS58/255-2) and 4230 (PC496) m water depth.

High variability in the sedimentation rate of PC494 in mid-MIS 6 may represent changes in ice dynamics or minor ice sheet disintegrations. The period 171-166 ka had a sedimentation rate of 15.4 cm/kyr with MAR_{terr} 14.1-14.8 g/cm²/kyr, which was followed during 166-158 ka by a sedimentation rate of 5.0 cm/ka with MAR_{terr} of 4.4-4.8 g/cm²/kyr. There is no accompanying significant change in $MAR_{IRD,}$ suggesting any change in the ice sheet was localised. This could represent ice retreating from the shelf edge temporarily, resulting in reduced volumes of sediment being deposited on the upper slope and transported via turbidity currents. The high-resolution chronology of PC494 suggests the ice may have begun to retreat from the shelf break approximately 143 ka, based on a halving in the mass accumulation rate of terrigenous material.

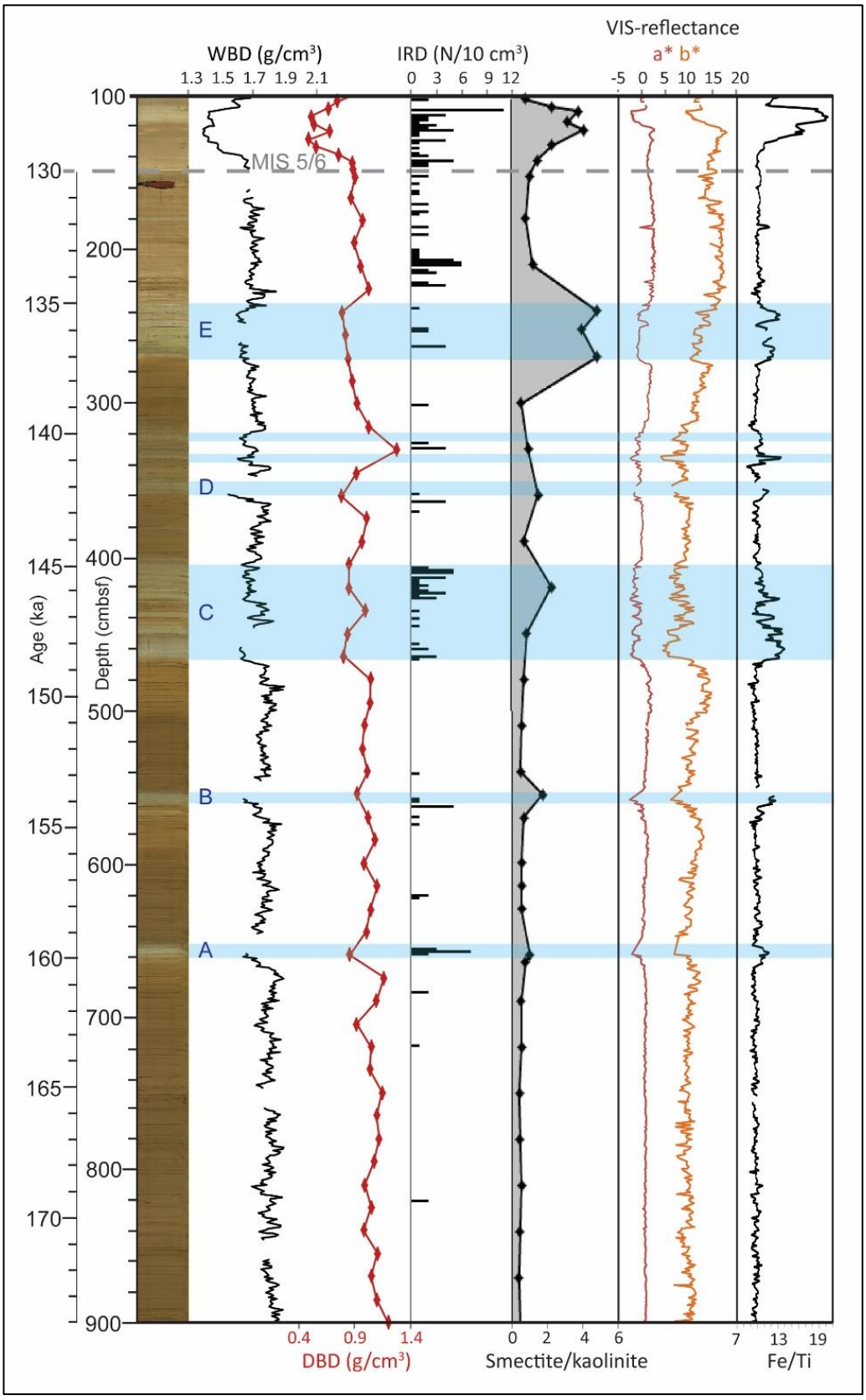

Figure 7.33: Physical properties and indicators of variability in terrigenous sediment supply and provenance in mid-late MIS 6 sediments of PS58/255-2. Sediment ages have been calculated assuming a linear sedimentation rate from the MIS 6/7 boundary at 1194 cmbsf to the MIS 5/6 boundary.

Sediments deposited in core PS58/255-2 during the latter half of MIS 6 (c.160-130 ka, based on a linear sedimentation rate) show colour variations. At least five (labelled A-E on Figure 7.33), 10-60 cm thick units of pale grey-green sediments with relatively low WBD and a moderate-high smectite:kaolinite ratio alternate with olive green, high WBD, low smectite:kaolinite ratio sediments that comprise most of the MIS 6 deposits in this core. Two further, thinner units of apparently similar sediment are indicated on Figure 7.33 between units D and E but are not marked as units as no samples were taken from these layers to confirm they show the same clay mineralogical and DBD changes. The number of IRD grains increases in some of the pale grey-green sediments compared to the olive green sediments.

The changes seen in the proxy data are similar to the changes seen during the transition from glacial to interglacial periods but of a lower magnitude. An exception is the smectite:kaolinite ratio of Unit E which exceeds the maxima of MIS 5. The variability is seen in colour and VIS reflectance, WBD and DBD, IRD content and clay mineralogy, but there is no notable difference in any of the productivity proxies. The sortable silt proxies, although highly variable in the MIS 6 sediments of PS58/255-2, do not show any consistent variation between the two differently coloured units. MIS 6 sediments in the other cores have lower sedimentation rates and do not show the colour and density variations and are almost entirely composed of the olive green, high WBD sediments (LF 1a in PC496 and LF 1b in PC494 and PS58/253-1).

The decreases in WBD and DBD in the pale olive-green unit with no accompanying change in Ba/Ti or biogenic silica suggest the density change reflects differences in the nature of the terrigenous sediment deposited. The increase in the smectite:kaolinite ratio may indicate an increase in the deposition of far-travelled, smectite-rich clay, despite the lack of consistent sortable silt proxy changes, if the bottom current was carrying more clay from increased inputs upstream. Alternatively, the amount of kaolinite-rich sediment supplied down-slope may have reduced, most likely as a result of fluctuations in the grounding line position, resulting in less dilution of the smectite-rich sediment supplied by bottom currents. However, the absence of any changes in productivity or TOC suggest the burial of organic, carbonate and siliceous material was similar in both the pale green-grey unit and the green unit.

A third suggestion is that the increased smectite:kaolinite ratio may reflect a change in the provenance of sediment delivered to the drifts via turbidity currents. This is preferred over oceanographic or sedimentation rate changes as illite percentages also increase in the pale olive-green units, and high illite contents are present on the surface of the shelf today (Ehrmann et al., 2011) suggesting a local illite-rich source. The clay mineralogy changes could reflect changes in the hinterland, such as a shifting ice divide meaning different geologies are eroded, or could reflect changes on the outer shelf, such as variations in the position or dominance of ice streams and/or the location of the initiation and pathway of turbidity currents to the drift. This latter hypothesis is favoured as the changes are seen only in PS58/255-2, the only core taken from the crest of Drift Three, with down-slope sediment apparently sourced from the eastern margin of PITE and the inter-trough area between PITE and PITW. Such changes could be caused by internal ice sheet dynamics. However, a further possibility that cannot be excluded, given the changes in the proxy data resemble that of glacial-interglacial transitions, is that the changes are climate-driven and could reflect millennial scale warming events. Similar events, known as Antarctic Isotopic Maxima, have been identified during MIS 2, when up to 2°C warming was recorded at the EPICA Dome C ice core on a 1470 year cyclicity (Jouzel et al., 2007). Based on a linear sedimentation rate between the MIS 6/7 and MIS 5/6 boundaries, the units A-E were each deposited over 2.1-4.6 kyrs. Temperature fluctuations of ≤4°C are present in the MIS 6 ice core record of EPICA Dome C, however, these occur earlier in MIS 6 than the assumed ages of the fluctuations in the PS58/255-2 WBD record (191-157 ka compared to 160 to 135 ka, respectively). The development of more robust age model for PS58/255-2 is therefore vital for investigating the timing of the changes in terrigenous flux and provenance, and to correlate the changes with further palaeoenvironmental records.

MIS 7 & 9

Ba/Ti reaches a maximum early in MIS 7 and 9, suggesting productivity increased rapidly following deglaciation and then declined gradually through the interglacial periods. Peak Ba/Ti values are comparable to those of MIS 5, suggesting sea ice coverage was similar. Low biogenic silica and $CaCO_3$ mass accumulation rates but moderate to large biogenic

silica and $CaCO_3$ contents reflect high productivity and minimal dissolution, despite low rates of burial and dilution by terrigenous material. The $CaCO_3$ and Ca/Ti record of PS58/253-1 show a double peak in MIS 7 separated by a minima, which may reflect fluctuations in the height of the CCD. Relatively high sortable silt values are indicative of a faster moving bottom current than during MIS 10, 8 and 6, with selective deposition preventing some clay deposition. The high smectite:kaolinite ratio reflects the decrease in the proportion of locally sourced terrigenous material compared to glacial periods. Input of material from the ice sheet is very low, suggesting a stable and distal ice sheet.

MIS 8 & 10

Sediments deposited during MIS 8 and 10 are relatively thin and feature very low mass accumulation rates of terrigenous sediments or IRD when compared to MIS 6 and 2-4, suggesting the ice sheet was more distal and is unlikely to have been at the shelf break. IRD content in MIS 8 in particular is very low. The low smectite:kaolinite ratio, however, is in keeping with the other glacial periods and does suggest that what little deposition occurred was dominated by input from local sources. Relatively moderate sortable silt values suggest the bottom current speed was weak with selective deposition of clay less common than in MIS 5 and 7. Productivity proxies suggest productivity was very low and/or that high rates of dissolution of silica and carbonate occurred.

Chapter 8: Conclusions

8.1. Introduction

This research had two primary aims: to reconstruct the Late Quaternary depositional environments recorded in the sediments from the Amundsen Sea continental rise and to draw conclusions about the mechanisms responsible for the formation of the sediment mounds. This chapter will review the findings of this research and address the two aims in the context of each of the five research objectives, which were outlined in Chapter 1.2 as follows:

1. To conduct sedimentological, geochemical and micro-palaeontological investigations on four sediment cores from Amundsen Sea sediment mounds.

2. To use the core data in conjunction with sub-bottom profiler data and published multi-beam swath bathymetry and multi-channel seismic data to examine the sediment composition and structure of the Amundsen Sea mounds. This will be used to interpret the depositional processes involved and to theorise the mechanisms of the formation and development of these features.

3. To compare the sediment mounds in the Amundsen Sea to the comparatively well studied sediment mounds west of the Antarctic Peninsula, which have been interpreted as contourite drifts.

4. To assess the evidence in the cores for past changes of the West Antarctic Ice Sheet (such as advance, retreat and collapse).

5. To reconstruct the Late Quaternary palaeoenvironmental history of the Amundsen Sea based on the sediment core data.

This chapter will also discuss the primary limitations of the research and make recommendations for future work on the eastern Amundsen Sea drifts.

8.2. Main Research Findings

8.2.1. Objective 1

Objective 1: To conduct sedimentological, geochemical and micro-palaeontological investigations on four sediment cores from Amundsen Sea sediment mounds.

A range of sedimentological, geochemical and mineralogical investigations have been carried out on four sediment cores in order to determine changes in the supply and provenance of terrigenous, biogenic and authigenic material. Age constraints for the ≤375 kyr records were derived from relative palaeomagnetic intensity, biostratigraphy, AMS ^{14}C dates and lithostratigraphy. Many of the results have been directly compared to those obtained from sediment core PS58/254-2 by Hillenbrand et al. (2009a).

Sediment characteristics are highly cyclic and correspond to glacial-interglacial cycles. Grey, laminated, IRD-rich, barren sediments, rich in locally-sourced kaolinite and illite, were deposited in glacial periods with sedimentation rates ranging from 0.1 to 17.2 cm/kyr reflecting the advance and retreat of the WAIS across the shelf. Olive-brown, bioturbated, diatom-bearing muds were deposited in interglacial periods, with a high smectite content reflecting deposition of far-travelled clay and sedimentation rates ranging from 0.2 to ≥3.7 cm/kyr reflecting changes in productivity that were mostly controlled by sea-ice coverage.

8.2.2. Objective 2

Objective 2: To use the core data in conjunction with sub-bottom profiler data and published multi-beam swath bathymetry and multi-channel seismic data to examine the sediment composition and structure of the Amundsen Sea mounds. This will be used to interpret the depositional processes involved and to theorise the mechanisms of the formation and development of these features.

Four sediment mounds had previously been identified by other authors in the eastern Amundsen Sea and interpreted as levee-drifts, based on multi-channel seismic data (Uenzelmann-Neben and Gohl, 2012, 2014). A sediment core taken from one of the mounds had been investigated with a view to examining indicators of ice sheet collapse (Hillenbrand et al., 2009a) and oceanographic responses to the Mid-Pleistocene transition (Konfirst et al., 2012). Further work to investigate how the mounds formed was important to understand their suitability as records of palaeoenvironmental change, given the pressing need to place modern ice sheet and oceanographic changes into a longer term context.

This thesis has presented the most comprehensive analysis of the eastern Amundsen Sea sediment mounds to date. Published multi-beam swath bathymetry data and multi-channel seismic data were used in conjunction with unpublished sub-bottom profiler data to examine the geometry and internal structure of the mounds, complemented by the four new sediment cores presented in this thesis and the published work of PS58/254-1 (Hillenbrand et al., 2009a). Geophysical and sediment core data were both used to support the interpretation of the mounds as mixed turbidite-contourite drifts and to identify a fifth drift lying north of Abbot Trough. The drifts were found to be long (250-433 km), narrow (38-130 km), stand up to 900 m above the sea floor and be asymmetric, with a gently-sloping western flank and steeper eastern flank resulting from sediment interaction with the eastwards flowing ACC.

The drifts are mostly composed of fine-grained, terrigenous sediment deposited during glacial periods. Sediments deposited during glacial periods thin offshore, reflecting a dominant supply of material down-slope. Geophysical data identified a concentration of gullies in the upper slope (as described in Noormets et al., 2009 and Dowdeswell et al., 2006), some of which connect to channels on the mid and lower slope and feed into large channels running between the drifts. The channel distribution suggests most turbidity currents were initiated in front of the eastern edge of PITW, the western edge of PITE and the inter-trough area separating PITW from PITE. This suggests meltwater dynamics associated with the slower-moving ice at the edges of the ice streams were important in initiating

turbidity currents at the shelf break in the eastern Amundsen Sea. Channels running between the drifts are typically 20 km wide, incised and run for hundreds of kilometres to the offshore end of the drifts before merging into the seafloor. The channels run along the bottom of the steep eastern flank of each drift and this flank may be further enhanced by deposition under the Coriolis force of fine sediments from the turbidity currents. However, much of the sediment suspended in turbidity currents was pirated by the eastwards-flowing bottom current and deposited to the east. Interaction with a faster-flowing bottom current associated with the sACCf may explain the eastwards change in alignment of the three eastern drifts.

The low slope gradient, and therefore long length of the continental slope, resulted in the transport of sediment in turbidity currents up to 400 km from the base of the slope and the erosion of a channel partially separating three of the drifts from the slope. The coarse-grained component of the turbidity currents was largely constrained to the channels running between the drifts, with occasional spill-over depositing sand and sandy muds on the drift flanks. The fine-grained fraction of the turbidity currents was largely suspended in the nepheloid layer and was entrained within the weak, eastwards-flowing bottom current, which may be AABW or LCDW within the ACC and possibly within the Ross Sea Gyre. Some sediment may have been deposited on the western flank of the channel under the Coriolis force. However, the majority of the suspended sediment was transported by the weak bottom current then deposited downstream on the next drift.

During interglacial periods, low sedimentation rates reflect deposition largely of far-travelled, smectite-rich clay from the bottom current, probably transported from the sub-Antarctic Southeast Pacific. This material is probably also deposited during glacial periods, but diluted by high inputs from local sources of relatively kaolinite-rich clay. Interglacial increases in productivity are reflected in the increased biogenic silica and $CaCO_3$ contents, with predominantly diatoms and planktonic foraminifera deposited via vertical settling.

8.2.3. Objective 3

Objective 3: To compare the sediment mounds in the Amundsen Sea to the comparatively well studied sediment mounds west of the Antarctic Peninsula, which have been interpreted as contourite drifts.

The drifts of the eastern Amundsen Sea are similar to the Peninsula drifts in their fine-grained, terrigenous nature, the glacial-interglacial variability in sediment composition, their position relative to turbidity current channels on the slope and rise, and their asymmetry with a more gently sloping flank facing into the main direction of bottom current flow. The Peninsula drifts are more frequently separated from the base of the slope than the Amundsen Sea drifts, which is probably a function of the steeper slope angle leading to erosion at the slope base. The two sets of drifts are of a comparable size in terms of maximum width and height. However, their geometry differs, with the Amundsen Sea drifts longer and narrower offshore, as opposed to the oval-shaped geometry and short length of the Peninsula drifts. This difference has been attributed to the lower gradient of the continental slope in the Amundsen Sea (2-4°, compared to 16° off the Peninsula) resulting in longer run-out distances of the turbidity currents, delivering sediment further onto the continental rise.

The location of the Peninsula drifts is controlled by the position of palaeo ice-stream troughs, with the drift crests aligning with the inter-trough areas and turbidity current channels located in front of the troughs. In contrast, the drifts in the Amundsen Sea are fed largely by channels originating from the trough margins and inter-trough area. This may be related to different ice dynamics and meltwater production between the two areas, or to the steeper slope angle off the Peninsula encouraging deeper gully erosion and more steering of subsequent turbidity currents. The contrasting clay mineralogy of the drifts reflects differences in the geology of their sediment source areas.

Both sets of drifts are deemed to be in the “drift maintenance stage” (Rebesco et al., 1996). In the Amundsen Sea drifts, the gently sloping flank is the western flank due to the influence of the eastwards-flowing LCDW or AABW within the

ACC, in contrast to the gently sloping eastern flank and steeper western flank of the Peninsula drifts under the influence of westwards-flowing WSDW. Both regions feature drifts which have amalgamated to form a particularly wide, plateau-shape drift. The clay-rich contents of both drifts suggest the bottom currents are similarly weak. The Amundsen Sea drifts contain more $CaCO_3$ during interglacial periods and more sediment waves than the Peninsula drifts, suggesting the bottom current may be less corrosive to carbonate but possibly less stable in terms of direction and/or speed.

The two sets of drifts have comparable sedimentation rates which are greatest during glacial periods: 1.1-4.3 cm/kyr (interglacial) and 1.8 to 13.5 cm/kyr (glacial) on the Peninsula drifts (Pudsey, 2000) and 0.2-2.2 cm/kyr (interglacial) and 0.1-17.2 cm/kyr (glacial) on the Amundsen Sea drifts. Sedimentation rates peak in the Amundsen Sea drifts during MIS 6, whilst the Peninsula drifts see peak sedimentation rates in MIS 2-4, which may be related to differences in the position of ice on the shelf between the two areas, or the mode of sediment delivery, with meltwater plumes common off the Peninsula in MIS 2-4 (Pudsey, 2000).

8.2.4. Objective 4

Objective 4: To assess the evidence in the cores for past changes of the West Antarctic Ice Sheet (such as advance, retreat and collapse).

The accumulation rate, clay mineralogy and grain size of terrigenous material in the four sediment cores have been used to infer changes in the supply and provenance of sediment sourced from the ice sheet. The accumulation rate of terrigenous material during glacial periods was on average seventeen times higher than that in interglacial periods. The relatively high kaolinite content of sediment deposited during glacial periods suggests a source area in the ASE and a northerly transport of material across the shelf and down the continental slope. This concurs with the position of gullies in the upper slope, some of which connect to channels on the mid and lower slope, which suggest highly erosive

flows, including turbidity currents, were initiated at the shelf break in front of the eastern edge of PITW, the western edge of PITE and particularly in front of the area separating these two troughs.

IRD contents are greater in sediments dating to glacial periods than interglacial periods, particularly during MIS 6 and MIS 2-4, which suggests the ice sheet had expanded across the continental shelf to a more proximal location. IRD contents also suggest the ice sheet was relatively stable with periodic, probably small calving events and a slow retreat beginning in the late glacial period. The high mass accumulation rate of terrigenous material during MIS 2-4 and particularly MIS 6 also suggests ice in these areas had expanded across the shelf and was grounded at or near the shelf break, probably for a longer period of time in MIS 6 than in MIS 2-4. The high-resolution chronology of PC494 suggests the ice may have begun to retreat from the shelf break at 145 ka, 15 kyr prior to the MIS 6/5 boundary, based on a decrease in sedimentation rate from 14.1 to 6.8 cm/kyr and a corresponding halving in the mass accumulation rate of terrigenous material.

Depositional anomalies present in PS58/255-2 show millennial-scale cyclical variations in the supply and provenance of terrigenous material during mid-late MIS 6 that may reflect changes in ice dynamics or minor ice sheet disintegrations and could be climatically driven. However, the changes are unlikely to be large enough to represent a major disintegration of the WAIS. IRD contents increase during the events but only to relative moderate contents and are not suggestive of a major iceberg rafting event. The absence of these changes in the other cores also suggests they are unlikely to represent a major event across the Amundsen Sea and may reflect local changes in sediment supply to that one drift. Alternatively, the cyclical variations may have occurred on such short timetables, they are only detectable in PS58/255-2 due to the high sedimentation rate.

In contrast to sediments from the Scotia Sea (Weber et al., 2014), there is no notable increase in IRD around the time of Meltwater Pulse 1a or other global climatic events during the Holocene.

Hillenbrand et al. (2002) noted that in the Amundsen Sea, evidence of collapse of the WAIS might include significant changes in the amount of lithogenic content, particularly gravel, and $CaCO_3$ contents, beyond those expected of glacial-interglacial cycles. No such occurrences have been identified in the cores. Sedimentology, geochemistry and mineralogy all exhibit strong variability according to glacial-interglacial cycles but show little variation within each MIS, with the exception of the changes in the supply and provenance of terrigenous material during late MIS 6 in PS58/255-2, described above. Where IRD is present in discrete layers, the layers are typically only a few centimetres thick and there are no significant layers that can be correlated between cores. The geology of the sand fraction is consistent, suggesting the source areas of icebergs remained similar. Although the cores appear to have lain below the CCD for some of the c. <375 kyr records, biogenic silica is present in all sediments and might also be expected to respond to an ice sheet collapse if a large input of freshwater led to ocean stratification and changes in sea ice coverage. However, no such signal is seen.

There are also no major depositional anomalies, of the sort identified by Hillenbrand et al. (2009a) in PS58/254-1, where it appears the sediments dated to MIS 14 are more characteristic of a prolonged interglacial period. However, this is limited by the age model of the cores and cannot be ruled out, particularly in the pre-MIS 6 sediments of PS58/253-1 and PS58/255-2 for which chronological constraints are particularly limited.

8.2.5. Objective 5

Objective 5: To reconstruct the Late Quaternary palaeoenvironmental history of the Amundsen Sea based on the sediment core data.

Diatom and planktonic calcareous foraminifera contents are greater during interglacial periods than glacial periods, reflecting increased productivity under the seasonal, rather than perennial, sea ice cover. The planktonic calcareous foraminifera contents are almost entirely of the polar species *Neogloboquadrina*

pachyderma sinistral. Biogenic silica contents at the most ice-proximal site (PC494) show no glacial-interglacial variability, reflecting the importance of burial in minimising post-depositional silica dissolution on the drifts. Productivity was higher during MIS 5 than the present day, which suggests either an open ocean or that sea ice coverage was at least reduced compared to the Holocene. $CaCO_3$ contents are low in the early part of MIS 5, including during the peak warmth of MIS 5e, suggesting the CCD was slow to rise following MIS 6. Comparison with PS58/254-1 suggests the CCD lay below 4014 m water depth from MIS 17 to MIS 6 and fluctuated between ≤4014 m and ≥4230 m water depth post-MIS 6.

Sortable silt data suggest average bottom current speeds over the drifts since MIS 10 of approximately 3.0 cm/sec^{-1}. The bottom current speed was faster at one of the four core sites during interglacial periods, at an average mean scalar flow speed estimated at 7.7 cm/sec^{-1} compared to 3.5 cm/sec^{-1} during glacial periods. This is at odds with the increased AABW production and transport that occurred at the LGM, so may reflect a change in the water mass over the drifts from LCDW during interglacial periods to AABW during glacial periods. Alternatively, it may reflect variation in the position of the sACCf.

Manganese contents suggest the bottom current was suboxic during MIS 6 and MIS 2-4, with an increase in oxygen content towards the end of the glacial periods seen in the precipitation of manganese into micro-nodules. This may relate to sea ice coverage in the Ross Sea restricting the ventilation of AABW during glacial periods.

8.3. Implications of the Research

This thesis has presented the first high-resolution study of Late Quaternary palaeoenvironmental change in the eastern Amundsen Sea. High sedimentation rates in sediments deposited during glacial periods mean the time of deposition between samples is frequently less than 1000 years and as small as 290 years (PS58/255-2, MIS 6). XRF scanning, completed at a 2 mm sampling frequency, equates to an average 12

years between readings in the MIS 6 sediments of PS58/255-2. Given the rapid increase in mass loss seen in the Amundsen Sea sector of the WAIS since the 1940s, such high sedimentation rates and high sampling frequencies are vital in looking for short-lived palaeoenvironmental changes. As a result, changes in the provenance and supply of terrigenous material were identified in mid-late MIS 6 sediments of PS58/255-2 which may reflect previously unidentified cyclical changes in the dynamics of the WAIS.

The inclusion of a wide range of sedimentological, geochemical and mineralogical analyses in combination with published data from core PS58/254-1 and geophysical data means this is the most comprehensive study of the drifts to date. The confirmation that the drifts contain reliable records of the history of the WAIS, productivity and oceanography, and that a chronology can be developed using multiple techniques, has shown great potential for further palaeoenvironmental information to be extracted from the drift sediments.

8.4. Limitations of the Research

Sparse Coverage of Cores

Three of the cores used in this research were taken from Drift Two, along with PS58/254-2 (Hillenbrand et al., 2009a), and one core was taken from Drift Three. The interpretation of how the drifts formed relies heavily on sediment analysis, such as the presence of a sand layer in PC496 interpreted as a turbidite spill-over deposit. It is also important to understand how sedimentation rates differ spatially over the drifts in order to assess the impact of both down-slope deposition and along-slope movement of sediment. The interpretation of how drifts One, Four and Five formed relies solely on the geophysical data and the assumption that they exhibit similar sedimentology to drifts Two and Three. This is a particularly significant limitation given the drifts all have unique source areas of the down-slope sediment and so may exhibit large differences in the nature of their sediments, e.g. clay mineralogy, grain size. The bottom current may also change speed as it flows eastwards and towards the westwards-flowing WSDW, which could be examined using sortable silt data.

Sparse Oceanographic Data

An assessment of the available oceanographic data for the eastern Amundsen Sea found AABW present at the base of some CTDs taken over the drifts and LCDW present in others. It is not currently possible to say whether this variation is related to spatial or temporal variability, or which is the dominant water mass affecting the drifts. Similarly, it is unclear whether WSDW extends westwards to the drifts (probably very weakly and confined to the base of the slope). Inferences about present and past bottom current direction are derived from the clay mineralogy of the sediments and geometry of the drifts.

The collection of current meter data from the bottom current in the eastern Amundsen Sea would benefit future study of the drifts for several reasons. First, the sortable silt value in surface sediments could be correlated to a modern bottom current speed to improve quantifications of past bottom current speeds. This is particularly relevant given recent work has shown large differences between the sortable silt of bottom current speeds in the Scotia and Weddell Seas compared to the sortable silt of the same current speeds in other oceans (McCave et al., 2017). Secondly, the influence of the bottom current on the drift sediments could be investigated, similar to the work of Camerlenghi et al. (1997) on the Peninsula drifts, in order to better understand sediment-current interaction and how the flow is affected by the presence of the drifts. Thirdly, a quantification of how fast the bottom current flows at the sACCf and how much the position of the sACCf can vary will aid in the discussion and understanding of why three drifts change orientation towards the east.

Core Chronology

With the exception of PC494, the chronology for the cores is relatively low-resolution and interpretations are restricted to changes between whole glacial-interglacial periods, rather than being able to date changes which happened within each individual period. This is particularly important for assessing the cause of millennial-scale variability in multiple proxies in the mid-late MIS 6 sediments of PS58/255-2. Relative palaeomagnetic intensity provided a robust and relatively high-resolution chronology

for PC494 but also relied heavily on the correlation of magnetic susceptibility records with other cores. A more robust chronology, such as oxygen isotope stratigraphy or carrying out relative palaeomagnetic intensity analysis on more than one core, would have allowed for the dating of changes within a glacial-interglacial period and identified hiatuses or episodes of non-deposition.

Lack of pre-LGM Palaeoenvironmental Records for Comparison

There are few records of either Amundsen Sea oceanographic changes or WAIS history that predate the LGM and offer a resolution suitable for comparison with the new data presented here. Some comparisons have been drawn with the one million year record of PS58/254-2 (Hillenbrand et al., 2009a), but more records are needed from this region in order to compare and contrast data and make more robust interpretations.

8.5. Recommendations for Future Research

Drilling the drifts for longer-term palaeoenvironmental records

Cores from Drifts Two and Three have been shown here and by Hillenbrand et al. (2009a) to offer continuous records of palaeoenvironmental change offshore of a region experiencing rapid, present day environmental change, where pre-LGM records are sparse and where a longer term context is vital. The drift sediments record both ice sheet and oceanographic change and a multi-proxy approach can provide a large range of valuable datasets. A reliable chronology can be obtained via oxygen isotope stratigraphy (Hillenbrand et al., 2009a) and relative palaeomagnetic intensity, if carried out on a proximal drift crest where sedimentation rates are relatively high. Coverage of the drifts by seismic lines is good and seismic profiles suggest the drifts are suitable for the drilling of deeper cores.

International Ocean Discovery Programme Expedition 379 (scheduled for January-March 2019) has identified three primary drill sites on Drift Four and Five and secondary sites on Drift Two and Four, with the aim of reconstructing WAIS behaviour since the Neogene (pp.1, Gohl et al., 2013). The expedition is expecting maximum penetration of

900-1400 m, producing sediments dating to the mid-Miocene, <18 Ma (Gohl et al., 2013). The long time span of the cores will allow for techniques such as the use of diatom and dinoflagellate cyst assemblages to reconstruct sea ice coverage, the use of Mg/Ca composition of calcareous foraminifera to reconstruct sea surface and deep-water temperatures, and the use of recently developed biomarkers such as TEX^{L}_{86} and IP_{25} to reconstruct sea surface temperature and sea ice limits (Gohl et al., 2013).

Improved spatial coverage of marine sediment cores

The cores presented in this research showed substantial variability in sedimentation rates between drifts, reflecting the different channels and source areas of the turbidity currents. PS58/255-2 showed cyclical changes in the sediments during MIS 6 which were not observed in the other cores. Taking more cores from the drifts could therefore provide further information regarding both how the drifts formed, by examining spatial differences, and regarding palaeoenvironmental change, given each drift has been supplied with terrigenous sediment from a unique catchment area. This may also help to identify areas of high silica and carbonate preservation suitable as future drilling targets, for which a chronology could be devised using diatom assemblages or oxygen isotope stratigraphy.

References

Ackley, S.F., Xie, H. and Tichenor, E.A., 2015. Ocean heat flux under Antarctic sea ice in the Bellingshausen and Amundsen Seas: two case studies. *Annals of Glaciology*, **56**(69), pp.200-210.

Alonso, B., Ercilla, G., Casas, D., Stow, D.A., Rodríguez-Tovar, F.J., Dorador, J. and Hernández-Molina, F.J., 2016. Contourite vs gravity-flow deposits of the Pleistocene Faro Drift (Gulf of Cadiz): Sedimentological and mineralogical approaches. *Marine Geology*, **377**, pp.77-94.

Amblas, D., Urgeles, R., Canals, M., Calafat, A.M., Rebesco, M., Camerlenghi, A., Estrada, F., De Batist, M. and Hughes-Clarke, J.E., 2006. Relationship between continental rise development and palaeo-ice sheet dynamics, Northern Antarctic Peninsula Pacific margin. *Quaternary Science Reviews*, **25**(9-10), pp.933-944.

Anderson, R.F., Ali, S., Bradtmiller, L.I., Nielsen, S.H.H., Fleisher, M.Q., Anderson, B.E. and Burckle, L.H., 2009. Wind-driven upwelling in the Southern Ocean and the deglacial rise in atmospheric CO2. *Science*, **323**(5920), pp.1443-1448.

Aoki, S. and Oinuma, K., 1980. Clay mineral composition in shallow water sediment samples near the Antarctic Peninsula and in deep-sea core samples from the pacific and the Indian-Antarctic Basins. *Journal of Oceanography*, **36**(1), pp.23-29.

Arndt, J.E., Schenke, H.W., Jakobsson, M., Nitsche, F.O., Buys, G., Goleby, B., Rebesco, M., Bohoyo, F., Hong, J., Black, J. and Greku, R., 2013. The International Bathymetric Chart of the Southern Ocean (IBCSO) Version 1.0—A new bathymetric compilation covering circum-Antarctic waters. *Geophysical Research Letters*, **40**(12), pp.3111-3117.

Arneborg, L., Wåhlin, A.K., Björk, G., Liljebladh, B. and Orsi, A.H., 2012. Persistent inflow of warm water onto the central Amundsen shelf. *Nature Geoscience*, **5**(12), pp.876-880.

Arzel, O., Fichefet, T. and Goosse, H., 2006. Sea ice evolution over the 20th and 21st centuries as simulated by current AOGCMs. *Ocean Modelling*, **12**(3), pp.401-415.

Assmann, K.M., Hellmer, H.H. and Jacobs, S.S., 2005. Amundsen Sea ice production and transport. *Journal of Geophysical Research: Oceans*, **110**(C12).

Baas, J.H., Manica, R., Puhl, E., Verhagen, I. and Borges, A.L.D.O., 2014. Processes and products of turbidity currents entering soft muddy substrates. *Geology*, **42**(5), pp.371-374.

Barker, P. F., Camerlenghi, A., Acton, G.D. and Ramsay, A. T. S. (Eds.) (2002) *Proceedings of the Ocean Drilling Program Scientific Results*, Volume *178.* Ocean Drilling Program, College Station, Texas.

Bentley, C.R., 1998. Rapid sea-level rise from a West Antarctic ice-sheet collapse: a short-term perspective. *Journal of Glaciology*, **44**(146), pp.157-163.

Bentley, M.J., Ó. Cofaigh, C., Anderson, J.B., Conway, H., Davies, B., Graham, A.G., Hillenbrand, C.D., Hodgson, D.A., Jamieson, S.S., Larter, R.D. and Mackintosh, A., 2014.

A community-based geological reconstruction of Antarctic Ice Sheet deglaciation since the Last Glacial Maximum. *Quaternary Science Reviews*, **100**, pp.1-9.

Berkman, P.A. and Forman, S.L., 1996. Pre-bomb radiocarbon and the reservoir correction for calcareous marine species in the Southern Ocean. *Geophysical Research Letters*, **23**(4), pp.363-366.

Bernard, B.B., Bernard, H. and Brooks, J.M., 1995. Determination of total carbon, total organic carbon and inorganic carbon in sediments. *TDI-Brooks International/B&B Laboratories Inc.* College Station, Texas, pp.1-5.

Bianchi, G.G., Hall, I.R., McCave, I.N. and Joseph, L., 1999. Measurement of the sortable silt current speed proxy using the Sedigraph 5100 and Coulter Multisizer IIe: precision and accuracy. *Sedimentology*, ***46***(6), pp.1001-1014.

Bindschadler, R., 2006. The environment and evolution of the West Antarctic ice sheet: setting the stage. *Philosophical Transactions of the Royal Society of London A: Mathematical, Physical and Engineering Sciences*, **364**(1844), pp.1583-1605.

Bingham, R.G., Ferraccioli, F., King, E.C., Larter, R.D., Pritchard, H.D., Smith, A.M. and Vaughan, D.G., 2012. Inland thinning of West Antarctic Ice Sheet steered along subglacial rifts. *Nature*, ***487***(7408), pp.468-471.

Bleil, U. and von Dobeneck, T. 1999. Geomagnetic events and relative palaeointensity records – clues to high-resolution palaeomagnetic chronostratigraphies of Late Quaternary marine sediments? pp. 635-654 *In* Fischer, G. and Wefer, G. *(Eds) Use of Proxies in Palaeoceanography: Examples from the South Atlantic.* Springer-Verlag, Berlin Heidelberg.

Blott, S.J. and Pye, K., 2001. GRADISTAT: a grain size distribution and statistics package for the analysis of unconsolidated sediments. *Earth Surface Processes and Landforms*, **26**(11), pp.1237-1248. http://www.kpal.co.uk/gradistat.html

Bouma, A.H., 1962. *Sedimentology of some flysch deposits. A graphic approach to facies interpretation, 168*. Elsevier, Amsterdam, 168 pp.

Boyer, T.P., Antonov, J.I., Baranova, O.K., Coleman, C., Garcia, H.E., Grodsky, A., Johnson, D.R., Locarnini, R.A., Mishonov, A.V., O'Brien, T.D., Paver, C.R., Reagan, J.R., Seidov, D., Smolyar, I.V. and Zweng, M.M. 2013. World Ocean Database 2013, NOAA Atlas NESDIS 72. Levitus, S. (Ed.), Mishonov, A.V. (Technical Ed.). Silver Spring, MD.

Brackenridge, R., Stow, D.A. and Hernández-Molina, F.J., 2011. Contourites within a deep-water sequence stratigraphic framework. *Geo-Marine Letters*, **31**(5-6), pp.343-360.

Camerlenghi, A., Crise, A., Pudsey, C.J., Accerboni, E., Laterza, R. and Rebesco, M., 1997. Ten-month observation of the bottom current regime across a sediment drift of the Pacific margin of the Antarctic Peninsula. *Antarctic Science*, **9**(04), pp.426-433.

Carter, P., Vance, D., Hillenbrand, C.D., Smith, J.A. and Shoosmith, D.R., 2012. The neodymium isotopic composition of waters masses in the eastern Pacific sector of the Southern Ocean. *Geochimica et Cosmochimica Acta*, **79**, pp.41-59.

Channell, J.E.T., Xuan, C. and Hodell, D.A., 2009. Stacking paleointensity and oxygen isotope data for the last 1.5 Myr (PISO-1500). *Earth and Planetary Science Letters*, **283**(1), pp.14-23.

Chase, Z., Anderson, R.F., Fleisher, M.Q. and Kubik, P.W., 2003. Accumulation of biogenic and lithogenic material in the Pacific sector of the Southern Ocean during the past 40,000 years. *Deep Sea Research Part II: Topical Studies in Oceanography*, **50**(3-4), pp.799-832.

Chester, R. and Jickells, T. (2012) *Marine Geochemistry*. Third Edition. Wiley-Blackwell, Oxford.

Cochran, J.R., Jacobs, S.S., Tinto, K.J. and Bell, R.E., 2014. Bathymetric and oceanic controls on Abbot Ice Shelf thickness and stability. *The Cryosphere*, **8**(3), pp.877-889.

Crosta, X., Romero, O., Armand, L.K. and Pichon, J.J., 2005. The biogeography of major diatom taxa in Southern Ocean sediments: 2. Open ocean related species. *Palaeogeography, Palaeoclimatology, Palaeoecology*, **223**(1), pp.66-92.

Dalziel, I.W.D. and Lawver, L.A., 2001. The lithospheric setting of the West Antarctic Ice Sheet, pp.29-44 in Alley, R.B. and Bindschadler, R.A. (Eds) *The West Antarctic Ice Sheet: Behavior and Environment*. American Geophysical Union, Washington, D.C.

DeMaster, D.J., 1981. The supply and accumulation of silica in the marine environment. *Geochimica et Cosmochimica acta*, **45**(10), pp.1715-1732.

DeMaster, D.J., Ragueneau, O. and Nittrouer, C.A., 1996. Preservation efficiencies and accumulation rates for biogenic silica and organic C, N, and P in high-latitude sediments: The Ross Sea. *Journal of Geophysical Research: Oceans*, **101**(C8), pp.18501-18518.

DeMaster, D.J., 2002. The accumulation and cycling of biogenic silica in the Southern Ocean: revisiting the marine silica budget. *Deep Sea Research Part II: Topical Studies in Oceanography*, **49**(16), pp.3155-3167.

Depoorter, M.A., Bamber, J.L., Griggs, J.A., Lenaerts, J.T.M., Ligtenberg, S.R.M., Van den Broeke, M.R. and Moholdt, G., 2013. Calving fluxes and basal melt rates of Antarctic ice shelves. *Nature*, **502**(7469), pp.89-92.

Dieckmann, G., Spindler, M., Lange, M.A., Ackley, S.F. and Eicken, H., 1991. Antarctic sea ice: a habitat for the foraminifer *Neogloboquadrina pachyderma*. *Journal of Foraminiferal Research*, **21**(2), pp.182-189.

Diehl, T.M., Holt, J.W., Blankenship, D.D., Young, D.A., Jordan, T.A. and Ferraccioli, F., 2008. First airborne gravity results over the Thwaites Glacier catchment, West Antarctica. *Geochemistry, Geophysics, Geosystems*, **9**(4).

Diekmann, B., 2007. Sedimentary patterns in the late Quaternary Southern Ocean. *Deep Sea Research Part II: Topical Studies in Oceanography*, **54**(21-22), pp.2350-2366.

DiVenere, V.J., Kent, D.V. and Dalziel, I.W.D., 1994. Mid-Cretaceous paleomagnetic results from Marie Byrd Land, West Antarctica: A test of post-100 Ma relative motion

between East and West Antarctica. *Journal of Geophysical Research: Solid Earth*, **99**(B8), pp.15115-15139.

Dowdeswell, J.A. and Ó Cofaigh, C. (Eds.) 2002. *Glacier-influenced sedimentation on high-latitude continental margins*. Geological Society of London.

Dowdeswell, J.A., Ó Cofaigh, C. and Pudsey, C.J., 2004. Continental slope morphology and sedimentary processes at the mouth of an Antarctic palaeo-ice stream. *Marine Geology*, **204**(1-2), pp.203-214.

Dowdeswell, J.A., Evans, J., Ó Cofaigh, C. and Anderson, J.B., 2006. Morphology and sedimentary processes on the continental slope off Pine Island Bay, Amundsen Sea, West Antarctica. *Geological Society of America Bulletin*, **118**(5-6), pp.606-619.

Dowdeswell, J.A., Ó. Cofaigh, C., Noormets, R., Larter, R.D., Hillenbrand, C.D., Benetti, S., Evans, J. and Pudsey, C.J., 2008. A major trough-mouth fan on the continental margin of the Bellingshausen Sea, West Antarctica: the Belgica Fan. *Marine Geology*, **252**(3), pp.129-140.

Dunbar, N.W., McIntosh, W.C. and Esser, R.P., 2008. Physical setting and tephrochronology of the summit caldera ice record at Mount Moulton, West Antarctica. *Geological Society of America Bulletin*, **120**(7-8), pp.796-812.

Dutrieux, P., De Rydt, J., Jenkins, A., Holland, P.R., Ha, H.K., Lee, S.H., Steig, E.J., Ding, Q., Abrahamsen, E.P. and Schröder, M., 2014. Strong sensitivity of Pine Island ice-shelf melting to climatic variability. *Science*, **343**(6167), pp.174-178.

Ehrmann, W., Hillenbrand, C.D., Smith, J.A., Graham, A.G., Kuhn, G. and Larter, R.D., 2011. Provenance changes between recent and glacial-time sediments in the Amundsen Sea embayment, West Antarctica: clay mineral assemblage evidence. *Antarctic Science*, **23**(5), pp.471-486.

Elverhøi, A., DeBlasio, F., Butt, F.A., Issler, D., Harbitz, C.B., Engvik, L. et al., 2002. Submarine mass-wasting on glacially-influenced continental slopes: Processes and dynamics, pp.73-87 *in* Dowdeswell, J.A. and Ó Cofaigh, C. (Eds) *Glacier Influenced Sedimentation on High-Latitude Continental Margins.* Geological Society, Special Publications 203: London.

Escutia, C., Nelson, C.H., Acton, G.D., Eittreim, S.L., Cooper, A.K., Warnke, D.A. and Jaramillo, J.M., 2002. Current controlled deposition on the Wilkes Land continental rise, Antarctica. *Geological Society, London, Memoirs*, **22**(1), pp.373-384.

Esper, O., Gersonde, R. and Kadagies, N., 2010. Diatom distribution in southeastern Pacific surface sediments and their relationship to modern environmental variables. *Palaeogeography, Palaeoclimatology, Palaeoecology*, **287**(1), pp.1-27.

Evans, J., Dowdeswell, J.A., Ó. Cofaigh, C., Benham, T.J. and Anderson, J.B., 2006. Extent and dynamics of the West Antarctic Ice Sheet on the outer continental shelf of Pine Island Bay during the last glaciation. *Marine Geology*, **230**(1), pp.53-72.

Faugères, J.C. and Stow, D.A.V., 2008. Contourite drifts: Nature, evolution and controls. Chapter 14 *in:* Rebesco, M. and Camerlenghi, A. (Eds.) van Loon, A.J. (Series Ed.) *Contourites: Developments in Sedimentology Volume 60*. Elsevier, Amsterdam. pp.259-288.

Faugères, J.C. and Mulder, T., 2011. Contour currents and contourite drifts. Chapter 3 pp.149-214 in Hüneke, H. and Mulder, T. *Developments in Sedimentology Volume 63: Deep-Sea Sediments.* Elsevier, Oxford.

Feldmann, J. and Levermann, A., 2015. Collapse of the West Antarctic Ice Sheet after local destabilization of the Amundsen Basin. *Proceedings of the National Academy of Sciences*, **112**(46), pp.14191-14196.

Ferrari, R., Jansen, M.F., Adkins, J.F., Burke, A., Stewart, A.L. and Thompson, A.F., 2014. Antarctic sea ice control on ocean circulation in present and glacial climates. *Proceedings of the National Academy of Sciences*, **111**(24), pp.8753-8758.

Folk, R.L. and Ward, W.C., 1957. Brazos River bar: a study in the significance of grain size parameters. *Journal of Sedimentary Research*, **27**(1).

Fragoso, G.M. and Smith Jr, W.O., 2012. Influence of hydrography on phytoplankton distribution in the Amundsen and Ross Seas, Antarctica. *Journal of Marine Systems*, **89**(1), pp.19-29.

Fretwell, P., Pritchard, H.D., Vaughan, D.G., Bamber, J.L., Barrand, N.E., Bell, R., Bianchi, C., Bingham, R.G., Blankenship, D.D., Casassa, G. and Catania, G., 2013. Bedmap2: improved ice bed, surface and thickness datasets for Antarctica. *The Cryosphere*, **7**(1) pp.375-393.

Gales, J.A., Larter, R.D., Mitchell, N.C. and Dowdeswell, J.A., 2013. Geomorphic signature of Antarctic submarine gullies: implications for continental slope processes. *Marine Geology*, **337**, pp.112-124.

García, M., Lobo, F.J., Maldonado, A., Hernández-Molina, F.J., Bohoyo, F. and Pérez, L.F., 2016. High-resolution seismic stratigraphy and morphology of the Scan Basin contourite fan, southern Scotia Sea, Antarctica. *Marine Geology*, **378**, pp.361-373.

Garcia, H.E., Locarnini, R.A., Boyer, T.P., Antonov, J.I., 2006. World Ocean Atlas 2005. *In*: Levitus, S. (Ed.), Nutrients (Phosphate, Nitrate, Silicate): *NOAA Atlas NESDIS 64*, U.S. Government Printing Office, Washington, D.C., Vol. 4.

Garcia, M., Ercilla, G., Alonso, B., Estrada, F., Jane, G., Mena, A., Alves, T. and Juan, C., 2015. Deep-water turbidite systems: a review of their elements, sedimentary processes and depositional models. Their characteristics on the Iberian margins-Sistemas turbidíticos de aguas profundas: revisión de sus elementos, procesos sedimentarios y modelos deposicionales. Sus características en los márgenes Ibéricos. *Boletín Geológico y Minero*, **126**(2-3), pp.189-218.

Gardner, J.V., Prior, D.B. and Field, M.E., 1999. Humboldt slide—a large shear-dominated retrogressive slope failure. *Marine Geology*, **154**(1-4), pp.323-338.

Gerringa, L.J., Alderkamp, A.C., Laan, P., Thuroczy, C.E., De Baar, H.J., Mills, M.M., van Dijken, G.L., van Haren, H. and Arrigo, K.R., 2012. Iron from melting glaciers fuels the phytoplankton blooms in Amundsen Sea (Southern Ocean): Iron biogeochemistry. *Deep Sea Research Part II: Topical Studies in Oceanography*, **71**, pp.16-31.

Gersonde, R. (2010) "Physical oceanography and chlorophyll a during Polarstern Cruise ANT-XVIII/5a". Online database available at: Pangaea, https://doi.org/10.1594/PANGAEA.735574 (Accessed 20th August 2016).

Gilbert, I.M., Pudsey, C.J. and Murray, J.W., 1998. A sediment record of cyclic bottom-current variability from the northwest Weddell Sea. *Sedimentary Geology*, **115**(1-4), pp.185-214.

Gohl, K., Nitsche, F., Vanneste, K., Miller, H., Fechner, N., Oszko, L., Hübscher, C., Weigelt, E. and Lambrecht, A., 1997. Tectonic and sedimentary architecture of the Bellingshausen and Amundsen Sea Basins, SE Pacific, by seismic profiling. pp.719-723 in Ricci, C.A. (Ed.) *The Antarctic Region: Geological Evolution and Processes.* Terra Antartica Publication, Siena.

Gohl, K., Teterin, D., Eagles, G., Netzeband, G., Grobys, J., Parsiegla, N., Schlüter, P., Leinweber, V.T., Larter, R.D., Uenzelmann-Neben, G. and Udintsev, G.B., 2007. Geophysical survey reveals tectonic structures in the Amundsen Sea embayment, West Antarctica. *US Geological Survey Open-File Report*, 2007-1047. Available at: http://pubs.usgs.gov/of/2007/1047/srp/srp047/.

Gohl, K., Uenzelmann-Neben, G., Larter, R.D., Hillenbrand, C.-D., Hochmuth, K., Kalberg, T., Weigelt, E., Davy, B., Kuhn, G. and Nitsche, F.O., 2013. Seismic stratigraphic record of the Amundsen Sea Embayment shelf from pre-glacial to recent times: Evidence for a dynamic West Antarctic ice sheet. *Marine Geology*, **344**, pp.115-131.

Gouretski, V.V. and Koltermann, K.P., 2004. WOCE Global Hydrographic Climatology: A technical report. *Berichte des Bundesamtes für Seeschifffahrt und Hydrographie* Nr. **35**, 52 pp. Quoted in: Esper, O., Gersonde, R. and Kadagies, N., 2010. Diatom distribution in southeastern Pacific surface sediments and their relationship to modern environmental variables. *Palaeogeography, Palaeoclimatology, Palaeoecology*, **287**(1), pp.1-27.

Graham, A.G., Larter, R.D., Gohl, K., Hillenbrand, C.-D., Smith, J.A. and Kuhn, G., 2009. Bedform signature of a West Antarctic palaeo-ice stream reveals a multi-temporal record of flow and substrate control. *Quaternary Science Reviews*, **28**(25), pp.2774-2793.

Graham, A.G., Larter, R.D., Gohl, K., Dowdeswell, J.A., Hillenbrand, C.-D., Smith, J.A., Evans, J., Kuhn, G. and Deen, T., 2010. Flow and retreat of the Late Quaternary Pine Island-Thwaites palaeo-ice stream, West Antarctica. *Journal of Geophysical Research: Earth Surface*, **115**(F03025), pp.1-12.

Graham, A.G., Jakobsson, M., Nitsche, F.O., Larter, R.D., Anderson, J.B., Hillenbrand, C.D., Gohl, K., Klages, J.P., Smith, J.A. and Jenkins, A., 2016. Submarine glacial-landform distribution across the West Antarctic margin, from grounding line to slope: the Pine Island–Thwaites ice-stream system. *Geological Society, London, Memoirs*, **46**(1), pp.493-500.

Grobe, H., 1987. A simple method for the determination of ice-rafted debris in sediment cores. *Polarforschung*, **57**(3), pp.123-126.

Guyodo, Y. and Valet, J.P., 1999. Global changes in intensity of the Earth's magnetic field during the past 800 kyr. *Nature*, **399**(6733), pp.249-252.

Hansen, L.A., Callow, R.H., Kane, I.A., Gamberi, F., Rovere, M., Cronin, B.T. and Kneller, B.C., 2015. Genesis and character of thin-bedded turbidites associated with submarine channels. *Marine and Petroleum Geology*, **67**, pp.852-879.

Hauck, J., Gerdes, D., Hillenbrand, C.-D., Hoppema, M., Kuhn, G., Nehrke, G., Völker, C. and Wolf-Gladrow, D.A., 2012. Distribution and mineralogy of carbonate sediments on Antarctic shelves. *Journal of Marine Systems*, **90**(1), pp.77-87.

He, Y., Duan, T. and Gao, Z., 2008. Sediment entrainment. Chapter 7 *in:* Rebesco, M. and Camerlenghi, A. (Eds.) van Loon, A.J. (Series Ed.) *Contourites: Developments in Sedimentology Volume 60*. Elsevier, Amsterdam. pp.101-118.

Hennekam, R. and de Lange, G., 2012. X-Ray Fluorescence core scanning of wet marine sediments: methods to improve quality and reproducibility of high-resolution paleoenvironmental records. *Limnology and Oceanography: Methods*, **10**(12), pp.991-1003.

Hepp, D.A., Mörz, T. and Grützner, J., 2006. Pliocene glacial cyclicity in a deep-sea sediment drift (Antarctic Peninsula Pacific Margin). *Palaeogeography, Palaeoclimatology, Palaeoecology*, **231**(1), pp.181-198.

Hernández-Molina, F.J., Llave, E., Stow, D.A.V., García, M., Somoza, L., Vázquez, J.T., Lobo, F.J., Maestro, A., del Río, V.D., León, R. and Medialdea, T., 2006. The contourite depositional system of the Gulf of Cadiz: a sedimentary model related to the bottom current activity of the Mediterranean outflow water and its interaction with the continental margin. *Deep Sea Research Part II: Topical Studies in Oceanography*, **53**(11-13), pp.1420-1463.

Hernández-Molina, F.J., Llave, E. and Stow, D.A.V., 2008. Continental slope contourites. *Developments in Sedimentology*, **60**, pp.379-408.

Hesse, R. and Schacht, U., 2011. Early diagenesis of deep-sea sediments. In *Developments in Sedimentology*, **63**, pp. 557-713. Elsevier.

Hillenbrand, C.-D., and Ehrmann, W., 2001. Distribution of clay minerals in drift sediments on the continental rise west of the Antarctic Peninsula, ODP Leg 178, Sites 1095 and 1096. *In* Barker, P.F., Camerlenghi, A., Acton, G.D., and Ramsay, A.T.S. (Eds.), *Proc. ODP, Sci. Results,* 178: College Station, TX (Ocean Drilling Program), 1–29. doi:10.2973/odp.proc.sr.178.224.2001

Hillenbrand, C.-D., and Fütterer, D.K., 2001. Neogene to Quaternary deposition of opal on the continental rise west of the Antarctic Peninsula, ODP Leg 178, Sites 1095, 1096, and 1101. *In* Barker, P.F., Camerlenghi, A., Acton, G.D., and Ramsay, A.T.S. (Eds.), *Proc. ODP, Sci. Results,* 178: College Station, TX (Ocean Drilling Program), 1–33. doi:10.2973/odp.proc.sr.178.215.2001

Hillenbrand, C.D., Fütterer, D.K., Grobe, H. and Frederichs, T., 2002. No evidence for a Pleistocene collapse of the West Antarctic Ice Sheet from continental margin sediments recovered in the Amundsen Sea. *Geo-Marine Letters*, 22(2), pp.51-59.

Hillenbrand, C.-D., Fütterer, D.K., Grobe, H. and Frederichs, T., 2002. No evidence for a Pleistocene collapse of the West Antarctic Ice Sheet from continental margin sediments recovered in the Amundsen Sea. *Geo-Marine Letters*, **22**(2), pp.51-59.

Hillenbrand, C.-D., Grobe, H., Diekmann, B., Kuhn, G. and Fütterer, D.K., 2003. Distribution of clay minerals and proxies for productivity in surface sediments of the Bellingshausen and Amundsen seas (West Antarctica)–Relation to modern environmental conditions. *Marine Geology*, **193**(3), pp.253-271.

Hillenbrand, C.-D. and Ehrmann, W., 2005. Late Neogene to Quaternary environmental changes in the Antarctic Peninsula region: evidence from drift sediments. *Global and Planetary Change*, **45**(1), pp.165-191.

Hillenbrand, C.-D., Camerlenghi, A., Cowan, E.A., Hernández-Molina, F.J., Lucchi, R.G., Rebesco, M. and Uenzelmann-Neben, G., 2008a. The present and past bottom-current flow regime around the sediment drifts on the continental rise west of the Antarctic Peninsula. *Marine Geology*, **255**(1), pp.55-63.

Hillenbrand, C.-D., Moreton, S.G., Caburlotto, A., Pudsey, C.J., Lucchi, R.G., Smellie, J.L., Benetti, S., Grobe, H., Hunt, J.B. and Larter, R.D., 2008b. Volcanic time-markers for Marine Isotopic Stages 6 and 5 in Southern Ocean sediments and Antarctic ice cores: implications for tephra correlations between palaeoclimatic records. *Quaternary Science Reviews*, **27**(5), pp.518-540.

Hillenbrand, C.-D., Kuhn, G. and Frederichs, T., 2009a. Record of a Mid-Pleistocene depositional anomaly in West Antarctic continental margin sediments: an indicator for ice-sheet collapse? *Quaternary Science Reviews*, **28**(13), pp.1147-1159.

Hillenbrand, C.-D., Ehrmann, W., Larter, R.D., Benetti, S., Dowdeswell, J.A., Cofaigh, C.Ó., Graham, A.G. and Grobe, H., 2009b. Clay mineral provenance of sediments in the southern Bellingshausen Sea reveals drainage changes of the West Antarctic Ice Sheet during the Late Quaternary. *Marine Geology*, **265**(1), pp.1-18.

Hillenbrand, C.-D., Kuhn, G. and Frederichs, T. 2009c. Sedimentology on core PS58/254-1. Pangaea dataset accessible at: https://doi.pangaea.de/10.1594/PANGAEA.701219. Accessed December 2014. Dataset is in supplement to: Hillenbrand, C.-D., Kuhn, G. and Frederichs, T., 2009a. Record of a Mid-Pleistocene depositional anomaly in West Antarctic continental margin sediments: an indicator for ice-sheet collapse? *Quaternary Science Reviews*, **28**(13), pp.1147-1159.

Hillenbrand, C.-D., Smith, J.A., Hodell, D.A., Greaves, M., Poole, C.R., Kender, S., Williams, M., Andersen, T.J., Jernas, P.E., Elderfield, H., Klages, J.P., Roberts, S.J., Gohl, K., Larter, R.D., Kuhn, G. (2017). West Antarctic Ice Sheet retreat driven by Holocene warm water incursions. *Nature*, **547**, pp.43-48.

Hiscock, M.R., Marra, J., Smith Jr, W.O., Goericke, R., Vink, S., Olson, R.J., Sosik, H.M. and Barber, R.T., 2003. Primary productivity and its regulation in the Pacific Sector of the

Southern Ocean. *Deep Sea Research Part II: Topical Studies in Oceanography*, **50**(3-4), pp.533-558.

Hochmuth, K. and Gohl, K., 2013. Glaciomarine sedimentation dynamics of the Abbot glacial trough of the Amundsen Sea Embayment shelf, West Antarctica. *Geological Society, London, Special Publications*, **381**(1), pp.233-244.

Howe, J.A., 1996. Turbidite and contourite sediment waves in the northern Rockall Trough, North Atlantic Ocean. *Sedimentology*, **43**(2), pp.219-234.

Howe, J.A., Pudsey, C.J. and Cunningham, A.P., 1997. Pliocene-Holocene contourite deposition under the Antarctic circumpolar current, western Falkland trough, South Atlantic Ocean. *Marine Geology*, **138**(1-2), pp.27-50.

Howe, J.A., Livermore, R.A. and Maldonado, A., 1998. Mudwave activity and current-controlled sedimentation in Powell Basin, northern Weddell Sea, Antarctica. *Marine Geology*, **149**(1-4), pp.229-241.

Howe, J.A., 2008. Methods for contourite research. Chapter 3 *in:* Rebesco, M. and Camerlenghi, A. (Eds.) van Loon, A.J. (Series Ed.) *Contourites: Developments in Sedimentology Volume 60*. Elsevier, Amsterdam. pp.19-33.

Huang, X. and Jokat, W., 2016. Middle Miocene to present sediment transport and deposits in the southeastern Weddell Sea, Antarctica. *Global and Planetary Change*, **139**, pp.211-225.

Hughes, T.J. (1981) Correspondence. The weak underbelly of the West Antarctic Ice Sheet. *Journal of Glaciology,* **27**(97), 518-525.

Jacobs, S.S., Jenkins, A., Giulivi, C.F. and Dutrieux, P., 2011. Stronger ocean circulation and increased melting under Pine Island Glacier ice shelf. *Nature Geoscience*, **4**(8), pp.519-523.

Jacobs, S., Giulivi, C., Dutrieux, P., Rignot, E., Nitsche, F. and Mouginot, J., 2013. Getz Ice Shelf melting response to changes in ocean forcing. *Journal of Geophysical Research: Oceans*, **118**(9), pp.4152-4168.

Jakobsson, M., Anderson, J.B., Nitsche, F.O., Gyllencreutz, R., Kirshner, A.E., Kirchner, N., O'Regan, M., Mohammad, R. and Eriksson, B., 2012. Ice sheet retreat dynamics inferred from glacial morphology of the central Pine Island Bay Trough, West Antarctica. *Quaternary Science Reviews*, **38**, pp.1-10.

Jenkins, A., Dutrieux, P., Jacobs, S., Steig, E.J., Gudmundsson, G.H., Smith, J. and Heywood, K.J., 2016. Decadal ocean forcing and Antarctic ice sheet response: Lessons from the Amundsen Sea. *Oceanography*, **29**(4), pp.106-117.

Johnson, J.A. and Hill, R.B., 1975, November. A three-dimensional model of the Southern Ocean with bottom topography. In Deep Sea Research and Oceanographic Abstracts (Vol. 22, No. 11, pp. 745-751). Elsevier. Cited in: Nowlin, W.D. and Klinck, J.M., 1986. The physics of the Antarctic circumpolar current. *Reviews of Geophysics*, **24**(3), pp.469-491.

Jordan, T.A., Ferraccioli, F., Vaughan, D.G., Holt, J.W., Corr, H., Blankenship, D.D. and Diehl, T.M., 2010. Aerogravity evidence for major crustal thinning under the Pine Island Glacier region (West Antarctica). *Geological Society of America Bulletin*, **122**(5-6), pp.714-726.

Jorissen F.J., 1999. Benthic foraminiferal microhabitats below the sediment-water interface. Chapter 10, pp.161-179 In: Gupta, B.K.S. (Ed) *Modern Foraminifera*. Springer, Dordrecht.

Joughin, I., Rignot, E., Rosanova, C.E., Lucchitta, B.K. and Bohlander, J., 2003. Timing of recent accelerations of Pine Island glacier, Antarctica. *Geophysical Research Letters*, **30**(13) 1706.

Joughin, I., Smith, B.E. and Holland, D.M., 2010. Sensitivity of 21st century sea level to ocean-induced thinning of Pine Island Glacier, Antarctica. *Geophysical Research Letters*, **37**(20) L20502.

Joughin, I. and Alley, R.B., 2011. Stability of the West Antarctic Ice Sheet in a warming world. *Nature Geoscience*, **4**(8), pp.506-513.

Joughin, I., Smith, B.E. and Medley, B., 2014. Marine ice sheet collapse potentially under way for the Thwaites Glacier Basin, West Antarctica. *Science*, **344**(6185), pp.735-738.

Jouzel, J., Masson-Delmotte, V., Cattani, O., Dreyfus, G., Falourd, S., Hoffmann, G., Minster, B., Nouet, J., Barnola, J.M., Chappellaz, J. and Fischer, H., 2007. Orbital and millennial Antarctic climate variability over the past 800,000 years. *Science*, **317**(5839), pp.793-796.

Keevil, G.M., Peakall, J. and Best, J.L., 2008. The formation and dynamics of sediment waves. Conference paper, pp.179-183, Marine and River Dune Dynamics, 1-3 April 2008, Leeds.

Kim, C.S., Kim, T.W., Cho, K.H., Ha, H.K., Lee, S., Kim, H.C. and Lee, J.H., 2016. Variability of the Antarctic Coastal Current in the Amundsen Sea. *Estuarine, Coastal and Shelf Science*, **181**, pp.123-133.

King, M.A., Bingham, R.J., Moore, P., Whitehouse, P.L., Bentley, M.J. and Milne, G.A., 2012. Lower satellite-gravimetry estimates of Antarctic sea-level contribution. *Nature*, **491**(7425), pp.586-589.

Kipf, A., Hauff, F., Werner, R., Gohl, K., van den Bogaard, P., Hoernle, K., Maicher, D. and Klügel, A., 2014. Seamounts off the West Antarctic margin: A case for non-hotspot driven intraplate volcanism. *Gondwana Research*, **25**(4), pp.1660-1679.

Kirshner, A.E., Anderson, J.B., Jakobsson, M., O'Regan, M., Majewski, W. and Nitsche, F.O., 2012. Post-LGM deglaciation in Pine island Bay, west Antarctica. *Quaternary Science Reviews*, **38**, pp.11-26.

Klages, J.P., Kuhn, G., Graham, A.G.C., Hillenbrand, C.-D., Smith, J.A., Nitsche, F.O., Larter, R.D. and Gohl, K., 2015. Palaeo-ice stream pathways and retreat style in the easternmost Amundsen Sea Embayment, West Antarctica, revealed by combined multibeam bathymetric and seismic data. *Geomorphology*, **245**, pp.207-222.

Klages, J.P., Kuhn, G., Hillenbrand, C.-D., Smith, J.A., Graham, A.G., Nitsche, F.O., Frederichs, T., Jernas, P.E., Gohl, K. and Wacker, L., 2017. Limited grounding-line advance onto the West Antarctic continental shelf in the easternmost Amundsen Sea Embayment during the last glacial period. *PloS one*, **12**(7) p.e0181593.

Konfirst, M.A., Scherer, R.P., Hillenbrand, C.-D. and Kuhn, G., 2012. A marine diatom record from the Amundsen Sea—insights into oceanographic and climatic response to the Mid-Pleistocene transition in the West Antarctic sector of the Southern Ocean. *Marine Micropaleontology*, **92**, pp.40-51.

Kneller, B., 2003. The influence of flow parameters on turbidite slope channel architecture. *Marine and Petroleum Geology*, **20**(6-8), pp.901-910.

Knutz, P.C., 2008. Palaeoceanographic significance of contourite drifts. Chapter 24 *in:* Rebesco, M. and Camerlenghi, A. (Eds.) van Loon, A.J. (Series Ed.) *Contourites: Developments in Sedimentology Volume 60*. Elsevier, Amsterdam. pp.511-535.

Kranck, K., 1984. Grain-size characteristics of turbidites. *Geological Society, London, Special Publications*, **15**(1), pp.83-92.

Kreutz, K.J., Mayewski, P.A., Pittalwala, I.I., Meeker, L.D., Twickler, M.S. and Whitlow, S.I., 2000. Sea level pressure variability in the Amundsen Sea region inferred from a West Antarctic glaciochemical record. *Journal of Geophysical Research: Atmospheres*, **105**(D3), pp.4047-4059.

Kuhn, G., Hillenbrand, C.D., Kasten, S., Smith, J.A., Nitsche, F.O., Frederichs, T., Wiers, S., Ehrmann, W., Klages, J.P. and Mogollón, J.M., 2017. Evidence for a palaeo-subglacial lake on the Antarctic continental shelf. *Nature Communications*, **8**, 15591.

Kurentsova, N.A., Udintsev, G.V., Teterin, D.E. and Roshchina, I.A., 2008. Geology of the Hubert Miller Seamount, Marie Byrd Seamounts province, Amundsen Sea, West Antarctic. *Russian Journal of Pacific Geology*, **2**(5), pp.377-384.

Kuvaas, B. and Leitchenkov, G., 1992. Glaciomarine turbidite and current controlled deposits in Prydz Bay, Antarctica. *Marine Geology*, **108**(3-4), pp.365-381.

Kuvaas, B., Kristoffersen, Y., Guseva, J., Leitchenkov, G., Gandjukhin, V., Løvås, O., Sand, M. and Brekke, H., 2005. Interplay of turbidite and contourite deposition along the Cosmonaut Sea/Enderby Land margin, East Antarctica. *Marine Geology*, **217**(1-2), pp.143-159.

Lamy, F., Gersonde, R., Winckler, G., Esper, O., Jaeschke, A., Kuhn, G., Ullermann, J., Martínez-Garcia, A., Lambert, F. and Kilian, R., 2014. Increased dust deposition in the Pacific Southern Ocean during glacial periods. *Science*, **343**(6169), pp.403-407.

Langereis, C.G., Dekkers, M.J., Lange, G.D., Paterne, M. and Santvoort, P.V., 1997. Magnetostratigraphy and astronomical calibration of the last 1.1 Myr from an eastern Mediterranean piston core and dating of short events in the Brunhes. *Geophysical Journal International*, **129**(1), pp.75-94.

Larter, R.D. and Cunningham, A.P., 1993. The depositional pattern and distribution of glacial-interglacial sequences on the Antarctic Peninsula Pacific margin. *Marine Geology*, **109**(3-4), pp.203-219.

Larter, R.D., Graham, A.G., Gohl, K., Kuhn, G., Hillenbrand, C.-D., Smith, J.A., Deen, T.J., Livermore, R.A. and Schenke, H.W., 2009. Subglacial bedforms reveal complex basal regime in a zone of paleo–ice stream convergence, Amundsen Sea Embayment, West Antarctica. *Geology*, **37**(5), pp.411-414.

Larter, R.D., Anderson, J.B., Graham, A.G., Gohl, K., Hillenbrand, C.-D., Jakobsson, M., Johnson, J.S., Kuhn, G., Nitsche, F.O., Smith, J.A. and Witus, A.E., 2014. Reconstruction of changes in the Amundsen Sea and Bellingshausen Sea sector of the West Antarctic ice sheet since the Last Glacial Maximum. *Quaternary Science Reviews*, **100**, pp.55-86.

Lee, H.J., Syvitski, J.P., Parker, G., Orange, D., Locat, J., Hutton, E.W. and Imran, J., 2002. Distinguishing sediment waves from slope failure deposits: field examples, including the 'Humboldt slide', and modelling results. *Marine Geology*, **192**(1-3), pp.79-104.

LeMasurier, W.E. and Rex, D.C., 1991, Marie Byrd Land volcanic province and its relation to the Cenozoic West Antarctic rift system, pp.249-284 *in* Tingey, R.J. (Ed) *The Geology of Antarctica*. Oxford University Press, Oxford.

Li, F., Ginoux, P. and Ramaswamy, V., 2008. Distribution, transport, and deposition of mineral dust in the Southern Ocean and Antarctica: Contribution of major sources. *Journal of Geophysical Research: Atmospheres*, **113**(D10207).

Lindeque, A., Gohl, K., Henrys, S., Wobbe, F. and Davy, B., 2016. Seismic stratigraphy along the Amundsen Sea to Ross Sea continental rise: A cross-regional record of pre-glacial to glacial processes of the West Antarctic margin. *Palaeogeography, Palaeoclimatology, Palaeoecology*, **443**, pp.183-202.

Lisiecki, L.E. and Raymo, M.E., 2005. A Pliocene-Pleistocene stack of 57 globally distributed benthic $\delta^{18}O$ records. *Palaeoceanography*, **20**(1) PA1003.

Locarnini, R.A., 1994. Water masses and circulation in the Ross Gyre and environs. Texas A&M University, Office of Graduate Studies.

Lowe, D.R., 1982. Sediment gravity flows: II Depositional models with special reference to the deposits of high-density turbidity currents. *Journal of Sedimentary Research*, **52**(1) pp.279-297.

Lowe, A.L. and Anderson, J.B., 2002. Reconstruction of the West Antarctic ice sheet in Pine Island Bay during the Last Glacial Maximum and its subsequent retreat history. *Quaternary Science Reviews*, **21**(16), pp.1879-1897.

Lu, Z., Hoogakker, B.A., Hillenbrand, C.D., Zhou, X., Thomas, E., Gutchess, K.M., Lu, W., Jones, L. and Rickaby, R.E., 2016. Oxygen depletion recorded in upper waters of the glacial Southern Ocean. *Nature Communications*, **7**, 11146.

Lucchi, R.G., Rebesco, M., Camerlenghi, A., Busetti, M., Tomadin, L., Villa, G., Persico, D., Morigi, C., Bonci, M.C. and Giorgetti, G., 2002. Mid-late Pleistocene glacimarine

sedimentary processes of a high-latitude, deep-sea sediment drift (Antarctic Peninsula Pacific margin). *Marine Geology*, **189**(3), pp.343-370.

Lucchi, R.G. and Rebesco, M., 2007. Glacial contourites on the Antarctic Peninsula margin: insight for palaeoenvironmental and palaeoclimatic conditions. *Geological Society, London, Special Publications*, **276**(1), pp.111-127.

MacAyeal, D.R., 1992. Irregular oscillations of the West Antarctic ice sheet. *Nature*, **359**(6390), p.29.

MacGregor, J.A., Catania, G.A., Markowski, M.S. and Andrews, A.G., 2012. Widespread rifting and retreat of ice-shelf margins in the eastern Amundsen Sea Embayment between 1972 and 2011. *Journal of Glaciology*, **58**(209), pp.458-466.

Majewski, W., Wellner, J.S. and Anderson, J.B., 2016. Environmental connotations of benthic foraminiferal assemblages from coastal West Antarctica. *Marine Micropaleontology*, **124**, pp.1-15.

Maldonado, A., Barnolas, A., Bohoyo, F., Escutia, C., Galindo-Zaldívar, J., Hernández-Molina, J., Jabaloy, A., Lobo, F.J., Nelson, C.H., Rodríguez-Fernández, J. and Somoza, L., 2005. Miocene to recent contourite drifts development in the northern Weddell Sea (Antarctica). *Global and Planetary Change*, **45**(1-3), pp.99-129.

Mangini, A., Eisenhauer, A. and Walter, P., 1990. Response of manganese in the ocean to the climatic cycles in the Quaternary. *Paleoceanography*, **5**(5), pp.811-821.

Mangini, A., Jung, M. and Laukenmann, S., 2001. What do we learn from peaks of uranium and of manganese in deep sea sediments? *Marine Geology*, **177**(1), pp.63-78.

Marinoni, L., Quaia, T., Setti, M., Lopez-Galindo, A. and Brambati, A., 2000. Mineralogy and crystal-chemistry of the clay fraction in core ANTA91-8 Ross Sea, Antarctica: palaeoclimatic and palaeoenvironmental implications. *Terra Antartica Reports*, **4**, pp.211-216.

Martos, Y.M., Maldonado, A., Lobo, F.J., Hernández-Molina, F.J. and Pérez, L.F., 2013. Tectonics and palaeoceanographic evolution recorded by contourite features in southern Drake Passage (Antarctica). *Marine Geology*, **343**, pp.76-91.

Mayall, M., Jones, E. and Casey, M., 2006. Turbidite channel reservoirs—Key elements in facies prediction and effective development. *Marine and Petroleum Geology*, **23**(8), pp.821-841.

Mazur, A.K., Wåhlin, A.K. and Krężel, A., 2017. An object-based SAR image iceberg detection algorithm applied to the Amundsen Sea. *Remote Sensing of Environment*, **189**, pp.67-83.

McCave, I.N., Manighetti, B. and Robinson, S.G., 1995. Sortable silt and fine sediment size/composition slicing: parameters for palaeocurrent speed and palaeoceanography. *Paleoceanography*, **10**(3), pp.593-610.

McCave, I.N. and Hall, I.R., 2006. Size sorting in marine muds: Processes, pitfalls, and prospects for paleoflow-speed proxies. *Geochemistry, Geophysics, Geosystems*, **7**(10) Q10N05.

McCave, I.N., 2008. Size sorting during transport and deposition of fine sediments: sortable silt and flow speed. Chapter 8 *in:* Rebesco, M. and Camerlenghi, A. (Eds.) van Loon, A.J. (Series Ed.) *Contourites: Developments in Sedimentology Volume 60*. Elsevier, Amsterdam. pp.121-142.

McCave, I.N., 2017. Formation of sediment waves by turbidity currents and geostrophic flows: A discussion. *Marine Geology*, **390**, pp.89-93.

McCave, I.N., Thornalley, D.J.R. and Hall, I.R. 2017. Relation of sortable silt grain-size to deep-sea current speeds: Calibration of the 'Mud Current Meter'. *Deep Sea Research Part 1: Oceanographic Research Papers,* **127**, pp.1-12.

McHargue, T., Pyrcz, M.J., Sullivan, M.D., Clark, J.D., Fildani, A., Romans, B.W., Covault, J.A., Levy, M., Posamentier, H.W. and Drinkwater, N.J., 2011. Architecture of turbidite channel systems on the continental slope: patterns and predictions. *Marine and Petroleum Geology,* **28**(3), pp.728-743.

Meiburg, E. and Kneller, B., 2010. Turbidity currents and their deposits. *Annual Review of Fluid Mechanics*, **42**, pp.135-156.

Merino, N., Le Sommer, J., Durand, G., Jourdain, N.C., Madec, G., Mathiot, P. and Tournadre, J., 2016. Antarctic icebergs melt over the Southern Ocean: climatology and impact on sea ice. *Ocean Modelling*, **104**, pp.99-110.

Michels, K.H., Rogenhagen, J. and Kuhn, G., 2001. Recognition of contour-current influence in mixed contourite-turbidite sequences of the western Weddell Sea, Antarctica. *Marine Geophysical Researches*, **22**(5-6), pp.465-485.

Michels, K.H., Kuhn, G., Hillenbrand, C.D., Diekmann, B., FÜtterer, D.K., Grobe, H. and Uenzelmann-Neben, G., 2002. The southern Weddell Sea: combined contourite-turbidite sedimentation at the southeastern margin of the Weddell Gyre. *Geological Society, London, Memoirs,* **22**(1), pp.305-323.

Middleton, G.V., 1993. Sediment deposition from turbidity currents. *Annual Review of Earth and Planetary Sciences,* **21**(1), pp.89-114.

Migeon, S., Savoye, B., Zanella, E., Mulder, T., Faugères, J.C. and Weber, O., 2001. Detailed seismic-reflection and sedimentary study of turbidite sediment waves on the Var Sedimentary Ridge (SE France): significance for sediment transport and deposition and for the mechanisms of sediment-wave construction. *Marine and Petroleum Geology*, **18**(2), pp.179-208.

Monterey, G. and Levitus, S., 1997. Seasonal variability of mixed layer depth for the world ocean. NOAA Atlas NESDIS, vol. 14. U.S. Gov. Printing Office, Washington, D.C., 96 pp. Quoted in: Esper, O., Gersonde, R. and Kadagies, N., 2010. Diatom distribution in southeastern Pacific surface sediments and their relationship to modern environmental variables. *Palaeogeography, Palaeoclimatology, Palaeoecology*, **287**(1), pp.1-27.

Mortlock, R.A. and Froelich, P.N., 1989. A simple method for the rapid determination of biogenic opal in pelagic marine sediments. *Deep Sea Research Part A. Oceanographic Research Papers*, **36**(9), pp.1415-1426.

Mouginot, J., Rignot, E. and Scheuchl, B., 2014. Sustained increase in ice discharge from the Amundsen Sea Embayment, West Antarctica, from 1973 to 2013. *Geophysical Research Letters*, **41**(5), pp.1576-1584.

Mulder, T., Faugères, J.-C. and Gonthier, E., 2008. Mixed turbidite-contourite systems. Chapter 21 *in:* Rebesco, M. and Camerlenghi, A. (Eds.) van Loon, A.J. (Series Ed.) *Contourites: Developments in Sedimentology Volume 60*. Elsevier, Amsterdam. pp.435-456.

Müller, P.J. and Schneider, R., 1993. An automated leaching method for the determination of opal in sediments and particulate matter. *Deep Sea Research Part I: Oceanographic Research Papers*, **40**(3), pp.425-444.

Mutti, E. and Carminatti, M., 2012. Deep-water sands of the Brazilian offshore basins: American Association of Petroleum Geologists Search and Discovery Article 30219.

Nakayama, Y., Schröder, M. and Hellmer, H.H., 2013. From Circumpolar Deep Water to the glacial meltwater plume on the eastern Amundsen Shelf. *Deep Sea Research Part I: Oceanographic Research Papers*, **77**, pp.50-62.

Nakayama, Y., Timmermann, R., Rodehacke, C.B., Schröder, M. and Hellmer, H.H., 2014. Modelling the spreading of glacial meltwater from the Amundsen and Bellingshausen Seas. *Geophysical Research Letters*, **41**(22), pp.7942-7949.

National Oceanographic Data Centre (2013) "CTD data from Amundsen and Ross seas 2010/2011 during the OSO1011 expedition" submitted by Anna Wahlin. Accessed August 2016.

National Snow and Ice Data Centre (2016) Sea Ice Index Data and Image Archive. https://nsidc.org/data/seaice_index/archives.html. Accessed September 2016.

Nayudu, Y.R., 1971. Lithology and chemistry of surface sediments in sub-Antarctic regions of the Pacific Ocean. *Antarctic Research Series* **15**, pp.247-282.

Nelson, C.H., Baraza, J. and Maldonado, A., 1993. Mediterranean undercurrent sandy contourites, Gulf of Cadiz, Spain. *Sedimentary Geology*, **82**(1), pp.103-131.

Nelson, C.H. and Nilsen, T.H., 1984. Modern and ancient deep-sea fan sedimentation: lecture notes for short course no. 14. Society of Economic Paleontologists and Mineralogists. In: Maldonado, A., Barnolas, A., Bohoyo, F., Escutia, C., Galindo-Zaldívar, J., Hernández-Molina, J., Jabaloy, A., Lobo, F.J., Nelson, C.H., Rodríguez-Fernández, J. and Somoza, L., 2005. Miocene to recent contourite drifts development in the northern Weddell Sea (Antarctica). *Global and Planetary Change*, **45**(1-3), pp.99-129.

Nicholls, K.W., Østerhus, S., Makinson, K., Gammelsrød, T. and Fahrbach, E., 2009. Ice-ocean processes over the continental shelf of the southern Weddell Sea, Antarctica: A review. *Reviews of Geophysics*, **47**(3).

Niessen, F., Gebhardt, A.C., Kuhn, G., Magens, D. and Monien, D., 2013. Porosity and density of the AND-1B sediment core, McMurdo Sound region, Antarctica: Field consolidation enhanced by grounded ice. *Geosphere*, **9**(3), pp.489-509.

Nitsche, F.O., Gohl, K., Vanneste, K. and Miller, H., 1997. Seismic expression of glacially deposited sequences in the Bellingshausen and Amundsen Seas, West Antarctica. *Geology and Seismic Stratigraphy of the Antarctic Margin,* **2**, pp.95-108.

Nitsche, F.O., Cunningham, A.P., Larter, R.D. and Gohl, K., 2000. Geometry and development of glacial continental margin depositional systems in the Bellingshausen Sea. *Marine Geology*, **162**(2), pp.277-302.

Nitsche, F.O., Jacobs, S.S., Larter, R.D. and Gohl, K., 2007. Bathymetry of the Amundsen Sea continental shelf: implications for geology, oceanography, and glaciology. *Geochemistry, Geophysics, Geosystems*, **8**(10).

Nitsche, F. Personal Communication on 14/05/2016.

Noormets, R., Dowdeswell, J.A., Larter, R.D., Ó Cofaigh, C. and Evans, J., 2009. Morphology of the upper continental slope in the Bellingshausen and Amundsen Seas–Implications for sedimentary processes at the shelf edge of West Antarctica. *Marine Geology*, **258**(1), pp.100-114.

Normark, W.R., Piper, D.J., Posamentier, H., Pirmez, C. and Migeon, S., 2002. Variability in form and growth of sediment waves on turbidite channel levees. *Marine Geology*, **192**(1), pp.23-58.

Nowlin, W.D. and Klinck, J.M., 1986. The physics of the Antarctic circumpolar current. *Reviews of Geophysics*, **24**(3), pp.469-491.

Ó Cofaigh, C., Dowdeswell, J.A. and Pudsey, C.J., 2001. Late Quaternary iceberg rafting along the Antarctic Peninsula continental rise and in the Weddell and Scotia Seas. *Quaternary Research*, **56**(3), pp.308-321.

Ó Cofaigh, C., Taylor, J., Dowdeswell, J.A. and Pudsey, C.J., 2003. Palaeo-ice streams, trough mouth fans and high-latitude continental slope sedimentation. *Boreas*, **32**(1), pp.37-55.

O'Grady, D.B. and Syvitski, J.P., 2002. Large-scale morphology of Arctic continental slopes: the influence of sediment delivery on slope form. *Geological Society, London, Special Publications*, **203**(1), pp.11-31.

Orsi, A.H., Whitworth, T. and Nowlin, W.D., 1995. On the meridional extent and fronts of the Antarctic Circumpolar Current. *Deep Sea Research Part I: Oceanographic Research Papers*, **42**(5), pp.641-673.

Orsi, A.H., Johnson, G.C. and Bullister, J.L., 1999. Circulation, mixing, and production of Antarctic Bottom Water. *Progress in Oceanography*, **43**(1), pp.55-109.

Orsi, A.H. and Wiederwohl, C.L., 2009. A recount of Ross Sea waters. *Deep Sea Research Part II: Topical Studies in Oceanography*, **56**(13-14), pp.778-795.

Otto-Bliesner, B.L., Hewitt, C.D., Marchitto, T.M., Brady, E., Abe-Ouchi, A., Crucifix, M., Murakami, S. and Weber, S.L., 2007. Last Glacial Maximum ocean thermohaline circulation: PMIP2 model intercomparisons and data constraints. *Geophysical Research Letters*, **34**(12).

Pankhurst, R.J., Weaver, S.D., Bradshaw, J.D., Storey, B.C. and Ireland, T.R., 1998. Geochronology and geochemistry of pre-Jurassic superterranes in Marie Byrd Land, Antarctica. *Journal of Geophysical Research: Solid Earth*, **103**(B2), pp.2529-2547.

Parkinson, C.L. and Cavalieri, D.J., 2012. Antarctic sea ice variability and trends, 1979-2010. *The Cryosphere*, **6**(4), p.871.

Parsons, J.D., Friedrichs, C.T., Traykovski, P.A., Mohrig, D., Imran, J., Syvitski, J.P., Parker, G.A.R.Y., Puig, P., Buttles, J.L. and Garcia, M.H., 2007. The mechanics of marine sediment gravity flows. *Continental Margin Sedimentation: From Sediment Transport to Sequence Stratigraphy, C. Nittrouer, J. Austin, M. Field, J. Syvitski, and P. Wiberg, eds., Blackwell, Oxford, UK*, pp.275-333.

Passchier, S., 2011. Linkages between East Antarctic Ice Sheet extent and Southern Ocean temperatures based on a Pliocene high-resolution record of ice-rafted debris off Prydz Bay, East Antarctica. *Paleoceanography*, **26**(4).

Petschick, R., Kuhn, G. and Gingele, F., 1996. Clay mineral distribution in surface sediments of the South Atlantic: sources, transport, and relation to oceanography. *Marine Geology*, **130**(3-4), pp.203-229.

Petty, A.A., Holland, P.R. and Feltham, D.L., 2014. Sea ice and the ocean mixed layer over the Antarctic shelf seas. *The Cryosphere*, **8**(2), pp.761-783.

Piper, D.J.W., 1973. The sedimentology of silt turbidites from the Gulf of Alaska. *Initial Reports of the Deep Sea Drilling Project*, **18**, pp.847-867.

Pratson, L.F., Imran, J., Parker, G., Syvitski, J.P. and Hutton, E., 2000. AAPG Memoir 72/SEPM Special Publication No. 68, Chapter 6: *Debris Flows vs. Turbidity Currents: a Modeling Comparison of Their Dynamics and Deposits.*

Pritchard, H.D., Ligtenberg, S.R.M., Fricker, H.A., Vaughan, D.G., Van den Broeke, M.R. and Padman, L., 2012. Antarctic ice-sheet loss driven by basal melting of ice shelves. *Nature*, **484**(7395), pp.502-505.

Pudsey, C.J. and Camerlenghi, A., 1998. Glacial–interglacial deposition on a sediment drift on the Pacific margin of the Antarctic Peninsula. *Antarctic Science*, **10**(3), pp.286-308.

Pudsey, C.J., 2000. Sedimentation on the continental rise west of the Antarctic Peninsula over the last three glacial cycles. *Marine Geology*, **167**(3), pp.313-338.

Pudsey, C.J. and Howe, J.A., 2002. Mixed biosiliceous-terrigenous sedimentation under the Antarctic Circumpolar Current, Scotia Sea. *Geological Society, London, Memoirs*, **22**(1), pp.325-336.

Pugh, R.S., McCave, I.N., Hillenbrand, C.-D. and Kuhn, G., 2009. Circum-Antarctic age modelling of Quaternary marine cores under the Antarctic Circumpolar Current: ice-core dust–magnetic correlation. *Earth and Planetary Science Letters*, **284**(1), pp.113-123.

Raiswell, R., Tranter, M., Benning, L.G., Siegert, M., De'ath, R., Huybrechts, P. and Payne, T., 2006. Contributions from glacially derived sediment to the global iron (oxyhydr) oxide cycle: implications for iron delivery to the oceans. *Geochimica et Cosmochimica Acta*, **70**(11), pp.2765-2780.

Rebesco, M., Larter, R.D., Camerlenghi, A. and Barker, P.F., 1996. Giant sediment drifts on the continental rise west of the Antarctic Peninsula. *Geo-Marine Letters*, **16**(2), pp.65-75.

Rebesco, M., Larter, R.D., Barker, P.F., Camerlenghi, A. and Vanneste, L.E., 1997. The history of sedimentation on the continental rise west of the Antarctic Peninsula. *Geology and Seismic Stratigraphy of the Antarctic Margin, Part 2. Antarctic Research Series, 71*, pp 29-49. American Geophysical Union.

Rebesco, M., Pudsey, C.J., Canals, M., Camerlenghi, A., Barker, P.F., Estrada, F. and Giorgetti, A., 2002. Sediment drifts and deep-sea channel systems, Antarctic Peninsula Pacific Margin. In: Stow, D.A.V., Faugeres, J.-C., Howe, J., Pudsey, C., Viana, A. (Eds) Deep-Water Contourite Systems: Modern Drift and Ancient Series, Seismic and Sedimentary Characteristics. *Geological Society, London, Memoirs*, **22**(1), pp.353-371.

Rebesco, M., Camerlenghi, A. and Van Loon, A.J., 2008. Contourite research: a field in full development. *Developments in sedimentology*, *60*, pp.1-10. Elsevier, Amsterdam.

Rebesco, M., Wåhlin, A., Laberg, J.S., Schauer, U., Beszczynska-Möller, A., Lucchi, R.G., Noormets, R., Accettella, D., Zarayskaya, Y. and Diviacco, P., 2013. Quaternary contourite drifts of the Western Spitsbergen margin. *Deep Sea Research Part I: Oceanographic Research Papers*, **79**, pp.156-168.

Rebesco, M., Hernández-Molina, F.J., Van Rooij, D. and Wåhlin, A., 2014. Contourites and associated sediments controlled by deep-water circulation processes: state-of-the-art and future considerations. *Marine Geology*, **352**, pp.111-154.

Reimer, P.J., Bard, E., Bayliss, A., Beck, J.W., Blackwell, P.G., Ramsey, C.B., Buck, C.E., Cheng, H., Edwards, R.L., Friedrich, M. and Grootes, P.M., 2013. IntCal13 and Marine13 radiocarbon age calibration curves 0–50,000 years cal BP. *Radiocarbon,* **55**(4), pp.1869-1887.

Richter, T. O., and others. 2006. The Avaatech XRF Core Scanner: Technical description and applications to NE Atlantic sediments, pp.39-50. In: Rothwell, R.G. [Ed.] *New Techniques in Sediment Core Analysis.* Geological Society, London, Special Publications, 267.

Rignot, E. and Jacobs, S.S., 2002. Rapid bottom melting widespread near Antarctic ice sheet grounding lines. *Science*, **296**(5575), pp.2020-2023.

Rignot, E., Vaughan, D.G., Schmeltz, M., Dupont, T. and MacAyeal, D., 2002. Acceleration of Pine Island and Thwaites glaciers, west Antarctica. *Annals of Glaciology*, **34**(1), pp.189-194.

Rignot, E., Bamber, J.L., Van Den Broeke, M.R., Davis, C., Li, Y., Van De Berg, W.J. and Van Meijgaard, E., 2008. Recent Antarctic ice mass loss from radar interferometry and regional climate modelling. *Nature Geoscience*, **1**(2), pp.106-110.

Rignot, E., Mouginot, J. and Scheuchl, B., 2011. Ice flow of the Antarctic ice sheet. *Science*, **333**(6048), pp.1427-1430.

Roberts, A.P., 2006. High-resolution magnetic analysis of sediment cores: strengths, limitations and strategies for maximizing the value of long-core magnetic data. *Physics of the Earth and Planetary Interiors*, **156**(3), pp.162-178.

Roberts, J., McCave, I.N., McClymont, E.L., Kender, S., Hillenbrand, C.D., Matano, R., Hodell, D.A. and Peck, V.L., 2017. Deglacial changes in flow and frontal structure through the Drake Passage. *Earth and Planetary Science Letters*, **474**, pp.397-408.

Rodriguez, A.B. and Anderson, J.B., 2004. Contourite origin for shelf and upper slope sand sheet, offshore Antarctica. *Sedimentology*, **51**(4), pp.699-711.

Rothwell, R.G. and Rack, F.R., 2006. New techniques in sediment core analysis: An Introduction. In: *New Techniques in Sediment Core Analysis*. Geological Society, London. Special Publications, 267, pp.1-29.

Rothwell, R.G. and Croudace, I.W., 2015. Twenty years of XRF core scanning marine sediments: What do geochemical proxies tell us? Chapter 2 *in* Croudace, I.W. and Rothwell, R.G. (Eds) Micro-XRF Studies of Sediment Cores: Applications of a non-destructive tool for the environmental sciences. Developments in Palaeoenvironmetnal Research 17, pp.25-102. Springer, Dordrecht, Netherlands.

Scherer, R.P., Aldahan, A., Tulaczyk, S., Possnert, G., Engelhardt, H. and Kamb, B., 1998. Pleistocene collapse of the West Antarctic ice sheet. *Science,* **281**(5373), pp.82-85.

Scheuer, C., Gohl, K. and Eagles, G., 2006a. Gridded isopach maps from the South Pacific and their use in interpreting the sedimentation history of the West Antarctic continental margin. *Geochemistry, Geophysics, Geosystems*, **7**(11).

Scheuer, C., Gohl, K. and Udintsev, G., 2006b. Bottom-current control on sedimentation in the western Bellingshausen Sea, West Antarctica. *Geo-Marine Letters*, **26**(2), pp.90-101.

Scheuer, C., Gohl, K., Larter, R.D., Rebesco, M. and Udintsev, G., 2006c. Variability in Cenozoic sedimentation along the continental rise of the Bellingshausen Sea, West Antarctica. *Marine Geology*, **227**(3), pp.279-298.

Schlitzer, R., Ocean Data View, odv.awi.de, 2017.

Schlüter, M., van der Loeff, M.M.R., Holby, O. and Kuhn, G., 1998. Silica cycle in surface sediments of the South Atlantic. *Deep Sea Research Part I: Oceanographic Research Papers*, **45**(7), pp.1085-1109.

Schoof, C., 2007. Ice sheet grounding line dynamics: Steady states, stability, and hysteresis. *Journal of Geophysical Research: Earth Surface*, **112**(F3).

Schweitzer, P.N., 1995. Monthly averaged polar sea ice concentration. U.S. Geological

Survey Digital Data Series: Virginia. CD-rom, Ed 1. DDS-27. Quoted in: Esper, O., Gersonde, R. and Kadagies, N., 2010. Diatom distribution in southeastern Pacific surface sediments and their relationship to modern environmental variables. *Palaeogeography, Palaeoclimatology, Palaeoecology*, **287**(1), pp.1-27.

Shanmugam, G., 1996. High-density turbidity currents: are they sandy debris flows?: Perspectives. *Journal of Sedimentary Research*, **66**(1).

Shanmugam, G., 1997. The Bouma sequence and the *turbidite m*ind set. *Earth-Science Reviews*, **42**(4), pp.201-229.

Shanmugam, G., 2000. 50 years of the turbidite paradigm (1950s—1990s): deep-water processes and facies models—a critical perspective. *Marine and Petroleum Geology*, **17**(2), pp.285-342.

Shanmugam, G. 2001. Slides, slumps, debris flows and turbidity currents. *In* Steele, J.H., Thorpe, S.A. and Turekian, K.K. (Eds) Marine Geology and Geophysics. Academic Press, Elsevier, London.

Shanmugam, G., 2002. Ten turbidite myths. *Earth-Science Reviews*, **58**(3), pp.311-341.

Shanmugam, G., 2008. Deep-water bottom currents and their deposits. *Developments in Sedimentology*, **60**, pp.59-81.

Shanmugam, G., 2013. New perspectives on deep-water sandstones: Implications. *Petroleum Exploration and Development*, **40**(3), pp.316-324.

Shanmugam, G. and Wang, Y., 2015. The landslide problem. *Journal of Palaeogeography*, **4**(2), pp.109-166.

Shanmugam, G., 2016. The Contourite Problem, Chapter 9 in: *Sediment Provenance*. Elsevier, Oxford. pp.183-254.

Shepherd, A., Wingham, D.J. and Mansley, J.A., 2002. Inland thinning of the Amundsen Sea sector, West Antarctica. *Geophysical Research Letters*, **29**(10).

Shipboard Party JR179, 2008. Marine biological and marine geological and geophysical studies in the Amundsen and Bellingshausen Seas. RRS James Clark Ross, February to April 2008.

Singer, B.S., Guillou, H., Jicha, B.R., Laj, C., Kissel, C., Beard, B.L. and Johnson, C.M., 2009. $^{40}Ar/^{39}Ar$, K–Ar and $^{230}Th–^{238}U$ dating of the Laschamp excursion: a radioisotopic tie-point for ice core and climate chronologies. *Earth and Planetary Science Letters*, **286**(1-2), pp.80-88.

Smith, J.A., Hillenbrand, C.-D., Kuhn, G., Graham, A.G.C., Larter, R.D., Johann, J.-P., Erhmann, W., Moreton, S.G., Williams, T., 2014. New constraints on the timing of West Antarctic Ice Sheet retreat in the eastern Amundsen Sea since the Last Glacial Maximum. *Global Planetary Change*, **122**, 224-237.

Smith, J.A., Andersen, T.J., Shortt, M., Gaffney, A.M., Truffer, M., Stanton, T.P., Bindschadler, R., Dutrieux, P., Jenkins, A., Hillenbrand, C.-D. and Ehrmann, W., 2017.

Sub-ice-shelf sediments record history of twentieth-century retreat of Pine Island Glacier. *Nature*, **541**(7635), pp.77-80.

Solli, K., Kuvaas, B., Kristoffersen, Y., Leitchenkov, G., Guseva, J. and Gandjukhin, V., 2007. A seismo-stratigraphic analysis of glaciomarine deposits in the eastern Riiser-Larsen Sea (Antarctica). *Marine Geophysical Researches*, **28**(1), pp.43-57.

Sprenk, D., Weber, M.E., Kuhn, G., Rosén, P., Frank, M., Molina-Kescher, M., Liebetrau, V. and Röhling, H.G., 2013. Southern Ocean bioproductivity during the last glacial cycle–new detection method and decadal-scale insight from the Scotia Sea. Geological Society, London, Special Publications, **381**(1), pp.245-261.

Sprenk, D., Weber, M.E., Kuhn, G., Wennrich, V., Hartmann, T. and Seelos, K., 2014. Seasonal changes in glacial polynya activity inferred from Weddell Sea varves. *Climate of the Past*, **10**(3), pp.1239-1251.

Steig, E.J., Ding, Q., Battisti, D.S. and Jenkins, A., 2012. Tropical forcing of Circumpolar Deep Water inflow and outlet glacier thinning in the Amundsen Sea Embayment, West Antarctica. *Annals of Glaciology*, **53**(60), pp.19-28.

Stow, D.A.V. and Bowen, A.J., 1978. Origin of lamination in deep-sea, fine grained sediments. *Nature*, **274**, pp.324-328.

Stow, D. A. V. and Bowen, A. J., 1980. A physical model for the transport and sorting of fine-grained sediment by turbidity currents. *Sedimentology*, **27**(1), 31-46.

Stow, D.A.V. and Lovell, J.P.B., 1979. Contourites: Their recognition in modern and ancient sediments. *Earth Science Reviews*, **14**, pp.251-291.

Stow, D.A.V., Reading, H.G. and Collinson, J.D., 1996. Deep Seas *in* Reading, H.G., *Sedimentary Environments* (3rd Edition) pp. 395-454. Oxford, Wiley-Blackwell.

Stow, D.A.V. and Mayall, M., 2000. Deep-water sedimentary systems: new models for the 21st century *Marine and Petroleum Geology*, **17** (2), pp. 125-135.

Stow, D.A.V., Faugères, J.-C., Gonthier, E., Cremer, M., Llave, E., Hernandez-Molina, F.J., Somoza, L., Diaz-Del-Rio, V., 2002a. Faro-Albufeira drift complex, northern Gulf of Cadiz, in: Stow, D.A.V., Pudsey, C.J., Howe, J.A., Faugères, J.-C., Viana, A.R. (Eds.) *Deep-Water Contourite Systems: Modern Drifts and Ancient Series, Seismic and Sedimentary Characteristics*. Geological Society London Memoir, Vol. 22, pp. 137–154.

Stow, D.A.V., Faugères, J.-C, Howe, J.A., Pudsey, C.J., Viana, A.R., 2002b. Bottom currents, contourites and deep-sea sediment drifts: Current state-of-the-art, in: Stow, D.A.V., Pudsey, C.J., Howe, J.A., Faugères, J.-C., Viana, A.R. (Eds.) *Deep-Water Contourite Systems: Modern Drifts and Ancient Series, Seismic and Sedimentary Characteristics.* Geological Society London Memoir, Vol. 22, pp. 7–20.

Stow, D.A.V. and Faugères, J.-C., 2008. Contourite facies and the facies model. Chapter 13 *in:* Rebesco, M. and Camerlenghi, A. (Eds.) van Loon, A.J. (Series Ed.) *Contourites: Developments in Sedimentology Volume 60*. Elsevier, Amsterdam. pp.223-256.

Stow, D.A., Hernández-Molina, F.J., Llave, E., Sayago-Gil, M., del Río, V.D. and Branson, A., 2009. Bedform-velocity matrix: the estimation of bottom current velocity from bedform observations. *Geology*, **37**(4), pp.327-330.

Stuiver, M., Reimer, P.J., and Reimer, R.W., 2017, **CALIB** 7.1 [WWW **program**] at http://**calib**.org, accessed 2017-9-07.

Sutterley, T.C., Velicogna, I., Rignot, E., Mouginot, J., Flament, T., Van Den Broeke, M.R., Van Wessem, J.M. and Reijmer, C.H., 2014. Mass loss of the Amundsen Sea Embayment of West Antarctica from four independent techniques. *Geophysical Research Letters*, **41**(23), pp.8421-8428.

Symons, W.O., Sumner, E.J., Talling, P.J., Cartigny, M.J. and Clare, M.A., 2016. Large-scale sediment waves and scours on the modern seafloor and their implications for the prevalence of supercritical flows. *Marine Geology*, **371**, pp.130-148.

Talling, P.J., Masson, D.G., Sumner, E.J. and Malgesini, G., 2012. Subaqueous sediment density flows: Depositional processes and deposit types. *Sedimentology*, **59**(7), pp.1937-2003.

Thatje, S., Hillenbrand, C.-D., Mackensen, A. and Larter, R., 2008. Life hung by a thread: endurance of Antarctic fauna in glacial periods. *Ecology*, **89**(3), pp.682-692.

Thoma, M., Jenkins, A., Holland, D. and Jacobs, S., 2008. Modelling Circumpolar Deep Water intrusions on the Amundsen Sea continental shelf, Antarctica. *Geophysical Research Letters*, **35**(18) L18602.

Tjallingii, R., Röhl, U., Kölling, M. and Bickert, T., 2007. Influence of the water content on X-ray fluorescence core-scanning measurements in soft marine sediments. *Geochemistry, Geophysics, Geosystems*, **8**(2) Q02004.

Turner, J., Comiso, J.C., Marshall, G.J., Lachlan-Cope, T.A., Bracegirdle, T., Maksym, T., Meredith, M.P., Wang, Z. and Orr, A., 2009. Non-annular atmospheric circulation change induced by stratospheric ozone depletion and its role in the recent increase of Antarctic sea ice extent. *Geophysical Research Letters,* **36**(8) L08502.

Turner, J., Phillips, T., Hosking, J.S., Marshall, G.J. and Orr, A., 2013. The Amundsen Sea low. *International Journal of Climatology*, **33**(7), pp.1818-1829.

Turner, J., Orr, A., Gudmundsson, G.H., Jenkins, A., Bingham, R.G., Hillenbrand, C.-D. and Bracegirdle, T.J., 2017. Atmosphere-ocean-ice interactions in the Amundsen Sea Embayment, West Antarctica. *Reviews of Geophysics*, **55**(1), pp.235-276.

Uenzelmann-Neben, G., 2006. Depositional patterns at Drift 7, Antarctic Peninsula: Along-slope versus down-slope sediment transport as indicators for oceanic currents and climatic conditions. *Marine Geology*, **233**(1), pp.49-62.

Uenzelmann-Neben, G. and Gohl, K., 2012. Amundsen Sea sediment drifts: archives of modifications in oceanographic and climatic conditions. *Marine Geology*, **299**, pp.51-62.

Uenzelmann-Neben, G. and Gohl, K., 2014. Early glaciation already during the Early Miocene in the Amundsen Sea, Southern Pacific: Indications from the distribution of sedimentary sequences. *Global and Planetary Change*, **120**, pp.92-104.

Vautravers, M.J., Hodell, D.A., Channell, J.E., Hillenbrand, C.-D., Hall, M., Smith, J. and Larter, R.D., 2013. Palaeoenvironmental records from the West Antarctic Peninsula drift sediments over the last 75 ka. *Geological Society, London, Special Publications*, **381**(1), pp.263-276.

Venuti, A., Florindo, F., Caburlotto, A., Hounslow, M.W., Hillenbrand, C.-D., Strada, E., Talarico, F.M. and Cavallo, A., 2011. Late Quaternary sediments from deep-sea sediment drifts on the Antarctic Peninsula Pacific margin: Climatic control on provenance of minerals. *Journal of Geophysical Research: Solid Earth*, **116**(B6).

Viana, A.R., Faugères, J.C. and Stow, D.A.V., 1998. Bottom-current-controlled sand deposits—a review of modern shallow-to deep-water environments. *Sedimentary Geology*, **115**(1-4), pp.53-80.

Wåhlin, A.K., Yuan, X., Björk, G. and Nohr, C., 2010. Inflow of warm Circumpolar Deep Water in the central Amundsen shelf. *Journal of Physical Oceanography*, **40**(6), pp.1427-1434.

Wåhlin, A.K., Kalén, O., Arneborg, L., Björk, G., Carvajal, G.K., Ha, H.K., Kim, T., Lee, S.H., Lee, J. and Stranne, C., 2013. Variability of warm deep water inflow in a submarine trough on the Amundsen Sea shelf. *Journal of Physical Oceanography*, **43**(10), pp.2054-2070.

Wåhlin, A. and University of Gothenburg, 2015. Temperature, salinity and oxygen data collected from the Oden in the Amundsen and Ross Seas, 2010 - 2011 (NCEI Accession 0104260). Version 1.1. NOAA National Center for Environmental Information. Dataset. [Accessed 02/02/2016]

Walker, R.G., 1967. Turbidite sedimentary structures and their relationship to proximal and distal depositional environments. *Journal of Sedimentary Research*, **37**(1).

Walker, D.P., Jenkins, A., Assmann, K.M., Shoosmith, D.R. and Brandon, M.A., 2013. Oceanographic observations at the shelf break of the Amundsen Sea, Antarctica. *Journal of Geophysical Research: Oceans*, **118**(6), pp.2906-2918.

Warnock, J.P., Scherer, R.P. and Konfirst, M.A., 2015. A record of Pleistocene diatom preservation from the Amundsen Sea, West Antarctica with possible implications on silica leakage. *Marine Micropaleontology*, **117**, pp.40-46.

Weber, M.E., Niessen, F., Kuhn, G. and Wiedicke, M., 1997. Calibration and application of marine sedimentary physical properties using a multi-sensor core logger. *Marine Geology*, **136**(3), pp.151-172.

Weber, M.E., Kuhn, G., Sprenk, D., Rolf, C., Ohlwein, C. and Ricken, W., 2012. Dust transport from Patagonia to Antarctica–a new stratigraphic approach from the Scotia Sea and its implications for the last glacial cycle. *Quaternary Science Reviews*, **36**, pp.177-188.

Weber, M.E., Clark, P.U., Kuhn, G., Timmermann, A., Sprenk, D., Gladstone, R., Zhang, X., Lohmann, G., Menviel, L., Chikamoto, M.O. and Friedrich, T., 2014. Millennial-scale variability in Antarctic ice-sheet discharge during the last deglaciation. *Nature*, **510**(7503), p.134.

van Weering, T., Stoker, M. and Rebesco, M., 2008. High-latitude contourites. Chapter 22 *in:* Rebesco, M. and Camerlenghi, A. (Eds.) van Loon, A.J. (Series Ed.) *Contourites: Developments in Sedimentology Volume 60*. Elsevier, Amsterdam. pp.457-489.

Wetzel, A., Werner, F. and Stow, D.A.V., 2008. Bioturbation and biogenic sedimentary structures in contourites. Chapter 11 *in:* Rebesco, M. and Camerlenghi, A. (Eds.) van Loon, A.J. (Series Ed.) *Contourites: Developments in Sedimentology Volume 60*. Elsevier, Amsterdam. pp.183-202.

Wilch, T.I., McIntosh, W.C. and Dunbar, N.W., 1999. Late Quaternary volcanic activity in Marie Byrd Land: Potential $^{40}Ar/^{39}Ar$-dated time horizons in West Antarctic ice and marine cores. *Geological Society of America Bulletin*, **111**(10), pp.1563-1580.

Whittaker, J.M. and Müller, R.D., 2006. Seismic stratigraphy of the Adare Trough area, Antarctica. *Marine Geology*, **230**(3-4), pp.179-197.

Whitworth, T., Orsi, A.H., Kim, S.J., Nowlin, W.D. and Locarnini, R.A., 1998. Water masses and mixing near the Antarctic Slope Front. Ocean, ice, and atmosphere: interactions at the Antarctic continental margin, pp.1-27.

Wilson, E., 2013. Reconstructing past storminess in Halifax Harbour through grain-size analysis of marine sediment cores. BSc thesis, Dalhousie University.

Wynn, R.B. and Stow, D.A., 2002. Classification and characterisation of deep-water sediment waves. *Marine Geology*, **192**(1-3), pp.7-22.

Wynn, R.B. and Masson, D.G., 2008. Sediment waves and bedforms. Chapter 15 *in:* Rebesco, M. and Camerlenghi, A. (Eds.) van Loon, A.J. (Series Ed.) *Contourites: Developments in Sedimentology Volume 60*. Elsevier, Amsterdam. pp.289-300.

Xie, H., Ackley, S.F., Yi, D., Zwally, H.J., Wagner, P., Weissling, B., Lewis, M. and Ye, K., 2011. Sea-ice thickness distribution of the Bellingshausen Sea from surface measurements and ICESat altimetry. *Deep Sea Research Part II: Topical Studies in Oceanography*, **58**(9), pp.1039-1051.

Xuan, C. and Channell, J.E., 2009. UPmag: MATLAB software for viewing and processing u channel or other pass-through paleomagnetic data. *Geochemistry, Geophysics, Geosystems*, **10**(10).

Yamaguchi, K., Tamura, Y., Mizukoshi, I. and Tsuru, T., 1988, September. Preliminary report of geophysical and geological surveys in the Amundsen Sea, West Antarctica. *Proceedings of the NIPR Symposium on Antarctic Geosciences*, **2**, pp. 55-67.

Yang, E.J., Jiang, Y. and Lee, S., 2016. Microzooplankton herbivory and community structure in the Amundsen Sea, Antarctica. *Deep Sea Research Part II: Topical Studies in Oceanography*, **123**, pp.58-68.

Zhang, J., 2007. Increasing Antarctic sea ice under warming atmospheric and oceanic conditions. *Journal of Climate*, **20**(11), pp.2515-2529.

Zielinski, U., Bianchi, C., Gersonde, R. and Kunz-Pirrung, M., 2002. Last occurrence datums of the diatoms *Rouxia leventerae* and *Rouxia constricta*: indicators for marine isotope stages 6 and 8 in Southern Ocean sediments. *Marine Micropaleontology*, **46**(1), pp.127-137.

Zielinski, U. and Gersonde, R., 2002. Plio–Pleistocene diatom biostratigraphy from ODP Leg 177, Atlantic sector of the Southern Ocean. *Marine Micropaleontology*, **45**(3), pp.225-268.

Zwally, H.J. and Giovinetto, M.B., 1997. Annual sea level variability induced by changes in sea ice extent and accumulation on ice sheets: an assessment based on remotely sensed data. *Surveys in Geophysics*, **18**(2-3), pp.327-340.